1-1-2017

Spacesuit Integrated Carbon Nanotube Dust Mitigation System For Lunar Exploration

Kavya Kamal Manyapu

SPACESUIT INTEGRATED CARBON NANOTUBE DUST MITIGATION SYSTEM FOR LUNAR EXPLORATION

by

Kavya Kamal Manyapu
Bachelor of Science, Aerospace Engineering, Georgia Institute of Technology, 2006
Master of Science, Aeronautics and Astronautics, Massachusetts Institute of Technology, 2010

A Dissertation
Submitted to the Graduate Faculty

of the

University of North Dakota

In partial fulfillment of the requirements

for the degree of

Doctor of Philosophy

Grand Forks, North Dakota
August
2017

APPROVAL

This dissertation, submitted by Kavya K. Manyapu in partial fulfillment of the requirements for the Degree of Philosophy in Aerospace Sciences from the University of North Dakota, has been read by the Faculty Advisory Committee under whom the work has been done and is hereby approved.

Dr. Pablo de León,
Professor in Department of Aerospace Sciences, UND
Ph.D. Committee Chair

Dr. Timothy Young,
Professor in the Department of Physics and Astrophysics, UND
Member, Ph.D. Committee

Dr. Richard Ferraro
Professor in the Department of Psychology, UND
Member, Ph.D. Committee

Dr. Leora Peltz
Senior Scientist and Technical Fellow, The Boeing Company
Member, Ph.D. Committee

Dr. James R. Gaier
Research Physicist, NASA Glenn Research Center
Member, Ph.D. Committee

This dissertation is being submitted by the appointed advisory committee as having met all of the requirements of the School of Graduate Studies at the University of North Dakota and is hereby approved.

Dr. Grant McGimpsey, Dean of the School of Graduate Studies

July 28, 2017
Date

PERMISSION

Title	Spacesuit Integrated Carbon Nanotube Dust Mitigation System for Lunar Exploration
Department	Aerospace Science
Degree	Doctor of Philosophy

In presenting this dissertation in partial fulfillment of the requirements for a graduate degree from the University of North Dakota, I agree that the library of this University shall make it freely available for inspection. I further agree that permission for extensive copying for scholarly purposes may be granted by the professor who supervised my dissertation work or, in his absence, by the Chairperson of the department or the dean of the School of Graduate Studies. It is understood that any copying or publication or other use of this dissertation or part thereof for financial gain shall not be allowed without my written permission. It is also understood that due recognition shall be given to me and to the University of North Dakota in any scholarly use which may be made of any material in my dissertation.

Kavya. K. Manyapu
July 27th 2017

ABSTRACT

Lunar dust proved to be troublesome during the Apollo missions. The lunar dust comprises of fine particles, with electric charges imparted by solar winds and ultraviolet radiation. As such, it adheres readily, and easily penetrates through smallest crevices into mechanisms. During Apollo missions, the powdery dust substantially degraded the performance of spacesuits by abrading suit fabric and clogging seals. Dust also degraded other critical equipment such as rovers, thermal control and optical surfaces, solar arrays, and was thus shown to be a major issue for surface operations. Even inside the lunar module, Apollo astronauts were exposed to this dust when they removed their dust coated spacesuits. This historical evidence from the Apollo missions has compelled NASA to identify dust mitigation as a critical path. This important environmental challenge must be overcome prior to sending humans back to the lunar surface and potentially to other surfaces such as Mars and asteroids with dusty environments.

Several concepts were successfully investigated by the international research community for preventing deposition of lunar dust on rigid surfaces (ex: solar cells, thermal radiators). However, applying these technologies for flexible surfaces and specifically to spacesuits has remained an open challenge, due to the complexity of the suit design, geometry, and dynamics. The research presented in this dissertation brings original contribution through the development and demonstration of the SPacesuit Integrated Carbon nanotube Dust Ejection/Removal (SPIcDER) system to protect spacesuits and other flexible surfaces from lunar dust. SPIcDER leverages the Electrodynamic Dust Shield (EDS) concept developed at NASA for use on solar cells. For the SPIcDER research, the EDS concept is customized for application on spacesuits and flexible surfaces utilizing novel materials and specialized design techniques. Furthermore, the performance of the active SPIcDER system is enhanced by integrating a passive technique based on Work Function Matching coating. SPIcDER aims for a self-cleaning spacesuit that can repel lunar dust.

The SPIcDER research encompassed numerous demonstrations on coupons made of spacesuit outerlayer fabric, to validate the feasibility of the concept, and provide evidence that the SPIcDER system is capable of repelling over 85% of lunar dust simulant comprising of particles in the range of 10 μm-75μm, in ambient and vacuum conditions. Furthermore, the research presented in this dissertation proves the scalability of the SPIcDER technology on a full scale functional prototype of a spacesuit knee joint-section, and demonstrates its scaled functionality and performance using lunar dust simulant. It also comprises detailed numerical simulation and parametric analysis in ANSYS Maxwell and MATLAB for optimizing the integration of the SPIcDER system into the spacesuit outerlayer. The research concludes with analysis and experimental results on design, manufacturability, operational performance, practicality of application and astronaut safety.

The research aims primarily towards spacesuit dust contamination. The SPIcDER technology developed in this research is however versatile, that can be optimized to a wide range of flexible surfaces for space and terrain applications-such as exploration missions to asteroids, Mars and dust-prone applications on Earth.

ACKNOWLEDGMENTS

***"All our dreams can come true, if we have the courage to pursue them**."- Walt Disney*

A strong support system is crucial to achieving any dream. Completion of this doctoral dissertation was possible only with the support of several people. I am indebted to them for helping me through what seemed to be an indomitable yet enjoyable journey. They have played an integral role not only in the professional development of this 4 + years of research effort, but also in the substantial growth I have experienced as a researcher and as a person. I would like to express my sincere gratitude to all of them. Growing up in a town far off in the east, every time I looked up to the night sky as a child, it was fascinating; the Moon never ceased to inspire me. I am extremely fortunate and grateful for being able to pursue my passion for space exploration through academic research and professional work, and make a small contribution to humanity's greatest endeavors.

First and foremost, I am thankful to my advisor **Dr.Pablo de León** for providing an opportunity to work with him and more importantly allowing me the academic freedom to explore new and interesting research ideas. His technical knowledge and experience on spacesuits, and his hands-on experience are outstanding which continuously motivates and inspires me. My gratitude to him goes beyond just being his student, for the support he has provided me personally, professionally and financially along the way. '*Can make this happen, you don't worry*' are the words he used to utter every time it seemed like I was hitting a dead end. His enthusiasm, creative thinking and helping nature encouraged me to look at the brighter side. Without his help, his belief in my abilities, confidence he provided and his generosity, this journey would not have been possible. Therefore, I'm immensely grateful for having him as my professor for the course of my Ph.D. I now eagerly look forward to continuing our collaboration beyond this Doctoral research and hoping to see some of our research being flown in space one day!

I would like to express my deepest gratitude to **Dr. Leora Peltz**, my mentor, guide, and dissertation committee member. She has been my pillar of support over the last few years. Her

admirable guidance, extreme patience, insights from her vast professional and personal experiences have helped me transform from an engineer to a researcher and experimentalist. Her mentorship and analytical skills both on the research topic and career goals have taught me to see the big picture in life. Her dedication and commitment as a mentor are priceless and without her generous support and time I would have not progressed this far. And I am also forever grateful that she took time to expose me to new opportunities that didn't seem possible and helped me get to the finish line making it an enjoyable journey. I look forward to continuing our collaboration beyond the Doctoral study. Along these lines, I should thank **Dr.Aditya Rajagopal,** my dear friend who to introduced me to Leora.

My special thanks to **Dr. James R. Gaier**, my dissertation committee member, whose knowledge and experience in the area of lunar dust and contamination have been of utmost significance for the progress of this research. When the new concepts were discussed with him, he immediately encouraged me to pursue the ideas and provided valuable suggestions. More importantly, he provided the needed contacts from Dexmat®/Rice University that led to a collaboration with the company and university on the use of CNTs. His valuable suggestions on the techniques used to test some of the concepts, his help to materialize the passive coating for spacesuit application and his guidance since the beginning of my Ph.D. have been paramount to the success of this research. My thanks to **Debbie Waters** at Jim's lab at NASA Glenn who supported coating some of the samples that were tested in this research.

I would like to thank my dissertation committee members for their valuable time and guidance through all these years. My appreciation to **Dr. Tim Young** for providing his insights and helping find a way with my modeling work when faced with a challenging issue. **Dr. Vadim Rygalov,** for his experience and insights into the human in the loop operations and guidance through an essential aspect of this research. **Dr. Richard Ferraro** for his time. I also want to thank all my committee members for letting my defense be an enjoyable moment.

I am extremely thankful and appreciative of **Dr. Carlos Calle** at NASA KSC who welcomed me into his lab. His generosity and kindness provided the opportunity to test the new concepts of this research at the Electrostatics and Surface Physics Laboratory (ESPL), use the power electronics and vacuum chamber which proved to be extremely critical to the progress of this research. Without his support, the technology concepts initiated in this research would not have advanced this far. My special thanks to **Paul Mackey** of ESPL for helping and supporting me

while testing at the lab and providing his valuable suggestions. I would also like to thank **Rachel Cox** and **Michael Hogue**, members of ESPL, for their support.

I am extremely thankful to **Dr.Dmitri Tsentalovich**, **Dr. Alberto Goenaga** and **Dr. Matteo Pasquali** at DexMat® and Rice University for generously providing CNT samples to experiment the new concepts. During my first encounter with the team, Dr. Pasquali encouraged the idea to support my research and generously provided access to their lab as a Visiting Researcher at the Rice University. With Dmitri's consistent help thereafter, I was able to obtain new insights into the CNT yarn technology. Special thanks to Dmitri who has for the last two years been consistently helping with providing CNT samples when needed which were fundamental to the progress of this research.

I would like to express my special appreciation and gratitude to **Barry Fox** who not only helped us navigate through patent applications based on this research, he has taken a keen interest to mentor me through the Ph.D. process, motivated me and found ways to help with the progress of my research. At many instances he shared his knowledge, provided valuable insights and facilitated networking opportunities that helped with the final stages of this research. I would also like to thank him for his time and dedication for reviewing the dissertation. His continuing interest in the research topic has motivated me and provided confidence in the future that this technology holds.

Special thanks to the **faculty of the UND Space Studies Department** for their encouragement and hospitality, and for their financial assistance in helping me present this research at various international avenues. I must thank **Bev Fetter**, Space Studies Department administrator for helping me through the Ph.D. process and making sure I did not miss any deadlines.

My gratitude to **Gary Harris**, a spacesuit expert who was key to building the scaled prototype for the experimental validation part of this project. My sincere thanks to him for helping make this come to fruition in time for the experiments. I would also like to thank **Carolyn Newton**, graduate student at UND who helped us with initial patterning of outerlayer material for the knee prototype.

Special thanks to **Richard Rhodes** and **Amy Ross** from NASA Johnson Space Center who generously provided spacesuit material for this research.

I would like to thank the **Boeing Company** for providing an opportunity to pursue my Ph.D. Special thanks to my management who have recognized the efforts and supported me along the way and provided the needed relief when needed.

My warm appreciation to my dear friend **Soumya Ashok** for designing an apt logo for the SPIcDER technology.

Finally, I would like to express my most sincere gratitude to my parents and family for their ongoing and sacrificial support throughout my educational journey and my entire life. My deepest gratitude to my husband for his unconditional support, patience and moral support. I would also like to specially recognize my mother who shares a piece of this work by helping me work through the prototype construction. Her simple ideas and artistic imagination often helped overcome challenges and have played a key role in helping set up my experiments. This journey would not have been possible without my family's love, blessings, inspiration and strength.

To my family who encouraged me to look up to the skies

"Shoot for the moon, even if you miss, you'll land among the stars"

TABLE OF CONTENTS

LIST OF FIGURES

Figure Page

LIST OF TABLES

Table Page

LIST OF ACRONYMS

2D	Two Dimensional
AC	Alternating Current
Ag	Silver
Al	Aluminum
ALSEP	Apollo Lunar Surface Experiment Package
ARM	Asteroid Redirect Mission
CM	Command Module
CNF	Carbon nanofibers
CNS	Central Nervous System
CNT	Carbon nanotubes
D&C	Display and Control
DC	Direct Current
DCS	Dust Cleaning System
DEM	Discrete element method
DEP	Dielectrophoretic Forces
DRM	Design Reference Mission
EDLR	Electrostatic Static Lunar Dust Repeller
EDS	Electrodynamic Dust Shield
EF	Electric Field
ELF	Extremely Low Frequency
EMF	Electromagnetic Field
EMU	Extravehicular Mobility Unit
ESA	European Space Agency
ESPL	Electrostatics and Surface Physics Laboratory
ETFE	Ethylene tetrafluoroethylene
EVA	Extra Vehicular Activity
FEP	Fluorinated ethylene propylene
FESEM	Field Emission Secondary Electron Microcopy
GRC	Glenn Research Center
GSFC	Goddard Spaceflight Center
ICNIRP	International Commission on Non-Ionizing Radiation Protection

IEC	International Electrotechnical Commission
ISRU	In-Situ Resource Utilization
ISS	International Space Station
ITMG	Integrated Thermal Micrometeorite Garment
ITO	Indium Tin Oxide
IVA	Intra Vehicular Activity
JSC	Johnson Spaceflight Center
KSC	Kennedy Space Center
LADEE	Lunar Atmosphere Dust and Environment Explorer
LADTAG	Lunar Airborne Dust Toxicity Advisory Group
LDAB	Lunar Dust Adhesion Bell Jar
LDEX	Lunar Dust Experiment
LED	Light Emitting Diode
LiOH	Lithium Hydroxide
LM	Lunar Module
LRV	Lunar Roving Vehicle
MARSWIT	Martian Surface Wind Tunnel
MISSE	Materials International Space Station Experiment
MLI	Multi-Layer Insulation
MMOD	Micrometeoroid Orbital Debris
MSC	Marshall Spaceflight Center
NASA	National Aeronautics and Space Administration
NASDIRT	NASA Smithsonian Dust Investigation Research Team
NDX-#	North Dakota Experimental Spacesuit-#
NIOSH	The National Institute for Occupational Safety and Health
NOAEL	No Observable Adverse Effect Level
np	Nanophase
NTE	Not-to-Exceed
OSHA	Occupational Safety and Health Administration
PEL	Permissible Exposure Level
PGS	Pressure Garment Assembly
PLSS	Portable Life Support System
PSD	Particle Size Distribution
PTFE	Polytetrafluoroethylene
RC	Resistance x Capacitance
RH	Relative Humidity
SEM	Scanning Electron Microscope
SPACLED	Space Plasma Alleviation of Regolith Concentrations by Discharge

SPIcDER	Spacesuit Integrated Carbon Nanotube Dust Ejection/Removal System
STR	Space Technology Roadmap
TDS	Thermal Degradation Sample
TWA	Time Weighted Average
UHV	Ultra-high vacuum
UND	University of North Dakota
UV	Ultraviolet
VAC	Volts Alternating Current
VdW	Van der Waal Forces
WFM	Work Function Matching Coating
WHO	World Health Organization
WSTF	White Sands Test Facility

PART I
DUST PROBLEMS DURING PLANETARY EXPLORATION:
Background, Previous Work and State of the Art

CHAPTER 1-INTRODUCTION

"That's one small step for man; one giant leap for mankind" - *Neil Armstrong*

Between 1969 and 1972, twelve astronauts walked the surface of the Moon. By the end of their surface operations, their white iconic spacesuits were covered with lunar dust. The surface of the Moon is covered in fine dust - gray, powdery, abrasive - which caused unforeseen problems that impacted mission operations. The primary objective of the spacesuit is to provide a safe environment for astronauts to perform their activities in the harsh environments of space. Therefore, it is imperative that the astronaut suit is capable of withstanding the environmental condition on the Moon, without degrading mission performance. This is particularly important for future long duration missions, where regular resupply of components is limited. Emergency or quick-return options due to system or spacesuit failures will not be feasible, and maintenance activities must be minimized– so that astronaut time can be dedicated to meeting mission objectives, and maximize their time on achieving science and mission goals.

The focus of this research is to develop a dust mitigation technology integrated into the spacesuit. The SPIcDER system (pronounced 'Spider') aims to enable long-term performance and durability of spacesuits in dusty extra-terrestrial environments, particularly the lunar surface. This chapter provides a brief overview of the detrimental effects of planetary dust on spacesuits, particularly lunar dust. This establishes the problem statement for the SPIcDER research. Hypothesis and research objectives are stated in this chapter, followed by an overview of the content and organization of this dissertation.

1.1. Background

Extra-Vehicular Activities (EVAs) on the moon during the Apollo missions have shown that lunar dust can rapidly degrade spacesuits and impede operations. Post-flight investigations of these suits also revealed damaging effects to the suits worn by the astronauts during their missions' due to the dust that adhered during EVAs (Gaier, 2005; Wagner, 2006; Christoffersen et al., 2009).

After the EVA tasks, when the astronauts doffed their suits, the adhered dust inadvertently transferred into the habitable volume of the lunar module, posing risk to crew health. Astronauts complained about the 'gunpowder' like smell and stickiness of the dust, and about dust getting into everything they did, impeding operations. It is important to point out that the Apollo missions comprised only a small number of EVAs on the lunar surface. Less than 24 hours of dust exposure was accumulated by the suits during these lunar sortie missions (See Figure 1.1-1 and Table 1.1-1), yet the lunar dust contaminated the spacesuits to the point where any further exposure would have significantly increased the risks to the astronauts.

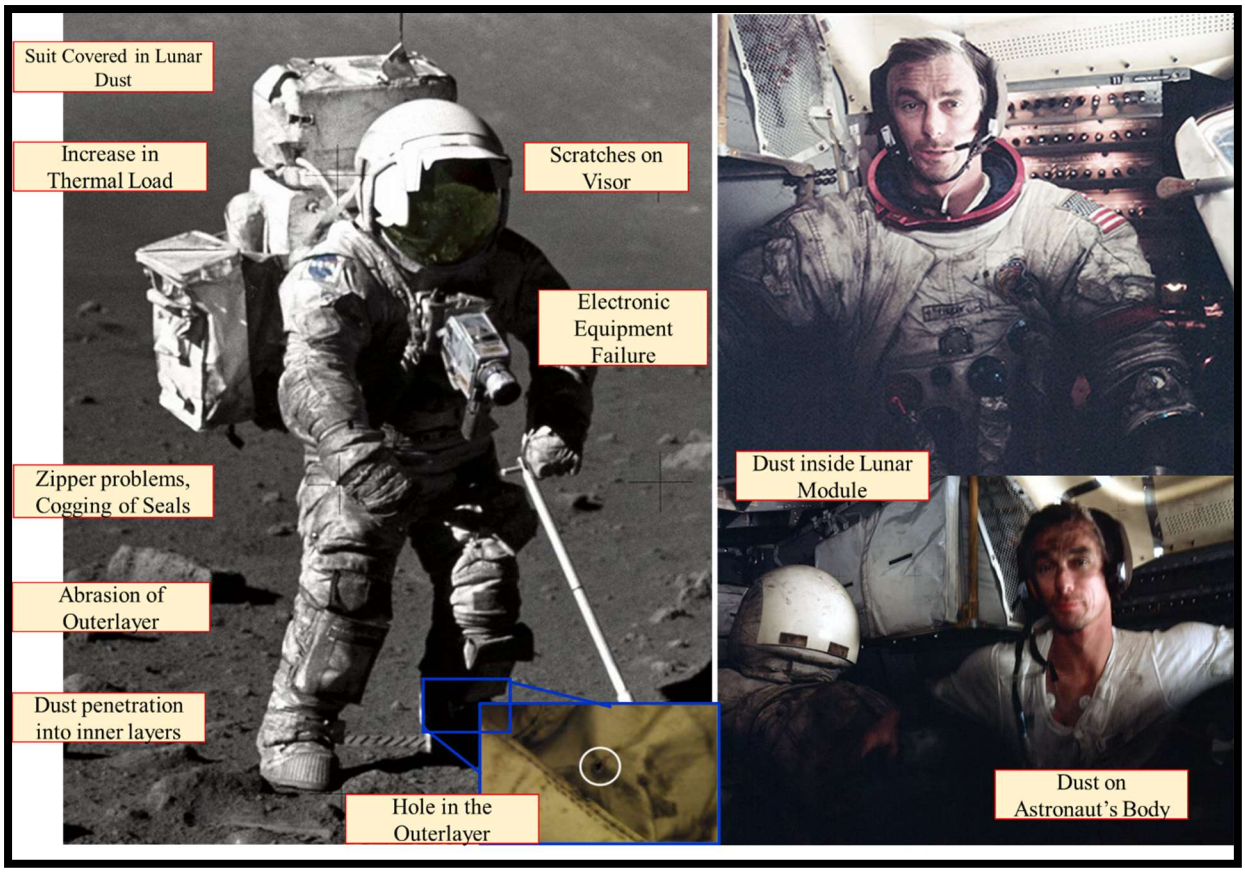

Figure 1.1-1. Lunar dust effects on spacesuits and operations (NASA). [Left] Astronaut Harrison Schmitt on the lunar surface during Apollo 17 mission. [Right- Top] Astronaut Gene Cernan inside lunar module-spacesuit covered in dust, [Right-Bottom] His face, body and surroundings covered in dust when he doffed his suit during Apollo 17 (Images from NASA).

Table 1.1-1. Total hours spent on surface EVA operations during each Apollo mission. Provides an estimate of spacesuit exposure to dust (*Information approximated from Lunar Planetary Institute and NASA Apollo Mission pages).*

Apollo Mission	Hours of Surface EVA Operations	No. of EVAs
Apollo 11	2.5	1
Apollo 12	7.5	2
Apollo 14	9	2
Apollo 15	18.5	3
Apollo 16	20.3	3
Apollo 17	22	3
TOTAL	79.8	14

Following these findings from the Apollo missions, NASA has identified dust mitigation as a critical path prior to sending humans on future lunar, planetary and asteroid exploration missions with dusty environments. A recent report published by NASA lists dust/particulate mitigation as high priority research for NASA (NASA, 2016). Future spacesuits and all other systems that may be exposed to planetary dust/regolith must be designed to be robust (compared with the Apollo missions), designed to have enhanced mobility features, and be durable, with minimal maintenance, for frequent use in the dusty environment of planetary surfaces.

1.2. Topic Motivation

While it has been nearly 50 years since the manned explorations to the moon, lunar exploration has always been a significant topic of interest to utilize resources of the moon in support of human space exploration and spacefaring capabilities. NASA is working towards an eventual return to the lunar surface, and the European Space Agency (ESA) plans to set up permanent human outpost on the moon to "assess the economic feasibility of using lunar resources for sustaining human surface-exploration activities" (David 2016 and ESA 2016). Such activities necessitate longer and rigorous EVAs by astronauts, which in turn require robust spacesuits. Therefore, NASA's 2015 Space Technology Roadmaps (STR) and Asteroid Redirect Mission (ARM) reports identify the need for highly mobile spacesuits that enable more frequent and rapid EVAs in dusty surface environments. Such endeavors require technologies for dust mitigation/protection and decontamination/removal.

NASA's 2015 STR identifies the need for EVA and spacesuit systems that can maintain full functionality in the following conditions:

1. Exposures to dusty environments of lunar surface (and other dusty planetary surfaces), for a minimum of 100 EVAs (800 hours of use)
2. Performance of EVAs without need for specialized servicing, maintenance, or ground support, for a minimum of 100 EVAs (800 hours of use)

This dust protection technology capability has been identified for the following potential missions in the near future:

Table 1.2-1. Design Reference Missions (DRM) as stated by NASA's STR requiring dust mitigation technologies for successful mission operations *(Reproduced from NASA STR, 2015)*

Technology Needed for the Following NASA Mission Class and Design Reference Mission	Enabling or Enhancing	Mission Class Date	Launch Date	Technology Need Date
Into the Solar System: DRM 5 Asteroid Redirect - Crewed in DRO	Enabling	2022	2022	2015-2021
Exploring Other Worlds: DRM 6 Crewed to NEA	Enabling	2027	2027	2021
Exploring Other Worlds: DRM 7 Crewed to Lunar Surface	Enabling	2027	2027	2021
Exploring Other Worlds: DRM 8 Crewed to Mars Moons	Enabling	2027	2027	2021
Planetary Exploration: DRM 8a Crewed Mars Orbital	Enabling	2033	--	2027
Planetary Exploration: DRM 9 Crewed Mars Surface Mission (DRA 5.0)	Enabling	2033	--	2027
Planetary Exploration: DRM 9a Crewed Mars Surface Mission (Minimal)	Enabling	2033	--	2027

Currently, the technology development programs at various NASA centers for dust mitigation focus on materials and coatings for dust mitigation for rigid surfaces. The dust protection of the spacesuit systems, which are comprised of flexible surfaces, remains an open challenge. A unique approach is the Suitport concept developed by NASA, which is attached to the exterior of the habitat and the suits are not brought inside the habitat. The Suitport approach avoids ingress of dust into the habitat, thus reducing the impact to crew health. However, the dust protection of suits themselves while stationed outside, on dusty planetary surfaces remains an open challenge.

These challenges motivate the SPIcDER research. The research focuses on development of a dust mitigation technology for flexible structures, applicable to lunar spacesuits. The SPIcDER research has a broad formulation, that can be customized and optimized for spacesuits or other flexible structures, operating on other planetary surfaces (such as Mars and asteroids), or on Earth. In summary, based on near term plans for NASA and ESA to establish potential long duration outposts on the moon and other planetary surfaces, the fundamental goals for the SPIcDER research are to:

- Increase the durability and reliability of spacesuits for long duration missions in dusty environments
- Develop a system that functions autonomously to prevent dust accumulation and repel adhered dust
- Decrease the time demands on the astronauts to perform spacesuit maintenance during a mission to maximize the allocation of crew time and performance towards mission objectives and science goals
- Reduce transport of dust into habitats, to prevent health issues

1.3. Research Questions and Hypotheses

The SPIcDER research addresses two questions:

1. How to mitigate dust contamination for planetary spacesuits for long duration missions, with specific focus on lunar operations?
2. How to integrate and enhance the dust mitigation technology into existing and future spacesuits for operations in lunar environments?

In order to address the above research questions, the following solutions are proposed and tested:

A. Utilize an active electrode technology embedded within the outerlayer of the spacesuit. Connecting a "cleaning signal" comprised of a multi-phase AC voltage signal to the electrodes, can create a surrounding electric field, which can prevent dust accumulation and can repel adhered dust particles off the surface. The main performance metric in the SPIcDER research is the residual (%) coverage of dust remaining after the cleaning. Successful mitigation is defined as residual dust coverage of less than 25% of the spacesuit fabric area embedded with electrodes. This value of the success metric is equivalent to residual dust of <= 0.25 mg/mm^2. This performance metric is driven by the requirement that the thermal effects of the residual dust on the spacesuit are allowed to degrade at most 20% of the localized area of the suit's radiative thermal capability (for details, the reader is referred to Chapter 7, section 7.3.3).

The SPIcDER research leverages the Electrodynamic Dust Shield (EDS) concept, developed by NASA for rigid surfaces such as solar cells, optical surfaces and thermal radiators, and

customizes it for application on the soft flexible areas of the spacesuit. Following innovations are developed in the SPIcDER research:

- Application of high performance flexible fibers made of Carbon nanotube (CNT) material as electrodes into the outerlayer of the spacesuit to overcome spacesuit design and operational complexities. The embedded CNT yarns are flexible, strong, and can conform to the spacesuit outerlayer, including existing weaves of the material. The flexibility, resilience and conformity of the CNT electrodes is critical for the performance of the SPIcDER system.

- Utilizing a unique fabrication method for electrode integration into spacesuit. Several automated and manual fabrication methods have been developed as part of this research to expand the application of the dust technology to flexible surfaces, including small (less than 3 inch x 3 inch area) and large (wearable garments, flexible solar panels etc. that require automated fabrication method) surfaces.

B. Combination of active and passive dust mitigation technologies is proposed to provide better dust removal/cleaning efficiency than using standalone individual technologies

- Evaluate the feasibility of enhancing the dust cleaning performance of SPIcDER by combining Work Function Matching (WFM) coating passive technology along with the active electrodes within the spacesuit outerlayer.

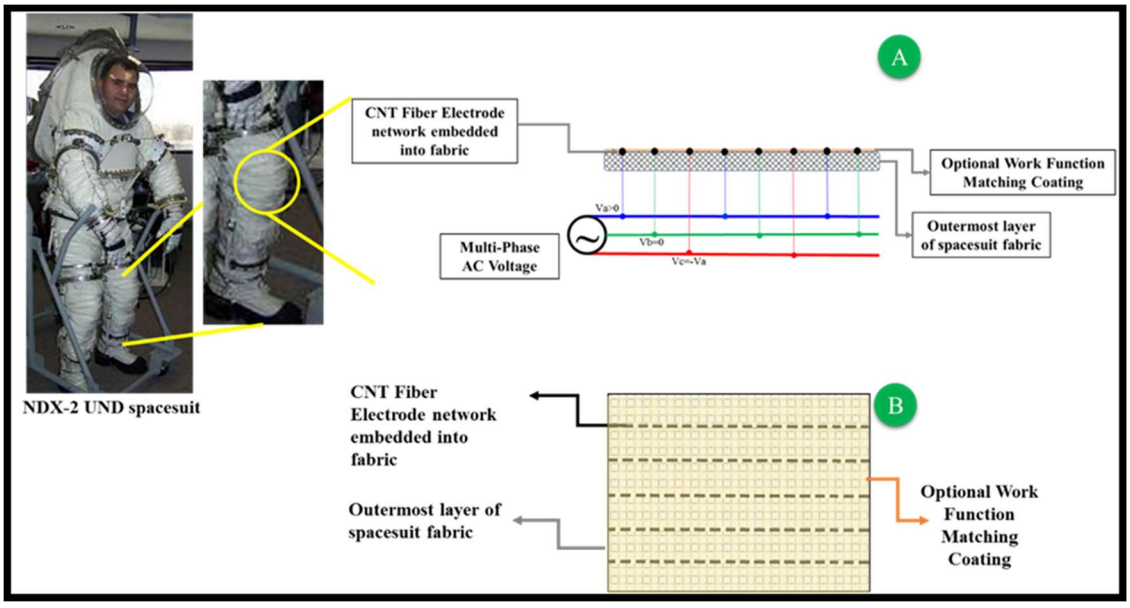

Figure 1.3-1. Concept of *SP*acesuit *I*ntegrated *C*arbon nanotube *D*ust *E*jection/*R*emoval (SPIcDER) System

1.4. Research Objectives

The research objectives listed below were developed and completed. For details, the reader is referred to Section 4.4.

1. Understand and characterize the dominant physical mechanisms of dust adhesion to surfaces in the lunar environment.
2. Investigate dust cleaning technology concepts that are viable for spacesuit implementation
3. Identify an approach for dust mitigation strategy of spacesuits, with emphasis on the soft areas of the spacesuit.
4. Outline the fabrication challenges for applying traditional electrode materials for spacesuit.
5. Investigate new materials that are suitable for conformal integration into the outerlayer of the spacesuit.
6. Develop a system design for a spacesuit integrated dust cleaning technology and implementation method specific to lunar application to achieve the performance metrics.
7. Proof of concept demonstration of the technology on coupons made of spacesuit outerlayer to assess the implementation (fabrication) method of the SPIcDER system into the spacesuit outerlayer, and to examine its performance capabilities to remove lunar dust simulant.
8. Demonstrate feasibility of coating the spacesuit fabric embedded with CNT electrodes with WFM coating. Assess viability of using a combination of the passive WFM coating with active CNT electrodes would not impact the cleaning performance of the active system in ambient conditions.
9. Develop an analytical model to characterize the key parameters impacting the dust cleaning performance of the SPIcDER system.
10. Assess the design parameters of the SPIcDER system to develop a framework of parameters and required tradeoffs for flight suit implementation.
11. Analyze parameters for astronaut safety and develop recommendations for SPIcDER implementation on a spacesuit to minimize hazards.
12. Provide an overview of the operational considerations required to implement the SPIcDER technology for flight operations.
13. Develop and assess the scalability and performance of a functional prototype of a scaled joint-section of the spacesuit embedded with SPIcDER based on NDX-2 spacesuit design and dimensions.

14. Provide recommendations for improvement and enhancement of the SPIcDER technology, subsequent to the research detailed in this dissertation.

The following topics are relevant to the SPIcDER technology; however, they are outside the scope of the SPIcDER research described in this dissertation:

1. Manufacturability of CNT fibers and CNT yarns.
2. Design, development and physical integration of the power supply into the spacesuit. The experiments conducted during the SPIcDER research utilize power electronics built by NASA Kennedy Space Center (KSC).
3. Dust mitigation on metallic areas /metal to electrode interaction. Recognized as a challenge that is not addressed in this research and provides direction for future.
4. Fidelity of lunar dust simulant: The experiments in the SPIcDER research utilize available lunar dust simulants at KSC and Glenn Research Centers (GRC), with the implicit assumption that these simulants are adequate.
5. For numerical analysis, particle-to-particle interactions are believed to constitute only secondary mechanisms and are not simulated. Obtaining such experimental data is difficult for the large spread of particle sizes, and modeling this does not provide additional data for the success criteria set for the dust cleaning performance and therefore the effort is not justified.
6. While the current research assumes that the SPIcDER system can be operated 100% of the time, there could be constraints based on science investigations and to minimize disruptions with payloads. The SPIcDER system is shown to be effective in other operational modes such as non-continuous pulse/burst mode. These modes of operations can be optimized for the type of EVA. Analysis of these operational modes are outside the scope of this research. Recommendations where applicable for safety aspects are provided within Chapters 8 and 9.

1.5. Approach

The overall research plan is formulated in a 5-step approach to efficiently address the research problem. Figure 1.5-1 provides the roadmap utilized to achieve the research objectives. The overall research methodology was based on using a combination of quantitative and qualitative assessments. The research utilized experimental work to investigate the feasibility of utilizing CNT

fibers integrated into spacesuit fabric to mitigate dust and numerical simulation to understand the effects of key parameters on dust cleaning performance to optimize the SPIcDER system.

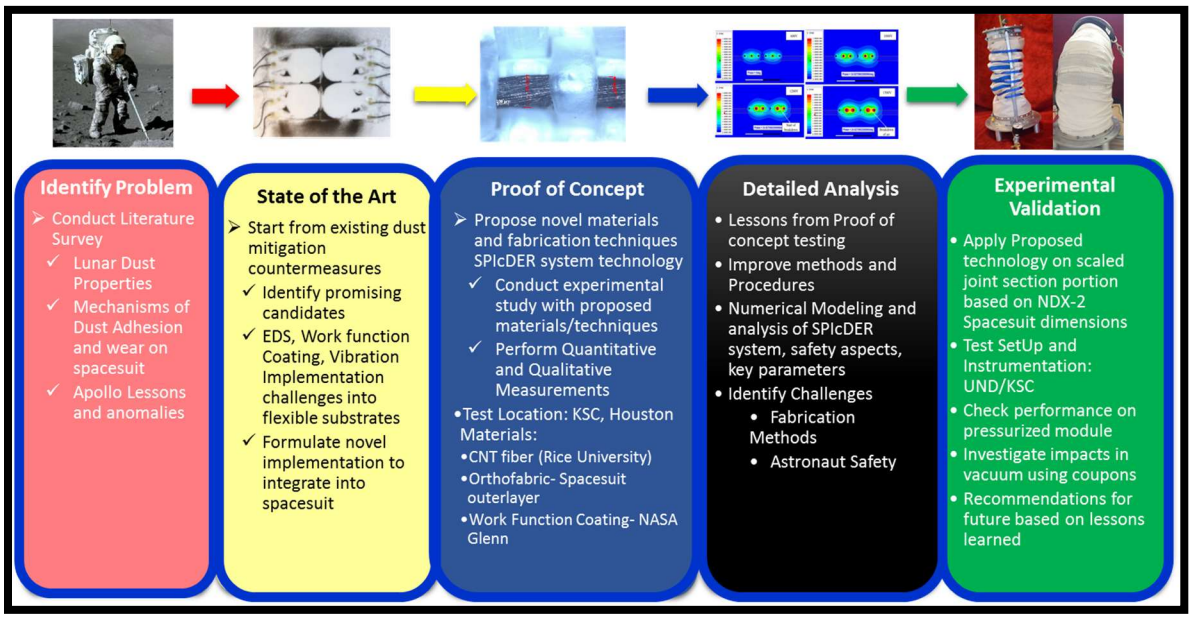

Figure 1.5-1. Overall research approach

1.5.1. Methodology

Numerical simulation using appropriate tools are utilized to perform the following

- Numerically simulate the SPIcDER system in ANSYS Maxwell to understand the electric fields generated and repulsion forces acting on the dust particles.
- Understand the trajectory of a single dust particle in MATLAB when exposed to the electric field generated by the SPIcDER system.
- Identify key parameters of the SPIcDER system impacting dust cleaning performance

Experimental portion of the research provides both quantitative and qualitative assessment to explore the feasibility of the proposed concepts.

- Qualitatively analyze the feasibility of embedding CNT yarns into the spacesuit outerlayer when compared to traditional electrode wires (example: copper wire).
- Quantitative data collected during the proof of concept tests to identify performance of the SPIcDER system.
- Quantitative data on dust coverage post cleaning operations on a scaled prototype.
- Quantitative data on dust coverage post cleaning operations on coupons in a vacuum chamber.

1.5.2. Performance Metrics

The key performance metric utilized to evaluate dust cleaning performance is the residual dust coverage on the spacesuit fabric post cleaning operations. Other relevant metrics to characterize the SPIcDER system during this research for both the experimental work and numerical simulation are provided in Table 1.5-1. Where applicable, recommendations are made for future studies on metrics.

Table 1.5-1. Metrics utilized in this research

Experimental / Numerical	Type	Metrics Utilized for Research	Coupons-Ambient	Coupons-Vacuum	Scaled Prototype	Constraints and Future Recommendations
Experimental Work	Quantitative	Number of dust particles on the suit fabric before and after activation electrodes	x			Thermal and Optical Reflectivity-Provides better metric for dust clearing performance. Limited by
		Dust particle sizes on the suit fabric before and after activation of SPIcDER system	x			
		Area of fabric covered in dust before and after cleaning operations using image processing techniques	x	x	x	Use sophisticated particle counting equipment such as Horiba particle size
		Activation time of the SPIcDER system for both Coupon and Scaled prototype tests	x	x	x	
		Applied operations voltages and frequencies	x	x	x	
		Threshold voltages where breakdown initiates	x	x	x	
	Qualitative	Visual observations on how fast or slow dust was cleared	x	x	x	
		Feasibility of fabricating flexible CNT yarns verses rigid Copper electrodes into spacesuit outerlayer fabric	x			
Numerical Simulation	Quantitative	**ANSYS Simulations**	**Flat Surface**	**Curved Surface**		
		Electric field Magnitudes	x	x		
		Electric field Vectors	x	x		
		Threshold voltage where breakdown starts	x	x		
		MATLAB				
		Understand trajectory of single dust particle due to Electric field force				COMSOL particle trajectory simulation that includes particle-particle interactions

1.6. Dissertation Overview and Structure

This dissertation is organized into five parts with a total of ten chapters that follow the above stated research approach. Following is a brief description of the chapters

Part I: ***Dust Problems during Planetary Exploration: Background, Previous Work and State of the Art***

Chapter 2: Why is Lunar Dust Problematic? Lessons from Apollo Missions

The chapter provides an overview of the lunar surface and lunar dust properties. A comprehensive overview of the dust problems confronted during the Apollo missions, with specific emphasis on spacesuits is discussed. Lessons from Apollo missions are outlined to address the dust problem.

Chapter 3: State-of-the-Art Dust Mitigation Technologies

A survey of state-of-the-art active and passive dust mitigation technologies are presented and discussed to determine viable candidates to address spacesuit dust contamination for lunar surface application. Published literature on these proven and proposed dust contamination countermeasures is analyzed. Limitations of these previously reported technologies for spacesuit application are outlined. Technologies with high dust cleaning efficacy are down selected for further study to integrate into spacesuits.

Part II: Current Research: Spacesuit Integrated Carbon Nanotube Dust Ejection/Removal Technology

Chapter 4: Overview of the SPIcDER Dust Cleaning System for Spacesuits

Challenges of spacesuit design for dust mitigation are discussed. A novel approach to address dust mitigation of spacesuits and flexible surfaces is proposed using the SPIcDER system that was developed as part of this research. Detailed discussion of the SPIcDER system and various fabrication techniques are presented.

Chapter 5: Proof of Concept Demonstrations

To investigate the feasibility of applying the proposed SPIcDER technique and its dust cleaning performance, experiments on coupons made of spacesuit outerlayer material were conducted at the NASA Electrostatics and Surface Physics Laboratory (EPSL) at KSC in both ambient and vacuum conditions. Tests were also conducted to identify the feasibility of integrating the active CNT fiber along with the passive WFM coating. Results from these demonstrations are detailed in this chapter.

Part III: Research Analysis: Numerical Modeling and Design Considerations

Chapter 6: Numerical Simulations and Key Parameters for the SPIcDER System

An analytical model describing the SPIcDER system and detailed investigation into the electric field forces generated by the electrodes is presented. This includes a discussion of: the electric field theory, numerical modeling of the electrode system using parallel cylindrical wire system and Gauss's law, ANSYS Maxwell 2D simulations of the electric field generated by the CNT electrodes embedded in the outerlayer, MATLAB modeling of the dust particle trajectory, and fundamental characterization of the SPIcDER system's key parameters.

Chapter 7. Design and Operational Considerations for Implementing the SPIcDER System

A review and analysis of the design and operational parameters that are to be considered and traded to integrate the SPIcDER system for flight suit implementation are detailed in this chapter. Whether designed for lunar dust mitigation or Mars and asteroids exploration missions, the spacesuit system integrated with SPIcDER must be able to provide a high degree of dust cleaning performance capabilities and, be safe and reliable. Key design and operational elements are reviewed and recommendations are provided for future work.

Chapter 8: Astronaut Safety

Detailed investigation of the spacesuit layers and material layout is presented to examine the feasibility and safety aspects of applying high voltages on the spacesuit outerlayer when the suit is donned by a crew. The chapter presents results on astronaut exposure to induced voltages and electric fields using numerical analysis considering the material lay-up and thicknesses of the Apollo suit and the International Space Station (ISS) Extravehicular Mobility Unit (EMU) spacesuit layers. Recommendations to address safety aspects are provided in this chapter.

Part IV Experimental Validation: Spacesuit Prototype

Chapter 9: Experimental Validation

A scaled version of the first-generation SPIcDER system on a knee joint-section of a spacesuit that is built based on the design and dimensions of the UND NDX-2 lunar spacesuit prototype is presented. Discussion of the prototype manufacturing process, series of tests conducted to assess the feasibility of the scaled SPIcDER system, its dust cleaning performance are detailed. Improved methods to fabricate the SPIcDER system into spacesuits based on lessons learned are discussed.

Additionally, initial investigation of the SPIcDER system in vacuum conditions utilizing coupons is detailed.

PART V: Conclusion-Research Contributions, Findings, Conclusions, Limitations, Future Recommendations

Chapter 10: Summary of Research, Contributions and Recommendations for Future

Summary of research conducted as part of this Ph.D. work is presented including- key findings, limitations, contributions and recommendations for future work. Recommendations for enhancing the SPIcDER system performance are discussed. Other applications beyond spacesuits where the SPIcDER system can be configured and implemented are discussed expanding the scope of implementation of this technology.

1.7. Brief Summary of Research Findings

Dust mitigation of spacesuits is a major challenge for planetary exploration (Moon, Mars and asteroids) and needs to be addressed for future long duration missions. This research investigates methods to address spacesuit dust contamination, specifically the soft areas of spacesuit in lunar environments. Investigations resulted in the design, development, modeling, manufacturing and testing of the SPIcDER system leveraging proven active dust mitigation methods, by applying novel materials and techniques. The research demonstrated the viability of integrating active electrodes into the spacesuit outerlayer (and similar flexible structures) to protect from dust contamination by utilizing CNT flexible yarns to overcome the constraints of the zero-adhesion Teflon coated spacesuit outerlayer and continuous flexure cycles due to astronaut movement. The proposed SPIcDER technology was shown to prevent dust accumulation and repel adhered dust to the spacesuit outerlayer with cleaning efficiencies ranging between 80-97%. A combination of active and passive dust control technology was also shown to be feasible. The system is shown to be scalable to larger portions of the spacesuit through development of a full scale knee joint-section of spacesuit embedded with the SPIcDER system to provide autonomous cleaning. Experiments conducted on the scaled prototype validate the dust cleaning performance of the system. Results show that activation of the SPIcDER can keep dust contamination of the suit area to within 3-16% of the suit fabric, cleaning as high as 97% of the dust adhered to the suit.

The technology developed during this research bridges the existing gap between dust mitigation of rigid surfaces and that of flexible surfaces with specific usability on spacesuits. Experimental work along with numerical simulations have been used to demonstrate working prototypes ranging from coupons to a scaled joint-section of a spacesuit to validate the manufacturability, dust cleaning performance and scalable functionality of the SPIcDER system as a primary mode of dust mitigation for spacesuits. While this research aims primarily towards spacesuit dust contamination, the versatility of SPIcDER technology is applicable to a wide range of flexible surfaces for both space and terrain applications.

CHAPTER 2: WHY IS LUNAR DUST PROBLEMATIC? LESSONS FROM APOLLO MISSIONS

"Lunar dust is fine, like a powder, but it cuts like glass"- *The Mystery of Moon Dust, The New Yorker*

The lack of atmosphere on the Moon and exposure to the various space weathering processes results in the electrostatic charging of lunar dust particles and their abrasive nature causing lunar dust to be problematic for exploration missions. First part of this chapter provides a background on the composition of lunar surface and details the reasons for lunar dust being detrimental to space operations. An overview of the characteristics of lunar dust particles relevant to this research are presented. Second part of the chapter provides an in-depth review and historical overview of the dust problems encountered by Apollo astronauts during lunar operations, with specific focus on spacesuits and EVA systems, and challenges for future lunar surface operations are discussed. Potential health effects due to lunar dust are covered in Chapter 8. Third part provides a generic overview of various mechanisms through which lunar dust adheres to exposed surfaces.

Part A: Background on Lunar Surface and Lunar Dust Characteristics

2.1. Lunar Surface

The lunar surface is categorized into two regions: the basaltic rich dark mare, and the anorthositic feldspar-rich highlands (See Figure 2.1-1). The surface of the Moon is covered by several layers of thick regolith formed by high-velocity micrometeorite impacts, and is characterized by steady bombardment of charged atomic particles from the sun and the stars (McKay, 1991). Variations in the mean thickness of the regolith covering the lunar surface range from 4-5 m in the lunar Maria and 10-15 m in the highlands (Slayut, 2014). Observations from the Apollo missions reveal that the regolith is a mixture of loose unconsolidated rocks, pebbles, and fine fragmental dust material made of a complex mixture of following particle types: crystalline rock fragments, mineral fragments, breccias, agglutinates, and glass (Carrier et al.,

1991). The properties of lunar soils have been measured in-situ by robotic missions, Apollo astronauts, laboratory studies on returned samples, and by remote sensing from Earth's surface and from the lunar orbit. Much research has been conducted on lunar samples collected by the Apollo missions, which returned a total of 382 kg of lunar rocks and soil. In addition to the Apollo program, a large volume of data on lunar soil and dust properties is available from the Soviet unmanned Luna 16, 20 and 24 sample return missions, which returned ~300 grams of lunar soil (Taylor, 1982; McKay, 1991; Slayut, 2014). Table 2.1-1 provides the environmental conditions on the Moon.

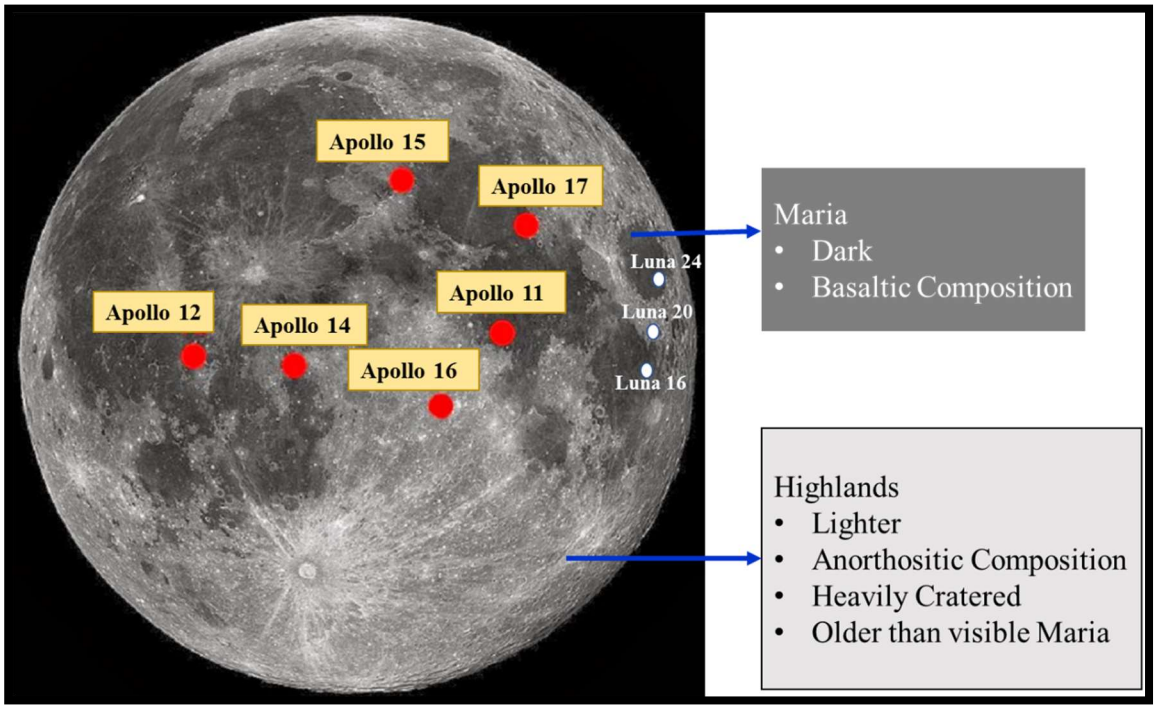

Figure 2.1-1. Visible face of the Moon from Earth. Locations of lunar return samples from Apollo and Luna missions. (*Author developed picture based on available data from NASA)*

Table 2.1-1. Environmental conditions on the Moon (Taylor, 1982)

Property	Value	
Radius of the Moon	1738 km	
Surface Gravity	1.622 m/s² (0.16 g)	
Atmospheric pressure	Vacuum	
Temperatures	Daytime High	Nighttime Low
Mean Surface	107ºC	-153ºC
Equator (0º latitude)	122ºC	-158ºC
Mid-Latitudes	77ºC	-143ºC
Poles	-43ºC	-63ºC
Dark Polar Crater	-233ºC	-233ºC
Magnetic Field	Negligible	

2.2. Characterization of Lunar Dust

The highly pulverized small particle portion of the lunar soil is considered lunar dust. Three basic components are determined to form the basis of lunar dust: rock fragments, mineral grains, and glass particles (Carrier et al., 1991). The top surface is very loose dust due to stirring by micrometeorites, although the soil is compacted at lower depths. The lack of an atmosphere on the Moon has exposed the upper layers of the regolith to harsh environments of space such as the bombardment of micrometeorites and to solar wind irradiation. As such, the major processes theorized for lunar soil formation on the moon are as follows (McKay, 1991):

- Comminution caused by the constant micrometeorite impacts with velocities greater than 30,000 km/h leading to mechanical fracturing and destruction of the fresh rock surfaces.
- Electrostatic charging of lunar surface by steady bombardment by charged atomic particles from sun and the stars.
- Agglutination caused by extensive bombardment by micrometeorites resulting in breaking-up of soil particles, shock melting portions of the soil and mixing with lithic (rock) fragments. This leads to formation of irregular clusters called agglutinates which are aggregates formed by welding of smaller soil particles bonded together by vesicular, micrometeorite-impact produced glass.

The following sections provide an overview of the lunar dust characteristics based on published data that have utilized various resources including sample return and remote sensing observations. Hands-on knowledge on the lunar soil and its characteristics are limited to the sites of the Apollo missions and the three Russian Luna sample return missions. While studies from these samples have provided a baseline for lunar soil characteristics, site-to-site differences in dust properties are anticipated as the sample return missions were limited to just a few locations.

2.2.1. Mineralogy

Lunar soil is dominated by silicate minerals and oxides based on studies using Apollo missions (Papike et al., 1991). Mineralogical studies of the lunar dust have shown silicate, calcium, aluminum, magnesium, and ferrous oxides along with impact glass (mostly agglutinitic glass) make up over 90% of the average soil composition on the moon (Papike et al., 1991; Taylor 1982; Liu 2011). Table 2.2-1 illustrates the major elemental composition of the soils from the Apollo landing sites. Commonly found silicate minerals on the lunar surface include pyroxene, plagioclase

feldspar, and olivine (Papike, 1991). Other minor components include ilmenite, olivine with rare grains of crystobalite, tridymite, chromite, ramacite, taenite, troilite (Colwell, 2007; Papike, 1991). Prior to recent investigations, it was thought that there is a total absence of water on the Moon and a lack of water containing minerals such as clay, mica, and amphiboles on the lunar surface (Papike, 1991). However, more recent observations from the Chandrayan-1, Lunar Reconnaissance Orbiter (LRO) and the Lunar Crater Observation and Sensing Satellite (LCROSS) suggest good evidence for water ice in the permanently shadowed craters in the Polar Regions, and the presence of hydrated minerals at least in the Polar Regions (Pieters et al., 2009; Colaprete et al., 2010).

Table 2.2-1. Major elemental composition of lunar soils at Apollo landing sites (Taylor, 1982 and Hill et al., 2007)

Apollo Mission:	11	12		14	15		16		17	
Sample #	10084	12001	120033	14163	15221	15271	64501	67461	70009	70051
SiO_2	41.3	46	46.9	47.3	46	46	45.3	45	40.4	42.2
TiO_2	7.8	2.8	2.3	1.6	1.1	1.5	0.37	0.29	8.3	5.09
Al_2O_2	13.7	12.5	14.2	17.8	18	16.4	27.7	29.2	12.1	15.7
FeO	15.8	17.2	15.4	10.5	11.3	12.8	4.2	4.2	17.1	12.4
MgO	7.9	10.4	9.2	9.6	10.7	10.8	4.9	3.9	10.7	10.3
CaO	12.5	10.9	11.1	11.4	12.3	11.7	17.2	17.6	10.8	11.5
Na_2O	0.41	0.48	0.67	0.7	0.43	0.49	0.44	0.43	0.39	0.24
K_2O	0.14	0.26	0.41	0.55	0.16	0.22	0.1	0.06	0.09	0.07
MnO	0.21	0.22	0.2	0.14	0.15	0.16	0.06	0.06	0.22	0.15
CrO	0.3	0.41	0.39	0.2	0.33	0.35	0.09	0.08	0.41	
Σ %	100.1	101.2	100.8	99.8	100.5	100.4	100.4	100.8	100.5	97.7

2.2.1.1. Agglutinates

Evidence from sample return missions have shown that more than a quarter of the lunar soil are agglutinate particles, with a smaller fraction of impact-generated glasses and breccia (Taylor, 1982). Recent studies showed that while these agglutinates and can make up a high proportion of many lunar soils, about 25-30% on average, their abundances may range from 5 to 65% (Eckart, 2006). These agglutinates are comprised of various particles (mineral grains, glasses) which are fused together by vesicular, flow-banded glass. They also contain submicron Fe^0 metal particles (nanophase Fe) and solar wind gases (He, H_2). The increase in the abundance of agglutinitic glass with deceasing dust grain size has been noted in literature (Liu, 2011). Recent investigations on

lunar dust note the presence of relatively large amounts of np-Fe^0 in the small portion of the lunar dust (< 50 μm) formed by vapor deposition that imparts considerable magnetic susceptibility to the lunar soil (Taylor et al., 2005). The constant influence of the solar wind and space radiation enriches the regolith particles with hydrogen, noble gases, cosmogenic isotopes of a wide spectrum, and other components. This also promotes the formation of Fe, Si, and other elements in the surface layers of the particles and their reduction to the elemental state. The shape and the surface of these agglutinic particles is caused by melting and agglomeration of lithic fragments, mineral and glass grains of the lunar regolith into a single particle in a high velocity micrometeorite impact. (See insets [C, D] in Figure 2.2-3 for agglutinate examples).

2.2.2. Physical and Mechanical Properties

2.2.2.1. Particle Size Distribution

Several interpretations related to the definition of lunar dust particle size have been reported in literature. By conventional planetary science definition, lunar soil is the less than 1 cm particle size portion of the lunar regolith, while lunar dust definitions range from particles less than 50 μm to less than 10 μm (McKay, 1991). In recent years the definition in the literature has tended to settle on less than 20 μm (Cain, 2010; Liu, 2011). With varying sizes of dust particles, studies. have reported lunar dust comprises of the following (Carrier, 1991; Colwell, 2007; Taylor et al., 2005; Cain 2010)

- 95% particles finer than 1 mm, of which
    - 50% of the particles are in the size range less than 60 μm
    - 10–20% are less than 20 μm, and
    - ~10% particles are made of 10 μm particles

Figure 2.2-1 illustrates the particle size distribution of soil taken from a mare region on Apollo 11 (McKay et al., 1989). Table 2.2-2 shows the median particle sizes for all Apollo samples and JSC-1A lunar dust simulant and Figure 2.2-2 illustrates the particle size distribution (PSD) for majority of Apollo surface soils from previous studies (Liu and Taylor, 2011; Graf, 1993).

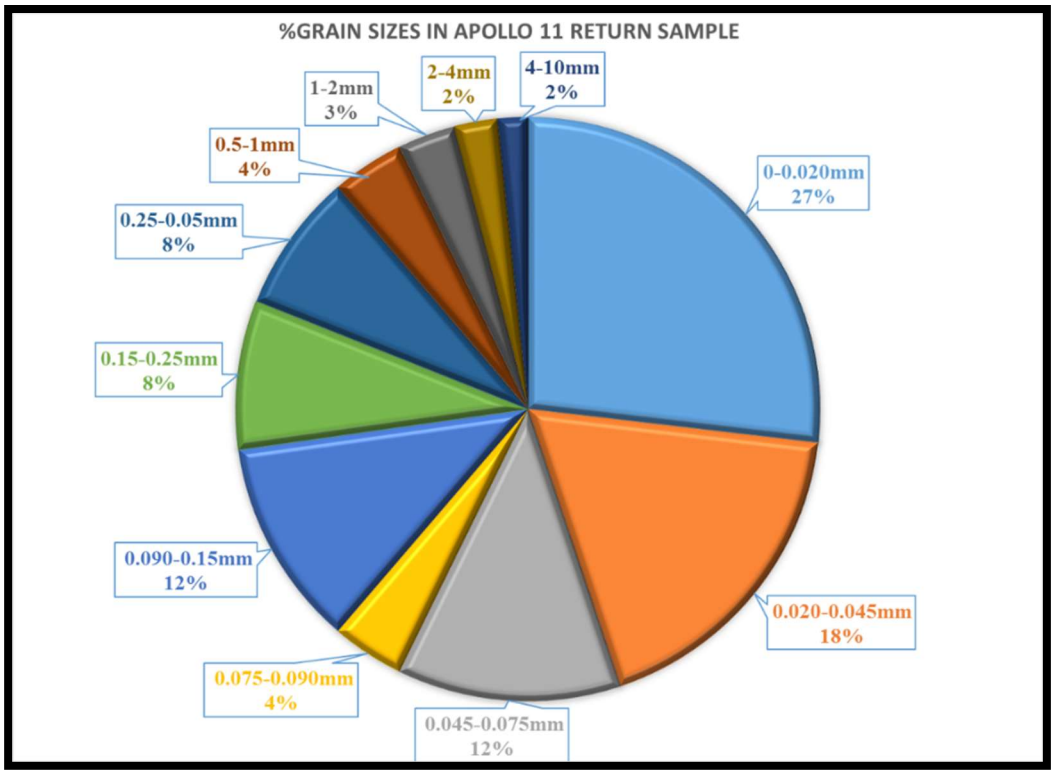

Figure 2.2-1. Percentage of dust particle (grain) size distribution of samples collected on Apollo mission (Data adapted from McKay et al., 1989)

Table 2.2-2. Median dust particle sizes reported in literature
(Apollo samples from Heiken et al., 1991 (The Lunar Sourcebook), JSC-1A from Orbitec®, 2007)

Sample	Median Particle Size range (μm)
Apollo 11	48-105
Apollo 12	42-94
Apollo 14	75-802
Apollo 15	51-108
Apollo 16	101-268
Apollo 17	42-166
JSC-1	98-117
JSC-1A	99-105

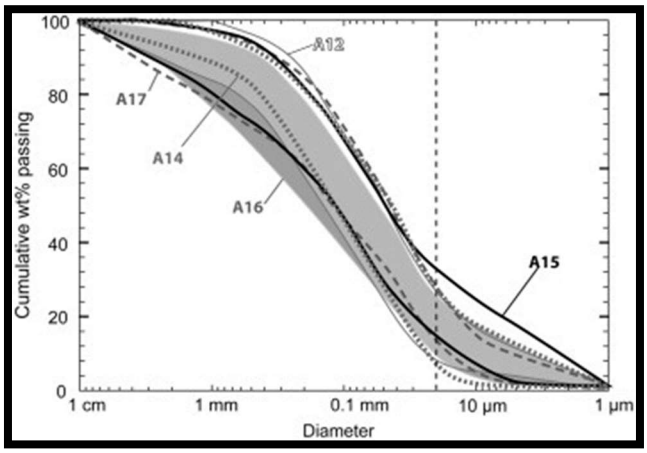

Figure 2.2-2. Particle size distribution of majority of Apollo samples. *The dotted line represents 20 μm dust size. Picture adapted from Liu and Taylor 2011 with original data from Graf, 1993.*

2.2.3. Shape/Morphology

Along with the variable particle size distribution (PSD) of the lunar soil, sample return soils provide evidence that the shapes of the individual lunar soil particles are highly variable ranging

from spherical, elongated, to extremely angular as shown in Figure 2.2-3. Due to the lack of atmosphere and water (presence of water in Polar Regions, but in general lunar surface is dry), there is an absence of atmospheric weathering on the lunar surface, because of which these dust particles have sharp and jagged edges. Furthermore, the soil is exposed to constant bombardment of micrometeorites and solar winds, the impacts of which have led to the formation of sharp edged particles making the lunar dust to be abrasive.

Apollo studies show soil fragments to be rough, with splashed glass coats, impacts, micro-craters, and iron particles (McKay, 1972). Agglutinates are noted to have varying morphologies depending on the size of their substituent grains. In the study conducted by Slayut et al. in 2014 on the physical and mechanical properties of lunar particles, they reported that the particles can be divided into three groups based on their order of increasing shape irregularity (data reported in Table 2.2-3). The high surface area, complex shapes, and hardness of the lunar particles are known to contribute to the abrasiveness of the lunar dust particles. The jagged and irregular shapes of the lunar dust lead to these particles mechanically adhering to spacesuit surfaces and getting trapped on the surfaces.

Table 2.2-3 Three categories of lunar dust grains based on their morphology *(Data adapted from Slayut et al., 2014)*

Morphology of Grains	Category
Spherical grains of glass and metal	Mostly regular in shape
Acute-angled fragments of different rocks, minerals and glassed	Intermediate in irregularity degree
Agglomerated and slagged grains (Agglutinates)	Usually irregular, dendritic like in shape

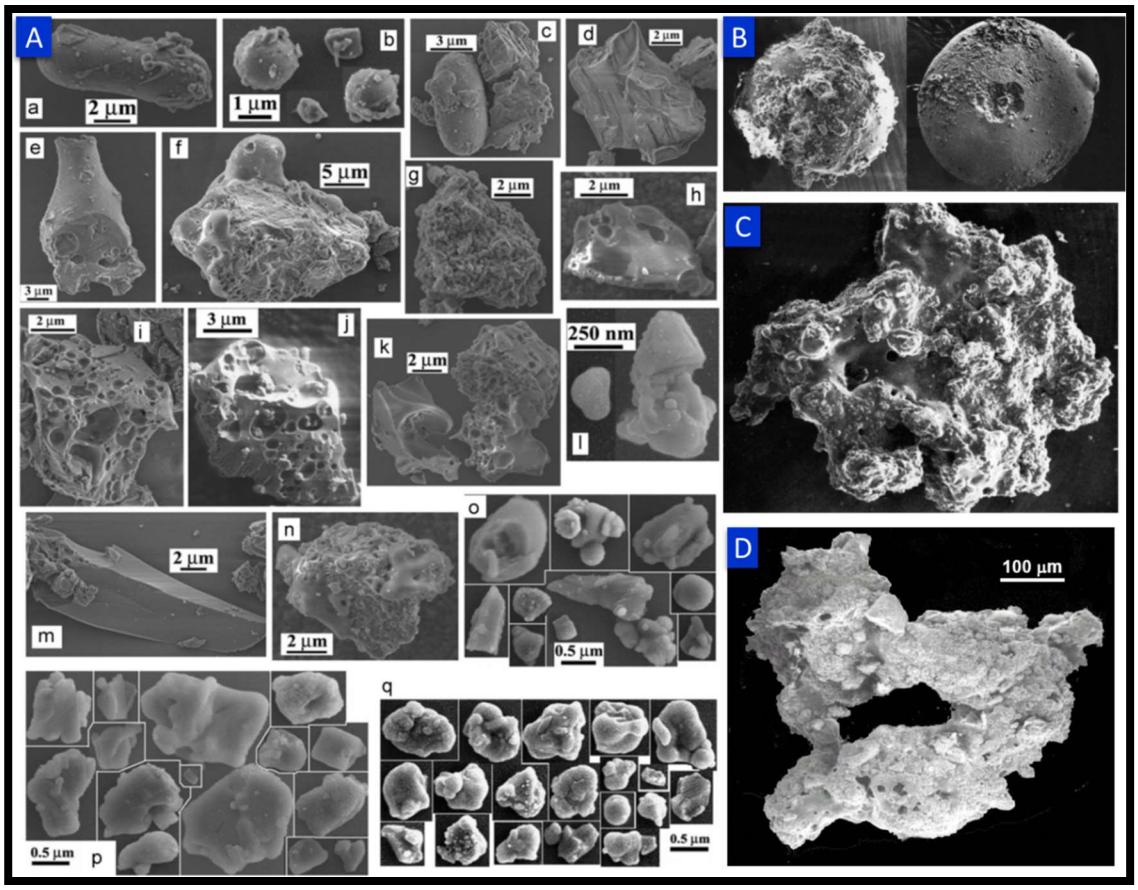

Figure 2.2-3. [A] Lunar dust particle morphology as seen from Secondary Electron images (Adapted from Liu, 2011), [B] Glass and spherical particles of regolith- (right) an impact microcrater on the surface of glass particles (Adapted from Slayut, 2014), [C, D] Typical agglutinate particles of lunar regolith (Adapted from Slayut, 2014 and McKay, 1991)

2.2.3.1. Bulk Density

The lunar sourcebook reports the bulk density of the soil ranging from 1.45 to 1.79 g/cm^3 depending on the depth. On average, the bulk density is reported to be approximately 1.50 g/cm^3 at the surface (Colwell et al., 2007). The density of individual soil grains has been estimated to be ~3g/cm^3 (Mitchell et al., 1972). Lunar soils show considerable variation in chemical composition, but properties such as density, packing, and compressibility are relatively uniform.

2.2.4. Electrical and Electrostatic Properties of Lunar Soil

Due to the lack of an atmosphere and weak magnetic field, the lunar surface is exposed to steady charged atomic particles of the solar wind, cosmic rays and solar radiation which leads to the electrostatic charging of the lunar dust grains. The charging processes on the lunar surface are illustrated in Figure 2.2.4. The photoemission effect due to bombardment of solar Ultraviolet (UV)

and X-ray photons drives the positive charge of the dust particles during the lunar dayside. The interaction with plasma electrons due to solar winds dominate the negative charge of the dust particles on the lunar night side (Carrier et al., 1991; Abbas et al., 2007). These effects make the lunar dust particles electrostatically charged. Table 2.2-4 provides a list of radiation particles that reach the moon leading to the electrostatic nature of the lunar dust particles. The average values predicted by a few previous studies show that the surface electrostatic potentials of the lunar surface can range from ~10 V on the dayside (Calle, 2011) to ~-200 V on the night side (Stubbs et al., 2007). More recent studies have reported that the electrostatic potentials can be as high as ~20 V on the dayside and -3.8 kV on the night side (Pabari and Banerjee 2016). The dryness of the lunar surface and the low electrical conductivity effectively make the lunar soil an insulator, and the conditions are conducive for these dust particles to hold the static charge developed. This characteristic of the dust particles in the lunar environment impacts equipment deployed on the surface of the Moon for exploration missions.

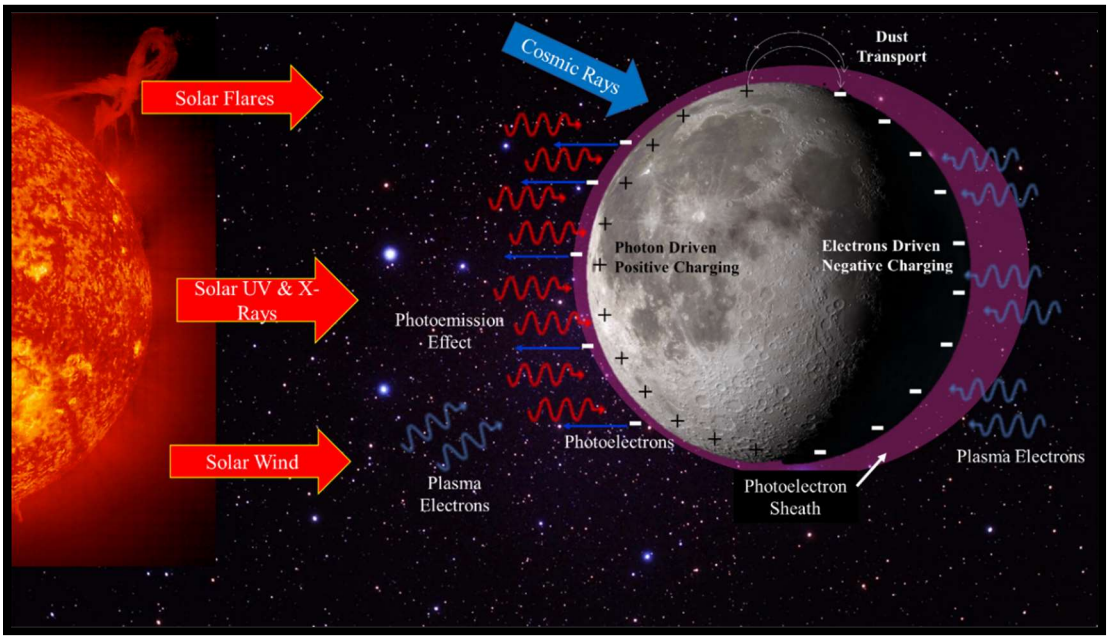

Figure 2.2-4. Processes driving lunar dart particle charges. *Graphic created by author based on information from several sources on lunar dust charging*

Table 2.2-4. Radiation sources and energy transferred on moon (*Bowell, 1971; Seybold 1995)*

Radiation Source	Energy	Flux ($cm^{-2}s^{-1}$)	Penetration Depth
Cosmic rays	1-10 GeV/nucleon	1	few meters
Solar flares	1-100 MeV/nucleon	100	1 cm
Solar wind	1000 eV/nucleon	108	10-8 cm

Due to the acquired static charge, the lunar soil can exhibit unusual behavior. Surface charging process and electrostatic charging of lunar dust particles was previously thought to drive dust levitation and transport across the lunar surface which were observed during Apollo and robotic missions (Carrier et al., 1991). Evidence for local stirring of the top dust layer has been inferred from the light scattering observed by the Apollo 17 astronauts (Taylor, 1982). The interpretation of this dust levitation higher in the altitude however has recently been questioned based on the observations made by the Lunar Dust Experiment (LDEX) onboard the Lunar Atmosphere Dust and Environment Explorer (LADEE) mission which did not see evidence of high elevations (3-250 km) of dust into the exosphere (Pabari and Banerjee 2016). Recent interpretations by O'Brien and Hollick (2015) do confirm however that local lofting of dust upto 100 cm could be driven by sunrise. This near surface lofted dust is of interest to the current research. The variations of the lunar surface potential which are known to occur due to charging from photoemission and plasma currents may cause the electrostatic transport of dust.

The charged dust particles would have a tendency to adhere to surfaces that come in contact and readily coat these surfaces. While there are ongoing studies with regards to understanding the exact charging and dynamic processes of lunar dust grains, such electrostatic adhesion of lunar dust presents significant hazards to future robotic and human exploration of the Moon. For long duration missions to the lunar surface, any equipment including spacesuits being exposed to this lunar dust, it is anticipated that they would accumulate high electrostatic charges on these surfaces that might lead to failure of equipment and impacts operations including but not limited to communication failure, discharge breakdown, electronic equipment failure etc.

The dielectric properties of lunar soil were investigated by Olheft and Strangway (1975) and Strangway et al. (1977). The dielectric constant is a measure of polarizability of a material when exposed to an electric field. The importance of dielectric constant of the lunar dust will be evident when the particles are exposed to the electric field generated by the SPIcDER electrodes (explained d in Section 6.8.4). Based on previous studies using regression analysis for more than 100 dust samples from Apollo (fine particle size < 1 mm) measured at 10e5 Hz, they generated a relation between the dielectric constant (k) and the bulk density (ρ in g/cm^3) as given by Equation 1.

$$k = (1.93 \pm 0.17)^{\rho} \quad (1)$$

The same studies identified that the effect of temperature on dielectric properties is very small over the range of temperatures found during typical lunar day. At surface, the dielectric constant may change ~ 5% and loss tangent 20-30%, and no changes at depth of few centimeters. Hence the temperature effects on dielectric constant in the top 100 m of lunar surface can be neglected. It was concluded from these studies that the dielectric constant varies with density, independent of temperature, frequency and ilmenite content. Also, during the Apollo mission specific experiments to measure dielectric constant was performed that showed that the Apollo 17 soils had a dielectric constant of 3.8 (Strangway et al., 1977). Other reviews from remote observations of lunar surface show a range between 1.5-3 (Calla and Rathore, 2012). Some studies conducted in the laboratory showed the dielectric constant to be close to 4 (Calle et al., 2008).

2.2.5. Thermal Properties

The mare and highland regions of the lunar surface have varied levels of brightness; thus, the albedo of the lunar surface is not uniform. The albedo of the moon varies from 0.50 for the brightest features on the surface to 0.07 for the darkest regions (Geiss et al., 1972). Studies have reported that lunar dust has high emittance (ε) nearing 0.93, however they also have high solar absorptance (α) on the order of 0.76, which means lunar dust absorbs more light, resulting in increased heating of the dust (Gaier and Jaworske, 2007). The high solar absorptancy and the thermal conductivity of the dust (~ 5×10^{-4} W/m-K) is thought to be of a major impact of lunar dust (Gaier and Jaworske, 2007). The impact of these thermal properties of lunar dust result in increased thermal load when lunar dust adheres/coats thermal control surfaces including the outerlayer of the spacesuits through conduction and radiation. Appendix A provides details on thermal impacts of lunar dust on thermal radiator surfaces during the Apollo missions and Chapter 7 provides an overview of impacts to radiation heat transfer of spacesuit outerlayer due to dust.

2.3. Lunar Dust Simulants

Limited availability of the actual lunar soil necessitates the development of lunar soil and dust simulants with closely matching properties for ground-based research investigating various candidate technologies for lunar exploration. Engineering and scientific investigations such as measuring the effects of lunar dust on spacesuits, planning for in-situ resource utilization (ISRU), toxicological impact of lunar dust and studies on lunar surface operations will require use of high

fidelity lunar simulants that can replicate the properties of lunar samples. Dust properties such as chemical composition, mineralogy, particle size, shape, surface morphology, electrical and thermal properties are critical to investigate and evaluate the effects of dust on thermal surfaces, astronauts, mission critical life support systems, mobility systems, EVA suit performance to name a few. However, synthesizing lunar simulants using terrestrial material sources to replicate all lunar dust properties is a considerable challenge due to variations in environmental conditions between Earth and Moon. Several institutions and research groups have developed lunar simulants to meet their research needs based on unique properties of lunar dust for specific investigations.

This section specifically reviews the Johnson Space Center (JSC) lunar soil simulant (JSC-1A) developed by Orbitec® and heavily utilized by NASA and for experiments conducted within this research.

2.3.1. Background

JSC-1 was the first lunar soil simulant standardized by NASA, and manufactured and distributed in the public domain in 1993 to facilitate lunar exploration studies (McKay et al., 1993). JSC-1 was created using basaltic pyroclastic sheet deposit in the San Francisco volcanic field near Flagstaff, AZ, which erupted from vents related to Merriam Crater to replicate the mare soil of the lunar surface (McKay et al., 1993). Since it was produced from glass-rich basaltic tuff, JSC-1 contains high proportions of volcanic glass (~49 wt%) and the bulk chemistry and PSD resembles the Apollo 14 samples (McKay et al., 1993; Hill et al., 2007). JSC-1 has been used for engineering studies of lunar surface exploration such as material handling, construction, excavation, dust control, spacesuit durability, oxygen production, and sintering to produce building blocks. However, supplies of JSC-1 are no longer available.

In 2004, NASA developed a suite of three simulant materials categorized into JSC-1A, JSC-1AF, and JSC-1AC to match as closely as possible the composition of the previous JSC-1 lunar regolith simulant. Additionally, NU-LHT-# simulant to represent lunar highlands was also developed by NASA Marshall Spaceflight Center (MSC). Figure 2.3-1 shows the two simulants developed to replicate the mare and highland simulants. Bulk amounts of the simulants were produced and distributed for use on lunar projects.

- **JSC-IA**

JSC-1A series was produced using the same quarry source of volcanic tuff/ash as JSC-1 and represents lunar mare soils. The geotechnical properties of JSC-1A are the same as JSC-1 due to the same original material used (Hill et al., 2007). While JSC-1A matches the composition and PSD of the original JSC-1 simulant, JSC-1AF is a 'fine-fraction' composition representing lunar mare regolith with <20 μm particle size distribution, and JSC-1AC is a 'coarse fraction' representing the coarser component of the lunar regolith (Hill et al., 2007; Liu et al., 2011; Gustafson, 2009).

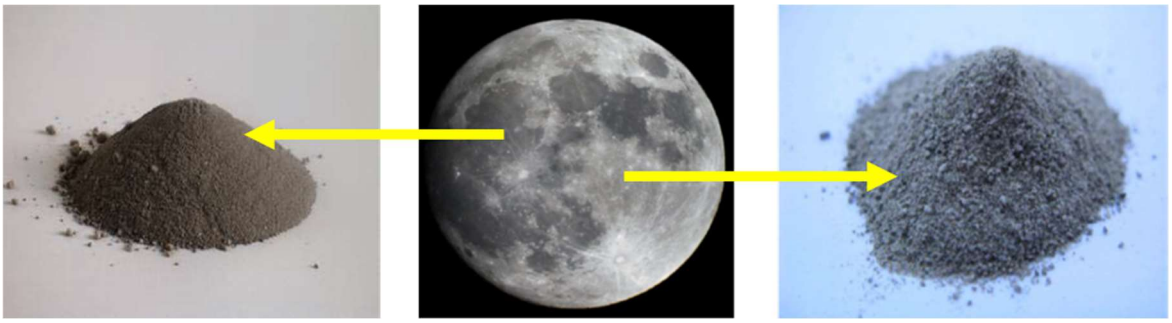

Figure 2.3-1 [Left] JSC-1A lunar mare simulant, [Right] NU-LHT-1M lunar highland simulant (Schrader et al., 2008)

2.3.2. Simulant Composition and Differences from Lunar Dust

The elemental compositions of JSC-1A and JSC-1AF (<50 μm portion of JSC-1A) simulants were analyzed by Hill et al. (2007). The bulk composition of the simulants compared to Apollo samples from their analyses is illustrated in Table 2.3-1. The JSC-1A simulant has a chemistry that contains abundant volcanic glass (~50 wt.%). The natural high-glass content with glass shards and angular grains of JSC-1A, combined with its PSD, approximates the engineering properties of lunar soil. As such, JSC-1A is suited to studies dealing with dust adhesion/abrasion, regolith handling, excavation and drilling. It was observed from their analyses that the trace element compositions differ between JSC-1A and JSC-1AF and suggest that the disparities are likely a result of differences in crushability of minerals holding these materials.

Table 2.3-1. Bulk chemical composition of lunar soils and simulants (Hill et al., 2007)

Mineral	Apollo 11	Apollo 14	Apollo 17	JSC-I	JSC-1A	JSC-1AF	JSC-1A (Orbitec, 2005)
	10084	14163	70051				
SiO_2	41.3	47.3	42.2	49.1	46.2	47.2	46-49
TiO_2	7.8	1.6	5.09	1.48	1.85	1.81	1.0-2.0
Al_2O_3	13.7	17.8	15.7	15.5	17.1	17.9	14.5-15.5
FeO	15.8	10.5	12.4	9.81*	11.2*	10.3*	7-7.5
MgO	7.9	9.6	10.3	8.48	6.7	5.93	8.5-9.5
CaO	12.5	11.4	11.5	10.1	9.43	10.5	10.-11
Na_2O	0.41	0.7	0.24	2.46	3.33	3.53	2.5-3.0
K_2O	0.14	0.55	0.07	0.85	0.85	0.82	0.75-0.85
MnO	0.21	0.14	0.15	0.18	0.19	0.17	0.15-0.2
Cr_2O_3	0.3	0.2					0.02-0.06
P_2O_5	0.1			0.61	0.62	0.71	0.6-0.7
Fe_2O_3							3.0-4.0
Total %	100	99.8	97.7	98.6	97.6	99.6	

*Total Fe as FeO

Differences between the JSC-1A simulant and lunar soil do exist since several properties of the lunar soils are difficult to simulate using terrestrial compositions including the dust charging mechanisms. Key differences between lunar soil and JSC-1A simulant identified by various studies are compiled and summarized in Table 2.3.2 (Sibille et al., 2006; Hill, 2007; Park et al., 2008; Liu, 2011; Gaier et al., 2012).

It is evident from the differences between the simulants and actual lunar soil that no one material/simulant can reproduce all the characteristics required to replicate lunar soil. In fact, the lunar regions visited by Apollo and robotic missions represent only a small fraction of the lunar surface mostly within the mare regions, and are not necessarily representative of other significant regions, such as the lunar highlands, polar regions and permanently illuminated or shadowed areas where the local environment factors are unique to these locations. Site-to-site differences in dust properties were also evident during the Apollo program when the Apollo 14 crew experienced non-adhesive dust compared to the rest of the missions whose spacesuits experienced relatively more abrasive and adhesive interactions (McKay, 1991). Therefore, the diversity of material compositions expected to be encountered on the Moon is a challenge to capture using terrestrial materials within one simulant.

Table 2.3-2. Comparison of lunar soil and JSC-1A simulant properties. Data consolidated form various sources

Property	Lunar Soil	JSC-1A Simulant	Use for dust contamination study
Source/ Formation	• **Formation methods**: Comminution Agglutination Vapor Deposition • **Major Weathering and Erosional Agent on the Moon** Meteorite and Micrometeorite impact	• Produced from basaltic pyroclastic sheet deposit in volcanic field near Flagstaff, AZ • Grounded to obtain essential PSD	• Formed under different conditions • Does not provide the same charging characteristics as lunar soil • Needs to be pre-treated prior to vacuum chamber testing for dust cleaning performance
Bulk Density	• Typical values for surface density ◘1.45 to 1.79 g/cm^3 (range from Lunar Sourcebook) • Individual grains ◘~1.27g/cm^3 (Olhoeft, 1975) ◘1.30g/cm^3 (Carrier et al., 1991) ◘1.50g/cm^3 (Colwell et al., 2007) ◘ For depth profile: $\rho=\rho0+kln(z+1)$ $\rho0$ is surface density 1.27 g/cm^3 (z=0), z is depth in cm, k is 0.121 is empirical constant (Olhoeft, 1975) ◘ Apollo 17 closer to 2 g/cm^3	1.4–1.9 g/cm^3 (Sibille et al., 2006)	• Similar density • Possible to use mass of dust as a performance metric
Specific Gravity	2.9-3.5 (Carrier et al., 1991)	Average 2.875 -2.9 (Zeng et al., 2009)	
Morphology	Ranges from spherical to very angular, sharp jagged edges	•Variety of shapes ranging from spherical to very angular • Substantial proportion of glass shards and angular grains • Abrasiveness and	• Works well for abrasion and dust contamination studies • Suitable engineering and geotechnical properties

Property	Lunar Soil	JSC-1A Simulant	Use for dust contamination study
		interlocking characteristics of lunar soil	
Mineral Composition	• Mainly consists of (70-98%) ◘ impact glass (mostly agglutinitic glass), ◘ plagioclase ◘ pyroxene • **Mare dust**: pyroxene and plagioclase nearly equal • **Highland dust**: contains about equal amount of plagioclase and agglutinic glass • 5%, 10%, 15% of Ilmenite (Feo+TiO_2) presence which covers most important ranges of lunar compositions (Taylor et al., 2000; Hill et al., 2007)	• Three major constituents of this simulant are ◘ glass (49.3 vol%), ◘ plagioclase (38.8 vol%) ◘ olivine (9 vol%) (Hill et al., 2007) Two separate simulants for mare and highlands (NU-LHT)	No major impact using for current study
Agglutinates	• Pieces of minerals, rocklets, and glass welded together by shock-melt glass called Agglutinates • Agglutinates are vesicular in nature due to solar wind particles escaping during melting and filled with myriad Fe0 globules Vesicular texture that gives lunar agglutinates their friable nature and are a major characteristic of lunar soils • Abundances of agglutinitic glasses increase with decreasing grain size • dust fraction (<20 μm) of most soils contains generally > 50 vol% of agglutinitic	• JSC-1A does not include agglutinates (impact glass) • Vesicular texture of lunar soils not captured • The glass in the simulant was not formed due to flash heating during impacts • Produced from glass-rich volcanic ash (Hill et al., 2007))	• Different density of glass might impact replicating charging effects of dust • Simulant does not replicate these properties entirely • Aggultinitic glass contributes to optical, electrical and toxic properties • More useful for health studies • Impacts when used for abrasion studies • May impact charging characteristics when pre-

Property	Lunar Soil	JSC-1A Simulant	Use for dust contamination study
	glass • < 10 µm fraction contains up to 70 vol% (Taylor et al., 2001a, 2001b, 2010)		treating with UV for vacuum studies
Dust Particle Mean Size	• Over 95% of the particles <1 mm ◘ 50% <60 µm ◘10-20% finer than 20 µm • ~ 10% less than 10 µm • 50% greater than 100 µm (Taylor et al., 2005)	• PSD of <20 µm fraction of JSC-1A shows dust fraction has a larger mean size than typical lunar soils (Park et al. 2008) ◘ JSC-1AF <50 µm ◘ JSC-1A <1 mm ◘ JSC-1AC <5 mm (Gustafson, 2009) ◘ JSC-1A PSD falls between +1 and -1 standard deviation of typical lunar soils (Zeng, 2010)	• Might provide skewed results for dust cleaning of specific particle sizes, particularly <10 µm • Works for initial investigations in current studies • For final flight implementation, suggest using real lunar dust to replicate properties
Moisture Content	• Dry and completely void of water containing minerals (not counting water ice in permanently shadowed crates/ polar regions)	• Contains approximately 0.7 wt% water incorporated mainly into clay minerals (McKay et al., 1994)	• Impacts dust cleaning performance due to charging characteristics • Dust needs to be pre-treated in vacuum
FeO composition	• Lunar mare (>15 wt%) and lunar highlands (5 wt%) in FeO composition (Sibille et al., 2006) None of iron present in Fe+3 form, only Fe+2 and np-Fe (see row below) Ilmenite - a potential toxic iron-titanium oxide also is present in all lunar soils	• Contains 10 wt% FeO Minerals formed on earth contain Fe+3 • Instead, presence of trivalent iron, nano-sized Ti- magnetite - highest magnetic susceptibility	• Chemically a misfit for most lunar soils as FeO content is half way between both type of soils • Different magnetic and chemical properties

Property	Lunar Soil	JSC-1A Simulant	Use for dust contamination study
Nanophase Fe^0	• Tiny Fe grains shown to be formed by vapor deposition due to energetic micrometeoroid impacts. Lunar soil crystallized in magmatic systems with low partial pressures of oxygen- conducive for stable metallic iron (Fe^0) (Hill et al., 2007; Liu and Taylor, 2011; Taylor et al., 2005). • Ubiquitous presence of np-Fe • Magnetic susceptibility of soil particles increases as grain size decreases	• Does not contain nano-phase iron (Fe^0) and ilmenite	• Possible impacts of Fe^0 on dielectric properties not representative in simulants • Nanophase Ti provides magnetic susceptibility but may be skewed with high magnetic susceptibility • Skews cleaning results if magnetic brushes tested
Electrical Properties	• Low electrical conductivity • Dielectric Constant (Olhoeft & Strangway 1975) ◘ k= (1.93+/- 0.17)^ρ ◘ ρ is the bulk density in g/cm^3. Eq based on All Apollo samples • Apollo (17,14) soils 3.18-3.8 at 24 GHz and 18 GHz (Calla and Rathore 2012) • Other reviews from remote observations of lunar surface show a range between 1.5-3 • Loss Tangent: Apollo 17 ~ 0.008	• Dielectric constant ◘ Ranges from 3.5 (-190ºC) to 4.5 (200ºC) within microwave frequencies (1.7GHz to 31.6 GHz) ◘ When measured at room temperature 3.61-4.22 loss tangent 0.11-0.29 (Calla and Rathore, 2012)	• Some laboratory measured data shows comparable values between JSC-1A simulant and some lunar soil samples • Variations in temperature and chemistry between simulant and soil impact values • One simulant may not completely envelop dielectric properties of all lunar soils
Thermal Properties	• High Solar Absorptance: 0.76 • High Emittance: 0.93 • Low Thermal conductivity 5×10^{-4} W/m-K (Gaier et al., 2007, 2012, 2013)	• α (thermal absorptivity) of the simulants range from 0.39 to 0.75 ◘ JSC-1A: α=0.66, ε=0.89 ◘ NU-LHT-1D: α=0.66, ε=0.89 • Lower than representative mare and highlands lunar soils (Gaier et al., 2007, 2012, 2013)	• Not recommended for investigating thermal properties of lunar dust • Does not impact dust cleaning conducted in this research. But results may be skewed if thermal measurement techniques utilized for residual dust coverage

2.4. Summary

To summarize, more than one property and characteristic of lunar dust contributes to the dust contamination problems of space hardware. Table 2.4-1 summarizes these core characteristics of lunar dust particles that have led to several dust problems during the Apollo missions and will be hazardous for future missions. The table also identifies the requirements for the SPIcDER system operation to mitigate the problems produced by these properties of lunar dust. Other properties of lunar dust that specifically contribute to potential health effects are detailed in Chapter 8.

Table 2.4-1. Summary of lunar dust characteristics that lead to dust contamination problems of space hardware including spacesuits

Property	Dust contamination issue	Requirements for the SPIcDER operations
Physical characteristics • **Sharp and jagged edges** • **Surface area**	Leads to mechanical adhesion of lunar dust particles	Remove dust deposited on the fabric (Static Mode of Operation, Chapter 5)
Electrical Properties: charged dust	Leads to electrostatic adhesion of lunar dust particles	Repel/levitate dust floating or in contact with the fabric (Dynamic Mode of Operation, Chapter 5)
Thermal Properties: high absorptivity	Leads to high thermal load when surface is coated with dust	Remove dust deposited on the fabric (Static Mode of Operation, Chapter 5)

Most geotechnical properties of JSC-1A simulant are similar to that of lunar soils. These primary characteristics of morphology and PSD of the JSC-1A are assumed to be sufficient for initial investigations of the SPIcDER technology. However, for final flight development, the SPIcDER performance parameters will need to be optimized using real lunar regolith and return samples.

Part B: Lunar Dust Problems on Spacesuit and EVA Systems

2.5. Dust Encounter during Apollo Missions and Lessons Learned

Several anomalies due to dust were encountered during the Apollo missions as reported by both flight crew during and after the missions, and by post-flight investigations of the suits (Gaier, 2005; Wagner, 2006; Christoffersen et al., 2008). Apollo suits were exposed to the lunar surface environment for less than 24 hours per mission compared to the training suits on Earth that were

used for over 100 hours of training prior to the missions. Even then, the EVA suits used on the lunar surface showed considerable degradation and worse suit abrasion than the training suits (Gaier, 2005). Steps taken during Apollo mission to clean dust particles from the dust contaminated suits were not sufficient to mitigate problems.

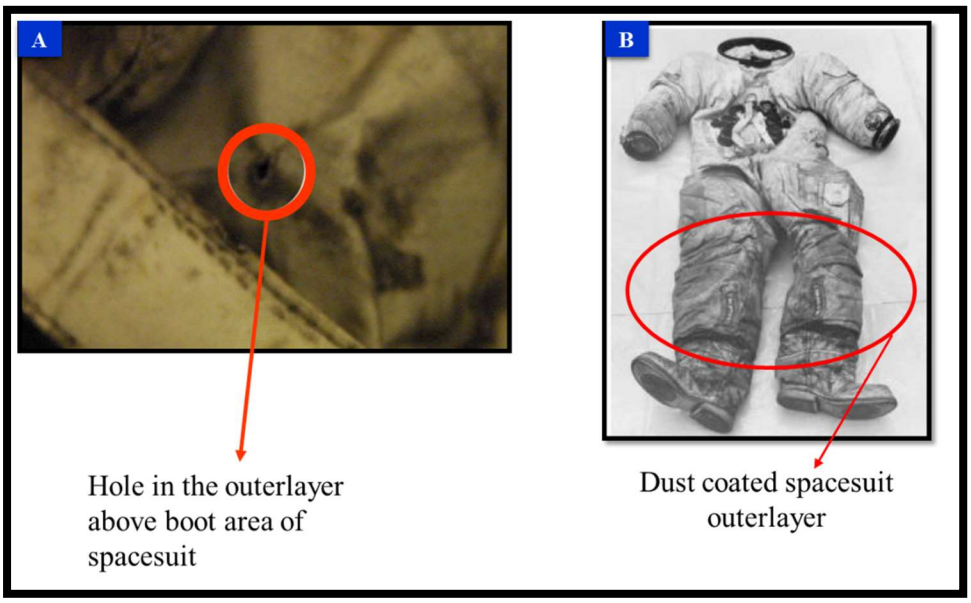

Figure 2.5-1. [A] Portion of Apollo 17 Harrison Schmitt's suit outerlayer showing a hole worn through the outerlayer above the boot (Gaier, 2005), [B] Apollo 12, Lunar Module pilot, Alan Bean's suit coated in lunar dust (Christoffersen et al., 2008).

In addition to dust problems while on EVAs, astronauts were exposed to dust directly when they returned to the Lunar Module (LM) and doffed their dust coated spacesuits. The dust that was accumulated on the suits ended up on the floor and floated within the LM. The exposures were brief but sufficient to cause acute health effects from dust inhalation that included sore throat, sneezing, and coughing (Cain, 2010).

The following sections summarize the problems faced by Apollo astronauts with lunar dust particularly in the context of anomalies associated with spacesuits and analysis from post-flight investigations conducted on the some of the suits.

2.5.1. Summary of Spacesuit Anomalies during Apollo Missions

Based on Apollo mission documentation and experience from the six Apollo missions, approximately 25% of the Apollo astronaut references seem to pertain to dust interactions with spacesuits during their post-mission reports (Gaier, 2005 and Wagner, 2006). These references to

dust effects by astronauts include directly observed effects such as dust adhering to spacesuit fabrics. Other indirectly related and subjectively interpreted references by astronauts also exist reporting on unusual system behaviors due to dust exposure such as suit pressure decay and problems with fittings. Table 2.5-1 provides a consolidated summary of dust effects primarily related to spacesuits and its components using data from multiple previous publications that evaluated the impacts of dust during Apollo missions.

Table 2.5-1. Summary of dust effects on spacesuits during Apollo missions

Category (Specific to spacesuits)	Apollo Missions	Dust Effects (Gaier, 2005; Wagner, 2006)
Seals and Connector Issues	Apollo 12, 15, 16, 17	▪ Apollo 12 wrist and suit hose locks became difficult to operate ▪ Apollo 15 crew hampered by difficulty in connecting and disconnecting Primary Life Support System (PLSS) Pressure Garment Assembly (PGA) ▪ Apollo 16 lunar operations affected by dust in zipper led to difficult operation; wrist ring pull connectors were covered with dust, degraded mobility ▪ Apollo 17 crew reported stiff glove connectors, stickiness in helmet and visor retraction ▪ Other equipment mechanisms jammed on every mission
Seal Failures/Pressure losses	Apollo 11,12	▪ Apollo 11 crew reported increased suit pressure losses ▪ Apollo 12 showed higher than normal suit pressure decay due to abrasion. Pete Conrad's suit was tight before first EVA. Leak after first EVA 0.15 psi/min, leak after second EVA 0.25 psi/min (Safety limit was 0.30 psi/min) ▪ Both Apollo 12 crewmen reported a higher than normal suit-pressure decay on the last pressure check ▪ Seals on return samples casing failed. Dust could not be completely cleared off fittings

Category (Specific to spacesuits)	Apollo Missions	Dust Effects (Gaier, 2005; Wagner, 2006)
Wear and Tear (Abrasion)	Apollo 12, 17	▪ Apollo 12: Conard and Bean's suit worn above knee. Several Kapton multi-insulation layers (MLI) and micrometeoroid protection layers breached. Considerable dirt adhesion to boots and gloves, suit material just beneath top of lunar boots chafed and worn out outer layer ▪ Apollo 17: Hole in outerlayer above the boot area of Harrison Schmitt's suit. Apollo 17 had several falls on lunar surface (See Figure 2.5-1A) ▪ Apollo 17: Cover gloves for core drill heavily abraded, worn within 2 EVAs (of 3)
PLSS (Thermal Control Problems)		▪ Blackbody effect observed due to increased dust on the outer layer of the Apollo suits leading to increased thermal load on the life support system
Visor/Displays	Apollo 14,16,17	▪ Apollo 14 Crew reported helmet visor scratches that decreased visibility. PLSS Remote Control Unit displays were abraded and could not be read ▪ Apollo 16: Mobility unit overvisor of the commander on 3rd EVA would not retract due to dust accumulation on helmet ▪ Apollo 17 Cernan's gold visor got very dirty and dusty and scratched up very early in the first EVA
Operational		▪ Astronaut time was devoted to ineffective cleaning of spacesuits and components

2.5.2. Post-Flight Investigations of Apollo Spacesuits

Limited post-flight investigations were conducted on Apollo EVA spacesuits to specifically determine the degree to which suits suffered contamination, abrasion, wear, and loss of function due to exposure to lunar dust. This section summarizes results from these limited studies where detailed post-flight investigations were conducted on selected suits.

2.5.2.1. Apollo Era Investigations

The only known post-flight investigation on Apollo suits during the Apollo era was conducted in 1970 at the White Sands Test Facility (WSTF) that examined Alan Bean's A7L suit after the Apollo 12 mission (See Figure 2.5.1B). The suit was dissembled and tested for detailed analysis of the outerlayer Integrated Thermal Micrometeorite Garment (ITMG) shortly after the flight. Though the results from these detailed post flight analyses are not available publicly and documented in internal NASA TRL-169-001 and TRL-169-00 reports, a later report in 2008 by Christoffersen et al., state that these WSTF tests were not specifically designed to evaluate lunar dust effects on the spacesuit materials themselves. However, preliminary data on PSD and relative total amounts of lunar dust adhering to and contained within the layers of ITMG fabric and other components were examined during this study. WSTF tests specifically evaluated fabric layers over the left kneecap and below the knee, as they were the most dust-coated regions as seen in Figure 2.5.1B. Measurements were taken on both the outer and inner surfaces of the 1a -Teflon and 1b-beta fabric layers, and on the outer surface of the aluminized Kapton® (details on Apollo fabric layers illustrated in Chapter 8). Optical microscopy with some limited application of the electron probe micro-analyzer was used for the analysis for a limited study of wear and degradation of the fabrics. Findings from these WSTF tests captured by Christoffersen et al. in their report confirmed the following

- Abrasion of the outerlayer was due to effects from the suits encountering lunar soil rather than the actual wear and tear of the spacesuit due to contact with hard surfaces
- Results provided evidence of dust particle penetration into the weaves of the 1a-Teflon 164 and 1b-beta cloth fabric layers. Additionally, Layer 2 Kapton was shown to be lightly contaminated
- Concentration of dust particles was observed to fall off rapidly between the outer and inner surfaces of the 1a-Teflon 164 first layer and 1b-beta cloth. 1b-beta cloth layer aided to reduce particulate penetration into the Kapton layer, particularly for <10 μm particles size.

2.5.2.2. Recent Investigations of Apollo Suits

There has been a lack of any follow-on studies or analysis on the flight suits beyond the WSTF tests up until 2008 where detailed forensic analysis was conducted by Christoffersen et al. as part of NASA Smithsonian Dust Investigation Research Team (NASDIRT) project. The project was

targeted towards strategic planning of future lunar exploratory spacesuits. The team conducted detailed evaluation of Apollo suit degradation to validate many of the crew and mission reports on lunar dust effects. This more recent study utilized suits from the Apollo time that were more than 35 years old.

Investigations were conducted specifically on the outermost soft fabric layers of the Apollo 12 (Alan Bean's suit) and Apollo 17 (Harrison Schmidt's suit, see Figure 2.5-2) ITMG assemblies, Apollo 17 EVA pressure gloves and lunar boots, and Apollo 16 EVA and Intra Vehicular Activity (IVA) pressure gloves. The study also included filter materials from the Lithium Hydroxide (LiOH) canisters from the Apollo Command Module (CM) to determine the amount and type of any lunar dust particles they may have captured from the spacecraft atmosphere. Observations and analysis were conducted using Scanning Electron Microscope (SEM), Field Emission SEM (FESEM), X-Ray Fluorescence Spectroscopy, optical imaging, high yield particle sampling with adhesive tape, restricted particle sampling, and microscopic imaging. Overall findings from this study are summarized in Table 2.5-2, with specific focus on the soft areas of the suit.

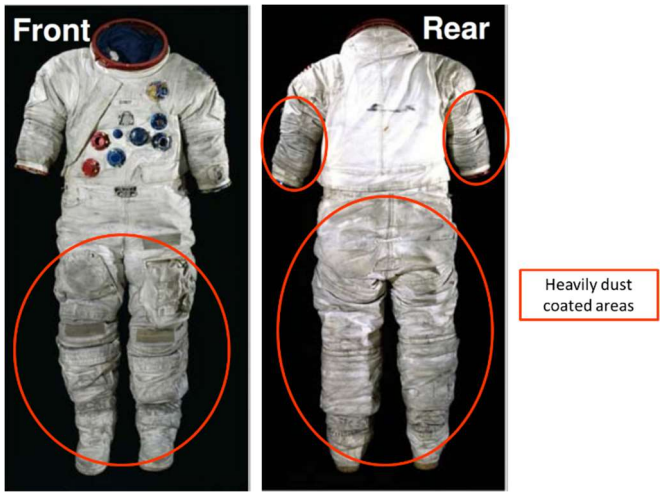

Figure 2.5-2. Apollo 17 Harrison Schmidt's spacesuit A7LB (Christoffersen et al., 2008)

Table 2.5-2. Summary of findings from Apollo suit investigations (Christofersen et al., 2008)

Category	Observations	Relevance to Current Research
Generic Observations	• Even after 35 years since spacesuit return, disassembly and/or physical handling, suits were still coated with lunar dust particles • Front part of legs had higher dust concentration compared to rest of the spacesuit • Visual inspection and optical microscopy showed that Apollo 17 suit had higher-level lunar dust contamination relative to Apollo 12 suit • Higher lunar particle quantity on Apollo 17 related to o Apollo 17 suit had over twice the EVA exposure time compared to Apollo 12 o Number of astronaut slips and falls during Apollo 17 significantly higher than Apollo 12 • Dust was more concentrated knees and elbows where significant wear on the fabric was also noted	• Focus on dust contamination of outerlayer of suit • Focus areas are knees, boots and elbows • Long-term exposure to dusty environment
Abrasion	• Outer layer of Apollo 17 (Harrison Schmidt's) suit had a hole in the area above the boot • Apollo 17 EVA pressure glove showed number of effects of physical abrasion of all components • Physical wear and abrasion appeared to increase the fabric's capacity to retain lunar dust contamination	• Focus area are knees • Easier to protect suits before dust accumulates to prevent abrasion
Particle Density	• T-164 Teflon outer fabric woven material retained considerable number lunar particles (up to 2.5 x 10^5 / cm^2 of the fabric) o Even after 35 years since spacesuit return, disassembly and/or physical handling o Most frequently found grains were lunar glass (400 grains) and plagioclase (350 grains)	• Minimize accumulation of dust particles
Particle Sizes and Type	• High-yield particle sampling using adhesive tape and X-Ray Fluorescence chemical analysis of Apollo 17 fabric surfaces confirmed o 80% particles on fabric to be lunar soil particles, averaging 10.5 µm in diameter with a positive skew to larger particles (Figure 2.5-3) o Analysis on 840 grains showed mean of 10.7 µm (Figure 2.5-3) o Rest of the particles were intrinsic fabric materials or environmental contaminants	• Focus on preventing <50 µm particle sizes

Category	Observations	Relevance to Current Research
	○ Number of particles are the loosely held particles removed by adhesive tape and not the penetrated particles ○ Lunar glass (mainly agglutinic) and plagioclase feldspar particles seemed to make up 80% of the total particle count ○ Although pyroxene was found to be lower count than plagioclase and glass particles, recalculation of particle population to a modal basis (volume %) shows the outer fabric preferentially "select" and retains pyroxene, but does not retain glass particles	
Wear and Tear	• SEM investigation of T-164 woven Teflon fabric confirmed presence of lunar soil particles on the outer fabric layer • Ability of dust particles to cause separation and fraying of the Teflon fibers was noticed • Progressive transformation of T-164 Teflon from its intact state, to a worn state on both suits. Shows physical wear, particularly ITMG T-164 woven Teflon • Individual Teflon fibers became progressively split and frayed • An increasing transfer of fragments of glass fibers from underlying beta cloth to exposed surface of Teflon fabric was observed	• Prevent dust settling on the outerlayer

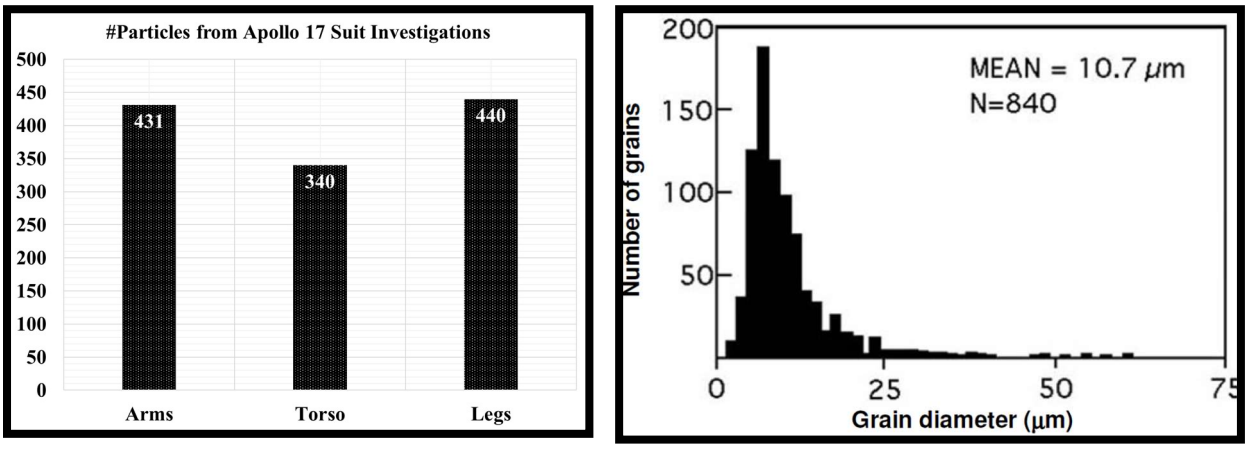

Figure 2.5-3. [Left] Number of lunar dust particles on 3 areas of the Apollo 17 suit (*Plotted by author using data from Christoffersen et al., 2008*), [Right] PSD of 840 particles from Christoffersen et al. (2008) study.

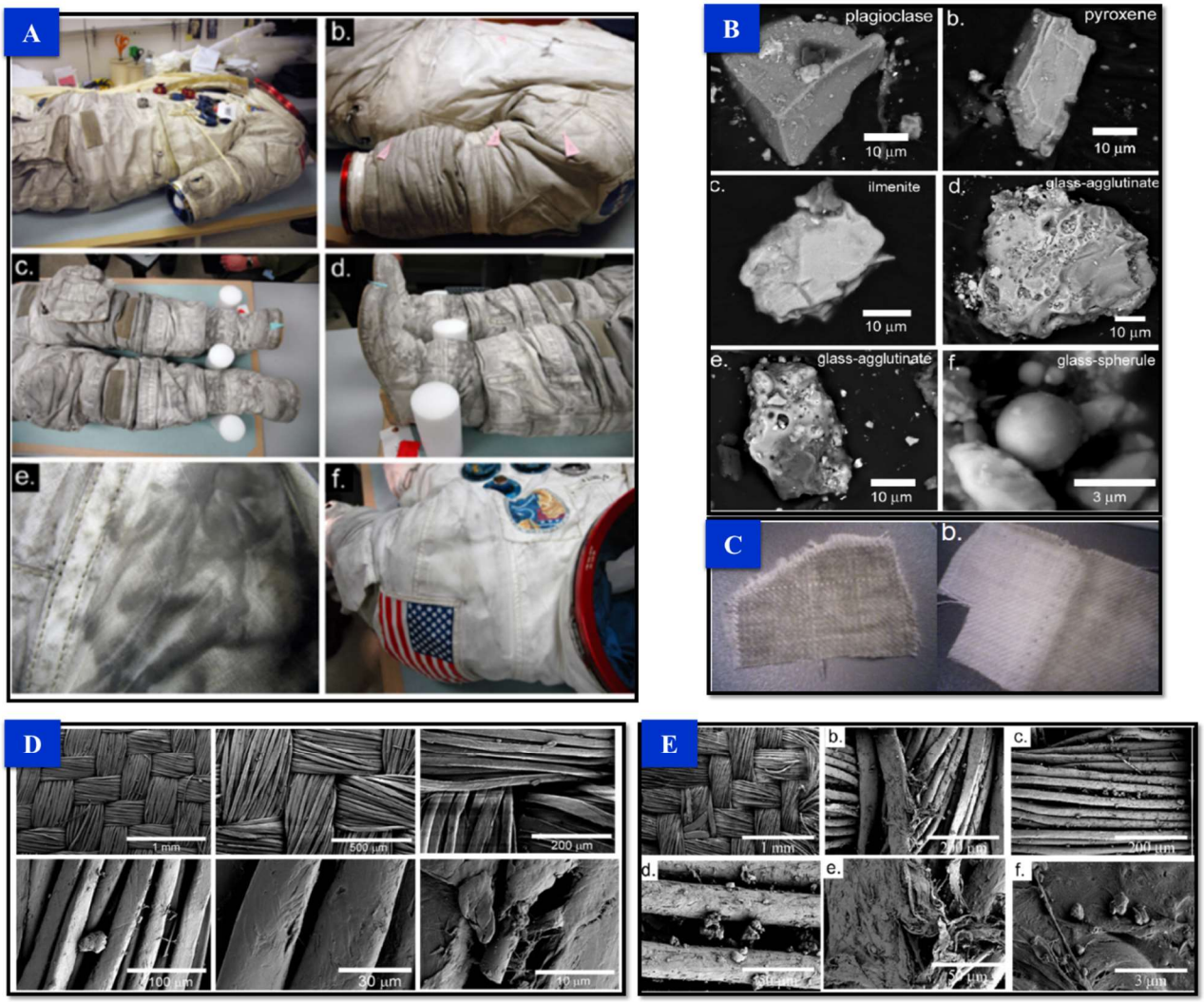

Figure 2.5-4. [A] Apollo 17 A7LB spacesuit during post flight investigations, [B] SEM images of particles from the surface of the Apollo 17 T-164 Teflon outerfabric, [C] Samples of outer fabric from Apollo 12 spacesuit, left is from left knee and right side is from left shoulder where the lighter area was covered under U.S. flag patch, [D] SEM secondary electron images of T-164 Teflon from left knee area of Apollo 12, [E] T-164 Teflon fabric from unexposed area on left shoulder on Apollo 12 ITMG covered by the flag patch (*All pictures from Christoffersen et al., study in 2008*).

Results from these detailed post-flight analyses emphasize the significant role for lunar soil interactions in causing physical wear and degradation of spacesuit outerlayer fabrics (and other components of spacesuits not reported here). It is evident from challenges faced during Apollo that if longer duration lunar expeditions in the future, dramatic measures are to be taken to mitigate the impacts of dust contamination to increase the durability of spacesuits.

2.5.3. Apollo Dust Mitigation Techniques

Apollo missions implemented several dust mitigation techniques for various equipment contaminated with dust with varying degrees of effectiveness. Techniques such as lubrication, wiping, dust covers, brushing and vacuuming to reduce dust contamination were implemented by Apollo astronauts during the missions (Gaier, 2005; Wagner, 2006). Cleaning materials and suits reduced some dust contamination; however, the root cause of dust problem, i.e. preventing dust accumulation and adhesion on the suits was still a major problem during the missions.

Reports from Apollo missions note that spacesuit cleaning primarily consisted of brushing and vacuuming. A nylon bristle brush was known to have been provided to dust off the suits and visors. However, it was reported to be effective only to remove coarse grains and not very effective for fine particles (Gaier, 2005; Wagner, 2006). Various crew reports note that brushing produced varying results, abraded surfaces and was time-consuming, often-exceeding operational timelines due to cleaning (Gaier, 2005; Wagner, 2006).

Apollo 12 crew reported wiping their wrist rings and neck rings to remove dust before putting them back on, but they had noticed that the connectors were harder to put on. Also, wiping only appeared to improve the situation in some cases, but was not as effective entirely. (Wagner, 2006).

Post-flight mission reports suggest that other techniques implemented by crew during these missions included crews banging against hard surfaces prior to ingress into the LM. Some loose dust to varying degrees was removed and helped particularly when crew were fatigued after long EVAs which greatly limited their manual dexterity to clean their suits (Wagner, 2006). Alan Shepard during Apollo 14 remarked, "*just banging the boots against the ladder was enough to shake off that dust"* (Wagner, 2006).

Problems with scratches on the visors and dust accumulation resulting in visibility reduction problems were also not corrected or addressed during the Apollo program. These simple mitigation strategies did not prevent dust contamination problems during the Apollo missions and in turn valuable astronaut time was spent in housekeeping activities like brushing off and wiping down equipment including spacesuits. Several astronauts noted that suits might not sustain more surface activities if longer stays on the lunar surface are to be continued. It's been agreed that more sophisticated and efficient dust removal techniques are necessary for longer duration missions.

2.5.4. Summary of Dust Effects on Spacesuits

Apollo missions proved the deleterious effects of dust on spacesuits. Table 2.5-2 summarizes possible impacts of dust for future missions on various spacesuit components based on lessons learned from Apollo thus far. It was concluded from the literature study conducted during this research that since the outerlayer of the spacesuit is the first element on the suit that is exposed to dust, focusing on preventing dust accumulation on this surface would help mitigate several of the below-mentioned issues for the soft suit areas and protects dust penetration into the inner layers.

Table 2.5-2. Possible effects of dust on Spacesuits (Wagner, 2006 and 2008; Gaier 2007; Christoffersen et al., 2008)

Suit Component	Effect of Dust	Secondary Effect
Outer Garment/Outerlayer Fabric	• Dust accumulation and coating • Degradation of material due to abrasion, fraying of fibers, penetration into inner layers • Possible pressure leaks if inner layers penetrated	Dust transfer to airlock-habitat Cleaning and maintenance time
Bearings	• Seal degradation and potential leakage • Chemical reactivity with metallic components, • Abrasion	Need for spares and maintenance
Visors	• Scratches/Pitting due to severe abrasion • Loss of coatings and therefore obscuration	
Lighting	• Reduced illumination due to dust coating	Vision impairments
Portable Life Support System	PLSS Cooling Systems: • Contamination of evaporative and venting membranes and transport blockage of PLSS cooling and venting systems • Seal degradation, and leaks in quick disconnects, connectors • Contamination of orifice and transport blockage of O_2 system regulators • PLSS Vent • Increased heat load due to coated outer layer	Requiring spares/maintenance
Suit electronics	• Effect on tribocharging due to changes in electrical conductivity of suit surfaces • Spurious discharge effects	Loss of communications, detrimental to suit electronics
Seals and Zippers	• Jammed seals and zippers • Leaks leading to depressurization	
Operations	• Additional maintenance time	Impact to science and mission objectives

Part C: Mechanisms of Dust Effects for Spacesuits

2.6. Mechanisms of Adhesion and Wear

As described in section 2.2, the dryness of the lunar surface (most of the surface except for permanently shadowed regions) and low electrical conductivity effectively make the lunar soil an insulator, and the conditions are conducive to holding the static charge developed. Lunar dust is thus characterized by its tenacious adhesive property, sticking to everything with which it encounters, causing abrasion and wear. This section specifically explores the various mechanisms through which lunar dust adheres and causes wear of spacesuits (and other components). Mechanisms of wear and adhesion due to lunar dust can be described using the science of interacting surfaces in relative motion termed as tribology.

2.6.1. Adhesion

Adhesion is the phenomenon that occurs when two surfaces are pressed together either under a pure normal load or under combined normal and shear forces (Israelachvili, 2011). Normal tension force must be then exerted to separate the surfaces. Adhesion of dust and powders to surfaces has been an area of study for many years (Zimon, 1969; Walton, 2007). Generally, the main factors facilitating adhesion are extensive such as the Van der Waals (VdW) forces, electrostatic forces, chemical bonding, capillary forces, oxidation, and magnetic forces. However, some of these forces of adhesion are reduced in the lunar environment due to the lack of atmosphere and the dry environment. It's been reported that the predominant forces that contribute to adhesion of lunar dust to surfaces are short range VdW forces (related to surface energy) and long range electrostatic forces (related to static electric image forces). The electrostatic forces are expected to be much higher due to the charging effects of lunar dust by solar wind and UV ionization (Walton, 2007 and 2008). These VdW and electrostatic interactions can be the driving force depending on the size and charge of the dust particles on the lunar surface. Surface energy, roughness, mechanical properties, and electrical properties are all known to contribute to the adhesion characteristics of lunar dust (Walton, 2007; 2008).

Therefore, to design an optimal solution to protect spacesuits from dust contamination it is necessary to identify the dominant components of the adhesive force (VdW and electrostatic) and

reduce that force by either modifying the surface, mechanically separating dust from surfaces or by electrostatically removing the dust particles or by a combination of these methods.

A detailed discussion of the underlying physics of VdW and electrostatic forces of adhesion is beyond the scope of this research. However, to quantify the adhesion forces involved for dust particles, the research explores simplified theory and provides a generic overview for approximating the values of adhesion forces. This allows to gain an understanding and approximation of the lunar dust particle interaction with a surface. For an in-depth discussion of the adhesion forces the interested reader is referred to references Ruths and Israelachvili, 2011; Walton, 2007 and 2008; Dove et al., 2007.

2.6.1.1. Van der Waals Forces

A generic overview of VdW forces is described. VdW forces are driven by inter-molecular or inter-particle forces acting between two materials in close contact (nearly touching), combining the effects of interactions between permanent or induced dipoles. The surface energies of the particle and the substrate in contact play a key role in VdW forces. Surface energy is defined as the work required to separate a unit area of two surfaces in contact on a molecular scale. Particle roughness and mechanical properties are also known to affect VdW forces as they affect the spacing between the two surfaces in contact (Dove et al., 2011; Ruths and Israelachvili, 2011). In addition to the collective VdW forces, materials in contact can also interact by other weak bonding interactions such as the Lewis acid-base interactions that can contribute to the surface energy (Walton, 2007). A detailed discussion of the underlying physics of VdW forces is beyond the scope of this research, however, informative to explore the simplified theory to gain an understanding of particle interaction with a surface. For an in-depth discussion of, the interested reader is referred to Ruths and Israelachvili, 2011 and Walton, 2007.

Equations for quantifying VdW forces have been derived in literature by approximating the dust particles as a sphere. While this may be a poor approximation for lunar dust particles as they come in various jagged and angular shapes (as described in section 2.2), for purposes of understanding VdW force, spherical particles are assumed. VdW force, F_{VdW}, between a spherical particle and a flat surface as shown in Figure 2.6-1 can be approximated using Equation 2 (Ruths and Israelachvili, 2011; Dove et al., 2011)

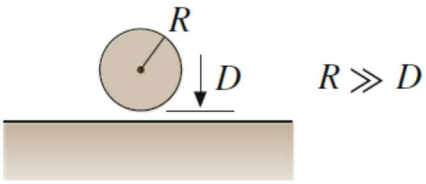

Figure 2.6-1. Schematic approximating dust particles as spheres to derive an equation for Van der Waal forces (Ruths and Israelachvili, 2011)

$$F = \frac{A_H R_p}{6D^2} \tag{2}$$

Where, *Rp* is the radius of the sphere (dust particle in this case), *D* is the spacing between the sphere and the surface (spacesuit is the surface in this case) and $R_p >> D$. A_H is the Hamaker constant and is material dependent. Negative value of force implies attraction between the surface and the dust particle causing adhesion of dust. The Hamaker constant A_H can be estimated from Equation 3.

$$A = 12\pi D^2 \Delta\gamma \tag{3}$$

Where, $\Delta y = \sqrt{(y_p, y_s)}$, where y_p and y_s are the surface energies of the dust particle and the substrate (spacesuit) in contact respectively. Typical values of the Hamaker constant are on the order of ~10^{-19}-10^{-20} J and is often difficult to measure experimentally. The value of *D* is typically on the order of ~4 Å (or ~0.4 nm) when the two surfaces are in contact (approximated molecular distances between the dust particle and the substrate) (Walton, 2007).

The VdW force acting between two nearly touching bodies as described by Equation 2, is a net attraction that scales linearly with particle size and varies with the inverse second power of the distance between surface molecule centers of the two bodies in contact. This force is therefore dominant in very short-ranges (on the order <10 nm) compared to typical dust particle dimensions. For example, for a 50 µm spherical dust particle, the F_{VdW}

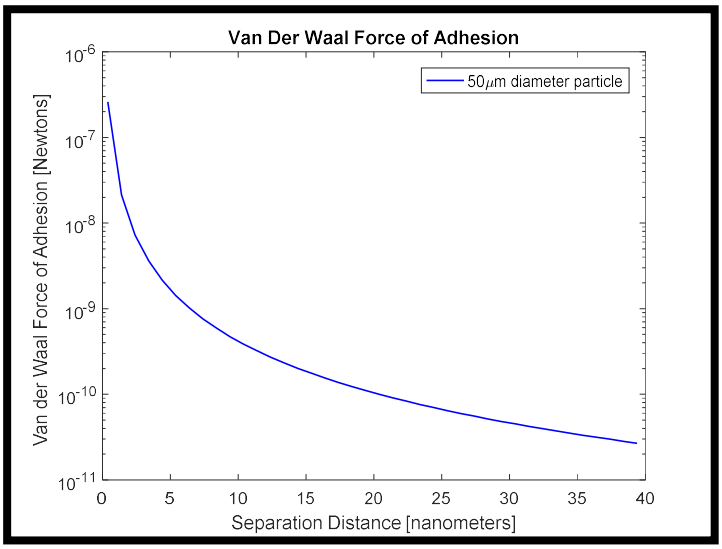

Figure 2.6-2 Van der Waal force of adhesion for a 50 µm particle plotted based on Equation 2

decreases by two orders of magnitude by the time the two surfaces are separated by 40 Å (~4 nm), and by four orders of magnitude by the time they are 40 nm apart as shown in Figure 2.6-2. Theoretically predicted VdW force magnitudes could be higher and could have considerable uncertainty in the estimates due to the jagged shapes of the lunar dust that would increase the contact separation. The VdW forces are sensitive to parameters such as, particle shape, roughness and separation distances and quantifying these parameters is beyond the current scope.

2.6.1.2. Electrostatic Forces

The other dominant adhesion force between particles are the electrostatic forces or the columbic attraction force. Two types of electrostatic interactions are possible. Spontaneous transfer of charge may occur between two dissimilar materials in contact, due to a phenomenon called contact electrification also known as triboelectric effect (Ruths and Israelachvili, 2011; Dove et al., 2011). The interaction is based on differences in work function. Electrostatic interaction is generally seen to be stronger with increasing difference in work function (or electron affinity) between the two materials (Ruths and Israelachvili, 2011). During the tribocharging process, the difference in work function of the materials during contact leads to electron transfer from the material of lower magnitude work function (example: dust particle) to the material with higher magnitude work function (example spacesuit material) that hold tightly onto its electron, resulting in modified charges on the surfaces leading to adhesion. A contact potential difference (Φ_c) is generated due to the transfer of electrons between the two materials that ranges between 0-0.5 V (Ranade, 1987). This transfer of charges produced in the surface layers of the particle and the surface can be approximated by Equation 4a. Where ε_o is the permittivity of free space and D is the separation distance that is approximated as ~4 Å.

$$F_{el} = \frac{\pi \varepsilon_O R_p \Phi_c^2}{D} \tag{4a}$$

The other type of electrostatic interaction occurs when charged dust particles are in the vicinity of the substrate (and other components). Coulombic force of attraction exists between the charged particle and the substrate, leading to the dust particles adhering to the surfaces. The lunar surface is devoid of atmosphere and is nearly dry and the minerals comprising the regolith are insulators (nonconductive). This means that once lunar dust particles acquire charge, they can maintain the charge on the particle surface and not conduct the charge to an interior "ground" potential as might

occur on earth. As explained in section 2.2, charging of lunar dust particles occurs through various sources such as UV and solar winds. The Coulombic force of attraction are long range forces and likely to dominate between distances of 100 nm to >0.1 μm (Walton, 2007).

Of the adhesion forces present at the lunar surface, it's been shown that only electrostatic forces have the capability of attracting dust particles to spacecraft surfaces from a distance (Dove et al., 2011, Walton, 2008). Therefore, by reducing the electron transfer between lunar dust particles and suit material, dust adhesion to surfaces can be minimized.

Equations for quantifying the Coulombic force of attraction between spherical particles with that of substrate forces have been derived in literature by approximating the dust particles as a sphere (Ruths and Israelachvili, 2011; Dove et al. 2011; Walton, 2007). The electrostatic force of adhesion is given by the electrostatic image force which is described as arising from bulk excess charges on the particle and the surface causing a coulombic attraction (Bowling, 1985). For a charged dielectric spherical particle contacting a planar conducting surface, the attractive Coulombic force is given by Equation 4b

$$F_i = -\alpha \frac{q^2}{16\pi\varepsilon_0 R_P^2} \tag{4b}$$

Where q is the particle charge with an assumption that it is uniformly distributed on the dust particle surface, Rp is the radius of the particle, ε_o is the permittivity of free space and α is a correction factor that depends on the polarizability of the dielectric particle (dust particle). This value of α is typically 1.9 for a dielectric constant of 4, which is similar to the lunar dust dielectric constant (Hays, 1988). For purposes of this research the electrostatic image force is utilized for analyzing adhesion and comparing with the electric forces generated by SPIcDER. The effective electron work function of lunar dust particles is unknown at this time and yet to be understood.

Using the theoretical equations described above for VdW and the image force for charged particles, the expected dominant force of adhesion are plotted for varying particle diameters and separation distances as shown in Figure 2.6-3. From a general overview standpoint, the VdW forces are expected to be dominant on particles that have already adhered (~4 Å separation distance, short range forces. 0.4 nm plot in Figure 2.6-3). For particles at very small separation distances on the order of < 1.5 nm, Vdw forces are dominant for particles with radii less than ~200 μm. As the separation distances increases as shown in the Figure 2.6-3 (4 nm plot in this case), the

electrostatic forces of adhesion start to dominate over the VdW forces for particle sizes above ~35 μm (long range forces).

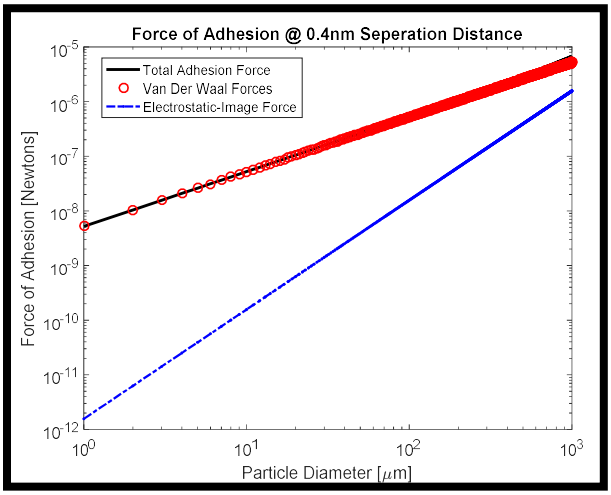

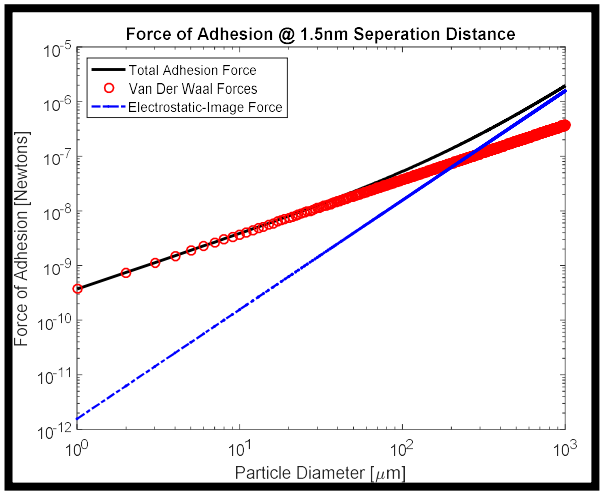

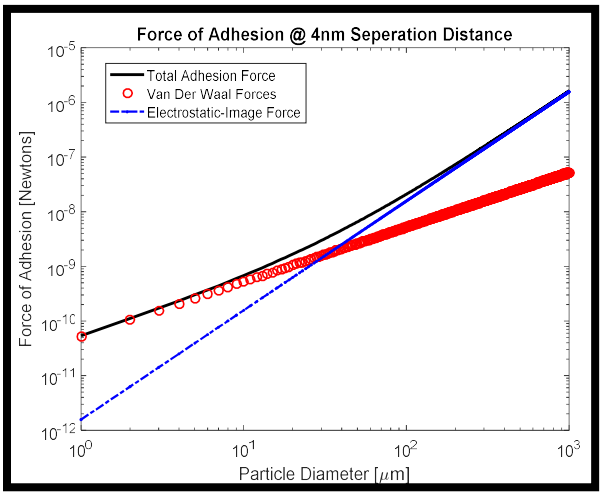

Parameter	Value	Units	Source
A_H	10^-21	Joules	Israelachvili, 2011, Walton 2007
Particle Diameter	1-1000	μm	Lunar dust particles of interest
R_p	Particle Diamter*0.5	μm	
D	0.4, 1.5, 40 (0.4 represents surfaces in 'contact')	nm	Israelachvili, 2011, Walton 2007
α	1.9		Hays 1988
Particle Charge Density (P_q)	-3.05E-06	C/m2	Chestnutt and Marshall 2013
q	P_q*Particle Surface Area	C	
εo	8.95E-12	F/m	

Figure 2.6-3 Dominant forces of adhesion on lunar dust particles at various separation distances. *Table shows values utilized for the plots*

The theoretical equations utilized for both types of adhesion forces are based on the assumption that the single dust particle in contact has a perfectly spherical shape, is interacting with a perfectly flat plan surface, and has a uniformly distributed charge. On the lunar surface however, the dust particles are rough with jagged surfaces as explained in section 2.2. These variations in geometry will increase the separation distances between the particle and surface. Furthermore, the particles may have localized charged-patch forces rather than uniformly distributed charge as modeled in the image force potentially dominating the VdW Forces. These differences in real lunar environments would impact the magnitude of the adhesion forces varying from the theoretically predicted particle adhesion and potentially increase the electrostatic adhesion forces over VdW

force. Quantifying these VdW forces and the contact potential difference are beyond the scope of this research.

It has also been proved in previous adhesion studies that the ultra-high vacuum (UHV) and dry conditions of the lunar environment can lead to strongly increased adhesion dominated by electrostatic interactions. Adhesion studies conducted by Gaier and Berkebile (2012) measuring forces under UHV vacuum conditions (10^{-10} torr) between a synthetic volcanic glass and commonly used space exploration materials indicated that electrostatic forces dominate over VdW forces in lunar environments. It was concluded from their study that dust mitigation strategies that target to reduce electrostatic forces would be more effective than if they attack VdW adhesion. Strategies such as textured surfaces and surface modifications such as the lotus coating may eliminate the effects of VdW forces, however these will be less effective as the decrease in the overall dust adhesion will be minimal. This theory was also proved by experimental verification that textured surfaces do not help shed lunar simulant dust under simulated lunar conditions (Gaier et al., 2011). Therefore, based on previous studies, the approach taken by the current research approach is built on reducing the electrostatic forces of adhesion.

2.6.2. Types of Wear

When the dust particles interact with the spacesuit surface, the motion of the particle on the suit, combined with the motion of the suit itself causes wear of the spacesuit fabric. Post-flight investigations of Apollo suits have shown severe wear of the outerlayer fabrics as discussed in section 2.5.2. This section provides a generic overview of types of wear and relates the interactions of lunar dust particles with spacesuit outerlayer.

Wear may be defined as the removal of material from solid surfaces because of mechanical action. Wear is caused by many mechanisms; however, four main forms of wear have been established in literature (Kopeliovic, 2015). Each wear process obeys its own laws and there may be instances when one of the modes of wear acts in such a way as to affect the others. The following are the four main wear mechanisms:

- Adhesion
- Abrasion
- Surface fatigue
- Tribochemical reaction (Oxidation/Corrosion)

The following sections provide a brief description of the primary wear types that may be the most relevant to lunar missions and lunar dust particles- abrasive, adhesive, and erosive (not mentioned above).

2.6.2.1. Adhesive Wear

The most generic form of wear, the adhesive wear occurs when two smooth bodies slide over each other, and fragments are pulled off one surface and adhere to the other. These fragments may come off the surface later on and be transferred back to the original surface, or may form loose wear particles (Ziemer et al., 2008; Kopeliovic, 2015).

Adhesive wear arises from the strong adhesive forces whenever atoms come into intimate contact as mentioned in in the previous section. During sliding, a small patch on one of the surfaces comes into contact with a similar patch on the other surface and there is a probability, that when this contact is broken, the break will occur not at the original adhesion interface, but within one of the materials. In consequence, a transferred fragment will be formed (Figure 2.6-4).

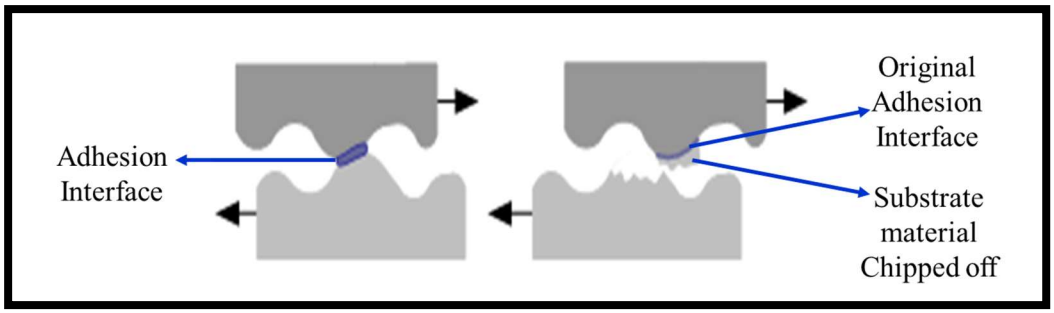

Figure 2.6-4. Adhesive wear schematic *(Author developed picture based on Kopeliovic. D, 2015)*

2.6.2.2. Abrasion/Abrasive wear

Abrasive wear occurs when either a rough, hard surface or a soft surface with hard particles (lunar dust particles in this case) embedded in its surface slides over a softer material (spacesuit fabric in this case). This causes grooves in the soft surface. The material extracted from the grooves is displaced in the form of loose wear particles.

Abrasion can be subcategorized into two types based on degree of freedom; two-body and three-body wear. Two-body abrasion occurs when hard particles or protuberances are fixed on the surface of a body and produce wear on another body (example sandpaper running against a

surface). When abrasive wear is the result of loose wear particles introduced or generated between the contacting two surfaces, it is called three-body abrasive wear (example, sand being poured into two plates rubbing against each other). Relevant to spacesuit contamination, two-body mode of abrasion may occur when the outerlayer of the suit is in direct contact with lunar dust particles, while the three-body mode of abrasion may occur when dust particles get embedded within two suit layers. Both modes of abrasion cause damaging effects on spacesuits (Figure 2.6-5).

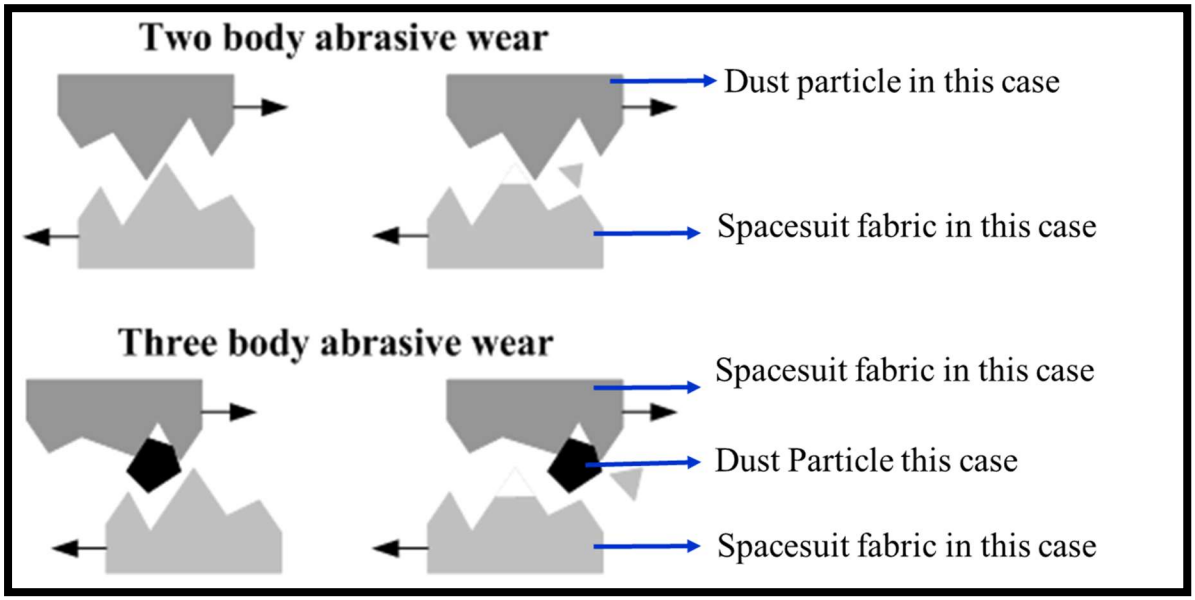

Figure 2.6-5. Abrasive wear schematic *(Author developed picture based on Kopeliovic. D, 2015)*

One of the most fundamental and detrimental attributes of lunar dust is its ability to wear surfaces. During the Apollo 17 lunar mission, lunar dust scratched (abraded) the sun shade of NASA astronaut Harrison Schmitt's helmet to the extent that it obscured his vision in certain directions. Lunar dust also abraded gauge dials that they were unreadable (Wagner, 2006). The lunar science community has identified the abrasive nature of lunar dust as one of the top five physical properties of interest (Kobrick et al., 2011). The importance of abrasion due to lunar dust is ranked high as it affects any material that moves or has a sealing surface and is considered the most severe and costly form of wear affecting lunar operations (Kobrick et al., 2011).

When defining abrasive wear, there could be confusion between fine abrasive wear and a form of relatively benign adhesive wear. In both cases, wear is caused by small hard particles (lunar dust). In one case, the hard particles are abrasives; in the other case, they are small adhesive particles. In both cases, the surfaces are covered by fine scratches in the sliding direction. The two

wear modes can be differentiated from each other because abrasive particles tend to produce a sharp scratch, deep when measured in a profile meter, while the adhesive-caused scratches are often irregular and shallow (Ziemer et al., 2008; Kopeliovic, 2015). For purposes of the current research, it is assumed that the adhesion of lunar dust particles to the spacesuit fabric results in abrasion of the suit materials during movement.

2.6.2.3. Erosion

Erosive wear is caused by impingement of particles (solid, liquid or gaseous), which remove fragments of materials from the surface due to momentum effect (Kopeliovic, 2015 and Mpagazehe et al., 2014). Two types of erosion are mainly encountered, low-speed erosion and high-speed erosion. This type of wear results from sharp particles impinging on a surface such as the cutting of materials by hard particles in a high velocity fluid impinging on a surface. This action is very much like that of sandblasting.

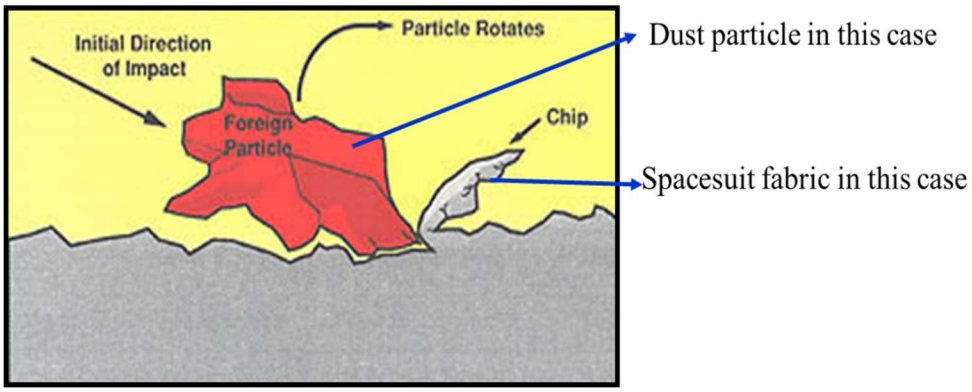

Figure 2.6-6. Schematic of Erosive wear (Ziemer et al., 2008)

During Apollo 12, lunar dust particles had been accelerated by the LM exhaust and caused erosive wear damage to the Surveyor III lander (Wagner, 2006; Mpagazehe et al., 2014). A study was conducted with the JSC-1AF lunar dust simulant to understand the erosive potential of lunar dust (Mpagazehe et al., 2014). Metallic and acrylic test specimens were exposed to erosive wear and the changes in mass, surface topography, transmittance, and reflectance were reported. It was observed that exposure to erosive wear from JSC-1AF, even at moderate velocities (approximately 10.5 m/s), resulted in a significant decrease in direct transmittance and total reflectance, greater than 70% in some cases. The results from their study suggest that optical components such as lenses and mirrors are highly susceptible to damage during lunar landings due to lunar dust particle impingement. While the effects of erosive wear due to sandblasting effects are more likely to occur

on Mars than on lunar missions, the relevance to spacesuits on lunar surface might occur when astronauts would be operating rovers (top speed of lunar rovers from Apollo missions was 8 mph (3.6 m/s). Their suits may be exposed to impinging dynamic dust in such cases.

2.7. Research on Abrasive Effects Of Spacesuit Materials

There have been ongoing research at NASA and by other groups to investigate the mechanisms of dust effects on space hardware and required techniques and technologies to mitigate dust contamination. This section captures some of these past and on-going research particularly focused on the abrasive dust impacts on spacesuits.

2.7.1. Spacesuit Outerlayer Abrasion Studies

2.7.1.1. Abrasion Studies Using Lunar Simulants

Gaier et al. (2009) and Mitchell (2010) evaluated the abrasion wear characteristics of various candidate EVA spacesuit outerlayer fabrics. The results from these abrasion experiments are captured in Table 2.7-1. The following section provides a summary of the tests and overall outcomes. Refer to the table for specific test methodology and results.

A. Abrasion Study 1

Gaier et al. in 2009 evaluated four candidate EVA spacesuit outerlayer fabrics (Kevlar, Orthofabric, Tyvek, Vectran) using simulated lunar dust at NASA Glenn Research Center (GRC). The study focused on characterizing the degree of wear due to abrasion and dust permeation into subsequent layers of the fabric. The candidate spacesuit fabrics were compared against the outer layer at the knee of the Apollo 12 (Alan Bean's) suit as a baseline. The simulant was processed to simulate solar wind exposure. Optical microscope and FESEM were used for analysis. Three variations of tests as listed below were conducted during the study

- Test 1: PTFE made abrasion wheel
- Test 2: leather covered brass wheel S-39
- Test 3: low wheel pressure outside of LDAB

General results from the study are summarized below based the low wheel pressure test and twill weave tests which were the only published results. Figures 2.7-1 and 2.7-2 provide imagery from this abrasion test

- Baseline sample (Apollo 12 knee sample) showed little plastic deformation of fibers but many filaments were shredded
- Uncoated woven fabrics were shown to be vulnerable to dust penetration
- Abrasion test results showed that woven structures were all abraded with the Orthofabric showing least abrasion, while Tyvek sustained little damage
- Plain and twill weave were noted to have had similar results, although twill weaves are noted to be less durable than plain weaves

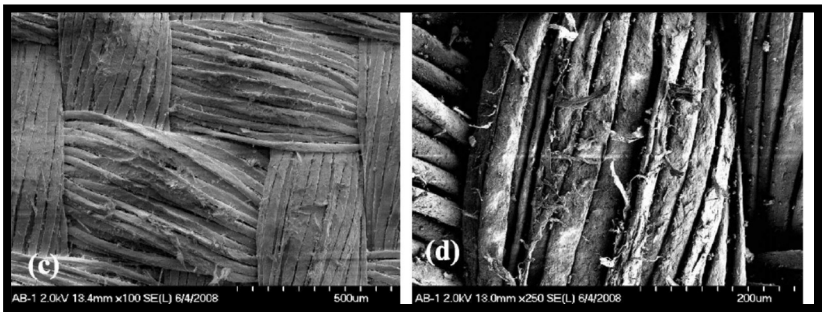

Figure 2.7-1. FESEM photos of Apollo 12: Alan Bean's suit, left knee (Gaier et al., 2009)

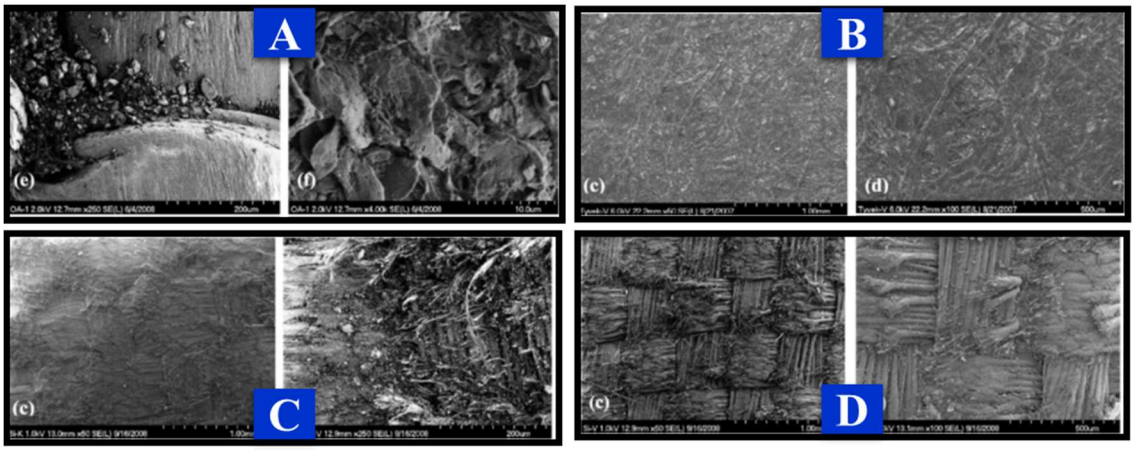

Figure 2.7-2. FESEM Photos of tested Fabrics using PTFE 8000 cycles abrasion. [A] Orthofabric, [B] Tyvek, [C] Kevlar, [D] Vectran (Gaier et al., 2009). *Shown within each section are different magnification scales*

B. Abrasion Study-2

Another test conducted by Mitchell (2010) at NASA JSC evaluated candidate outer layer fabrics for planetary spacesuits comparing abrasion wear characteristics. The degree of wear due to abrasion, dust permeation into subsequent layers using heat seal seam and strength of the fabrics after being abraded were analyzed. The fabrics were arranged in cylindrical elements representing

upper leg assemblies integrated with outerlayer fabric, bladder, and restraint layer. The fabric was abraded with an exposure time of 8 hours, which is representative of future long-term planetary surface EVAs. General results from the study are summarized below and images from the study are shown in Figure 2.7-3. Refer to Table 2.7-1 for details on specific fabrics

- The fabrics using JSC-1 simulant turned a darker shade of gray than NU-LHT-2. The change in color may reflect the probable effect of solar absorbance/ thermal load
- There was little or no difference in the performance of fabrics due to the two simulant types
- There was abrasive wear on end-caps on all test articles due to sharp corners. This may suggest limiting sharp corners in suit design. Tyvek showed tear while others did not
- Dust penetration and migration testing results were inconclusive and further investigation and mitigation of dust migration through suit components will be required.

Figure 2.7-3. [Left] Comparison of hue between simulant types. Top picture using JSC-1 simulant and bottom using NU-LHT-2C, both using W.L. Gore 4 fabric. [Right] Close-up of damaged Tyvek fabric with a tear (Mitchell ,2010)

Overall conclusions from these two abrasion tests are:

- The lunar simulant was embedded in all fabrics changing color even after vacuuming
- Orthofabric and both Gore-Tex® materials are viable candidate planetary spacesuit materials
- Soft Tyvek is not recommended as a durable suit outer layer
- Non-woven Tyvek is only viable option as a disposable garment
- Dust penetration into inner layers and migration testing results were inconclusive and further investigation and mitigation of dust migration through suit components will be required

Table 2.7-1. Summary of spacesuit material abrasion tests conducted at NASA. *Data compiled from published literature*

Fabrics Tested	Fabric Features	Gaier 2009 Overall Results		Mitchell 2010 Overall Results	
Test Methodology			ASTM D3884-01 Standard Guide for Abrasion resistance of textile fabrics protocol using a Rotary Platform Double head method		-Test methodology included NASA JSC developed large rotary drum tumbler with rocks and loose lunar simulant material -Strength testing before and after abrasion
Conditions			Vacumm (10^{-4} Pa) using NASA Glenn's Lunar Dust Adhesion Bell Jar (LDAB) with abrasion wheels (8000 cycles)		Abraded with an exposure time of 8 hours in the tumbler
Simulant			JSC-1A lunar Simulant		JSC-1A Lunar (Mare Simulant) and NU-LHT-2C (Highland Simulant)
Orthofabric	Standard Shuttle and ISS EMU	X	Vulnerable to dust peneration when compared to silicone coated Orthofabric	X	-Less degradation in Orthofabric compared to other materials -Orthofabric proved to be the strongest fabric among all, followed by the two Gore-Tex. -Percent strength degradation in both Orthofabric and Gore-Tex before and after abrasion test was similar
Orthofabric	Silicone coated (Candidate Fabric) to keep dust from reaching the inner layers (Candidate Fabric)	X	Effective at keeping dust from penetrating		
Kevlar	Silicon Coated (Candidate Fabric)	X	Effective at keeping dust from penetrating		
Vectran	Silicon Coated (Candidate Fabric)	X	-Unable to keep dust from penetrating -Not a viable option for spacesuit outer layer fabric		
Plain Weave FEP	Used on most Apollo suits	X	Plain and twill weave were noted to have had similar results (but see note on twill)		
Twill weave FEP	Apollo 12 suit (Alan Bean). Left knee area sample	X	Twill weaves noted to be less durable than plain weaves -Baseline sample (Apollo 12 knee sample) showed little plastic deformation of fibers but many filaments were shredded		
Tyvek®	Non-woven fabric Paper structure (Candidate for disposable covers)	X	-Effective at keeping dust from penetrating -Tyvek's paper structure was dense enough to block dust -Sustained least abrasion and penetration		
Tyvek® 1443R	Soft Structure non-woven fabric			X	-Tyvek showed tear while others did not -Tyvek showed severe degradation -Tyvek was by far the weakest material across all strength measurements. Tyvek is not recommended as a durable suit outer layer.
W.L. Gore #R8127	5 Harness Satin with back face coated with Teflon			X	-Gore-Tex was the second strongest after Orthofabric -Percent strength degradation in both Orthofabric and Gore-Tex before and after abrasion test was similar
W.L. Gore #V 112671	3x1 Right-hand Twill with back face coated with Teflon			X	-Gore-Tex was the second strongest after Orthofabric -Percent strength degradation in both Orthofabric and Gore-Tex before and after abrasion test was similar

2.7.1.2. Abrasion Studies Using Mars Simulant

Although there are environmental differences between Martian and lunar surfaces, abrasion studies conducted on candidate spacesuit fabrics using Martian simulants are noted here as there may be some evidences and commonalities in how dust effects spacesuits, and may aid in designing future planetary spacesuits with common dust mitigation technologies that can be optimized for various environments. Summary of two abrasion testing studies performed using Mars simulants on spacesuit outerlayer fabrics are summarized here.

A. Abrasion Study-3

Gaier et al. (2010) assessed the durability of current spacesuits in the Martian environment. The study used University of North Dakota NDX-1 suit and nine candidate spacesuit fabric patches strapped onto NDX-1 (15 mm x 17 mm patches) for the test. The study evaluated the degree of wear due to abrasion and dust permeation into subsequent layers.

Table 2.7-2. Spacesuit Fabrics tested by Gaier et al. (2010)

Fabrics Tested	Features
FEP	Apollo-era lunar suit outer fabric
Orthofabric	Standard Shuttle EMU
Silicone backed Orthofabric	To keep dust from reaching the inner layers (Candidate Fabric)
Silicone backed Kevlar	Soft Structure non-woven fabric (Candidate Fabric)
Silicone backed Vectran	Candidate Fabric
Tyvek®	Paper like structure which has been suggested as a disposable over-garment (Candidate Fabric)
NDX1OL	Blue cotton-nylon fabric NDX-1 Outer layer (Candidate Fabric)
NDX1RL	NDX-1 Restraint layer (Millenia™ XT)
NDX2OL	An advanced double layer fabric

The test methodology included using Martian simulant in the NASA Ames Martian Surface Wind Tunnel (MARSWIT). The NDX-1 suit upper torso and helmet were blasted with wind-borne simulant for 5 types of tests, each for 10 minutes long in both terrestrial and Martian pressures (1 atm and 10 mbar respectively). JSC-Mars-1 simulant and quartz sand were used for the test. To add additional abrasive particles, powdered walnut shells of ~150 μm size we used during the test. NDX-1 was pressurized to 7 KPa (1psid). A total of four runs at terrestrial atmospheric pressure and four runs at Martian atmospheric pressures were conducted.

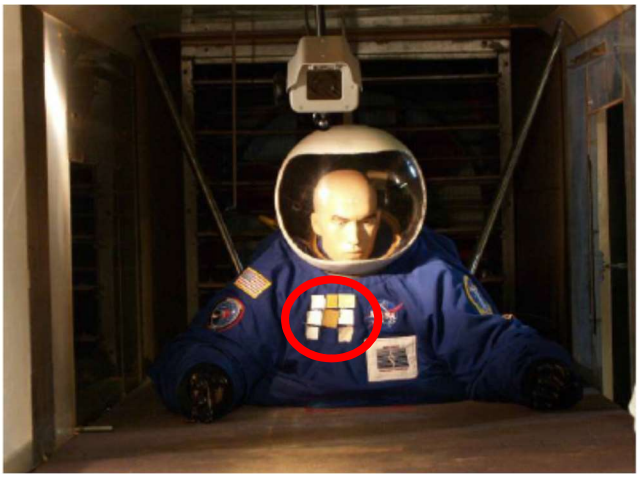

Figure 2.7-4. NDX-1 spacesuit in the test position in MARSWIT. The 9 sample patches are seen on the right of the mannequin (Gaier et al., 2010)

Pre-and post-test analyses was conducted using photographic evidence, Optical imaging microscopy and FESEM. Results from the study are summarized below

- No dust penetration or infiltration was observed into the NDX-1 PGA
- Penetration through the outer layers at high wind speeds was observed at terrestrial pressures
- Significant dust on the visor only at 10 m/s wind speed which is a concern for visor damage, but no degradation of visor observed after removal of dust with a brush
- Significant amount of dust flew up the sleeve of the suit and around neck, however did not impair glove attachment mechanism or other mechanisms
- High magnification of the fabrics provided insight into abrasion. Those results are categorized into terrestrial and Martian results and noted below

- *Abrasion at Terrestrial pressures*
  - No abrasion was observed at terrestrial pressure and there were minimal defects in the pristine FEP at 3 m/s wind speed
  - Fiber damage was observed at wind speeds >3 m/s and penetration occurred only at higher wind speeds
- *Abrasion at Martian pressures*
  - No penetration and abrasion was observed at Martian pressures but the fibers were densely covered with fine particles.

It was concluded from the tests that high velocity smaller particles would coat the rather than abrade fabrics in Martian atmospheres. Hence, coating and clogging of mechanisms would likely be a major issue than abrasion on Mars.

B. Abrasion Study-4

Bratton et al. (1999) conducted a study to evaluate spacesuit materials to windblown soil in Martian atmospheres (wind and pressure). They investigated the susceptibility of the materials to dust contamination and sand abrasion of spacesuit. Similar to Gaier et al. (2010), tests were performed at the NASA Ames MARWIT. Wind conditions of 10 m/s and 80 m/s were used for the test at both Martian pressures (10 mbar) and Earth atmosphere.

Materials included 3 cm in diameter samples of suit structure fabrics and visor/helmet material. Samples were tested by placing them at 5-10 cm from tunnel floor (boundary layer-maximum sand flux), and at 50 cm from floor (free stream –maximum wind and dust speeds). Soil simulants used for the test included 1. Carbondale Red: 1-2 μm with clay and silicate material, 2. JSC Mars-1 simulant with a large grain size and, 3. Sub grounded quartz sand of 100 μm to simulate dune materials. Data was collected using microscope CCD camera and video film in the tunnel, while analysis was performed using profilometry and SEM to quantify abrasion and adhesion. Results from Brantton et al. (1999) study are summarized here

- PVC-based products used for gloves and boots were extremely prone to dust adhesion
- Fabric materials for the spacesuit body were also readily contaminated by dust adhesion
- Teflon fabric was much less prone to contamination than Gore twill fabric or composite Orthofabric
- Ortho weave fibers of unit strands were uncontaminated, while composite strands became highly dust impregnated
- Helmet visor material was moderately contaminated with dust adhesion, above acceptable limits for maintenance of transparency
- No information on pitting/abrasion below dust on samples is available. The study did not attempt to remove any dust from the samples
- Dust seemed to cling tenaciously seven months after the tests. This may suggest semi-permanent stable bond between surfaces and dust. No effects to variations in temperature, humidity, long-term surface mobility of static charges observed

- Outward curling of fabric materials due to sand bombardment was observed. This was attributed to the elastic tension induced in the impacted side of the material, perhaps due to work hardening of the plastic fibers
- Contamination in the fabrics was observed to be similar using Carbondale red and JSC-Mars simulants
- Adhesion seemed to be a function of grain-size
- Abrasion effects could not be observed other than in the visor with linear patterns

2.7.2. Effects of Radiation on Dust Coated Fabrics

Another aspect of dust contamination of spacesuits (and the outerlayer material) is understanding the increase in material degradation when the dust coated/ abraded suit materials are exposed to radiation, a relevant environmental condition during lunar exploration. While this topic is outside the scope of this research, a summary of a previous study has been provided to show the importance of keeping spacesuit fabrics free from dust contamination for future long duration missions.

Gaier et al. (2012) studied the long-term exposure of suit fabrics to space to understand the effect of radiation on dust-coated and abraded surfaces. The objectives of the study were to understand radiation effects on dust coated and abraded spacesuit materials, degradation and changes in thermal absorptance, and changes in tensile strength. Since dust abrasion increases the surface area of a material, there is a concern that abrasion may increase radiation degradation.

As part of their study, six pristine and dust-abraded spacesuit material samples were sent to the International Space Station (ISS) as part of the Materials International Space Station Experiment-7 (MISSE-7), where the samples were exposed to the wakeside for a period of 18 months (554 days) on STS 129 in 2009 (See Figure 2.6-5). Prior to sending the samples to ISS, the fabric samples were abraded using ASTM standard using JSC-1A simulant. Figure 2.7-5 shows the fabric samples tested and layout on the metal plates of MISSE-7. One of the Orthofabric samples was abraded to the same level as the Apollo sample, while the other Orthofabric sample was abraded twice as long. Only Alan Bean's suit sample was tested for tensile strength due to limited sample lengths. Pre-and post-test data collection and analysis was conducted using optical microscopy,

energy dispersive X-Ray spectroscopy, total reflectance (optical) spectroscopy, FESEM and atomic force microscopy.

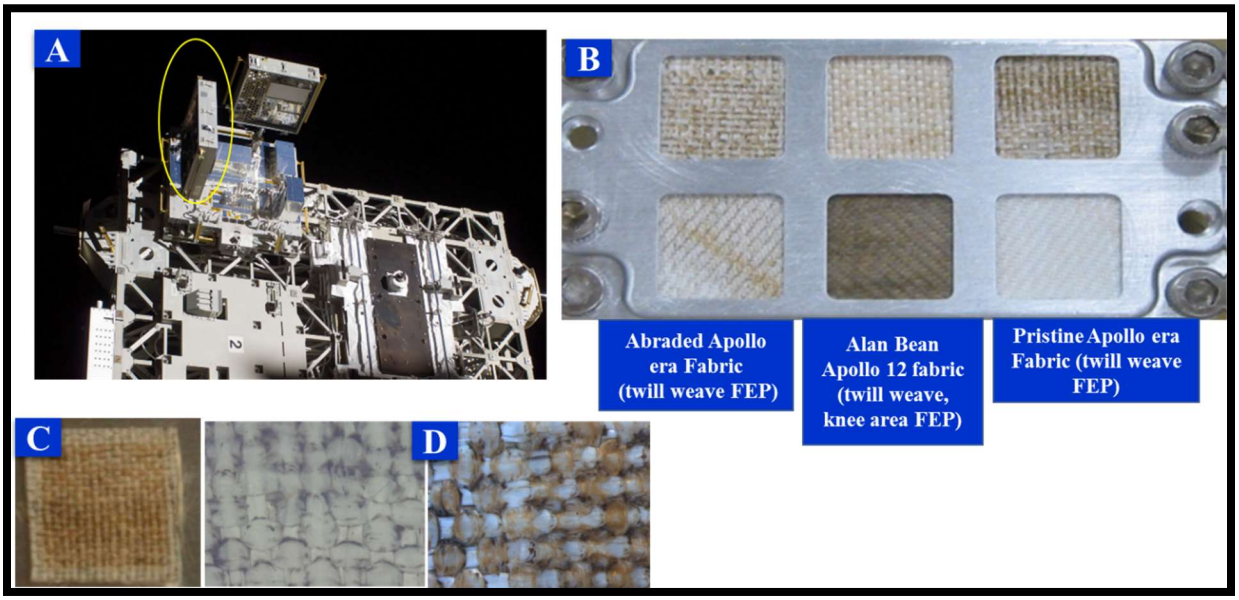

Figure 2.7-5. [A] MISSE-7 as mounted on the ISS. *Circled is the Rig on which the spacesuit fabric samples were mounted*, [B] Layout of the Spacesuit Fabric Exposure Experiment Samples, [C] Discoloration of dust-abraded Orthofabric pre-flight, [D] Optical pictograph of dust abraded orthofabric at 25X pre-flight and post-flight (Gaier et al., 2012)

Observations and results from this study are summarized here

- Exposing samples to the space environment darkened and reddened all fabrics (both FEP and Orthofabric). A conspicuous red streak appeared in the abraded FEP. Initial explanation for these results alluded to exposure to unintended atomic oxygen for approximately ~38 days causing etching of fibers
- Energy Dispersive X-Ray Spectroscopy of FEP and Orthofabric pristine and dust-abraded samples were identical, showing only carbon and fluorine peaks. Based on the results from the spectroscopy, it was concluded that darkening was not caused by contamination, but by an interaction of the fabrics with radiation in the space environment
- Thermal absorptancy changes were observed using solar absorptancy (α) measurements. Increased solar absorptancy by 7% to 38% was observed in the fabrics.
    - α of the pristine FEP fabric post flight increased by 27 %, while the abraded FEP sample showed only 7% increase.
    - α of the pristine Orthofabric post flight increased by 38 % while the abraded Orthofabric showed only 9% increase

- Tensile Test on the Apollo 12 Alan Bean's fabric sample from the knee area that was exposed to lunar dust abrasion showed while there was an increase in the elastic modulus by a factor of 2, the ultimate tensile strength and elongation to failure decreased by a factor of four

The study concluded that there is substantial degradation in the tensile properties of dust abraded spacesuit fabrics when exposed to the space radiation environment. Such exposure is highly relevant during lunar exploration missions. Therefore, for long duration missions it is imperative that the spacesuit fabrics need to be protected from dust contamination to prevent further degradation due to radiation exposure.

2.8. Summary and Relevance to Current Research

Crew reports from Apollo missions, evaluation of their spacesuits post flight and ongoing research on lunar dust effects show the substantial degradation caused by lunar dust on spaceflight hardware, specifically spacesuits. The significant role of lunar dust causing physical wear of spacesuit fabrics is highly evident from mission reports. Dust contamination caused negative effects on multiple components and systems during Apollo EVA activities, however, the problem was never seriously manifested because of the brief utilization of the spacesuits, and the suits were never reused. Simple dust mitigation strategies utilized during Apollo missions were not effective but aided in completing the short lunar sorties that lasted less than 3 days. However, the case for future lunar missions where suits will be utilized for more than just 24 hours of exposure and will be reused (estimated 800 hours over 6 months), spacesuits need to remain functional after repeated exposure to lunar dust particles over extended stays on the moon. Appropriate dust mitigation techniques are hence imperative if this is to be achieved. Table 2.8-1 summarizes key outcomes from the literature survey that are of relevance to this research to help develop a dust mitigation strategy for spacesuits.

Table 2.8-1. Summary of parameters to consider for developing spacesuit dust mitigation

Relevance to Current Research	Inputs from Literature Survey and Lessons Learned from Apollo missions
Lunar Dust Characteristics resulting in dust problems	Electrostatically charged
	High thermal absorption
	Jagged and sharp
Particle sizes of relevance	<75 μm

Relevance to Current Research	Inputs from Literature Survey and Lessons Learned from Apollo missions
Spacesuit areas highly prone to dust	Knees, elbows, boots
	Coating of outerlayer (increased thermal load, further degradation due to radiation exposure)
	Abrasion and wear of outerlayer (Less durable for long durations, cause of leak)
	Penetration into inner layers and mechanisms (cause of leak)
	Other effects
	Viewing obscuration through visors and scratching/pitting of visor surfaces,
	Create spurious discharge effects detrimental to suit electronics/radio systems.
Spacesuit outerlayer candidates	Orthofabric is a viable choice Silicone coated Orthofabric could be a secondary choice
Strategy for dust contamination	Brushing causes scratches, time consuming
	Focus on minimizing electrostatic forces of adhesion
	Making spacesuit fabric surface of similar work function as lunar dust particle-minimizes electrostatic force of adhesion
	Focus on minimizing dust accumulation (prevents several secondary issues) Dust mitigation system also capable of removing already adhered dust on outerlayer

CHAPTER 3: STATE-OF-THE-ART DUST MITIGATION TECHNOLOGIES

"Let's go invent tomorrow instead of worrying about what happened yesterday" *- Steve Jobs*

Several dust mitigation concepts have been successfully investigated by the international research community for preventing deposition of lunar and Martian dust on rigid surfaces such as solar cells and thermal radiators. However, applying these technologies for flexible surfaces and specifically to spacesuits has remained an open challenge due to the complexity of the suit design, geometry, and dynamics. A broad survey of these state-of-the-art dust mitigation techniques that are based on different mechanisms, active and passive, are presented in this chapter while focusing on assessing their capabilities and limitations for spacesuit applicability. Candidate technologies for potential spacesuit dust mitigation are evaluated and selected for further development.

3.1. Dust Mitigation Technologies

As explained in Chapter 2, the Apollo program used a few basic and manual dust mitigation strategies without much success which is evident from the suit degradation studies conducted. Rather than using valuable crew time for cleaning and maintaining suits after every EVA, it is beneficial to incorporate elements and cleaning system into the spacesuit design. This will help prevent dust contamination, maintain performance and functionality of suits after long duration dust exposures, provide reuse capability, and minimize crew time on maintenance. Survey of past and ongoing research on countermeasures for addressing dust contamination captured in the following sections are divided into passive and active methods based on their mitigation strategy.

3.1.1. Passive Technologies

Passive methods for dust mitigation are generally based on material design, engineering design and operational design which do not contain moving parts, control feedback loops, or energy requirements to actively control dust contamination, but are embedded elements that passively mitigate or prevent dust contamination. Both NASA and other research groups have been

investigating passive methods for dust cleaning. Figure 3.1-1 captures some of the passive technologies explained in the sections below

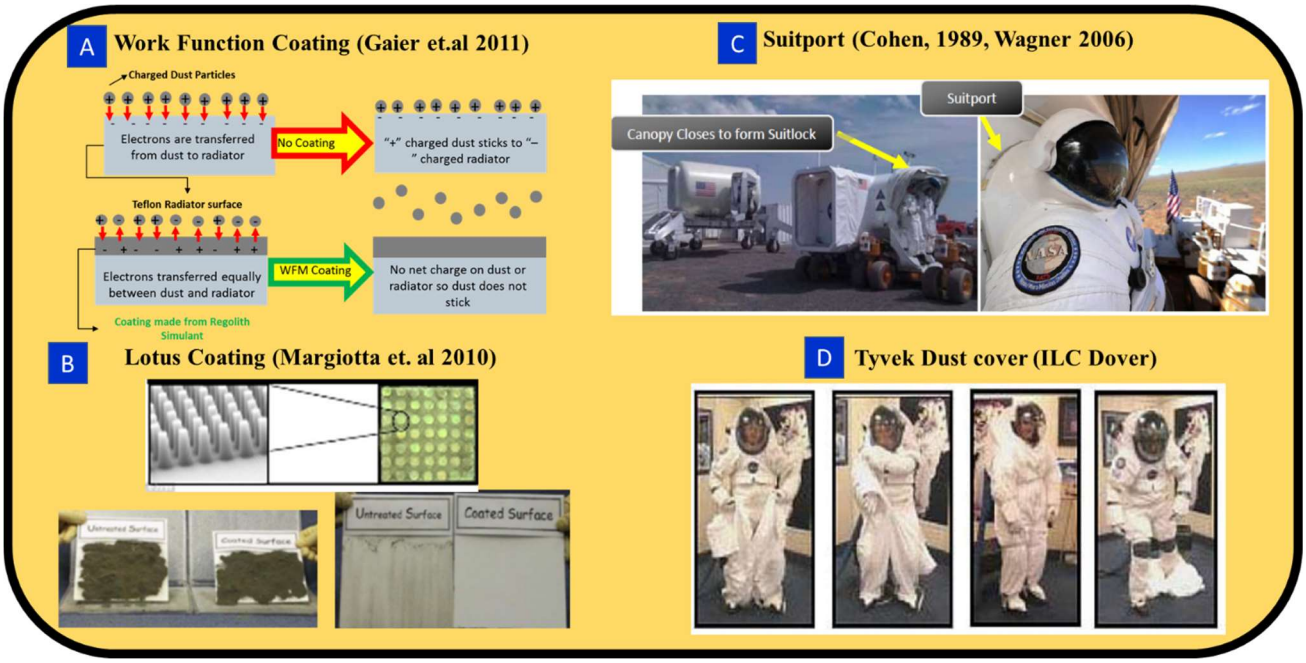

Figure 3.1-1 List of passive dust mitigation technologies under investigation for space and commercial utilization [A] Work function matching coating, [B] Lotus coatings, [C] Suitport concept [D] Dust covers

3.1.1.1. Dust Resistive Coatings

This concept includes specialized materials and coatings that can passively prevent accumulation of dust by chemical and/or textural modification of the external surface exposed to dust. The coatings work to reducing dust adhesion by either controlling charge transfer in an effort to minimize the electrostatic adhesion, and/or to minimize surface energy to decrease the VdW forces of adhesion, or both, by restructuring the external surface exposed to dust.

- ***Work Function Matching Coating***

The WFM coating works by altering the chemistry of the surface exposed to dust, particularly designed to minimize the electrostatic forces of adhesion. Among the multiple charging mechanisms at work in the lunar environment, the electrostatic forces and triboelectric-charging have been shown to be important and dominating mechanisms in cohesion and adhesion of lunar dust particles (details in Chapter 2, Berkebile and Gaier, 2012). The work function is the energy required to remove an electron from a material. During triboelectric-charging, electrons are

transferred from a material that easily loses electrons (i.e., has a low work function) to a material that holds tightly onto its electron (i.e., has a high work function) as illustrated in Fig 3.1-2 causing the two materials to adhere. Triboelectric-charging can be minimized if the work function of the two surfaces coming into contact with each other are similar.

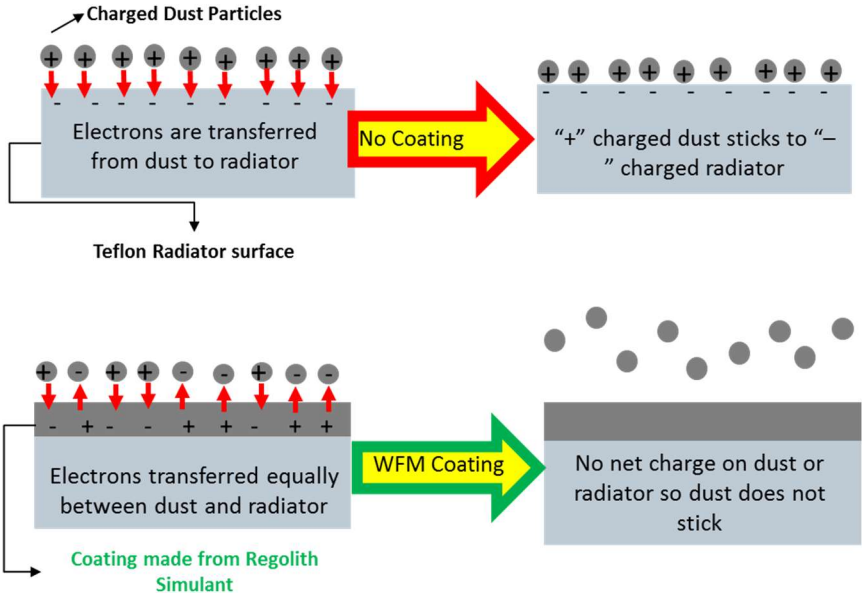

Figure 3.1-2. Working concept of WFM coating. [Top] Mechanism of dust adhesion when no coating is present. [Bottom] Having a work function for the surface that matches the work function of the lunar dust minimizes dust adhesion to the surface

The WFM coating application and surface treatments were evaluated by a study conducted by Gaier et al. in 2011. The study investigated the thermal performance of the three thermal control surfaces under simulated lunar conditions using three different surface treatments 1. Oxygen ion beam texturing, 2. Deposition of 100 nm thick layer WFM coating using lunar dust simulant composition and 3. Ball proprietary ion beam process, each of which worked to alter the surface chemistry of the thermal control surface samples. Three types of lunar simulants were used to test the adhesion to the three types of surface treatments. Results did not show favorable outcome for lowering dust accumulation using the Oxygen ion beam texturing, but both the WFM coating and the Ball surface treatment were reported to substantially decrease the adhesion of lunar simulant on two thermal control surfaces. Results of the WFM coating from Gaier's studies suggest that WFM coatings, combined with a puff of gas, could be an effective way to remove dust from metal-backed FEP thermal control surfaces on the lunar surface.

- ***Lotus and Gecko Coatings***

Another example of dust resistive coating includes Lotus and Gecko coatings with self-cleaning properties based on the lotus leaf concept. The coatings work by reducing surface energy and contact area required for adhesion, thereby reducing VdW forces of adhesion (See section 2.6.1.1 for details on VdW forces). Leaves of a lotus plant are composed of micro and nano scale structures that prevent water, dust and other contaminants from adhering to the surface. Same principles are being applied to manufacture lotus coatings.

The Lotus coating concept is currently in development by NASA Goddard Spaceflight Center (GSFC) (and partnered with nGimat for formulation) (Margiotta et al., 2010). Made of silica, zinc oxide, other oxides and mixtures of layers, these coatings create nano-texture on the surface simulating the lotus effect which reduces the surface area on which dust can cling. The coating creates super hydrophobic boundary preventing dust accumulation by shedding dust particles from surfaces. Initial investigations by Margiotta et al. were conducted in air to evaluate and characterize durability, stability, and cleanability of multiple lotus-coated substrates (See Figure 3.1-1B). Results from their studies showed:

- Lotus-coated coupon surfaces shed dust (JSC-1 lunar dust simulant) more effectively than when not coated when investigated in air. No significant increase in thermal property values of coated substrates was observed
- UV exposure tests showed that the anti-contamination properties were maintained but had mixed results with thermal radiative properties
- Thermal cycling testing showed retention of self-cleaning and thermal radiative properties from 100^{o} to -100^{o}C
- Solar wind testing that exposed the samples to low energy electrons and protons for 23 hours showed samples were browned and thermal radiative properties were degraded but self-cleaning properties were maintained
- SEM and EDX analyses showed variations in roughness across surfaces and differences in nanostructure layer among samples. There was concern regarding application, reproducibility and quality control

Based on these initial investigations, it is evident that lotus coating formulation needs to be modified to withstand the harsh space and lunar environments over time when applied to external

surfaces and performance values are still unknown. Research is underway by the NASA team to investigate application of these coatings using a patented combustive chemical vapor deposition method to substrate surfaces, survivability in the harsh lunar environment and minimize lunar dust from accumulating on spaceflight hardware (Margiotta et al. 2010). If successful, this technique can be used as external coating for multiple applications such as spacecraft radiators, solar arrays, suits, visors, habitat walls etc. However, the effectiveness of dust shedding by this coating was tested only in air and has not been examined in vacuum. Whereas in vacuum conditions it's been shown by Gaier e al. (2012) that electrostatic forces dominate in the lunar environments. The textured coating targets to only minimize VdW forces, therefore using lotus coating alone won't address the dust contamination problem entirely and could be combined with another method to also reduce the electrostatic forces of adhesion.

3.1.1.2. Suitports / Canopy on Suitports

Suitports, a concept designed and developed by NASA, such as those used in hazardous materials cleanup operations, allow crewmembers to ingress habitats/rovers without bringing regolith into the habitable volume (Cohen 1989). In addition to minimizing pressure losses and pre-breath time, the Suitport allows astronauts to dock their spacesuits outside of a pressurized structure before and after an EVA minimizing dust transport inside the habitable volume. This decreases potential human health impacts due to dust. (See Figure 3.1-1C)

However, this approach still necessitates periodical cleaning and maintenance of the suits as they are positioned outside the habitat for long durations. Even the inclusion of retracting dust covers/canopy structures proposed by NASA does not eliminate dust exposure and suit degradation due to dust and might potentially decrease the reuse capability of suits if left uncleaned. These covers/canopy structures may however protect the suit from unfiltered solar UV radiation exposure minimizing possible mechanical degradation of the suit material. Additional considerations must be given to designing suit elements (suit fabric and other exposed elements of the suits) to prevent dust contamination utilizing dust resistance materials and coatings. A combination of multiple dust contamination approaches might need to be implemented while using the Suitport concept.

3.1.1.3. Dust Covers and Fabric Structures

Incorporating exterior dust covers for spacesuits and sensitive equipment is another approach for passive dust contamination. Simple, reusable coveralls, worn over clean spacesuits prior to

conducting an EVA can protect the suit from the deleterious effects of dust and prevent transfer of dust into habitats. This concept can be adopted from terrestrial applications where disposable dust coveralls are common in industrial and hazardous operations. A modular system could be donned when beginning EVA and doffed prior to airlock (or suitlock) ingress. The design of such dust covers for future systems should be a simple and easy to don/doff without compromising mobility, be tear resistant in addition to being dust resistant, and should be of minimal weight impact.

- ***Dust Covers***

ILC dover designed and tested two prototype dust covers to understand the potential for creating a dust cover that can be easily donned and doffed to protect suits from dust degradation without encumbering mobility (Cadogan et al., 2007). The study investigated mobility impacts, suit-cover interface, sizing and closure methods. Dust covers were fabricated using 9 mm thick DuPont Tyvek® and were tested using their I-suit EVA demonstrator built for planetary missions. Donning operations with a fully pressurized suit (4.3 psi) were evaluated. Initial investigations showed that a stiffer material would help with the donning process, and it was a challenge to design dust covers that are conformal to the spacesuit.

These dust covers may be combined with dust resistive coatings to make them more durable and act as a flexible dust barrier. The fabric component of the dust cover should be lightweight and high strength material. While dust covers are a feasible option for dust contamination, making the covers conformal to the suit, addition of weight and storage volume if new covers must be used on every EVA for long-term missions, disposal of contaminated covers and constraints for emergency ingress are some of the challenges that need to be resolved.

- ***Fabric Structures***

Evidence from Apollo missions and abrasion test studies (Chapter 2, section 2.7) also show that future planetary spacesuit fabrics should have tightly woven structures (or non-woven like Tyvek®) and incorporate a smooth coating to sustain repeated cleaning without degradation to withstand the abrasive action of dust. Test results have shown that the hard paper structured Tyvek is a feasible option but the challenge is to conform Tyvek as an outer layer fabric. Tyvek can be used as dust cover as explained in the previous section. Silicone coated orthofabric is also another option as an outerlayer for suit fabric to help minimize penetration. Initial investigations by Gaier

et al. (2009) showed evidence that the silicone coated orthofabric was effective at minimizing dust penetration into inner layers, however it adds weight and silicones darken upon UV exposure. Studies conducted on silicone coatings in low earth orbit also showed degradation due to oxidation of surface when exposed to atomic oxygen (Banks et al., 1999). The use of silicones in lunar environments is yet to be validated.

3.1.2. Active Technologies

Active technologies incorporate active or moving elements, generally requiring energy input (electrical or mechanical). Some of these may also incorporate controllers with a feedback loop. Several active dust technologies have been proposed and published in literature for both spaceflight use specifically over solar panels, and in commercial applications. Most of these technologies are in their preliminary stages of development. Figure 3.2-1 provides an overview of the active technologies described in subsequent sections.

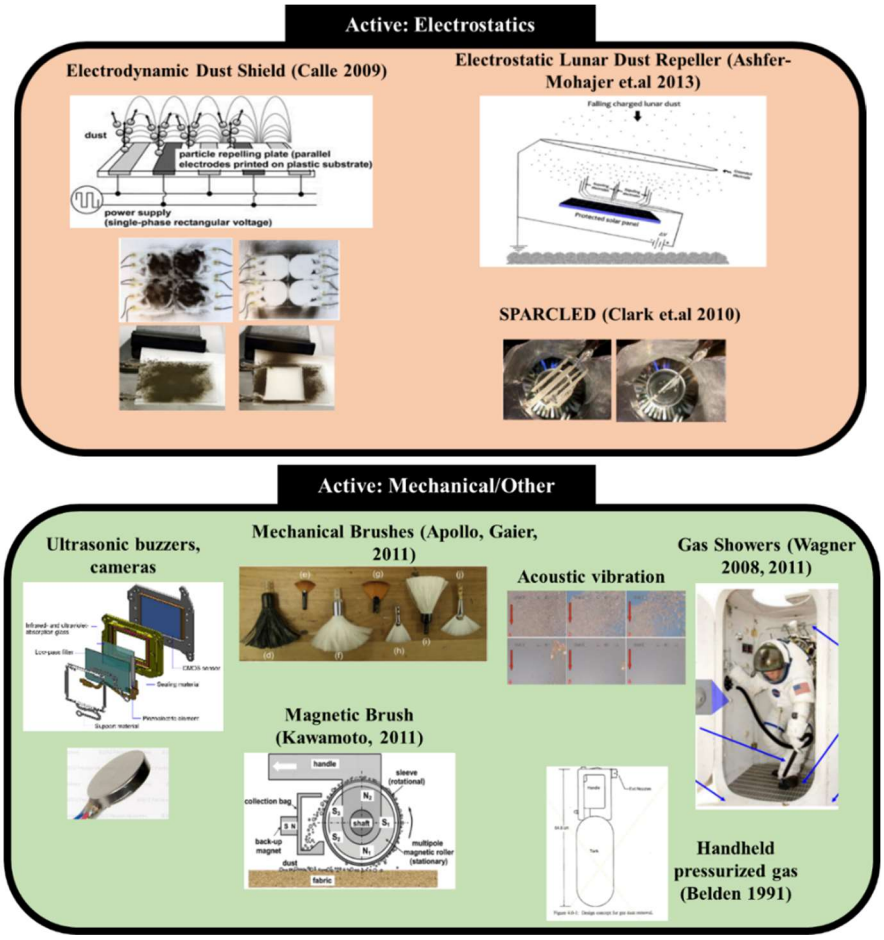

Figure 3.2-1. Various active dust mitigation technologies proposed in literature

3.1.2.1. Electrostatics and Electrodynamic Methods

- ***Electrodynamic Dust Shield***

EDS is an active technology developed by NASA that uses electrostatic and dielectrophoretic forces to carry charged and uncharged dust particles off surfaces by generating a travelling electric field. The shield contains a series of parallel electrodes through which an alternating current (AC) of voltage is applied as shown in Fig 3.2-1 (Calle et al., 2008 and 2011). The electric field generated by the electrodes levitates and repels dust particles off the surface and prevents further accumulation of dust when kept activated. The electrodes can be excited using a single or multi-phase AC voltage to remove charged and uncharged dust particles on the surface. First introduced by NASA in the 1960s as the Electric Curtain concept, this EDS technology was further developed for dust removal on rigid surfaces at NASA KSC.

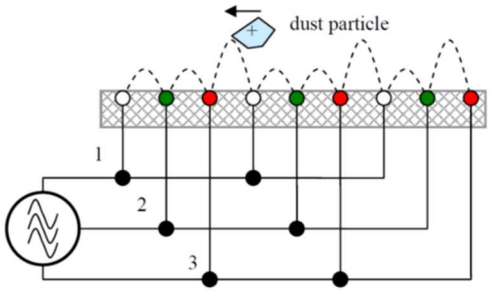

Figure 3.2-2. Concept of the Electrodynamic Dust Shield or electric curtain. *Three-phase curtain shown here* (Calle et al., 2011)

Several experiments previously conducted at NASA KSC demonstrate the feasibility and high efficiency of the EDS system for surface cleaning of solar panels, optical systems, glass structures and thermal radiators (Calle et al., 2008 and 2011). For example, in one of the experiments it was shown that when dust loading conditions using lunar dust simulant caused solar cell performance to drop to 11–23% of the baseline performance, activating EDS restored solar cell performance values to above 90%. Of the active dust mitigation technologies developed thus far, EDS proves to be the most promising, efficient and feasible path for rigid surface application.

- ***Electrostatic Lunar Dust Repeller***

Another similar dust removal technology was developed by Ashfer-Mohajer et al. (2013) called the Electrostatic Static Lunar Dust Repeller (EDLR) that was proved to efficiently protect sensitive surfaces exposed to dust deposition. The ELDR consists of an arrangement of thin,

needle-shaped electrodes in front of the protected surface to repel like-charged lunar dust (Figure 3.2-1). The study conducted by the research group used a discrete element method (DEM) to track particle trajectories for determining the removal efficiency. The study investigated electrode arrangement for maximum performance and X-shaped electrodes arrangement was identified to be the most effective dust-repelling pattern among various electrodes arrangements. The electrical particle-particle interaction enhances repelling efficiency. This study was analytically performed with no experimental evidence available to understand the feasibility of the concept, and the system is shown to work only for charged particles.

- ***Space Plasma Alleviation of Regolith Concentrations by Discharge***

Space Plasma Alleviation of Regolith Concentrations by Discharge (SPARCLED) is another electrostatic tool designed by NASA to remove contaminating lunar regolith from surfaces in lunar environments primarily for the lunar habitat airlock (Clark et al., 2010 and Hyatt, 2010). SPARCLED uses a charged particle gun combined with an oppositely charged plate electron beam to rapidly charge dust contaminating a surface to a sufficiently high charge-to-mass ratio. This causes rapid and complete removal of the dust grains by mutual repulsion and controls electrostatic potential of the surface and flow of dust (Hyatt, 2010). SPARCLED allows near radial removal of dust from surfaces, minimizing abrasive tangential forces. It utilizes only electrons and hence no consumables such as gases are needed for operation. Experiments are ongoing at NASA ton this patent protected technology o measure the performance and dust mitigation effectiveness. It is unknown however if this technology can be modified for spacesuit application with the limited information available.

3.1.2.2. Mechanical Methods

- ***Vibratory Surface Cleaning***

Dust mitigation strategies used in non-space related domains such as the camera industry may be adopted to spacesuits with modifications. Some commercially available cameras use piezo crystal ultrasonic vibration technology which function by vibrating a thin filter surface that covers the image sensor to many tens of thousands of times per second (35,000 to 50,000 hertz) to remove particles from the filter (Irhazy, 2007). The system consists of a very thin piece of filter glass placed in front of the image sensor (also known as the CMOS sensor); the area between the filter and the sensor is sealed, so no dust can enter. Whenever the camera is turned on, a piezoelectric

driver induces a vibration in the filter glass, effectively shaking and loosening dust particles so they fall off (Irhazy, 2007). A piece of adhesive located inside the camera traps removed dust. Other studies of vibratory surface cleaning technologies using piezoelectric buzzers located under a transparent film over a solar panel are being studied for space applications (William et al., 2007). When activated, these vibratory buzzers would generate standing modes of oscillation to "shake off" dust from the solar panel.

The potential application of this technology for spacesuits needs further investigation into studying the impacts of suit material stiffness, integration with the suit fabrics, size of vibratory sensors, mobility and reliability impacts. The current systems used in cameras do not completely remove dust and require maintenance of camera lens by externally cleaning the lens. The same might be the case for spacesuit as well, where more than one method may be integrated with other concepts for effective dust mitigation.

- ***Manual Brushing***

Apollo missions used brushing as their main approach to remove dust that proved to be ineffective. Nylon brush used on Apollo was ineffective in restoring α (solar absorptance) on the LRV (Gaier and Jaworske, 2007). However, recent tests were conducted by Gaier et al. (2011) using various brush types (bristle material, geometry and length) to evaluate brushing as a lunar dust mitigation strategy on thermal control surfaces (AZ93, AlFEP, AgFEP) with improved brushing systems. Results from Gaier's investigations using NU-LHT-1D lunar simulant showed that metallic brushes were too stiff and too hard. The fan and round brush designs were more effective than strip brushes. Longer bristles were more effective than short brushes. Nylon Escoda and round fiberglass Zephyr were effective as lunar dust removal brushes (Gaier et al., 2011). These studies suggest that brushes may be used as a supplementary method of cleaning but not as a primary dust cleaning technique. In-depth experimental data may be required for specific use on spacesuit and abrasion of suit materials due to brushes as seen on Apollo missions. Furthermore, using brushes as a primary means of cleaning is labor intensive requiring substantial crew time.

- ***Magnetic Brushes/Devices***

Another solution to remove dust may be the use of magnetic devices that take advantage of the magnetic properties of the fine lunar dust (nanophase Fe^0). A magnetic cleaning device that utilizes magnetic force was developed and demonstrated by Kawamoto and Inoue (2011) to capture and

separate lunar dust continuously with a multi-pole magnetic roller (See Figure 3.2-3 and 3.2-4). The device utilizes a permanent magnet with no electrical power. It is a simple, lightweight and easily operated device producing no waste (Kawamoto and Inoue 2011).

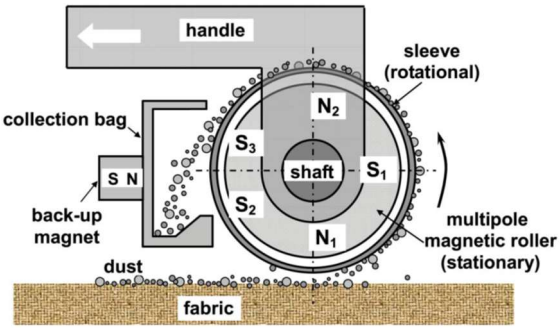

Figure 3.2-3. Magnetic cleaning device (Kawamoto and Inoue, 2011)

The study group conducted experiments with a prototype device on spacesuit fabrics (80 mm X 80 mm area). The suit fabric samples were rubbed with FJS-1 lunar simulant (similar to JSC-1A) using particles <53 μm diameter. The magnetic roller device was pushed against the fabric surface and pulled manually in the lateral direction (see figure 3.2-3). High-speed microscope camera was used to observe particle dynamic behavior from lateral side of device and the observed behavior was compared to calculated behavior. Results from their experiment showed high separation rate (90%) but low overall capture rate (<40%) using the magnetic device (See figure 3.2-4). The low magnetic permeability of lunar simulant results in low capture rate. ~5% of the lunar simulant by weight was not magnetic. Magnetic attractive force of the roller was less than the adhesion force between the dust and the suit fabric. It is believed that the performance of the device with actual lunar dust would generate better results due to the higher magnetic permeability and lower nonmagnetic particles in the lunar dust. The capture rate was observed to be independent of the rotational speed.

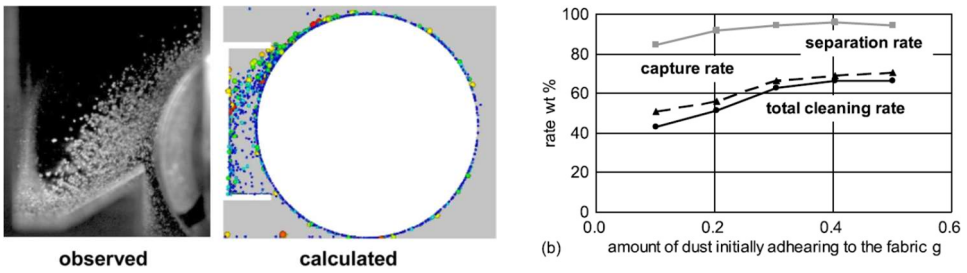

Figure 3.2-4. [Left] Observed and calculated particle motion at the separation area, [Right] Effect of amount of dust initially adhering to the fabric (Kawamoto and Inoue, 2011)

Some of the challenges of using such a magnetic device include the difficulty in capturing smaller particles trapped between fabric fibers and ability to increase capture rate. Similar to manual brushing, it requires manual action by the crew and such a device could be used as a supplementary tool in addition to other techniques for lunar operations rather than just rely on using this one device as the primary method to mitigate dust.

3.1.2.3. Pressurized Gas Methods

- ***Pressurized Gas Showers***

Showers using pressurized air or CO_2 are principle cleaning technologies used in commercial industries for dust contamination, which can be perhaps aided by brushes with magnets attached (Wagner, 2008). The air/ CO_2 shower techniques proposed for long term space missions by NASA features directional jets inside an airlock or similar enclosed area after an EVA that create turbulence to remove dust from spacesuits and equipment with the general flow downward, moving the dirt under a grated floor to be collected by filters (Wagner, 2014). Figure 3.2-1 shows a concept proposed by NASA for shower systems (bottom part of the figure). A water shower has also been suggested as part of planetary surface airlocks.

However, these techniques result in increased system mass and complexity to carry or generate additional water for suit cleaning purposes. In addition, whether it is air, CO_2 or water, there are several disadvantages of such shower systems due to their low efficiency. These systems require high energy consumption and additional consumables. Showers and mechanical parts of the system require regular maintenance and are susceptible to degradation themselves.

- ***Handheld Pressurized Gas cylinder***

A handheld pressurized gas device concept was proposed by Belden (1991) for dust removal utilizing short bursts of gas. The concept uses small astronaut/robotic compatible device using either CO_2 or N_2 as the cleaning medium. The device consists of removable pressurized storage tank (600 psi) and a handle with 3 gas exist nozzles in a triangular configuration. The proposed design would have changeable nozzles to increase performance for spacesuit applications and can have other uses such as a fire extinguisher with CO_2. The study only provides conceptual description and no experimental data is available to compare the performance of the technique to other dust mitigation strategies.

The challenges of using such an approach include several areas of development. For example, thermal insulation and cooling system for the pressurized tank to overcome temperature variations, payload mass, buildup of gas on the lunar surface and suspension of dust, nozzle configuration, condensation effects due to environmental temperatures, fatigue and thermal analysis for long term usage and reliability due to cyclical stress on tank need to be addressed. Furthermore, this requires manual operation by the crew resulting in additional crew time. The concept may be integrated with other techniques as a supplemental tool where the pressurized gas cylinder can be used to remove any residual particles after automatic cleaning operations.

3.1.2.4. Integrated Technologies

There have been studies to essentially combine one or more dust mitigation technologies for more effective performance to protect from dust contamination.

One such test was conducted by Margiotta and Calle et al. (2011) utilizing a combination of Lotus coating (passive) and EDS (active) technology using 8 x10 inch rigid panels mounted on an analog habitat at Desert RATs. They investigated the performance increase of dust mitigation by combining two technologies. Initial testing in ambient conditions showed that the dust mitigation properties using EDS were enhanced by addition of Lotus coating to EDS surfaces. Lotus coating reduced the amount of dust (JSC-1 simulant) that can attach to the EDS surface thus optimizing the EDS's particle removal abilities. These preliminary tests using solar absorbtance measurements showed that the combined passive (Lotus coating) and active (EDS) dust mitigation technique was more efficient than standalone technique to protect from dust contamination.

Similarly, Kawamoto and Hara (2011) experimented with integrating their electrostatic flicker, (similar to EDS) with mechanical vibration in both air and vacuum conditions. The electrostatic flicker used polyester insulated copper wire electrodes stitched into spacesuit fabric and were energized using single-phase rectangular voltage. Mechanical vibration was generated using a bolt clamp Langevin ultrasonic transducer under the fabric. They reported improved cleaning performance to a maximum of 90% at 10 Hz using the combined method when compared to cleaning performance of 75% with the electrostatic flicker alone and cleaning operation time reduced to half. Particles >20 μm were removed with combined vibration which otherwise did not come off. However, the use of rigid copper wires stitched into the spacesuit fabric will ultimately

break with repeated flexure cycles. Therefore, further improvement in this concept is important for long term repeated usage of the dust cleaning strategy.

3.2. Limitations of Previous Work to Spacesuit Applications

Survey of the various techniques for dust mitigation demonstrate that:

1. *Rigid versus Soft Surfaces*: Several techniques identified in literature were proven for rigid surface application such as solar panels, thermal radiators, and optical surfaces. Very few techniques such as brushing was experimentally proven for spacesuit fabrics. Calle et al. (2007) applied printed electrodes on a cotton fabric using ink jet printing, and Kawamoto et al. (2011) stitched copper electrodes into the spacesuit fabric, however, these efforts do not address all the complexities of overcoming the spacesuit design constraints to fabricate the EDS system into spacesuit outerlayer and have not proven scaled functionality.
    - Newer suit designs may contain both soft and hard areas on the suit. Some of the techniques surveyed can be easily implemented on hard surfaces. The challenge will be to address soft surface areas of the suit (More details in Chapter 4).
2. *Dust prevention and removal*: Except for the EDS concept, other techniques in literature focus on either removing already adhered dust or preventing dust accumulation, but not both.
3. *Redundancy*: Each proposed countermeasure was not capable of completely mitigating dust problems and/or did not have redundancy when applied individually.
4. *Cleaning Efficiency*: Except for the EDS system that demonstrated high cleaning efficiencies for use on solar panels and optical surfaces (>90%), other cleaning methods surveyed were either proven analytically with no experimental validation and/or did not have cleaning efficiencies to prevent the thermal degradation of surfaces (<25% residual dust coverage) established in this research.
5. *Combined Technologies*: One of the conclusions from the survey was that each proposed countermeasure was not capable of completely mitigating dust problems and/or did not have redundancy when applied individually. It may be beneficial to recognize how combining several technologies in an incremental method or using hybrid technologies, where more than one technology can be applied at various levels or operational timeline can be utilized to optimize solutions for dust contamination (primary mode of dust mitigation embedded in

spacesuits, secondary supplemental tool, post EVA maintenance etc.) such as the layered approach proposed by NASA (Wagner, 2014; Afshar-Mohajer et al., 2015).

6. *Pressurized versus unpressurized suits*: Most of the ground tests conducted to investigate dust contamination effects on spacesuits (from Chapter 2) were not performed using pressurized suits. Abrasion and penetration properties may be different for pressurized suits versus unpressurized suits and dust mitigation strategies might work differently based on suit pressurization. Including suit pressurization for future tests may help understand these effects.

3.3. Candidates for Spacesuit Dust Mitigation Techniques

The fundamental goal of this research is to design a dust cleaning system that can be integrated into the spacesuit outerlayer requiring minimal crew actions to operate and clean the suit while conducting surface exploration activities and minimize post EVA maintenance time. To downselect cleaning concepts that are viable for spacesuit implementation, specifically for the soft areas of the suit, each of the dust technologies surveyed was assessed against the following criteria. Table 3.3-1 provides an overview of these results.

1) Able to prevent dust accumulation *and* removal of adhered dust
2) Target Electrostatic forces of adhesion
    - Electrostatic forces have been demonstrated to be 100 times more effective than VdW forces in the 'sticking' of silicate grains (Dominik and Tielens, 1997 and Berkebile, 2012)
3) Works to reduce dust contamination of fabric with less than 25% of fabric area covered in residual dust post cleaning operations
4) Feasibility proven using experiments
5) Capable of integrating with multiple methods
    - Does not diminish individual cleaning effect
6) Conformal to spacesuit shape and structure
    - Minimal impact to mobility
7) Requires minimal manual action as a primary dust cleaning method

Table 3.3-1. Feasibility trade study of passive and active dust mitigation concepts for spacesuit application.
(Legend in the Table: Electrostatic- ES, Van der Waal Forces- VdW, Mechanical/Physical -Mech/Phy)

Type: Active/ Passive	Dust Mitigation Strategy	Technology	Details	Adhesion Force Targeted			Dust Contamination		Mass Impact	Power Reqs	Feasibility Testing	Dust Cleaning Efficiency	Spacesuit Applicability/ Challenges	Assessment/ Comments	Source
				ES	VdW	Mech/ Phy	Prevent Accumu-lation	Remove Adhered Dust							
Passive	Surface Coatings & Modifica-tions	Work Function	• Modifies chemistry of the external surface exposed to dust to reduce electron affinity reducing dust adhesion • Uses Lunar dust simulant to make work function of surface same as that of dust	X			X	X* (with puff of gas/manual action)	Negligible	N/A	Completed on Thermal radiator samples	• 50-80% of JSC-1AF dust removed on coated surfaces • Easy to clean off using puff of gas/dust comes of easily • WFM coatings, combined with a puff of gas will provide dust mitigation	• Thin, transparent coating, ~100nm • Conformable to spacesuit flexible surface • Technique to coat Teflon surface proven • Consistency over all fabric weaves	• Made of Lunar dust simulant • Can be used as a coating over EDS due to its insulative nature	NASA developed Gaier et al., 2011
		Lotus Coating	• Based on lotus leaf self-cleaning characteristics • Changes surface texture		X		X	X (with manual action)	Negligible	N/A	Completed on Thermal radiator samples	unknown	• Conformable to spacesuit flexible surface • Technique to coat Teflon surface unknown Consistency over all fabric weaves	•Electrostatic forces shown to dominant • May not provide sufficient cleaning	NASA Developed, Margiotta et al., 2010)
Passive	Dust Covers and Fabric Structures	Dust Covers	Reusable suit covers worn over clean spacesuit	N/A	N/A	X	X		~25lb per astronaut for 800hrs EVAs	N/A	Initial prototypes using pressurized I-suits	Assuming >95% no data available on actual dust contamination	• Challenge to conform to spacesuit shape and structure • Doffing and donning • Additional cover to remove for emergency ingress • Disposal issues	Mass estimated : ~1lb per cover, estimating 25 covers for 800 EVA hrs., 6 months, reuse upto 4 times	ILC Dover
		Fabric Structures	-Tightly woven structures (or non-woven like Tyvek)			X	X		~145 g/m^2 increase if silicone backed orthofabric	N/A	Abrasion tests on candidate outerlayer	N/A	• Suit Outerlayer material choice silicone coated Outerlayer • Minimize pockets on outerlayer	No cleaning, only choice of material for better strength and tear resistance post dust exposure	Gaier, 2010; Mitchell 2010

Table 3.3-1 cont.

Type: Active/ Passive	Dust Mitigation Strategy	Technology	Details	Adhesion Force Targeted			Dust Contamination		Mass Impact	Power Reqs	Feasibility Testing	Dust Cleaning Efficiency	Spacesuit Applicability/ Challenges	Assessment/ Comments	Source
				ES	VdW	Mech/ Phy	Prevent Accumu-lation	Remove Adhered Dust							
Active	Electrostatics based Technologies	Electrodynamic Dust Shield	-The concept of the electrodynamic electrostatic and dielectrophoretic forces to carry dust particles off surfaces and to generate an electrodynamic shield that prevents further accumulation of dust -Series of electrodes over the surface with high voltage application	X			X	X	<100grams for electrodes ~2lbs for electrical equipment	~0.06 Wh	Solar panels, thermal radiators, optical systems	• 98% in lunar conditions, 97% in Martian conditions for solar panels • 99% in Optical Systems • 96-99% on thermal radiator performance	• Integrating heavily flexed electrical wiring into spacesuit outerlayer • Metallic wire not conformal to suit movement • Potential impacts to mobility unless flexible electrodes integrated with weaves • Address high voltage application with humans inside	• Removes both charged and uncharged particles • If proper material available can be used as a primary mode of dust mitigation • Need to overcome challenges with novel materials and fabrication techniques	NASA developed, Calle, 2009
		Electrostatic Lunar Dust Repeller	Arrangement of thin, needle-shaped electrodes in front of the protected surface to repel like-charged lunar dust. Similar to EDS concept	X* (only works on charged particles)			X	X	unknown	unknown	• No experimental data • analytical studies only on solar panels	92%, on works on charged particles	unknown	• Only suitable to remove charged particles • Suitable for surfaces larger than 900cm^2	Ashfer-Mohajer et al., 2013
		SPARCLED	• Uses a charged particle gun combined with an oppositely charged plate electron beam •Rapidly charges dust on a surface to a sufficiently high charge-to-mass ratio • Causes rapid and complete removal of the dust grains by mutual repulsion and controls electrostatic	X				X	unknown	Relatively high/unknown	20 mm JSC-1A , dust migration proved with 1000VDC pin probe 2mm above it	Unknown	• Limited to very small surface areas • A robotic lever that scans the surface line by line not feasible to operate during real time EVAs	• Removed both charged and uncharged particles • Takes a long time to remove particles Not feasible for integration into suits for real time ops	NASA developed, Clark et al., 2010

Table 3.3-1. cont.

Type: Active/ Passive	Dust Mitigation Strategy	Technology	Details	Adhesion Force Targeted			Dust Contamination		Mass Impact	Power Reqs	Feasibility Testing	Dust Cleaning Efficiency	Spacesuit Applicability/ Challenges	Assessment/ Comments	Source
				ES	VdW	Mech/ Phy	Prevent Accumu-lation	Remove Adhered Dust							
Active	Mechanical	Mechanical Vibration	• Using ultra sonic vibration technology vibrating the surface on which dust is deposited			X	X	X	Within 2 lbs. if microsensros utilized	X	Combined electrostatic flicker with vibration on spacesuit material	• Improved cleaning performance with vibration to max 90% at 10Hz compared to 70-80% with electrostatic flicker alone	• Impacts of suit material stiffness, integration with the suit fabrics, size of vibratory sensors, mobility and reliability impacts. • May be integrated with one or more technologies for spacesuits to for enhancement dust mitigation enhancement	• Utilized in camera industry with micro vibration transducers • Can be combined with EDS and coating	Kawamoto, 2011; Camera industry
		Acoustic Levitation	• This Concept uses acoustics to levitate and remove dust from surface. • An acoustic force strong to overcome Van der walls adhesive forces between the surface and dust can potentially be used for dust mitigation.			X	X	X	X	X	• 4 different reflector materials (9X9cm^2 size) • 90s acoustic excitation and airflow • Mars simulant	• Restoration of solar cell performance post dust removal to 98.4% • For smaller particle acoustic radiation force was too weak	• Usage is limited to pressurized enclosures with an atmosphere and cannot be used in open planetary surfaces such as during EVAs	• Useful for rigid surfaces and industrial uses • Usage is limited to pressurized enclosures with an atmosphere and cannot be used in open planetary surfaces such as during EVAs	Chen and Wu, 2009
		Manual Brushing	• Manual removing adhered dust using brushes • Nylon brush used on Apollo was ineffective and caused abrasion			X		X	Lightweight <1lbs	N/A	• Thermal radiators • No testing on spacesuit fabrics except for experience from Apollo	• >80% α/ε restoration using Round fiberglass Zephyr brush and Nylon Escoda Fan brush • Apollo mission showed further abrasion	• Requires manual action by crew •Time consumption and abrasion of spacesuit material	• With softer bristles, can be able to use as secondary mode/supplementary tool of cleaning after EVAs and during maintenance	Apollo Program
		Magnetic Devices	• Magnetic cleaning device that utilizes magnetic force was developed and demonstrated by Kawamoto and Inoue (2011) to capture and separate lunar dust continuously with a multi-pole magnetic roller. The device utilizes a permanent magnet with no electrical			X		X	Lightweight <1lb	N/A	Spacesuit fabric with FJS-1 simulant <53μm particles	• High separation rate (90%) but low capture rate • difficulty in capturing smaller particles trapped between fabric fibers	Capturing smaller particles trapped in between fabric fibers	• Can be used as a supplementary tool like regular brush • Not for primary mode of dust mitigation mitigate dust	Kawamoto and Inoue, 2011

Table 3.3-1. cont

Type: Active/ Passive	Dust Mitigation Strategy	Technology	Details	Adhesion Force Targeted			Dust Contamination		Mass Impact	Power Reqs	Feasibility Testing	Dust Cleaning Efficiency	Spacesuit Applicability/ Challenges	Assessment/ Comments	Source
				ES	VdW	Mech/ Phy	Prevent Accum u-lation	Remove Adhered Dust							
Active	Pressurized Gas Jets	Showers	• Showers using air or CO2 are principle-cleaning technologies used in commercial industries for dust contamination • Air/ CO2 shower techniques have been proposed for long term space missions by NASA featuring directional jets creating turbulence to remove dust from space suits and equipment			X		X	Substantial additional consumables	High Energy consu m-ption	NA	• Low efficiency for high energy used	• Cannot be integrated into spacesuits for automatic cleaning during real time operations • Showers and mechanical parts of the system will require regular maintenance and are susceptible to degradation themselves	• Could be built into airlocks, but not useful during EVAs as primary mode of dust cleaning • Limited by gas consumables	Industrial Uses, Wagner, 2008 & 2011
		Handheld Pressurized gas cylinder	•A handheld pressurized gas device concept was proposed by Belden (1991) for dust removal utilizing short bursts of gas. The device consists of a small astronaut/robotic compatible device using either CO_2 or N_2 as the cleaning medium			X		X	unknown	unkno wn	No experimental testing	NA	• Cannot be integrated into spacesuit for automatic use • Time consumption, constrained by condensation effects due to environmental temperature and others,	• Manual action • Can be utilized for supplemental tool but not primary mode of dust mitigation	Belden, 1991

Based on the above set criteria, a list of candidate concepts that demonstrate their viability of being used for spacesuits as a primary mode of dust cleaning have been selected (Table 3.3-2). Developing a method that utilizes a combination of these candidate active and passive concepts to reduce adhesion of dust to the spacesuit outerlayer and removal of already adhered dust on the soft areas of the suit may provide for a more efficient and optimal dust mitigation technique.

Table 3.3-2. Candidate technology concepts for integration into spacesuits for dust mitigation

Type	Mitigation Strategy	Technology	Effects on Adhesive forces
Passive	Surface Modification	Work Function Matching coating or similar processes	Reduces charge transfer (electrostatic forces)/contact charging
Active	Electrostatics	Electrodynamic Dust Shield	Reduces charge transfer (electrostatic forces)/contact charging Actively works to prevent dust accumulation and remove adhered dust
Active	Mechanical	Mechanical Vibration	Mechanically breaks the adhesive forces

Due to the high efficiency proven for the EDS concept, it has been down-selected as the primary consideration for spacesuit dust mitigation. However, several challenges remain to integrate EDS into spacesuits, particularly the active metallic electrodes. Various methods were investigated to incorporate electrodes into the spacesuits, and Chapter 4 provides details on challenges for spacesuit implementation and proposed techniques per this dissertation to integrate the concept for spacesuit dust mitigation.

3.4. Summary

Based on the survey conducted on state-of-the-art dust mitigation techniques, three candidate technologies (EDS, WFM and potentially vibrating surfaces) of the several techniques are identified as viable techniques for integration into spacesuits as a primary strategy to address dust contamination. Other techniques surveyed did not seem feasible to be applied as a primary mode for dust protection of spacesuits due to limitations in their performance (low cleaning efficiency, no experimental data, requires manual action by crew) and challenges in integrating for spacesuit application. Survey has also shown that efficiency of dust removal performance using a combination of technologies types can be higher than standalone technology.

While initial investigations show EDS based concepts would be a preferred option for dust mitigation due to its very high cleaning efficiency proven on rigid surfaces, challenges remain to identify techniques to integrate EDS type system into spacesuits. The challenge is to design suits and provide protection from dust without compromising mobility. Identifying the most effective technical solutions and concentrating on developing those technologies further in a complementary fashion will be most beneficial. For the remainder of this dissertation, electrostatic levitation and transport based concepts that are specifically optimized for spacesuit dust mitigation will take primary focus, and the implementation methods for EDS based dust mitigation concept, modeling, and integration into spacesuit outerlayer will be investigated and tested in detail. Additionally, a combination of EDS and WFM coating concept will be studied using small samples of spacesuit outerlayer to identify the most promising combination of technology and the most effective and feasible integration and fabrication methods for spacesuit application.

PART II
CURRENT RESEARCH:
Spacesuit Integrated Carbon Nanotube Dust Ejection/ Removal (SPIcDER)

CHAPTER 4: OVERVIEW OF THE SPIcDER DUST CLEANING SYSTEM FOR SPACESUITS

"Problems are nothing but wake up calls for Creativity" *- Gerhard Gschwantner*

The goal of this research is to develop an autonomous dust cleaning system that is embedded into the outerlayer of the spacesuit which can operate during and after EVAs to continuously repel and remove dust and protect spacesuits from dust contamination. The specific application of the dust cleaning system that can be integrated into the spacesuit outerlayer proposed in this research is known as the SPIcDER system. This chapter provides an overview of this proposed concept that utilizes novel materials and fabrication methods to overcome spacesuit integration challenges based on candidate concepts that were down-selected in Chapter 3. The chapter begins with a summary of challenges for dust mitigation of spacesuits. Overall research contributions to this field with emphasis on dust mitigation of flexible structures are provided in this chapter.

4.1. Relevance and Challenges of Spacesuit Dust Mitigation

Lessons from the Apollo missions emphasize the need and relevance of addressing dust contamination of spacesuits for future long duration lunar missions. The spacesuit is a complex system providing a safe environment for astronauts during EVAs for surface exploration activties. The suit system consists of several layers of material, PLSS, oxygen rich atmosphere, and communication system and electronics. As noted earlier, while the Apollo program utilized basic dust cleaning methods such as manual brushing to remove dust from spacesuits and other equipment, it proved to be ineffective causing further abrasion of the spacesuit outerlayer and required precious crew time to clean the suits.

Based on experiences with dust during the Apollo missions and observations of dust contamination of solar panels during Mars missions, several state-of-the-art active and passive technologies have been proposed in literature for dust mitigation in the recent years. However, most of these techniques, specifically the highly proven EDS using active electrodes, have been demonstrated for use mostly on rigid surfaces such as solar panels, optical planes, glass structures

and thermal radiators (Calle et al., 2011; Margiotta et al., 2010). Application of these technologies for spacesuits has remained a challenge due to the complexity of the suit design.

The particular complexities of spacesuits that challenge the integration of existing dust cleaning technologies into suits can be categorized into the following areas

1. Flexible structure of the soft areas of the suit:
    - Irregular Contours: A major portion of the spacesuits are covered with soft materials as the spacesuit needs to provide sufficient flexibility for mobility of the astronauts and minimize launch mass. The spacesuit system is also shaped to conform to the human body and therefore has irregular contours and uneven surfaces.
    - Fatigue resistant materials/electrode wires: The continuous flexure cycles due to astronaut movement requires high fatigue resistant materials in order to withstand the bending, twisting, folding motions during EVAs and prevent fatigue breakage of materials. In the context of using electrode wires on the outerlayer to implement the EDS dust mitigation concept, high fatigue resistance electrodes will be required.
2. Outerlayer is Teflon® coated surface
    - Adhesion of Electrodes: Due to the chemical inertness of Teflon® and its resistance to VdW forces, traditional methods such as bonding, ink jet printing etc. of adhering materials or electrodes wires on the suit surface would not work. In the context of implementing EDS dust mitigation concept, new methods to attach electrodes to spacesuit surface are required. The conformity of the electrodes to the surface is crucial to utilize electrostatic levitation and transport.

4.1.1. Importance of this Research Field

Dust has been recognized as a major environmental factor for planetary exploration and needs to be addressed prior to sending humans on long duration missions to Moon, Mars and asteroids. Both government agencies, such as NASA and ESA, and commercial entities have plans of furthering space exploration efforts to the Moon, asteroids, Mars and beyond. As such, it becomes imperative to address this basic yet challenging environmental factor that poses challenges to operating in these harsh environments to facilitate maximum utilization of scientific equipment and astronaut time to accomplish mission and science objectives. Providing space hardware and

components that are robust and can withstand such environmental factors become key for long duration space missions.

Long duration space missions will undoubtedly make efforts to maximize astronaut's ability for real time operations using EVAs. It is anticipated that these future EVAs for surface operations could potentially last for long durations (upto 8 hours at a time and upto 6 month long missions, and as long as 500 days on the surface for a Mars mission). Therefore, providing spacesuits that can be utilized for such extended durations without fearing the loss of their functionality with repeated usage due to dust contamination and requiring minimal maintenance time will be imperative for future missions.

4.1.2. Complexity of Ph.D. Research

Dust mitigation of spacesuits involves interdisciplinary research areas of high-level of technical complexity requiring innovative research to address technical and fabrication complexities, operations in harsh environments and astronaut safety. This research specifically focuses on developing a dust cleaning system that can be an integral part of the spacesuit outerlayer, capable of being operated real time during EVAs repelling dust during operations, thereby minimizing crew time to clean the spacesuits.

Developing a technology that can minimize the effects of dust contamination of spacesuits in harsh environments of planetary surfaces is technically challenging due to the complexity of the spacesuit system. The irregular contours of the suit, Teflon® coated surfaces and flexible materials require novel methods to implement dust cleaning systems for a spacesuit. The challenge is to not only to address what type of cleaning system would work for spacesuits but also generate innovative techniques to integrate the cleaning system into the spacesuit. Additional challenges involve addressing how to operate the system in extreme environments of planetary surfaces, design and technical considerations, operational constraints and astronaut safety.

This research involved system design and analysis of spacesuit dust mitigation, understanding of the lunar dust problem, knowledge of lunar soil/dust, generation of a dust cleaning concept that is applicable to spacesuits, implementation and development of the SPIcDER system, fabrication methods for embedding electrodes, materials for high voltage application, analysis of safety aspects, electromagnetic field radiation, prototyping of small scale hardware (3 inch coupons) and

a large scale functional system (knee portion of suit), proof of concept experiments, and validation of the proposed concepts. Figure 4.1-1 is an illustration of the inter-related aspects and complexity of the problem addressed by this research.

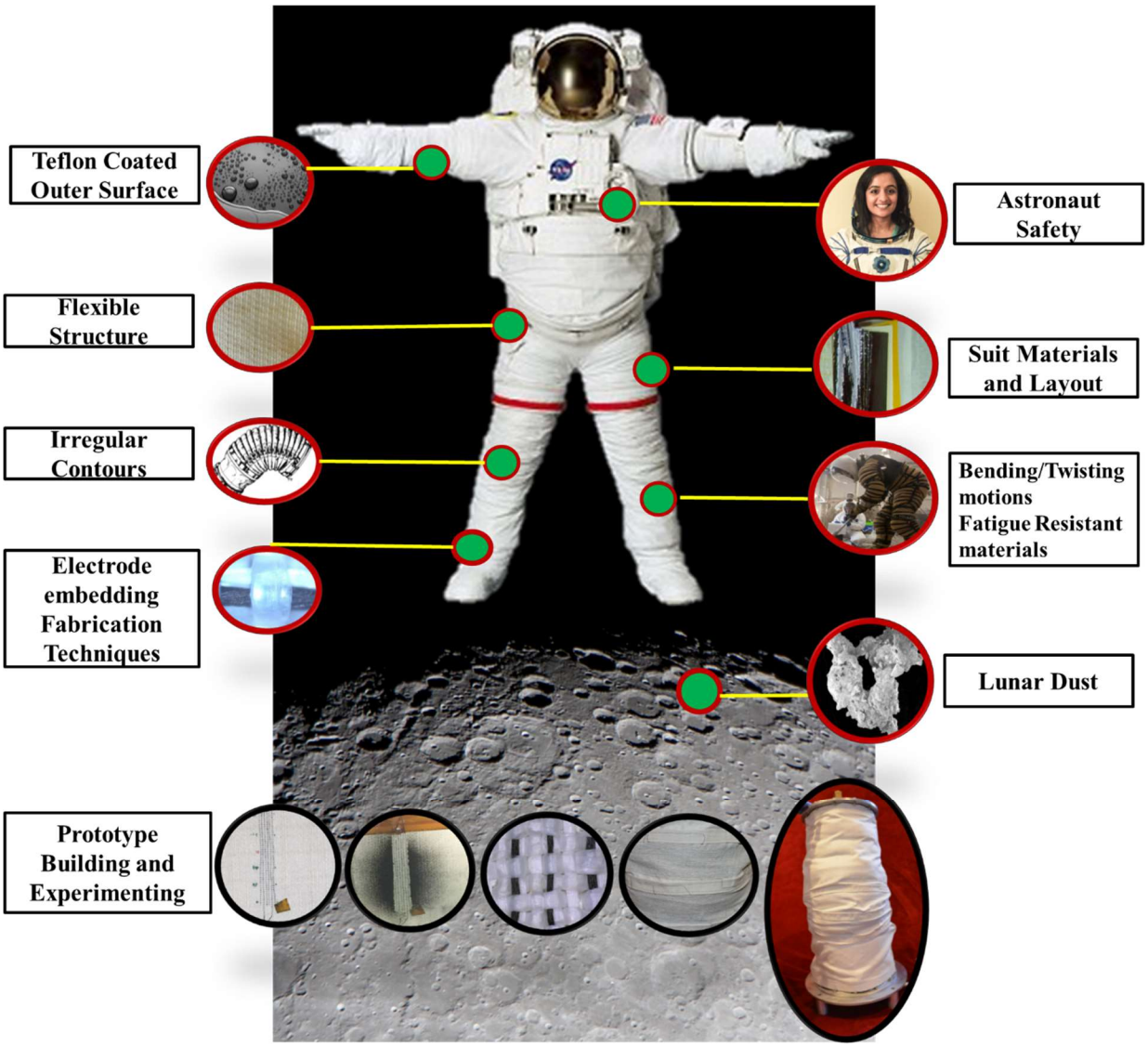

Figure 4.1-1. Complexity of spacesuit dust mitigation for lunar operations

4.2. Proposed Concepts

4.2.1. Concept Overview SPIcDER System

The SPIcDER system proposed for spacesuit dust mitigation consists of parallel yarns made of CNT flexible fibers embedded into the outerlayer of the spacesuit that act as electrodes wires. These CNT fibers when activated utilizing a multi-phase AC voltage signal, would levitate and push the dust off the surface of the material. The system can be further augmented with WFM coating made of lunar dust (in this case lunar simulant) that works to lower the adhesion of dust to the surface, thereby preventing further accumulation of dust. The combination of the CNT electrode network along with the WFM coating is proposed to provide an enhanced dust cleaning strategy for use in spacesuits for lunar missions. The SPIcDER system is proposed to help protect the soft areas of the spacesuit system from dust contamination. The coating may be extended to protect the hard areas (such as the hard-upper torso in new spacesuit prototypes) as well. This technology can be extended to be compatible for other flexible structures requiring dust mitigation and optimized to be used for Mars and asteroid surfaces as well.

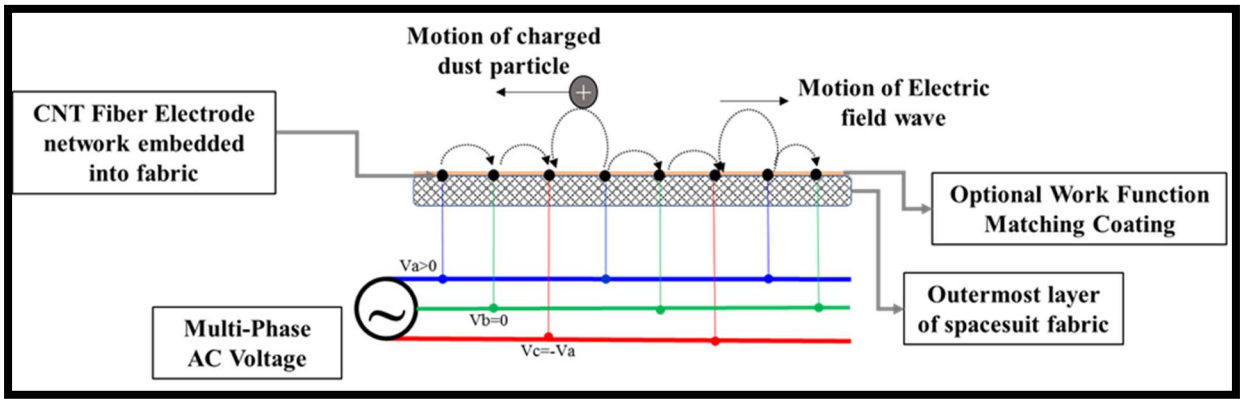

Figure 4.2-1. Working concept of the SPIcDER system

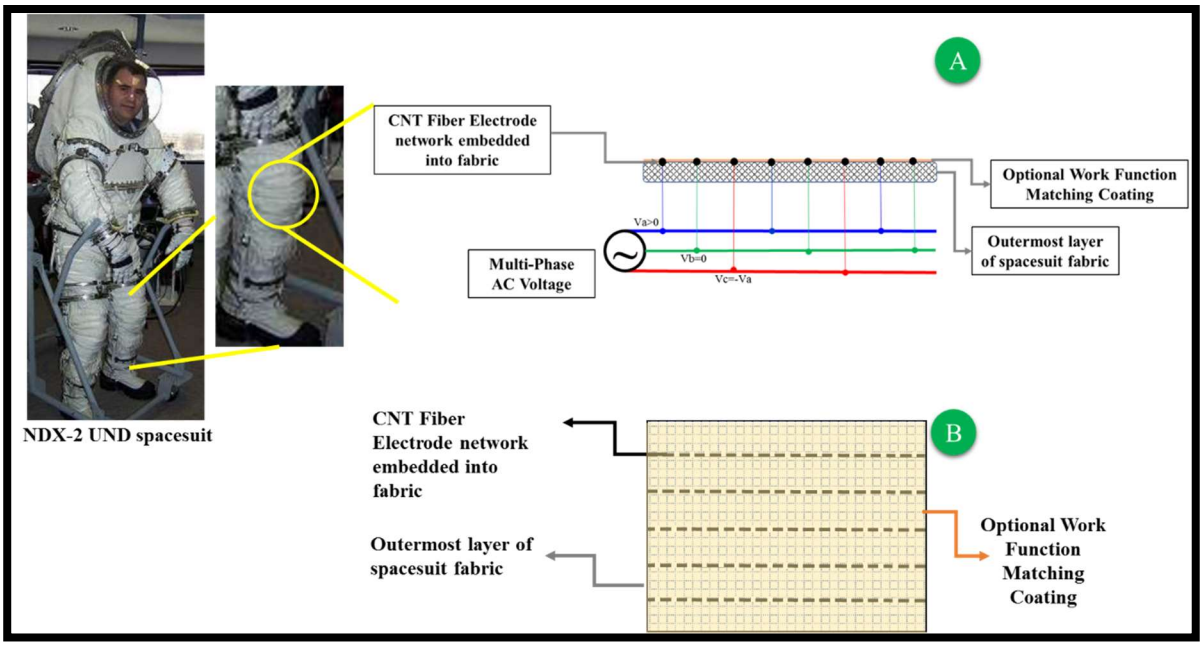

Figure 4.2-2. Schematic showing one potential location on the suit with the SPIcDER system

4.2.2. Novelty of Research

The goal of this research is to develop a spacesuit integrated dust cleaning system concept for operation on the lunar surface to minimize dust contamination of spacesuits. The research can be broadly categorized into two parts

- ***Identify and develop a concept for dust mitigation for spacesuits suitable for soft areas and flexible structures***
- ***Develop and validate a fabrication method to implement the proposed dust cleaning system into spacesuit outerlayer***

This Ph.D. research investigated novel techniques to develop a dust cleaning concept for flexible surfaces and specifically developed the SPIcDER system to be implemented for spacesuits. The proposed concept is based on utilizing a combination of active and passive dust cleaning technologies. The research leverages previously proven EDS active technology and WFM coating passive technology for rigid surfaces and applies new techniques to enable integration of the combined system into spacesuits to mitigate dust contamination. The research specifically focuses on addressing the technical and fabrication challenges of implementing the active electrostatic system into spacesuit outerlayer and defines a fabrication method (s) to blend the active technology using CNT network with traditional craftsmanship of garment making (spacesuit).

The SPIcDER system utilizes conductive yarns made of CNT flexible fibers weaved into the outerlayer of spacesuit to overcome challenges posed by spacesuit design defined in section 4.1. The embedded electrode network can be coated with WFM coating. This new kind of spacesuit outerlayer material mitigates dust contamination in two ways, one active and one passive. The CNT yarns when energized utilizing a AC voltage signal allows the fabric to create a travelling wave of electric field that actively prevents accumulation of dust particles and repels dust particles accumulated. This 'dust repellant smart fabric' performance is enhanced by adding the passive system. The passive strategy using the WFM coating is a novel polymer-based coating that is applied to the top of existing spacesuit fabric such as orthofabric. The coating is of uniform thickness which has the chemical composition of lunar dust simulant, which makes it harder for real lunar dust that has equivalent properties to stick to the fabric.

4.2.3. Problems addressed by this Research

The research addresses mitigation of space dust contamination. Specifically, it addresses two areas of challenges to integrate the active EDS system into spacesuits

1. **Selection of Electrode material for flexible substrates**

Based on the challenges posed by spacesuit complexity, electrode materials to be used for spacesuit application for dust mitigation must meet the following requirements:

- Flexibility
- High mechanical strength: Fatigue resistant
- Low density

This research therefore specifically investigated insertion of a new technology by using yarns made of CNT fibers as electrode wires to integrate EDS into spacesuits due to their ability to meet the electrode requirements for spacesuit application.

Current materials used as electrodes for EDS for dust removal on rigid structures are metal electrodes such as copper, silver and indium tin oxide (ITO). These metallic materials have high electrical conductivity with low mechanical strength, specifically low flexure tolerance and are therefore challenged by fatigue breakage. When flexed, they often exhibit high cycle fatigue due to cyclic loading under repeated mechanical loads. In the context of spacesuits, during planetary EVAs, suits undergo repeated motions that flex, bend, fold or twist suit materials, especially within the leg or arm portions demanding highly flexible and nearly fatigue-free electrode materials.

CNTs are proposed to overcome the challenges of integrating the active dust technology utilized in this research over using metal wires or strips as electrodes for the following reasons:

a. The CNT yarns are flexible and can conform to the spacesuit outerlayer and the existing weaves of the material when embedded. The significance of this flexibility and conformity of the CNT flexible fiber electrodes is fundamental to the performance of the dust cleaning system when the suit flexes, bends or twists.
b. The mechanical properties of CNTs are an order of magnitude higher than highly conductive metallic materials such as copper (details in section 4.3.2).
c. The CNT fibers have superior resistance and resilience to flex fatigue compared to metal electrodes.
d. The low density of CNT fibers makes it an ideal material over using metallic electrodes.

CNT fibers are flexible and have high mechanical strength and fatigue cycle limits that make it a valuable choice as electrode wires compared to the metal electrodes that are currently used for EDS application.

2. Electrode application technique into the spacesuit system

New methods to address adhesion/bonding of electrode material onto the outerlayer of the spacesuits are investigated in this research due to the Teflon (non-stick) coated Orthofabric material and uneven surface of the Orthofabric material. Traditional methods such as sputtering or ink jet printing have been used to adhere electrode wires to rigid surfaces in previous EDS studies. These studies usually incorporated smooth and flat surfaces (such as solar panels, radiators) using a dielectric substrate, which were conducive to using such techniques to attach the electrodes. For application on spacesuits however, due to their irregular contours, weave of the spacesuit fabric and Teflon® coating of outerlayer, novel fabrication methods are needed to integrate electrodes into the suit system. Sputtering and bonding require adhesion to the substrate which is impaired on nonstick materials such as Teflon®. Consequently, this research focused on developing and testing a fabrication technique to implement the SPIcDER system and investigated other fabrication techniques using traditional craftsmanship of garment making to develop this smart material that is capable of repelling dust. Section 4.5. details various fabrication techniques.

4.2.4. Theoretical Foundations

The salient features of the spacesuit outerlayer material that will be embedded with the CNT electrode network are characterized as follows

1. Electrode Layout
    a. Alternative conductive (electrode wires) and non-conductive threads
    b. Pre-determined minimum spacing between conductive threads
2. Connection to external multi-phase AC voltage generator
    a. Conductive threads should be terminated methodically to be attached to external voltage signal supply
    b. Conductive threads of distinct phases of the electric signal must be isolated from one another
3. Material properties
    a. Non-conducting substrate
    b. The dielectric properties of the underlying materials
4. Waveform Characteristics
    a. Single phase system produces a standing wave of electric field where the dust is just levitated but not pushed off
    b. Multi-phase signal helps generate a travelling wave to provide lateral transport of particles away from the electrodes
    c. Frequency of the waveform (details in Chapter 6)
    d. Amplitude of the voltage- dust removal performance is directly proportional to the voltage levels which increases the electric field. However, the applied voltage is limited by breakdown characteristics (details in Chapter 6)

4.3. Technologies Integrated for the SPIcDER system

4.3.1. Electrodynamic Dust Shield

The SPIcDER system leverages the EDS active technology concept developed and proven by NASA for rigid surfaces that uses electrostatic and dielectrophoretic forces to carry dust particles off surfaces by generating a travelling electric field. Chapter 3 provides a more detailed explanation of this EDS technology. Despite proof that EDS performs effectively as a dust mitigation strategy on rigid surfaces implementing this technology for use on spacesuits has remained a challenge. The materials and fabrication techniques utilized for applications such as solar cells, optical surfaces and radiators which have smooth and even surfaces are not directly applicable to the spacesuit system. The complexity of spacesuit design described previously

necessitate new active materials with enough flexibility and strength to serve as electrodes. Moreover, novel fabrication methods are needed to integrate these materials into the suit system to embedded a parallel electrode system into the surface of the spacesuit outerlayer. As such, this research addresses the challenges of selecting an electrode material and fabrication technique to enable the application of EDS technology to spacesuits.

Prior to identifying and proposing use of yarns made of CNT fibers to create the electrode network within the spacesuit outerlayer for dust mitigation, several techniques were initially investigated to integrate electrodes into the suit fabric. Below is an overview of these ideas.

1. Electrodes woven into Teflon fabric

One way to introduce electrodes into the outerlayer of the spacesuit is to weave the electrode wires into the Teflon (Orthofabric or Beta cloth) fabric of the spacesuit. Teflon has a high dielectric strength and some basic calculations yield the thickness of the fabric needed to withstand the voltage and insulate the astronaut (details of thickness in Chapter 8).

2. Electrodes deposited on fabric using films

Previous experiments by Calle et al. utilized films that were already printed with electrodes and then adhered them to the rigid surfaces as needed. The challenge using the same process on Teflon coated suit material is being able to adhere these electrode films to Teflon due to its non-stick properties. By using special adhesives or perhaps etching the surface of Teflon, we may be able to attach the EDS film to the Teflon outer layer. However, the films would not conform to the fabric and movement of the astronaut which would impact the dust cleaning capability.

3. Electrodes embedded between two fabric layers (Sandwich method)

Another option surveyed was to embed the electrodes in between two thin layers of the outer layer fabric of the spacesuits. In this case, the first layer may be etched or an adhesive can be used to adhere the EDS film, which contains the electrodes and then covered with another layer of Teflon (outerlayer of spacesuit). However, the electric field intensity generated by the electrodes sandwiched between two layers may have reduced intensity on the outside of the outerlayer (electric field reduces by square of the distance from the electrode) and may not be sufficient to break the adhesive forces and repel dust repel dust particles. Chapter 8 shows a few experiments that were conducted showing this effect with electrodes in between two orthofabric layers.

4.3.2. Work Function Coating

The WFM coating is a thin layer (~100nm) of coating that has the same composition of lunar dust simulant. This coating is applied over the spacesuit outerlayer embedded with the CNT electrode network. The coating works by altering the chemistry of the surface exposed to dust, particularly designed to minimize electrostatic forces of adhesion. The work function is the energy required to or remove an electron from a material. During triboelectric-charging, electrons are transferred from a material that easily loses electrons (i.e., has a low work function) to a material that holds tightly onto its electron (i.e., has a high work function) shown in Fig 4.3-5 causing the two materials to adhere (Gaier et al., 2011). Triboelectric-charging can be minimized if the work function of the two surfaces coming into contact with each other are similar.

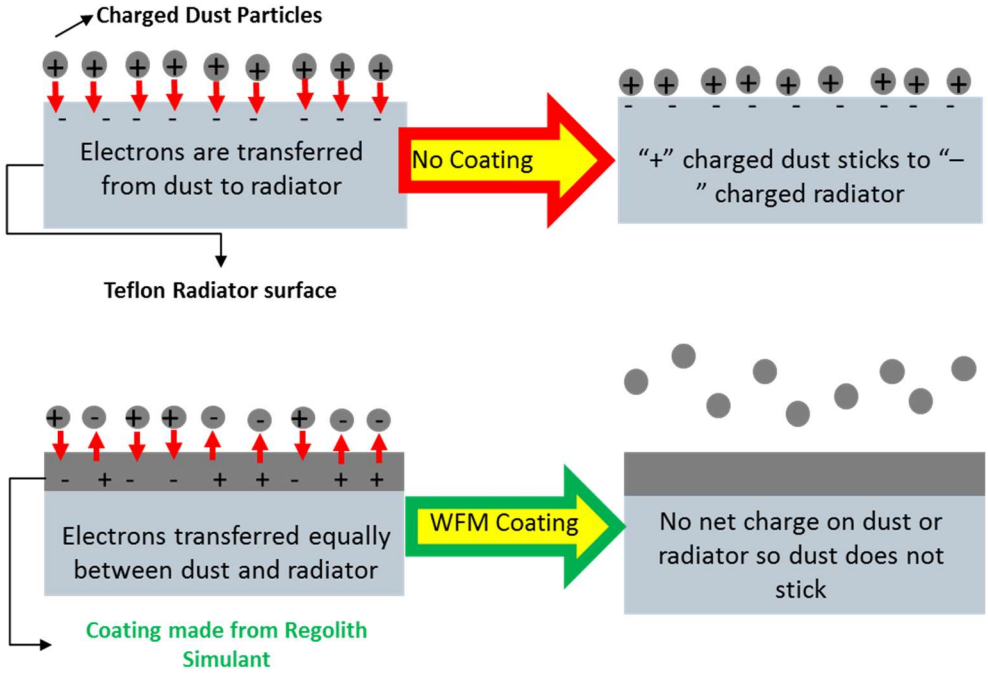

Figure 4.3-5. Working concept of WFM Coating. [Top] Mechanism of dust adhesion when no coating is present. [Bottom] Having a work function for the surface that matches the work function of the lunar dust minimizes dust adhesion to the surface.

The underlying concept of the WFM coating being assessed in this study has been previously developed and demonstrated by NASA GRC using the NU-LHT-1D highland lunar simulant (Gaier et al., 2011). Experiments conducted by Gaier et al. on fluorinated ethylene propylene (FEP) and other thermal control surfaces in vacuum and dry conditions showed that modifying the surface chemistry of these dust exposed surfaces by applying ~100 nm thick WFM coating showed

promising results in the reduction of dust adhesion. In the context of the current research, matching the work function of the outerlayer of spacesuits to that of the lunar dust (lunar dust simulant for experiments) is proposed to minimize triboelectric charging, thereby reducing dust adhesion and further dust accumulation. Since the effectiveness of WFM coating is prominent in vacuum and dry conditions as shown in previous studies, the scope for the research conducted in ambient conditions is limited to evaluating the feasibility of applying WFM over CNT fiber embedded orthofabric coupons and evaluating the effectiveness of the integrated active and passive system. Results from coupons experiments are used to understand if the WFM coating had any effect on the cleaning performance using energized CNT electrodes.

4.3.3. Carbon Nanotube Fiber Technology

Discovered in 1991 by Professor Sumo Iijima, CNTs are an allotrope of carbon with a cylindrical structure with diameters on the order of 1 nanometer (10^{-9}), which are a high-performance technology breakthrough material with applications in nanotechnology, electronics, material science, optics, etc. CNTs have exceptional properties of mechanical strength and stiffness, electrical and thermal conductivity, and low density (on the order of ~1.6 g/cm^3, versus ~8.96 g/cm^3 for copper), making them ideal multifunctional materials combining the best properties of polymers, carbon fibers, and metals (Behabtu et al., 2013). While single molecule strength and electrical conductivity of CNTs are far superior to most materials, translating these properties to a macroscopic scale has been a significant challenge. Handling CNTs with sufficient length, stiffness, and chemical inertness introduces major challenges in material processing. However, researchers at Rice University and their affiliate DexMat® have invented a manufacturing process to continuously produce lightweight CNT fibers on the order of tens of meters in length (See Fig.4.3-1) (Ericson et al., 2004). They have reported the properties of their fibers approaching the high specific strength of polymeric materials and carbon fibers, while also achieving high specific electrical conductivity of metals and specific thermal conductivity of graphite fibers.

While the individual CNT's at the microscopic level are very stiff, the yarns made from these CNT fibers are on the contrary, very flexible. This is possible because the individual stiff CNTs are only on the order of a few microns long while the yarns are made up of strands (trillions and trillions of individual CNTs) of well aligned fibers that can slide over one another. The CNT yarns

produced by Rice University/Dexmat® are capable of surviving greater than million cycles of flexure fatigue (unpublished internal tests). Other studies in literature on CNT yarns demonstrated their excellent resistance to flexural fatigue (Xu F et al., 2014). CNT yarns are therefore proposed to overcome the challenges of integrating the active dust technology utilized in this research over using metal wires or strips as electrodes for reasons specified in section 4.2.3- high flexibility and mechanical strength, resistance to flexure fatigue, and low density. Figures 4.3-2 through 4.3-4 illustrate the superior properties of the CNT electrodes when compared to other materials generally used for EDS electrodes. The numbers are normalized using Equation 5 where *x'* is the normalized value of each data point *x*.

$$x' = \frac{x - \min(x)}{\max(x) - \min(x)} \tag{5}$$

As an illustration, Figure 4.3-4 shows a comparison of mass of electrodes required to cover the knees, elbows and boot areas of a lunar spacesuit to prevent dust contamination using various materials estimated based on the quantity of electrodes and properties shown in Table 4.3-1. As seen, the mass of the CNT yarn electrodes is an order of magnitude lower than other frequently used metallic materials in EDS applications. The comparison is conducted utilizing the best value of CNT fiber density reported by Behabtu et al. (2013). The density values of the yarns utilized in current research from DexMat® are close to 1 g/cm^3. The calculations assume that each of the areas of the suit are covered with 100 electrodes (2 knees, 2 elbows, 2 boots). Use of CNTs for space applications detailed in Chapter 7.

Figure 4.3-1. [Left] DexMat's CNT fibers utilized in current research experiments, [Right] Display of strength and utilization of CNT fiber developed by Rice University. *Suspending a 46g light-emitting diode lit using two 24-µm-thick CNT fibers (Behabtu et al., 2013)*

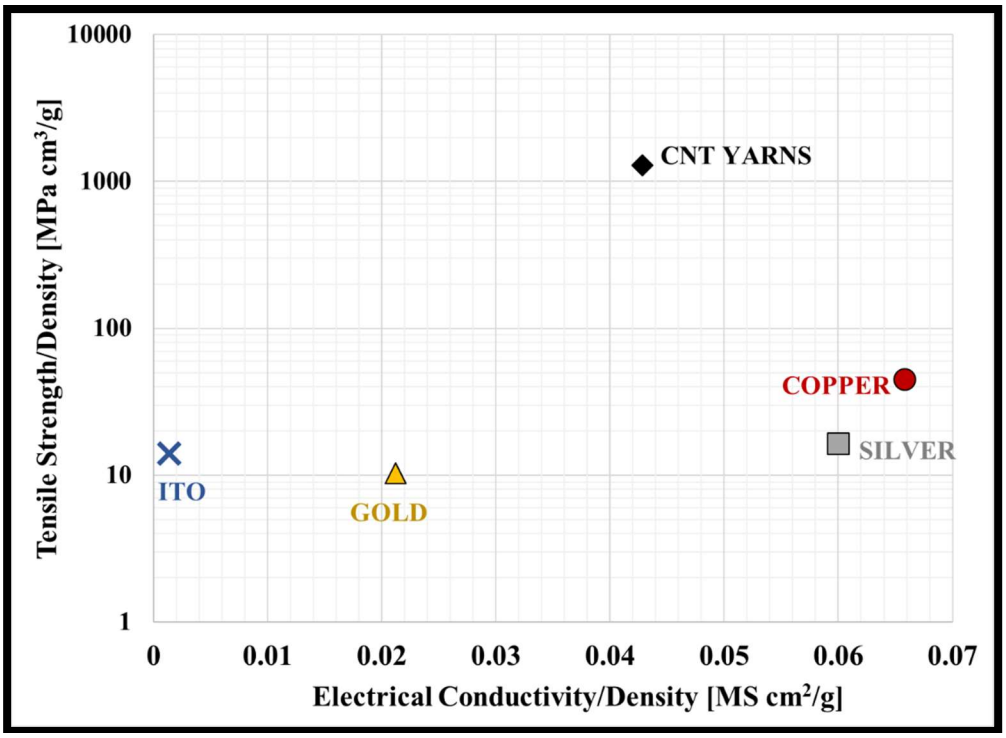

Figure 4.3-2. Ashby plot of specific tensile strength versus specific electrical conductivity of commonly used electrode metals compared to CNT yarns. *CNT data based on best properties reported by Behabtu et al. 2013*

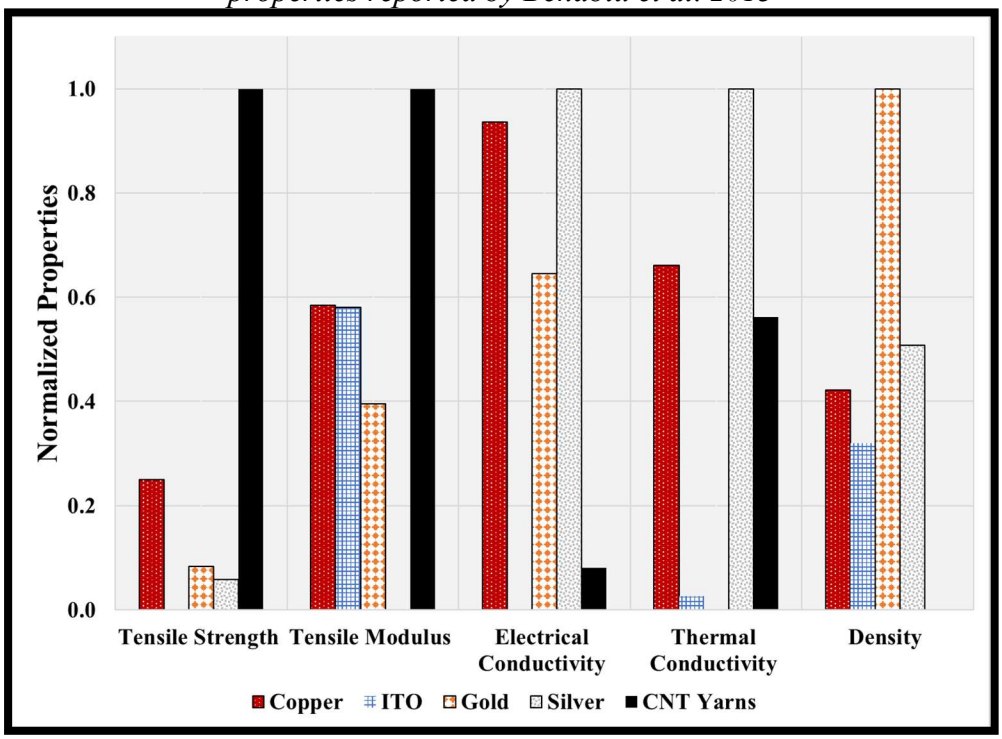

Figure 4.3.-3. Comparision of normalized properties. CNT modulus based on ~20 mm individual filament from ~100-500 m spools. *Best properties of CNT reported in Behabtu et al. 2013 and utilized for analysis.*

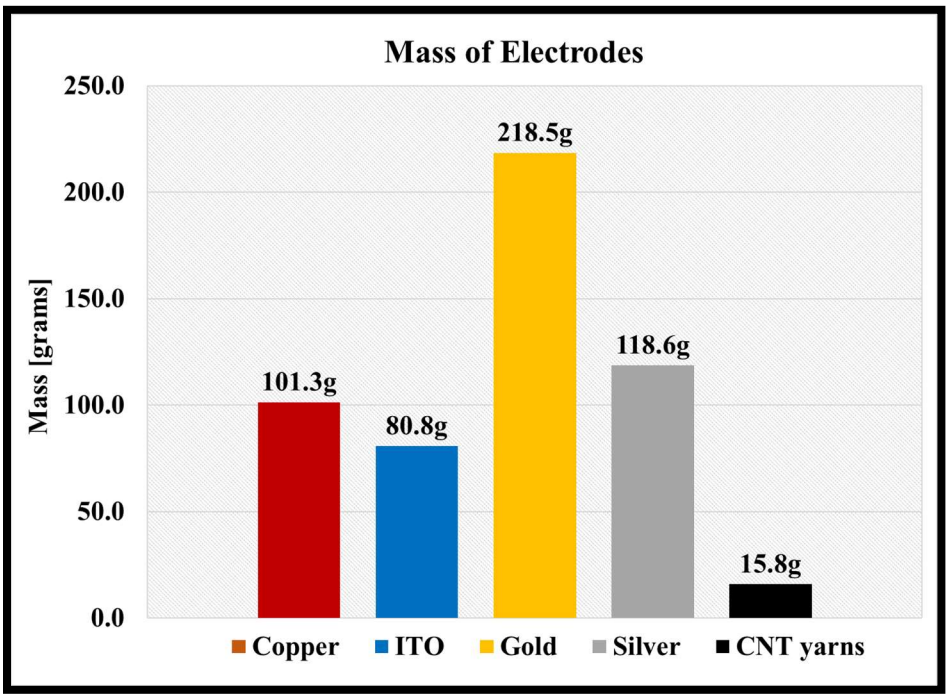

Figure 4.3-4. Comparing mass of electrodes required to cover the knees, elbows and boot areas of the suit

Table 4.3-1. Data used to calculate mass comparison of electrodes of various materials

	Silver	Copper	Gold	ITO	CNT yarns
Conductivity (S/m)	6.30E+07	5.90E+07	4.10E+07	1.00E+06	6.00E+06
Resistivity (Ω.m)	0.0	0.0	0.0	0.0	0.0
Resistance (Ω)	0.3	0.3	0.5	19.1	3.2
Mass Density (g/cm3)	10.5	9.0	19.3	7.1	1.4
Diameter of Electrodes (mm)	0.2	0.2	0.2	0.2	0.2
Number of electrodes (2 knees,2 elebows, 2 boots 100 each)	600.0	600.0	600.0	600.0	600.0
Length of Electrodes (m) (~25")	0.6	0.6	0.6	0.6	0.6
Total Length (m)	360.0	360.0	360.0	360.0	360.0
Volume of Electrodes (m3)	0.0	0.0	0.0	0.0	0.0
Volume Conversion into cm	11.3	11.3	11.3	11.3	11.3
Total Mass (grams)	118.6	101.3	218.5	80.8	15.8
% mass compared to copper	117.1	100.0	215.6	79.7	15.6
Source of Data	Goodfellow, 2013	Li and Zinkle, 2012	AZoM, 2013	Indium Corporation ®; Neerinck, & Vink, 1996	Behabtu et al., 2013 (*Reports best properties. Also based on yarns from current supplier)

4.4. Overall Research Contributions, Scope and Assumptions

4.3.1. Research Contributions

The contributions of this research can be summarized as follows:

1. *Comprehensive assessment* of *state-of-the-art* active and passive dust mitigation technologies and *down-selection of viable technologies* for spacesuit application -***See Chapter 3***
2. Development of a *novel dust cleaning system design concept*- the ***SPIcDER system*** for implementation within the spacesuit outerlayer with particular emphasis on flexible/soft areas of the suit -***See Section 4.2, Chapters 5 and 9***
3. Development of *Fabrication Technique (s)* to integrate the SPIcDER system using traditional craftsmanship into spacesuits- ***See Section 4.4, Chapter 5 and 9***
    - Developed several conceptual processes for manufacturing a smart fabric characterized by a combination of electrically conductive CNT yarns and insulative threads to form multi-ply strands capable of repelling dust when connected to a multi-phase AC voltage signal that provides dust mitigation
4. *Design, technical and operational considerations* for implementation of the SPIcDER system – ***See Chapter 7***
5. *First demonstration* of a fabrication method and application of CNT flexible yarns into a spacesuit outerlayer material utilizing coupon sized prototypes (3 inches) -***See Chapter 5***
6. *Proof of concept* of dust cleaning performance using the SPIcDER system through experiments conducted on coupons made of spacesuit material embedded with CNT yarns with lunar dust simulant - ***See Chapter 5***
    - *Demonstrated feasibility* of utilizing CNT fiber technology for repelling lunar dust simulant when applied with a multi-phase AC voltage
    - *Experimentally examined and characterized* the *dust cleaning performance* of the SPIcDER System
    - *Performance demonstration in both ambient and vacuum conditions*- ***Chapter 9***
7. First demonstration of integrating conductive CNT electrodes with passive WFM coating through coupons made of spacesuit material - ***See Chapter 5***
    - Evaluated and demonstrated feasibility of combined active and passive concept of applying WFM over CNT fiber embedded orthofabric coupons

- Experimentally characterized the effectiveness of dust cleaning performance of the combined system using coupon sized samples in laboratory conditions using lunar dust simulant

8. Development of E*ngineering methods* and *Simulation tools* for practical implementation of the SPIcDER system suitable for Spacesuits. Simulation tools would help conduct design trade-offs in the future - ***See Chapters 6,7 and 8***
9. Comprehensive assessment of SPIcDER operations relative to flight suit implementation. Development of simulation tools to analyze spacesuit material layout for astronaut safety and recommendations for design and operational implementation- ***See Chapter 8***
10. Development and *experimental validation of a scaled functional prototype* of a knee joint section of the spacesuit (knee-portion) with embedded SPIcDER system-***See Chapter 9***
11. Generation of a list of other applications and techniques using the proposed SPIcDER concept beyond spacesuits for dust mitigation of flexible surfaces -***See Chapter 10***
12. Proposed improvements, alternative architectures, and future work to further mature the SPIcDER system- ***See Chapters 9 and 10***

4.3.2. Underlying Assumptions

This section captures assumptions that were made as part of this research to allow the progress of ideas and implementation techniques. Further details for some of these assumptions are discussed in detailed in subsequent chapters where applicable.

1. CNT electrodes
    a. The CNT electrodes utilized in this research for simulation are assumed to be of uniform thickness and properties throughout the length of the electrodes. - ***See Chapter 5 for experimental and 6 for simulation assumptions.***
    b. The quality of the CNT electrodes is based on the manufacturing techniques for CNT fibers by the supplier. Optimizing quality of CNT fibers is beyond the scope of this research.
2. Spacesuit Material Layout
    a. The ISS EMU spacesuit layout has been utilized for analyzing the safety aspects related to electric field exposure for safety and parametric analysis. The EMU is an

improvement from the Apollo mission spacesuits that utilizes optimized set of material layout based on lessons learnt from Apollo missions- ***See Chapter 8.***

b. The Orthofabric material has been utilized as the outerlayer for all experimental purposes as this is the material used for ISS EMU spacesuit and a potential material for future spacesuits.

c. The Orthofabric material is a combination of Gore-Tex® on the front side and Nomex®-Kevlar® on the back side. For simulation analysis during this research the outerlayer of the spacesuit is modeled as Teflon throughout the thickness of the outerlayer-***See Chapter 6.***

d. The Aluminized Mylar layer in a spacesuit is backed by a Dacron Scrim. For simulation purposes, the entire thickness of this layer has been modeled using as a 6 μm Aluminum sheet, followed by Mylar. Dacron scrim was ignored for the analysis.

e. The materials of the spacesuit are assumed to be of high quality. The simulations did not investigate consequences due to defects in the materials. The properties of the layers are assumed to be consistent and degradation of their properties are not modeled

f. It is assumed that adding the CNT fibers and WFM coating to the outerlayer does not compromise the pressure garment mechanical and thermal properties.

3. High Voltages through outerlayer of spacesuit with crew inside

    a. Assumption is that the thicknesses and layers of spacesuit provide the required insulation for the crew inside.

    b. A parametric estimation of spacesuit thicknesses needed to provide astronaut protection and the amount of insulation provided by the existing layers is provided in ***Chapter 8.***

4. SPIcDER System Operation

    a. The dust cleaning system is assumed to be operating (Power ON) 100% of the time during EVAs. It is recognized that there could be constraints with scientific equipment for operating the system continuously. The system is shown to be effective in continuous and burst mode. These modes of operations can be optimized for the type of EVA. Recommendations on operational modes are provided, however specific timeline of operations not analyzed - ***See Chapters 7,8,9.***

5. Lunar Simulant
    a. JSC-1A simulant is utilized for experiments and NU-LHT lunar simulant is utilized for WFM coating. The simulants utilized in conducting the experiments during this research is assumed to provide a good basis to replicate lunar dust properties.
    b. Utilized simulant sizes that were pre-sorted into respective PSDs.

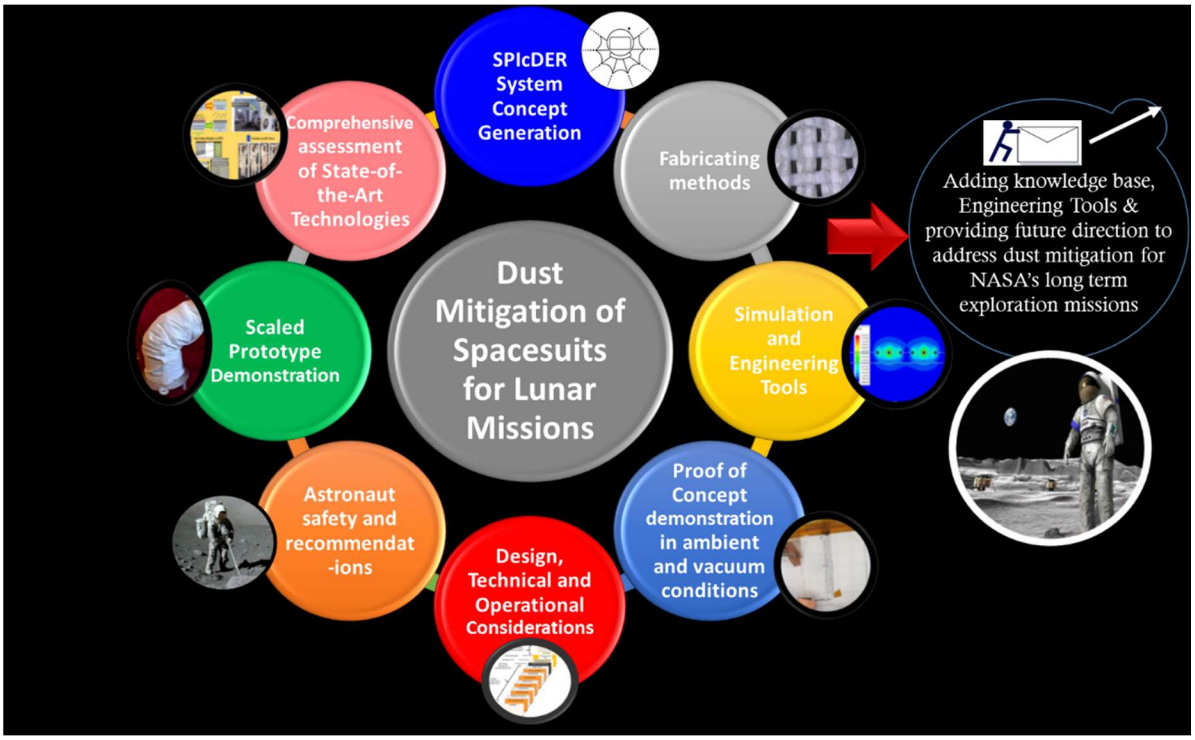

Figure 4.3.-1. Expected outcomes of this research

4.5. Fabrication Techniques

This research specifically developed and validated the feasibility of one of many conceptualized fabrication methods to embed CNTs into spacesuit outerlayer. An important aspect of this research is to identify and develop a fabrication method (s) to integrate the conductive CNT yarns into the outerlayer of the spacesuit to implement the SPIcDER system. The intent is to be able to identify a technique that can exploit the use of traditional craftsmanship of garment making so that electrodes can be easily integrated and replaced when necessary into the spacesuit outerlayer and other similar flexible materials (space habitats, flexible antennas etc.). Consequently, several fabrication methods have been identified to help integrate a CNT yarn based electrode network into the spacesuit outerlayer fabric.

The fabrication methods described here can be implemented with a broad range of weaving patterns and can be optimized for specific applications (garments, glove, tents, etc.). The identified fabrication methods can be manually applied or automated into the fabric production process which can be implemented at the fabric manufacturing level itself or at the product (ex: garment, spacesuit) preparation level.

During this research one of these proposed fabrication methods was experimentally validated that employs manually embedding CNT electrodes into the spacesuit orthofabric material. Demonstration of both the fabrication technique and the dust cleaning capability of the embedded SPIcDER system was conducted by building several coupons (~3 inches) made of spacesuit material and a scaled prototype of a joint knee section based on the NDX-2 lunar spacesuit prototype dimensions. Experiments conducted provided insights into the feasibility and challenges of the manufacturability of the SPIcDER system.

The following sections describe the fabrication method validated using experiments during this research and other conceptualized fabrication methods that can be implemented on various flexible surfaces requiring protection from dust contamination such as space habitats, inflatable structures, flexible solar panels etc.

A. Fabrication technique developed and validated in the current experiments

The fabrication technique utilized to integrate the conductive CNT yarns into the orthofabric material in this research is based on basic technique of weaving and embedding the CNT yarns only on the front side of a finished orthofabric material.

Using a pre-specified spacing, and leveraging the spacing characteristics of the orthofabric material, the CNT electrodes were embedded into the weaves of the material using a simple sewing needle by carefully following the warp direction of the orthofabric material weave and embedding the CNT yarns by lifting alternate weft threads methodically, going under and over every weft thread to embed the CNT yarn. Figure 4.5-1 provides an overview of the fabrication method and the finished product. The embedded CNT electrodes are all oriented in the warp direction parallel to each other, spaced at 1 mm or 2 mm intervals and with the electrodes exposed only on the outer surface of the orthofabric. By maximizing the exposure of CNT yarn on the front side of the orthofabric material, the electric field generated by the electrodes on the front side is maximized in order to enhance the dust repelling performance. The CNT yarn exposure on the backside is minimized for safety concerns. Such a configuration would help reduce the electric field intensity

and exposure on the inner side of the fabric that faces the astronaut. This fabrication technique as described is applicable to already produced/finished fabric materials that include warp and weft threads, in this case the orthofabric material of the spacesuit.

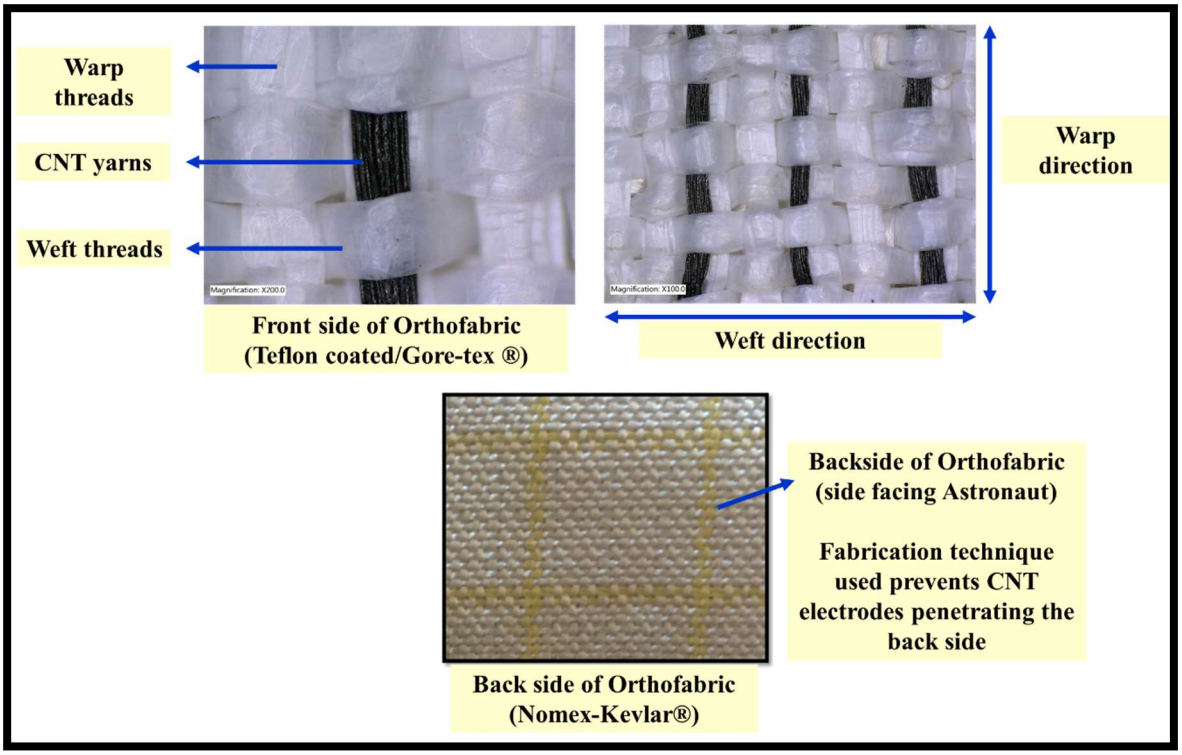

Figure 4.5-1. Fabrication technique developed and validated in this research

Other fabrication techniques conceptualized during this research can be categorized into two levels (implementation at the fabric making level and implementation at the finished product level) and are described in the following sections

B. Implementation of conductive electrodes at the fabric making level

Conductive fibers can be embedded into flexible materials/fabrics during the process of producing the fabric itself. The conductive fibers are utilized as an integral part of the fabric manufacturing process. Methods in this category may be applied either manually using hand looming processes or designed into an automated loom. Three fabrication methods are identified within this method.

B.1. Conductive fibers/yarns/threads implemented into the warp threads

The warp threads of the fabric during the fabric making process will include conductive fibers where, the warp threads will alternate between conductive and insulative threads based on pre-specified spacing of the electrodes. Spacing of the conductive and insulative threads can be

controlled by warp arrangement and/or by thickness of each warp thread. In this method while the warp threads have conductive and insulative threads alternatively placed based on the pre-specified electrode spacing, the weft threads should be insulative. The arrangement of these threads in such a specified manner can be achieved while the fabric is being manufactured using an automated loom or a handloom where the required conductive and insulative threads are pre-situated on bobbins. After weaving is completed the conductive threads of the respective phase are to be collected and terminated into one connection. No two conductive threads of distinct phases should touch each other. Details on terminal connections described in Chapter 7.

B.2. Conductive fibers/yarns/threads implemented into the weft threads

In this method, during the fabric making process the warp threads will be insulative, while the weft thread will be a continuous conductive fiber. The spacing of the weft conductive thread can be controlled by either the thickness of the weft thread or an additional insulative weft thread may be woven in the same weft direction. Once the weft thread is woven, each end of the weft turn of the conductive fiber should be terminated to remove any continuity within the adjacent conductive thread. The conductive threads of the respective phase are to be collected and terminated into one connection. No two conductive threads of distinct phases should touch each other.

B.3. Conductive fibers/yarns/threads implemented into both warp and weft threads

For complex patterns of conductive fibers for dust mitigation and other applications that might be benefited from the high voltage electric field, both the warp and waft threads may be embedded with conductive fibers during the fabric making process to create a smart fabric. These conductive fibers can be connected to an AC voltage signal and parameters of voltage, frequency and phase may be optimized appropriately for required application. The main requirement is to make sure that conductive fibers of the distinct phases do not touch/overlap.

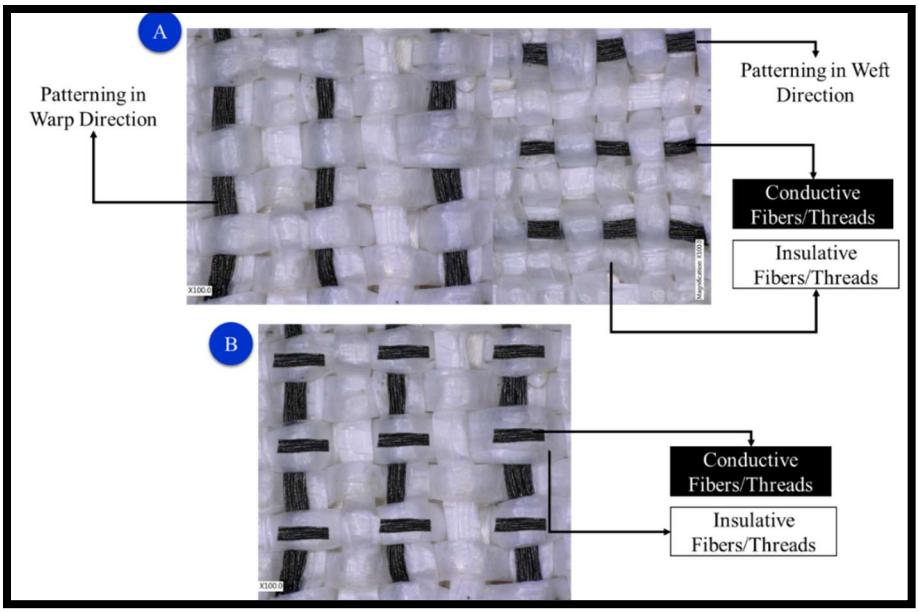

Figure 4.5.-2 [A] Areas with "vertical" weave, and areas with "horizontal weaves" [B] Superimposed "vertical" weave and "horizontal" weave, insulated by a thin film of insulating material or fabric material.

C. Implementation of conductive electrodes on the finished fabric

The method utilized for experiments in this research embedded CNT yarns on a finished orthofabric material. A few techniques may be used to embedded CNTs in a finished fabric. Attachment to the finished fabric (dust mitigation electrodes added onto the finished fabric)

C1. Manually weaving/sewing (Similar to that explained in section A)

C2. Using a sewing machine

A sewing machine may be utilized to easily embed the conductive yarns on to a finished fabric by pre-defining the spacing between electrodes similar to embroidering patterns on fabric materials. The conductive thread may be combined with an insulative thread to sew the electrodes on the fabric for strength or for ease of fabrication. See Figure 4.5-3

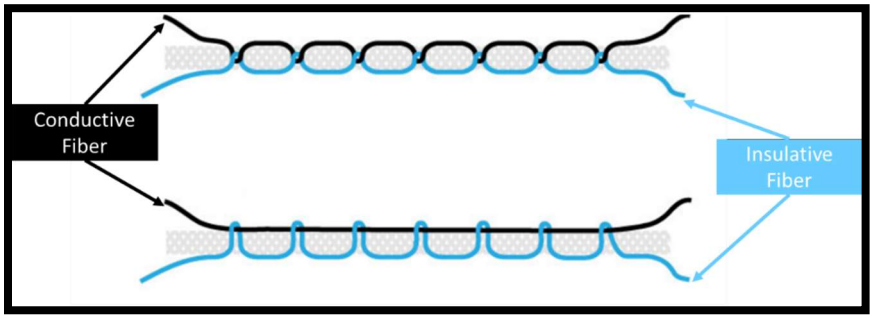

Figure 4.4-5. Technique to embed CNT fibers on the top layer of the spacesuit fabric using sewing machine techniques

C3. Crochet

C4. Methods for Non-Teflon Surfaces

- Bonding (for non-Teflon surfaces)

While the current research focused on embedding conductive fibers into spacesuit outerlayer which is a Teflon coated surface, other flexible materials made of non-Teflon surfaces pose less constraints on being able to utilize traditional methods of attaching electrodes to their surfaces. CNT yarns can be bonded to non-Teflon surfaces using adhesives with dielectric properties that are compatible and do not impact the dust cleaning performance of the embedded electrodes.

- Finished patterns, Applique methods

Other methods that can be utilized on non-Teflon surface include preparing optimized electrode patterns using CNT yarns on separate dielectric film/substrate specific to the application in the required shaped and orientation needed, and bonding the substrate to the flexible surface as needed.

Several of the above described fabrication methods are applicable to many applications and flexible surfaces. While the current research employs a manual method of embedding conductive yarns into finished spacesuit material, it is recognized that manual methods restrict customization of the weave and use of materials. Furthermore, manual methods are practical for only small areas (~inches) and difficult to scale (time consuming) for larger areas such as astronaut suits, space habitat structures, flexible antennas etc. For implementing predefined complex conductive electrode patterns that may correspond to superior dust cleaning performance and corresponding waveforms characteristics for large areas, some of the automatic techniques described in this section at the fabric manufacturing process would be appealing to develop large quantities of dust repelling material. Further details on an automatic method to weave the fibers into the fabric making process are captured in a patent application submitted during the timeline of this research (Manyapu and Leora, 2017).

4.6. Technical Design and Operational Aspects for the SPIcDER system

The SPIcDER system concept consisting of active electrodes and a AC voltage signal generator might be easily applied to large, stationary and static flexible surfaces with less complexity such as space habitats, flexible solar panels etc. However, application of the dust cleaning system for the spacesuits is complex due to the intricacy of suit design and operational

complexity of EVAs. Below is a list identified as areas of considerations involved in implementing the SPIcDER system. These aspects are described in further detail in Chapters 7 and 8

- Material Properties
- Mass
- Power
- Thermal
- Safety (See Chapter 8)

4.7. Summary

The goal of this research is to build a dust cleaning system that is an integral part of the spacesuit to protect suits from the deleterious effects of dust for long duration lunar surface. This research demonstrates the viability of integrating active electrodes into the soft areas spacesuit system via the development the SPIcDER concept. The research explored usage of high performance CNT flexible yarns as electrode wires and novel fabrication techniques. CNT yarns are embedded into the outerlayer of the suit by utilizing the fabrication techniques developed in this research. The system can be further augmented by applying the passive WFM coating over the CNT electrodes. The combined active and passive strategy provides a basis for self-cleaning spacesuits to prevent dust contaminating. The dust cleaning technology using CNT yarns and the fabrication methods developed in this research bridge the gap for using existing technologies for spacesuit application. The overall contributions of this research provide a foundation to explore potential applications of the SPIcDER system for various other flexible structures (space habitats, flexible solar cells etc.). The concept can be extended to be compatible for future Mars and asteroid missions as well.

CHAPTER 5: PROOF OF CONCEPT DEMONSTRATIONS

"Extraordinary claims require extraordinary evidence"- *Carl Sagan*

Preliminary proof-of-concept studies were undertaken to investigate the feasibility of embedding CNT flexible fibers utilizing the proposed fabrication techniques into spacesuit outerlayer, and to characterize the performance of the dust cleaning capability of the SPIcDER system. Several coupons made of Orthofabric material are prepared and tested. Experiments were conducted in ambient and vacuum conditions using JSC-1A lunar dust simulant to study the viability and dust cleaning performance of the concepts. The demonstrations presented in this chapter provide preliminary evaluation of the techniques and an understanding of the challenges involved in utilizing this technology for flight suit implementation.

5.1. Description of Experiments

Two experimental test series were conducted. An overview of these test series is highlighted in Table 5.1-1. Details of these experiments and results are discussed in the following sections.

Table 5.1-1. Overview of proof of concept experiments conducted

Information	Test Series-1	Test Series-2
Timeframe	Nov 2015-Feb 2016	June 2016-August 2016
Location	NASA Electrostatics and Surface Laboratory (ESPL), KSC, FL	Boeing Innovation Cell, Houston, TX
Environments	• Ambient • Preliminary Vacuum	Ambient
Samples Evaluated	• 3 in x 3 in spacesuit outerlayer orthofabric coupons • Embedded with uninsulated CNT fibers • 3 phase AC signal, 2 coupons @ 2 phase signal	• 3 in x 3 in spacesuit outerlayer orthofabric coupons • Embedded with CNT fibers and coated with WFM coating • 3 phase AC signal
Lunar Dust Simulant	• JSC-1A • 50-75 μm • 10-50 μm	• JSC-1A • 50-75 μm • 10-50 μm
Objectives		
Primary	• Investigate feasibility and provide preliminary evaluation of dust cleaning capability utilizing CNT fibers • Compare fabrication using copper electrodes and	• Evaluate combination of passive WFM coating and active CNT flexible fibers • Understand if WFM coating has any effect on the cleaning performance of active
Secondary	• Understand challenges involved in utilizing SPIcDER techniques and fabrication methods for flight suit implementation • Future direction for refining the implementation methods	• Validate repeatability of cleaning performance from previous tests

5.2. Methods and Materials

5.2.1. Test Samples for Test Series-1:

Multiple test coupons made of orthofabric material of approximately 3 in x 3 in (76 mm x 76 mm) were applied with multiple configurations of the CNT fiber electrode network. Yarns made of CNT fiber were embedded using a sewing needle, carefully following through the warp of the orthofabric material under each weft thread and covering only the front face of the fabric. These samples were tested to assess the feasibility of utilizing CNT fibers as electrodes and the dust removal capability when applied with a multi-phase AC voltage. Current ISS EVA suits use orthofabric as the outermost layer and it is a potential material identified for future planetary spacesuits. Orthofabric is a complex weave of Nomex® (DuPont) and Kevlar® (DuPont) with an outer layer of Gore-Tex® (W.L. Gore & Associates), which is made from expanded Polytetrafluoroethylene (PTFE). Additionally, one coupon was prepared with copper magnet wire as electrode wires to compare the fabrication process and performance with the CNT fiber embedded coupons. Figure 5.2-1 shows the features of these samples prepared. Table 5.2-1 provides an overview of all the test coupons prepared and tested. A test plan was developed to qualitatively evaluate and characterize the SPIcDER system.

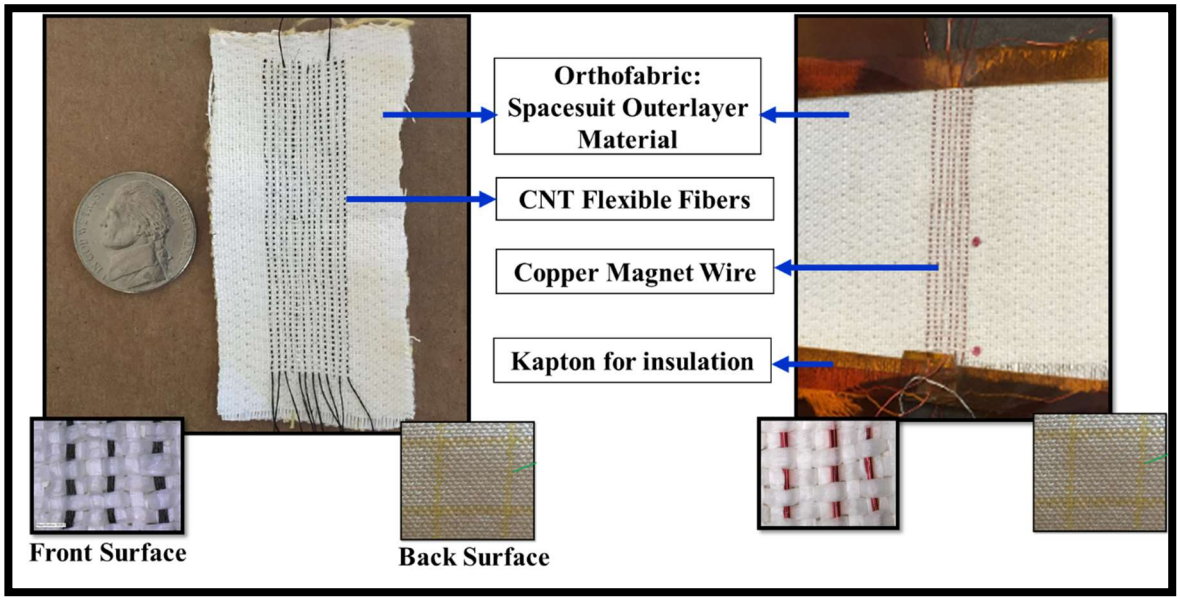

Figure 5.2-1. Features of the spacesuit fabric samples prepared for demonstrating proof of concept

Table 5.2-1. Samples prepared for Test Series-1. *Several other samples were prepared that are not shown here*

#	Material, Thickness	No. Electrodes	Electrode Spacing	No. Of Phases	
1	CNT Fiber ~200mm	6	~1.2mm	3	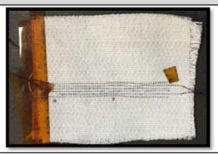
2	CNT Fiber ~200mm	6	~1.6mm	3	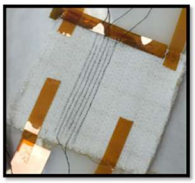
4	CNT Fiber ~200mm	12	~1.2mm	3	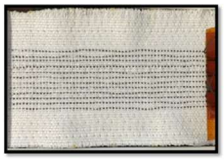
5	CNT Fiber ~200mm	4	~1.2mm	2	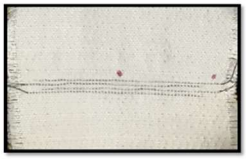
6	Magnet Wire (Copper) ~200mm	6	~1.2mm	3	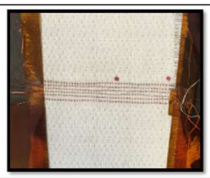

5.2.2. Test Samples for Test Series-2:

For this test series, a total of six coupons were used for testing with similar dimensions as Test Series-1 samples. Of these six coupons, three of them were reused from Test Series-1, and the other three were newly prepared and coated with WFM coating at NASA GRC after the CNT electrodes were embedded. The coating is extremely thin, on the order of 100 nm and transparent. These six samples were tested to evaluate the feasibility of applying passive coating over the embedded active CNT electrodes and their dust cleaning capability when applied with a multi-phase AC voltage. Table 5.2-2 provides an overview of the samples prepared for Test Series-2. A test plan to qualitatively evaluate and characterize the performance of the coated and uncoated samples embedded with active and passive dust mitigation technologies was developed and utilized.

Table 5.2-2 Multiple coupons made of orthofabric material embedded with CNT fiber electrodes and coated with WFM coating

Uncoated Samples (Only CNT fiber electrodes)	Coated Samples (CNT fiber electrodes + WFM coating)	Description
	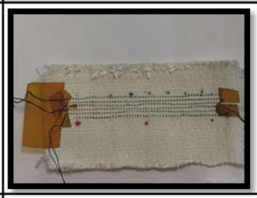	•6 CNT electrodes •~200 µm thickness •~1-1.2 mm spacing •3 phase system
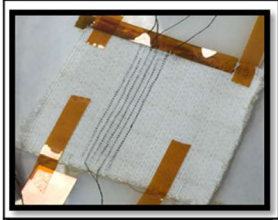	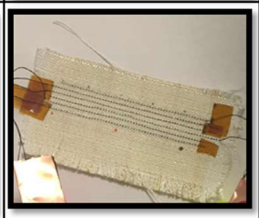	•6 CNT electrodes •~200 µm thickness •~1.6 mm spacing •3 phase system
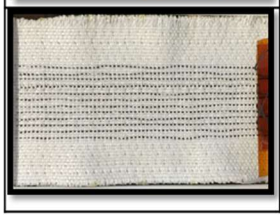	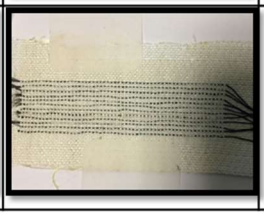	•12 CNT electrodes •~200 µm thickness •~1-1.2 mm spacing •3 phase system

5.2.3. CNT Flexible Electrodes

This research utilizes yarns made of CNT fibers manufactured by Rice University and their affiliate, DexMat®. These yarns were produced from raw CNTs dispersed in concentrated solutions of chlorosulfonic acid via wet-spinning process, as described in prior work using their proprietary process (Erickson et al. 2004). CNTs were provided by Meijo Nano Carbon Company and purified by DexMat® prior to fiber spinning. The process produced meters of multi-strand filaments made of pure CNT that were then assembled into twisted, two-ply yarn to achieve the thicknesses needed for this research as shown in Figure 5.2-2 using Planetary 3.0 ropemaking apparatus from the Domanoff Workshop.

The yarns used for this work consist a total of 28 uninsulated individual CNT filament fibers, each with a cylindrical cross-section which are then plied together (two ply, with each ply comprising of 14 individual filaments) to obtain the required electrode thicknesses. Therefore, each electrode of the SPIcDER system embedded into the orthofabric sample consists of CNT yarn from the same spool made up of multiple filament fibers made from pure CNT.

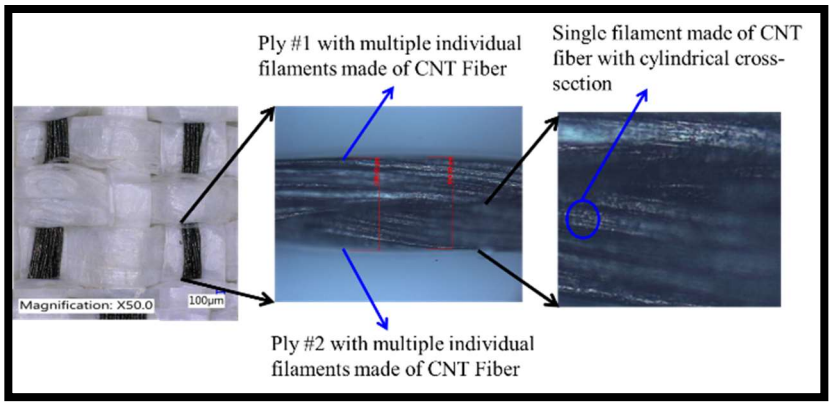

Figure 5.2-3. CNT flexible electrodes embedded into the orthofabric samples. *Each electrode is a yarn made up of multiple filaments, each filament fiber is made up of several aligned CNT.*

Both test series utilized material from the same spool. The individual filaments within each ply measure 26+/-2 µm in diameter with an average linear density of 0.81+/- 0.2 tex. Electrode properties relevant to this research for the materials utilized in the experiments are highlighted in Table 5.2-3. Evidence from characterization of materials show that the tenacity of the CNT yarns is 30 times stronger than the copper magnet wire used. (Tenacity is a measurement used in textile application as a measure of strength of a fiber or yarn calculated using the breaking force by linear density, similar to tensile strength of materials).

Table 5.2-3. Characterization of properties of the CNT fiber electrodes and copper magnet wire relevant to this research

Electrode Materials Used	CNT Yarns	Copper (Magnet wire)
Diameter (µm)	200-215	218
Density (g/cm^3)	0.81	7.86
Linear Density (tex)	29.4	280
Strength (MPa)	1260* (Single filament) 760 (2 ply with 28 filaments)	214
Tenacity (mN/tex)	940	30
Conductivity (MS/m)	3.1	49
Specific Conductivity (Sm^2/kg)	3850	6275
Insulated	No	Yes
Electrode shape	2-ply twisted yarn Single filaments have cylindrical cross section	Cylindrical rigid wire

5.2.4. WFM Coating Process for Test Series-2

After embedding the CNT yarns into the orthofabric samples, three coupons fabricated for Test Series-2 were sent to NASA GRC, where WFM coating with a thickness of approximately 100 nm was sputter deposited onto the fabric. The coatings were deposited utilizing ion beam sputter deposition using an argon ion beam source in order to sputter the lunar simulant targets made of

lunar highlands simulant NU-LHT onto the coupons. The resulting coating has a composition similar to the lunar dust simulant, and thus would also have similar work function as the simulant. The samples are coated in a dual beam chamber where they are mounted to the sample holder on the chamber door with Kapton tape (yellow) as seen in Fig. 5.2-4. The grid of the ion source is noticeable in the figure just below the samples. When the door of the chamber is closed and the chamber is evacuated, the argon ions are accelerated through that set of grids to a target that is about 15 cm^2 and made of the NU-LHT lunar highlands simulant. The ions sputter clusters of simulant atoms off the target and they arrive line-of-sight on the fabric samples. A second ion beam is located above the target and is directed into the fabric samples to microscopically roughen up the surface before deposition. This decreases the intrinsic stress that tends to build up during deposition. The samples are rotated through three positions at 120° apart to minimize fibers shadowing each other and obtain a uniform coating over the samples.

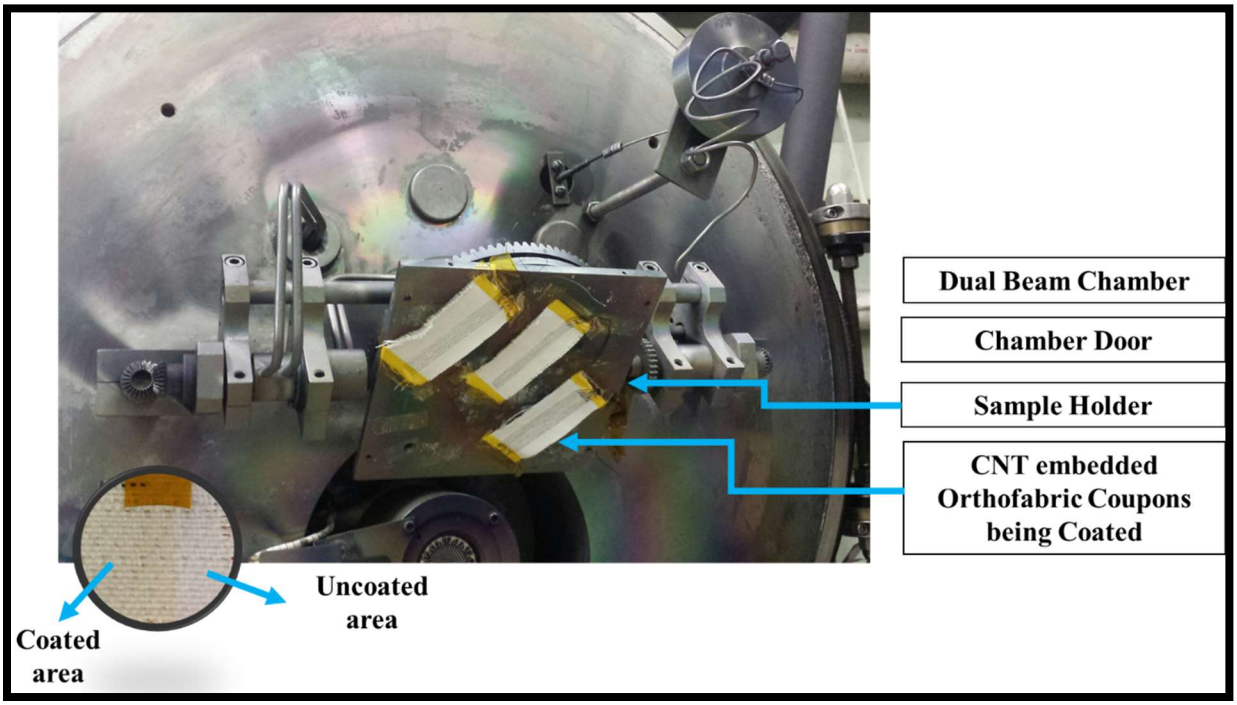

Figure 5.2-4. Three of the CNT embedded orthofabric coupons placed in the dual beam chamber to apply WFM coating at NASA GRC. *The inset shows that the coated area on the sample is visible by its yellowish tint post-coating process.*

5.2.5. Power Supply

Generation of multi-phase voltage for the active electrode portion of the experiments was performed using a tunable power electronics system developed by NASA KSC that can generate up to 3000 VAC between 1 Hz-200 Hz. Except for two samples of Test Series-1, all Test Series-1

and 2 experiments were conducted using the three-phase AC voltage, square waveform signal, at 10 Hz and 5 Hz frequency, with 120^{o} phase shift. Voltage levels for the coupons varied based on the electrode spacing. For the 1-1.2 mm spacing electrodes, a 1000 V input was applied, while a 1400 V input was applied for the ~1.6 mm spaced electrodes, for both coated and uncoated samples. The power electronics equipment utilized in the current experiments was previously used to demonstrate the EDS concept for rigid surfaces (example: solar panels).

Two samples of Test Series-1 were also tested using 2 phase voltage signal at 180^{o} phase shift, also using NASA developed power unit that has been demonstrated for their EDS studies (Calle et al., 2015). Figure 5.2-5 illustrates the two power supplies utilized for the experiments.

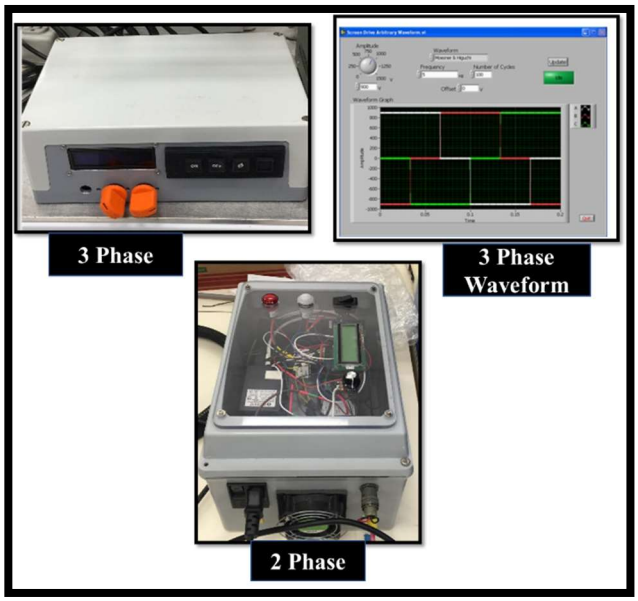

Figure 5.2-5. Three phase and two-phase power electronics generating AC signals. *Multi-phase waveform timing diagram shown on top right.*

5.2.6. Lunar Simulant

JSC-1A lunar simulant was used for all the experiments. Specifications for this simulant developed by Orbital Technologies Corporation are summarized in their specification database (Orbitec®, 2007). Simulant with two particle size ranges; larger grain size particles between 50-75 μm and relatively smaller grain size particles between 10-50 μm was used to test the feasibility of the dust cleaning system in the current experiments. These simulants were obtained from NASA KSC which were pre-sieved into their specific grain sizes. PSD of each of the simulant sets used for the test was characterized prior to beginning the experiments. Figure. 5.2-6. illustrates the

distribution and percentage of the particle sizes that was determined using microscopic images of the simulant and analysis conducted using ImageJ® particle counting software.

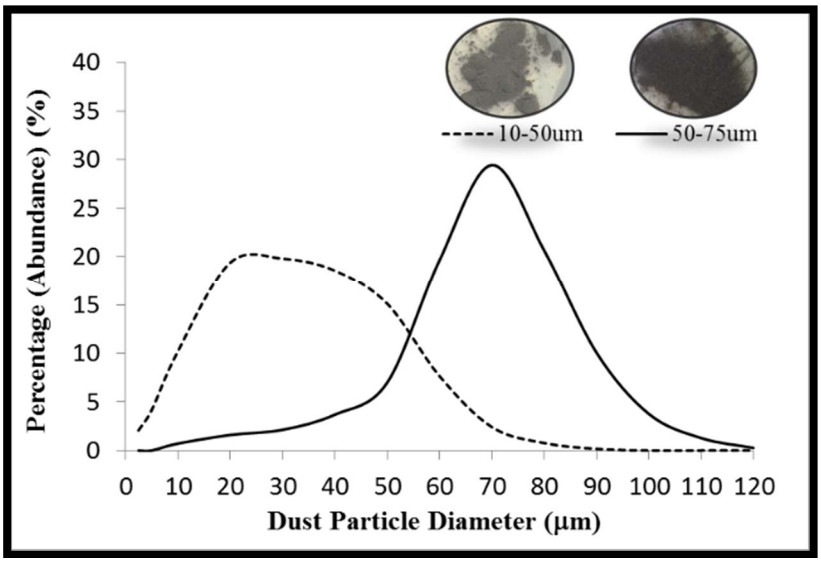

Figure 5.2-6. JSC-1A lunar dust simulant particle size distribution

5.2.7. Experimental Set-Up, Test Procedures and Test Conditions

5.2.7.1. Ambient Conditions

Figure 5.2-7 illustrates the experimental set-up for Test Series-1 conducted at NASA KSC at ESPL and Test Series-2 at the Boeing Innovation Cell. The test coupons with the SPIcDER system were placed in a test box and necessary connections were made to the terminals of the electrodes.

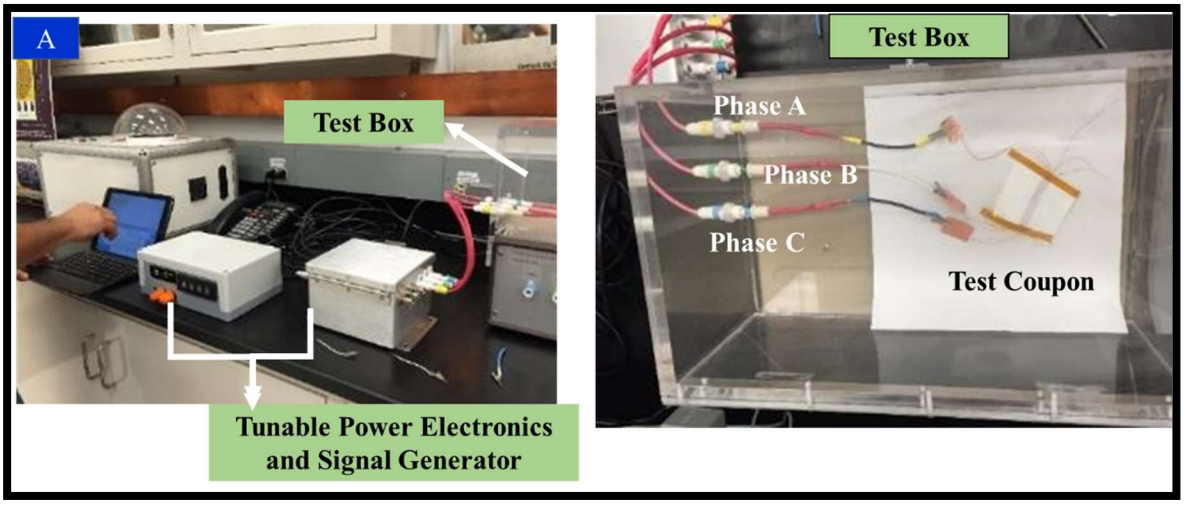

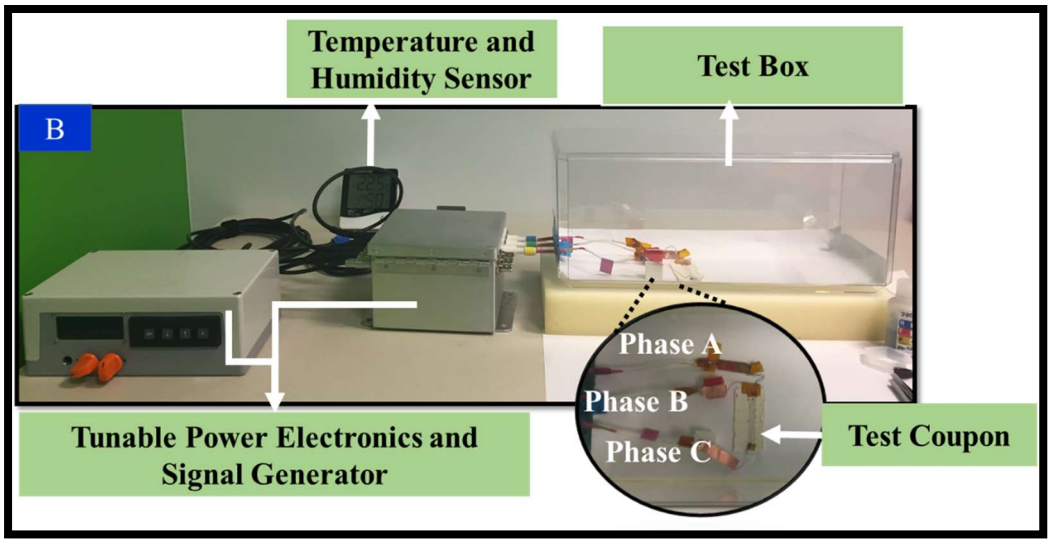

Figure 5.2-7. Experimental Set-up for Test series 1 and 2. [A] Set-up at NASA KSC [B] Test Set-Up replicated at Boeing Innovation Cell

5.2.7.2. Vacuum Conditions

For vacuum chamber testing in Test Series-1 at NASA KSC, coupons were placed in a bell jar that contained a metal box with insulative interior plates to mount coupons and connect the terminals as shown in Figure 5.2-8. The set-up consisted of an internal dust container which could be loaded with dust and actuated using an external controller to drop dust on the coupon. The coupon was first cleaned with pressurized air puffs, imaged using microscope, mounted in the box terminals connects, and the lid of the box was then closed. A camera was placed on the box that had a provision to hold a GoPro® session sized camera. Dust was then loaded into the dust container prior to closing the bell jar. An external turbo pump was activated to draw vacuum. After reaching a pressure level of 6.7×10^{-5} mbar (5×10^{-5} Torr), the electrodes were activated using the power supply situated outside the bell jar. The dust from the container inside the jar was dropped by controlling the actuator.

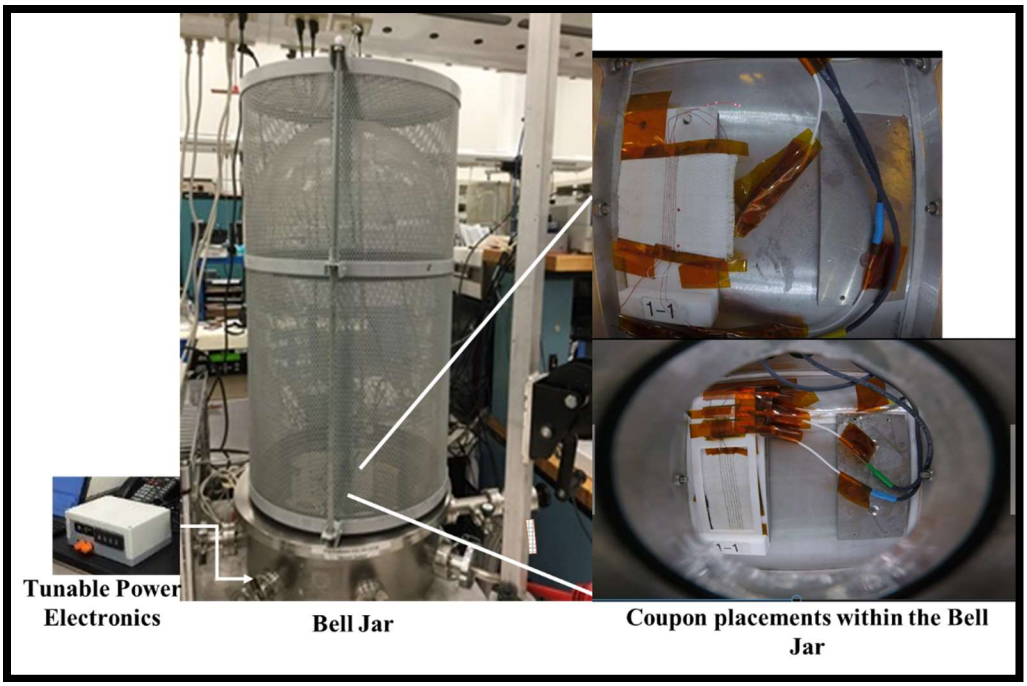

Figure 5.2-8. Vacuum chamber set up during Test Series-1 experiments at NASA

5.2.8. Test Conditions

All tests conducted in ambient conditions (Test Series-1 and Test Series-2) were performed at room temperature (~ 22-25 ºC), pressure (1 atm) and Relative Humidity (RH) (~ 40-45%). The SPIcDER system was evaluated by employing two specific dust depositing conditions:

1. Dynamic Drop test
2. Static test

In the first case of the 'Dynamic Drop test', CNT electrodes were activated prior to depositing the dust simulant over the coupon. When the electrodes were active, a measured amount of dust (~1.5 g) was continuously deposited/dropped (termed 'drop test') on the coupons within the area where electrodes were embedded (~6 mm wide stream of dust). The coupons were placed horizontally while the angle of the dust dropped was perpendicular to the coupons. This dynamic dust test case is presumed to represent lunar dust interacting with the suit when an astronaut is walking on the surface of the moon during an EVA. In the second test case (static test), approximately 10 mg of simulant is deposited over the area on the coupon covered with electrodes prior to activating SPIcDER. This condition represents a scenario where the suit is pre-disposed to dust which has statically adhered and coated the spacesuits during an EVA.

5.2.9. Test Procedures

For both test series conducted in ambient conditions, each coupon was first cleaned with pressurized air puffs and imaged using a microscope. The coupon was placed horizontally in the casing. For three phase tests, each of the three terminals (to receive the three-phase voltage signal) of the electrodes within the coupon was connected to the respective phases (A, B, C) of the power supply. For initial characterization of the SPIcDER system and to evaluate the voltages where breakdown starts for each coupon, the power supply was activated starting from low voltages (~100 V) at 10 Hz, in 50 V increments. Threshold voltages where breakdown initiated were noted for each coupon. Experiments that followed were conducted at ~100-150 V below the threshold voltage. Similar process was followed when two coupons in Test Series-1 were experimented with the two-phase power supply.

Dynamic Drop Test Procedures: For the dynamic drop test, after the coupon was connected to the respective terminals, the power supply was turned ON. Appropriate voltage and frequency levels were selected to activate the CNT electrodes. Following SPIcDER system activation, ~1.5 g of lunar dust simulant was continuously dropped over the active area of the coupon approximately 6 inches above the coupon. For a few scenarios in Test Series-1, heavy dust loading (~5 g) was used. The test was conducted for 1-3 minutes to assess the capability of the fabric dust cleaning system to repel the simulant. Subsequently, dust deposition was halted and the power was turned OFF. The coupon was then imaged in place for post-test analysis. These procedures were repeated for both the coated and uncoated samples for both 50-75 μm and 10-50 μm dust particles.

Static Test Procedures: For the static test case, after the coupon was connected to the respective terminals, 10 mg of lunar dust simulant was deposited over the coupon in the area where the electrodes were embedded. A stencil with dimensions of the electrodes area was used to make sure the dust was deposited only in the area covered with the electrodes. The coupon with the dust adhered to the fabric was imaged. After obtaining images for the 'before electrode activation' state of the coupon, the lid of the protective casing was closed, followed by activation of the electrodes system by turning ON the power supply at the needed voltage and frequency values. The system was kept activated for approximately 60 seconds until no further dust particles visually seemed to repel. The power was then turned OFF and the coupon was imaged in place.

Figure 5.2-9. Stencil to aid with depositing dust over electrode area

5.2.10. Data Collection and Analysis

Qualitative and quantitative data was used to assess the feasibility of the SPIcDER system. Both the dynamic and static tests were repeated multiple times during Test Series-1 and 2, both for the coated and uncoated samples. Data was obtained for three consecutive runs. For analysis, data was collected using video and microscopic images. For the dynamic drop test method, where the SPIcDER was first activated, continuous video was recorded while dust was dropped over the coupon. The coupon was imaged in place after the test using a handheld digital microscope. Similarly, for the static test, the coupon was imaged prior to dust deposition, after dust deposition, and after SPIcDER was activated. Microscopic images were taken at 20X magnification to record the state of the coupons and dust distribution. Operating voltages that provided the best cleaning performance was collected. Threshold voltages where breakdown starts to initiate was also collected for each electrode configuration. The capability of the dust cleaning system was evaluated using:

1) Visual inspection via the videography data and images collected during the experiments to document observable dust cleaning capability for the qualitative aspect of the analysis

2) ImageJ software was subsequently used to estimate dust particle size and distribution using microscopic images of the 6 electrodes, 1 mm electrode spacing configuration coupons to approximate the amount of dust remaining on the fabric and to derive the percentage of fabric covered in residual dust for the quantitative portion of the analysis.

5.3. Results

5.3.1. Test Series-1 (CNT only)

Part 1: Dynamic Drop Test

Real time observations of the drop test experiments clearly demonstrated the ability of the SPIcDER system consisting of CNT flexible electrodes to remove dust when applied to spacesuit material using fabrication techniques proposed in this research. When the SPIcDER was activated and dust was continuously dropped over the coupon, it was evident that dust was constantly being repelled over the active area of the coupon. Heavy dust loading (>5 g) was dropped over these coupons. Table 5.3-1 provides an illustration of the dust removal capability of the system.

The capability of the system to repel dust during drop tests was qualitatively assessed. The amount of dust dropped during these preliminary test series was not measured as the goal was to evaluate if the system was capable of repelling dust dropping over the electrodes. From the table below, visual observations showed that the CNT coupons could repel most of dust dropped as observed by the amount of dust on the outside of the active area. The system could reproduce similar cleaning results on repeated drop tests on the same coupons. Experiments showed that cleaning depends on electrode configuration and applied waveform characteristics. As expected, for a respective coupon with specific electrode configuration, the performance of the system was observed to be better (faster clearance of dust and relatively more particles removed) at higher voltages than at lower voltages due to the higher electric field strength generated with increase in the applied voltage. Observations from the tests showed the coupons with CNT electrodes performed on par (and better in some cases) than the Copper magnet wire embedded coupons.

Table 5.3-1. Test Series-1 Dynamic Dust Drop Test Results. (*Dust is continuously dropped over the entire coupon while the electrodes are active***)**

Coupon Information	Voltage	Before Activation	After Activation
• CNT fiber • 6 electrode lines • ~1-1.2mm electrode spacing • ~ 200micron electrode thickness	3 phase 1000V		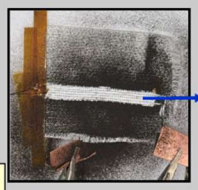 Active area: Cleared Dust
• CNT fiber • 4 electrode lines • ~1-1.2mm electrode spacing • ~ 200micron electrode thickness	2 phase 1000V	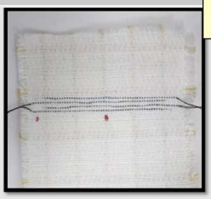 Simulant dropped over coupon	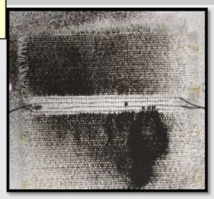
• CNT fiber • 6 electrode lines • ~1.6 mm electrode spacing • ~ 200micron electrode thickness • Note that this coupon had preexisting dust prior to the drop test. The amount of dust dropped was also in large quantities, that may not be the case in real EVAs	3 phase 1400V	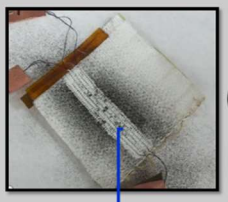	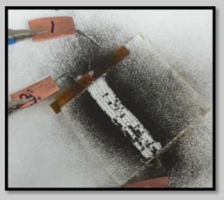 Left over dust from previous runs with heavy dust loading
• Copper Magnet wire, insulated • 6 electrode lines • ~1mm electrode spacing • ~ 200micron electrode thickness • Note that this coupon had preexisting dust prior to the drop test.	3 phase 1600V	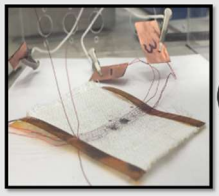	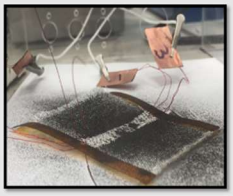 Heavy loading used for Test series-1 (>5g)

The coupons could repel dust particles of both larger (50-75 μm) and smaller (10-50 μm) grain sizes. However, a characteristic difference noticed between the large grain size (50-75 μm) and small grain size (10-50 μm) simulant particles was that, the smaller grain size simulant was more cohesive (particles grouped/stuck together) compared to the larger grain size particles when dropped over the coupon. During such scenarios when the particles were cohesive during drop tests, it was difficult to repel dust. Nonetheless, these clusters of particles were localized and only covered a minor portion of the coupon.

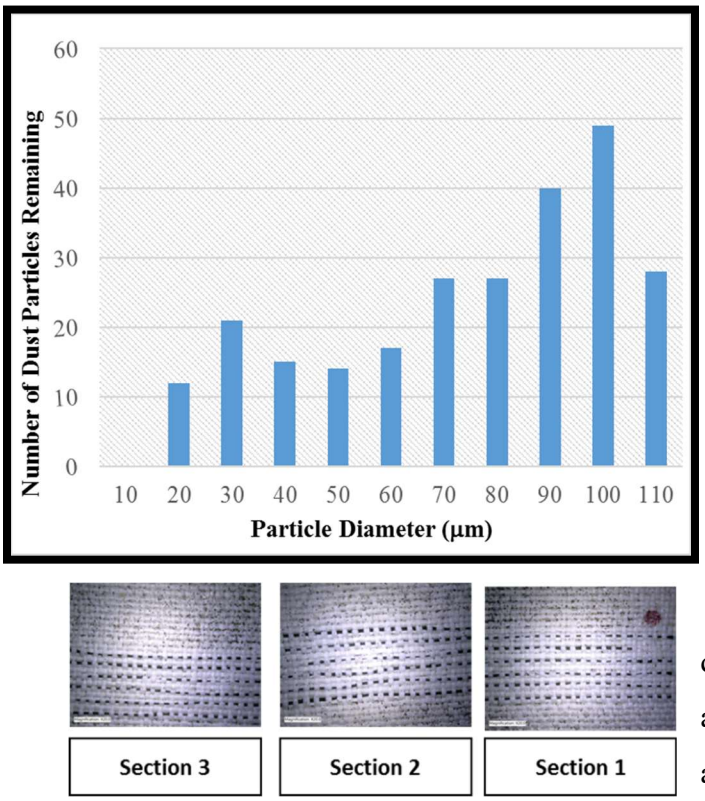

Figure 5.3-1. [Top] Dust PSD on one section of a drop test coupon averaged over three sections and three runs, [Bottom] An example of how each coupon was imaged in three sections to perform particle-counting analysis. *Results shown here are for the 3 phase, 1000V, 6 wire, 1~1.2mm spacing configuration coupon*

ImageJ® software was used to quantitatively estimate dust particle size and distribution remaining on the coupon after the test. Each coupon was imaged in three separate sections along the longitudinal axis of the electrodes covering the entire active area as shown in the bottom part of Figure 5.3-1. This method was adopted due to constraints on imaging the entire coupon with the needed magnification within a single image. ImageJ® analysis was performed on each of the three sections of the active area on the coupon. The approximate dimensions of each section were 9.85 mm X 6.23 mm. Results obtained were averaged over three repeated runs on the same coupon. As an example, Figure 5.3-1 provides an estimate of the residual dust PSD on the coupons on a single section after SPIcDER activation was halted using the 3-phase system with 50-75μm simulant. Results similar to that depicted in Figure 5.3-1 were obtained for rest of the coupons on all three sections, as well as for the two-phase drop tests. No significant difference was observed between the 3-phase and 2-phase voltage signals during the drop tests. Note that although the dust simulant

used had a size range of 50 - 75 μm, the coupon had particles both larger (> 75 μm) and smaller (< 50 μm) than that range remaining on the coupon. For the smaller grain size tests (10-50 μm), ImageJ® analysis was not accurate in estimating particle size and count is because particles were cohesively grouped together in various places on the coupon making it challenging to precisely distinguish the contours of individual particles. Future tests will address this by using estimating fractional coverage by dust using color scheme.

Part 2: Static Dust

The second type of experiments were conducted to understand if the system was capable of repelling dust when the fabric was pre-exposed to dust (static dust) prior to SPIcDER activation. Initial runs for the static test were conducted using general distribution of dust over the coupon, where the amount of dust deposited on the coupon was not quantified and the distribution was random. For subsequent runs, approximately 10 mg of dust was distributed over the electrode area using the stencil.

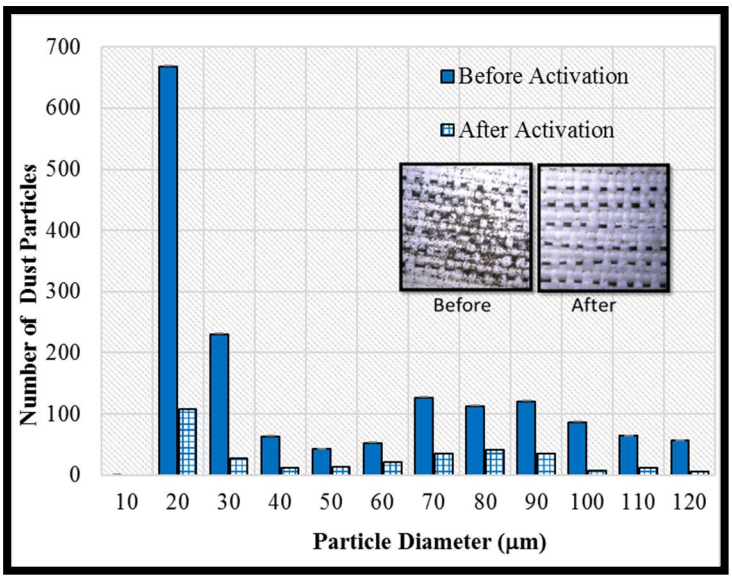

Figure 5.3-2. Dust particle size distribution on a section of the coupon before and after activation averaged over three runs. (Inset) Example of before and after picture of a section of the coupon. *Results shown here are for the 3-phase, 1000V, 6 wire, ~1mm spacing configuration coupon*

Tests were repeated to examine the reproducibility of system performance. The coupons were capable of repelling dust on repeated test runs. Experiments revealed that the system can repel between 80-95% of the dust that was statically attached to the coupon as shown in Table 5.3-2 (average of three repetitions). Figure 5.3-2 illustrates the amount of dust particles before and after activating the CNT electrodes on a section of a coupon for the static test averaged over all three sections and three repeat runs on the coupon.

Other observations showed no significant differences between the 3-phase and 2-phase voltage signals. As expected for a given coupon with specific electrode configuration, the system's capability to remove dust was greater (faster clearance of dust and relatively greater number of particles removed) at higher voltages. For example, Table 5.4-1 in the later part of this chapter

shows the increase in performance of dust clearance as the voltage was increased from 400 V to 900 V.

Table 5.3-2. Test Series-1 Static Test Results. *(Fabric pre-disposed to dust)*

Coupon Information	Voltage	Before Activation	After Activation
• CNT fiber • 6 electrode lines • ~1-1.2mm electrode spacing • ~ 200micron electrode thickness • 10mg Dust	3 phase 1000V	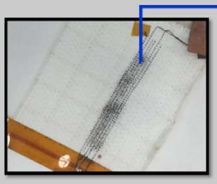	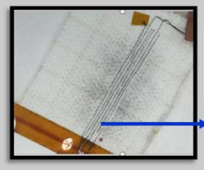 10mg of Lunar Dust simulant adhered to fabric Active CNT area: Cleared dust
• CNT fiber • 6 electrode lines • ~1-1.2mm electrode spacing • ~ 200micron electrode thickness • Heavy Dust Loading*	3 phase 1000V	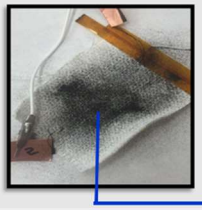	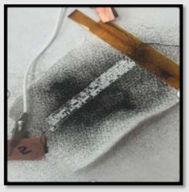 Heavy dust loading case >10mg
• CNT fiber • 4 electrode lines • ~1-1.2mm electrode spacing • ~ 200micron electrode thickness • 10mg Dust	2 phase 1000V	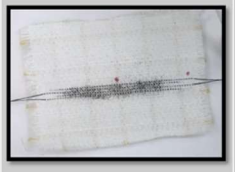	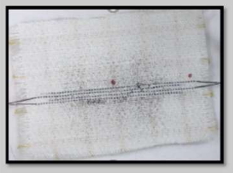
• CNT fiber • 6 electrode lines • ~1.6 mm electrode spacing • ~ 200micron electrode thickness • >10mg Dust	3 phase 1400V	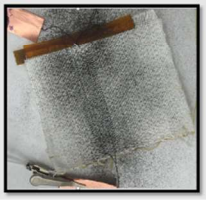	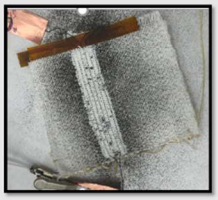
• Copper Magnet wire, insulated • 6 electrode lines • ~1.6 mm electrode spacing • ~ 200micron electrode thickness • >10mg Dust	3 phase 1600V	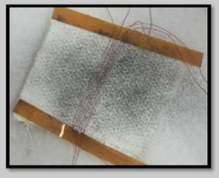	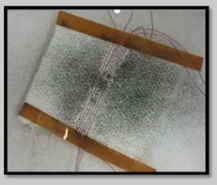

5.3.2. Test Series-2 (CNT+WFM)

Part 1: Dynamic Drop Tests

Similar to Test Series-1, real time observations during Test Series-2 dynamic drop tests and microscopic images provided compelling evidence that the integrated dust removal system is capable of repelling nearly 90% of lunar dust simulant that was dropped over the samples estimated using visual observations. The SPIcDER system here is also applied with WFM coating on three coupons. When the embedded CNT fiber electrodes on both the coated and uncoated samples were

activated and dust was dropped on the sample, dust was continuously being levitated and repelled away from the active area of the coupons. Evidence of these visual observations is illustrated in Table 5.3-3 where the active area is shown to be clear of dust while the surrounding area accumulated the repelled dust.

Specific observations made during these experiments are summarized here:

1. The system can reproduce similar cleaning results on repeated drop tests on the same coupons as observed during Test Series-1.
2. On a macro scale, both the WFM coated and uncoated samples performed relatively similar
3. Cleaning depends on electrode spacing configuration and applied waveform characteristics. As expected, for a respective coupon with specific electrode configuration, the performance of the system was observed to be better (faster clearance of dust and relatively more particles removed) at higher voltages than at lower voltages due to the higher electric field strength generated with increase in the applied voltage.
4. A visual comparison between the 1 mm electrode spacing and 1.6 mm electrode spacing coupons showed that the spacing in the later coupons was wide enough for the dust to accumulate in between the electrodes. These observations validate previously conducted experiments at NASA KSC described in the previous section.

The system performance was relatively straightforward to evaluate for the 50-75 μm grain sizes when compared to 10-50 μm. The difficulty with the small grain sizes was the extensive cohesion that existed among the particles posing problems while dropping dust over the coupon, similar to observations during Test Series-1. Due to its cohesive nature, dust simulant could not be consistently deposited on repeated runs over the coupons as the dust would often get accumulated in areas due to internal cohesion. However, these clusters of accumulated dusts were localized and the system was still able to repel most of the dust that was directly deposited on the active area (See row 3 in Table 5.3-3).

Table 5.3-3. Test Series-2 Dynamic Dust Drop Test Results. *WFM Coated and uncoated Samples*

Uncoated Samples (Only CNT fiber electrodes)	Coated Samples (CNT fiber electrodes + WFM coating)	Description
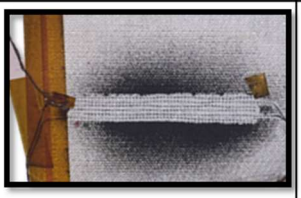	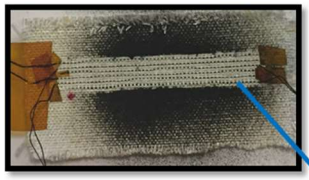	• 6 CNT electrodes • ~1 mm spacing •50-75µm JSC-1A lunar simulant •1000V, 10Hz Active Area that cleared the dust
	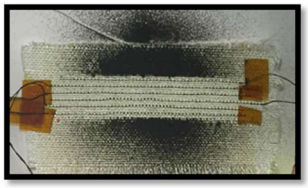	•6 CNT electrodes •~1.6 mm spacing •50-75µm JSC-1A lunar simulant •1400V, 10Hz
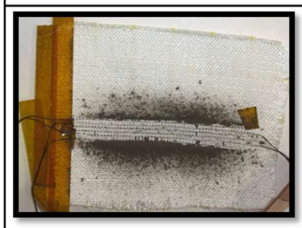	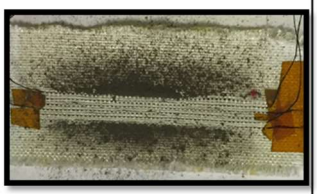	•6 CNT electrodes •~1 mm spacing •10-50µm JSC-1A lunar simulant •1000V, 10Hz

An approximation of the residual dust PSD and frequency (number of particles) was estimated using Image J® software for the 6 electrodes, ~1 mm spacing configuration coupons for the 50-75 µm tests. Each coupon was imaged using seven separate sections along the longitudinal axis of the electrodes covering the entire active area to accommodate the magnification needed to count the particles. Dimensions of each section analyzed was approximately 6.2 mm x 5.6 mm (see inset in Figure 5.3-3). Analysis was performed on each of the seven sections, for three repeated runs, for both the coated and uncoated coupons. Results obtained were averaged over the repeated runs for each coupon. As an example, Figure 5.3-3 provides an estimate of the average residual PSD on a section of both the coated and uncoated coupons. Figure 5.3-3 shows that the coated samples had fewer number of dust particles remaining compared to the uncoated samples.

An independent t-test statistical method was utilized to further evaluate the effectiveness of coating on particle sizes remaining on the coupons. Analysis showed that coating was effective for specific grain sizes: 0-10 μm (*p value*=0.041), 70-80 μm (*p value*-0.027), 80-90 μm (*p value*=0.008) and 90-100 μm (*p value*= 0.04) particles. For the smaller grain size experiments (10-50 μm), ImageJ® analysis was not accurate providing highly variable results while estimating particle size and count for the same sections of the coupons for the same reasons described in Test Series-1 (cohesive clusters of dust). Previous studies revealed that performing optical spectral measurement may provide more accurate results in estimating the performance of the dust cleaning system (Gaier et al., 2011).

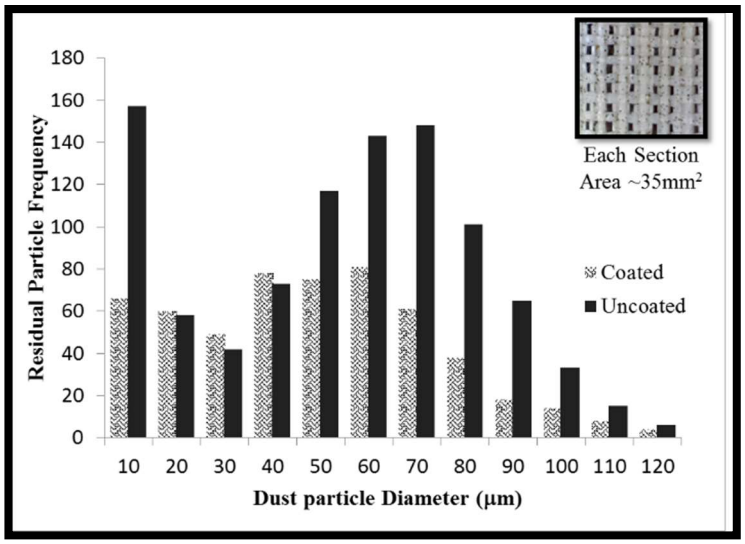

Figure 5.3-3. Residual dust particle size and distribution averaged over repeated runs on a section of the coated and uncoated samples after the dynamic drop test

Part 2: Static Tests

For the static tests, 10 mg of dust was deposited on the active area of the coupons prior to electrode activation. Visual observations and microscopic images revealed that the system can repel between 80-95% of the dust statically attached to the coupons similar to Test Series-1. Once again the coupons were capable of repelling dust on repeated test runs. Table 5.3-4 shows an illustration of the before-after pictures from the static tests for the 6 electrode configuration coupons. To quantify the amount of dust repelled on the coupon, ImageJ® particle counting analysis was conducted on the microscopic images. Figure 5.3-4 provides a snapshot of the dust particle size distribution before and after SPIcDER activation showing that the system was able to repel >80% of the particles after SPIcDER was activated. The figures provide data on a section of the coated and uncoated samples for the 6 electrodes, ~1 mm spacing configuration coupons. The data is averaged over seven sections and three repeated runs for each coupon. Additionally, Figure 5.3-5 shows a comparison of performance between the coated and uncoated samples by plotting

the number of particles repelled. Further analysis showed no statistical significance between the performance of the coated and uncoated coupons (*p value* >0.05). Therefore, coating did not affect the performance of the SPIcDER system as expected.

Using the smaller grain size particles (10-50 μm) also showed significant amount of dust being repelled using visual observations. There seemed to be remnants of less than 10 μm sized particles on the coupon. However, similar to Test Series-1, the cohesion between the particles proved to be a challenge to perform image analysis in order to quantify the data. Other observations from the static tests include, for the wider electrode spacing (1.6 mm) coupons, system performance was similar to the 1 mm spacing electrodes when the voltage was increased by 400 V above the voltage range of the former coupons (See row 3 in Table 5.3-4).

Table 5.3-5. Test Series-2 Static Test Results for WFM coated and uncoated samples.
(Fabric pre-disposed to dust)

Before Activation	After Activation	Description
	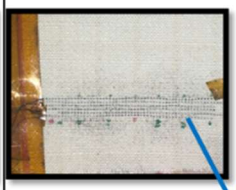	• **Uncoated Sample** • 6 CNT electrodes • ~1 mm spacing •50-75μm JSC-1A lunar simulant •1000V, 10Hz Active Area that cleared the dust
		•**Coated Sample** •6 CNT electrodes •~1 mm spacing •50-75μm JSC-1A lunar simulant •1000V, 10Hz
	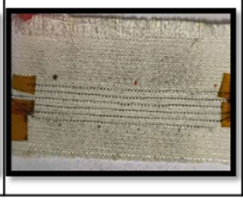	•**Coated Sample** •6 CNT electrodes •~1.6 mm spacing •50-75μm JSC-1A lunar simulant •1400V, 10Hz

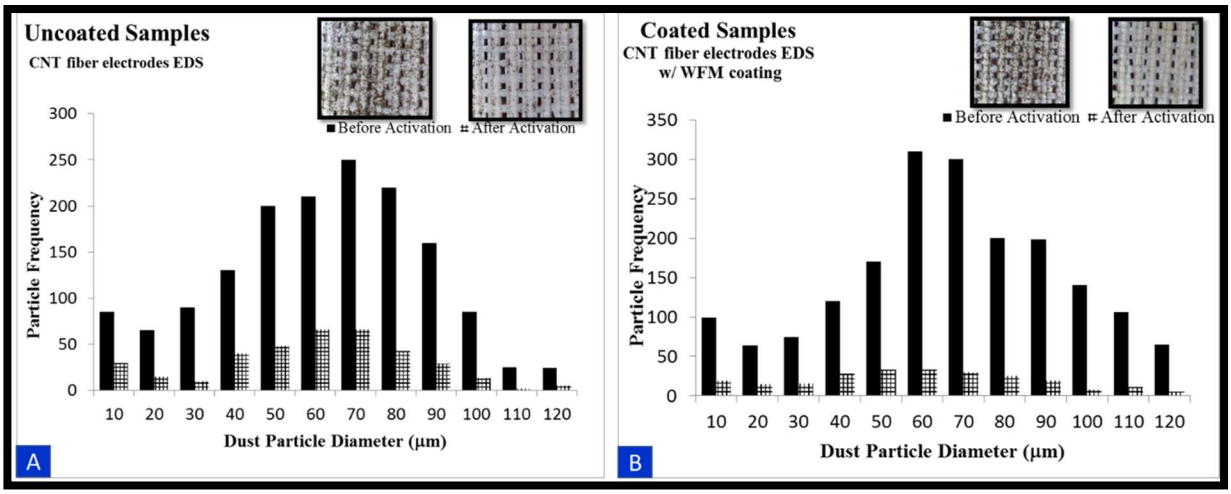

Figure 5.3-4. Dust particle size and distribution on a section of uncoated and coated coupons before and after SPIcDER activation

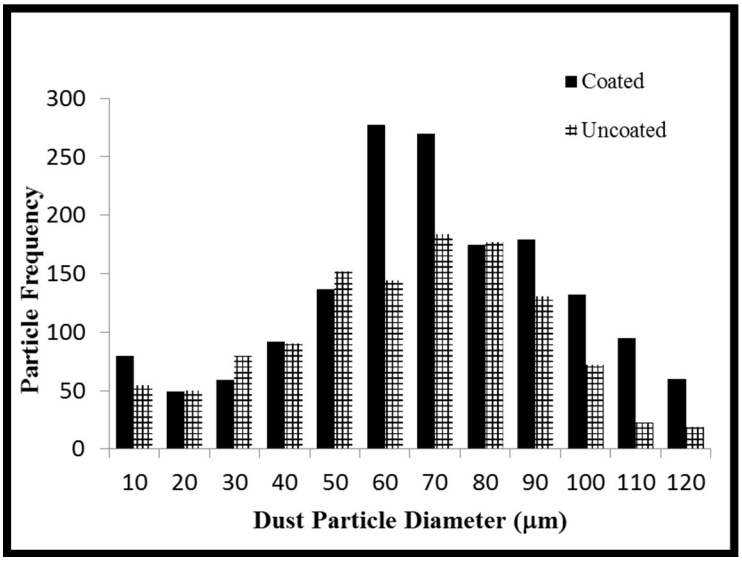

Figure 5.3-5. Comparing the number of dust particles repelled by the coated and uncoated samples

5.3.3. Vacuum Testing results from Test Series-1

During Test Series-1, several attempts were made to test two coupons in vacuum conditions. However, due to some inconsistencies in the mounting methods of coupons in the vacuum test chamber, a comprehensive set of vacuum chamber tests could not be accomplished. Therefore, those results are not presented here. One of the observations made during the initial vacuum chamber investigations however was that the coupon was discolored after chamber testing. The discoloration of the fabric around the CNT electrodes was revealed during visual inspection of the coupon after vacuum chamber operations at 1.3e-5 mbar (1e-5 Torr) (See Figure 5.3-6). It is

anticipated that the reason for this discoloration is outgassing of the CNT material. Since the manufacturing process of the CNT yarns involves dissolving the material in cholorsuphuric acid/ other similar solvents, the effects of these materials are seen in low pressures as outgassing. One possible solution to resolve this condition was determined, which is to bake the CNT yarn at high temperatures (300^{o}C) prior to embedding into the orthofabric material. The acid acts as a dopant, the degassing of which would decrease the conductivity of the electrode. However, the decrease in conductivity is still within the range that is usable for the current application. The yarn needs to degassed of any solvents prior to inserting them into the suit material to prevent outgassing of the powerful oxidant while operating in lunar environments. These procedures were implemented for vacuum chamber experiments described in Chapter 9.

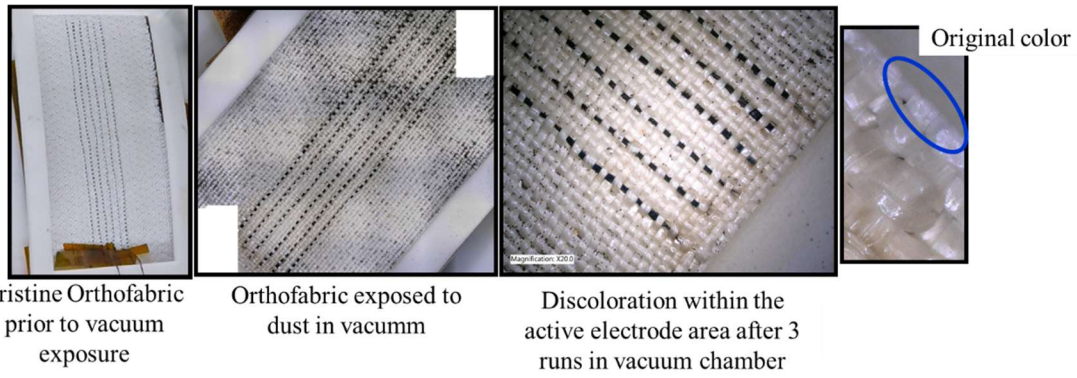

Figure 5.3-6. Fabric discoloration observed within the electrode area covered embedded with CNTs during vacuum chamber testing

5.4. Discussion

The proof of concept experiments qualitatively and quantitively demonstrated the ability of CNT yarns to overcome two specific challenges identified in Chapter 4 to integrate EDS based active technology into spacesuits for dust mitigation: i) Flexible electrode material to conform to spacesuit material and irregular contours and ii) fabrication techniques to apply electrodes into the spacesuit system. Furthermore, Test Series-2 demonstrated the feasibility of applying a passive WFM coating over the electrode system to minimize adhesion of dust particles.

.

5.4.1. SPIcDER System Concept Demonstration from Experiments

Results from both the Test Series-1 and 2 experiments demonstrate the feasibility of utilizing the proposed SPIcDER system that combines active and passive dust cleaning system for spacesuit dust mitigation.

- ***Demonstration and Effectiveness of CNT yarns for active dust mitigation***

Experiments conducted in ambient conditions (Temperature 22-25 ºC, RH=40-45%) with the CNT fiber embedded dust cleaning system was capable of repelling between 80-95% of dust that came in contact with the suit fabric. The efficiency of the dust cleaning performance (D_p) was calculated using the number of dust particles before and after SPIcDER activation using Equation 6 below, where N_{pB} represents the number of particles before dust cleaning and N_{pA} represents number of particles remaining on the fabric after SPIcDER activation. This is applicable specifically for the static tests.

$$\%Dp = \frac{N_{pB} - N_{pA}}{N_{pB}} \times 100 \quad (6)$$

Based on this equation, the efficiency of the SPIcDER system for coated samples was 87% for static tests and uncoated samples was 80%. For dynamic tests, it is estimated that the efficiency of the system is greater than 90%.

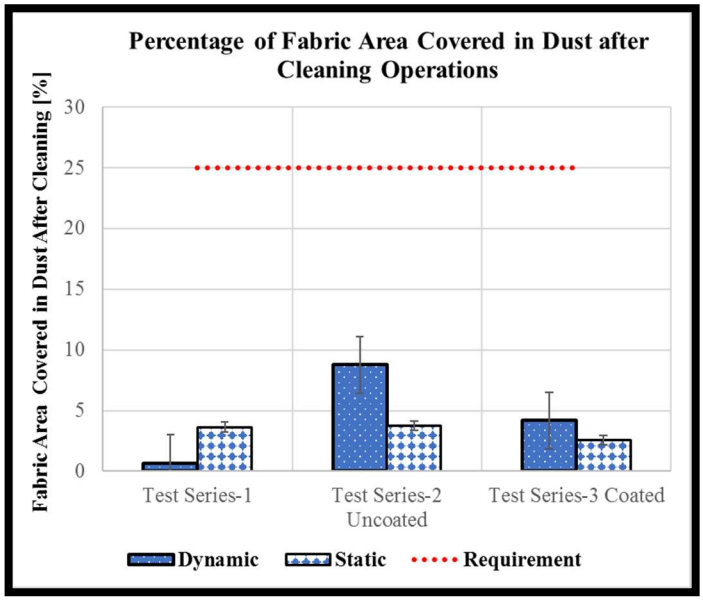

Figure 5.4-1. Percentage of fabric area covered in dust after cleaning operations on both test series. *Analysis based on PSD presented in section 5.3. 15% margin added.*

Based on the dust PSD data presented in section 5.3, the performance metric established to identify the dust cleaning performance of the system in Chapter 1- the percentage of orthofabric covered by dust after cleaning operations, was evaluated using a density value of dust of 3520 kg/m^3 (Liu and Marshall, 2010). Based on this, results showed that less than 10% of the orthofabric area was covered in dust post cleaning operations (Figures 5.4-1 and 5.4-2). This value is less than half the value imposed as a requirement (<25%) for cleaning performance based on thermal performance degradation.

It was observed that due to the flexibility of the CNT yarns, the ability of integrating the fiber electrodes into the spacesuit orthofabric material was effective. The CNT yarn electrodes conformed to the surface of the orthofabric and the existing weaves of the material. The significance of this flexibility and conformity of the CNT electrodes is fundamental to the performance of the SPIcDER system when the suit flexes, bends or twists. In comparison, the copper magnet wire, due to its rigidity was difficult to conform to the surface of the orthofabric material and the fabrication process was relatively longer than the coupons embedded with CNT yarns. The CNT electrode system performed on par (and better in some cases) with the copper magnet wire electrode system.

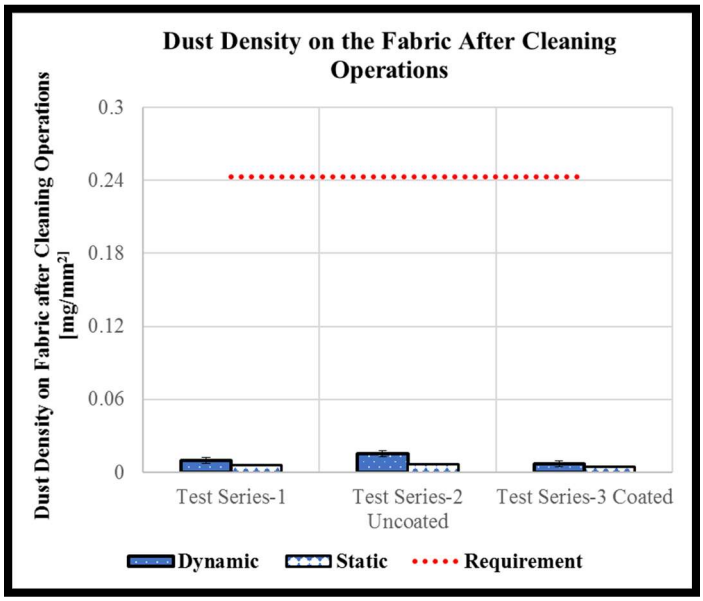

Figure 5.4-2. Dust areal density (kg/mm^2) on the fabric after cleaning operations on both test series. *Analysis based on PSD presented in section 5.3. 15% margin added.*

Dust cleaning performance of the SPIcDER was observed to be higher at higher voltages (Table 5.4-1). The applied operating voltage is however limited by breakdown of the surrounding medium that is characterized by electrode spacing and environmental conditions as determined by Paschen's law (further explained in Chapter 6). Therefore, insulating the CNT electrodes would permit an increase in the applied voltage, allowing an increase in the electric field intensity generated, prior to reaching breakdown. This would further improve the dust cleaning performance. Table 5.4-2 summarizes the operating voltages applied using the SPIcDER electrodes that provided the highest dust cleaning performance for all configurations tested. All CNT samples from Test Series-1 and 2 of the same configuration (electrode material, spacing and waveform characteristics) performed their best consistently at the same voltages. Test Series-2 provided evidence that dust cleaning was best at a frequency of 5 Hz when real time observations were conducted and slow-motion videography was analyzed. The breakdown voltage characteristics for both test series using CNT material, and both coated and uncoated samples within Test Series-2 were similar.

Table 5.4-1. Increase in dust cleaning performance of SPIcDER system with increase in voltages

Voltage	Before Activation	After Activation
3 phase **400V**	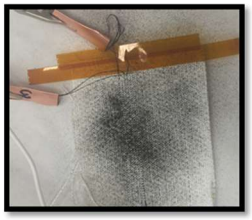	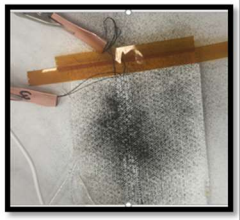
3 phase **800V**		
3 phase **900V**		

Increase in performance with increase in Voltage. Highest Voltage limited by Paschen's Law

Table 5.4-2. Applied waveform characteristics and summary of voltages for best performance

Electrode Material	Sample Type	Insulated	Electrode Spacing	No. Phases	Frequency	Voltages Used	Best Results	Threshold (Breakdown Voltage)
Test Series-1								
CNT	Uncoated	No	~1-1.2 mm	3	10 Hz	800-1000	1000 V	1200 V
CNT	Uncoated	No	~1.6 mm	3	10 Hz	1200-1500	1400 V	1600 V
CNT	Uncoated	No	~1 mm	2	10 Hz	900-1000	1000V	1200 V
Cu Magnet Wire	Uncoated	Yes	~1 mm	3	10 Hz	1200-1600	1600V	1800 V
Test Series- 2								
CNT	Uncoated	No	~1-1.2 mm	3	5,10 Hz	900-1000	1000 V, 5 Hz	1200 V
CNT	Uncoated	No	~1.6 mm	3	5,10 Hz	1400 V	1400 V, 5 Hz	1600 V
CNT +WFM	Coated	No	~1 mm	3	5,10 Hz	1000 V	1000 V, 5 Hz	1200 V
CNT+WFM	Coated	No	~1.6 mm	3	10 Hz	1400 V	1400 V, 5 Hz	1600 V

- ***Demonstration of Effectiveness of WFM Coating***

It is expected that coating provides another layer of defense for dust contamination by reducing adhesion of dust particles due to triboelectric charging, enhancing the overall dust cleaning performance when combined with the active CNT system. Coating the spacesuit fabric with WFM coating over the electrodes was performed after incorporating the electrode network into the suit fabric. Particle counting analysis from section 5.3 from both the dynamic and the static tests showed that coating did not seem to affect the CNT electrodes or the performance of the dust cleaning ability of the active electrode system and its breakdown characteristics in comparison with the uncoated samples. This validates that the two technologies can be combined without diminishing the effects of each of their dust cleaning performance and capability.

Furthermore, the effects of WFM are known to be significant and effective in vacuum and dry conditions, and when the dust is charged, as shown in previous studies (Gaier et al., 2011). In ambient conditions such as the current experiments, it is believed that the presence of water vapor in the atmosphere would diminish the effectiveness of the WFM coating. Despite the scope of the current experiments being limited to ambient conditions, it is noticed that the coated samples had a statistically significant effect over uncoated samples in repelling specific particle sizes during the dynamic tests (0-10 μm and 70μm, 90-100 μm). Moreover, visual observations during post-test operations while cleaning the coupons using puffs of air revealed that the coated coupons required a maximum of two air puffs to remove any residual dust particles on the coupons compared to more than two air puffs required for the uncoated samples on a consistent basis. Therefore, the effectiveness of WFM coating on minimizing adhesion of dust particles and enhancing the overall performance of the dust cleaning system alongside the CNT embedded SPIcDER system should be further evaluated in vacuum and dry environments.

5.5. Summary

Preliminary investigations of the SPIcDER system utilizing experimental samples made of orthofabric material, integrated with CNT yarns and WFM coating, show proof that the concepts proposed in this research to develop a spacesuit outerlayer integrated dust cleaning system to protect suits from the hazardous effects of lunar dust are viable. Experiments conducted in ambient conditions provide sufficient evidence for the feasibility of a combined passive and active dust cleaning system using CNT flexible fiber material in concert with design techniques to integrate

active electrostatics based technology and WFM coating passive technology into the spacesuit outerlayer fabric. From the data analyzed during these repeated preliminary tests, it is possible to conclude that the dust cleaning performance of the SPIcDER system is greater than 80% for lunar dust simulant with particle sizes between 10-75 μm in both dynamic and static dust settings in ambient conditions. It was also shown that cleaning performance is repeatable. Table 5.5-1 summarizes the overall optimal dust cleaning parameters for the SPIcDER configuration from this preliminary study.

Table 5.5-1. Summary of optimal performance parameters of the SPIcDER system

Parameter	Optimal Values	Comments
Electrode Spacing	~1-1.2 mm	
Voltage	1000 V	
Frequency	5 Hz	Square wave form utilized. Limited investigation with waveforms due to constraints on availability of power electronics system
Dynamic Dust Performance		Estimated using visual observations
WFM coated and uncoated samples	>90%	
Static Dust performance		Estimated using ImageJ® and clearing factor equation
WFM coated Samples (Average)	87%	Best performance 95%, range between 85-95% on repeated runs
Uncoated Samples (Average)	82%	Best performance 85%, range between 80-85% on repeated runs
Percentage of fabric area covered in residual dust post SPIcDER activation	<10%	Requirement less than 25%

The next steps as detailed in Chapters 6 and 9 are concentrated on optimizing different design techniques for scaling this technology on larger portions of a spacesuit and understand the key parameters governing system performance by developing numerical models to optimize the various technical aspects of the SPIcDER system. Furthermore, the SPIcDER system embedded samples were re-evaluated in vacuum conditions. These results are presented in Chapter 9.

PART III
RESEARCH ANALYSIS:
Numerical Modeling and Design Considerations

CHAPTER 6: NUMERICAL SIMULATION AND KEY PARAMETERS FOR THE SPIcDER SYSTEM

"It is magic until you understand it, and it is mathematics there after"- *Bharat Krishna*

In Chapter 5, experiments demonstrated that CNT yarns embedded into the spacesuit outerlayer can remove greater than 80% of lunar dust simulant particles, when energized using a multiphase AC voltage signal. In this chapter, the underlying physical laws governing the SPIcDER system are described, and the derivation of the associated equations are shown. A simplified representation of the SPIcDER experimental setup described in Chapter 5 is modeled using finite element methods in ANSYS Maxwell, and the corresponding electric field distributions are simulated, analyzed, and reviewed in correlation with the experimental data. The simulations are extended with MATLAB code which models the dynamics behavior of the dust particle in SPIcDER. This dynamics code takes inputs on the electric field forces acting on a dust particle coming in contact with the spacesuit outerlayer from ANSYS Maxwell, and computes the motion of individual dust particles. The key parameters that affect the dust cleaning performance of the SPIcDER system are identified as electrode geometries, signal waveform characteristics, and particle charge to mass ratio. This chapter presents the simulation results, and the derived assessment of effects of changing the parameters and limitations on the dust cleaning performance.

The main objectives of this chapter are to

- Understand the electrostatic effects applied in SPIcDER dust mitigation system and numerically model them to quantify the dynamic effects on the movement of dust particles.
- Identify and quantify by simulation the key design parameters that affect performance efficacy, such as: voltage waveform, electrode material properties, electrode geometry (spacing, alignment and size), particle properties.
- Apply the simulation models to optimize the key design parameters for the scaled prototype of the SPIcDER system on a knee joint section of a spacesuit. Assess the correlation between the simulation results and the experimental tests of the system performance.

6.1. Scope

The simulations developed here aim towards developing a fundamental understanding of how SPIcDER system repels particles, to derive a simplified model. A 2D model of the system is developed, starting with representation of flat substrate geometry of the spacesuit fabric comprising 6 electrodes connected to 3 phase sinusoidal AC voltage. This representation in flat-plate geometry gives insight into quantitative effects of key design parameters. The analysis is further extended to simulate and analyze the electric field distributions and intensities on a curved substrate, representative of a knee portion of the spacesuit, in four chosen bending positions. Differences in the electric field distributions and intensities between flat and curved geometries, are identified, and analyzed for lessons learned relevant to the optimization of SPIcDER key design parameters. Particle trajectory in the MATLAB dynamic model is simulated, to determine the motion of a single dust particle during one full cycle of the 3-phase sinusoidal AC voltage applied to the SPIcDER electrodes.

The assumptions and ground rules used in the ANSYS Maxwell simulations, and the MATLAB simulations are described in section 6.3. These are comparable with published studies which have previously investigated modeling efforts to simulate dust particle motion on EDS. For example, Horestein et al. (2013) modeled particle trajectories on EDS screens for use in desert environments, Liu and Marshall (2010) have modeled particle transport for standing waves and traveling waves. Additionally, Green and Morgan (2002) modeled the dielectrophoretic force for interdigitated electrodes and Malnar et al. (2003) investigated 3D simulation of the dielectrophoretic forces on particles in a traveling wave.

The forces and dynamic interactions of particles in EDS are complex, and the simulations in literature apply only simplified representations. Therefore, the technology development in EDS/electrostatic travelling-wave is guided primarily by experimental results. Simulations only come to aid in elucidation of mechanisms, and in proof of concept analysis. A similar approach has also been followed in the research presented in this dissertation. Simulation results gave guiding pointers, while the optimization of key design parameters for the SPIcDER prototype was achieved by experimenting with various configurations.

6.1.1. SPIcDER System

The SPIcDER system utilizes electrostatic and dielectrophoretic forces to repel charged and uncharged dust particles. Dielectrophoresis is the physical mechanism of a non-uniform electric field exerting a force on a dielectric particle immersed in this field. The SPIcDER system proposed in this research for spacesuit application consists of a series of parallel flexible electrodes made of yarns made of CNT fiber embedded into the spacesuit outerlayer material. The outerlayer acts as a dielectric (non-conducting) substrate for the electrodes, which are connected to an input signal source that provides an AC voltage signal.

The CNT fiber electrodes can be excited using either a single-phase or a multi-phase AC voltage signal. The SPIcDER research indicates that sinusoidal (single frequency) AC voltages are adequate for repelling dust, yet this concept could be easily extended in the future for broader frequency bands, should there be an advantage. When the electrodes are activated/energized, the AC voltage generates a surrounding electric field, as shown in Figure 6.1-1. An electric field which is sufficiently strong, levitates the dust particles and transports them away from the surface area which contains the electrodes (e.g. the spacesuit fabric, in this case).

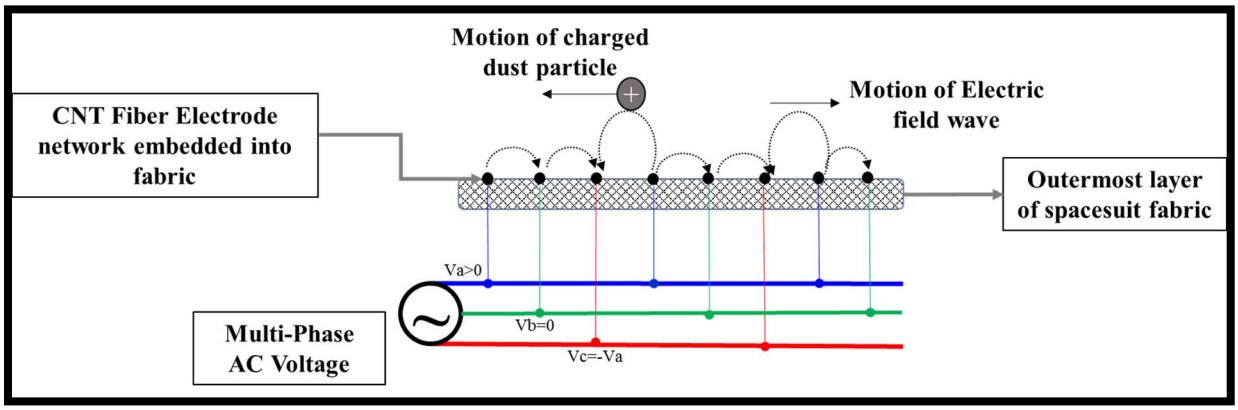

Figure 6.1-1. SPIcDER system mechanism. *Three-phase input voltage shown here.*

When a single-phase AC voltage is applied, the electrodes generate an electric field whose direction oscillates back and forth as the polarity of the waveform changes. Since all the electrodes are at the same phase, a travelling wave is not generated, instead a standing wave of electric field is generated. The standing wave of electric field lifts the particles from the surface but lacks strong translational component of force to effectively move the particles across the substrate. Hence the process of cleaning dust from the substrate is not as effective using a single-phase system.

In multi-phase input signal, as shown in Figure 6.1-1, the electric potentials vary between adjacent electrodes, with a phase shift (120° phase shift for 3 phase signal), generating a travelling wave of electric field. A charged particle introduced in this region will move along this traveling wave as the electric field generated has both strong vertical and translation components. Depending on the polarity of the charged particle, its movement is either along the direction of the electric field wave, or in the opposite direction. (for details, the reader is referred to Section 6.6.5).

6.2. Governing Equations of the SPIcDER System

This section details the governing equations of the active electrode system, and derives the forces acting on a charged dust particle that comes in contact with the SPIcDER surface. There are three governing principles to model the SPIcDER system as shown in Figure 6.2-1. The figure shows where each of these three aspects (Electric field solution, dust particle charge, and motion of dust particle using SPIcDER system) are modeled. Following sections provide details on this modeling effort with underlying assumptions described in section 6.3.

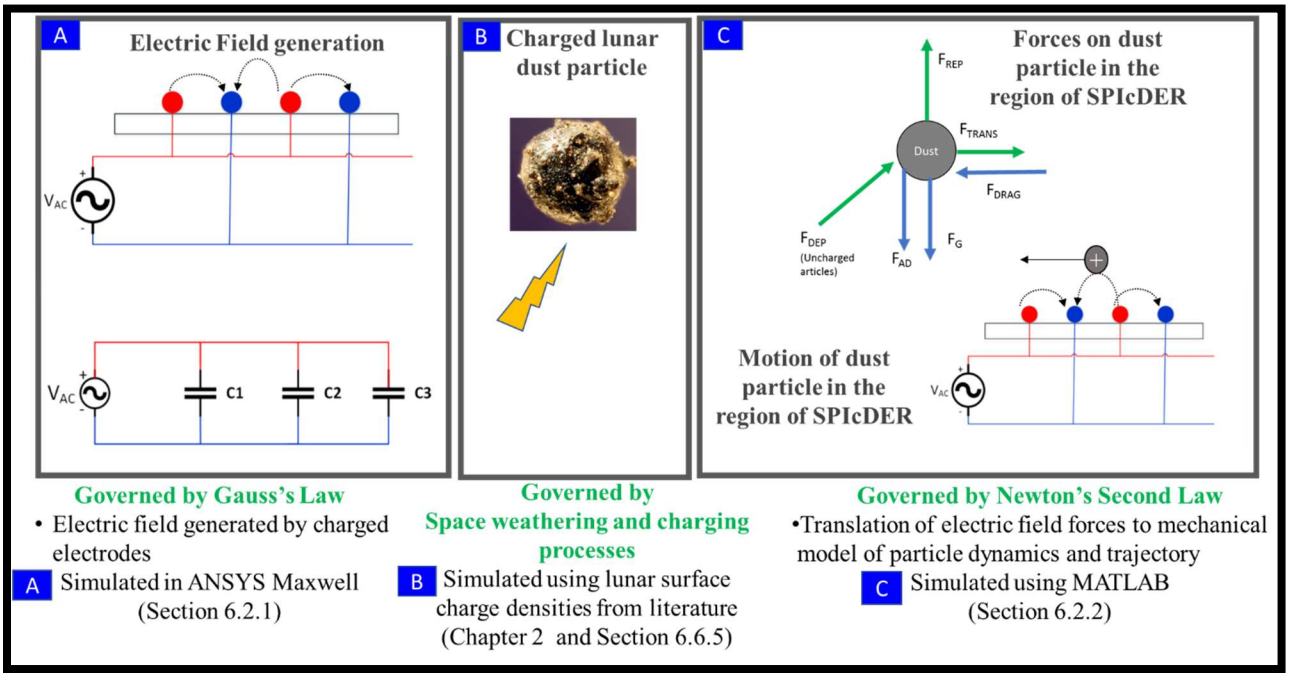

Figure 6.2-1. Governing principles of the SPIcDER system.

6.2.1. Electric Field Generated by SPIcDER

The SPIcDER system employs electrostatic and dielectrophoretic forces to levitate dust particles and move them across the surface of the substrate. These forces arise as a result of the

electric field distributions and magnitude. The electric field distribution generated by the SPIcDER system represents an electrostatics problem governed by Gauss's law. The assumptions in using Gauss's law is that the electric field for a point charge is inversely proportional to the square of the distance from the surface of the conductor and the field generated is radial.

Gauss's law states that the total electric flux *(Φ)* out of a closed surface *(S)* is equal to the net charge *(Q)* enclosed by that surface divided by the permittivity of the medium as given by Equation 7 (Jones, 1995).

$$\Phi = \oint_S \vec{E}.\overrightarrow{dA} = \frac{Q}{k\varepsilon_0} \tag{7}$$

Where ε_o is the permittivity of free space, k is the dielectric constant of the medium. Few values of k relevant to the experiments conducted as part of this research are given in Table 6.2-1.

Table 6.2-1. Values for the dielectric constant *k* utilized in this research based on the applicability of experiments

Medium	Dielectric Constant (k)	Applicability to current research
Air	1.00059 (@1 atm)	For experiments conducted in laboratory ambient conditions
Vacuum	1	For experiments conducted in the vacuum chamber
Teflon	2.1 (@1 atm)	Spacesuit outerlayer fabric is a Teflon coated material
Dust particle	4	Polarizability of particle impacts its movement in the electric field

The SPIcDER system can be modeled as a pair of charged cylindrical parallel wires. For a pair of cylindrical parallel wires of radius r_0, length L, separated by a distance d, as represented in Figure 6.2-2, Equation 7 above can be solved for the radial electric field intensity for each of the parallel cylinders separately. Superposition can be then used to add the two components (Kiousis et al., 2014).

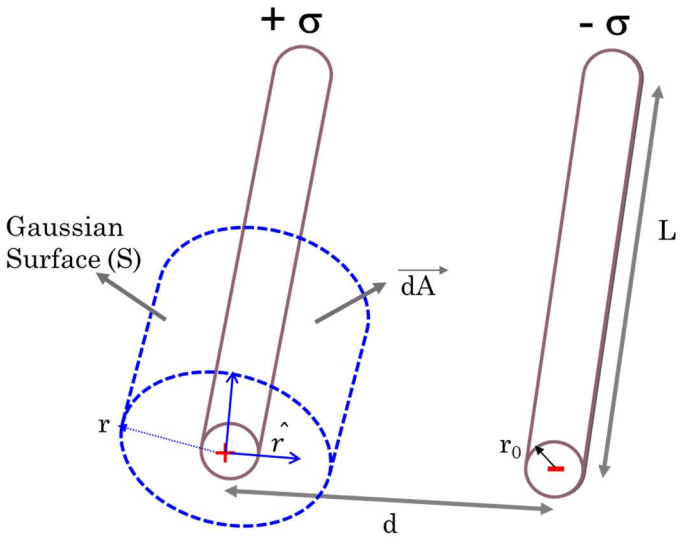

Figure 6.2-2. Representation of a pair of CNT electrodes in the SPIcDER system using Gauss's law to derive the electric field generated by the electrodes

The electric field due to wire 1 (on the left) that is charged with a linear charge density σ when external voltage is applied can be given by

$$\vec{E}_{Left} \cdot 2\pi r L\, \hat{r} = \frac{\sigma L}{k\varepsilon_0} \tag{8}$$

The electric field due to wire 2 (on the right) that is also charged with linear charge density σ when external voltage is applied can be given by

$$\vec{E}_{Right} \cdot 2\pi (d-r) L(-\hat{r}) = \frac{-\sigma L}{k\varepsilon_0} \tag{9}$$

where $r>r_0$ is the distance from the axis of the wire electrode, and r_0 is the electrode radius, with the assumption that both electrodes have the same radius.

The total electric field at each point is the sum of the radial electric fields from each of the parallel wires. Using superposition principle, the total electric field of the electrode pair can be given as

$$\vec{E}_{Total} = \vec{E}_{Left} + \vec{E}_{Right} \tag{10}$$

$$\vec{E}_{Total} = \frac{\sigma}{2\pi k\varepsilon_0}\left[\frac{1}{r} + \frac{1}{(d-r)}\right]\hat{r} \tag{11}$$

The electric field generated has both magnitude and direction. The direction of the electric field generated by the pair of electrodes with opposite charges, is depicted in Figure 6.2-3 which show the field lines starting on positive charges and terminating on negative charges

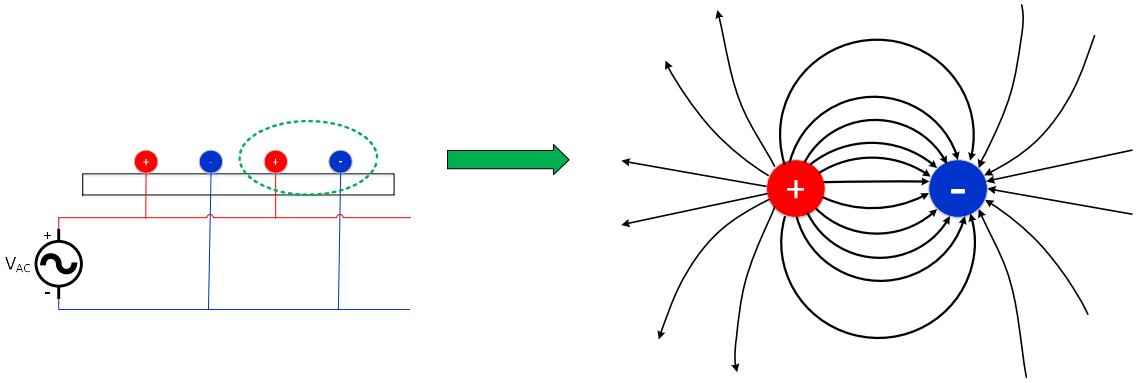

Figure 6.2-3. Illustration of electric field lines of between cylindrical electrodes with opposite charges representative of a pair of CNT fibers embedded in the spacesuit fabric

The potential difference between the two conductors can be found by integrating the total electric field over the path connecting the surface of the two conductors as shown in Equation 12

$$\Delta V = -\int_{r_o}^{d-r_o} \vec{E}_{Total}.\overrightarrow{dL} \tag{12}$$

Since E is conservative, taking a straight-line path along $\hat{r}$ a line connecting the centers of the two conductors, $\hat{r}$ dr. Then Equation 12 transforms to

$$\Delta V = -\frac{\sigma}{2\pi k\varepsilon_0}\int_{r_o}^{d-r_o}\left(\frac{1}{r}+\frac{1}{(d-r)}\right).\hat{r}\,dr \tag{13}$$

Solving the integral gives Equation 14

$$\Delta V = -\frac{Q}{2\pi Lk\varepsilon_0}\ln\left[\frac{(d-r_o)^2}{{r_o}^2}\right] \tag{14}$$

In other words, electric field is the negative gradient of the electric potential, and therefore is directly impacted by the input voltage levels

The electric force (Coulomb force) due to the electric field generated by the electrodes acting on a charged dust particle with charge q in the region of the field can be described as

$$\vec{F} = \vec{E}.q \tag{15}$$

For a sinusoidal waveform, this electric force is given by Equation 16, were ω is the angular frequency *(ω=2πf)* of the input signal

$$\vec{F} = \vec{E}\cos(\omega t)\,.\,q \tag{16}$$

This force generated by the electric field has both a lateral (translational) and vertical (lifting) component. When a charged particle is in the region, the vertical component of the electric field force levitates the particles. The lateral component transports the particle off to the next set of electrodes, and process continues until particles are swept away from the surface due to the travelling electric field generated. The electric potential at each electrode changes in steps within a time period. The frequency of the applied voltage determines how fast the polarity of the electrodes is changing over time.

6.2.1.1. Capacitor-Resistance Model

The basic principles of the SPIcDER system can be described with a simplified capacitor-resistance model. The parallel CNT electrodes in SPIcDER system form small interstitial capacitors, generating an electric field when a voltage is applied. The electric field produced between the electrode pairs together repel charged particles that are in the region of the electric field. As an example, Figure 6.2-4 shows how the SPIcDER system with four electrodes can be modeled as an equivalent capacitor-resistance system shown (6.2-4C). While the capacitors represent the CNT electrodes in a parallel configuration, the resistance of these electrodes is small enough (on the order of 0.4-2 Ω for CNT yarns utilized in the coupon experiments) to ignore the effects of the resistance of the wire and simplify the schematic to that shown in Figure 6.2-4D. The total equivalent capacitance of the system shown by the circuit schematic in Figure 6.2-4D for four electrodes can be expressed as

$$C_{eq} = C_1 + C_2 + C_3 \tag{17}$$

For system that has *n* electrodes, the total equivalent capacitance of can therefore be given by

$$C_{eq} = C_1 + C_2 + C_3 \ldots\ldots + C_{n-1} \tag{18}$$

Capacitance can be defined by relating the electric potential created across the electrodes and the amount of charge on the electrodes given by Equation 19a, where Q is the electric charge on each electrode, *V* is the electric potential and *C* is the capacitance in Coulombs/Volt or Farad.

$$\Delta Q = C\Delta V \tag{19a}$$

$$Q = CV\left[1 - e^{\frac{-t}{RC}}\right] \tag{19b}$$

When the electrodes are connected to the input voltage, the power system transports charge to the electrodes where t is the time starting from when the signal is applied. The charging characteristic of the electrodes (capacitors) is given by Equation 19b with the rate of charging defined by the value RC (resistance x capacitance), where R is the value in ohms and C in Farads, also known as time constant τ, which represents the transient response time. In the current case, the value of RC is very small (on the order of 10^{-11}-10^{-10} seconds) and is defined as the time it takes for the capacitors to charge to 63.2% of the maximum charge. The initial instantaneous current is high when the power system is turned on, during the transient, and approaches zero when the electrodes are charged. An electric field is generated as a result of this process. The currents passing through the electrodes are essentially negligible during the transient charging process (on the order of micro-amps) and happens very quickly (τ ~10^{-11}-10^{-10} seconds), thus any magnetic forces acting as a result of moving charges can be neglected. Substituting Q from Equation 19a into Equation 14 described earlier provides the capacitance for the two conducting wires shown in Equation 20.

$$C = \frac{2\pi L k \varepsilon_0}{\ln\left[\frac{r_o^{\,2}}{(d - r_o)^2}\right]} \tag{20}$$

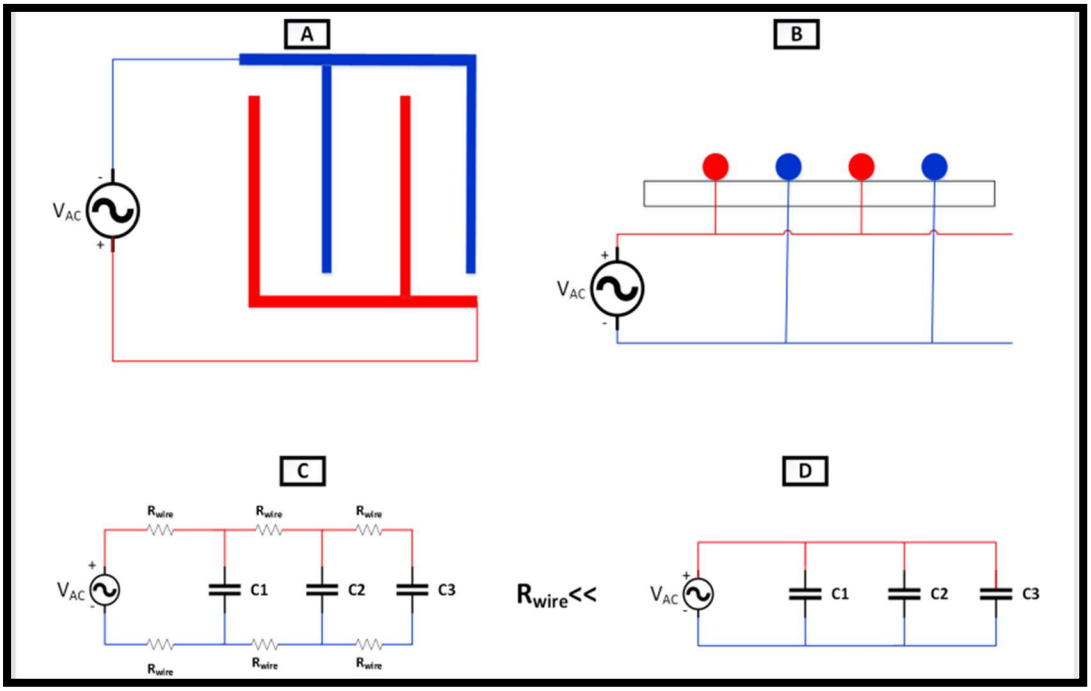

Figure 6.2-4. [A, B] 4 electrodes on a substrate (spacesuit fabric) connected to a AC power supply, [C] Equivalent capacitor-resistance model of the SPIcDER system shown in A, B, [D] Simplified capacitor model of the SPIcDER system shown in A, B for the 4-electrode system

6.2.2. Forces on the Dust Particle

The forces acting on a dust particle in the region above the spacesuit fabric when the SPIcDER system is activated are shown in the free body diagram in Figure 6.2-4. The net forces acting on the dust particle with charge q can be explained by a combination of the Coulomb force, the viscous force, the gravitational force and dielectrophoretic forces as given by the equation of motion (EOM) in Equation 21.

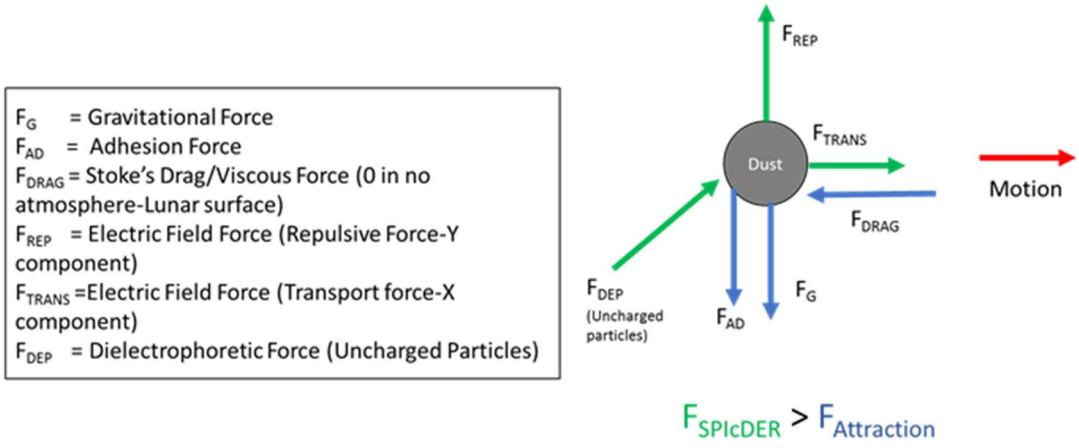

Figure 6.2-4 Free body diagram of a dust particle in the region above the fabric when SPIcDER system is activated.

$$m\frac{d^2r}{dt^2} = qEc \quad (\omega t) - 6\pi\eta\frac{dr}{dt} - mg + 2\pi R_P^3 \left(\frac{\varepsilon_P - \varepsilon_m}{\varepsilon_P + 2\varepsilon_m}\right)\nabla|E^2| - \alpha\frac{q^2}{16\pi\varepsilon_0 R_P^2} \qquad (21)$$

Where m, q, R_P , ε_p represents the properties of the dust particle (mass, particle charge, radius, dielectric constant respectively), r is the position of the dust particle.

- The electric field is a measure of force per unit charge. Therefore, $qEcos(\omega t)$ is the Electric force (or the Coulomb force) generated by activating the SPIcDER system on a dust particle with charge q. E is the electric field generated by applying an AC voltage input signal with frequency f (ω=2πf).
- $6\pi\eta\frac{dr}{dt}$ is the viscous force generated due to the friction between the particle and the surrounding fluid, where η is the viscosity of the fluid around the particle. With no atmosphere on the lunar surface, this force is zero when considering lunar environments. However, this force would need to be considered if cleaning operations for the suit are conducted inside a pressurized module such as an airlock, crew-lock, or similar module for post EVA operations.
- mg is the gravitational force where g is the acceleration due to gravity

- $\alpha \frac{q^2}{16\pi\varepsilon_0 R_P^2}$ is the electrostatic image force of adhesion of the charged dielectric spherical particle (dust particle) contacting a planar conducting surface (spacesuit fabric with electrodes) as described in chapter 2, section 2.6.1.
- The term $2\pi R_P^3 \left(\frac{\varepsilon_P - \varepsilon_m}{\varepsilon_P + 2\varepsilon_m}\right) \nabla |E^2|$ is the dielectrophoretic force for spherical particles. Dielectrophoretic (DEP) force refers to the force experienced by an uncharged particle when exposed to a non-uniform electric field. The DEP process governs the movement of these particles with internal electric dipole moments when exposed to non-uniform electric fields (Jones, 1995). The lunar dust is composed of both charged and uncharged particles. Therefore, even dust particles that are neutral will respond to the electric field generated by the SPIcDER system. The term represents the time-averaged DEP force experienced by polarizable spherical particles. The strength and direction of DEP force depends on the size of the dust particles, the electrical properties of the medium and dust particles, and the frequency and distribution of the electric field. Here ε_p and ε_m are the dielectric permittivities of the particle and the medium respectively and ∇E is the electric field gradient. On the lunar surface, ε_m corresponds to ε_o, the permittivity of free space. The term $\left(\frac{\varepsilon_P - \varepsilon_m}{\varepsilon_P + 2\varepsilon_m}\right)$ is called the Clausius-Mossotti function on which the strength of the dielectricphoretic force depends. The Clausius-Mossotti function defines whether the dust particle experiences a positive or negative a dielectrophoresis force. A positive dielectrophoresis indicates that particles are attracted to the electric field intensity maxima, and negative dielectrophoresis when particles are repelled from maxima and attracted towards minima. If the particle ε_p is greater than the medium ε_m, this often results in particles experiencing positive DEP and vice versa. This phenomenon of dielectrophoresis is heavily utilized to transport, sort and separate particles in medical applications generally related to biological processes.

The trajectory of the dust particle is obtained by solving for the differential Equation 21. Due to the complicated nature of the particle-field interaction, where the motion of the particles is nonlinear and coupled, this EOM cannot be solved analytically. A solution to a linear approximation to the EOM assuming small oscillations for the particles was previously proposed by Masuda (1971). While a few studies were previously conducted to simulate particle motion over an EDS system on which the SPIcDER system is based, due the complex nature of the forces,

much of this technology development has been driven by experimental investigations. Due to similar complexities, much of the efforts of this research is also geared towards experimental investigations and as such this chapter performs simulations of the net force experienced by a single dust particle considering only the electrostatic force and force due to gravity.

6.3. Underlying Assumptions for Simulations

Due to the complex nature of the problem involved, simplifying assumptions were made to represent the basic physical mechanisms of the SPIcDER system into a first order numerical model. This is a multi-physics simulation, comprising of the electric field distribution (modeling of electric fields and forces in ANSYS) and particle trajectory (mechanical model of dynamics and trajectory in MATLAB).

- Electrode and Substrate Properties
    - The CNT flexible electrodes are assumed to be uniformly cylindrical in the ANSYS model. In reality, and for the experimental work in this research, the CNT fibers being utilized are two ply strands (yarns of CNT) twisted together. Each ply is in turn made up of multiple (7-14) filaments, which are individually cylindrical in cross section. Figure 6.3-1 shows the two ply twisted CNT fibers utilized for the experiments.

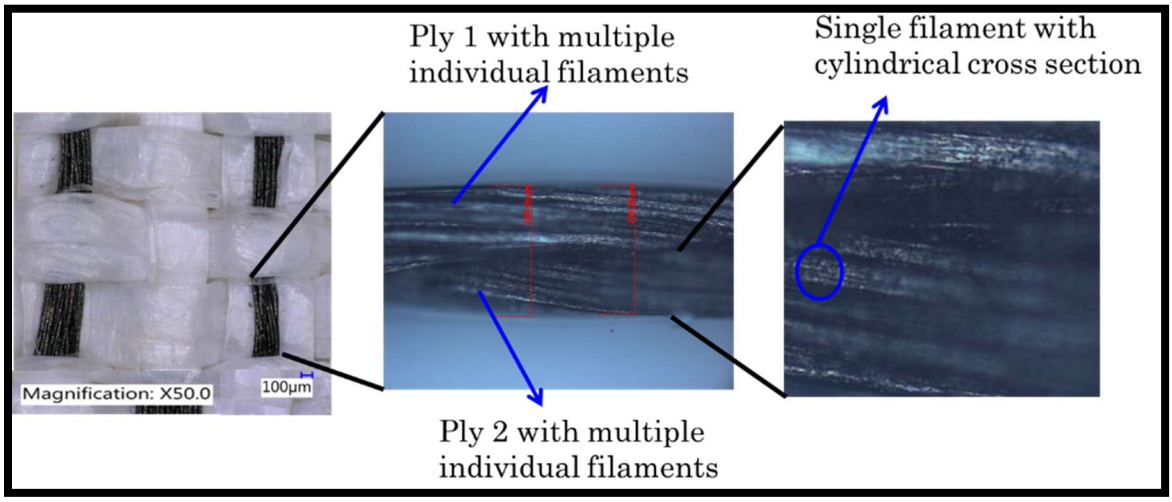

Figure 6.3-1. Illustration of the electrode shape utilized for testing the CNT material as embedded in the spacesuit outerlayer. Each electrode is a twisted two-ply CNT yarn. Each ply has multiple single filament fibers. Each filament fiber is cylindrical in shape

    - For the analysis, half of the electrode is exposed to the environment while the other half is embedded into the spacesuit fabric represented as the substrate. In the ANSYS

model, the electrodes are modeled by having the top half of the electrode exposed to the surrounding medium and the bottom half surrounded by the substrate.

- The perturbing effects of any protective or dielectric coating, or work function coating is neglected in the ANSYS model.
- The spacesuit outerlayer material used for experimental investigations is Orthofabric material which is a combination of Gore-Tex® on the front side and Nomex®-Kevlar® on the back side. In the ANSYS model, the outerlayer of the spacesuit is modeled as Teflon throughout the entire thickness of the outerlayer.

- Electric Field Solution in ANSYS
  - The electric field solution is derived using ANSYS Maxwell software, using the AC conduction solver, which defaults the input signal to a sinusoidal waveform as shown in Equation 16. The input signal waveform cannot be modified in ANSYS Student Edition used in this research. Due to this constraint, variations in the waveform type (square wave, triangular etc.) using the student edition have not been analyzed in the simulations. The representative equation of the sinusoidal wave utilized in ANSYS model is shown in Equation 22, where V_0 is the maximum voltage amplitude, $\omega=2\pi*frequency$, and θ is the phase angle

$$V = V_0 cos(\omega t + \theta) \quad (22)$$

  - Analysis in ANSYS is conducted in 2D for a flat substrate and a curved substrate. The curved surface is approximated to represent the profile of the knee section of the spacesuit, when in four pre-determined bent positions.
  - Fringing/edge effects are ignored in the analysis.
- Particle Trajectories in MATLAB
  - Particle trajectory is generated for a single particle. The forces created by interactions between adjacent dust particles (particle-to-particle interactions) are assumed to be negligible compared to the primary forces exerted by the traveling wave. Therefore, particle-to-particle interactions are neglected in the MATLAB model, and deemed outside the scope of this research, as detailed in Section 1.4.
  - The MATLAB model for particle trajectories includes gravitational force. This is a parameter, that can be adjusted to represent gravity on Earth (for experimental tests), or on the Moon (for potential operating scenarios).

- Dust Properties
    - Dust particles are assumed to be spherical. Lunar dust particles can be jagged and sharp, but accurately replicating different shapes in the numerical methods is very difficult, hence particle trajectories are shown for single spherical shaped particles. Therefore, the MATLAB model neglects those dust particles that may get entangled into the spacesuit surface with their jagged edges (nano-hooks). This assumption is supported by the experimental data, which shows no evidence of significant number of particles entangled on the orthofabric).
    - The dust particles are assumed to be charged (either positive or negative charge). The magnitude of the electric charges on the particle are based on literature values of the surface charge density of particles on the order of -3.05e-6 Cm^{-2} (Chesnutt and Marshall, 2013; Horenstein et al., 2013) and confirmed by analytical calculation based on the electric potentials on the lunar surface (~20 V day side and -3.8 kV during night side) using a simplified capacitive model for spherical particles that showed particle charges to range between -10^{-11} to 10^{-17} C. Uncharged particles are neglected, under the assumption that if uncharged particles are deposited on the spacesuit with the SPIcDER system, the dust becomes charged through tribocharging effects, or through collisions with the surface, or with the electrodes.

6.4. Numerical Modeling and Simulation Set-up

The objective of the modeling work presented herein is to gain quantitative understanding of the physical mechanisms in SPIcDER system, and to advance and support the experimental work in this research. The numerical modeling employed in this research is a two-step process, which was implemented in incremental steps.

- The first step involves utilizing a finite-element method to calculate the electric fields generated by the SPIcDER system electrodes in a 2D plane utilizing the student version of the ANSYS Maxwell 2015 software using the AC conduction solution solver.
- The second step involves solving the EOM (Equation 21) for a single dust particle in MATLAB to compute particle trajectory (position and velocity). The electric field vectors and magnitudes obtained from ANSYS are exported into MATLAB to solve the EOM.

The ANSYS model was first built to analyze a 3-phase electrode system with 6 electrodes for a flat substrate. The geometry and dimensions modeled replicate the coupon tests conducted, described in Chapter 5. Then, the MATLAB model was implemented and applied to calculate trajectories of dust particles of various sizes and dielectric constants. The next step comprised an upgrade of the ANSYS model to curved surface for four knee flex angles. The variations in the electric field intensities and threshold voltages between the flat and curved surfaces was analyzed. Key design parameters affecting the net repulsive forces on the particle are analyzed. Figure 6.4-1 provides an overview of the simulation process conducted for this research. Table 6.5-1 provides a list of all simulation runs conducted during this research to investigate key parameters impacting SPIcDER performance along with associated chapters where the results are illustrated. Each of the varying parameters are highlighted in colors. Experiments conducted using coupons and the scaled prototype that correspond to specific simulation runs are specified within the Table.

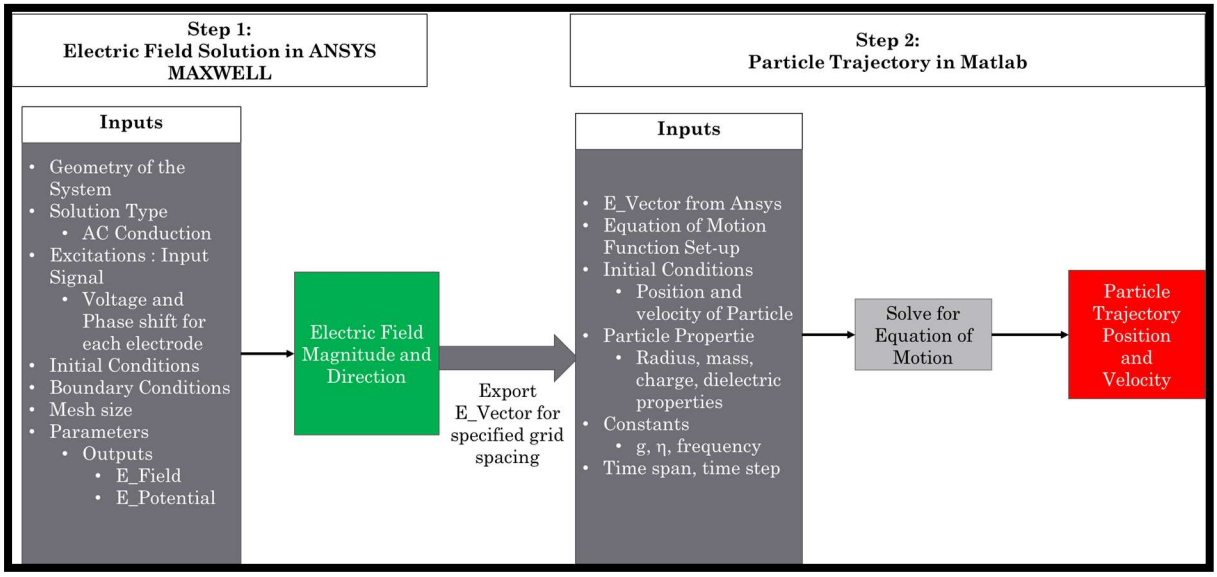

Figure 6.4-1. Approach for numerical modeling and simulation to generate electric field distribution an dust particle trajectories in ANSYS and MATLAB.

6.5. Electric Field Solution using ANSYS

A 2D model was created for a flat geometry of the substrate (spacesuit fabric) on which the 6 CNT electrodes were modeled. Dimensions of the system used for these simulations match closely to the spacesuit fabric coupons developed and tested in Chapter 5. The inner layers of the spacesuit are not included in the simulations of this chapter, however these layers are modeled and simulated in the safety analysis in Chapter 8. The electric solver best suited to the model is the AC conduction

solver, which computes steady-state 2D electric fields in conductors, due to applied potentials. A balloon boundary condition was applied, as represented by the large outer circle in Figure 6.5-1. The boundary models the region outside the drawing space as being nearly 'infinitely' large, effectively isolating the model from other sources of current or magnetic fields. The medium within the boundary is set to air for simulations that replicate the experiments. It is set to vacuum for scenarios of lunar operations. The boundary condition is set to have a voltage of 0 V, corresponding to virtual ground zero voltage at infinity. Table 6.6-1 provides the list of parameters utilized for the simulations.

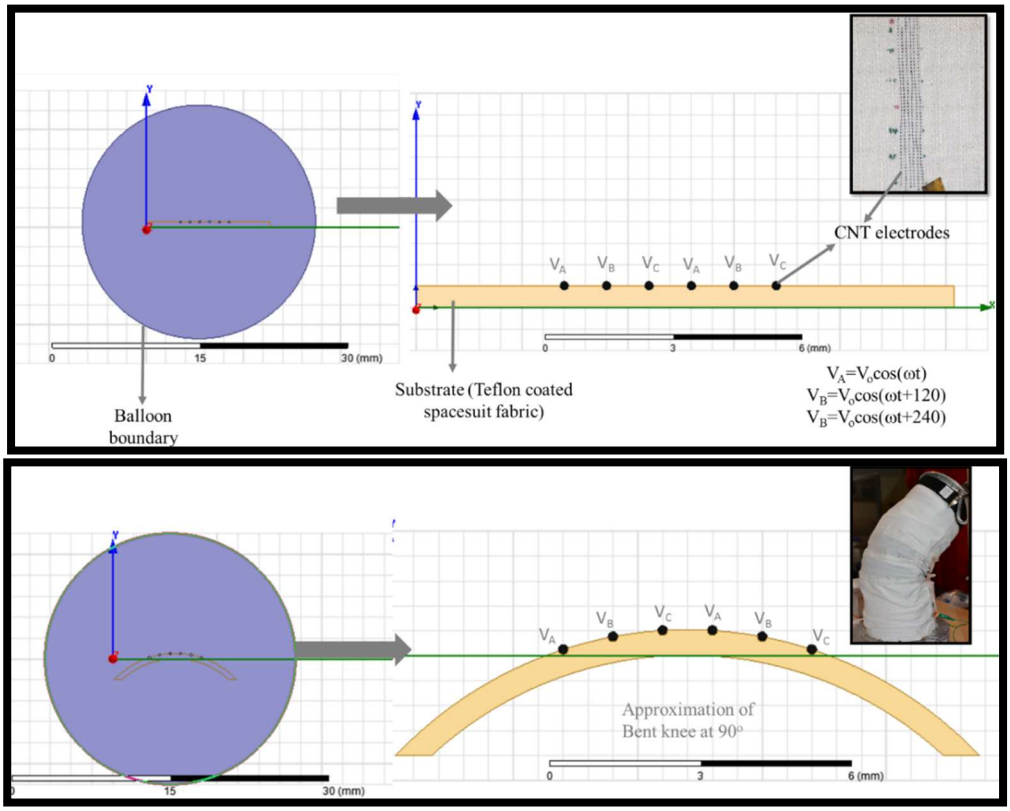

Figure 6.5-1. Modeling the SPIcDER system with the 6 CNT electrodes ANSYS. *[Top] Flat geometry (approximation of coupon testing) [Bottom] Curved geometry (approximation of knee joint curvature)*

The voltage excitation is defined at each electrode as a reference for computing the electric potentials. The voltage at each electrode is defined using a maximum voltage input V_0 and a phase angle representing a sinusoidal wave as described in Equation 22. A 3-phase input AC voltage with a phase shift of 120° is utilized for the simulations (shown in Figure 6.5-1). The number of phases in the model is a parameter that can be easily adjusted (single or multiphase) by redefining the excitations at each electrode and reanalyzing the problem.

The electrostatic field solver in the software solves a Poisson type partial differential equation for the electric potential V_E, with appropriate boundary condition shown in Equation 23.

$$\nabla(\varepsilon_r . \varepsilon_o \nabla V_E) = -\rho_v \tag{23}$$

Where, $V_E(x,y,z)$ is the electric potential as a function of position, ε_r is the relative permittivity of the medium, ε_o is the permittivity of free space and ρ_v is the volume density of the electric charge. This equation is derived from Gauss's law and from Faraday's law of induction. When the electric potential is obtained by solving the above second order differential equation using finite element method, Maxwell's equations and the applicable constitutive equation are then used to obtain the electric field strength, *E*, and the electric flux density *D*, vectors as shown in equations 24 and 25. The electric field is the negative gradient of electric potential.

$$\vec{E} = -\nabla V_E \tag{24}$$

$$\vec{D} = \varepsilon_r \varepsilon_o \vec{E} \tag{25}$$

The frequency of the AC voltage input is defined. Based on results from experiments in Chapter 5 it was found that frequency of 5 Hz provided the best cleaning performance. Therefore, most simulations were conducted at a frequency of 5 Hz.

Default mesh was used for the analysis. Maxwell generates an initial mesh, which includes surface approximation settings. To create a finite element mesh, Maxwell first divides all true surfaces into triangles. Figure 6.5-2 shows the meshing operations for the flat plate geometry. Number of adaptive passes to be made and percent error for the solution are also defined. The AC conduction field solver allows to analyze conduction currents due to time-varying electric fields in conductors and lossy dielectrics. This solver is used to analyze the current distributions, electric field distributions and potential differences for the SPIcDER system. The solver as mentioned previously assumes that all sources are sinusoids, oscillating at the same frequency with the different phase provided.

After the solution setup is defined, the program applies the provided boundary conditions, and initial excitations and solves each node equation in the mesh to get nodal results. The results are the set of equations that defines the electric potential at nodes of each element as previously defined in Equations 23-25. The analysis goes through an iterative process using the AC conduction field

solver then computes the electric potential for the model. From the electric potential, it derives the electric field *E(t),* the electric flux density *D(t)*, and the current density, *J(t)*.

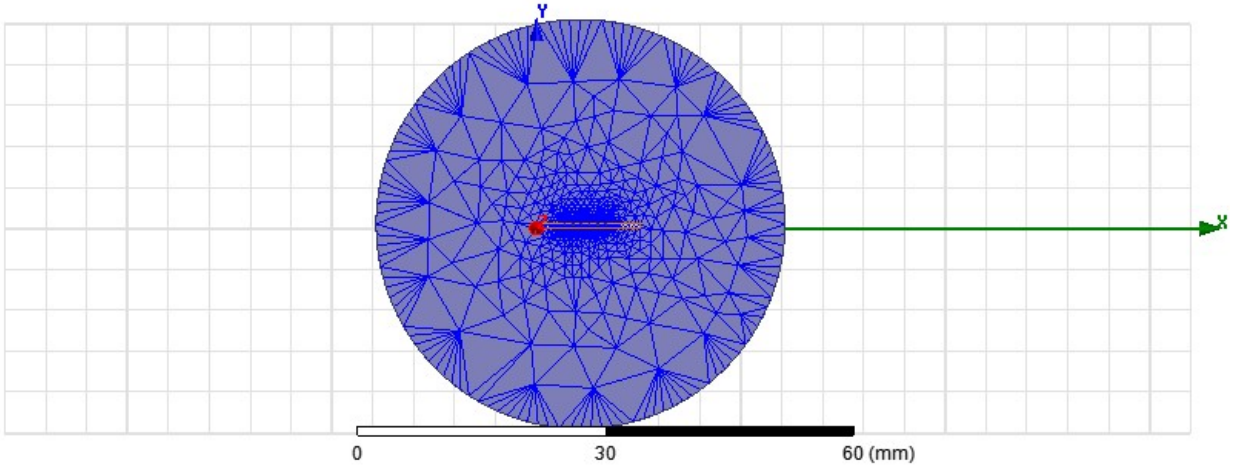

Figure 6.5-2. Discretization of the model into several finite elements using meshing operations in ANSYS. Mesh plots shown for the flat plate substrate as an example

Table 6.5-1. Simulation runs conducted to investigate key parameters impacting SPIcDER performance

	In Chap	Analysis	Simulation Type	Medium	Insulation	Insulation Material	Spacing	Electrode diameter	Freq	Voltage	# Phase	Dielectric Substrate	Test Case
1	Ch.8	Safety	All layers, 6 electrodes, no insulation	Air	NO	N/A	1 mm	200 μm	5 Hz	1000 V	3	Teflon (k=2.1)	
2	Ch.8	Safety	All layers, 6 electrodes, no insulation	Vacuum	NO	N/A	1 mm	200 μm	5 Hz	1000 V	3	Teflon (k=2.1)	
3	Ch.8	Safety	All layers, 6 electrodes, insulation	Air	YES, Around	Teflon, 20μm	1 mm	200 μm	5 Hz	1000 V	3	Teflon (k=2.1)	Ch.8 2 orthofabric layers
4	Ch.8	Safety	All layers, 6 electrodes, insulation	Vacuum	YES, Around	Teflon, 20μm	1 mm	200 μm	5 Hz	1000 V	3	Teflon (k=2.1)	Ch.8 2 orthofabric layers
5	Ch.8	Safety	All layers, 6 electrodes, WFM -no insulated	Air	WFM-layer on	Lunar dust 10 μm (k=3.6)	1 mm	200 μm	5 Hz	1000 V	3	Teflon (k=2.1)	
6	Ch.8	Safety	All layers, 6 electrodes, WFM -no insulated	Vacuum	WFM-layer on	Lunar dust 10 μm (k=3.6)	1 mm	200 μm	5 Hz	1000 V	3	Teflon (k=2.1)	
7	Ch.6	Medium	Flat sheet, 6 electrodes, uninsulated	Air	NO	N/A	1 mm	200 μm	5 Hz	1000 V	3	Teflon (k=2.1)	Ch 5. Coupon Tests
8	Ch.6	Medium	Flat sheet, 6 electrodes, uninsulated	Vacuum	NO	N/A	1 mm	200 μm	5 Hz	1000 V	3	Teflon (k=2.1)	Ch 9. Coupon vacuum test
9	Ch.6	Insulation	Flat sheet, 6 electrodes, insulated	Air	WFM	Lunar dust 10 μm (k=3.6)	1 mm	200 μm	5 Hz	1000 V	3	Teflon (k=2.1)	Ch.5 Coupon Test series2
10	Ch.6	Insulation	Flat sheet, 6 electrodes, insulated	Air	YES, Around	Teflon, 20μm	1 mm	200 μm	5 Hz	1000 V	3	Teflon (k=2.1)	Ch.5 Coupon Test series2
11	Ch.6	Insulation	Flat sheet, 6 electrodes, insulated	Air	YES, Around	Teflon, 20μm	1.2 mm	200 μm	5 Hz	1000V	3	Teflon (k=2.1)	
12	Ch.6	Spacing	Flat sheet, 6 electrodes, uninsulated	Air	NO	N/A	0.6 mm	200 μm	5 Hz	1000 V	3	Teflon (k=2.1)	
13	Ch.6	Spacing	Flat sheet, 6 electrodes, uninsulated	Air	NO	N/A	0.6 mm	200 μm	5 Hz	600 V	3	Teflon (k=2.1)	
14	Ch.6	Spacing	Flat sheet, 6 electrodes, uninsulated	Air	NO	N/A	1.6 mm	200 μm	5 Hz	1000 V	3	Teflon (k=2.1)	Ch.5 Coupon Test series
15	Ch.6	Spacing	Flat sheet, 6 electrodes, uninsulated	Air	NO	N/A	2 mm	200 μm	5 Hz	1000 V	3	Teflon (k=2.1)	
16	Ch.6	Curved	Curved sheet, 8 electrodes, 15°	Air	NO	N/A	1.2 mm	200 μm	5 Hz	1000 V	3	Teflon (k=2.1)	Ch. 9 Prototype, Neutral Angle
17	Ch.6	Curved	Curved sheet, 8 electrodes, 30°	Air	NO	N/A	1.2 mm	200 μm	5 Hz	1000 V	3	Teflon (k=2.1)	Ch. 9 Prototype, Intermediate Angle
18	Ch.6	Curved	Curved sheet, 8 electrodes, 45°	Air	NO	N/A	1.2 mm	200 μm	5Hz	1000 V	3	Teflon (k=2.1)	Ch. 9 Prototype, Intermediate Angle

Table 6.5-1 cont.

	In Chap	Analysis	Simulation Type	Medium	Insulation	Insulation Material	Spacing	Electrode diameter	Freq	Voltage	# Phase	Dielectric Substrate	Test Case
19	Ch.6	Curved	Curved sheet, 8 electrodes, 90°	Air	NO	N/A	1.2 mm	200 μm	5Hz	1000 V	3	Teflon (k=2.1)	
20	Ch.6	Electrode diameter	Flat sheet, 6 electrodes, uninsulated	Air	NO	N/A	1 mm	50 μm	5 Hz	1000V	3	Teflon (k=2.1)	
21	Ch.6	Electrode diameter	Flat sheet, 6 electrodes, uninsulated	Air	NO	N/A	1 mm	100 μm	5 Hz	1000V	3	Teflon (k=2.1)	
22	Ch.6	Electrode diameter	Flat sheet, 6 electrodes, uninsulated	Air	NO	N/A	1mm	300 μm	5 Hz	1000V	3	Teflon (k=2.1)	
23	Ch.6	Electrode diameter	Flat sheet, 6 electrodes, uninsulated	Air	NO	N/A	1 mm	400 μm	5 Hz	1000V	3	Teflon (k=2.1)	
24	Ch.6	Phase comparison	Flat sheet, 6 electrodes, uninsulated	Air	NO	N/A	1 mm	200 μm	5 Hz	1000V	2	Teflon (k=2.1)	Ch5. Coupon Test Series1
25	Ch.6	Phase comparison	Flat sheet, 6 electrodes , uninsulated	Air	NO	N/A	1 mm	200 μm	5 Hz	1000V	4	Teflon (k=2.1)	
26	Ch.6	Phase comparison	Flat sheet, 6 electrodes, uninsulated	Air	NO	N/A	1 mm	200 μm	5 Hz	1000V	1	Teflon (k=2.1)	
27	Ch.6	Frequency comparison	Flat sheet, 6 electrodes, uninsulated	Air	NO	N/A	1 mm	200 μm	15 Hz	1000V	3	Teflon (k=2.1)	Ch5. Coupon Test series
28	Ch.6	Frequency comparison	Flat sheet, 6 electrodes, uninsulated	Air	NO	N/A	1 mm	200 μm	50 Hz	1000V	3	Teflon (k=2.1)	Ch5. Coupon Test series
29	Ch.6	Frequency comparison	Flat sheet, 6 electrodes, uninsulated	Air	NO	N/A	1 mm	200 μm	100 Hz	1000V	3	Teflon (k=2.1)	Ch5. Coupon Test series
30	Ch.6	Voltage comparison	Flat sheet, 6 electrodes, uninsulated	Air	NO	N/A	1 mm	200 μm	5 Hz	600 V	3	Teflon (k=2.1)	Ch.5 Coupon Test series
31	Ch.6	Voltage comparison	Flat sheet, 6 electrodes, uninsulated	Air	NO	N/A	1 mm	200 μm	5 Hz	1200 V	3	Teflon (k=2.1)	Ch.5 Coupon Test series
32	Ch.6	Voltage comparison	Flat sheet, 6 electrodes, uninsulated	Air	NO	N/A	1 mm	200 μm	5 Hz	1500V	3	Teflon (k=2.1)	Ch.5 Coupon Test series
33	Ch.6	Dielectric substrate	Flat sheet, 6 electrodes, uninsulated	Air	NO	N/A	1 mm	200 μm	5 Hz	1000V	3	3.5	
34	Ch.6	Dielectric substrate	Flat sheet, 6 electrodes, uninsulated	Air	NO	N/A	1 mm	200 μm	5 Hz	1000V	3	5	
35	Ch.6	Dielectric substrate	Flat sheet, 6 electrodes, uninsulated	Air	NO	N/A	1 mm	200 μm	5 Hz	1000V	3	10	
36	Ch.6	Dielectric substrate	Flat sheet, 6 electrodes, uninsulated	Air	NO	N/A	1 mm	200 μm	5 Hz	1000V	3	20	

6.6. Results

This section provides an overview and interpretation of the results for the electric field solution obtained from the ANSYS and particle trajectory using MATLAB simulations. The solution interpreted in this section corresponds to the steady state values of the electric field obtained using parameters in Table 6.6-1 (explained in this section are results corresponding to simulation #7 in Table 6.5-1). Visualization using contour plots of both the field magnitude and direction (electric field lines) are obtained.

Table 6.6-1. Parameters used for SPIcDER system simulation in ANSYS Maxwell for simulation run #7. *These values are updated accordingly for all simulation runs and interpreted in section 6.8 for key parameter effects.*

Parameter	Flat Geometry Value	Approximated Curved Geometry Value
Electrode diameter	0.2 mm	0.2 mm
Electrode spacing	1.0 mm, 1.2 mm	1.2 mm
Electrode Material	CNT	CNT
CNT conductivity	310000 S/m	310000 S/m
Surrounding Medium	Air (Vacuum for lunar simulation)	Air (Vacuum for lunar simulation)
Electrode Voltages	Vo=1000 V, 3phase, sinusoidal wave Phase_A $=V_oCos(\omega t+0^o)$ Phase_B $=V_oCos(\omega t+120^o)$ Phase_C $=V_oCos(\omega t+240^o)$	Vo=1000 V, 3phase, sinusoidal wave Phase_A $=V_oCos(\omega t+0^o)$ Phase_B $=V_oCos(\omega t+120^o)$ Phase_C $=V_oCos(\omega t+240^o)$
Excitation Frequency	5 Hz	5 Hz
Boundary Condition	Balloon Boundary V=0 at 10 meters diameter	Balloon Boundary V=0 at 10 meters diameter
Suit Layer and Thickness		
Length of substrate	12.7 mm (0.5 in)	12.7 mm (0.5 in)
Thickness of Substrate	0.51mm	0.51mm
Substrate Material	Teflon	Teflon
Dielectric constant of Teflon	2.1	2.1
Geometry	Flat, horizontal	Curved, horizontal Angle-1: 15º (neutral angle when pressurized) Angle-2: 30º Angle-3: 45º Angle-4: 90º

6.6.1. Electric Field Distribution

Electric field magnitudes and vectors are obtained from ANSYS simulation for one full cycle of the input signal (0º-360º). For 5 Hz frequency, this corresponds to a time period of 0.2 seconds as shown in Figure 6.6.-1. The input signal to each of electrodes is at 120º phase shift from their adjacent electrodes.

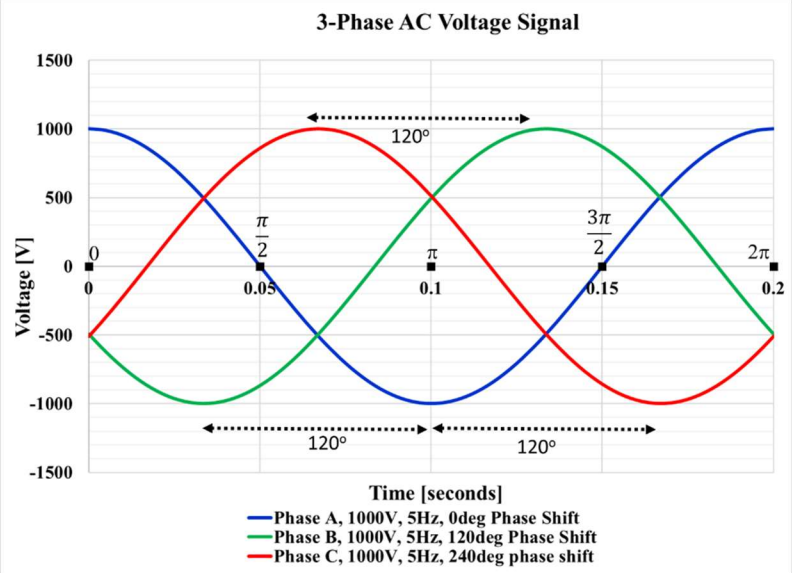

Figure 6.6-1. Applied 3-phase AC voltage signal. ***The plot shows the phase shift occurring at each of the 3-phases of the input signal***

6.6.2. Electric Field Magnitude

As expected, the simulated system produced a travelling wave of electric field with a magnitude of the field that is strongest near the electrode surfaces (E~ 5 x 10^6 V/m) and decreases radially outward as a function of the square of the distance from the surface of the electrodes. Table 6.6-2 provides an overview of the distribution (magnitude) of electric field for the flat geometric simulation, for the 3-phase sinusoidal AC input signal. In this table, the first graphic shows the electric field distribution at phase angle (ωt) of 0º at the first electrode at t=0s. In this setup, the adjacent electrode has a phase angle of 120º, the next electrode has phase angle of 240 º and so on. Similarly, the second graphic shows the electric field distribution at time t=0.067 sec, when the phase angle on the first electrode is 120º.The last graphic in the table corresponds to time t=0.135 sec, when the phase angle is 240º (-120º). A steady-state 3 phase AC input signal at 5Hz (cycle time of 0.2 s) repeats every 0.2 seconds. The electric field is shown to be travelling (left to right in

this case) from one electrode to the other corresponding to the phase angle and the polarity of the electrode changes during this phase (corresponding effect is shown at the bottom of Table 6.6-2). Although only 3 angles for the electrode are shown here, a steady-state animation in ANSYS can show the electric field wave travelling (moves) from one electrode to the next electrode corresponding to the phase angle. Frames from the steady-state animation are shown at the bottom of Table 6.6-2.

Table 6.6-2. Electric field distribution for a 6 electrode SPIcDER system

Phase Angle at each Electrode	Electric Field Magnitude Contour Plots
e1, e4= 0° e2, e5= 120° e3, e6= 240° Time, t=0s Initial Condition	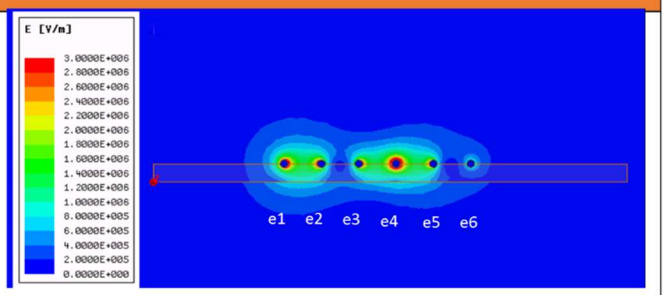
e1, e4= 240° e2, e5= 0° e3, e6= 120° Time, t=0.067s	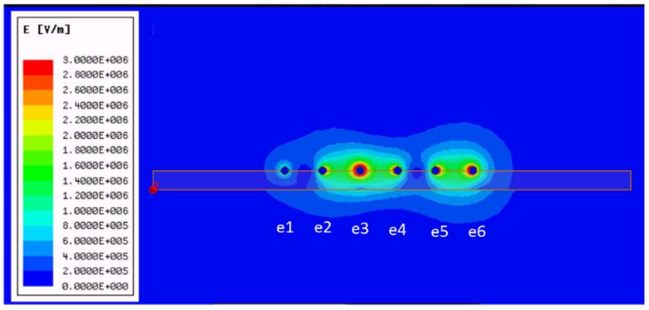
e1, e4= 120° e2, e5= 240° e3, e6= 0° Time, t=0.133s	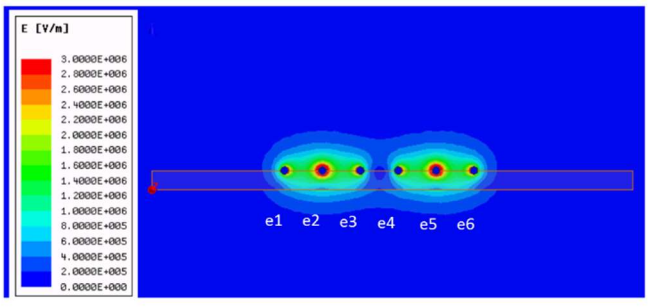

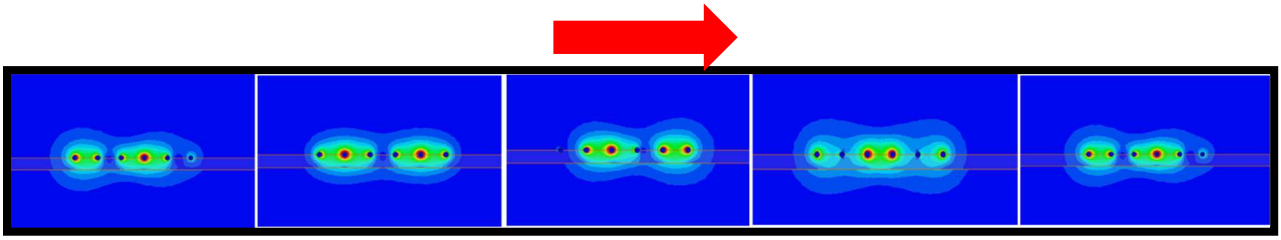

6.6.3. Electric Field Vectors

The electric field magnitude represents the overall strength of the electric field generated by the charged electrodes. The direction of the field, in vector representation are illustrated by vector arrows commonly called electric field lines. These field lines are always directed from a positive charge to a negative charge, i.e. from high potential energy to low potential energy, and ANSYS outputs electric field vectors along with electric field magnitudes. Figure 6.6.-2 shows the electric field lines for the flat plate and curved geometries at the start of the input signal (t=0). At t=0, the field lines originate from the positively charged electrodes (e1, e4) and are directed towards the negatively charged electrodes (e2, e3, e5). This pattern continues for the entire cycle of the input wave. As the input AC signal changes polarity, these field lines change direction. The electric field magnitudes and vectors are exported from ANSYS to generate particle trajectories in MATLAB. The ANSYS analysis is setup to update parameters and re-run analysis for variations in the system.

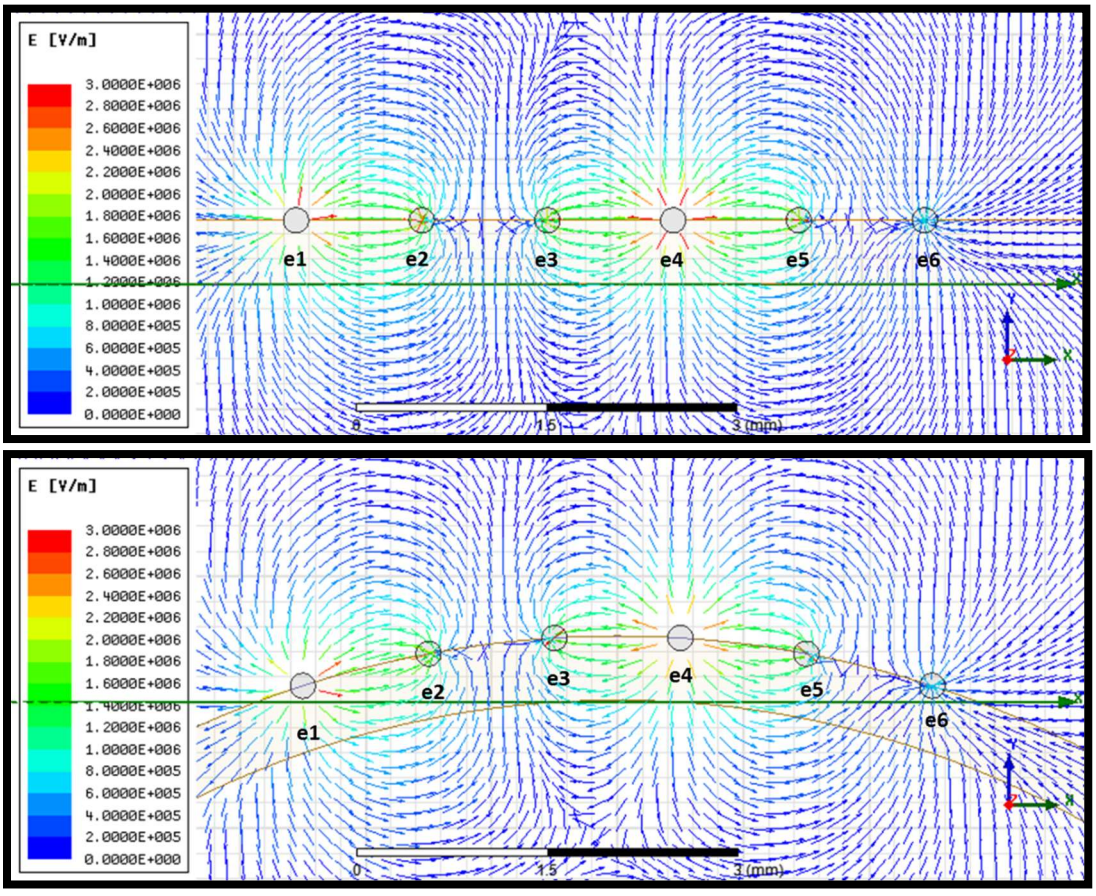

Figure 6.6-2. Snapshot of electric field lines for 3 phase, 1000 V sinusoidal input signal with 120^{o} phase shift. [Top] for Flat Plate Geometry, [Bottom] for curved geometry. *Shown here are the field lines at t=0 where the phase angle at the first (left most) electrode is 0^{o}.*

6.6.4. Electric Potentials

Electric potential is defined as the electric potential energy per unit charge. The relation between electric field and electric potential is defined in Equation 12. Figure 6.6-3 shows the electric potentials around the electrodes of the SPIcDER system at t=0. The contours around the charged electrodes are equipotential surfaces which carry equal potential within the field.

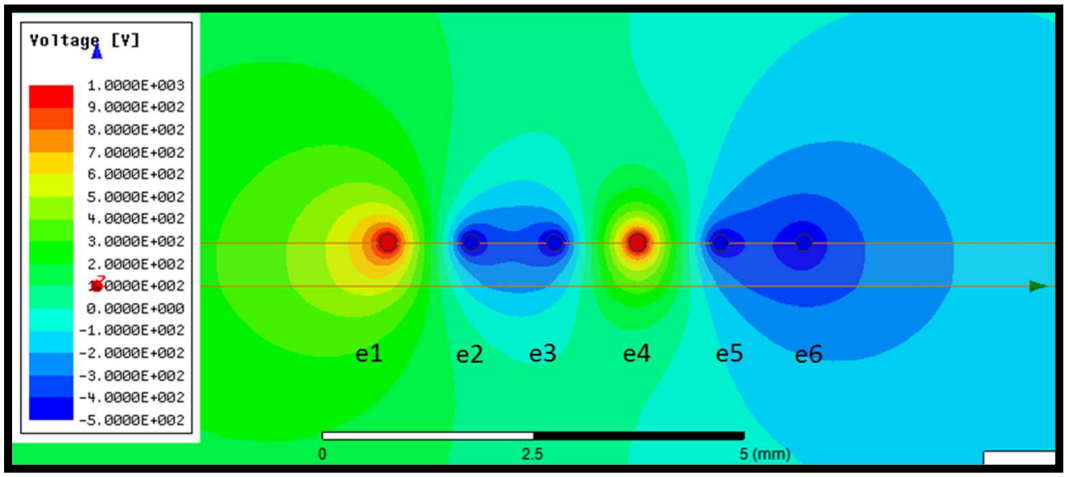

Figure 6.6-3 Electric potentials at t=0 s for the flat plate geometry with 6 electrodes

6.6.5. Particle Trajectory in MATLAB

To understand the particle motion due to the electric field generated by the electrodes, trajectory of a single charged dust particle is analyzed in MATLAB based on a simplified version of Equation 21 (described in section 6.2.2) as shown in Equation 26a

$$m\frac{d^2r}{dt^2} = qEcos(\omega t) - mg \tag{26a}$$

The ode45 MATLAB solver is utilized to solve the EOM to obtain the position and velocity of the dust particle. This function implements a Runge-Kutta method with a variable time step for efficient computation. ode45 is designed for equations of the form shown in Equation 27. (MATLAB Documentation 2016):

$$\frac{dx}{dt} = f(t,x), \qquad x(t_o) = x_0 \tag{27}$$

The EOM of the dust particle described in Equation 26 is a second order differential equation. This is translated by MATLAB into two first order differential equations by rearranging Equation 26a to utilize ode45 solver. The two first order equations are illustrated by Equations 26b and 26c

below. Here *r(x,y)* and *v(x.y)* are the position and velocity of the dust particle respectively, *E(x,y)* is the electric field vector in x and y direction, q is particle charge, m is the particle mass.

$$\frac{dr_x}{dt} = v_x \quad \frac{dr_y}{dt} = v_y \tag{26b}$$

$$\frac{dv_x}{dt} = \frac{q(E_x \cos 2\pi f t)}{m} \; ; \quad \frac{dv_y}{dt} = \frac{q\left(E_y \cos 2\pi f t\right)}{m} - g \tag{26c}$$

Initial conditions for the particle position and velocity are specified (Table 6.6-2). Values for electric field are exported from ANSYS Maxwell in a grid format for 6 specific points within a time period (0°, 100°, 120°, 240°, 300°, 360°) with subsequent interpolation in MATLAB for finer resolution. The solver is set up in a 2D format to provide the position and velocity of the particle in the x and y directions. The simulation time span and the time steps (Δt) are defined as constants in the MATLAB program. Additional physical parameters are defined, as shown in Table 6.6-2. Analysis and results are provided and explained for particle trajectory due to the electric field force generated over one complete cycle of the input voltage. The MATLAB code is set up to automatically update the particle position and velocity as initial conditions for every time step. The process repeats itself when multiple cycles of the time signal are provided.

Table 6.6-2. Parameters used for particle trajectory computation in MATLAB

Parameter	Value	Units	Source
No of Phases	3	AC_Voltage	Current research
Frequency	5	Hz	Optimal performance from tests
Input Voltage	1000	V	120° phase shift
Time Period	0.2	s	1/f
Cycles	1		Number of cycles
Particle Diameter	50	μm	
Particle Charge	-2.26e-17	Coulomb	Horenstein et al., 2013. ~ 140 electron charges
Particle Density	3520	kg/m^3	Liu and Marshall, 2010
Particle Mass	1.474e-08	g	Density*Volume
Particle Charge to Mass Ratio	9.81e-8	C/kg	Charge/Mass
Particle relative permittivity, εp	3.9		Horenstein et al. 2013
Initial Position	(6, 0.64)	mm	Between electrodes 3, 4
Initial Velocity	0.00	m/s	Particle at rest/adhered to fabric

The trajectory of a single dust particle for one complete cycle of the input signal is shown in Figure 6.6-4. The progression of the particle trajectory as the number of increasing cycles of the input signal is shown in Figure 6.6-5. The number of cycles of the input signal corresponds to the

amount of time the SPIcDER system is activated. For example: 1 cycle at 5 Hz represents 0.2s of SPIcDER operation, 5 cycles at 5 Hz represents 1 second of SPIcDER operation. The figures show results for particle trajectory due to electric field force. Gravity can be added based on the environment where SPIcDER is operated.

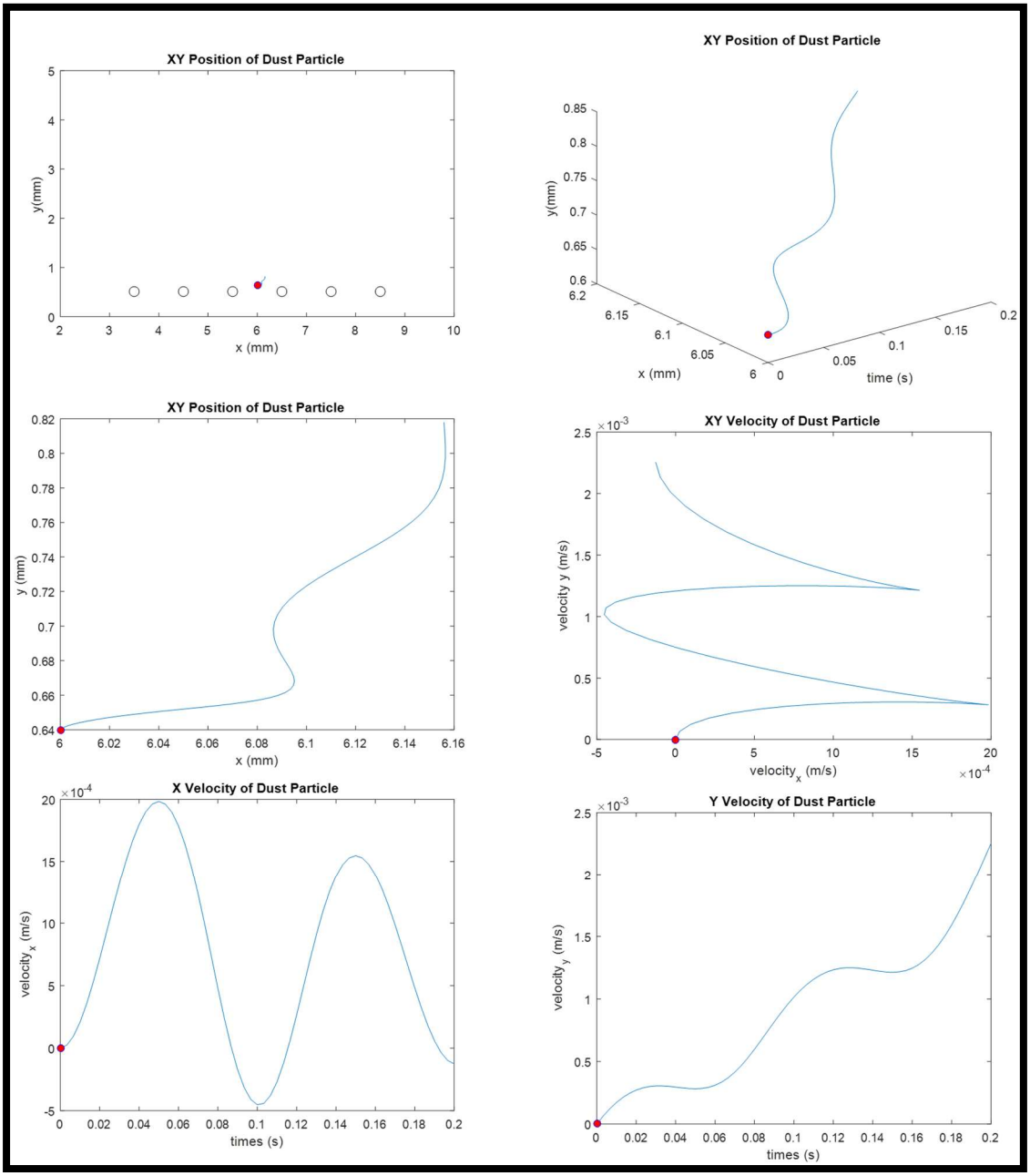

Figure 6.6-4. Particle trajectory for one complete cycle of the input signal for the flat plate geometry. *This picture shows trajectory due to Electric force generated. Gravitational force can be added to the analysis using Equation 26c.*

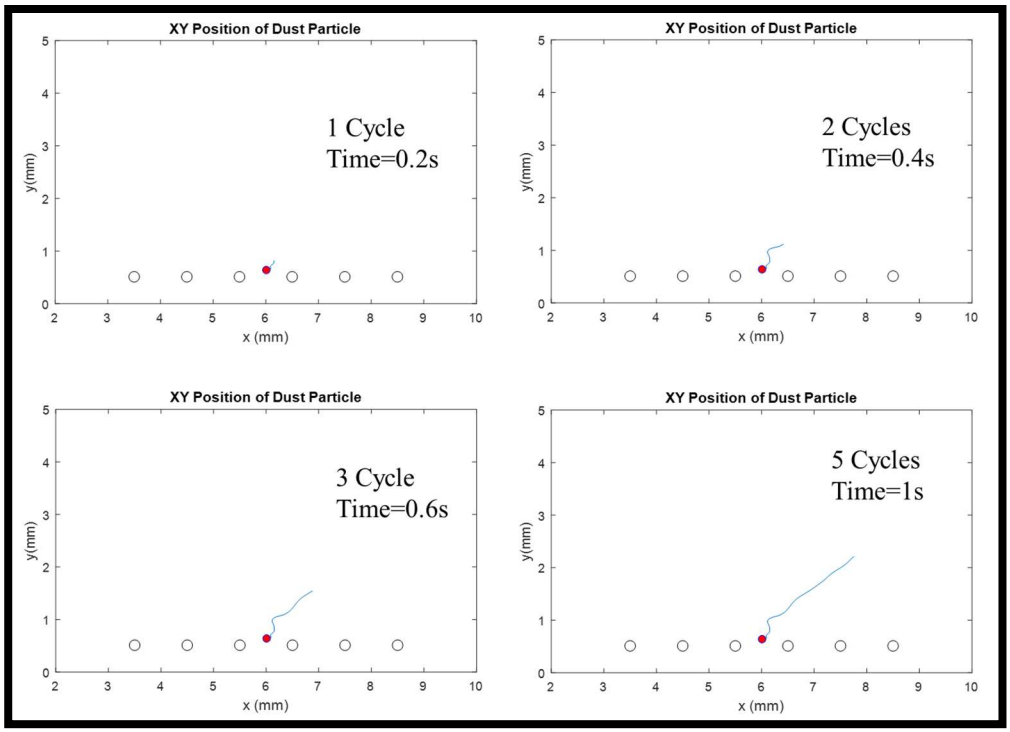

Figure 6.6-5. Progression of the trajectory of a single dust particle (50 μm) over increasing activation time of the SPIcDER system. *This picture shows trajectory due to Electric force.*

6.6.5.1. Correlation between Particle Trajectory and Electric Field

The trajectory of the dust particle for one cycle (0-360°) of the input signal is explained using electric field vector snapshots from ANSYS and MATLAB (Figure 6.6-6). The figures illustrate field vectors overlaid on voltage contours at each electrode and the position of the particle at five phase angles for the 1000 V sinusoidal signal. Regions around the positive electrodes are high potential, and regions around the negative electrode are low potential. In the electric field generated, the negatively charged particle moves from low potential to high potential by the action of the electrical (Coulomb) forces. The negatively charged particle experiences an attractive Coulomb force by the positively charged electrode and a repulsive force by the negatively charged electrode. As the electrodes change their polarity throughout the cycle of the input signal, the direction of the attractive and repulsive forces changes aiding particle translation along, and levitation above the substrate. A positively charged dust particle in the same position experiences a repulsive force from the positive electrode and attraction force from the negative electrode and the trajectory would be in the opposite direction. The simulated trajectories correlate well with experimental results, and illustrate the efficacy of the SPIcDER system for repelling lunar dust simulant particles.

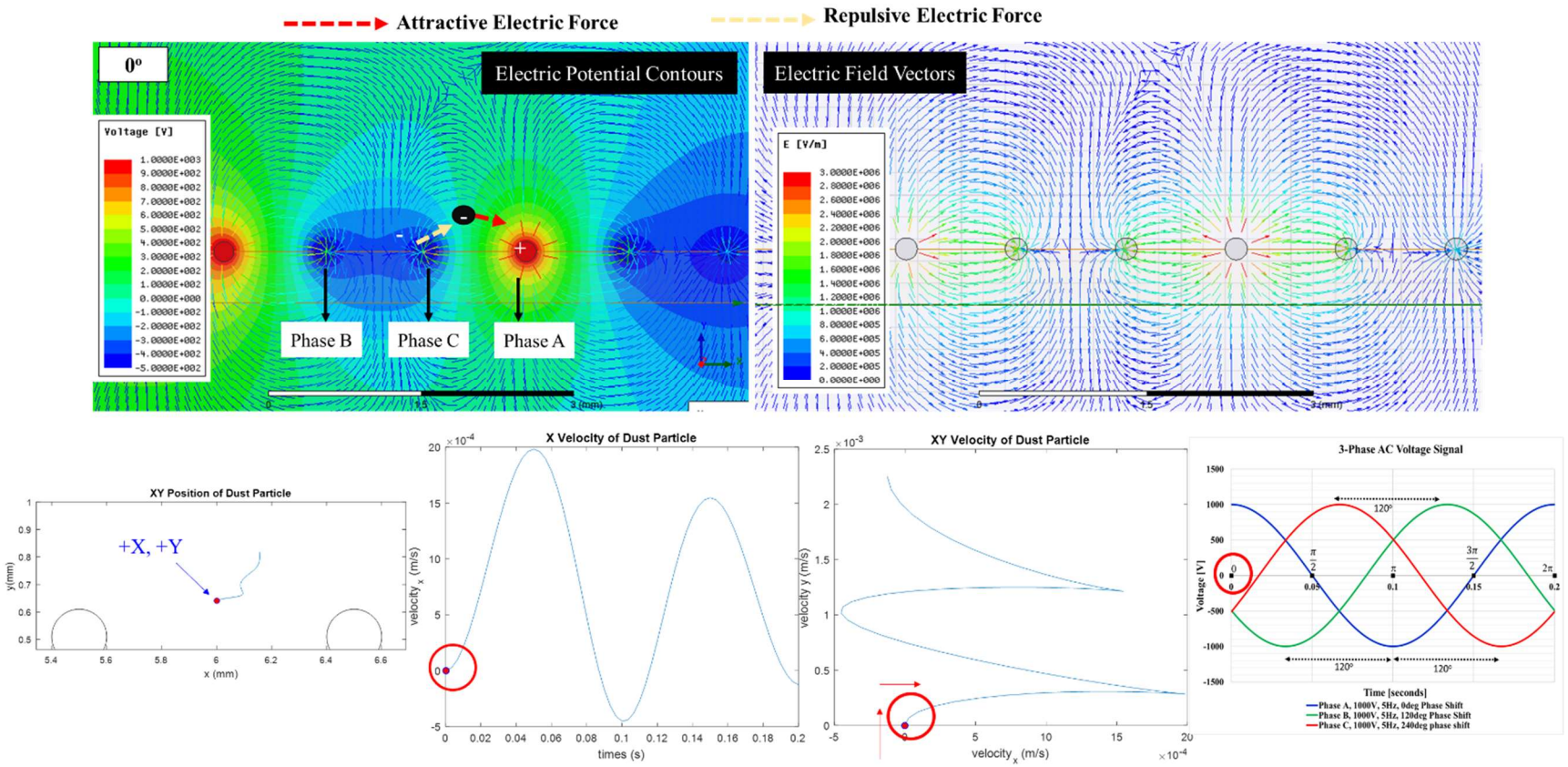

Figure 6.6-6. Trajectory of the dust particle due to the electric force generated over one cycle of the input voltage correlated with the electric field vectors and voltages at each electrode

Figure 6.6-6 cont.

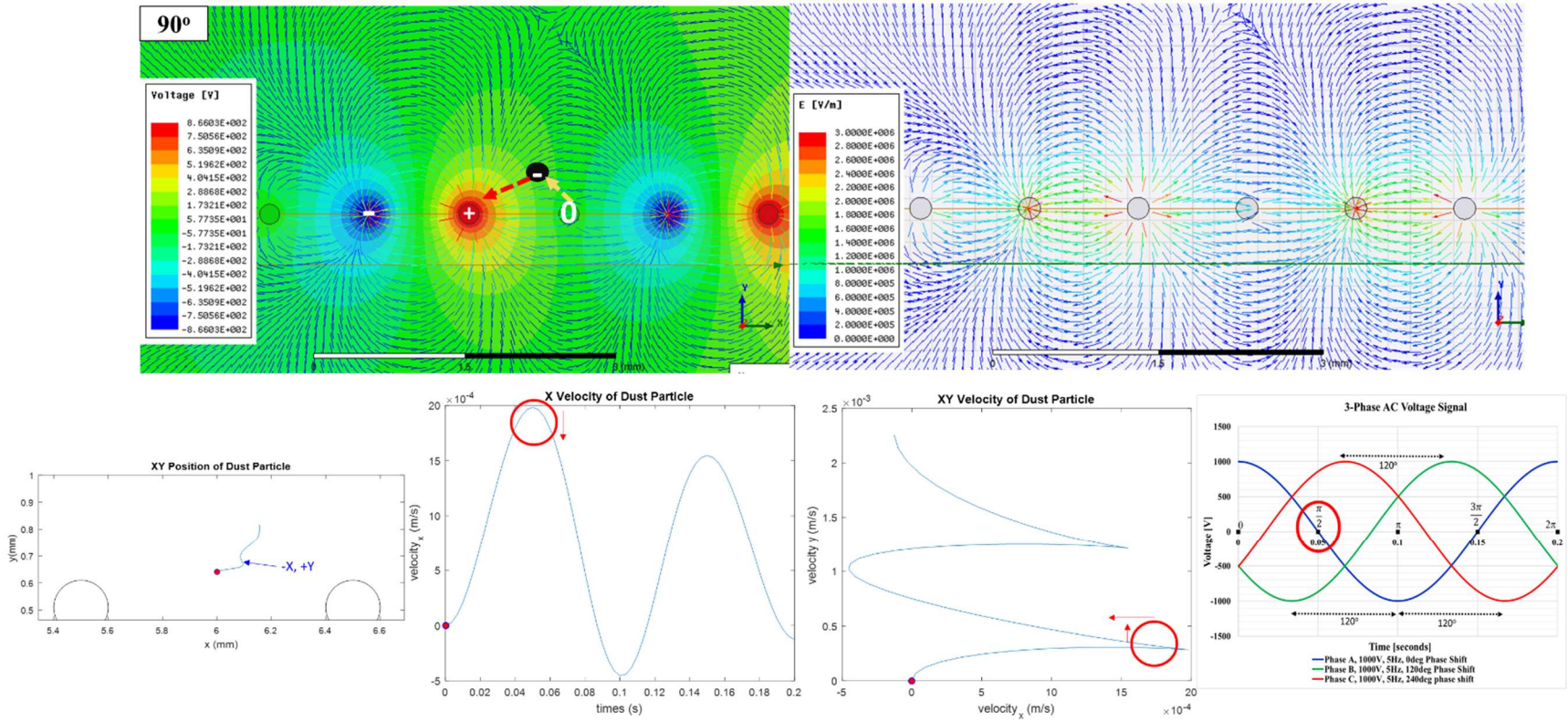

Figure 6.6-6 cont.

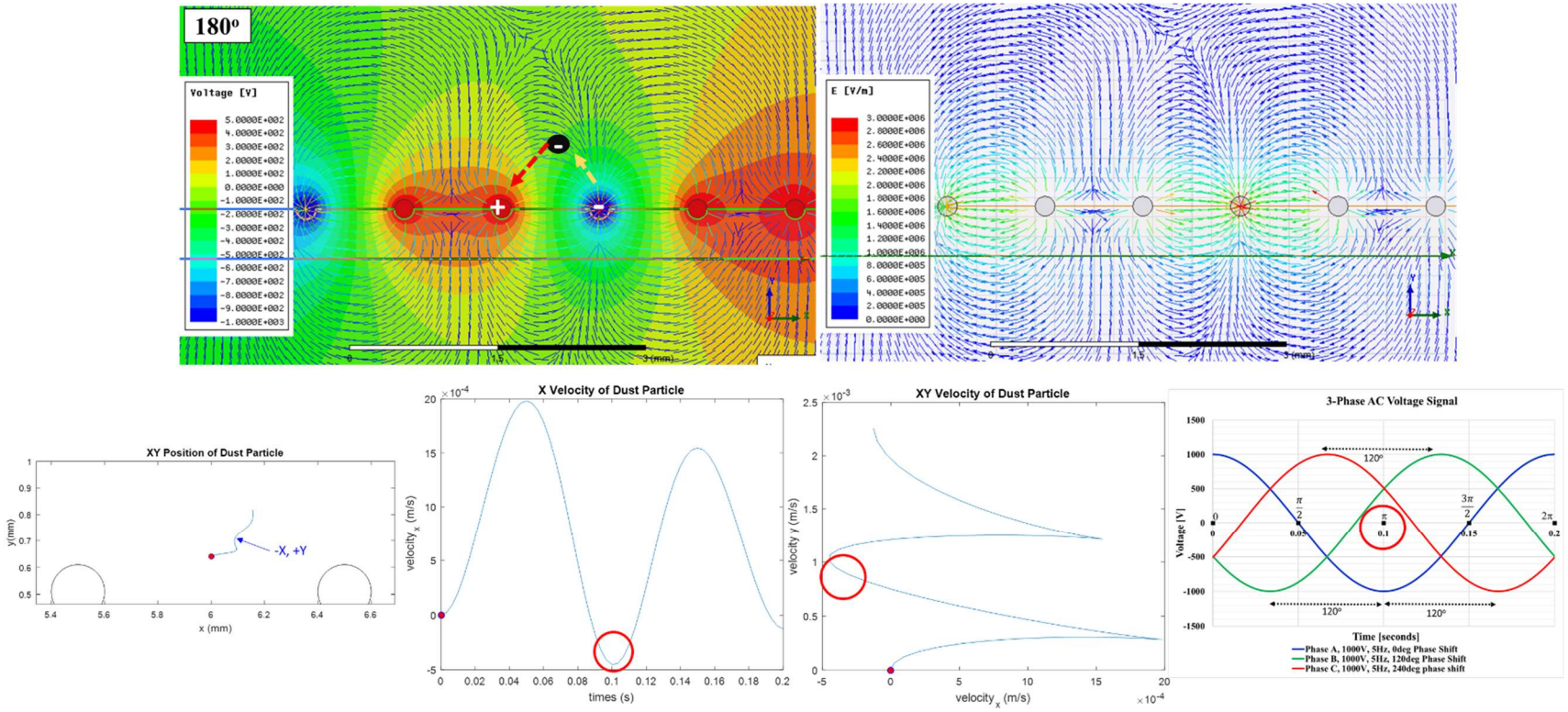

Figure 6.6-6 cont.

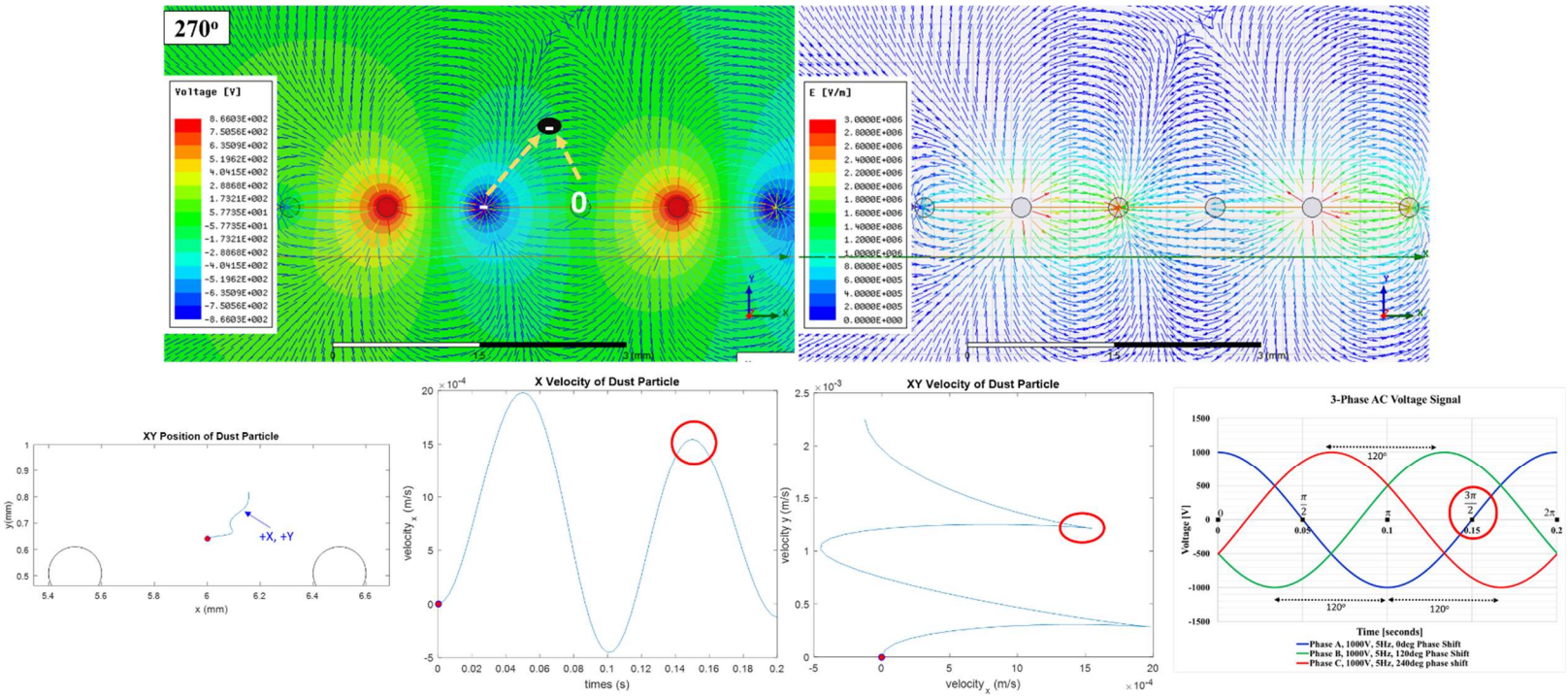

Figure 6.6-6 cont.

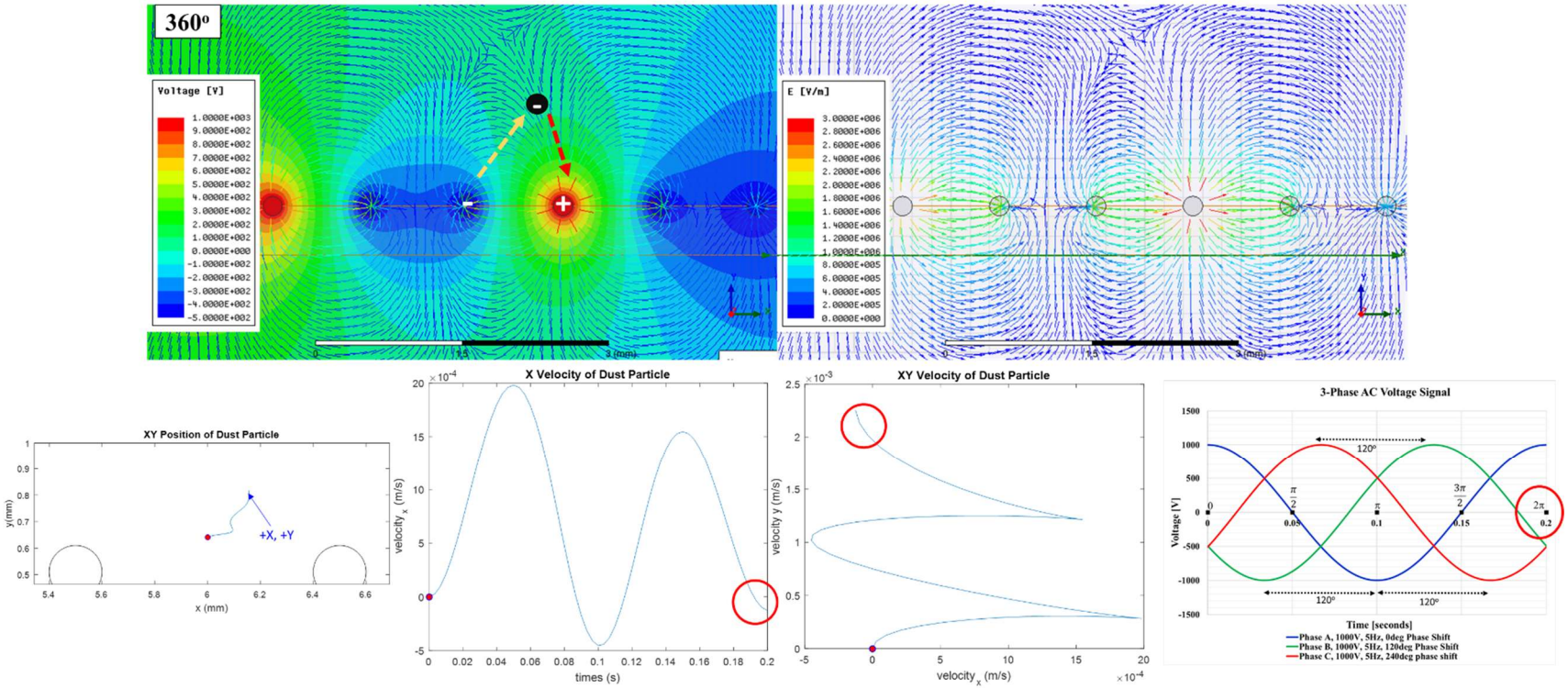

6.6.5.2. Comparison of Electrostatic Adhesion Force and Electric Field Force from the SPIcDER system

The electric force due to the electric field generated by the SPIcDER system is compared to the electrostatic adhesion force that might exist between the charged particle and the substrate if the SPIcDER system were not activated. Figure 6.6-7 plots the magnitude of the electrostatic image force of adhesion (explained in Chapter 2, section 2.6) along with the magnitude of the Coulomb force produced by the SPIcDER system in two locations on the substrate- a distance representative to be above the electrode where the electric field would be at its maximum, and a distance in between two consecutive electrodes (particle's initial position in the trajectory example in section 6.6.5.1). Figure 6.6-7 illustrates that the magnitude of electric force generated by the SPIcDER system can overcome the electrostatic adhesion force of the charged particle and will be able to repel the dust particle from the surface of the substrate. This is observed in the trajectory plots shown earlier for a 50 μm diameter particle. While the electrostatic force of adhesion is an approximation based on Equation 4b and can be higher than the theoretical predictions, experiments thus far in this research have shown that the SPIcDER system is able to repel 10-120 μm sized particles to sufficiently clean the spacesuit fabric maintaining the residual dust on the fabric much below 25% of the fabric area in both ambient and vacuum conditions.

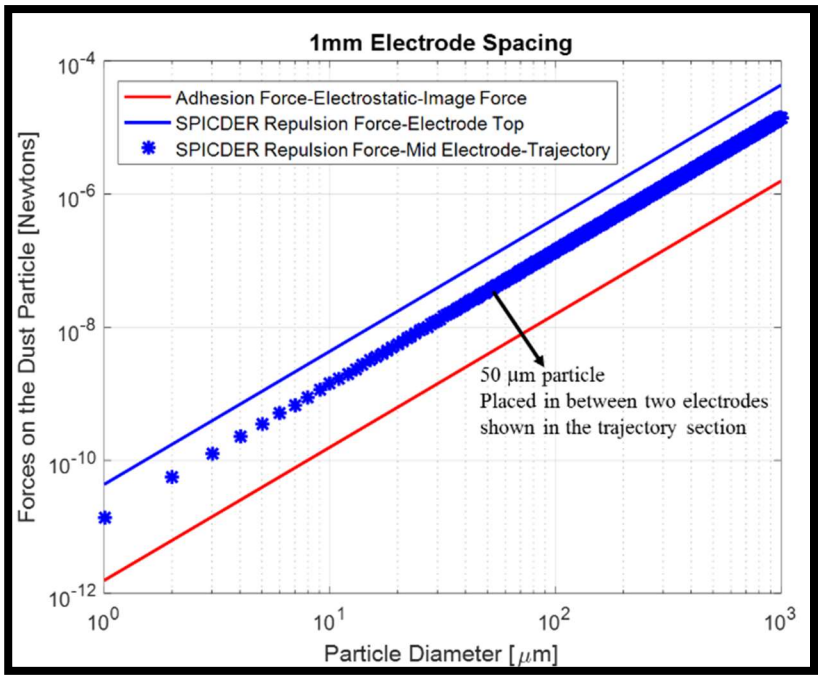

Figure 6.6-7. Electric force generated by the SPIcDER system compared to the electrostatic force of adhesion at the particle initial condition (Using -3.05e-6 Cm^{-2} charge density)**.**

6.7. Approximation of Bent Knee

The electric field generated by the SPIcDER system is analyzed for a case where the knee of the spacesuit is bent during walking motion of the astronaut during EVAs. Three angles corresponding to the knee angles utilized in the scaled experiments described in Chapter 9 are analyzed by numeric simulation. Additionally, a fourth angle is also included in the simulation, even though it does not have an experimental counterpart (it could not be tested due to limitations in the flex range of the knee prototype, as noted in Chapter 9). Figure 6.7-1 shows the simulation set-up approximating a 15º, 30º, 45º, 90º flex angles of the knee. the angle of 15º of the knee corresponds to the neutral angle when the suit is pressurized (assuming the NDX-2 spacesuit prototype) and the remaining angles correspond to flexed knee positions.

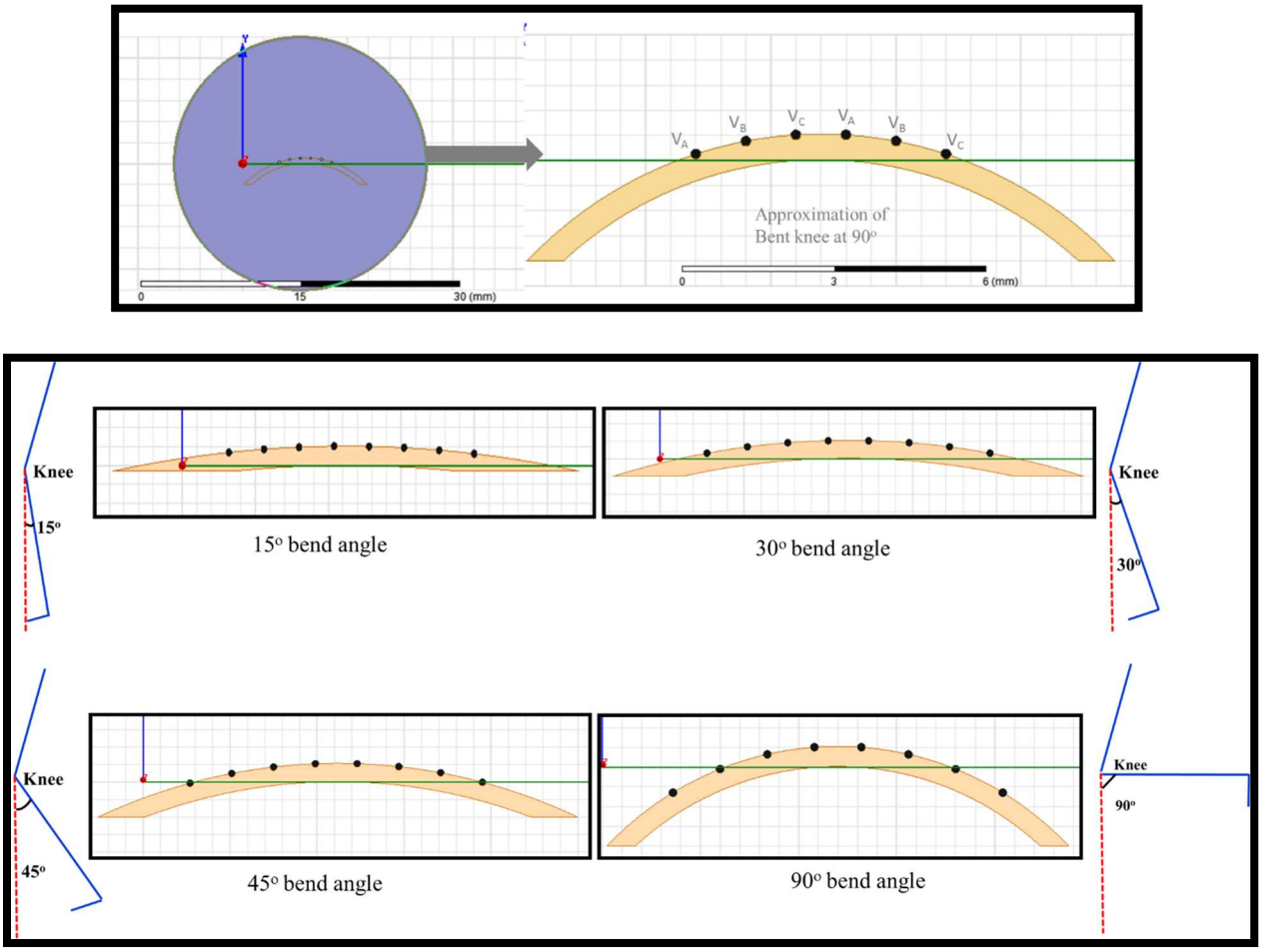

Figure 6.7-1. [Top] Approximating flex angle of the knee in ANSYS simulation, [Bottom] Simulation set-up in ANSYS for the four angles

6.7.1. Simulated Performance of the SPIcDER System on Curved Surface

Two metrics were used to compare the performance of the SPIcDER system on a curved geometry, approximating bending of the knee, to that of a flat geometry: (i) threshold voltage, at which breakdown discharge occurs between electrodes through the surrounding medium and (ii) magnitude of electric field. specifically,

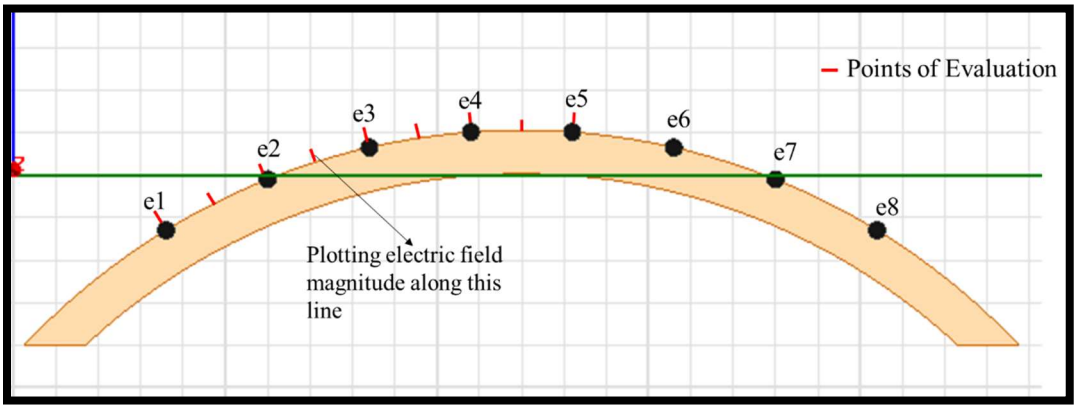

Figure 6.7-2. Points of evaluation to compare curved and flat geometries

1. The voltage at which breakdown occurs on the flat and curved geometries with the same electrode arrangement (spacing and diameter) are compared. It is anticipated that the breakdown on the curved surface would occur at a higher voltage value than the flat surface since the relative distance between the electrodes on the curved area increases slightly when the knee is bent as the fabric is stretched (on the order of 0.2-140 μm). Results from all four angles are provided.

2. To compare the electric field distribution between the flat and curved geometries, the electric field magnitude midway between two consecutive electrodes at a relative distance of 0.1 mm above the substrate was analyzed (shown as point between e1-e2, e2-e3, e3-e4, e4-e5 in Figure 6.7-2)

Comparative results for the threshold voltages where breakdown occurs and the electric field magnitude midway between two consecutive electrodes that are parameters of interest due to the impact on spacing between the electrodes are presented in the next section.

6.7.1.1. Impact of Curvature on Electric Field Distribution

- ***Threshold Voltages***

Evaluation of threshold voltages where breakdown initiates for the flat and curved surface shows that with the increase in the curvature, the voltage at which breakdown occurs increases for

the same electrode spacing configuration (evaluated 1 mm spacing). This is anticipated because of the slight increase in the distance between consecutive electrodes due to the curvature. The fabric surface connecting the electrodes stretches along a curved line and the spacing between the electrodes increases anywhere in the range of 0.03-12% (15° to 90° bend angle from experiments) depending on the curvature compared to the flat surface (See inset Figure 6.7-3 next to Table 6.7-1). Table 6.7-1 shows the values for the threshold voltages observed between the flat and curved geometries from the simulation.

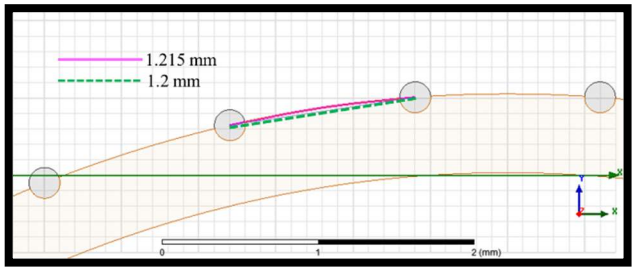

Figure 6.7-3. Example: difference in distance between the two consecutive electrodes for the 90° bend angle of the knee

Table 6.7-1. Threshold Voltage

Curvature	Simulation (Threshold Voltage)
Flat	1350
15°	1350
30°	1390
45°	1430
90°	1470

The increase in the threshold voltages as the angle of curvature increases implies that, higher operating voltages are required to repel the dust particle on higher curvature angles to match the cleaning performance of the SPIcDER system to that of the flat surface. This prediction was validated during the experiments conducted on the scaled prototype. Chapter 9 captures results from experiments for the same angles and provides an in-depth analysis on the observed differences.

- ***Electric Field Magnitude Midway Between Two Consecutive Electrodes***

Analysis was performed to evaluate the electric field magnitudes at the midpoint of two consecutive electrodes. Figure 6.7-4 shows the electric field magnitudes between electrodes e1-e2, e2-e3, e4-e5. As the angle of the curvature increases from 15° to 90°, it is observed that the electric field magnitudes between the electrodes, especially the ones on the sides (e12, e23) decreases. For the 90° case the percentage reduction in the electric field magnitude at the midpoint between e1 and e2 is 14% when compared to the flat surface. This is anticipated because, as the curvature increases, the spacing between the electrodes increases, as discussed in the Threshold

Voltage section (also refer to Figure 9.3-4 in Chapter 9 that shows the stretch values). This increase in spacing decreases the electric field magnitude which is dictated by Equation 11 where the electric field is inversely proportional to the distance between the electrodes.

The implication of this decrease in the field magnitude means, when a dust particle is in this region of the knee, higher operating voltages are needed to obtain the same performance as that of the flat geometry. This was clearly observed during the experiments of the scaled prototype in Chapter 9. This increase for operating voltages is also accompanied by increase in threshold voltages as the angle increases as explained previously. Which means, EVA walks do not increase the risk of breakdown (assuming that the fabric surface is not otherwise damaged during the EVA). Additionally, close attention to the percentage decrease in the electric field magnitudes between the curved surface and the flat surface show that the impact of curvature on the electric field is within 6% for all knee angles analyzed except for the 90° case and the decrease is on the electrodes on the very end of the curvature. Therefore, it is evident through simulations that SPIcDER can function effectively during EVAs.

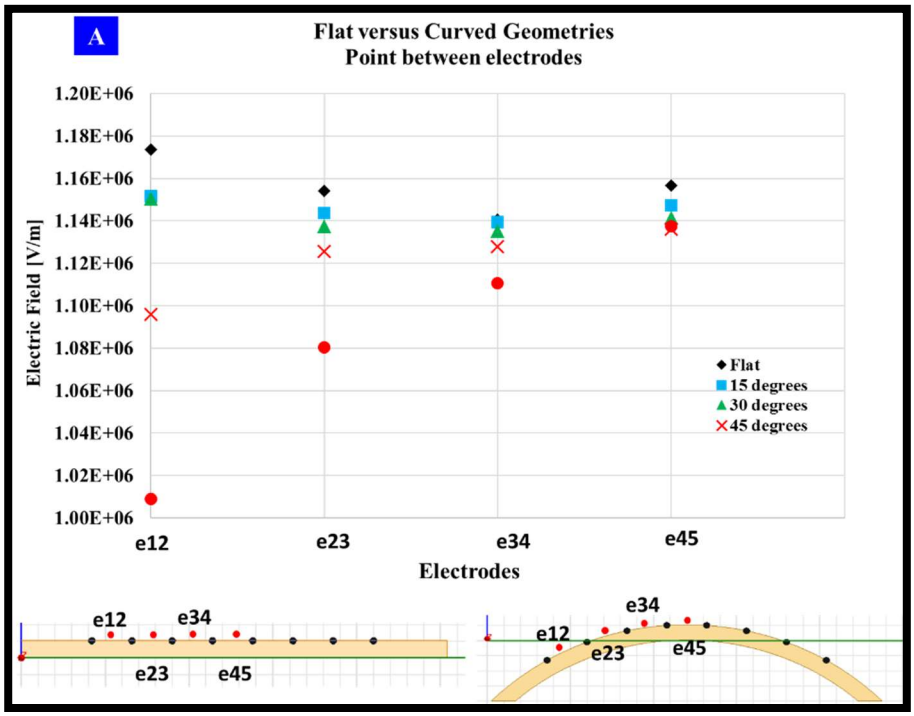

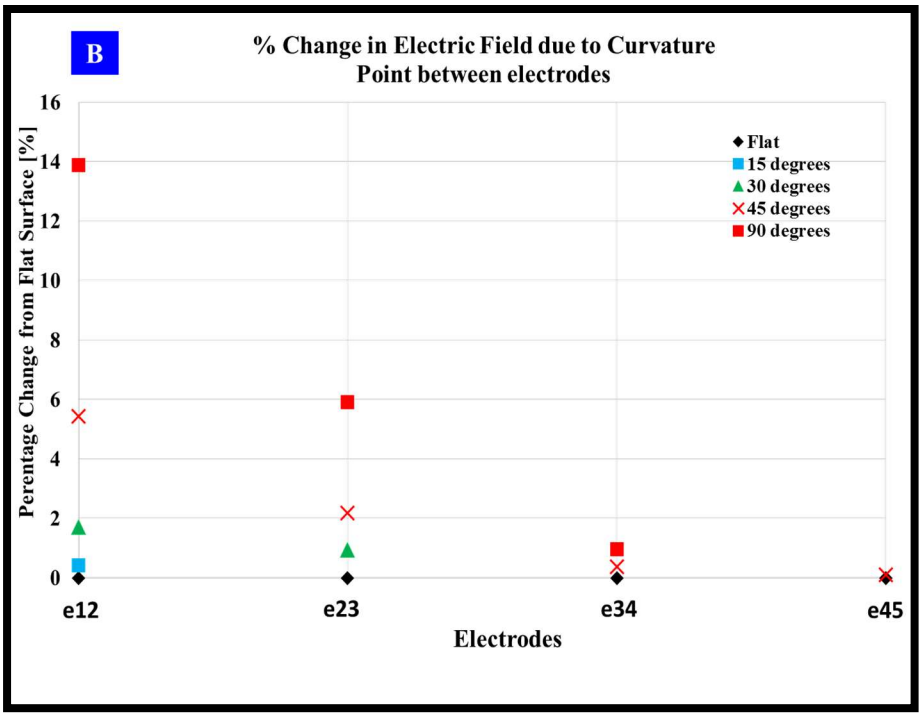

Figure 6.7-4 [A]. Electric field magnitudes at 0.1 mm above the substrate midway between two consecutive electrodes, [B] Percentage decrease in electric field magnitude on curved substrate compared to flat substrate

The difference noticed in the electric field magnitude between the electrodes (decrease in field magnitude at higher angles at the same point over the substrate, for electrodes on the sizes) can be further explained using the electric field vectors. Figure 6.7-5 illustrates the electric field vectors for the flat and curved surfaces, at the input phase angle of 0º. As seen in the figure, the variation in the electric field vector distribution is noticeable between the two geometries for electrodes with same spacing configuration. The areas with red dots represents where the electric field vectors on the curved surface are spread out when compared to the flat geometry due to the curvature and slight increase in the spacing between the electrodes on the curved surface. If the electric field vectors in the local region with the two red dots and arrows on the curved geometry (right side in Figure 6.7-5) is compared to that of the same localized region with the two red dots on the flat geometry (left side in Figure 6.7-5), it is visible that the relative separation of electric vectors on the curved surface is increased compared on the flat surface. These variations result in the differences in the field magnitudes observed in the previous section.

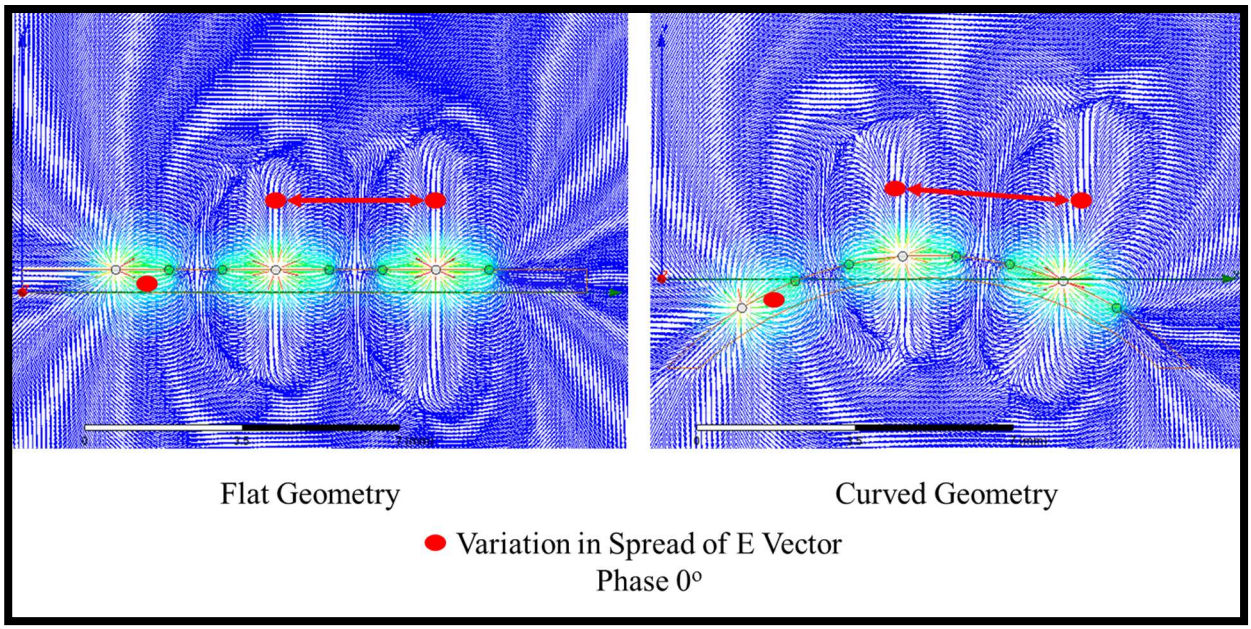

Figure 6.7-5. Comparing electric field vectors between flat and curved geometries. Shown here is an instance of one cycle of the input signal corresponding to phase angle of 0°

6.8. Parameters Affecting Dust Cleaning Performance

In this section, key parameters affecting the dust cleaning performance of the SPIcDER system are identified and, where possible, quantified using simulation runs conducted in Table 6.5-1. An assessment of the effects of changing these parameters and limitations on the dust cleaning performance using 2D ANSYS simulations are provided.

6.8.1. Effect of Input Signal Characteristics

The repulsion and translational forces acting on the dust particles are due to the forces generated by the electric field and are proportional to the strength of the electric field generated. The strength of the electric field generated is a function of the input voltage, frequency and waveform in addition to the other physical parameters of the electrode network (such as electrode spacing) that influence the forces on the particle.

6.8.1.1. Input Voltage

The electric potential between two points separated by an infinitesimal distance *ds* is given by Equation 28. This equation along with Equation 29 provide the relation between electric potentials and the electric field, previously described in Equations 11 and 12.

$$V_A - V_B = -\int \vec{E}\,\overrightarrow{d_s} \tag{28}$$

$$E = -\nabla V \tag{29}$$

Since the electric field is a function of the negative gradient of the electric potential, any change in the input voltage to the SPIcDER system has a direct impact on the electric field generated by the electrodes, and consequently has an impact on the repelling forces on the dust particles (per Equation 29). As the amplitude of the input voltage increases, the intensity of the electric field generated by the electrodes increases. This parameter has the largest impact on the electric forces generated on the dust particles resulting in greater repulsion and translation forces on the particles across the substrate. The impact of increasing the peak input voltage on electric field magnitude is shown in Figures 6.8-1a and 6.8-1b using four values of voltage levels for 1 mm electrode spacing in ANSYS simulation.

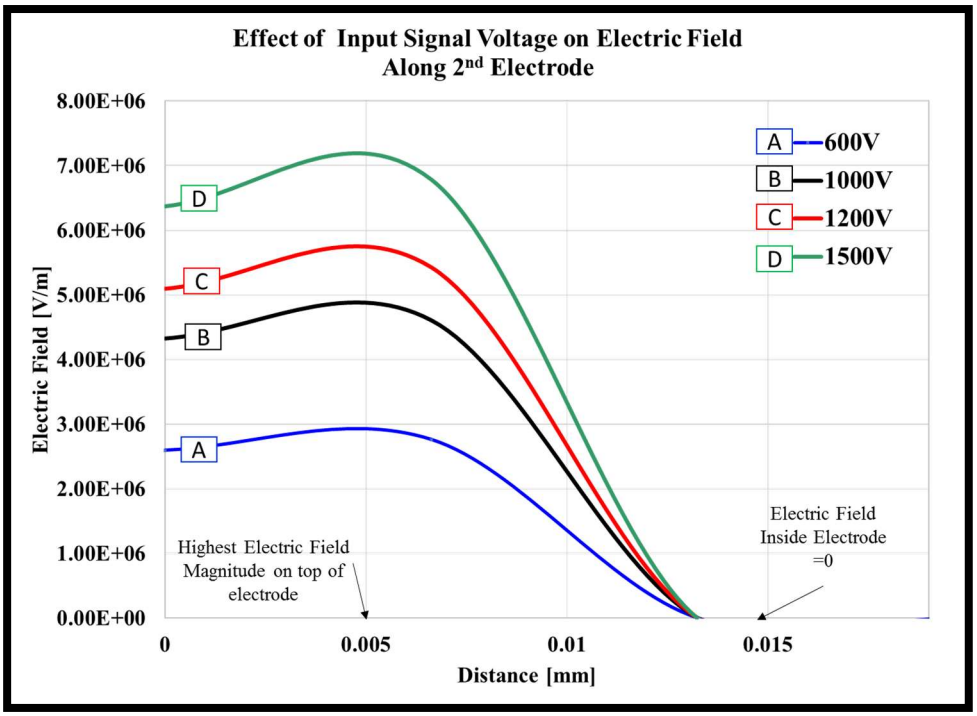

Figure 6.8-1a. Effect of input voltage on electric field magnitude. Shown here is the electric field magnitude on the top of a single electrode of the SPIcDER system

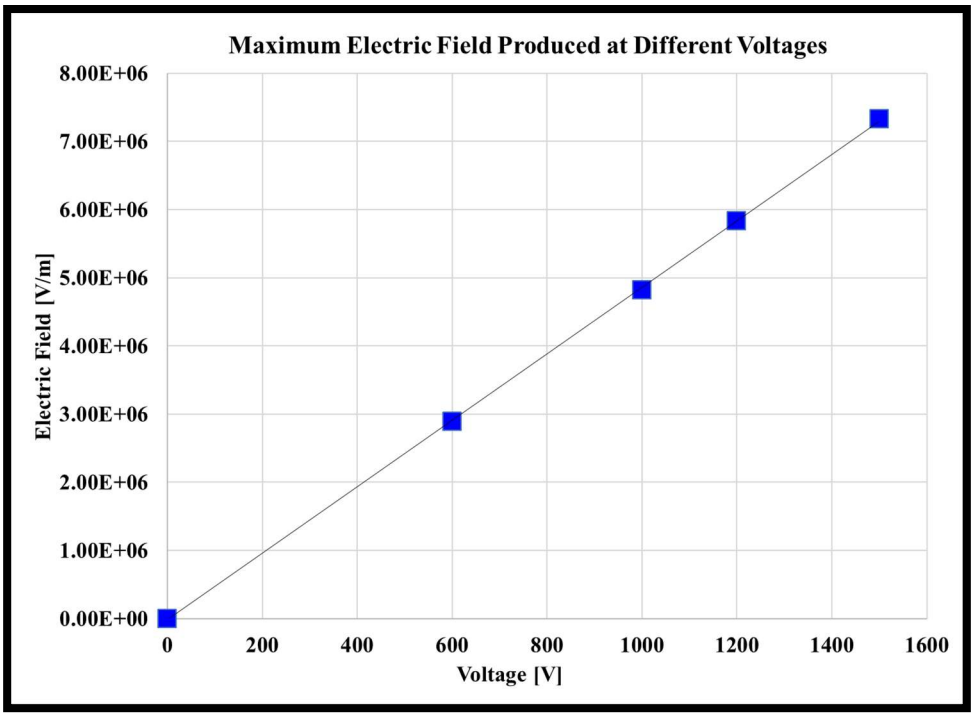

Figure 6.8-1b. Effect of input voltage on maximum electric field generated across the electrodes

It is apparent from the figure that electric field increases linearly as voltage is increased. The increase in electric field strength on the top of the electrode with voltage increase from 600 V to 1200 V is almost double the value at 600 V. Therefore, the input signal voltage has a significant impact on the electric field strength. Experiments in Chapter 5 showed this impact of voltage on the dust cleaning performance. Experimental results showed that for 1-1.2 mm spacing of electrodes, the dust cleaning performance starts to decrease drastically below 700 V.

However, the increase in the voltage and its effect on electric field and consequent performance of the dust removing capability of the SPIcDER system is limited by Paschen breakdown for a given spacing of the electrodes and the surrounding medium. (Paschen curve limitations further described in section 6.8.5). The voltage of the input signal can be increased only until a threshold value, after which breakdown occurs. From experiments conducted in air (ambient conditions) as described in Chapter 5, for 1 mm spacing of electrodes on the spacesuit fabric, dust removal performance increases as expected with increase in voltage from 600 V to 1000 V. However, the maximum voltage that can be applied is limited by breakdown of air which was shown to occur at 1200 V. The operating range of the SPIcDER system for a 1-1.2 mm spacing of electrodes is in between 800V -1100 V, providing sufficient margin for dust cleaning (>700V) and protection from breakdown and arcing (<1200 V).

The simulation conducted in ANSYS Maxwell using a sinusoidal wave shows an increase in the electric field for four input signal voltages in Figure 6.8-2. However, once the voltage of the input signal starts to increase beyond 1200 V, we can observe from Figure 6.8-2 that the electric field in between the electrodes starts to reach the breakdown voltage of air (set to 3 MV/m in 1 atm) leading to electrical breakdown of the surrounding medium. Since higher the voltage, higher is the electric field generated prior to breakdown, one way to increase voltage and delay the occurrence of breakdown is to insulate the electrodes in a high dielectric strength material. The guiding criteria for this trade-off is three-fold, (i) maintain the required dust cleaning performance (<25% of fabric covered in residual dust post cleaning), (ii) to prevent arcing hazards for astronaut safety (explained in detail in Chapter 8) (iii) provide protection for the CNT yarns that could fray and deteriorate due to use (explained in detail in Chapter 9, vacuum experiments).

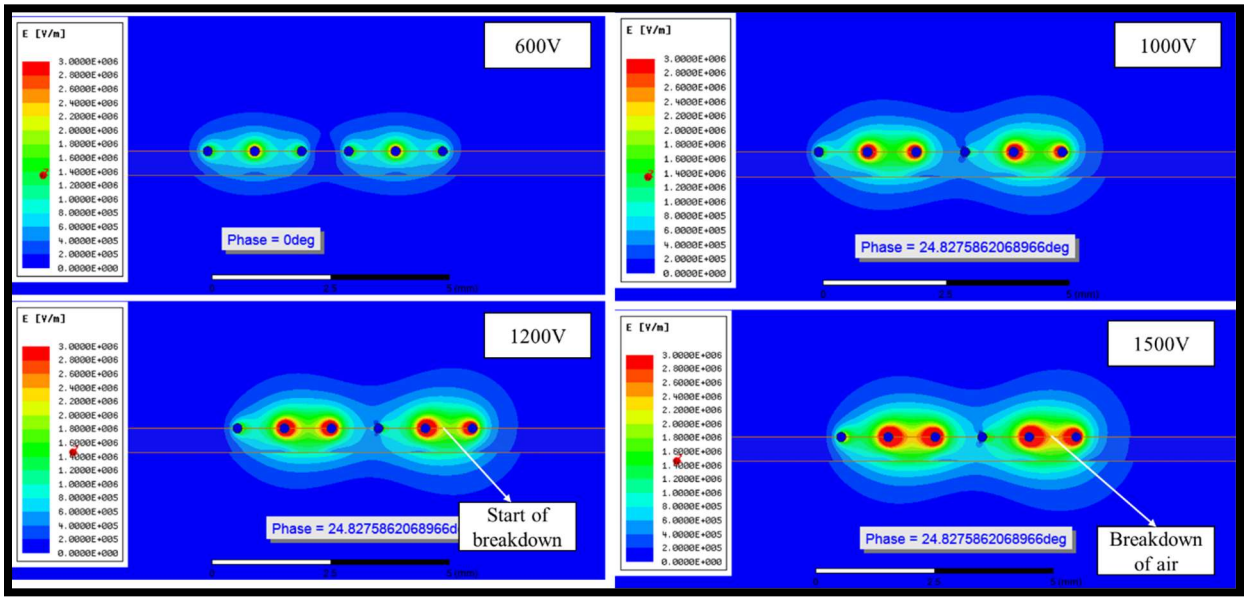

Figure 6.8-2. Simulation showing effect of input voltage on electric field distribution

6.8.1.2. Number of Phases of Input signal

The SPIcDER system can be designed to be operated using a single-phase or a multi-phase input signal. The main difference between using some single-phase versus a multi-phase input signal is the dynamic pattern of the electric field wave and the strength of the electric field generated by the electrodes.

When the electrodes are energized using a single or two-phase AC input signal, a standing wave of electric field is generated which oscillates back and forth between the electrodes with

changing polarity of the input signal. The standing wave of electric field generates a force on dust particles levitating the dust particles from the substrate. While the single and two-phase signals are capable of levitating dust particles within the region, they are limited by absence of lateral forces to transport the particles across the substrate efficiently.

When a multi-phase (>2 phases) AC voltage signal with waveforms that are out of phase from each other is utilized to energize the electrodes, it creates a travelling wave of electric field that propagates across the substrate. This effect levitates the dust particles from the substrate and laterally transports the particles away from the electrodes due to strong translational energy.

Simulation in ANSYS Maxwell was performed to show the effect of single, two, three and four phase input signal waveforms on the magnitude of electric field generated at the top surface of the electrodes. The four simulation scenarios are conducted using sinusoidal waveforms with characteristics described in Table 6.8-1. Figure 6.8-3 illustrates the input signal waveform for one cycle of the input wave for each simulation.

Table 6.8-1. Input signal phases evaluated using ANSYS Maxwell

No. of Phases	Peak Voltage V_p [V]	Phase shift [degrees]	Frequency [Hz]	Input waveform at alternating electrodes
Single	1000	0^o	5	• $V_A=V_p\sin(\omega t)$ • $V_B=0$
Two	1000	180^o	5	• $V_A=V_p\sin(\omega t)$ • $V_B= V_p\sin(\omega t+180^O)$
Three	1000	120^o	5	• $V_A=V_p\sin(\omega t)$ • $V_B= V_p\sin(\omega t+120^O)$ • $VC=V_p\sin(\omega t+240^O)$
Four	1000	90^o	5	• $V_A=V_p\cos(\omega t)$ • $V_B= V_p\cos(\omega t+90^O)$ • $V_C=V_p\cos(\omega t+180^O)$ • $V_D=V_p\cos(\omega t+270^O)$

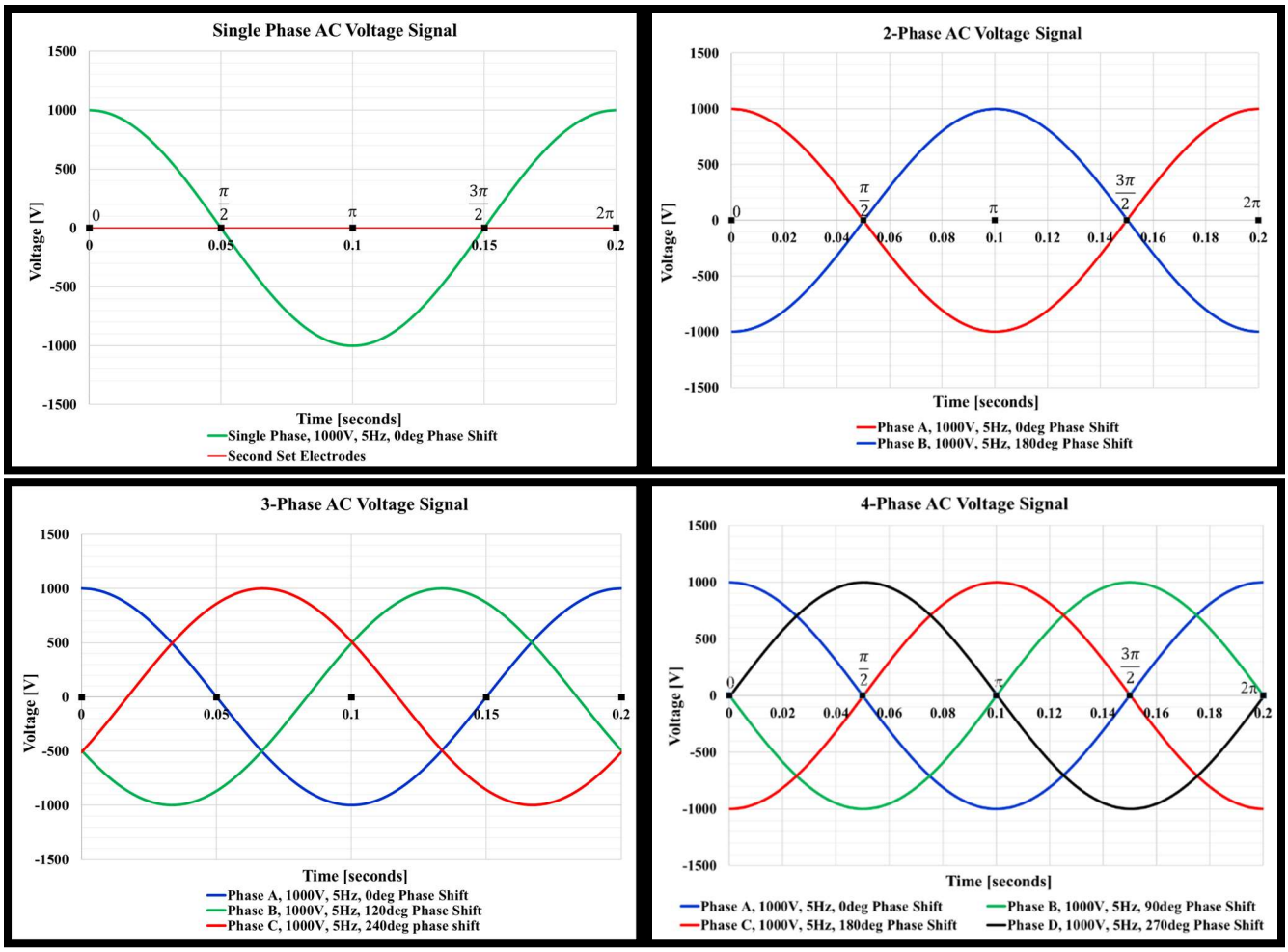

Figure 6.8-3. Single and multi-Phase AC Voltage Input Signal

- ***Effect on Electric Field***

For a specified electrode spacing, peak voltage and frequency, simulations demonstrate that single-phase signal generates the lowest electric field intensity when compared to multi-phase signals as shown Figure 6.8-4. Results illustrate that the two-phase signal provides the highest electric field intensity measured at the top surface of the electrodes when compared to three and four phases. However, the electric field intensity generated by three and four phase signals at their lowest points on the sinusoidal signal maintain a minimum electric field intensity that is an order of magnitude higher than that generated by the single and two-phase signals (See Figures 6.8-5a and Table 6.8-2). This indicates that with the increase in number of phases of the input signal, the dust particles have lower probability of settling on the substrate and in between the electrodes. The minimum electric field required to levitate the particles from the spacesuit substrate should compensate for the adhesion force that attracts the dust particles to the substrate (See Figure 6.8-6).

Therefore, it is expected that using a multiphase voltage signal (>2) increases the dust cleaning performance of the SPIcDER system.

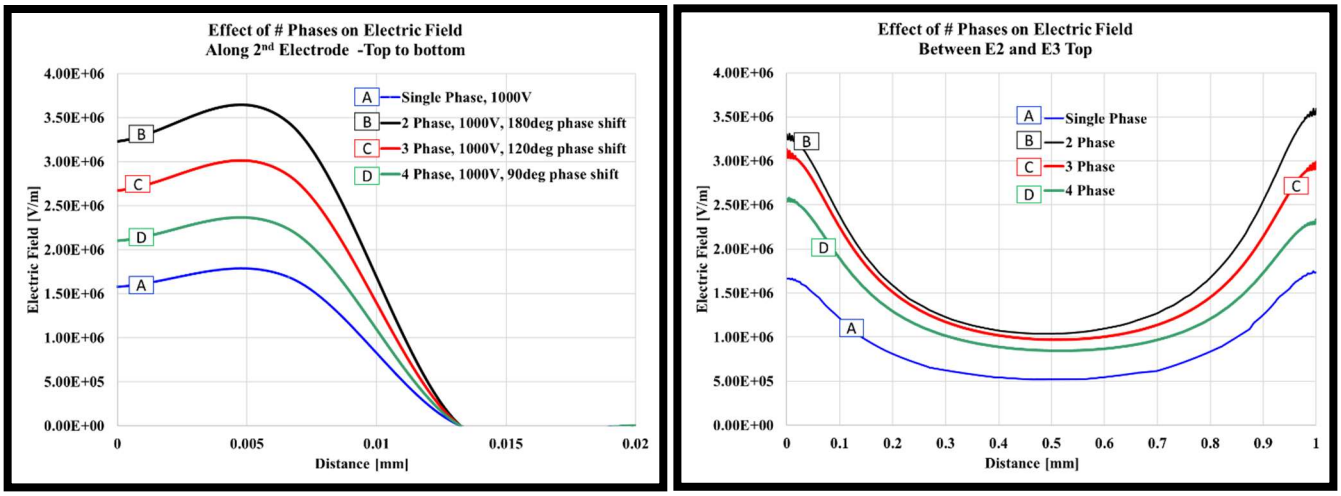

Figure 6.8-4 [Left] Effect of number of phases of input signal wave utilized for the SPIcDER system as seen on a single electrode, [Right] Effect shown on electric field intensity in between 2 electrodes

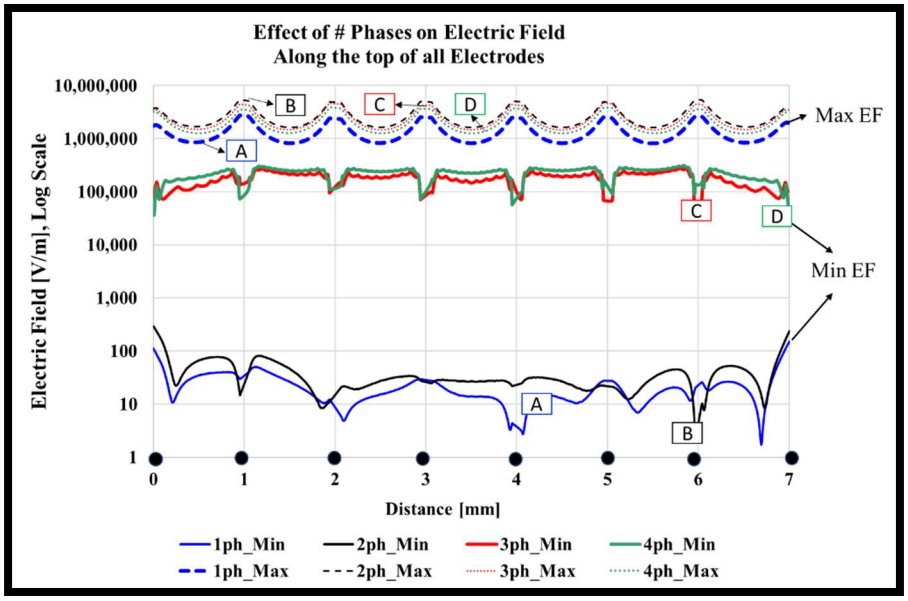

Figure 6.8-5. Electric field maxima and minima generated by the electrodes using a single versus multi-phase input voltage signals

Table 6.8-2 Visualization of electric field showing single and multi-phase input signals

Phases	Electric Field Magnitude 0º	Electric Field Magnitude 99º
Single Phase • Standing wave • Levitates particles • Minimal translational forces • Electric Field Minima is lowest compared to 3 and 4 phases	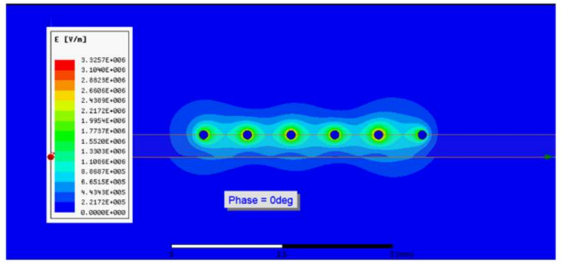	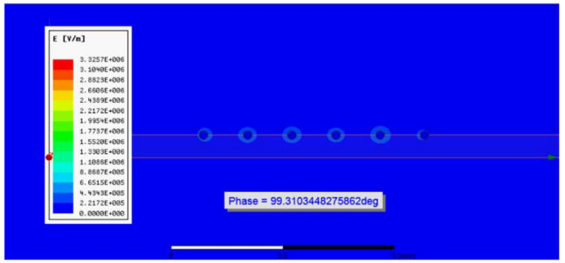
Two Phase • Standing wave • Levitates particles • Minimal translational forces • Electric Field Minima is lowest compared to 3 and 4 phases	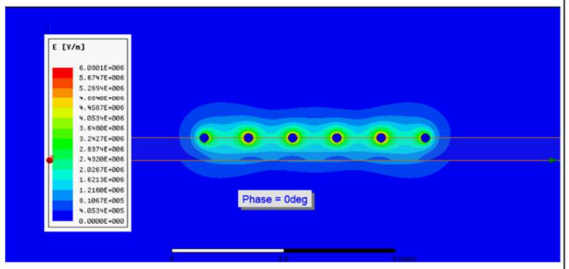	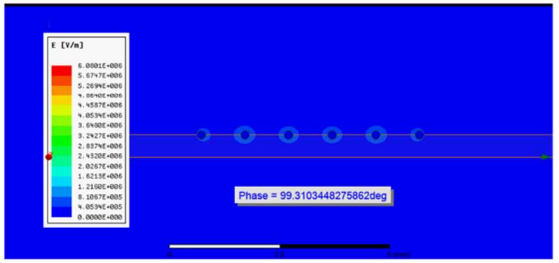
Three Phase • Travelling wave • Levitates and translates particles • Translational forces helps translate particles across the electrodes	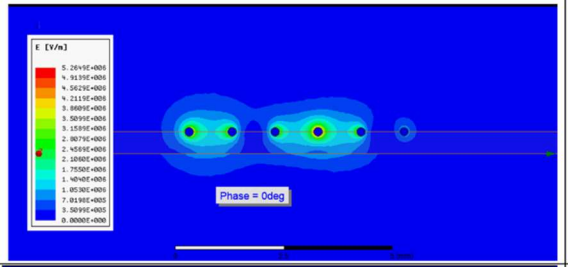	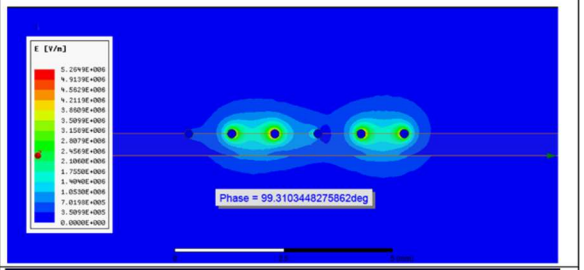
Four Phase • Travelling wave • Levitates particles • Translational forces helps translate particles across the electrodes	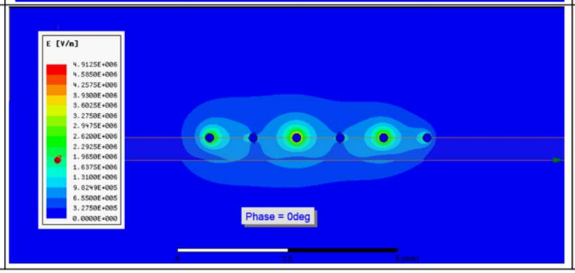	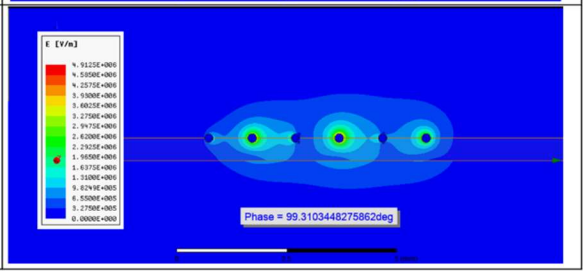

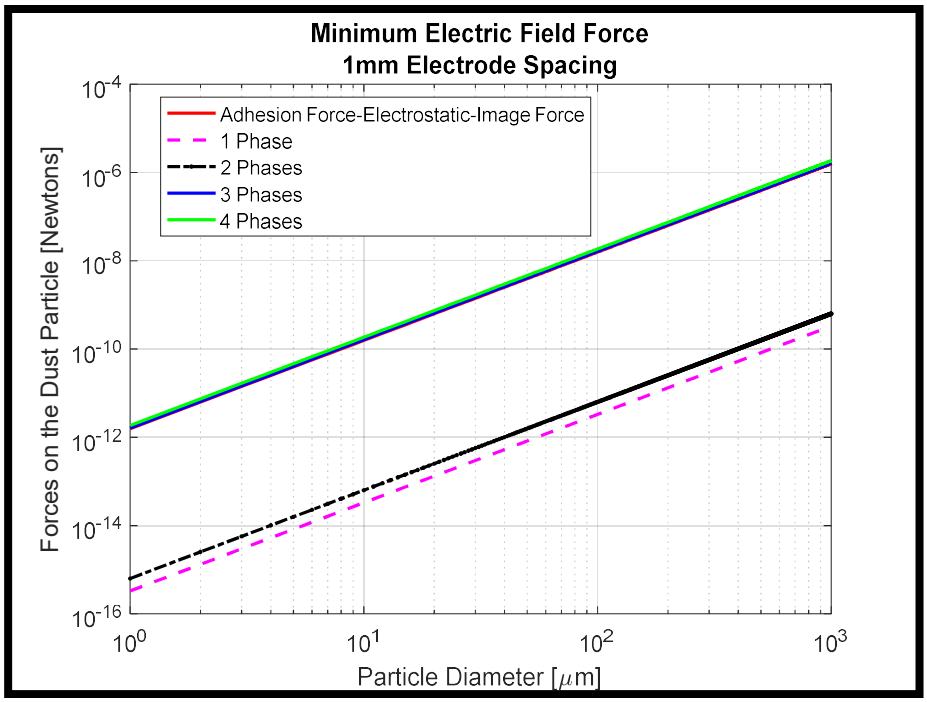

Figure 6.8-6. Illustration of electric force generated by the different phases when compared to the adhesion force. *Field intensity at mid-point between the electrodes plotted*

While higher number of phases (4+ phase) provides better cleaning performance, to minimize fabrication challenges of multi-phase electrodes, the SPIcDER system currently uses a 3-phase configuration.

6.8.1.3. Frequency

Frequency of the input signal determines how rapidly the polarity of the electrodes changes and electric field wave propagates across the substrate. This in turn impacts how rapidly the particles move across the substrate when acted upon by the electric field force. Equation 21 in section 6.2.2 shows the relation between the frequency and movement of particles both in the electrostatic force and the dielectrophoresis forces on the charged and uncharged particles.

Experimental work showed that the performance of the SPIcDER system to repel dust particles was best at low frequencies (<30 Hz). Visual observations during experiments showed that the optimal frequency at which the dust particles over the spacesuit fabric cleared with highest effectiveness was 5 Hz when compared to a range of frequencies between 1 Hz to 200 Hz at the same voltage amplitudes for electrode spacing of 1 mm. Frequencies higher than 30 Hz seemed to

have minimal to no impact on improving the cleaning performance with dust particles in the size range of 10-75 μm.

The impact of the input frequency can be theorized using the motion of the dust particle. At low frequencies, the dust particles are likely to have sufficient time to react (to reach steady state velocity) to the changing electric field and synchronize their movement with the travelling electric field wave. Whereas at higher frequencies (>30Hz) it is predicted that the electric field is rapidly changing prior to the dust particle reaching its steady state velocity and does not have enough time to respond to the lateral component of the electrostatic force from the electric field. This might inhibit the movement of the dust particle to translate from one electrode to the next. This was validated via experimental work that showed low frequencies are more effective at removing dust.

6.8.2. Effect of Electrode Characteristics

6.8.2.1. Effect of Diameter

The effect of electrode diameter on the electric field distribution is analyzed using the 2D Ansys Maxwell simulation. The simulation performed for four electrode diameters at a specific voltage (1000 V) and frequency (5 Hz). Simulations illustrate that electric field is associated with the wire electrode radius r showing that, smaller wire radii result in higher field intensities around the wire for the same voltage input, especially at the wire's surface, where E_{max} is observed.

- Results on electric field strength with varying electrode diameter illustrated in Figure 6.8-7 show that the electric field strength at the top of each electrode with the smallest (50 μm) diameter is 2-3 times higher than the electric field strength on larger diameters (200-400 μm) for the same voltage and spacing characteristics. This is consistent with the characteristic of electric field lines which are strongest at locations along the surface where the object is most curved.
- Though the smallest diameter has the highest electric field on top of the electrode, results also show demonstrate how the field intensity for the smaller diameter has a sharp decrease (drops an order of magnitude) in between two adjacent electrodes. This is because, the relative spacing between the surfaces of the adjacent electrodes is larger for smaller diameters than for larger diameter electrodes. Per Equation 11, electric field is inversely proportional to the distance between the two electrodes. Therefore, for larger diameters, the electric field between adjacent

electrodes is higher when compared to the smallest diameter electrodes and the electric field does not sharply subside in between the electrodes. This consistent electric field around electrodes with larger diameters is conducive to carry the dust particles with consistent repulsion and translation forces minimizing the effects of the dust particles getting 'trapped' in the space between the electrodes.

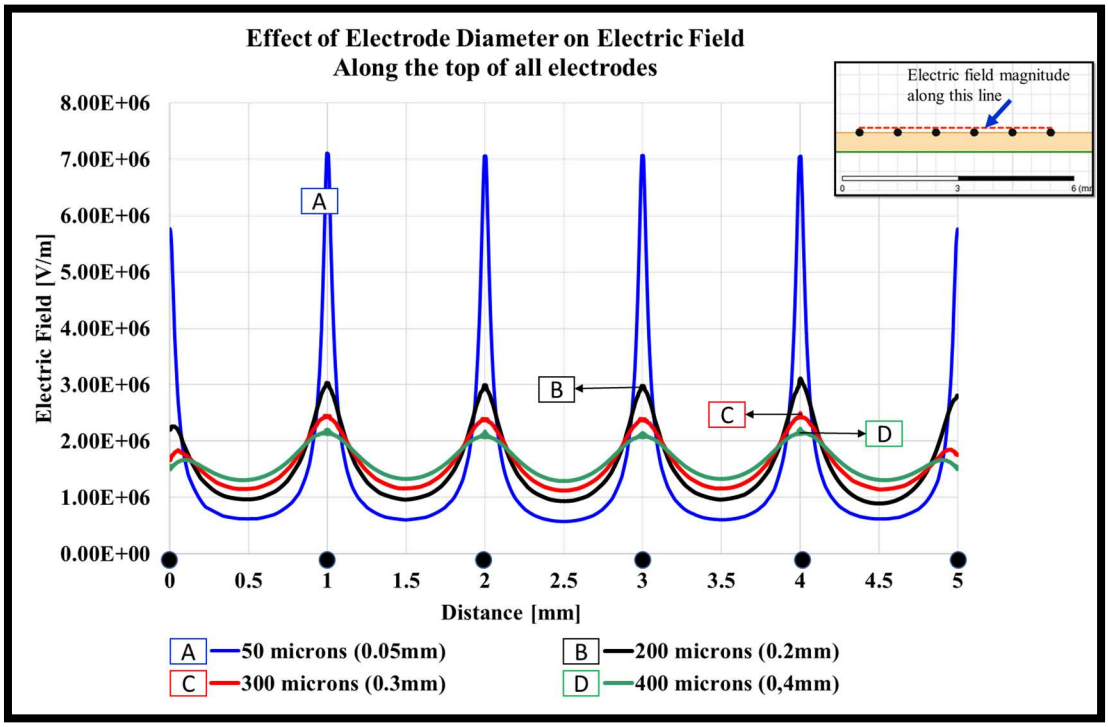

Figure 6.8-6. Effect of electrode diameter on electric field magnitude. X-axis represents the line joining the top of all electrodes and the y axis represents the average electric field value taken across one cycle of the input signal respectively. Black circles represent electrodes.

Another major parameter that affects the choice of the electrode diameter is the size of the weaves within the spacesuit fabric. Using orthofabric material as the outerlayer and one specific fabrication technique utilized in the current experiments, we are limited by the size of the electrode diameter that can be used due to the size of weave of the fabric to appropriately align the parallel CNT electrodes. For current experiments and research analysis, results show that the 200 μm sized electrodes provide consistent performance and results. Other fabrication techniques described in Chapter 4 would permit implementing larger diameters of electrodes with automated fabrication techniques. The choice of the size may also be affected by the CNT yarn properties as thicker yarns are stronger than single filaments.

6.8.2.2. Effect of Electrode Spacing

The electrode spacing determines the highest voltage that can be applied to the electrodes before breakdown (or arcing) occurs which is governed by the Paschen's law as shown in Figure 6.8-7. The higher the voltage, higher is the electric field generated which in turn generates higher forces to repel the dust particle for a given electrode configuration. However, there is a trade-off on how much voltage can be applied given the spacing between the electrodes before arcing occurs.

The electric field decreases rapidly as a function of the radius square from the electrode as shown in Equation 14 from section 6.2.1 derived for two parallel conductors. The electric field is therefore inversely proportional to the distance between the electrodes. However, the minimum spacing between the electrodes for a given voltage is limited by the Paschen breakdown (described in Section 6.8-5).

$$E_{Total} = \frac{\sigma}{2\pi k\varepsilon_0}\left[\frac{1}{r} + \frac{1}{(d-r)}\right] \qquad \textit{(Equation 14 from section 6.2.1)}$$

$$E = \frac{V}{d} \tag{30}$$

The effect of electrode spacing is analyzed using 2D ANSYS Maxwell simulation for a given voltage (1000 V) and diameter (200 μm) of the electrodes for 4 different variations in electrode spacing (spacing here is described from electrodes center to center) conditions. Results agree with the analytical solution that the electric field is higher for smallest spacing when compared to larger spacing as shown in Figure 6.8-8. Due to Paschen breakdown however, in the Figures 6.8-8 and 6.8-9 we notice that while the smallest spacing (0.6 mm) yields highest electric field magnitude for a given voltage of 1000 V, Figure 6.8-9 shows that breakdown of air occurs when the spacing of electrodes is 0.6 mm for a voltage of 1000 V. For 0.6 mm spacing the highest voltage that can be applied is limited to 600 V (Refer to section 6.8.5 for Paschen curve explanation and figure). Applying low voltages (600 V versus 1000 V) with smaller spacing is beneficial from a safety standpoint. However, the tradeoff will be to embed the electrodes close enough to increase electric field intensity while decreasing operating voltage levels, yet far apart to minimize contact/overlap between consecutive electrodes when the fabric creases due to movements to protect from arcing.

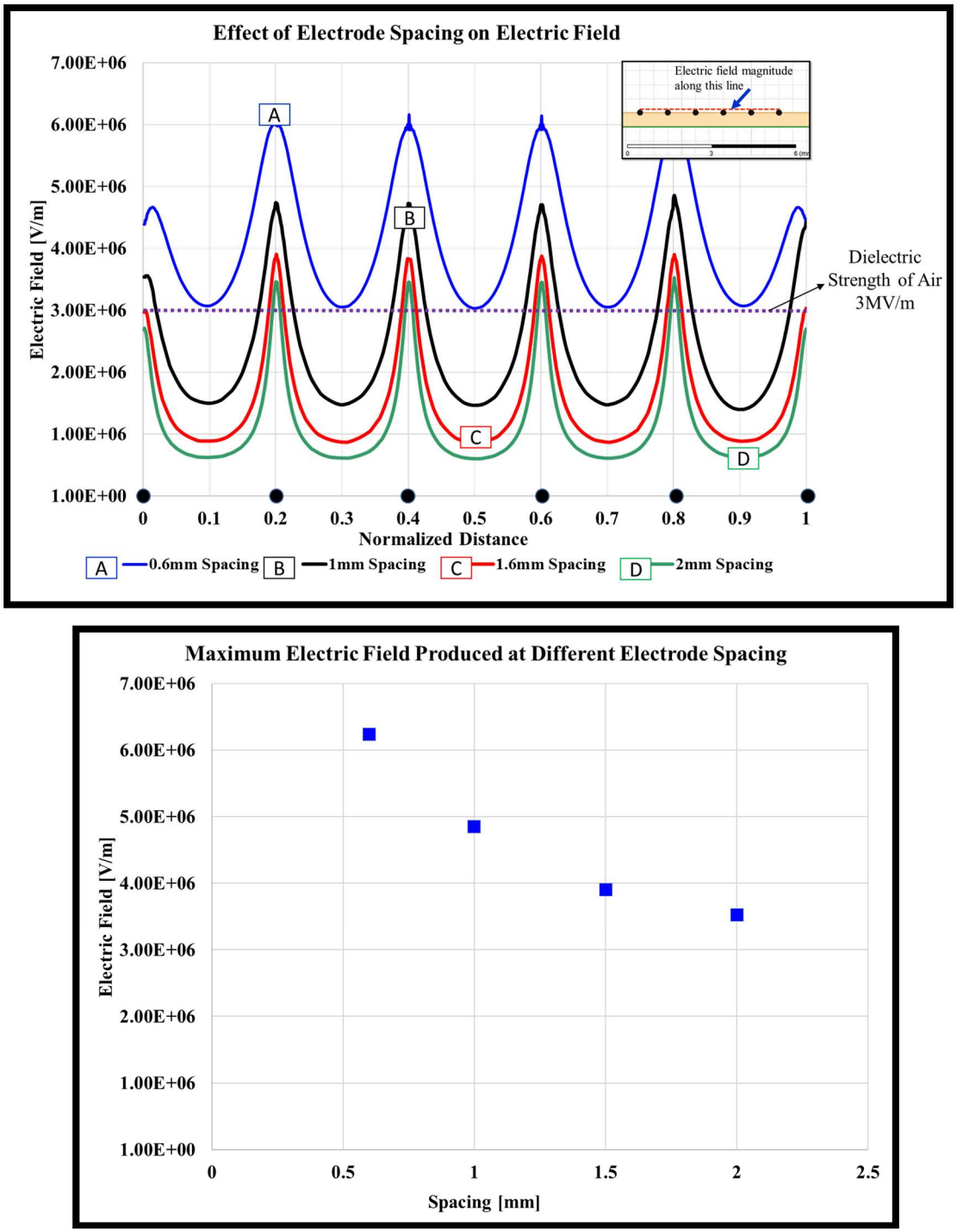

Figure 6.8-8. [Top] Effect of electrode spacing on electric field magnitude generated, [Bottom] Maximum electric field variation with electrode spacing

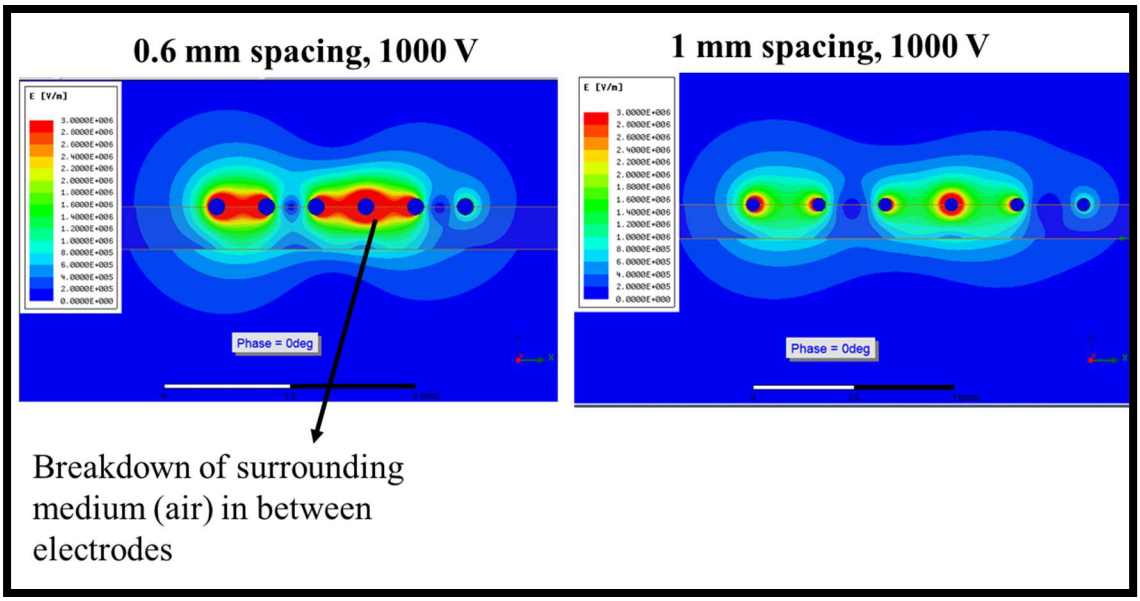

Figure 6.8-9. Impact of electrode spacing on input voltages applied before breakdown occurs. *Shown here is 0.6 mm spacing where breakdown occurs at 1000 V and 1 mm where breakdown does not occur at 1000 V*.

6.8.3. Effect of Substrate Properties

6.8.3.1. Effect of Dielectric Constant

The effect of the dielectric constant of the underlying substrate was studied using the 2D Ansys Maxwell simulation. The underlying substrate for the spacesuit application is modeled as Teflon with a dielectric constant of 2.1. Four additional values for *k* are applied in the simulation to assess the effect of this parameter. Results as shown in Figure 6.8-10 illustrate that the electric field intensity is inversely proportional to the dielectric constant of the substrate. The lower the dielectric constant, higher the electric field. However, the effect is minor (<1%) compared to effect on electric field due other parameters such as input voltage and electrode spacing. The results are consistent with Equation 11. Polarization of the dielectric material reduces the electric field by a factor of *k*. The impact of dielectric constant on the electric field is not highly evident in this case partly because the electrodes are not completely embedded within the substrate. However, materials with low dielectric constant are preferred to maximize the electric field intensity generated for the SPIcDER application. The main requirement is that the substrate needs to be a non-conductive material.

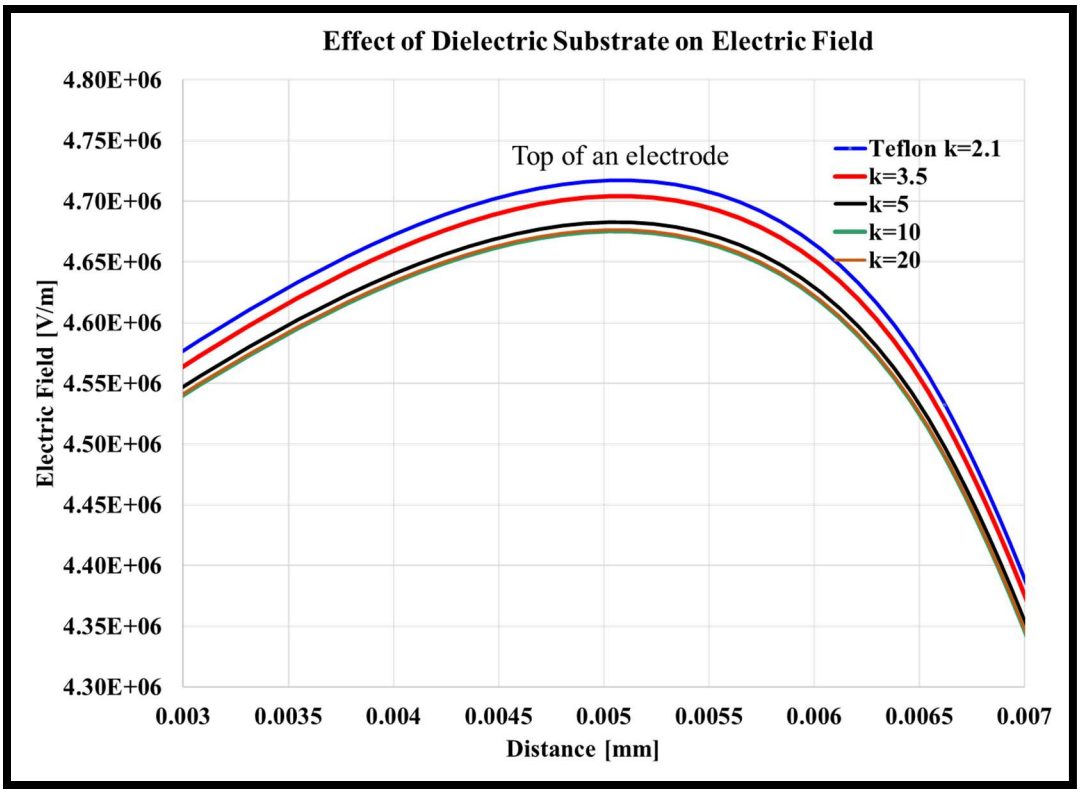

Figure 6.8-10. Impact of dielectric constant of substrate material where the electrodes are embedded

6.8.3.2. Dielectric Strength

The main parameter important for the substrate properties for this application is the dielectric strength of the underlying material. The spacesuit outerlayer is made up of an insulating material with high dielectric strength such as Teflon® (600 V/mil, ~20 MV/m). The high dielectric strength of Teflon prevents breakdown of the substrate material at high voltages where the SPIcDER system operates (600-1000 V). The insulating properties of Teflon help minimize the effects of electric field and high voltages on the inner layers of the suit. This effect of the dielectric strength is described in more detail in Chapter 8. Based on the analysis, a material with a combination of high dielectric strength and low dielectric constant is preferable to help increase the dust cleaning performance of the SPIcDER system.

6.8.4. Dust Particle Properties

The properties of the dust particles play an important role in the cleaning performance of the SPIcDER system. The dust properties impact both the adhesion forces resulting in the dust adhering to the substrate and the repulsive forces generated by the SPIcDER system. The

magnitude and direction of the force acting on the dust particles in an electric field generated by the SPIcDER system are impacted by the physical and electrostatic properties of the dust particles. The two most important properties are particle size and charge as described below

6.8.4.1. Particle Size

The particle size has an impact on the forces of adhesion where the Van der Waals forces scale linearly to the first power of the radius of the particle. The equation for the VdW forces from Chapter 2 indicates that the VdW adhesion forces increase with particle size. However, the VdW forces also depend on the particle shape and roughness which influences the real area in contact with the surface. For jagged shapes, the contact area would potentially be lower than a perfectly spherical particle. Therefore, it is anticipated that the predicted VdW forces from theoretical equations are higher than real scenarios and electrostatic forces of adhesion are dominant on the lunar surface. The electrostatic image force scales inversely to the second power of the particle radius, i.e., when comparing electrostatic adhesion force on a small sized particle with a larger particle of the same charge, the adhesion force on the small particles is much higher (see Figure 6.8-11 for example). As a result, these particles adhere to the substrate which reduces the performance of the cleaning system when operated at the same levels (voltage) as that of the larger particles as it is difficult to mobilize fine particles at the same repulsion forces generated (See Figure 6.8-11 for example). Therefore, for small particles, higher repulsive forces are needed to levitate and repel the particles, which translates to higher voltages and optimizing electrode characteristics.

The cleaning performance of the SPIcDER system improves for larger particles as the repulsive forces scale with the particle size, specially the dielectricphoretic forces that scale to the third power of the particle radius. However, this performance reduces on particles with radius >500 μm (700 μm in lunar gravity) where gravity overtakes the repulsive Coulomb force and constraints the levitation of the particles above the surface (see Figure 6.8-11 for example). For particles larger than 500 μm in diameter, the gravitational force is high at 1G, as the gravitational force is proportional to the cube of the particle diameter and hinders the levitation and transport of these particles. Furthermore, it's been shown through previous experiments on the EDS system that particle diameters cannot be greater than 3.5 times the distance between the electrodes to be cleaned (Kawamoto and Hayashi 2006). In such cases, the Coulomb force between the particle

and the electrodes is canceled since the particle will cover nearly four consecutive electrodes which are at opposite polarities, resulting in cancellation of the Coulomb repulsive force with no transport of the particles. In the experiments conducted in this research utilizing electrode spacings between 1-1.2 mm, this corresponds to particles greater than 3.5 mm.

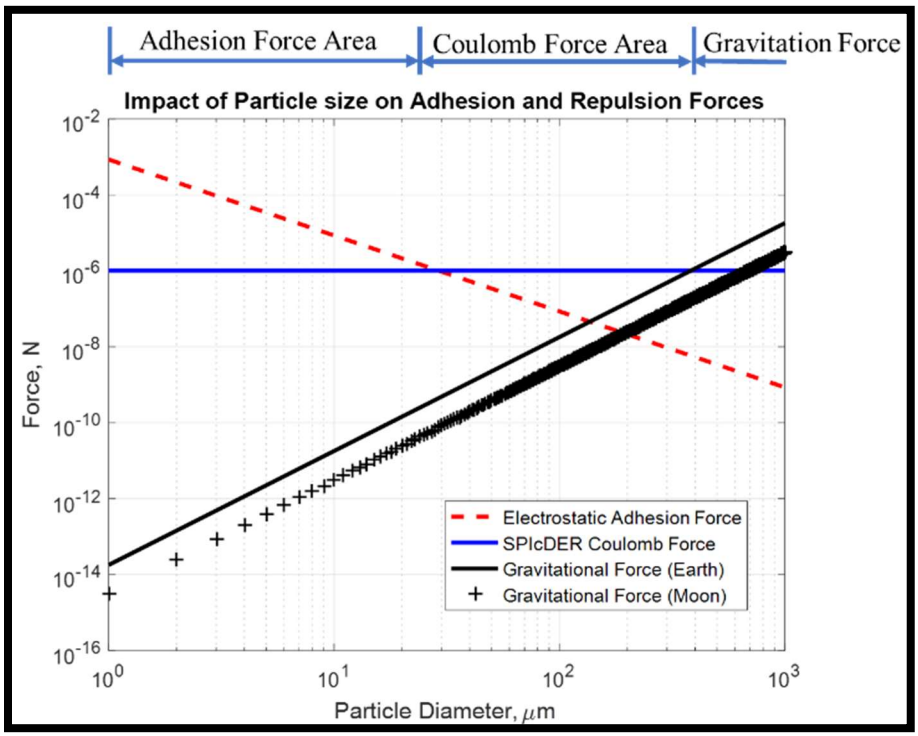

Figure 6.8-11. Impact of dust particle size on electrostatic adhesion force, and repulsion forces generated by SPIcDER system for particles of various sizes with same charge (-2.24e-13 C)

6.8.4.2. Particle Charge

Particle charge has a major impact on the electrostatic adhesion force and the repulsion force provided by the SPIcDER system. The electrostatic image force scales linearly with the second power of the particle charge (Equation 4b in Chapter 2). This is specifically prominent for small particles with high charge (high charge to mass ratios). Therefore, higher repulsion forces are required to levitate these smaller particles. Similarly, the Coulomb repulsive forces generated by the SPIcDER system are higher for particles with higher charge. Examining Equation 21 in section 6.2.2, the Coulomb force qE on the particle is directly proportional to the charge on the dust particle. For two particles of the same size, the particle with higher charge will be repelled much easier (*Force =q*Electric field produced*) than the one with lower charge, i.e. higher charge to mass ratio is desired (See Figure 6.8-12 for example).

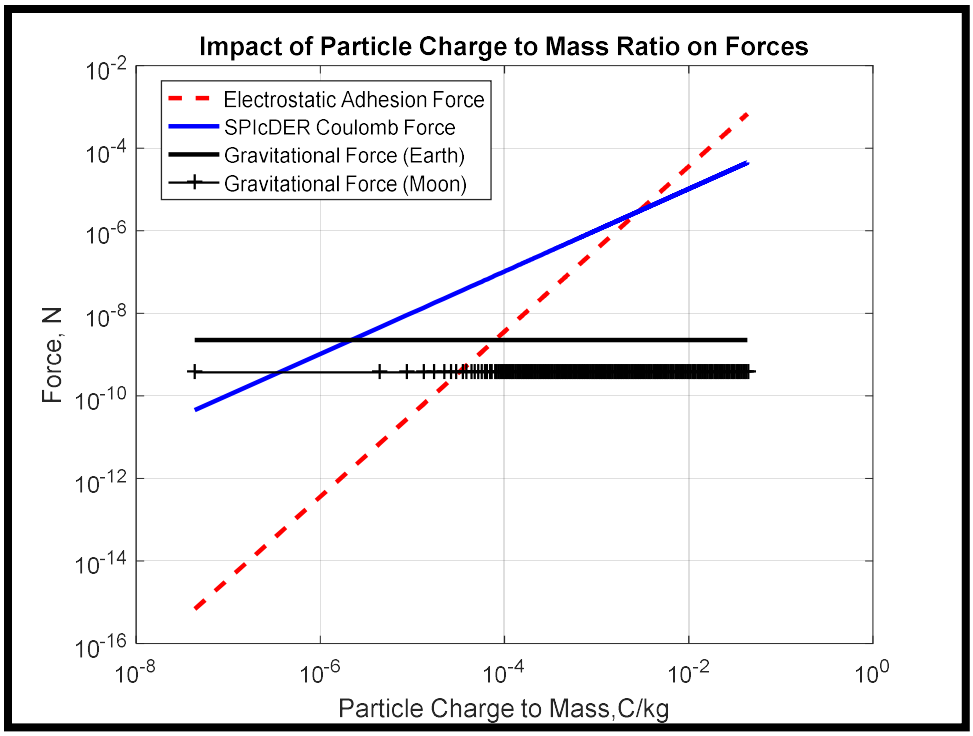

Figure 6.8-12. Impact of dust particle charge- to- mass ratio on the adhesion forces plotted for a 50 µm particle (constant mass) with varying charges (1e-17 to 1e-11 C)

The velocity of the dust particle in the electric field and thus its movement and trajectory are directly influenced by its charge and size (mass). Because finer particles have a greater impact than coarser particles (smaller radius and smaller charge density) on the performance of a SPIcDER system, the cleaning system and its operational scheme must be optimized to enhance its performance in cleaning small particles. This can be achieved by controlling the electrode width, spacing and voltage levels to provide higher electric fields.

6.8.5. Impact of Environmental Conditions

6.8.1.4. Paschen Curve Limitations

Applying an electric field of strength E between two electrodes separated by a distance within a gas medium can cause an electric discharge, i.e. a sudden occurrence of electric current between the electrodes and the surrounding medium when the applied voltage reaches a sufficiently high value. This is known as the point of electrical breakdown. Paschen Law as derived by Friedrich Paschen in 1889, provides the relationship between the breakdown voltage V_B between two electrodes separated by distance d in a medium of gas operating at pressure p and the composition

of the gas. The breakdown voltage is a function of the product of *pd* as derived in Equation 31, where *A,B* and γ are constants and have been experimentally established for many gases.

$$V_B = \frac{Bpd}{\ln\left(\frac{Apd}{\ln\frac{1}{\gamma}}\right)} \tag{31}$$

The processes primarily responsible for the breakdown of a gas are ionization by collision, photo-ionization, and the secondary ionization processes (Naidu and Kamaraju 1996). Currently two types of theories, (i) Townsend theory, and (ii) Streamer theory are known which explain the mechanism for breakdown under different conditions. These physical processes leading to the breakdown of the surrounding medium when electrodes are applied with a voltage can be explained as follows (See Figure 6.8-13):

Ionization by Collison: Based on the pressure of the surrounding medium and external ionizing sources several free electrons exist within the medium. When voltage is applied to the electrodes, these electrons start accelerating towards the anode. In higher pressure where the gas (in this case air) is sufficiently dense, the moving electrons may collide with neutral atoms within the surrounding medium thereby leading to ionization of these neutral atoms. The process of liberating an electron from a gas molecule with the simultaneous production of a positive ion is called ionization. As such, the free electrons collide with neutral gas molecules and gives rise to new electrons and positive ions.

Secondary Ionization Processes: These positive ions formed due to ionization by collision now accelerate towards the cathode and can cause emission of electrons from the cathode by giving up their kinetic energy on impact. If the total energy of the positive ion, that is, the sum of its kinetic energy and the ionization energy, is greater than twice the work function of the metal, then one electron will be ejected and a second electron will neutralize the ion (Naidu and Kamaraju 1996). Therefore, these positive ions colliding with the cathode lead to emission of secondary electrons, the probability of which is determined by the secondary electron emission coefficient γ of the gas (or the ionizing potential of the gas) dependent on the kind of gas and electrode material . These secondary electrons in turn ionize other surrounding neutral atoms.

When this discharge process becomes self-sustaining, where electrons create sufficient ions and these ions in turn release sufficient secondary electrons from the cathode, it leads to a continuous conducting path between the electrodes, thus causing a short circuit and build-up of high current flow leading to breakdown of the surrounding medium which manifests as a spark. To summarize, according to this theory, an electric spark occurs if free electrons accelerated by an electric field gain enough energy between successive collisions with neutral atoms (or molecules) to ionize the atoms. Ionization releases an additional electron which also accelerates, collides with atoms, and causes more ionizations. The various physical conditions of gases, such as pressure, temperature, electrode field configuration, nature of electrode surfaces, and the availability of initial conducting particles are known to govern these ionization processes.

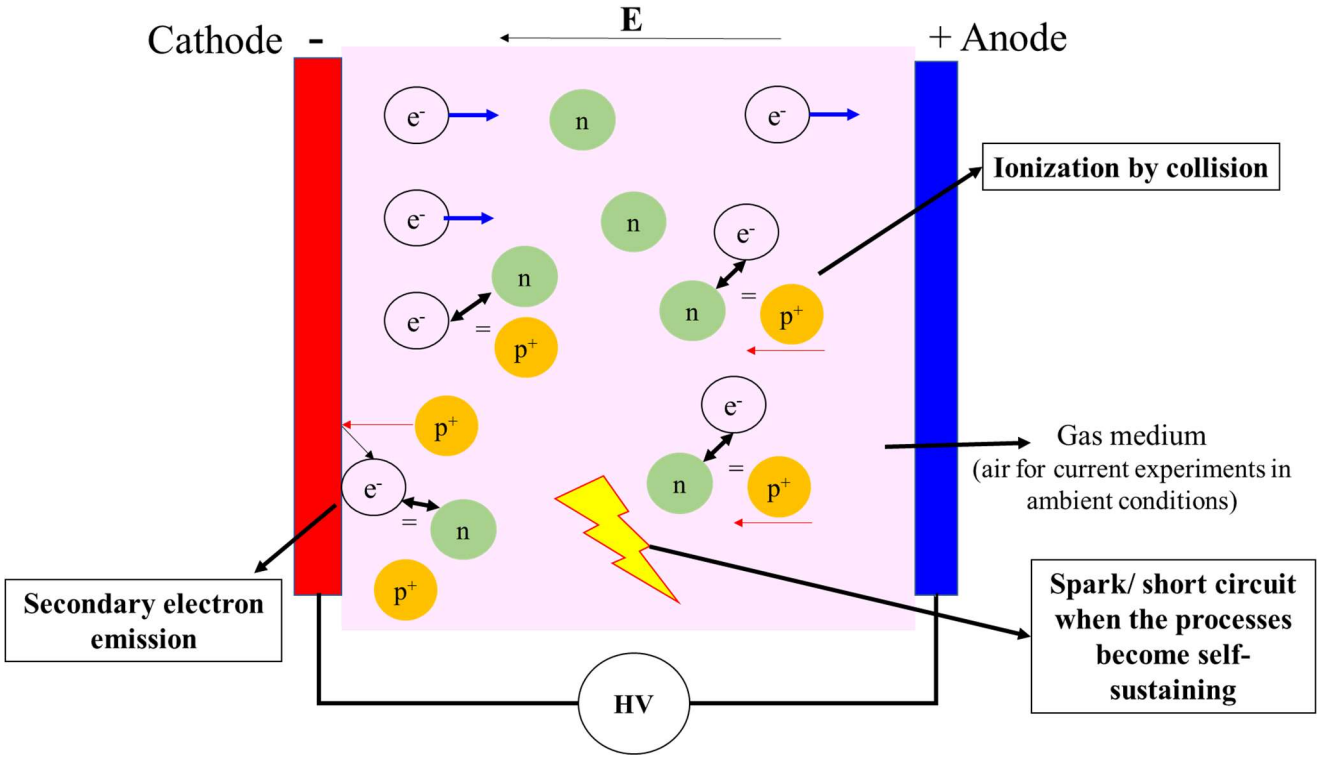

Figure 6.8-13. Visualization of the processes leading to breakdown of the surrounding medium when two electrodes separated by a distance are applied by high voltage

The behavior of the breakdown characteristic of gases is captured by the Paschen curve as represented in Figure 6.8-14. Focusing on the curve for air, the minimum V_B in the curve occurs at the condition where the electronic mean free path is just barely sufficient to allow electrons to gain the ionization energy. Starting from the left most side of the curve upto $(V_B)_{min}$, the curve has a negative slope. At high vacuum conditions (left most side of the curve) even if a large number of

secondary electrons are emitted within this regime, there is a low probability that these electrons will collide with neutral atoms during their movement from one electrode to the next, therefore the V_B at which breakdown occurs is high. Therefore, under high vacuum conditions, where the pressures are below ~10^{-4} torr, the breakdown cannot occur due to these collisional processes like in gases, and hence the breakdown strength and voltage V_B is high for a specified electrode distance. As we follow the curve from left to right and getting closer to the $(V_B)_{min}$ with increase in *pd*, collisions are more likely and thus V_B is lower. The breakdown voltage decreases with an increase in *pd* in this regime, where the electrodes are either very close (high electric field) or the gas is slightly dense (high mean free path). On the contrary, to the right of the $(V_B)_{min.}$ the curve has a positive slope, indicating that the breakdown voltage increases with either the increase in the spacing between the two electrodes, or with increase in the gas pressure. In this regime, the collisions by electrons may be too frequent unlike the lower pressures. An electron on its way to the anode might collide so frequently that it requires higher voltage input to build up enough energy to ionize a neutral atom.

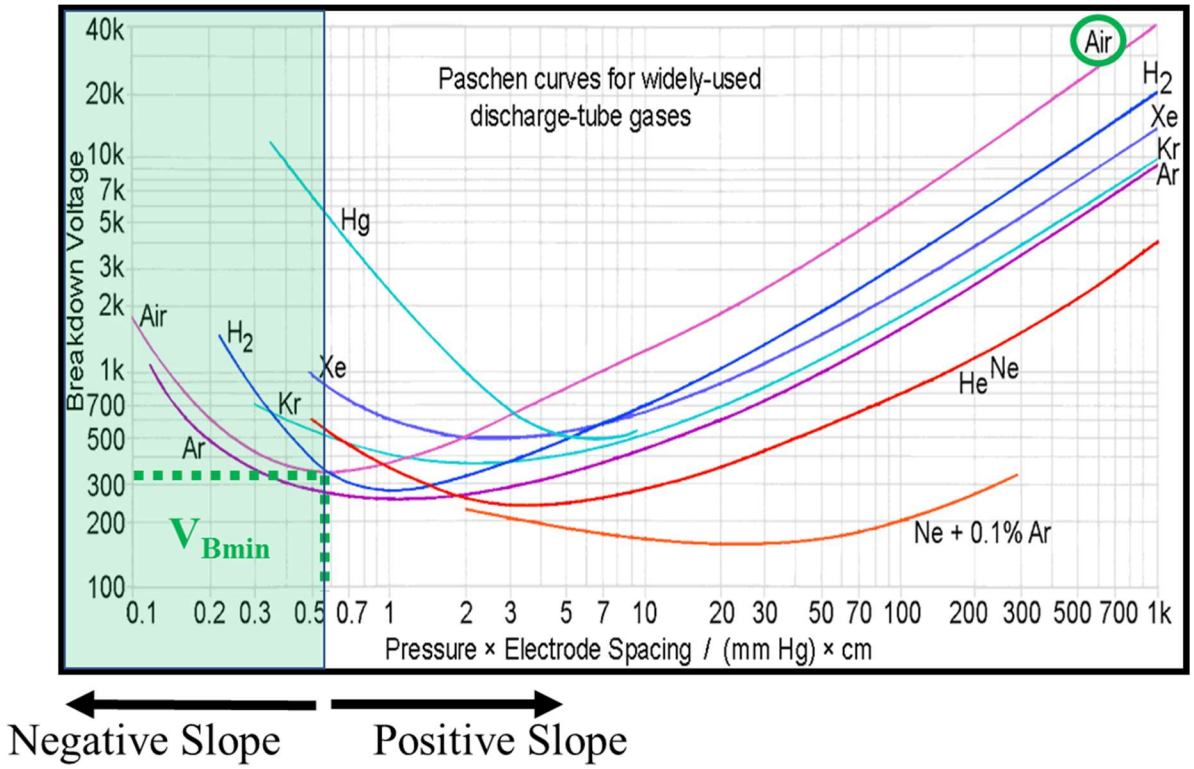

Figure 6.9-14. Paschen curves used to determine breakdown voltages (Wittenberg 1962). *This curve is utilized to determine the maximum voltage we may operate the active electrode system for a given thickness and spacing.*

Experimental investigation of the SPIcDER system embedded in orthofabric material in ambient conditions provided the voltages where breakdown occurs. These values are listed in Table 6.8-3 along with values from simulation where applicable. These values are for uninsulated CNT electrodes. Values for vacuum conditions are listed in Chapter 9 and a comparison between ambient and vacuum is captured in Section 9.4.4.

Table 6.8-3. Breakdown Voltages for various SPIcDER configurations

Electrode	Insulation	Electrode Spacing (mm)	Breakdown Voltage [Experimental]	Breakdown Voltage [Simulation]
CNT	No	0.6	650	650
CNT	No	1	1200	1230
CNT	No	1.2	1200	1350
CNT	No	1.6	1600	1700
CNT	Yes, Teflon 20 µm around each electrode	1		1300
CNT	Yes, Teflon 20 µm around each electrode	1.2		1600
CNT	WFM Coating, 10 µm thick over entire substrate	1.2	1200	1400
CNT	WFM Coating, 10 µm thick over entire substrate	1.6	1600	1750
Copper	Magnet wire, enamel insulation	1.6	1800	

6.8.5.1. Effect of Humidity

The presence of water vapor in the surrounding medium where the SPIcDER system operates impacts the dust cleaning performance of the system. Water conducts electricity; therefore, humidity can reduce static electricity since the water vapor in the air will allow static electricity to leave the objects. In the current case, if a charged dust particle contacts water vapor, the charge on the dust particle is dissipated when it encounters the water vapor. Higher humidity levels conduct static electricity much easier, as there are more moisture droplets in the air. In addition, humidity can create thin layers of moisture on object surfaces, which also helps increase adhesion of particles to the substrate. Therefore, the best dust cleaning performance of the SPIcDER system can be realized in low humidity conditions as the static electricity is more active when the air and materials are dry. The impact of humidity was clearly observed during experiments. The dust cleaning performance of the SPIcDER system on coupons and the knee prototype demonstrated nearly 30-50% reduction when the relative humidity of the surrounding air increased from 39% to 50%. This will however not be a major factor impacting cleaning performance on the surface of

the Moon due to lack of atmosphere and dry conditions. However, in order to apply the SPIcDER system for earth applications, this impact of humidity would need to be considered while optimizing the SPIcDER system parameters.

6.9. Summary

This chapter presented the physical laws and governing equations influencing the SPIcDER system performance. An analytical tool to predict the electric field distribution generated by different configurations of the electrode-substrate arrangement and the influence of key parameters on the dust cleaning performance of the SPIcDER system has been constructed, employing ANSYS Maxwell and MATLAB. The efforts described in this chapter have been utilized to 1) obtain a fundamental understanding of the working processes of the SPIcDER system and 2) to optimize the SPIcDER system for scaled functionality based on key parameters that influence the dust cleaning performance. Based on the analysis conducted in this chapter, Table 6.9-1 captures a list of variables influencing the performance of the SPIcDER system and the specific components of the system they influence. Table 6-9-2 provides a summary of the impacts of key parameters for the SPIcDER system performance.

Table 6.9-1. Table of parameters and components of SPIcDER system they influence

Variable	Units	Input for performance	Output	Description	System Design			Dust particle Influence
					Substrate design	Electrode Design	Power System design	
Voltage	V	*		Input AC voltage		X	X	
Waveform	-	*		AC singal waveform (sinusoidal, square, pulsed etc)		X	X	
f	Hz	*		Freqquency of input AC signal			X	
Phases				Number of Phases		X	X	X
t	seconds	*		Operating time of SPIcDER				
ε_p	-	*		Dielectric constant of dust particle** -used in dielectrophoresis]				X
ε_m	-	*		Dielectric constant of medium	X	X		
Dielectric strength	V/m	*		Dielectric strength of insulation, substrate and medium	X	X		
Rp	microns	*		Dust particle diameter				X
q	Coulombs	*		Dust particle charge		X		X
m	grams	*		Dust particle mass		X		X
Conductivity	MS/m			Conductivtiy and resitance have minimal influence on the SPIcDER performance due since electrodes are capacitive load and not resistive load in SPIcDER system		X		
Tensile Strength	MPa			Not a model input for SPIcDER performance, but influences long term use and electrode materials chosen		X		
Fatigue resistance	# cycles			Electrode fatigure life, not a model parameter, but influences electrode materials needed for spacesuits		X		
Electrode diameter	mm	*			X	X		
Electrode gap	mm	*			X	X		
g	m/s^2	*		gravity		X		
η	m^2/s	*		Kinematic viscosity (does not apply on Lunar surface)		X		
Electric Field	V/m		*	Electric field generated by SPIcDER	X	X	X	X
r	mm		*	Position of dust particle				X
Repelling and Translating Force	N		*	Repulsion force experienced by dust particles				X

Table 6.9-2. Summary of key parameters influencing the dust cleaning performance of the SPIcDER system. *Parameter explained in each row is highlighted using red font in the equations.*

	Parameter	Effect on electric field/ Adhesion or Repulsion Forces	Mathematical Relation	Constraints
Input Signal characteristics	Voltage	Magnitude of EF is directly proportional to voltage. Highest influence	• E=**V**/q	Voltage increase constrained by electrode spacing governed by Paschen law/breakdown of surrounding medium
	Frequency	Effects how fast the polarity of the electrodes changes, electric field propagation and particle velocity	• qEcos(**ω**t) Electrostatic force • $2\pi R_P^3 \left(\frac{\varepsilon_P - \varepsilon_m}{\varepsilon_P + 2\varepsilon_m}\right) \nabla \lvert E^2 \rvert$ DEP force	Low frequency <30Hz conducive for particle movement
	#Phases	Magnitude and direction proportional to number of phases	• qEcos(ωt) Electrostatic force • $2\pi R_P^3 \left(\frac{\varepsilon_P - \varepsilon_m}{\varepsilon_P + 2\varepsilon_m}\right) \nabla \lvert \boldsymbol{E}^2 \rvert$ DEP force	Manufacturability of electrode terminations. Lower number of phases allows relatively easier isolation between phases
Electrode	Diameter	Relatively higher EF at the surface of smaller diameter electrodes, but lower EF in between consecutive electrodes	$\oint_S \vec{E}.\overrightarrow{dA} = \frac{\sigma L}{k\varepsilon_0}$	Constrained by size of the weaves of the substrate material
	Spacing	Magnitude of EF inversely proportional to electrode spacing	$\vec{E}_{Total} = \frac{\sigma}{2\pi k\varepsilon_0}\left[\frac{1}{r} + \frac{1}{(\boldsymbol{d} - r)}\right]\hat{r}$	Smallest spacing for a given voltage constrained by Paschen breakdown
	Conductivity, Resistivity	Very minor influence on performance. Electrodes act as capacitive load, not resistive load. Impacts charge -	RC<<1	

	Parameter	Effect on electric field/ Adhesion or Repulsion Forces	Mathematical Relation	Constraints
		discharge cycle, but on the order of 10^{-10}- 10^{-11} seconds		
Substrate Properties	Dielectric Constant	EF is inversely proportional to the Dielectric constant. Polarizable dielectrics will reduce EF magnitudes	$\vec{E}_{Total} = \frac{\sigma}{2\pi k\varepsilon_0}\left[\frac{1}{r} + \frac{1}{(d-r)}\right]\hat{r}$	
	Dielectric Strength	Property is influenced by EF magnitude		Higher dielectric strength needed to prevent breakdown of underlying substrate and eventual loss of insulation to the wearer
Dust Particle Properties	Charge	Electrostatic force on particle proportional to particle charge. Influences both repulsion forces generated by SPIcDER and electrostatic force of adhesion	• qEcos(ωt) SPIcDER generated force • $\alpha \frac{q^2}{16\pi\ {}_0 R_P^2}$ Force of Electrostatic Adhesion	
	Size	Force of adhesion inversely proportional to particle size - Need for higher repulsive forces DEP force directly proportional to size	• $\alpha \frac{q^2}{16\pi\varepsilon_0 R_P^2}$ Force of Electrostatic Adhesion • $2\pi R_P^3 \left(\frac{\varepsilon_P - \varepsilon_m}{\varepsilon_P + 2\varepsilon_m}\right)\nabla\lvert E^2\rvert$ DEP force	
	Dielectric constant	Influences DEP force due to influence on electric dipole moment	$2\pi R_P^3 \left(\frac{\varepsilon_P - \varepsilon_m}{\varepsilon_P + 2\varepsilon_m}\right)\nabla\lvert E^2\rvert$ DEP force	

	Parameter	Effect on electric field/ Adhesion or Repulsion Forces	Mathematical Relation	Constraints
Environmental Conditions	Pressure	Higher voltages in lower pressures	$V_B = \frac{Bpd}{\ln\left(\frac{Apd}{\ln\frac{1}{\gamma}}\right)}$	Operating voltage constrained by Paschen's law
	Humidity	Higher humidity lowers static charge and influences the Electrostatic force on the particle		

CHAPTER 7: DESIGN AND OPERATIONAL CONSIDERATIONS FOR IMPLEMENTING THE SPIcDER SYSTEM

"The important thing is to never stop questioning"- *Albert Einstein*

The SPIcDER system that involves embedding a series of parallel CNT flexible yarns into the spacesuit outerlayer and energizing them with an AC voltage signal is identified as a technique to protect suits from dust contamination in this research. This chapter provides an overview of the design and operational elements that are important for developing, optimizing and operating the SPIcDER system.

7.1. Design and Operational Elements for the SPIcDER System

Key technical parameters that impact the dust cleaning performance of the SPIcDER system were analyzed in Chapter 6. There are other salient elements that affect the performance, manufacturability and operations to implement the SPIcDER system for a flight suit which can be categorized into the following segments. The next few sections of the chapter provide an overview on these aspects in combination with key parameters explained previously.

A. Key Design Elements
    - Material Properties
        - Underlying fabric/substrate
            - Electrical properties of underlying fabric/substrate
            - Structure and composition of fabric threads
        - Properties of Conductive fibers
    - Electrode Alignment
    - Termination of Electrodes
B. Operational considerations
    - Mass
    - Power
    - Thermal
    - Safety

7.2 Design Elements

7.2.1 Material Properties

The physical and electrical properties of both the fabric substrate, where the CNT conductive electrodes will be embedded, and the properties of the conductive fibers themselves are crucial to the performance of the dust cleaning system.

7.2.1.1. Properties of the Underlying Fabric/ Substrate

- Electrical properties

Dielectric strength: Dielectric strength is a measure of the maximum voltage required to produce dielectric breakdown through a material (insulation) and is a material property that can be varied with thickness. The underlying fabric where the dust repelling active electrodes are embedded should be an insulating dielectric medium with high dielectric strengths to provide sufficient insulation to the underlying layers of the spacesuit. This would prevent breakdown due to the high voltages being supplied to the electrode network. The material and thickness of the substrate can be varied to achieve the required minimum dielectric strength based on SPIcDER operating voltages. A preliminary analysis on the minimum thicknesses required to prevent insulation breakdown utilizing ISS EMU spacesuit fabric layout is presented in Chapter 8.

Dielectric constant: In addition to providing high dielectric strength to prevent breakdown and provide insulation for the user covered with the fabric, the dielectric constant k (also called relative permittivity, also ε_r) of the substrate and that of an insulation coating used over the substrate should be compatible with entire system to generate the required electric field strength. As explained in Chapter 6, the performance of the dust cleaning system is directly proportional to the strength of the electric field generated. However, the electric field is a function of the dielectric constant of the substrate/medium in which the electrodes are embedded. Equation 10 in Chapter 6 showed that the electric field is inversely proportional to the dielectric constant of the material. A material with high dielectric constant will decrease the effective electric field between the electrodes. Such as in a capacitor (two consecutive parallel electrodes of the SPIcDER system can be modeled as a capacitor), if the dielectric contains polar molecules, the electric field from the polarized dielectric will partially cancel the electric field from the charge on the capacitor plates. This decreases the net field inside the capacitor. This decrease in the electric field strength affects the forces on the

dust particle and thus the dust cleaning performance. In situations where the underlying facric of the flexible system is a conductive material, a layer of dielectric coating may be applied to the fabric over which the electrodes can be embedded and/or the individual fabric yarns may be coated with insulating/dielectric material so that the fabrication techniques described in this research may be directly applied.

$$\oint_S \vec{E}.\overrightarrow{dA} = \frac{Q}{k\varepsilon_0}$$ Equation 10 from Chapter 6

7.2.1.2. Structure and Composition of Fabric Threads

The structure of the underlying fabric weave in combination with the material properties is crucial for the implementation of the CNT yarns. The composition of the underlying fabric threads must be an insulative material as described in the previous section in both the warp and weft directions.

If the underlying fabric is made of Teflon®/Teflon coated threads:

- The weave of the fabric must be conducive to embed the conductive fibers in a parallel configuration with pre-described spacing between each conductive thread.
- The CNT flexible fibers can be applied either during the fabric manufacturing process or on a finished fabric using various methods (weaving on finished fabric, sewing etc.) using some of the techniques described in Chapter 4.
- Allow maximum exposure of the conductive yarns to the outer side where the fabric is exposed to dust.
- The yarns may be embedded in the weft or the warp direction.
- Consecutive conductive yarns should be parallel to each other.

For non-Teflon materials and other flexible structures in addition to the above requirements, the conductive yarns can be adhered in required patterns using one of the fabrication methods (bonding, adhesives, etc.) described in Chapter 4.

7.2.1.3. Properties of Conductive threads (CNT yarns or other conductive flexible threads)

The most important characteristics required of the conductive yarns/threads that are embedded into the fabric as part of the SPIcDER system are as follows

- The conductive threads are *highly flexible* in order to conform to the shape of the fabric during bending and twisting motions of the suit during EVAs.
    - Electrodes should not be lifted away from the fabric during different motions of the fabric
- The conductive threads have *high mechanical strength* and *fatigue resistance* to survive repeated motions for applications such as spacesuits involving repeated motions
- The conductive threads are of *low density* to minimize overall mass due to addition of electrodes to the system
- The conductive yarns utilized should be aligned on their outer surfaces with no/minimal fraying.
    - Flexible insulative coating with compatible dielectric constant may be utilized to overcome this. Alvarez et al. (2014) have designed a simple dip-coating process using hydrogenated nitrile butadiene rubber (HNBR), a flexible insulator, to provide unique continuous and uniform insulative coating of the CNTs fibers. Their results confirm that HNBR solution creates a few microns uniform insulation and mechanical protection over a CNT fiber used as the electrically conducting core (see Figure 7.2-1, excerpt from Alvarez et al., 2014). However, further testing to understand the characteristics and performance of HBNR material in the space environments is yet to be conducted if this will be the insulative material choice for the current application. Other space rated materials for insulating the CNT fibers include using Fluoropolymers such as Fluorinated Ethylene-Propylene (FEP), ETFE (polyethylene tetrafluoroethylene) which can be utilized for the current application. Some methods to insulate CNT fibers have be proposed and tested that are available in published literature (Lekawa-Raus et al., 2014; Kozoil et al., 2016; Kukoswki 2012). A manufacturing method to insulate CNT fiber is outside the scope of this research.

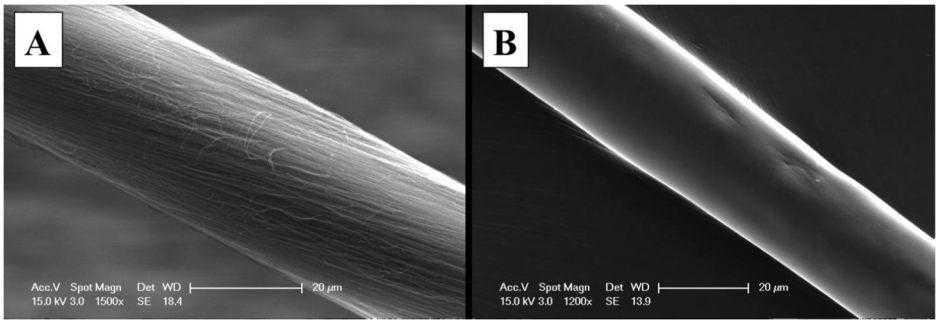

Figure 7.2-1. (A) Uninsulated CNT fiber, (B) HNBR insulation over CNT yarn using dipping process (Alvarez et al., 2014)

- The conductive fibers/yarns must withstand radiation hazards and the vacuum of space.
    - The first use of CNT material for space application was on the Juno spacecraft, where dry CNT sheets developed by Nanocomp Technologies Inc. were incorporated as the outermost ply on several composite structures of the spacecraft (Rawal et al., 2013). The spacecraft has been in operation since 2011 using space qualified CNT material for protection from electrostatic discharge.
    - Other previous studies such the one conducted by Hong et al. in 2006, have reported on the ability of CNT network to withstand high-energy proton irradiation that are comparable to the aerospace radiation environment with no significant compromise in their electrical properties, suggesting the radiation hardness of CNTs. Another study reported the effects of gamma irradiation treatments of pure CNT yarns in air, which showed significant improvement in the yarn strength and modulus (Cai, 2014). The electrical properties of macroscopic CNT structures are generally sensitive to defects of constituent CNTs and to the overall structural flaws, which are related to the quality of the as-made material, fiber making process and the presence of foreign molecules/chemical compounds in the fibers. Investigations that reported on the thermo-electrical properties of both pure CNT fibers and CNT composite fibers have shown that the electrical conductivity increases with increasing temperatures (Lekawa-Raus et al., 2014), however, much evidence for temperatures beyond 300 K are not readily available.

The successful technology insertion of a CNT sheet for Electrostatic Discharge (ESD) protection on the Juno spacecraft is paving the path forward for future space applications of the CNT material. However, further investigation is needed to characterize the capability of the CNT fibers to survive

in space environments, and the pre- and post-processing treatments of CNTs are to be considered prior to flight suit implementation. It is anticipated that insulating the CNT fiber in one of the space rated materials such as ETFE/ PTFE would help prevent extreme radiation exposure of the CNT yarns. This is outside the scope of this dissertation.

7.2.2. Alignment of Electrodes

The performance of the dust cleaning system is affected by the *placement, orientation* and *spacing* accuracy of the conductive threads. The electric field generated is dependent on the spacing of the electrodes. The characteristics of the electrode alignment that are crucial for dust cleaning are as follows

- The conductive fibers need to be *placed on the outer surface* of the fabric/flexible material where the material is exposed to dust for maximum dust cleaning performance.
- The conductive fibers should maintain a *nearly parallel orientation* throughout the length of the conductive fibers with *specific pre-defined spacing* to provide avoid breakdown at operating voltages and provide consistent electric field throughout the fabric to repel dust particles.
- It is important to define the width of the electrodes and the spacing (distance) between the adjacent electrodes as they affect the movement of the particles and therefore the dust removal efficiency. Precisely controllable alignment of conductive fibers and pre-determined minimum spacing between conductive fibers are dictated by a combination of the input voltage, frequency, Paschen curve and insulative properties of the substrate material. Alignment of the electrodes can be controlled in two ways:
    - The first method is to embed the CNT fibers during the fabric manufacturing process where a pre-specified width and spacing of electrodes is provided based on required dust cleaning properties and key parameters (voltage, frequency, waveform, dust particle size, environmental conditions). Insulative fibers of pre-described diameter are used to alternate between the conductive fibers. The advantage of applying the CNT fibers/other flexible conductive fibers during the fabric manufacturing process is that it allows for precisely controlled alignment and spacing of electrodes with the fabric.

- The second method applies to embedding the conductive fibers over a finished fabric. The weaves of the fabric itself (in this case orthofabric) have a certain width which minimizes the movement of the electrode when embedded within that weave (See Figure 7.2-2). To minimize lateral movement of electrodes, the diameter of the conductive fibers can be made to match the diameter of the warp and weft threads, while maintaining the required spacing between consecutive conductive strands. Additionally, tension must be applied to the ends of the CNT fibers to remove slack and maintain the alignment. Since the SPIcDER system is to be used during EVA surface operations, the tension needed should consider expansion of the fabric when the spacesuit is pressurized. The concern of alignment is applicable only to manual methods of weaving the conductive fibers on a finished fabric, such as the method utilized for all the proof of concept testing conducted during this research. This concern is greatly minimized if the conductive fibers can be embedded during the fabric manufacturing process.

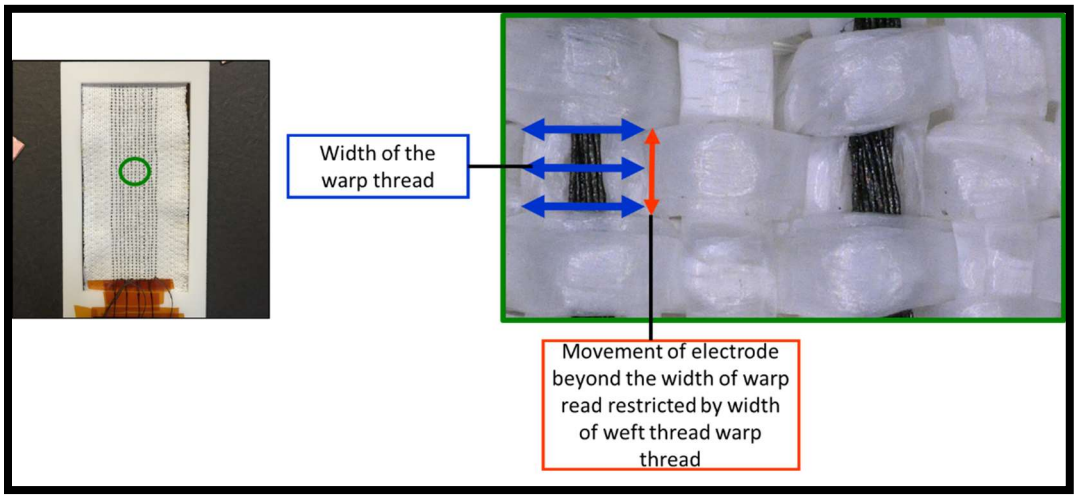

Figure 7.2-2. Illustration of electrode alignment restricted by the fabric warp and weft threads.

7.2.3. Termination of Electrodes and Connection to the AC Signal Generator

The SPIcDER system electrodes are segmented conductive fibers based on the number of phases used to generate the electric field (single or multi-phase). These conductive fibers need to be terminated (utilized serrated scissors for experiments in Chapter 5) and gathered into the respective signal phase they correspond to in order to supply the appropriate electrical signal to generate a travelling or standing wave of electric field (Manyapu and Leora, 2017).

An important aspect of fabrication and embedding conductive fibers (electrodes) is that the *conductive fibers of different phases must be isolated*. For example, a three-phase AC voltage signal will have conductive fibers representing three phases with each phase 120° phase shift (first phase electrodes at 0° phase shift, second at 120° and third at 240°). The fibers connecting to each of these 3 phases must be isolated from one another to avoid short circuiting which inhibits the generation of electric field and produces arcing. Isolation of each conductive fiber may be accomplished by implementing insulative threads in between the conductive threads and insulating the conductive threads themselves. Additionally, automated manufacturing process of the dust cleaning fabric may utilize conductive and insulative adapters for terminating and grouping the respective conductive fibers representing a particular phase (See Figure 7.2-3). Insulating adapters with very high dielectric strengths and required thickness to sustain breakdown should be used. Tools to calculate the thicknesses required are presented in Chapter 8 as part of safety analysis.

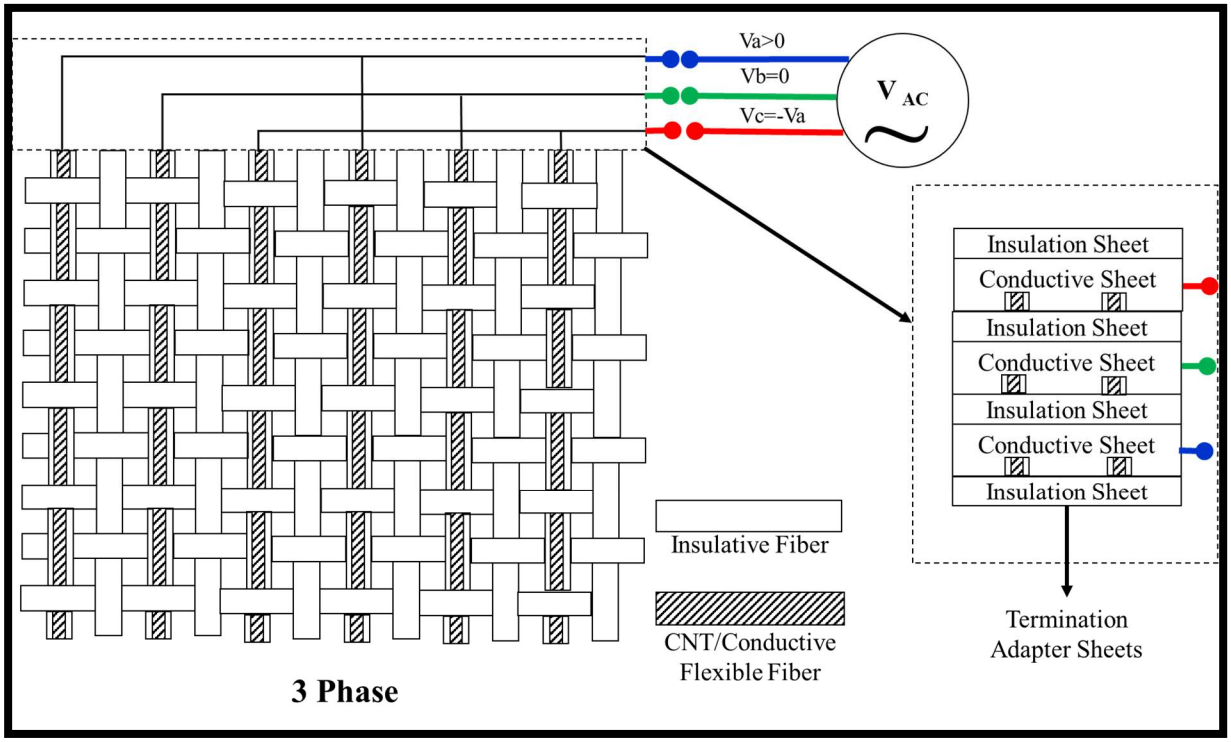

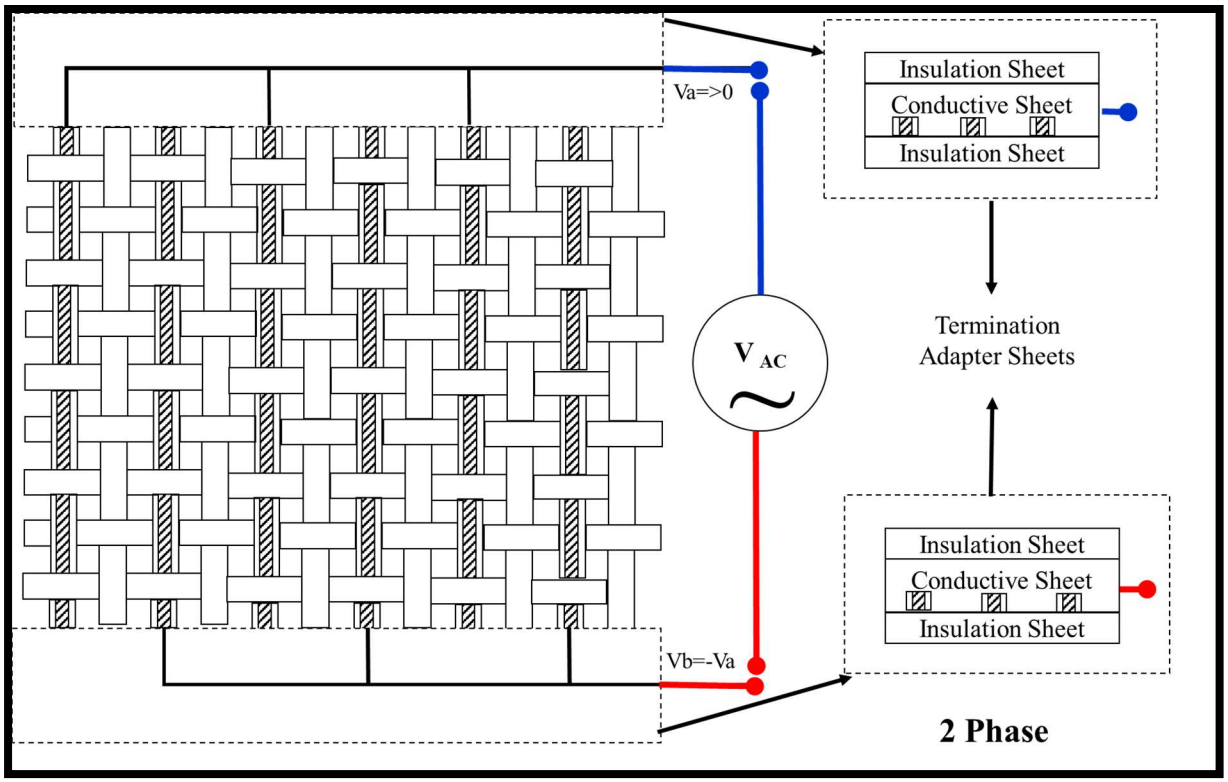

Figure 7.2-3. A method terminating groups of conductive fibers. [Top] Example for three-phase, [Bottom] Example for two-phase

7.3. Elements for Operational Considerations

This section describes the operational aspects that should be considered to implement the SPIcDER system. The proposed system with flexible active electrodes enhanced by WFM passive coating and AC voltage signal generator can be applied to large, stationary and static flexible surfaces with less complexity such as space habitats, flexible solar panels etc. Previous EDS experiments also showed that the system can be applied to rigid surfaces using metallic conductors. However, application of this system for larger areas of spacesuits is complex due to the intricacy of suit design and operational complexity of EVAs.

7.3.1. Mass

Figure 4.3-4 in Chapter 4 illustrated that the mass of the CNT flexible fibers over the area covering both knees, elbows and boots will be negligible when compared to the overall mass of the spacesuits (~91.3 kg of Apollo suit versus 16 g of CNT electrodes). However, the power system and electronics generating the multi-phase AC voltage signal should be designed to be lightweight and compact for launch mass constraints and portable so that astronauts can carry it during EVAs.

The power electronics should be designed to be compatible in a way it can be integrated within the suit system without interfering with other electronic equipment of the suit. Designing a miniaturized high voltage power supply to be portable for the spacesuit system is critical, however this topic is outside the scope of this dissertation. Previous studies conducted by Calle et al. (2011), Kawamoto (2011) and Mazumder et al. (2013), have developed simple, lightweight and compact power supplies. It is estimated that the mass impact of this unit will be less than 2 lbs based on prototypes built by the above published reports. The overall mass of the total SPIcDER system is estimated no more than 5 lbs (< 2.27 kg) when electrodes are applied to cover both knees, elbows and boots on the suit. The increase in the mass to cover additional areas will be less than 2 lbs since the majority of the mass is pertained to the power electronics. The density of CNT electrodes is insignificant (1-1.6 gm/cm^3). Table 7.3-1 provides an estimation of the mass of the SPIcDER system based on available data from literature.

Table 7.3-1. Mass estimation of the SPIcDER system to cover both knees, elbows, boots

Parameter	Mass	Units	Basis of Estimates
Electrodes	8	grams	CNT Flexible fibers on both knees, elbows, boots; 1 gm/cm^3, 600 electrodes
Electrode insulation	11	grams	Flexible Teflon® Tape 1.3 g/cm^3, 2 mil, includes 15% margin
Termination Insulative adapters	9	grams	Kapton (1.42 g/cm^3) (6 inch by 4 inch by 2 mil)
Termination Conductive adapters	54	grams	Copper films (8.96 g/cm^3) (6 in by 4inch by 2 mil)
Termination Cables	19	grams	estimating
Connectors	455	grams	Estimating 1lb for space rated connectors
Power Electronics (DC Voltage Source, HVDC-AC converter, Voltage/frequency regulartor)	1364	grams	Estimating 3 lbs including protection/casing based on previous studies by Mazumder et al 2013 and Kawamoto and Hara 2011
Total	1.9	kg	
	4.9	**lbs**	(~2.23 kg) includes 15% margin

7.3.2. Power

7.3.2.1. Modes of Operation

The SPIcDER system can be operated in two modes 1. Continuous mode 2. Pulse mode.

- *Continuous Mode/Dynamic Dust:* When the SPIcDER system is continuously operated, the area on the fabric embedded with the CNT yarns maintains an active electric field. Any dust that may come in the proximity of this area on the fabric will be continuously repelled away

from the fabric. The dynamic drop test in Chapter 5 represents this case. This mode of operation continuously works to prevent any dust particles to accumulate on the fabric. This case is specially observed when the astronauts are walking /traversing the lunar surface where dust is constantly being kicked and raised up that may *'fall'* on the fabric. Observations from Apollo missions showed that walking on the Moon with large boots resulted in lunar dust being kicked and spread out. The dust that raises tends to stay levitated for longer periods due to the lower gravity and drier environment than the Earth. A study conducted by Katzan and Edwards (1991) estimated the velocity and maximum height of the kicked off particles due to astronauts walking to be 3.6 m/s and 4 m, respectively. Similarly, astronauts were exposed to continuous dust in motion when they traversed the lunar surface on the LRV (See section 2.6.2.3).

- *Pulse mode/Static Dust:* The SPIcDER system can also be operated in a pulse mode where the system is powered on for brief periods (experiments showed less than 2 minutes of power on time is sufficient to clear adhered dust) to clear dust. This mode is particularly useful when the suit is predisposed to dust and there is a need to remove the adhered dust on the fabric.

Experiments conducted in this research have shown that the SPIcDER system performs efficiently to remove dust particles from the suit fabric in both modes of operation.

7.3.2.2. Power Requirements

The SPIcDER system operates at high voltages on the order of 600-1200 V, however because the electrodes represent a capacitive load rather than a resistive load, the current draw by the system to charge the electrodes to create the electric field is very low, minimizing the overall energy requirements to operate the SPIcDER system (~ 100 mW for 60 seconds, Calle et al., 2011). Since the SPIcDER system can be operated in two modes during EVA operations, a tradeoff between the most effective method to operate for specific surface operations will be required prior to EVA operations. The power consumption of the SPIcDER system varies depending on electrode spacing, operating voltage, and frequency. Using power consumption values from literature of 100 mW for 60 seconds, it is estimated that the overall energy required to operate the SPIcDER system on a long duration mission per EVA in pulse mode is within 5% of the energy required to operate the suit during a single EVA (SPIcDER operational energy values from analysis below compared to an estimated 540 Wh capacity of the Lithium Ion battery on the ISS EMU (Campbell, 2012)).

As an approximation of the operational time and energy required for SPIcDER operations, a modest analysis was conducted using a scenario for both pulse mode and continuous mode for a long duration mission. The following list explains the assumptions made for the analysis.

- Future EVAs on the moon are estimated to last 6-8 hours per EVA
- As such, for the pulse mode operation, SPIcDER may be activated for 4 times every hour lasting 60 seconds' operational time when activated each time
- Similarly, for continuous operation, it is estimated that the SPIcDER is operated continuously for the entire 8 hours over an EVA (See Figure 7.3-1)
- Based on NASA STR 2015 publication, is estimated that for a 6-month long term stay on the moon, approximately 4 EVAs are conducted every week (during the initial lunar base settlement).
- Based on these assumptions, the approximate energy required to operate the SPIcDER for an 8-hour long EVA for an overall 6-month mission to moon (~ 100 EVAs) with
    - Pulse mode operation: 4 times every hour, for 60 seconds each time, the energy consumption is estimated to be 3.2 Wh per EVA and 320 Wh for total of 100 EVAs.
    - Continuous mode operation: the energy consumption is estimated to be 48 Wh for an 8-hour EVA and 4.8 kWh for a 6-month mission with 100 EVAs.

Although the power requirements are low for operating SPIcDER, the tradeoff will be in the energy required to operate the SPIcDER in pulse versus continuous mode. It is shown that the energy requirements to operate the SPIcDER continuously over a period of 8 hours is ~15 times more, and operating continuously may pose operational safety risks (see next section and Chapter 8) when compared to pulse mode operations. Therefore, for flight suit implementation and future lunar missions, a trade study will be needed to understand how and when the SPIcDER may be operated based on mission requirements, payloads and EVA objectives. An adjustable duty cycle based on the operation and EVA task may be beneficial. The operation may also be automated with pulse mode operation with specific duty cycle during EVA operations. Additionally, the power system and electronics should include tunable inputs to adjust/optimize voltage, frequency and waveform of the SPIcDER system to optimize dust removal performance. Designing a system that can operate at low voltages (<=than 12 V using DC power generating a high output voltage (>=2kV) would be beneficial. Mazumder et al. (2015) have designed such a system for use to clean solar panels.

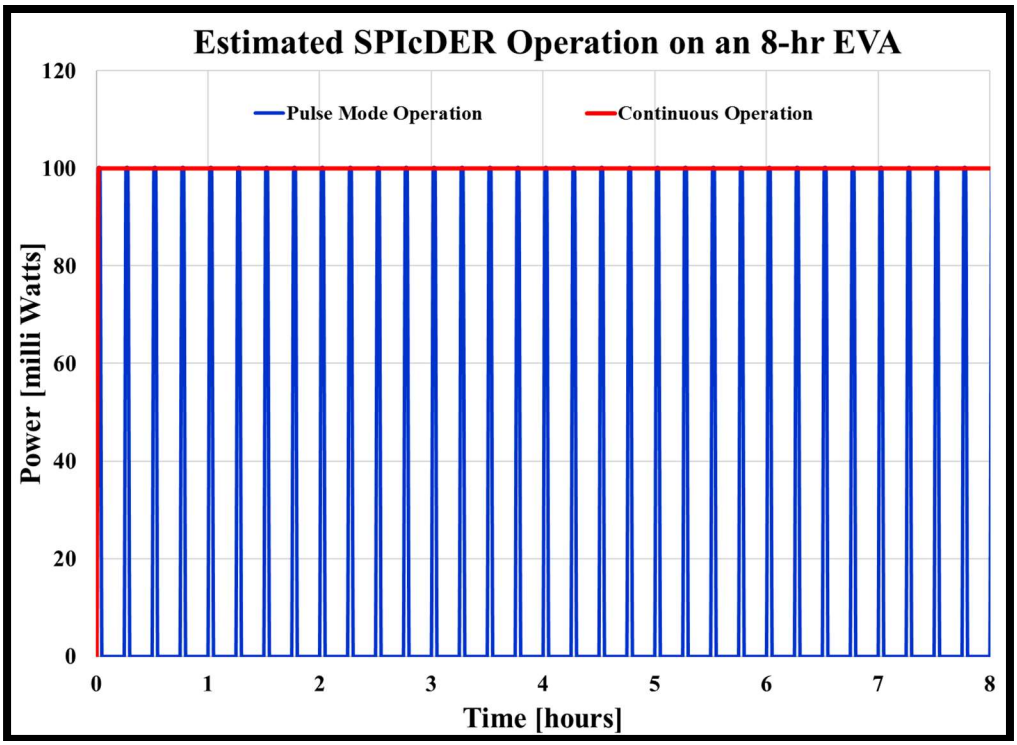

Figure 7.3-1. Example of SPIcDER duty cycle over a single EVA

7.3.2.3. Monitoring Amount of Dust Accumulation

An area for further investigation to optimize energy requirements to operate the SPIcDER system could be to functionalize the CNT yarns with embedded sensors and/or separately embed micro-sensors on critical areas on the outerlayer to detect quantity of dust contamination. The sensors can be programmed to detect a specific amount of dust coverage over a specific area (thermal or optical sensors for example) and signal the power electronics to turn on and off the system. The operational time and t energy used by the SPIcDER system can then be optimized.

7.3.3. Thermal

Spacesuit thermal control is a dynamic process with a need to regulate thermal effects from both the internal generation of heat loads due to metabolic and electronics equipment, and the external environment. Lunar surface temperatures can range from 122°C at the subsolar point (equator) to -233°C in dark polar craters (Taylor, 1982). While the primary means of heat rejection within the spacesuits so far has been its active water sublimation system (for the Apollo and ISS missions), the outerlayer of the suit provides a means to passively regulate the thermal energy of the suit system to maintain suit internal temperatures (Thomas and McMann, 2011). Therefore,

the white outerlayer seen on EVA spacesuits (microgravity and Apollo missions) besides serving as a Micrometeoroid Orbital Debris (MMOD) shield and an outer cover, plays a key role in passively regulating the heat dissipation to maintain the internal temperatures largely by means of radiative heat transfer. The radiative heat transfer capacity of the outerlayer is primarily dependent on the material's thermal properties (solar absorptivity α and emissivity ε), along with the surface temperature of the material and the local thermal environment.

Studies from Apollo missions have shown that spacesuits contaminated by lunar dust impacted thermal loads on the suit system. Therefore, the goal of the SPIcDER system is to reduce dust accumulation to prevent thermal degradation performance of the spacesuit. Furthermore, in the context of using the SPIcDER system, since the CNT yarns are black, if transparent insulation is used and/or uninsulated yarns are used, covering the spacesuit (various areas such as knees, legs, elbows, shoulders, boots) with black material has potential impacts to the passive radiative thermal management of the spacesuits. To minimize these impacts, an understanding of the critical areas of suit that are prone to dust and effects on spacesuit thermal management due to CNT coverage is essential. This allows identifying localized and specific areas of the suit that need to be embedded with the CNT electrodes permitting for an optimized solution to clean and protect the most severely impacted areas of spacesuits from dust.

A preliminary assessment was performed to understand how the addition of the SPIcDER system electrodes on various areas of the suit would affect the radiative heat transfer capability of an EVA suit on the lunar surface due to the inherent differences in the α/ε ratios between the outerlayer orthofabric material of the suit and the CNT yarns embedded on the surface of the suit. This assessment provides an understanding of the suit surface area that can be covered by CNT fibers in order to implement the SPIcDER system without reducing the radiative heat capability of the suit. Additionally, degradation of the radiative thermal regulation of the spacesuit outerlayer due to dust coverage of local areas of the suit is assessed. This assessment was conducted to establish a guideline for evaluating the dust cleaning performance of the SPIcDER system.

7.3.3.1. Thermal Assessment

To understand the thermal effects, this initial assessment compares the net heat dissipation by the outerlayer of the suit with and without CNT electrodes by assuming that the outerlayer of the suit acts as a radiator. A first order thermal model for radiative heat analysis was built based on a

research study conducted by Massina et al. (2014) on incorporating a full suit flexile radiator for thermal control in spacesuits. Elements from this study were utilized to build a thermal model for the current assessment. Conduction of heat to the lunar surface is not included in this analysis and is considered to be negligible for these initial investigations on radiative heat transfer impacts.

- **Background Calculations**

The net heat dissipation ($Q_{radiated}$, *Watts*) via radiation governed by the Stefan-Boltzmann law as shown Equation 32 is the dominant heat transfer mechanism from the suit on the lunar surface due to the lack of atmosphere. Here ε is the surface's emissivity (outerlayer), σ is the Stefan-Boltzmann constant (W/m^2K^4), A is the radiator area (here, it is the area of the spacesuit outerlayer), T_{surf} is the radiator's surface temperature and T_{sink} is the effective sink temperature to which the suit with a given α and ε equilibrate to in a radiative flux environment.

$$Q_{radiated} = \varepsilon A \sigma \left(T_{surf}^4 - T_{sink}^4\right) \tag{32}$$

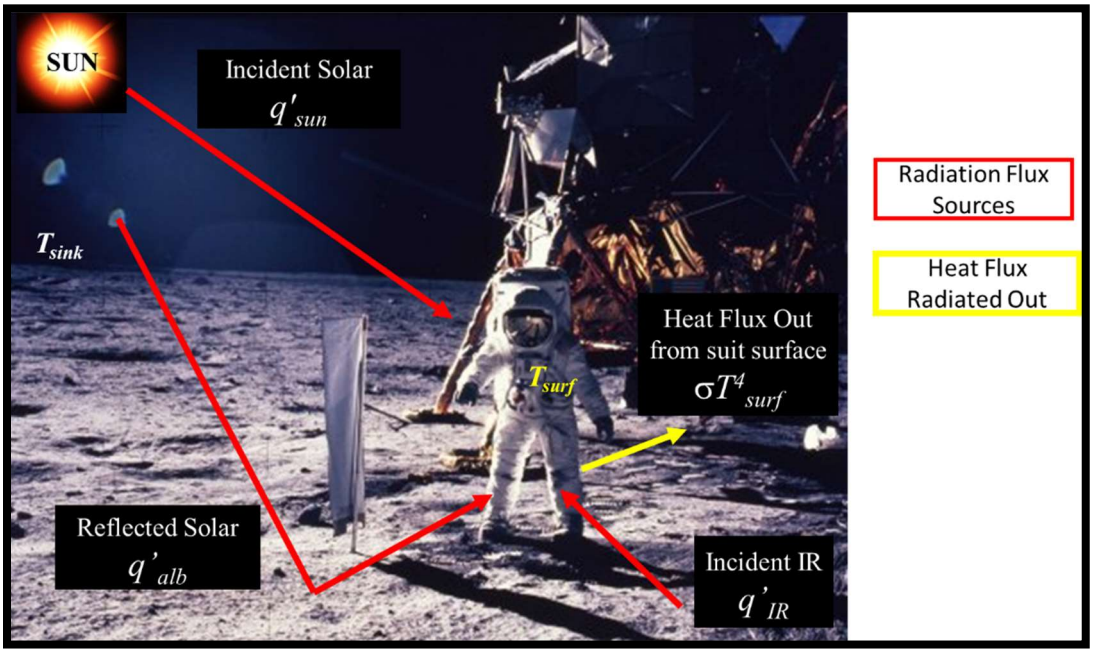

Figure 7.3-2. Overview of radiation heat fluxes on the lunar surface during an EVA
(Background image credit: NASA)

Figure 7.3.2 illustrates the primary radiation flux sources experienced by astronauts/ spacesuits during a lunar surface EVA. The radiative flux sources are modeled using Equations 33-37. The generic equation for the total net heat dissipation can be rearranged as shown in Equation 37. Definition of all the parameters in the equations below and their values along with assumptions used for the assessment are described in Table 7.3-2.

$$T_{sink} = \left(\frac{1}{\sigma}\left(\frac{\alpha}{\varepsilon}(q'_{sun} + q'_{alb}) + \varepsilon(q'_{IR})\right)\right)^{\frac{1}{4}} \quad (33)$$

$$q'_{IR} = \cos\theta * VF * S\alpha_{Lunar} \quad (34)$$

$$q'_{sun} = VF * S \quad (35)$$

$$q'_{Alb} = \cos\theta * VF * S(1 - \alpha_{Lunar}) \quad (36)$$

$$Q_{radiated} = A\left(\varepsilon\left(\sigma T_{surf}^4 - q'_{IR}\right) - \alpha(q'_{sun} + q'_{alb})\right) \quad (37)$$

Analysis was conducted in two steps

1. *Localized analysis*: First, the net heat dissipation ($Q_{radiated}$) was calculated for the area that would be covered by CNT electrodes using O*rthofabric material properties* using Equation 38 (based on Equation 37). This value was then compared with the net heat dissipation of the same area covered with CNT electrodes using Equation 39 (also based on Equation 37)
2. *Suit level analysis*: Second, the net heat dissipation was calculated for the entire suit area using Orthofabric material. This value was compared with the net heat dissipation when parts of the suit are covered with CNT electrodes. The percentage change that would be seen in the total net heat dissipation of the entire suit due to local areas covered in CNT was analyzed.

$$Q_{radiated_{Ortho}} = A_{Ortho}\left(\varepsilon_{Ortho}\left(\sigma T_{surf}^4 - q'_{IR}\right) - \alpha_{Ortho}(q'_{sun} + q'_{alb})\right) \quad (38)$$

$$Q_{radiated\_CNT} = A_{CNT}\left(\varepsilon_{CNT}\left(\sigma T_{surf}^4 - q'_{IR}\right) - \alpha_{CNT}(q'_{sun} + q'_{alb})\right) \quad (39)$$

Two configurations of the CNT electrode coverage were considered for the analysis: 1. both knees embedded with CNT electrodes and 2. both knees, boots and elbows embedded with electrodes.

For the analysis on thermal impacts due to local dust coverage on the suit, similar approach as that described above for the CNT electrodes was performed (Localized analysis and Suit level analysis). Equation 39 was updated with values for lunar dust solar absorptivity emissivity to resulting in Equation 40. Analysis was conducted for dust coating on both knees, elbows and boots.

$$Q_{radiated\_Dust} = A_{Dust}\left(\varepsilon_{Dust}\left(\sigma T_{surf}^4 - q'_{IR}\right) - \alpha_{Dust}(q'_{sun} + q'_{alb})\right) \quad (40)$$

Table 7.3-2. Equation parameters, their descriptions, and values used in the assessment

Parameter	Value	Units	Description	Source
Constants				
σ	5.67E-08	$W/(m^2.K^4)$	Stefan Boltzmann Constant	
VF (View Factor)	0.5		View Factor. Evaluated as if the astronaut is in a fully erect posture and the spacesuit is apprimated as a flat plate	Massina et.al 2014
θ	70º		Angle from Subsolar point. Using threshold angle based on 300 W load from previous study	Massina et.al 2014
Environmental Parameters				Massina et.al 2014
S	1368	W/m^2	Mean incident solar flux/solar constant	
α_{Lunar}	0.92		Lunar surface solar absorptivity , assuming Lunar albedo coefficient of 0.08 for worst case (Bright side. The value is highly variable ~0.5-0.08 depending on dark or bright areas respectively)	
q_{IR}'	Equation 34		Infrared Heat Flux	
q_{Sun}'	Equation 35		Direct Solar heat flux	
q_{Alb}'	Equation 36		Albedo/Reflected solar heat flux	
T sink			Sink (equilibriuum) Temperature	
Suit Parameters				
Outerlayer Material	Orthofabric		Based on ISS EMU and current research	
Surface Area of suit	3.9	m^2	Based on EMU evaluations	Tepper et.al 2014
Radiating area factor	0.86			Massina et.al 2014
A_{Suit}	3.35	m^2	Effective radiating surface area after applying Radiating area factorfactor	
α_{Ortho}	0.18		Solar Absorptivity of orthofabric outerlayer	Larson 1999
ε_{Ortho}	0.84		Emissivity of orthofabric outerlayer	Larson 1999
T_{surf}	17-37	degree C	Based on minimum and maximum mean skin temperature	Larson 1999 and Massina et.al 2014
Electrode Parameters				
Electrode Material	Carbon Nanotube Yarn, Uninsulated		Current research	
α_{CNT}	0.95		Based on Carbon fiber/black paint	
ε_{CNT}	1		Using ideal black body	Aliev et al 2009
Diameter of single electrode	0.2	mm	Based on prototype development	
Length of single electrode	12	inches	Based on prototype development	
Area of single electrode	10.2	mm^2	Diameter*Length (assuming a rectagular shape)	
Number of electrodes per location each	100		1knee=100, 2 knees=200, knees+elbows+boots= 600	
1 knee	100			
2 knees	200			
2 knees+2 boots	400			
2 knees+2 boots+2 elbows	600			
A_{CNT}		mm^2	Area covered by all CNT electrodes	
2 knees	2032	mm^2		
2 knees+2 boots+2 elbows	6096	mm^2		
Dust Parameters				
α_{Dust}	0.76		Solar Absorptivity of lunar dust from literature	Gaier and Jaworske 2007
ε_{Dust}	0.93		Emissivity of luanr dust from literature	Gaier and Jaworske 2007
$A_{dust\ (for\ 100\%\ dust\ coverage)}$	0.17	m^2	Area of suit covered in lunar dust. For simiplified analysis assuming 2 knees, 2 elbows, 2 boots based on ptototype measurements (11 *4 in^2)* 6 sections	
$A_{dust\ (for\ 25\%\ dust\ coverage)}$	0.04	m^2	0.25* Adust (for 100%)	
Length of each section	11.0	in	Measurements from prototype experiment in Chapter 9. Section represents- knee, boot, elbow	
Width of each section	4	in	Measurements from prototype experiment in Chapter 9. Section represents- knee, boot, elbow	
Assumption	6 sections		To simpyfy area covered in dust for 2 knees, boots, elbow, assuming each section is of the same area (11 in x 4 in)	

7.3.3.2. Thermal Assessment Results: CNT Coverage

Net heat dissipated by the local area covered by CNT electrodes: As illustrated by Figure 7.3-3, the net heat dissipated by the local suit area is decreased when portions of the suit are covered in CNT yarns (uninsulated). The change in the net heat dissipation is illustrated in the figure for both configurations of the electrode placements (just knees, knees, boots and elbows).

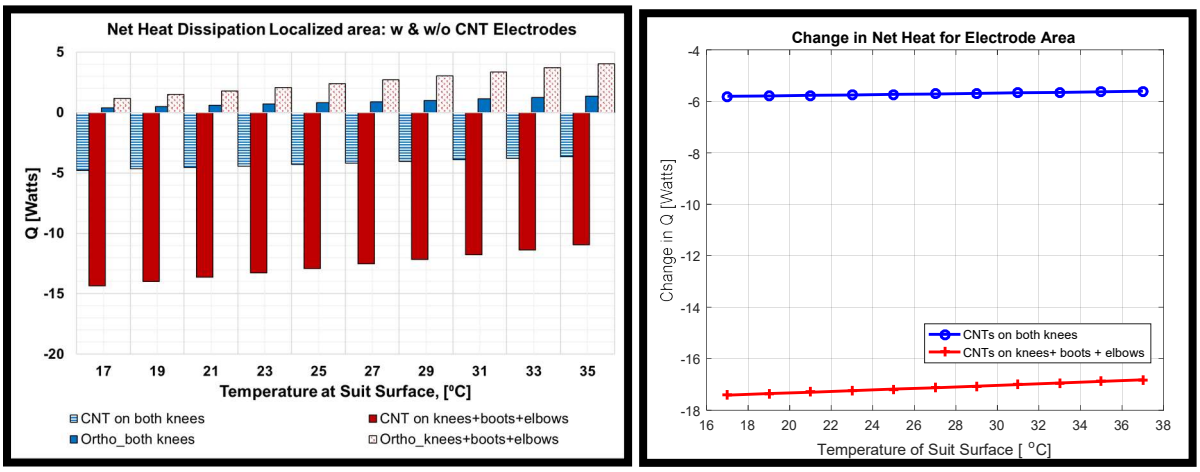

Figure 7.3-3 [Left] Comparison of net heat dissipation by the local area of the outerlayer with and without embedded CNT electrodes at various suit surface temperatures, [Right] Change in net heat dissipation due to CNT electrodes based on data from the left graph

Similarly for the full suit analysis, Figure 7.3-4 illustrates the percentage change in the overall net heat disspation by the full suit when portions of the suit are covered by CNT electrodes. For temperatures of the suit surface below 25 ºC, the efficiency of the outerlayer to dissipate heat when covered in CNT electrodes decreases rapidly (16% decrease at 17 ºC) . The value (17 °C) was chosen as the lowest end as it represents minimum liquid cooling garment water temperature of 16 °C for the ISS EMU. This value also corresponds to maintaining an optimum mean skin temperature of 27 ºC that needs to be maintained at the astronaut skin using an average metabolic load of 300 W (Massina et al. 2014; Larson, 1999).

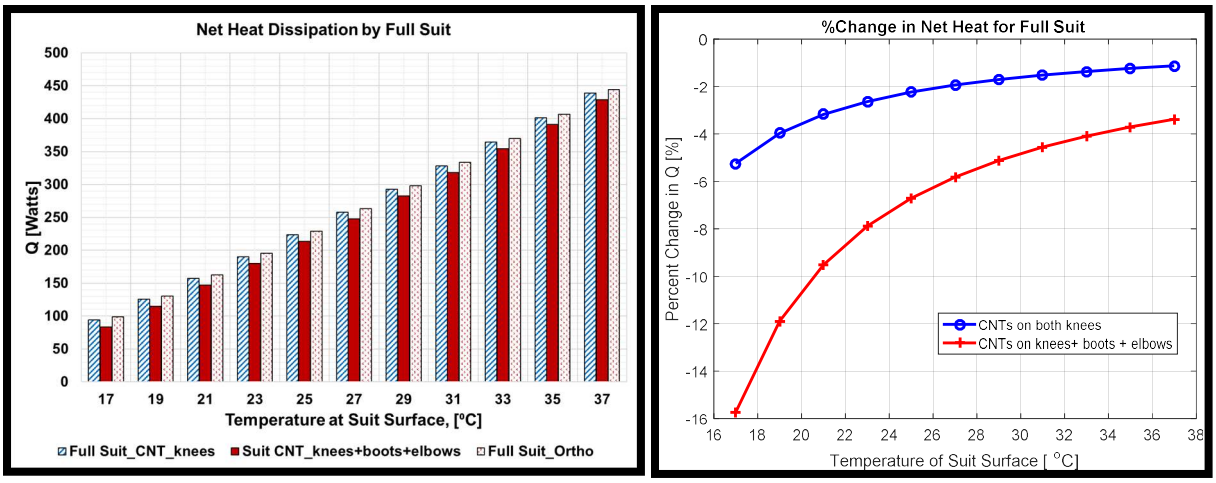

Figure 7.3-4. [Left] Comparison of net heat dissipation by the entire suit covered in orthofabric with and without CNT electrodes at various suit surface temperatures. [Right] % Change in net heat dissipation for the entire suit area based on data from the left graph due to embedded CNT electrodes

Percentage decrease in the total net heat dissipation when the local areas of the suit are covered in CNT yarns shown using preliminary analysis suggest that thermal calculations and analysis is an essential element to consider when planning to implement the SPIcDER system over the entire suit. Based on data generated in this section, it is recommended that CNT yarns be insulated with materials where the overall suit emissivity is maximized and solar absorptivity minimized to help mitigate thermal management challenges using bare electrodes. If materials with such thermal properties in combination with material flexibility are not available, the application of the SPIcDER system can optimized to be applied to just the highly dust prone areas of the suit such as the legs (knees, boots and area between the knees and boots) and elbows.

7.3.3.3. Thermal Assessment Results: Dust Coverage

Thermal analysis for dust coverage on the knee, boots and elbow area of the suit was performed to i) estimate the degradation in thermal radiation capability of the Orthofabric suit layer when local areas of suit are covered in a layer of dust and ii) establish a requirement guideline to evaluate the SPIcDER system dust cleaning performance. Two scenarios are assessed, one where 100% of the knee, elbows and boot areas are covered in a complete layer of dust and the second where only 25% of this area is covered in dust. These specific areas are chosen for the thermal assessment as previous investigations have shown the most affected areas of the suit were the knees and the boots. Measurements for the areas are estimated using values from the experimental prototype

from Chapter 9. For simplification, the areas of each section (knee section, elbow section, boot section) are assumed to be the same (11 in x 4 in each). Figure 7.3-5 and 7.3-6 show the results from the analysis and Table 7.3-2 captures the dust thermal parameters utilized for the analysis.

Net heat dissipated by the local area covered by lunar dust: As illustrated by Figure 7.3-5, when the local suit areas are covered by a layer of lunar dust, the net heat dissipated is decreased drastically when compared to a clean suit. The area of the suit covered in dust (knees, elbows and boots) absorbs heat due to the high solar absorptivity of the dust as seen in the 100% dust coverage results in Figure 7.3-5

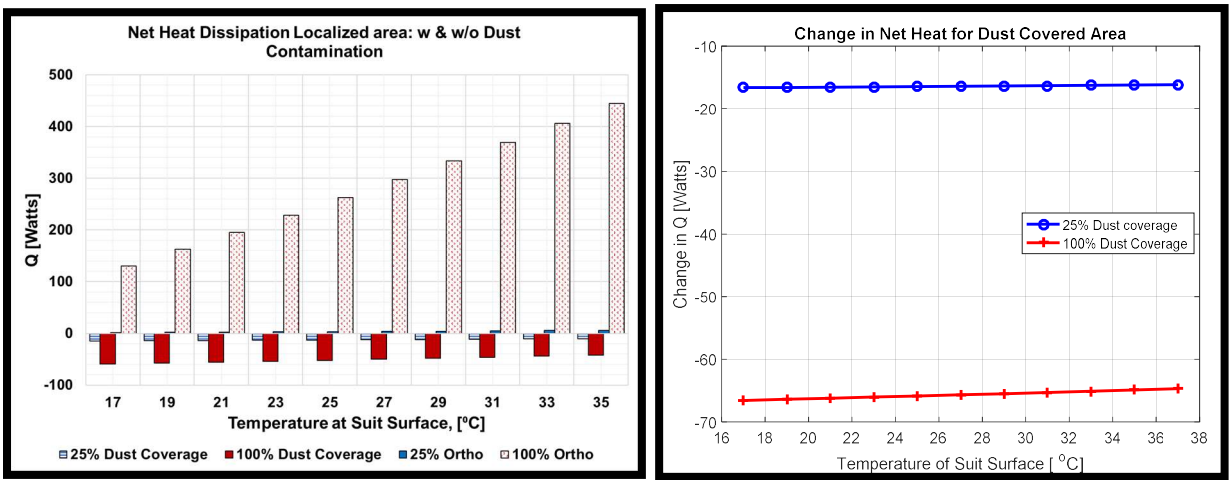

Figure 7.3-5 [Left] Comparison of net heat dissipation by the local area of the outerlayer covered in dust at various suit surface temperatures. [Right] Change in net heat dissipation by the local area based on data from the left graph due to 25% and 100% dust coverage.

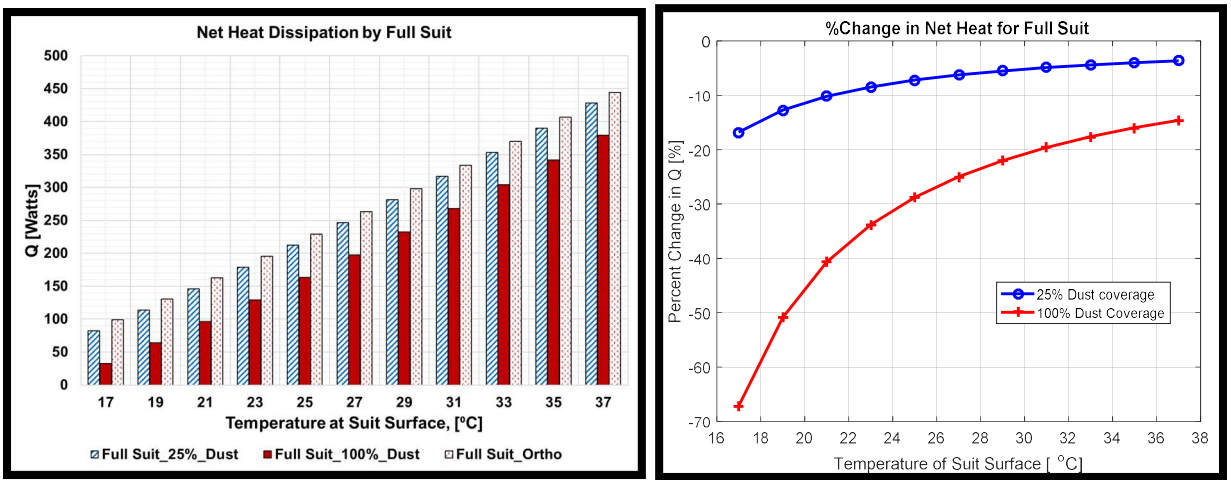

Figure 7.3-6. [Left] Comparison of net heat dissipation by the entire suit covered in orthofabric with and without dust coverage on knees, elbows and boots at various suit surface temperatures, [Right] %Change in net heat dissipation for the entire suit area based on data from the left graph due dust coverage.

When this change in the net heat dissipation caused by a layer of dust coverage of the local areas of the suit is viewed from the overall suit thermal radiative capability, the result is a 70% thermal performance degradation of the suit system, specially at low surface temperatures (Figure 7.3-6). If the dust coverage is reduced to 25% or less, we notice that the heat absorbed by the local area due to dust decreases from ~ 65 Watts to ~15 Watts, which is ~75% improvement in the thermal performance from the degraded thermal performance caused by 100% dust contamination (Figure 7.3-5). The percentage change in the net heat dissipated by the full suit is illustrated in the Figure 7.3-6 for both 100% and 25% dust coverage of the local areas (knees, knees, boots and elbows).

Using simplified thermal analysis, results indicate that if dust coverage of the fabric is reduced to <25%, the impact to radiative heat transfer of the entire suit at low temperatures will be less than 20%. When this analysis is extended to the entire suit, it is evident that it is imperative to protect the spacesuit from dust contamination from a thermal perspective. If the SPIcDER system can remove this adhered dust such that the residual percentage of the fabric dust coverage drops to <25%, thermal performance is greatly improved and thermal impacts due to dust contamination can be significantly minimized. This value has been therefore established as a guideline to evaluate the dust cleaning performance of the SPIcDER system. Results from Chapter 5 experiments demonstrated that the SPIcDER system is capable of meeting (in most cases far exceed) this requirement on small scale prototypes, of keeping the dust coverage of fabric well below 25%.

7.4. Safety

While the voltages required for using the SPIcDER system are on the order of 600-1400 V, the currents passing through the electrodes is very low (on the order of micro-amps) as the electrodes act as capacitive loads. However, application of high voltages still needs attention for astronaut safety. Due to the high voltage operation of the SPIcDER system, it is particularly important to make sure there is minimal contact between the astronaut inside the suit and the electrodes during operation of the SPIcDER system. The safety risks involved in operating the SPIcDER include Electrostatic discharge, electrical shock due to arching or contact, and electric field exposures. The safety risks include both human aspect as well as electromagnetic interference and electrostatic discharge with other electronics equipment. Spacesuits are made up of several layers (upto 11-13 layers). The fabrics and materials used in the spacesuit system are made of materials such as

Orthofabric and Kapton which are insulating and have high dielectric strengths. The presumption is that the layers of the spacesuit will provide the needed protection to the crew in the suit from the electric field forces generated by the SPIcDER system. Chapter 8 captures the safety aspects of operating the SPIcDER system in detail. A parametric analysis considering the layers and material properties of a planetary spacesuit and experiments using orthofabric coupons are conducted to characterize the safety issues. Results from the analysis and experiments, and recommendations to minimize hazards are presented in Chapter 8.

7.5. Summary

Table 7.5-1 summarizes findings from this chapter based on analysis of parameters that are critical for the manufacturability, performance and operation of the SPIcDER system for spacesuit application.

Table 7.5-1. Summary of key aspects for manufacturing and operational considerations of the SPIcDER system

Element	Key Aspects
Manufacturability and Performance	
Material/Substrate Properties	• Non-conducting substrate • High dielectric strength substrate materials
Conductive Fibers	• Spacing • Highly flexible • Fatigue resistant/ Flexure tolerance • Insulated fibers
Alignment of Electrodes	• Weaving methods • Consider automated weaving for large areas • Consider width of conductive fiber and width of warp/weft threads
Termination of Electrodes	• No overlap between conductors of distinct phases • Consider using insulative and conductive termination adapter films
Operational Considerations	
Power consumption/Duty Cycle	• Pulse versus continuous mode operation • Automated duty cycle • Considerations for embedded sensors for automated duty cycle
Thermal Management	• Utilize insulation materials with high emissivity and low solar absorptivity • Consider optimizing locating CNT electrodes to highly dust prone areas • Optimize SPIcDER system application to maintain atleast 75% of the suit fabric clean from dust (< 25% local residual dust coverage)
CNT yarns	• Qualification testing for space rated operations

CHAPTER 8: ASTRONAUT SAFETY: HEALTH EFFECTS OF LUNAR DUST AND SPIcDER SAFETY CONSIDERATIONS

"No Safety, Know Pain. Know Safety, No Pain"-*Anonymous*

This chapter provides an overview and brief analysis of the safety aspects for human-in-the-loop operation using the SPIcDER system. The chapter is divided into three parts. Parts I and II of focus on the hazards due to lunar dust and SPIcDER system implementation. Specifically, Part I emphasizes the toxicological effects of lunar dust on astronaut health and safety, and Part II details safety considerations that need to be addressed to implement the proposed SPIcDER dust cleaning system to effectively remove dust from spacesuit outerlayer. Part III of the chapter focuses on analysis conducted through experiments and numerical simulations to investigate the electric field and voltage exposures at the inner layers of the suit due to SPIcDER system operation. Recommendations for future flight implementation of the SPIcDER system to overcome some of the hazards identified in Part II of the chapter are provided.

Part I: Impacts of Lunar Dust on Astronaut Health and Operations During Lunar Exploration

Chapter 2 focused on the adverse effects of lunar dust on spacesuits, performance of scientific and life-support instruments, and other spacecraft components on the lunar surface. In addition to these impacts, Apollo astronauts reported undesirable effects to their skin (dermal), eyes (ocular), and airways (respiratory) during the Apollo missions (specific details in section 8.2). These effects have been related to exposure to the lunar dust that had adhered to their spacesuits during the EVAs and was subsequently brought into the habitable volume of LM when astronauts doffed their suits. This directly exposed the astronauts to lunar dust. A summary of health effects faced by Apollo mission astronauts along with other health considerations due to lunar dust are reported here.

During the Apollo era, dust toxicology was in its infancy when Apollo samples were initially returned to earth. Furthermore, during the Apollo days, NASA did not have a space toxicology group to pose questions regarding possible toxicity of inhaled lunar particles. However, with potential future long duration exploration missions to Moon, Mars and asteroids, we need to be concerned with the health of the astronauts to repeated (chronic) and acute episodic exposures to lunar dusts (Taylor and James 2007). As such, research is underway at NASA to characterize lunar dust, understand its toxicity, effects to health and components, and to develop dust mitigation techniques to address the problem.

Figure 8.1-1. Astronaut Gene Cernan, Apollo 17 regolith contamination in lunar module (Image credit: NASA)

8.1. Toxicity of Lunar Dust

With lessons learned from Apollo on lunar dust being abrasive and toxic, it is speculated that prolonged exposure to lunar dust would be detrimental to human health. Evidence from the Apollo flights and sample return investigations provide sufficient confirmation that lunar dust poses a challenge and has proved to be an important environmental factor to be considered not only for hardware and spacesuit designs but also for astronaut health for future missions to the moon. Reports from Apollo missions and health effects due to toxic terrestrial dust exposures that serve as an analog provide basis for concern on prolonged exposure of future crews to lunar dust that would potentially impact operations and performance of the crew.

The lunar surface does not have the earth's protective atmosphere, exposing the lunar soil directly to the harsh space environments such as constant hypervelocity micrometeorite impacts and solar winds. Unlike terrestrial dusts, which are mostly a product of atmospheric and

hydrodynamic modification, lunar dusts particles (specially the <20 μm fraction of lunar soils) have sharp and jagged edges due to the lack of atmospheric weathering and erosion, and lack of presence of water on the moon. Additionally, due to the reduced gravity on the moon ($1/6^{th}$ that of Earth), the time that the lunar dust remains airborne increases, increasing the probability that these dust particles will be inhaled.

To study the potential health effects for long term lunar exploration missions, NASA established the Lunar Airborne Dust Toxicity Advisory Group (LADTAG) to understand and characterize the toxicity of lunar dust (Khan-Mayberry, 2008). The research conducted by LADTAG on lunar dust has demonstrated that lunar soil contains several types of reactive dusts, including an extremely fine respirable component (<10 μm). Their studies revealed that approximately 10% of lunar dust is in the respirable range, and that lunar dust has a very large surface area (~8 times that of a sphere of equivalent external size (James, 2007). Based on studies conducted by this group and consultation with expert pulmonary toxicologists, a preliminary Permissible Exposure Level (PEL) of 0.3 mg/m^3 for episodic exposure to airborne lunar dust during a six-month stay on the lunar surface has been established (Meyers and Scully, 2015).

8.2. Reported Health Effects During Apollo Missions

Apollo astronauts reported experiencing several problems with lunar dust during their missions. When they removed their helmets and spacesuits inside the LM, the dust permeated all areas of the LM and the astronauts were in direct contact with this fine dust. Reports published on the missions noted that these dust exposures were uncontrolled and brief, but were sufficient to cause acute health effects during the Apollo missions (Cain, 2010; Wagner, 2006). Throughout every Apollo mission, astronauts remarked about the "gun powder" smell when they took off their helmets in the LM, upon returning from an EVA (Wagner, 2006). Several astronauts reported respiratory or eye irritations. Jack Schmitt from Apollo 17 was affected the most with coughing and transient congestion (Wagner, 2006). Some astronauts remarked that it was obvious that there was something unusual about the lunar dust. It was reported in a study conducted by NASA that on the Apollo 12, when removing their clothing on the return journey to earth, astronauts discovered that their skin was covered in dust (Wagner, 2006). Post-flight allergic-type responses were also observed in astronauts. A selected set of health-related comments directly reported by Apollo astronauts when exposed to lunar dust is presented in Table 8.2-1.

Table 8.2-1. Health related Lunar dust effects during Apollo missions (Adapted from Wagner, 2006)

Apollo Mission	Apollo Astronauts	Selected Comments from Mission Reports
Apollo 11	Neil Armstrong and Buzz Aldrin	- Commander removed his liquid-cooling garment in order to clean his body. One grain of material got into the ***Commander's eye***, but was easily removed and caused -***Dust under fingernails*** not able to be removed -Crew noticed ***distinct pungent odor*** from Lunar material -Crewmembers reported sleeping with their helmets on, in part, so they "***wouldn't be breathing all that dust***"
Apollo 12	Charles Conard	"... .. The LM was filthy dirty and it has so much dust and debris floating around in it that I ***took my helmet off and almost blinded myself***. I ***immediately got my eyes full of junk***, and I had to put my helmet back on. I told Al to leave his on. We left the helmets on and took off our gloves." "..... "[w]e chose to remain in the suit loop as much as possible because of the dust and debris floating around"; and "[t]o ***keep our eyes from burning and our noses from inhaling these small particles,*** we left our helmet sitting on top of our heads"
Apollo 13	Alan Bean	"…..We were plagued by it (dust) when we finally did get back into the Command Module. Pete and I had to remove our hoses so that we could use them for vacuum cleaners. ..... We had to remove our helmets from our suits, to keep our ***eyes from burning and our noses from inhaling these small particles floating*** around....."
Apollo 15	David Scott	"…..When you took your helmet off, you could ***smell the lunar dirt***. It ***smelled like*** – the nearest analogy I can think of is ***gunpowde***r."
Apollo 16	Charles Duke	" John and I both doffed the suits in the LM. I thought it was quite a hazard over there floating through the LM with all the dust and debris. A number of times I ***got my eyes full of dust and particulates***. I felt like ***my right eye was scratched slightly*** once."
Apollo 17	Gene Cernan	".....I didn't feel any aerosol problems at all until after rendezvous and docking when I took off my helmet in zero-g and we had the lunar module cabin running the whole time. I did all the transfer with my helmet and gloves off, and I'm sorry I did because the ***dust really began to bother me.*** It ***bothered my eyes, it bothered by throat, and I was tasting it and eating it*** and I really could feel it working back and forth between the tunnel and the LM"
Apollo 17	Harrison Schmidt	"After the first EVA, there was considerable dust in the cabin. It would be stirred up by movements of the suit and the gear that we had. Almost immediately upon removing my helmet, I started to pick up the symptoms that you might ***associate with hay fever symptoms.*** I never had runny eyes or runny nose. It was merely a ***stuffiness in the nose*** and ***maybe in the frontal sinuses*** that ***affected my speech and my respiration considerably.***..."

8.3. General Health Effects of Lunar Dust

The abrasive nature of lunar dust, fractional gravity of the lunar surface, sharp and irregular shapes of the lunar dust particles, particle size and chemical composition of lunar dust, all contribute to causing severe health effects. Dust exposure and inhalation could have a range of toxic effects on human lunar explorers specially if longer EVAs are planned for future human exploration missions, increasing time exposed to dust. Harmful effects on human health by dust include effects on mucus membranes, visual and respiratory systems (Cain, 2010 and Linnarsson et al., 2012). Typical maladies that occur due to dust contamination is silicosis, quoted by NASA as perhaps the most representative model to the lunar environment because of the particles size distribution, shape, and chemical reactivity. Due to the limited spaceflight data on lunar dust, evidence from ground-based studies suggests that human exposures to dust from mineral deposits have caused respiratory problems (Linnarsson et al., 2012). Below are some of the characteristics of the lunar dust particles that have been recognized to impose health effects.

8.3.1. Characteristics of Lunar Dust Causing Health Effects

- **Chemical composition effects**

Lunar dust which consists of over 50% of silica oxide, is chemically reactive and chronic inhalation exposure to these dust particles could result in a progressive silicosis type respiratory disease (Cain, 2010; Liu and Taylor 2011, Khan-Mayberry, 2008). Another factor that may increase the toxicity of lunar dust is its iron content. Smallest-sized fraction of lunar dust contains a substantial portion of nanophase (np) Fe^0 metal particles. These $npFe^0$ particles adhere to the surface of respirable-sized dust particles in sufficient concentration to give them magnetic properties (Linnarsson et al., 2012). The presence of $npFe^0$ in these dust particles affect toxicity and type of cellular injury. In-depth investigations to understand the chemical toxicity of lunar dust are still ongoing to set an appropriate health standard for future lunar missions.

- **Fractional gravity effects**

In a micro/hypo-gravity environment, the risk of inhalation of dust is increased due to reduced gravity-induced sedimentation and durations of airborne dust. The fractional gravity of the moon will enable the small particles to penetrate deep into the lungs increasing the risks of lung disease.

Inhaled particles tend to deposit more peripherally and may be retained in the lungs for longer periods in reduced gravity (Linnarsson et al., 2012).

- **Particle Size effects**

Particles of lunar dust of less than 20 μm or less may cause damage to the upper airways including the nasal passages, pharynx, and larynx (Cain, 2010 and Linnarsson et al., 2012). Particles of 10 μm or less would be expected to cause potential damage to the lower respiratory airways, including the trachea, and as particles decrease in size to 5 μm or less they would penetrate deeper into the lung and bronchioalveolar regions where symptoms such as edema, inflammation, fibrosis, and potentially carcinogenic effects may occur (Cain, 2010 and Linnarsson et al., 2012).

- **Abrasiveness of lunar dust particles**

Because of the abrasive properties of lunar dust, dermal abrasion may cause skin damage induced by pressure on the skin at sites of anatomical prominence (finger tips, knuckles, elbows, knees), and result in breakdown of the outermost layer of the skin (Khan-Mayberry, 2008; Cain, 2010 and Linnarsson et al., 2012). In addition, it could irritate the dermal water vapor barrier and could lead to dermatitis and/or sensitization.

8.3.2. Other Health Considerations

Even though most concern about the health effects of lunar dust is dominated by pulmonary (respiratory) considerations, many operational scenarios have the potential to result in eye and skin exposures to lunar dust. Other toxic effects that are expected based on Apollo experience include dermal irritation and penetration, and ocular injury including mechanical and possibly chemical irritation.

For eye exposure, at least two scenarios are envisioned: deposition of airborne particles onto the surface of the eye, and transfer of particles from contaminated objects, such as fingers, that may touch the eye. Eye contact could result in minor irritation, physical or chemical injury leading to conjunctivitis eye (Linnarsson et al., 2012).

Exposure of the skin to lunar dust could occur due to airborne particles once astronauts doff their suits in a habitat. This can be avoided to a certain extent if suits are doffed in a separate module outside the habitable volume. However, other operations performed by astronauts that

involve handling dust contaminated EVA suits or tools such as suit cleaning, maintenance and repair procedures would also present risk of exposure to dust. Skin exposure to lunar dust may also be of concern if the interior of the spacesuit becomes contaminated with lunar dust. During operations, such as donning a suit using contaminated hands, dermal abrasion may take place at sites where the suit rubs against the skin. For future missions, it may be necessary to study abrasive skin exposures and determine a PEL for entry into the spacesuits.

The risk of adverse effects caused by inhalation of lunar dusts to the nose, pharynx, trachea, and larger air conducting areas of the respiratory system and irritation or damage to the mucosa of the gastrointestinal system by ingested dust remains to be assessed. The risk of effects of lunar dusts on other systems such as the cardiovascular, nervous systems and immune systems that may be secondary, or indirectly affected by inhaled or ingested dusts also remains to be characterized. For example, research findings on air pollution related to dust is also linked to cardiovascular effects and, dysfunction of the autonomic nervous system and chronic inflammation, which is believed to exacerbate cardiovascular disease (Tranfield et al., 2010). These effects have known to manifest as irregularities in heart rate, heart rhythm, and blood pressure. Considering terrestrial analogs, dust effects on health would be distressing for future human lunar exploration missions if proper protection and decontamination methods are not established.

8.4. Lunar Dust Toxicity using Animal Studies

Pulmonary Effects: The toxicological effects of lunar dust have also been investigated using animal studies by various groups. Russian studies of lunar dust returned on the Russian Luna spacecraft have also been previously reported. One study by Batsura et al. in 1981 reported that instillation of 50 mg of lunar soil into the lungs of rats caused inflammation and fibrotic changes; this amount of material would severely overload the lungs of rats. Another study reported that rats given 50 mg of lunar soil showed lung fibrogenic effects and increased lung weights, but the effects were much less severe than concomitant exposures of other rats (Kustov et al., 1981). Another such study by Holland and Simmons in 1973 reported intratrachael instillation of 20 mg of Apollo dust to small groups of guinea pigs. The study reported alveolar cell hypertrophy, septal edema, mononuclear cell infiltration, and macrophage proliferation around spikules of dust (Holland and Simmonds, 1973). However, the findings were inconclusive as both the exposed and control animals had a significant degree of spontaneous pathology, thought to be caused by a respiratory.

A recent study conducted by James et al. in 2013 investigated the effects of pulmonary toxicity of lunar dust in rats. They exposed rats to four different concentration levels of respirable size lunar dust for 4 weeks (6 h/day, 5 days/week). Their results showed that at higher exposure concentrations histopathology, including inflammation, septal thickening, fibrosis and granulomas, in the lung was observed. Their 4-week exposure study in rats showed that 6.8 mg/m^3 was the highest no-observable-adverse-effect level (NOAEL) of toxicity exposure to lunar dust. Such studies are useful for assessing the health risk to humans' due to lunar dust exposure and would help establish human exposure limits and provides guidance for the design of dust mitigation systems in lunar landers or habitats.

Dermal Effects: The abrasive effect of lunar dust on skin has been evaluated by studies conducted by Jones et al. in 2009 using pig skin. After abrasion with JSC-1A lunar soil simulant and with authentic lunar dust, results of these studies show that both the simulant and authentic dust is abrasive as commercial sandpaper (Jones et al., 2009). Future studies involving classical skin toxicology studies, including chemical irritancy evaluation and sensitization tests remain to be performed.

Ocular Effects: Findings from a study conducted using rabbits to assess acute irritation in the eye suggested that exposure to lunar dust for 120 hours at a concentration as low as 20 mg/m^3 is sufficient to elicit a molecular response in the cornea (Lam et al., 2103; Theriot et al., 2014). Investigators noted that additional studies are required to fully assess the risk of vision impairment and the potential for long-term effects to astronaut health due to lunar dust exposure.

8.5. Further Lunar Dust Toxicity Studies

Research is currently underway to further investigate the physical and chemical determinants of lunar dust toxicity using lunar dust simulants. These simulants are commonly synthesized from terrestrial volcanic material and have been found to exhibit toxic effects. However, the lunar simulants do not necessarily capture all the unique features of actual lunar dust, which are a result of formation by micrometeoroid impacts and extended radiation exposure in the absence of oxygen and humidity. The toxicity and interaction of $npFe^o$ in lunar dust are also yet to be characterized and determined. These unique features such as the npFe, activated surfaces due to micrometeoroid impacts of lunar dust could lead to toxic effects significantly exceeding those of simulants made

from Earth materials. Therefore, further research to understand the health effects and development of effective countermeasures are imperative if future lunar missions need to be successful. Dust mitigation strategies and technologies should be developed to overcome the effects of dust contamination. The SPIcDER system is presumed to play a key role to help mitigate some of these challenges by preventing dust accumulation on the spacesuits and reducing astronaut exposures to dust when doffing the suits. In addition, other decontamination techniques for habitable volume and PEL levels should be defined and established for future lunar (and Martian) missions to minimize health risks. A summary of dust exposure limits from various studies surveyed are summarized in Table 8.5-1.

Table 8.5-1. Lunar dust exposure limits to minimize health effects from various studies

Limit Type	Exposure Limits	Notes from Study	Source
Safe Exposure levels	0.5-1 mg/m^3	Study estimates this value of lunar dust to be safe for periodic human exposures during long stays in habitats on the lunar surface. Study conducted on rats via instillation	James et al., 2013
Permissble Exposure Level (PEL)	0.3 mg/m^3	For episodic exposure to airborne lunar dust during a six-month stay on the lunar surface has been established. These were initial studies, more extensive studies recommended	Meyers and Scully 2015
No-observable-adverse-effect level (NOAEL)	6.8 mg/m^3	The highest no-observable-adverse-effect level (NOAEL) of toxicity in rats exposure to lunar dust for 4 weeks	Lam et al., 2013

Part II: Astronaut Safety Considerations for Designing the Proposed SPIcDER System

The proposed SPIcDER system utilizes high voltage AC signals at very low currents to produce time-varying electric fields using CNT yarns as electrodes wires. Accordingly, some of the elements of the system embedded into the outerlayer of the spacesuit might be of potential concern to the health and safety aspects of astronauts operating in those spacesuits. These potential hazards are illustrated in Figure 8.6-1 and can be categorized into three areas which should be addressed for full implementation of the system into flight suits.

1. First, exposure of astronauts to electric fields inside the suit when the SPIcDER system is active: Electric fields are generated at the outerlayer of the suit by applying high voltages (>600 V) to the electrodes embedded into the outerlayer. Concern will be if the electric field intensity is high enough to pose health risks at the inner layer (pressure bladder of the suit) in

proximity to the astronaut. This exposure on the inner layer of the suit may be due to reasons such as insufficient insulation within the suit layers, manufacturing quality, and wear/tear. Exposure to the generated electric fields may result in two hazards

   a. Potential electric field exposure/non-ionizing radiation
   b. Contact potential (touch voltage) resulting in induced electric currents leading to electrical shocks
   c. Additionally, the pressure inside the suit is maintained by using pure oxygen. Therefore, it is imperative to address both the effects on human health due to exposure to electric fields as well as possibility and prevention of the flammability of the suit

2. Second, the possibility and prevention of electrical arcing between the electrodes on the outerlayer of the suit if any two electrodes come in close contact as defined by Paschen's law.
   a. If the astronaut comes in direct contact with arcing or the energized electrodes, it's an electric shock hazard
3. Toxicity of CNT material exposure. There have been animal studies on the potential toxicity of exposure of raw CNT material. While the studies on toxicity of CNTs are still in their early stages, the National Institute for Occupational Safety and Health (NIOSH) recommends that exposures to CNT and Carbon nanofibers (CNF) be kept below a recommended exposure limit of 1 $\mu g/m^3$ for 8-hr Time Weighted Average (TWA) of respirable elemental carbon during a 40-hr work week.

A description of the hazards mentioned above are provided in detail in the following sections. Recommendations to overcome these safety aspects are presented towards the end of the chapter.

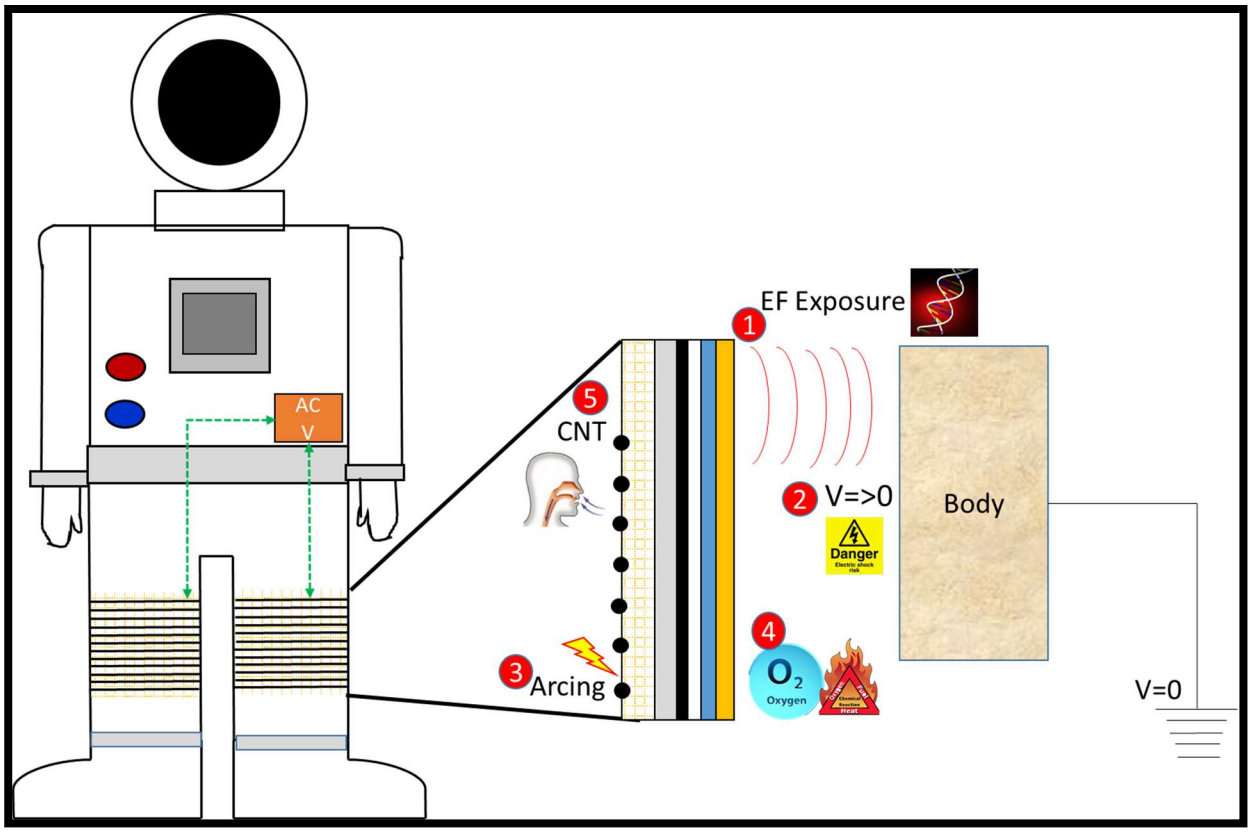

Figure 8.6-1. Possible hazards to be addressed for SPIcDER system integration into the spacesuit outerlayer

8.6. Possible Hazards to be Addressed for SPIcDER System Implementation

8.6.1. Electric Field Exposure

Electric fields (EF) exist whenever a positive or negative electrical charge is present. They exert forces on other charges within the field as shown in Figure 8.6-2. When the SPIcDER system is activated on the spacesuit, an EF is generated on the outerlayer of the spacesuit where the CNT electrode network is embedded. The intensity/strength of the EF is proportional to the voltage applied. Electric fields are strongest close to the electrodes and their strength rapidly diminishes with the square of the distance from the conductor as described in Equation 11 (previously derived in Chapter 6), where *r* is the radial distance from the center of the electrode. The spacesuit is made up of several layers of material (11-21 layers) that is presumed to minimize the intensity of the EF at the inner layers of the suit. An analysis to characterize the EF at the inner layer of the suit (in this case pressure bladder) is conducted in section 8.7 modeling the several layers of the spacesuit. A preliminary investigation using experiments has been performed and explained in section 8.7.

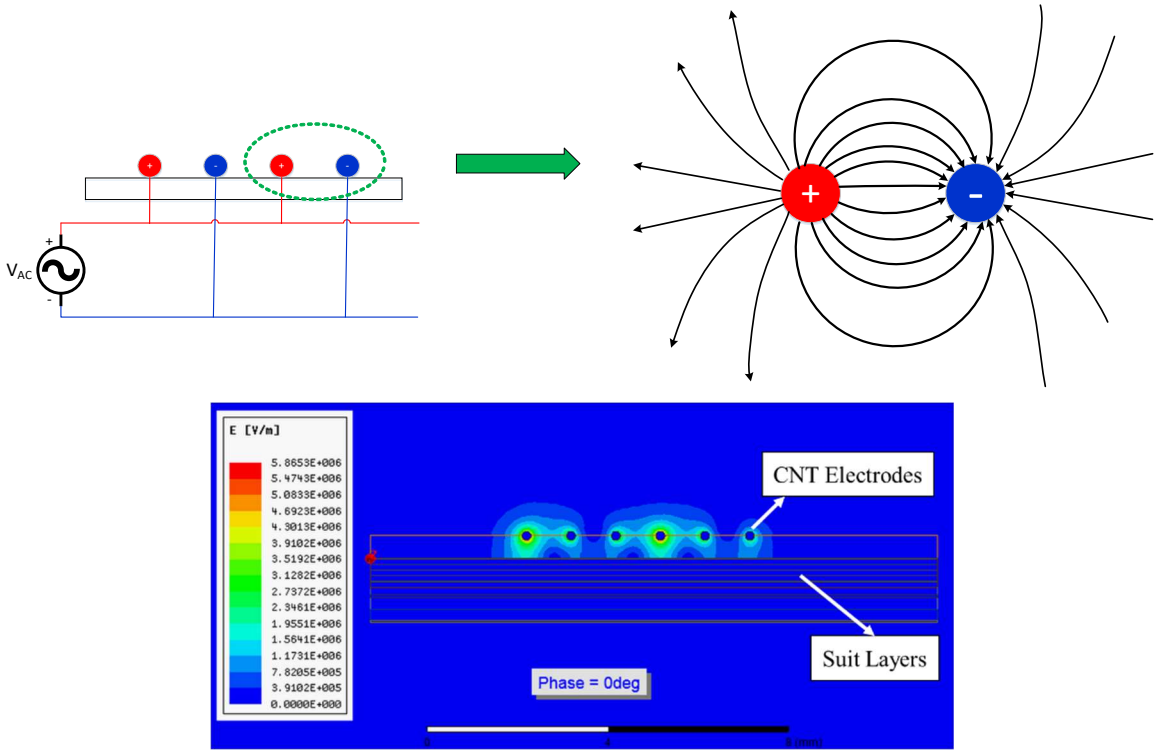

Figure 8.6-2. [Top] Representation electrodes on a substrate and electric field lines generated between adjacent electrodes. [Bottom] Representation of electric field magnitude using multiple layers of spacesuit. *Details on electric fields with spacesuit layers in section 8.7*

The effects of electromagnetic fields on the human body depend on the type of the exposure field (electric vs. magnetic), their characteristics (frequency, magnitude, orientation, etc.), and the size, shape, and electrical properties of the exposed body. Extremely Low Frequency (ELF) fields are defined as generally having frequencies up to 300 Hz (WHO, 2007).

The time-varying electric fields produced by the SPIcDER system is an example of ELF as the cleaning system may be operated between 5-200 Hz, with current research being performed using 5-10 Hz. As described in Chapter 6, the electrode network of the SPIcDER system act as a capacitive load which charge and discharge the electrodes within a time frame less than nanoseconds (10^{-10}-10^{-11} seconds). This time constant is insignificant when compared to the actual frequency and time period of the system operating at 5 Hz (0.2 seconds). Therefore, the currents passing through the electrodes is essentially negligible (on the order of nano to microamps). Since the charge-discharge cycle of the dust cleaning system relative to the time period of the signal is very low, the magnetic fields generated by the low currents diminish within the nanosecond timeframe. Therefore, the impacts of magnetic fields as a result of moving charges are negligible

compared to the electric fields generated by the SPIcDER system. Section 8.8 provides further quantification on the extent of electric and magnetic forces generated by the SPIcDER system

- ***Effects of Electric Field Exposure***

Exposure of the human body to external electric fields induces surface charges on the exposed body resulting in electric currents within the body. If these induced electric currents are sufficient, they can produce a range of effects such as heating of internal tissues and electrical shock. The extent of the intensity and damage of the EF on the human body depends on the field's amplitude and frequency range; and fields of different frequencies interact with the body in different ways. In addition to direct interaction and effect on the body, the ELF fields may cause interference with active and passive medical devices on the astronaut body located for biomedical monitoring. These effects may be extended to the life support systems and electronics on the spacesuit system. Below is a summary of some of the noted effects due to EF exposure based on a study conducted by the World Health Organization (WHO) (WHO, 2007)

- External electric fields acting on the outer surface of the body can lead to hair movements and sensory effects.
- Electric fields impact transmission of electric impulses by nerves disturbing nominal signal transmission within the body.
- Electric fields may cause time varying electric charges and currents within the body tissues causing undesired interactions with the chemical and biochemical reactions occurring within the body. For sinusoidal electric fields, the magnitude of currents produced inside the body increases proportionally with the frequency.
- When external electric fields are high enough, cells/ cell membranes within the body are most affected by exposure to these fields interrupting the normal electric signals within the body.
- If the current densities in tissue induced by external fields are large enough, it would depolarize the cell membrane potential up to their excitation threshold causing biological reactions and disturbances. These effects are mainly caused at levels of induced current densities exceeding 100 mA/m^2 to several hundred mA for frequencies between 1Hz-1kHz. SPIcDER analysis shows current densities on the order of 3 mAm^{-2} at the outerlayer to 0.00025 mAm^{-2} at the inner layer.
- Per WHO research, evidence for other neuro-behavioral effects due to electric field exposure in volunteer studies, such as the effects on brain electrical activity, cognition, sleep,

hypersensitivity and mood, is still lacking. Based on a few studies conducted on the gross electrical activity of the brain, there is some evidence suggesting existence of field-dependent effects on reaction time and reduced accuracy in the performance of some cognitive tasks. Other studies reported by WHO investigating Electromagnetic Field (EMF) induced changes in sleep quality seem to have reported inconsistent results. Reports exists that a small population of people claim to be hypersensitive to EMF as reported in WHO studies. However, there no compelling evidence on the correlation of these symptoms with EMF exposure.

8.6.1.1. Threshold Values for Electric Field Exposures

Electric field exposure limits based on the acute effects on electrically excitable tissues, particularly those in the Central Nervous System (CNS) have been proposed by several international organizations. The threshold limits for EMF exposures as standardized by the International Commission on Non-Ionizing Radiation Protection (ICNIRP) are summarized in Table 8.6-1 and shown in Figure 8.6-3 (ICNIRP, 1998a). For occupational groups, the IEEE levels are 20 kV/m and 2710 μT at 60 Hz. The differences in the guidelines, derived independently by the IEEE and the ICNIRP result from the use of different adverse reaction thresholds and different safety factors. There is however a factor of safety added to threshold values to derive the guideline limits (a safety factor of 10 for occupational exposure and a factor of 50 for public at which first behavioral changes become apparent). The occupationally exposed population consists of adults who generally experience known EMF conditions. These workers are trained to be aware of potential risk and to take appropriate precautions. For conservatism in this research, the ICNIRP levels of public exposure limits will be used as a standard for safety analysis of the SPIcDER system. The electric field exposures at the inner layer of the suit (pressure bladder) should be lower than the 4200 V/m and the magnetic field exposure limited to 83 μT as highlighted in the table.

Table 8.6-1. Summary of ICNIRP established guideline limits for EMF exposures

Field	Electric Field (V/m)		Magnetic Field(μT)	
Frequency	50 Hz	60Hz	50 Hz	60Hz
Public exposure limits	5000 V/m	4200 V/m	100 μT	83 μT
Occupational exposure limits	10,000 V/m	8300 V/m	500 μT	420 μT
Occupational exposure limits per IEEE*		20,000 V/m*		2710 μT*

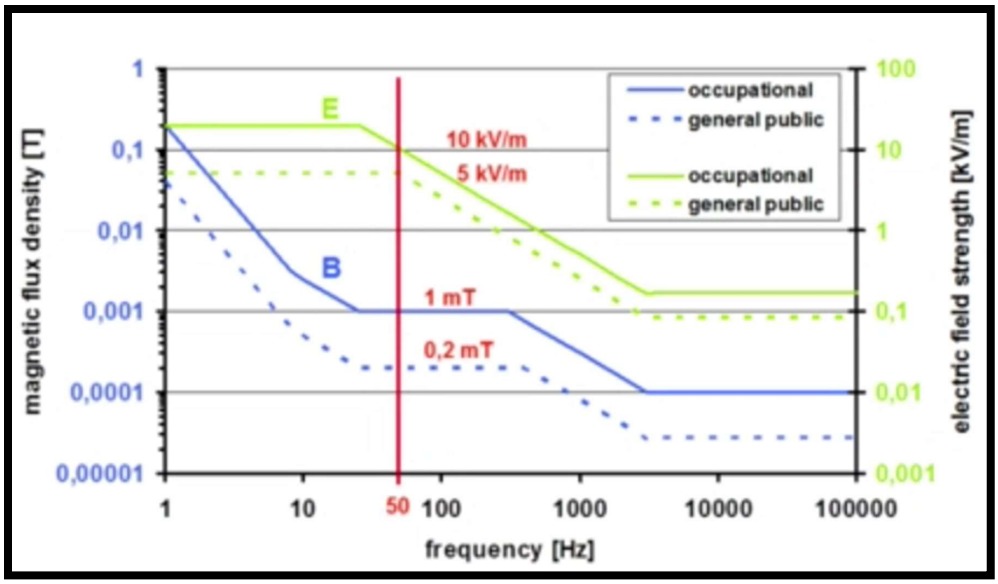

Figure 8.6-3. ICNRP guidelines for EMF exposure at 50Hz (Taken from ICNIRP standards)

Studies conducted on volunteers exposed to power frequency electric fields (50-60 Hz) provide an insight into biological responses due to electric field exposure. Studies conducted by WHO (2007) revealed that

- 10% of volunteers direct perception of electric field varied between 2 and 20 kVm^{-1}
- 5% found 15–20 kV m^{-1} annoying
- Spark discharge from a person to ground is found to be painful by 7% of volunteers in a field greater than 5 kV m^{-1}

The threshold levels also depend on the relative positions of the head, trunk and limbs, as a consequence of the different perturbations of the incident field. Above a certain threshold, the current to ground is perceived by the person as a tingling or prickling sensation for frequencies below 100 kHz and as heat at higher frequencies. Although these effects are not considered to be hazardous, hair vibration and tingling if sustained can become an annoyance, specially during EVAs. Some studies conducted using ELF electric fields on volunteers reported that EF can be perceived because of the field-induced vibration of body hair or occurrence of space discharges on contact with clothes or ground subjects.

In the low frequency range (between 1 Hz and 10 MHz) the current basic restriction is the current density (*J*, in A m^{-2}) for preventing effects in excitable tissues such as nerve and muscle cells. The ICNIRP (1998a) identified a threshold current density of 100 mAm^{-2} for acute changes in functions of the CNS (brain and spinal cord, located in the head and trunk) and recommended

basic restrictions on current density induced at 10 mAm^{-2} for workers, and 2 mAm^{-2} for members of the public. Values for the current densities generated by the SPIcDER system at the inner layer (pressure bladder) are on the order of 0.00025 mAm^{-2}, more than an order of magnitude lower than the numbers established for general population (Details in section 8.8).

8.6.2. Contact Currents/Touch Potential

When the human body comes in contact with conductive surfaces at different potentials and serves as a path for current flow, the potential difference induces currents in the body. If the currents are sufficient through the skin and the body, it would lead to severe injuries. This hazard is possible in two ways while operating the SPIcDER system (i) astronaut coming in direct contact with the electrodes at the outerlayer when CNTs are energized and (ii) high potential difference at the inner layer of the suit enough to cause currents to flow in the body when the inner layer touches the astronaut body. The contact currents that are induced in the body can be estimated using Ohm's Law, depicted in Equation 41. The contact current is determined by the voltage (V) of the source and the body/skin resistance (R), and the pathway the electricity takes through the body. Predictions and measurements of electrical resistance of human skin and body have been previously reported. Table 8.6-2 lists the electrical resistance values for human skin and body as reported by NIOSH, International Electrotechnical Commission (IEC) and another study (Aga et al., 2016).

$$V = IR \tag{41}$$

Table 8.6-2. Human body/skin resistance values reported by various standardized sources

Description	Resistance (Ohms, Ω) at 60Hz AC	Source
Dry Skin (NIOSH)	100,000	NIOSH
Wet Skin (NIOSH)	1000	NIOSH
50% population at 25 V	3250	IEC
50% population at 100 V	1875	IEC
Internal Body resistance using numerical model	1181	Aga et al., 2016

In the current context, assuming that the astronaut is at a local ground plane ($Va=0$), voltages at the inner layer of the suit (pressure bladder) should be maintained at a level lower than the value that would cause currents beyond the threshold levels within the astronaut's body (when the astronaut comes into contact with the inner layer) leading to injuries. Section 8.6.1.2 details the

effects of electric current on the human body and threshold values to be maintained to prevent injuries. Part III of this chapter analyses the voltages at the inner layers when the SPIcDER system is active.

8.6.3. Electrical Arcing

Electrical arcing on the SPIcDER system would occur when adjacent electrodes connected to separate phases of the AC electric signal come in close contact and there is electrical discharge or breakdown. Arching is characterized by Paschen's law and is a form of electric discharge as described in Chapter 6, section 6.8.5. When arching occurs, it produces visible continuous spark with high current densities. Exposure to such high current densities would lead to hazards. The energy released by the arc creates a rise in the temperature and pressure in the local surrounding area. This causes mechanical and thermal stress to nearby equipment and creates possibility for serious injuries within the vicinity if not mitigated.

When the SPIcDER system is operational, if human body comes into contact with the electrodes or during arcing, it would short circuit the system and cause electrical shock to the human body. Effects of arcing due to the release of energy generated may include burns, injuries, inhalation of toxic gases and electric shock. Because of the high voltages used in the SPIcDER system, high electric currents would be conducted through the body causing sever electric shock (Equation 41). However, because the electrodes are on the outerlayer of the suit along with several insulating layers of the suit, the astronauts don't directly contact the electrodes while inside their suits. Therefore, there is minimal hazard from the astronaut coming in contact with energized electrodes during EVAs. Additionally, arcing can be stopped by turning the power off to prevent arcing hazards. If the SPIcDER system is operated post EVAs when the suits are not in operation, precautions and procedures must be established to avoid direct contact with the energized electrodes.

8.6.3.1. Threshold Values for Currents Leading to Hazards

According to standards set by Occupational Safety and Health Association (OSHA), while any amount of current over 10 mA can produce painful to severe shock, currents between 100 and 200 mA are lethal. Currents above 200 mA produce severe burns and unconsciousness. The physiological effects of electric shock at various current levels are shown in Figure 8.6-4 and the

threshold value under which the SPIcDER should be operated. Section 8.8.2 analyses the voltages and currents that the astronauts will be exposed to due to implementation of the SPIcDER system.

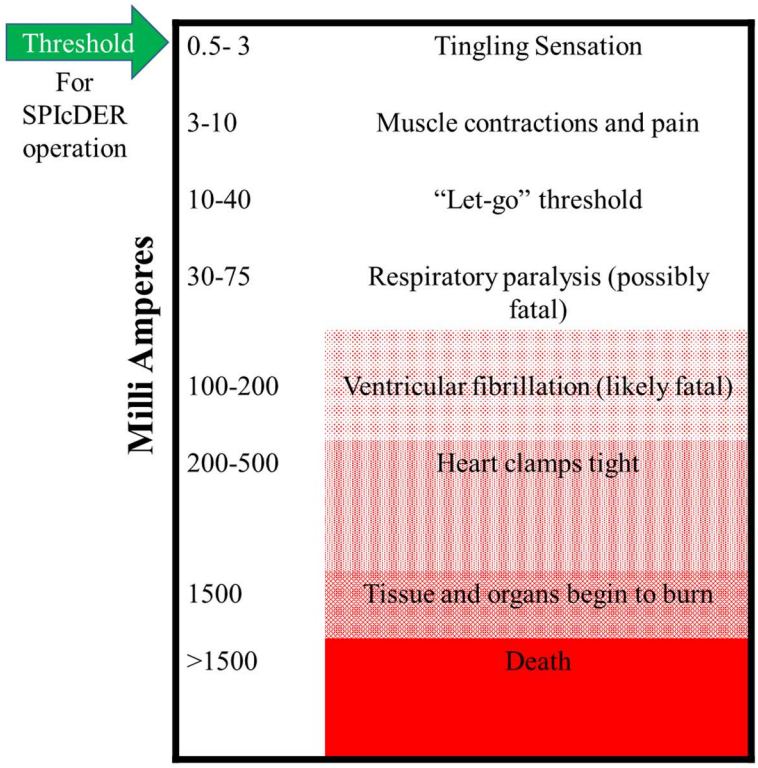

Figure 8.6-4. Physiological effects of exposures at various electric current levels (Reproduced using material from OSHA Regulations)

8.6.4. Oxygen Rich Atmosphere-Spark Ignition Hazard

Spacesuits provide breathable atmosphere for astronauts during EVAs. The pressure bladder of the spacesuit holds a 100% oxygen atmosphere at operating pressures ranging between 3.5-5.5 psi. Therefore, care must be taken to minimize any potential for ignition inside the suit and at leakage areas within the suit (generally the areas near the seams, disconnects). For example, the maximum leak rate requirement (not to exceed) for the ISS EMU is 1.38 kPa/min. For this analysis, an assumption is made that the gas does not spread beyond the leakage point (at the seals for example).

To avoid any hazards due to flammability with O_2 leakage, the dielectric strength of the pressure bladder material (and other layers of the suit) should be high enough to prevent any breakdown of the material that might lead to electric discharges and arcing becoming an ignition source to cause the hazard. Based on a parametric estimation using the thicknesses of layers and

material properties from the ISS EMU spacesuit, the dielectric strength and thickness of all the materials within the spacesuit are able to provide the required insulation to prevent insulation breakdown at operating voltages of 1000 V and the maximum voltage before which breakdown might occur at atleast one of the inner layers is estimated to be 1200 V. Table 8.7-2 provides details on the minimum thickness required to prevent dielectric breakdown of materials within the suit for a 1000 V and the ability of the current materials and thicknesses of the ISS EMU spacesuit to provide the required insulation.

Furthermore, the voltages at the inner layer should also be within the dielectric breakdown characteristics of O_2 gas. Experiments conducted by Radmilovic-Radjenovic et al. (2012) as shown in Figure 8.6-5 demonstrate that the minimum breakdown voltage for O_2 is 400 V. Results from analysis described in Part III section 8.8 indicate that the voltages at the inner layer of the spacesuit with SPIcDER system operating at 1000 V, 5 Hz frequency are two orders of magnitude below the breakdown voltage for oxygen (<4 V).

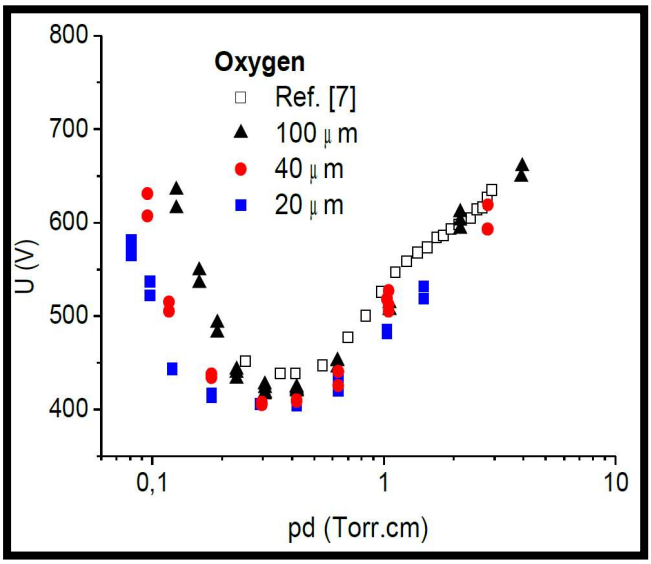

Figure 8.6-5. Breakdown voltages for oxygen gas experimentally measured (Radmilovic-Radjenovic et al., 2012)

It is recommended that ignition characteristics of spacesuit materials be measured for flight qualification to characterize the minimum current levels necessary for combustion of spacesuit materials (at a given voltage). If materials introduced into enriched oxygen environment cannot be controlled, measures to control static charge development within the suit can be implemented. These measures may be focused on preventing of charge accumulation by providing low resistance paths to ground by various grounding systems within the suit.

8.6.5. Toxicity of Carbon Nanotube Fibers

Safety concerns about the toxicity of CNT material have been raised in the recent years similar to those raised for asbestos. The concern is that if CNTs enter the working environment as suspended particulate matter of respirable sizes, they could pose an occupational inhalation exposure hazard (Lam et al., 2006). Crew exposure to CNTs embedded in the outerlayer of the spacesuit can result via inhalation, skin absorption or ingestion if not properly protected when astronauts doff their helmets and suits inside an airlock/crew-lock. It is therefore vital to assess the potential hazards and risks of using CNTs and provide guidance for the SPIcDER system.

To date, there is limited information on the toxicity levels of CNTs. A report published by NIOSH stated observing no cases of adverse health effects in workers using or producing CNT or CNF (NIOSH, 2013). Nonetheless, NIOSH and Lam et al.'s systematic review of several short-term and subchronic laboratory studies on animals (rodents) indicated CNT/CNF could cause non-cancerous adverse pulmonary effects including inflammation, epithelioid granulomas, fibrosis, and biochemical toxicity changes in the lungs that might impair pulmonary functions in animals.

There is limited data on dermal exposure and effects due to CNT/CNF. Due to established correlation between results of animal studies and adverse effects and similar lung effects in workers exposed to respirable particulates and air contaminants in dusty jobs, there is a concern that the observed effects due to CNT/CNF in animals could be relevant to human health risks (NIOSH 2002, 2006, 2011a, 2011b). In animal studies where CNTs were compared with other known fibrogenic materials such as silica, asbestos, ultrafine carbon black, the effects due to CNTs on animals were shown to be similar to that of other fibrogenic materials (Lam et al., 2004; Muller et al., 2005; Shvedova et al., 2005; Murray et al., 2012). However, due to the lack of sufficient evidence on the toxicity of the CNT material on humans, more research is needed to fully characterize the health risks of CNT/CNF. Even so, NIOSH reports approximately 0.5% to 16% of estimated risk of developing early-stage lung effects (slight or mild) over a working lifetime if exposed to CNT. This estimation was based on measurements conducted using NIOSH Method 5040, of 1 $\mu g/m^3$ (8-hr time-weighted average (TWA) as respirable elemental carbon). Based on these studies, NIOSH recommends that exposures to CNT and CNF be kept below the recommended exposure limit of 1 $\mu g/m^3$ 8-hr TWA of respirable elemental carbon during a 40-hr work week. Additionally, given the limited amount of data on dermal toxicity due to exposure to

CNT/CNF, it is suggested that protective clothing and gloves be worn when handling CNT based material. The use of such protective equipment might be necessary for post EVA operations when the SPIcDER system may be operated for post EVA cleaning.

All the toxicological studies conducted so far used free-form CNT/CNF products made from different manufacturing processes. The SPIcDER system however does not use raw CNT (power form) and uses the material in the form of yarns. In its finished form, the CNT yarns used as electrodes are internally aligned and non-fibrous in the yarn state, making them less prone to being a respirable particulate material. Toxicity of respirable material is greatly influenced by particle size of the material, with toxicity generally being greater with smaller particle size. In the finished form of a yarn, the CNT electrodes of the SPIcDER system are macroscopic and do not have airborne particles. Additionally, to increase the performance of the SPIcDER system, the electrodes are recommended to be insulated using flexible insulation material (Chapter 7). This insulation material will encapsulate the CNT yarns minimizing any direct exposure to the CNT material. For these reasons, CNT fiber used in SPIcDER system appear to pose little to no risks to astronauts that may occur due to inhalation.

Part III: Managing Exposure to Electric Fields and Arcing within Spacesuit

8.7. Spacesuit Material Layout

Spacesuits are made up of several layers of material, specifically the on-orbit and planetary suits that protect the astronaut from the harsh environments of space and planetary surface environments (example: Moon). For SPIcDER system operation, the presumption is that these several layers of the suit contribute to minimizing the electric field intensity at the pressure bladder and comfort layers generated by the electrodes embedded on the outerlayer, thus sufficiently insulating the astronaut inside the pressure bladder. Furthermore, it is anticipated that the layers also prevent any flammability issues due to pure O_2 within the pressure bladder. To explore the feasibility of this assumption, electric field analysis in ANSYS Maxwell has been conducted using the material layout of the spacesuit from the Apollo and ISS programs. The analysis is substantiated by coupon level experiments conducted as part of this research demonstrating how the diminishing effect of the EF intensity as a function of distance from the electrodes using spacesuit material layers. Table 8.7-1 provides a consolidated list of the several layers of the

Apollo and ISS EMU spacesuits, their functionality and thicknesses. Figures 8.7-1 and 8.7-2 provide an illustration of the layers from the Apollo and EMU spacesuits respectively.

Table 8.7-1. Material layout of the Apollo and ISS EMU spacesuits

Layer Description (Outside In)	Purpose	General Material Choice	Apollo Suits Layer #	Apollo Layer Materials	EMU Layer #	EMU Layer Materials	Thickness (mm)
Outer Protective Layer	Abrasion/Flame Resistance and MMOD protection over the integrated into the TMG	Ortho-Fabric, Beta Cloth/Teflon coated materials.[Highly reflective, flame resistant, poor heat conducting material]	1a 1b	Teflon cloth (T-164 8.5 oz woven Teflon fabric)- For Abrasion Resistance Teflon coated filament beta Cloth (beta 4484)-For Flame Resistance	1	Orthofabric-a multi-weave material with an outer surface primarily of Teflon Fiber (Goret0tex) and inner surface primarily of Nomex reinforced by Kevlar (Harris 2001).	0.51
Thermal Micro Meteoroid Garments (TMG)	Multi-functional layer providing thermal insulation and protection, micrometeoroids protection, radiation protection. Made of multiple layering of thermal layers under the outer layer. Retains metabolic temperature of suited crew.	Multilayer Insulation	2- 12	-Aluminized Kapton film/beta marquisette laminate (2 layers) -Alternating 5 layers of Aluminize Mylar (5 layers) Non-Woven Dacron (4 layers)	2-6	Aluminized Mylar backed with unwoven Dacron (five layers)	0.64
Second Micrometeoroid Layer /TMG Liner	Final layer of the MMOD protection/Liner		13	Neoprene-coated Nylon rip-stop	7	Neoprene-coated Nylon rip stop	0.23
Restraint Layer	Restraint (Shaping Layer) and control of longitudinal extension providing shape and mobility to pressure bladder	Generally been constructed using Nomex, Kevlar-Nomex weaves, High Tenacity Nylon, Rip Stop Nylon , Dacron, Capon etc.	14	Nylon restraint structure	8	Dacron woven with primary and secondary axial lines	0.28
Pressure Bladder	An elastic bladder that retains the gas pressure in the suit.	-Natural rubber, neoprene, polyurethane and latex compounds	15	Neoprene-coated nylon	9	Polyurethane- coated nylon	0.28
Liquid Cooling and Ventilation Garment	A tight fitting undergarment with a network of fine tubing circulating water for body cooling. Located closest to the skin	Ethylene Vinyl Acetate tubing Spandex as an attachment restraint member for the cooling tubes, bio medical instrumentation and comfort lining	16-18	Nomex Lycra Spandex Vinyl Tubing	10-12.	Nylon Spandex 1/16" ethyl vinyl acetate tubing for Water cooling	0.51
Body Comfort Suit	Layer of Nylon Chiffon between LVCG and astronaut's skin to prevent chaffing	Nylon Chiffon	19	Nylon restraint Structure	13	Nylon Chiffon	

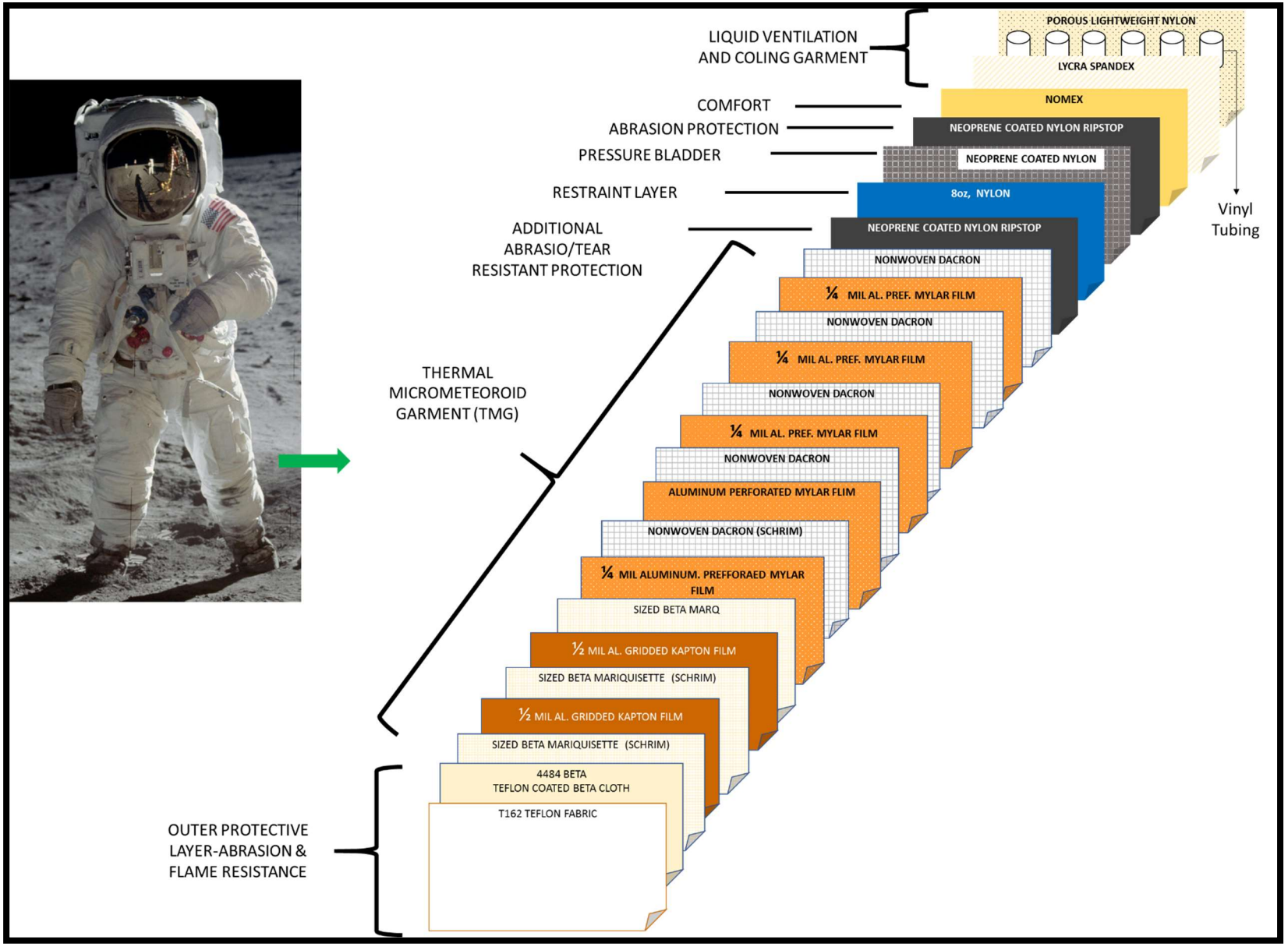

Figure 8.7.1. Apollo spacesuit material lay-up (information reproduced from NASA material)

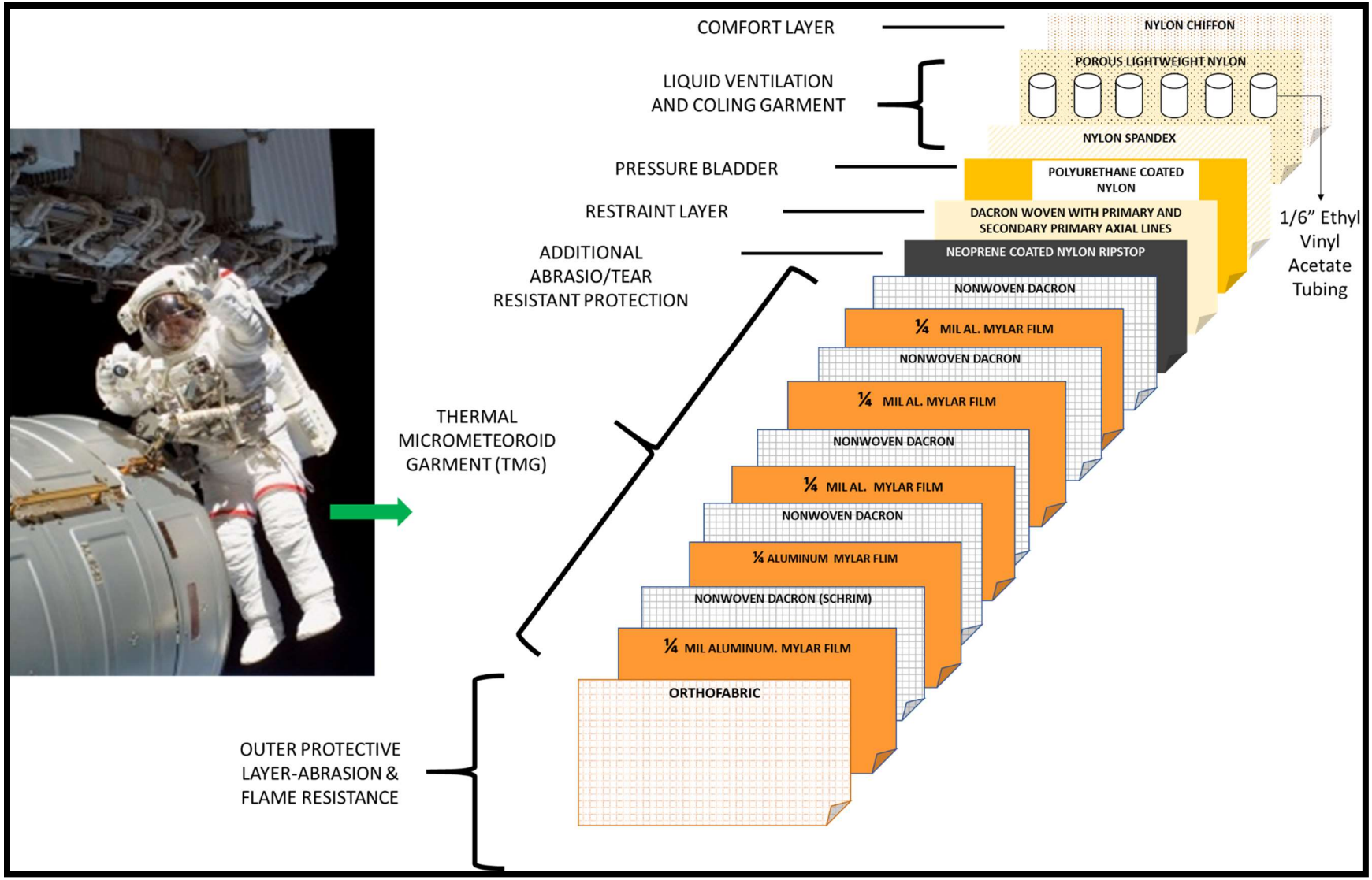

Figure 8.7.2. ISS EMU material lay-up (information reproduced from NASA material)

8.7.1. Breakdown Voltage

To understand the level of protection provided by the spacesuit layers from the high voltage input signal, the dielectric strength of each layer was identified using the material thickness information from the ISS EMU spacesuit layers. Subsequently, analysis was performed to evaluate the following parameters:

1. Evaluated the breakdown voltage for each layer based on the thickness of materials utilized in the spacesuit (ISS EMU)
2. Evaluated the thickness required to support the 1000 V input signal to operate the SPIcDER system

Table 8.7-2 shows the results from this analysis. Results show two values: (i) the evaluated voltage levels where breakdown occurs for each layer of material with its respective thicknesses currently utilized within the EMU spacesuit (column 8 in Table 8.7-2 and 2), and (ii) the thickness required per layer to withstand a 1000 V voltage without breakdown (Column 9 in Table 8.7-2). Assumptions were made on individual material thickness of materials where information on specific thickness of individual layers within the composite materials of the spacesuit were unavailable. The dielectric strength of the composite material such as Aluminized Mylar and Neoprene coated nylon would be different from individual values utilized for the analysis (conservative approach utilized in analysis). Nonetheless, results indicate that the current EMU spacesuit layers are capable of withstanding voltages within the range of SPIcDER operations (600-1000 V). Analysis shows that each layer is capable of withstanding up to at least 1180 V (lowest value among all layers). For future suit designs it is anticipated that additional layers might be added for thermal control (Apollo suit had more layers than EMU). Previous Apollo suits included two additional Kapton layers. These materials have very high dielectric strength similar to ones already evaluated in this analysis. Therefore, we can conclude that the layers of the suit will not pose safety hazards due to electric breakdown of materials. Other aspects of the SPIcDER operations-the electric field leakage and contact currents are described in section 8.8.

Table 8.7-2. Analysis for breakdown voltage of the individual layers of the ISS EMU suit lay-up

EMU Layer Materials	Thickness in suit (mm)	Material	Thickness for calculations (mm)	Dielectric Constant	Dielectric Strength (V/mil)	Dielectric Strength (V/mm)	Breakdwn voltage calculation based on EMU Suit thickness (V)	Thickness to prevent breakdown for 1000 V input signal (mm)	Thickness needed with 15% Safety Factor (mm)	Notes/Assumptions	Data Source
Ortho-Fabric-a multi-weave material with an outer surface primarily of Teflon Fiber (Gore-tex) and inner surface primarily of Nomex reinforced by Kelvar (Harris 2001).	**0.51**	Teflon	0.292	2.1	600	23622	6898	0.043	0.044	Gore tex in EMU Teflon in Apollo -Dielectric strength of composite material might be different	Miller, 1985
		Nomex	0.292	2.5	800	31496	9197	0.032	0.032		Dupont Material Data Sheet
Aluminized Mylar backed with unwoven Dacron (five layers)	**0.64**	Aluminized Mylar	0.00635	3.2	7000	275591	1750	0.004	0.004	Unknown thickness. Assumption is 1/4 mil. Composite material may have different dielectric strength. Using Mylar values	Grafix Plastics Company Material Daa Sheet
		Non-Woven Dacron	0.12165	2.6	1167	45932	5588	0.022	0.022	Unknown thickness. (7000V for 0.011inch)	The Gund Company Material Data Sheet
		Aluminized Mylar	0.00635	3.2	7000	275591	1750	0.004	0.004		
		Non-Woven Dacron	0.12165	2.6	1167	45932	5588	0.022	0.022		
		Aluminized Mylar	0.00635	3.2	7000	275591	1750	0.004	0.004		
		Non-Woven Dacron	0.12165	2.6	1167	45932	5588	0.022	0.022		
		Aluminized Mylar	0.00635	3.2	7000	275591	1750	0.004	0.004		
		Non-Woven Dacron	0.12165	2.6	1167	45932	5588	0.022	0.022		
		Aluminized Mylar	0.00635	3.2	7000	275591	1750	0.004	0.004		
		Non woven Dacron	0.12165	2.6	1167	45932	5588	0.022	0.022		
Neoprene Coated Nylon	**0.23**	Neoprene	0.05	6.7	600	23622	1181	0.043	0.044	Unknown individual thickness. The composite material might have different dielectric strength	Berger, 2009
		Nylon	0.2	3.5	400	15748	3150	0.064	0.065	Unknown individual thickness. The composite material might have different dielectric strength	Berger, 2009
Dacron woven with primary and secondary axial lines	**0.28**	Dacron	0.28	2.6	1167	45945	12865	0.022	0.022		The Gund Company Material Data Sheet
Polyurethane- coated nylon	**0.28**	Polyurethane	0.05	3.2	650	25591	1280	0.040	0.041	Unknown individual thickness. The composite material might have different dielectric strength	Prospector database
		Nylon Fabric	0.23	3.5	400	15748	3613	0.064	0.065	Unknown individual thickness. The composite material might have different dielectric strength	Berger, 2009
Liquid Ventilation Cooling Garment	**0.51**	Nylon-Spandex Tubing Nylon tricot	0.51	3.5	400	15748	8031	0.064	0.065	Assuming all 3 layers of LVCG are nylon	Berger, 2009

8.7.2. Voltages at the Inner Layers

Using the skin/body resistance values from Table 8.6-2, a simplified analysis was conducted to establish a requirement for maximum voltage level that cannot be exceeded at the inner suit layer (pressure bladder for conservatism) to prevent high currents passing through the astronaut body using Ohm's Law. Table 8.7-3 shows the currents in the body for voltages ranging from 1 V-120 V for the four body resistance values reported by different standards (NIOSH, IEC and Age et al., 2016) in Table 8.6-2. The table highlights the maximum voltage that cannot be exceeded at the inner layer for each body resistance standard based on the threshold current levels from Figure 8.6-3.

For conservatism and to envelope worst case scenarios, the lowest body resistance value for wet skin is utilized to establish the not-to-exceed (NTE) voltage levels at the inner layer of the spacesuit to prevent hazards due to electric shock (highlighted in Table 8.6-2). In reality, the PLSS and the thermal control of the spacesuit constantly perform to keep the temperatures and humidity of the astronaut's body at an optimal level and the skin may be dry. Additionally, the voltage level requirement is set for the pressure bladder layer. There are three more layers beyond the pressure bladder prior to contact with the body. Per the analysis conducted here, the maximum voltage at the inner layer cannot exceed 3V based on the body resistance value for wet skin from NIOSH standards corresponding to maintaining current levels below 3 mA. This value is anticipated to be higher than 3 V due to conservatism applied in this analysis. Results from the simulation study using ANSYS Maxwell, for a 1000 V input signal to the electrodes, the voltages at the inner layer of the spacesuit were analyzed. Results from the ANSYS simulation with spacesuit layers in section 8.8 show that voltages at the inner layer are infact less than 0.5 V which is an order of magnitude less than the threshold voltage of 3 V established here. Details of the numerical analysis and simulation are provided in the next section.

Table 8.7-3. Calculating NTE Voltage values at the inner layer of the spacesuit

Voltage (V)	Resistance-dry skin (Ω)	Current (mA) (I=V/R)	Resistance-wet skin (Ω)	Current (mA) (I=V/R)	Resistance-50% pop @ 25V, 100V (Ω)	Current (mA) (I=V/R)	Resistance (Ω)	Current (mA) (I=V/R)
1	100,000	0.0	1000	1	3250	0	1181	1
2	100,000	0.0	1000	2	3250	1	1181	2
3	100,000	0.0	1000	3	3250	1	1181	3
5	100,000	0.1	1000	5	3250	2	1181	4
10	100,000	0.1	1000	10	3250	3	1181	8
20	100,000	0.2	1000	20	3250	6	1181	17
30	100,000	0.3	1000	30	1875	16	1181	25
40	100,000	0.4	1000	40	1875	21	1181	34
50	100,000	0.5	1000	50	1875	27	1181	42
60	100,000	0.6	1000	60	1875	32	1181	51
70	100,000	0.7	1000	70	1875	37	1181	59
80	100,000	0.8	1000	80	1875	43	1181	68
90	100,000	0.9	1000	90	1875	48	1181	76
100	100,000	1.0	1000	100	1875	53	1181	85
110	100,000	1.1	1000	110	1875	59	1181	93
120	100,000	1.2	1000	120	1875	64	1181	102
	NIOSH Standard: Dry Skin		NIOSH Standard: Wet Skin		IEC Standard		Aga.et al	

8.8. Numerical Analysis for Electric Field and Voltage levels at the Inner Layers

To understand the electric field intensity and voltages at the inner layers of the spacesuit, numerical simulation was performed using ANSYS Maxwell. A 2D model of the spacesuit layers with material information from the ISS EMU suit layup and thickness values was developed and analyzed. Results from this analysis show that the electric field intensity and the voltages at the last layer (using pressure bladder as the last layer for conservatism) are an order of magnitude less than the OSHA EMF exposure limit of 4200 V/m and 3 V respectively. Figure 8.8-1 shows the model analyzed using the AC conduction solver in ANSYS and Table 8.8-1 shows the simulation parameters used for the analysis. For conservatism and due to unavailability of specific data on some layers of the spacesuit certain engineering assumptions were made for the analysis. These assumptions are listed below.

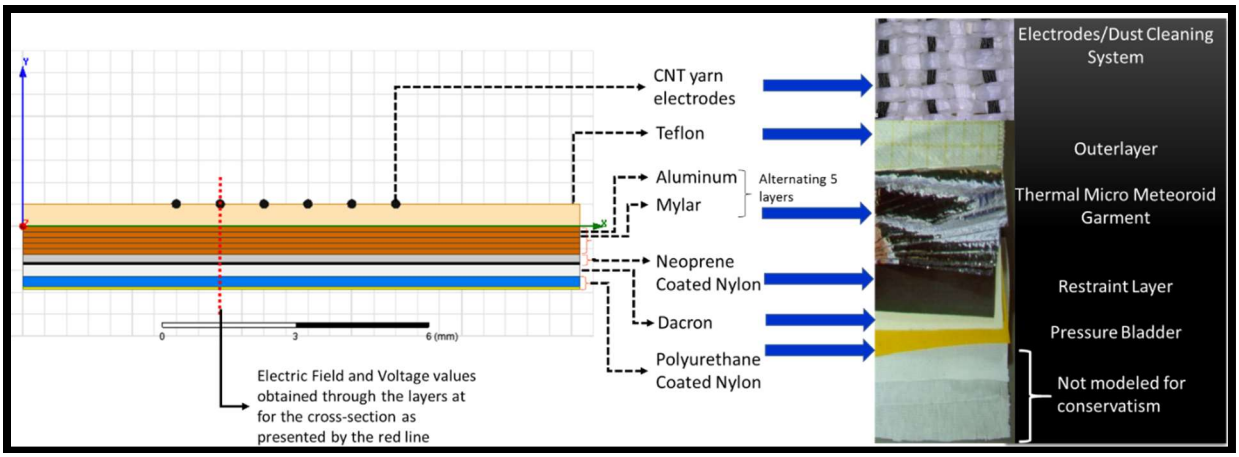

Figure 8.8-1. Modeling the spacesuit material layers in ANSYS Maxwell for electric fields and voltage values at the inner layer

Table 8.8-1. Parameters used for simulation

Parameter	Value_Safety Analysis
Electrode diameter	0.2 mm
Electrode spacing	1.0 mm
Electrode Material	CNT
CNT conductivity	310000 S/m
Surrounding Medium	Air
Electrode Voltages	1000V, 3 phase, sinusoidal wave
Excitation Frequency	5 Hz
Boundary Layer Distance	V=0 at 10 meters diameter
Suit Layers and Thickness	
Width of all layers	12.7 mm (0.5 in)
Outerlayer- Teflon	0.51 mm
Thermal Insulation- Aluminized Mylar (5 layers)	Total 0.64 mm thickness
Aluminum	0.00635 mm (1/4/ mil) 1 Ω/sq sheet resistance
Mylar	0.121 mm
Second MMOD Layer- Neoprene Coated Nylon	Total 0.23 mm
Neoprene	0.05 mm
Nylon	0.18 mm
Restraint Layer- Dacron	0.28 mm
Pressure Bladder- Polyurethane Coated Nylon	Total 0.28 mm
Nylon	0.23 mm
Polyurethane	0.05 mm

8.8.1. Assumptions for the Simulation

1. The outerlayer on the ISS EMU is orthofabric which has also been identified as a potential candidate fabric for future planetary spacesuits. This material is a proprietary material blend of Gore-Tex® (Teflon), Nomex® and Kevlar® for which there is no publicly available data on its specific composition and properties. Therefore, for this simulation the outerlayer and its properties are modeled as Teflon®.
2. Aluminized Mylar® for the simulation is depicted as a sheet of Aluminum ~6.35 microns thick (1/4 mil) over a Mylar layer. The Dacron Scrim that is part of the Aluminized Mylar fabric in the suit was not utilized as a separate layer but was made part of Mylar. This assumption was made due to unavailability of specific data on the composite material.
3. Aluminum sheet resistance of 1 Ω/sq was used which results in conductivity that is an order of magnitude lower than aluminum bulk conductivity.
4. The Neoprene coated Nylon composite material was depicted as two separate layers- Neoprene and Nylon due to unavailability of data on specific electrical properties of the entire composite material. Similar assumption was made for Polyurethane Coated Nylon Polyurethane coating and nylon were depicted as separate layers.
5. The model included all layers upto the pressure bladder. The last three layers that are the comfort layers and the liquid cooling garment was not modeled in the simulation. This is for maintaining margin and conservatism since the pressure bladder is what holds the oxygen.
6. The materials are modeled with uniform properties. Wear/ tear and manufacturing defects are not modeled.

8.8.2. Assessment Results

ANSYS analysis provided the magnitude of electric field and voltages at each layer of the suit. Specifically, these values were obtained from the top surface of an electrode through the cross-section of all layers of the suit, represented with a red line in Figure 8.8-1. For conservatism, the pressure bladder is considered the final layer where the electric field intensities and voltages are expected to be below the threshold values minimizing any hazards to the astronaut due to EF exposure and touch potential (contact current). Figures 8.8-3 through 8.8-5 show the values of the electric field intensities and voltages at each layer. These values represent the maximum and minimum values for a single cycle of the 3 phase AC input signal on the electrode (max and min

values of all phases). The electric filed intensity is an order of magnitude less than the threshold value (<500 V/m, compared to 4200 V/m requirement) at the pressure bladder (Polyurethane coated Nylon) and the voltages are less than 0.5 V (3 V requirement established) which correspond to current values within the safe range (see Figure 8.6-4). Results from this numerical simulation substantiate the earlier assumption that the many layers of the spacesuit provide sufficient protection from the EF exposures sue to SPIcDER system operation.

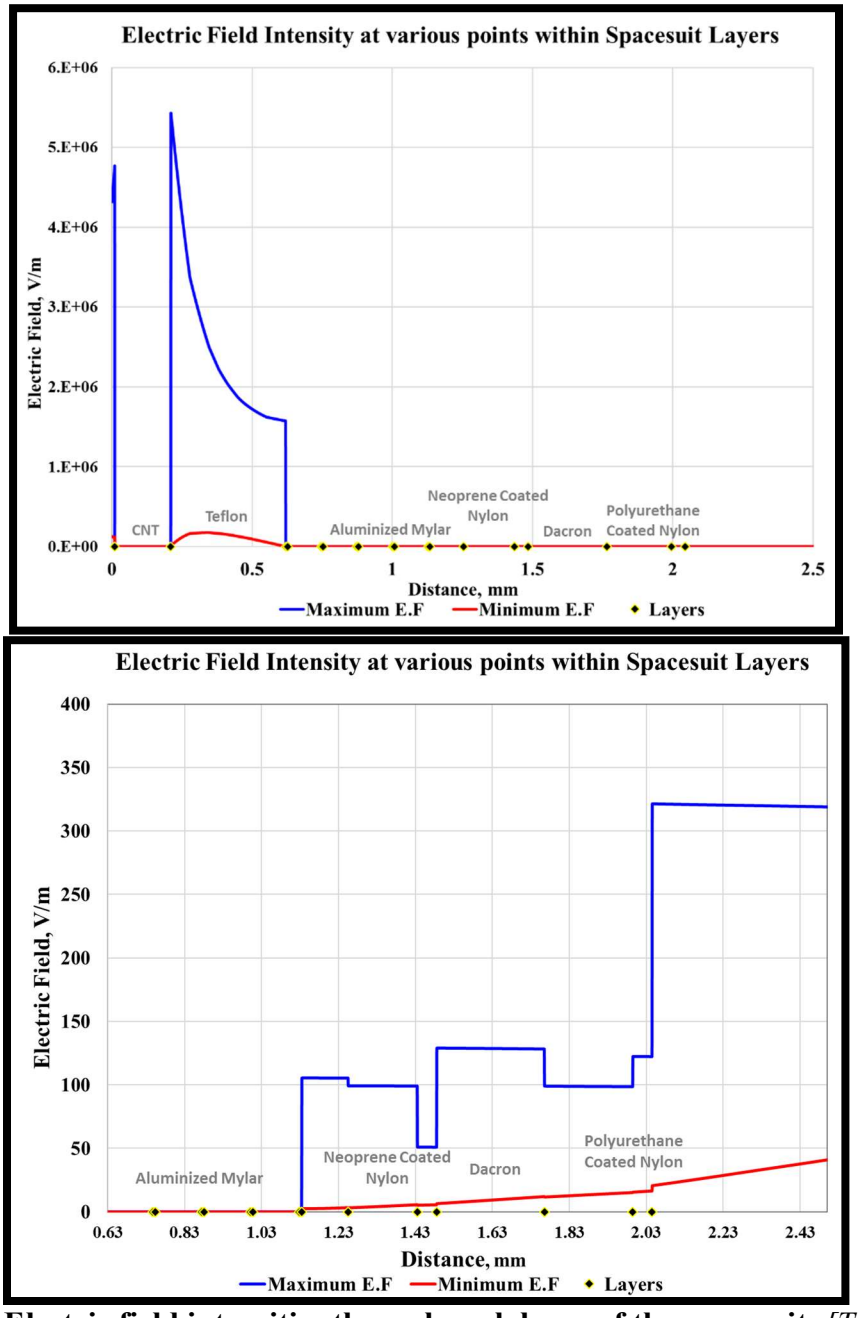

Figure 8.8-3. Electric field intensities through each layer of the spacesuit. *[Top] All layers [Bottom] Zoomed in to the show the last layer*

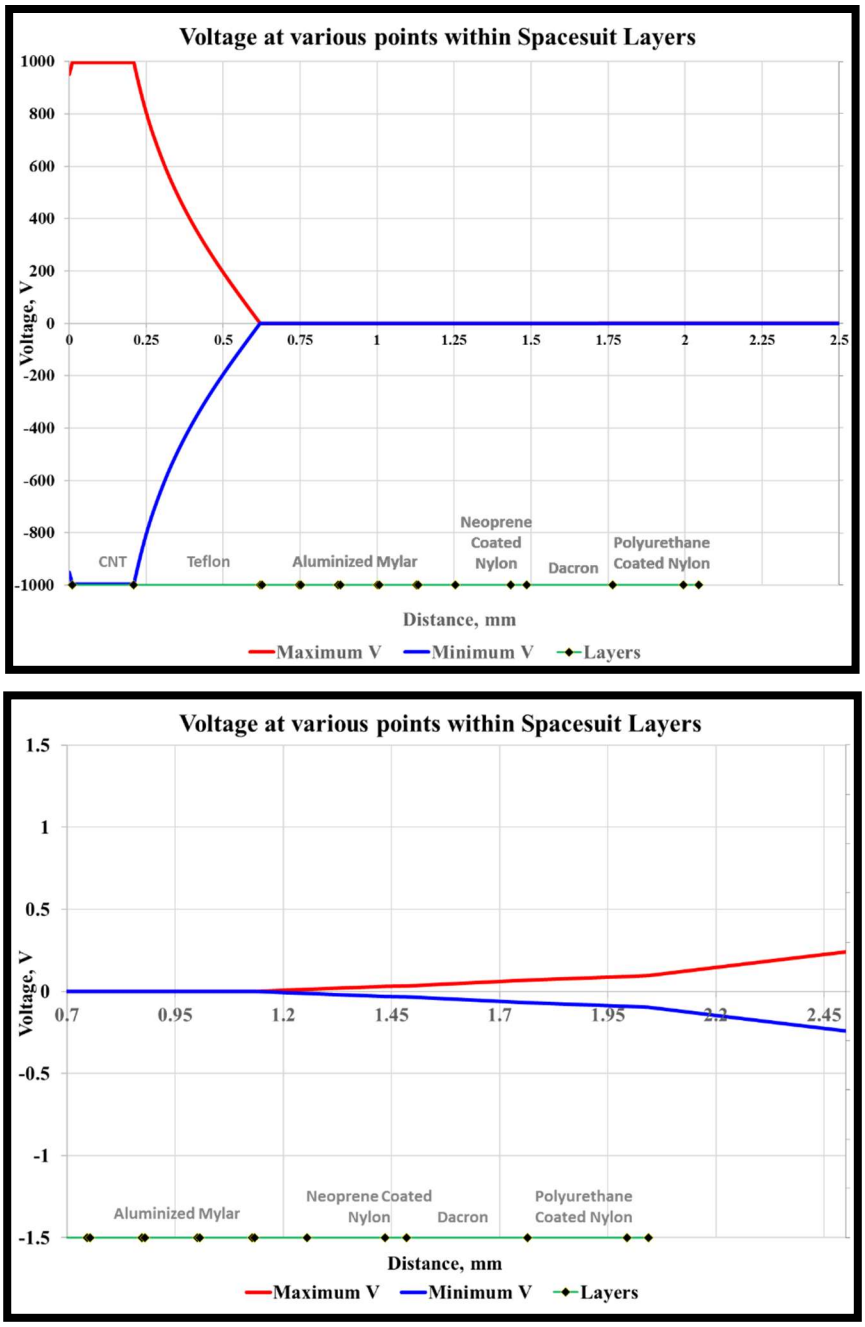

Figure 8.8-4. Voltage levels through each layer of the spacesuit. *[Top] All layers [Bottom] Zoomed in to show the last layers*

The current densities and magnetic field generated by the SPIcDER system were also evaluated using values from this simulation. Utilizing the Ampere-Maxwell equation as stated in Equation 42, the magnetic field generated around the electrode was calculated. Here B is the magnetic field, μ_o is the permeability ($4\pi \times 10^{-7}$ N.A^{-2}), I_{enc} is the conduction current through the electrodes, ε_o is the permittivity and ΦE is the electric flux given by Equation 43. Rearranging the equation for

magnetic field around the conducting electrode gives Equation 44. Since the electrodes are in an open circuit, I_{enc} can be considered negligible. The time to charge-discharge cycle relative to the frequency of the signal is on the order of 10^{-11} seconds. When the electrodes are charging and discharging, there is conduction current momentarily for that negligible amount of time, and once the electrodes are charged, there are no moving charges. Since the transient effect of moving charges happens within the picosecond range, the impact of magnetic field during this transient can be ignored. The term I_D represents the change of electric displacement field due to the electric field generated, k is the dielectric constant, for vacuum it is equal to 1. Equation 45 provides the overall magnetic field generated by an electrode at a distance r around the electrode

$$\oint \boldsymbol{B}.\boldsymbol{dl} = \boldsymbol{\mu_o I_{enc}} + \boldsymbol{\mu_o \varepsilon_o} \frac{\boldsymbol{d\Phi E}}{\boldsymbol{dt}} \tag{42}$$

$$\boldsymbol{\Phi E} = \oiint \boldsymbol{E}.\boldsymbol{dA} = \frac{\boldsymbol{Q}}{\boldsymbol{k\varepsilon_o}} \tag{43}$$

$$\oint \boldsymbol{B}.\boldsymbol{dl} = \boldsymbol{\mu_o I_{enc}} + \boldsymbol{\mu_o} \frac{\boldsymbol{I_D}}{\boldsymbol{k}} \tag{44}$$

$$\boldsymbol{B} = \frac{\boldsymbol{\mu_o I_D}}{\boldsymbol{2\pi r}} \tag{45}$$

From the simulations, the displacement current densities at the last layer of the spacesuit for a 1000 V, 5 Hz operation of the SPIcDER system results in a value on the order of 0.00025 mAm^{-2}. Using this value, the local magnetic field at the inner layer (r=~3 mm from the electrode) due to the displacement current by 1 electrode is approximated to be within the range of 4.5e−16 T. When this value is summed over approximately 10000 electrodes on the entire suit, it results in a field magnitude of 4.5e-12 T. This value is still negligible compared to the exposure level of 83 μT established by ICNRI given in Table 8.6-1.

8.9. Experimenting Electric Field leakage through Suit Layers

In addition to performing numerical analysis to analyze the intensity of electric field at the inner layers of the suit using ANSYS Maxwell, experiments were conducted to demonstrate the diminishing characteristic of the electric field intensity as a function of distance from the outerlayer layer of the spacesuit. A series of experiments described here facilitated visual demonstration of the electric field propagation across the spacesuit fabric and the minimum required insulation needed to protect astronauts wearing spacesuits embedded with the proposed SPIcDER system.

8.9.1. Methodology and Discussion

Experiments for electric field leakage through the spacesuit layers were conducted using one of the previously tested coupons embedded with CNT material from Chapter 5. The coupon made of orthofabric material, ~3 in x 2 in was embedded with six lines of CNT electrodes spaced approximately 1 mm apart. Experiments were conducted in ambient conditions using the same 3 phase power supply previously used.

A series of tests that utilized the same coupon in different configurations along with an additional layer of Orthofabric for insulation were performed to analyze how the electric field intensity minimized through the fabric layers. Furthermore, a second test series was performed using partial spacesuit material layup with fiver layers of Aluminized Mylar and a pressure bladder layer. Described below is the sequence utilized for the tests.

1. First, a set of experiments were performed to identify the performance of the EF with the coupon faced-up (CNTs exposed on top)
2. For the second set of experiments the orthofabric coupon was flipped (faced down) such that the CNTs electrodes were on the bottom side
3. For each of these face-up and face-down experiments, another plain Orthofabric coupon (with no CNTs) was placed over and under the main coupon to understand if the EF intensity is minimized through this second layer of the orthofabric or if the second layer made a difference in the EF propagation
4. For the partial material layup, five layers of Aluminized Mylar material was placed over the flipped Orthofabric material. Here CNT electrodes are facing the bottom.
5. The material layup test was repeated using a pressure bladder layer (Polyurethane coated Nylon material) over the Mylar layers

The approach used to identify whether the electric field intensity diminished through the layers was based on the dust cleaning performance. Dust was continuously dropped over each configuration while SPIcDER was active. If the dust dropped over the coupon while SPIcDER repelled, then the electric field intensity generated was high enough, if no dust repelled (in case when an insulation layer or Mylar layers were added,), then the intensity of electric field was assumed to diminished.

Tables 8.9-1 and 8.9-2 provide a list of these configurations tested and illustrates the results from the experiments. Experiments demonstrate that the intensity of the electric field generated at the outerlayer diminishes rapidly by adding just one additional layer of the orthofabric material with an average thickness of 0.51 mm on the backside (underside) of the main coupon (#5,6 in the Table 8.9-1). Results from Table 8/9-2 illustrate that adding just five layers of Mylar resulted in reduced electric field effect. In a real spacesuit, as seen in Table 8.7-2, the combined thickness of all the layers is on the order of 2.5-3.5 mm and most of the layers are made of electrically insulating materials with high dielectric strengths. Visual observations from these experiments substantiated by numerical analysis using ANSYS simulation described in the previous section with all the spacesuit layers validate the assumption that the many layers of the spacesuit provide sufficient buffer to protect the astronaut from high EFs generated on the outerlayer due to SPIcDER system operation.

Table 8.9-1. Experiments with two layers of orthofabric to understand the effects of insulating layers on electric field

LEGEND

Goretex Front-side of orthofabric	CNT Fiber Electrodes	Electric Field Observed/ Dust Repulsion
Nomex+Kevlar Back-side of orthofabric	Lunar Dust simulant being dropped over the coupon	Electric Field Intensity Diminished/ No Dust Repulsion

	Configuration	Explanation	Results from Tests	Comments
1	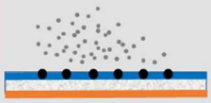	• Nominal Operation • Front-side up (Gore-Tex) • Dust dropped over the top side (CNTs facing towards dust)		• Nominal operation of the dust cleaning system • Dust is repelled • Strong electric field observed
2	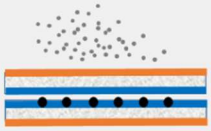	• Extra Layer of OrthoFabric on top of original coupon • Gore-Tex touching Gore-Tex • Dust dropped over the top most layer		• Nominal operation of the dust cleaning system with insulation on top • No dust repulsion observed • Assumed electric field intensity diminished
3	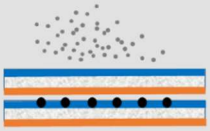	• Extra layer of Orthofabric on top of original coupon • Nomex of new layer touching Gore-Tex side of original coupon (where CNTs are embedded) • Dust dropped over the top most insulating layer • Provides indication if an extra layer of orthofabric (insulation) diminishes Electric field intensity	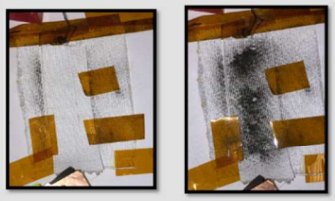	• Nominal Operation of the dust cleaning System with insulation on top • No dust repulsion observed • Assumed electric Field intensity diminished with one additional layer of orthofabric
4	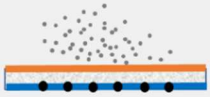	• CNT embedded coupon flipped with Back-side Up (Nomex/Kevlar) • CNT facing down • Dust dropped over the back-side • Provides indication if Electric Field propagates into the back side of the coupon		• Dust repulsion observed • Electric field propagates through first layer of ortho fabric

Table 8.9-1 cont.

	Configuration	Explanation	Results from Tests	Comments
5	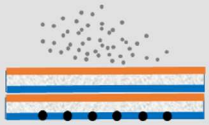	• CNT embedded coupon flipped with Back-side Up (Nomex/Kevlar) • CNT facing down • One extra layer of Orthofabric over main coupon (Gore-tex touching Nomex) • Dust dropped over the back-side of top layer • Provides indication if Electric Field propagates into the top insulating layer from the bottom	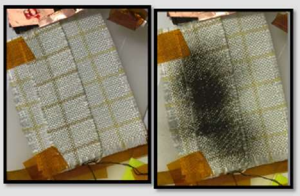	• No dust repulsion observed • Electric field diminishes through second layer • Therefore 1 insulating layer seems to remove effect of electric field
6	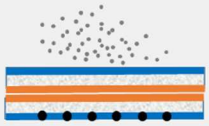	• CNT embedded coupon flipped with Back-side Up (Nomex/Kevlar) • CNT facing down • One extra layer of Orthofabric **over** main coupon (Gore-tex touching Nomex) • Dust dropped over the back-side of second layer • Provides indication if Electric Field propagates into the second insulating layer		• No dust repulsion observed • Electric field diminishes through second layer • Therefore 1 insulating layer seems to remove effect of electric field
7	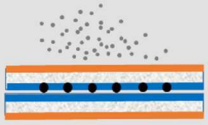	• CNT embedded coupon flipped with Back-side Up (Nomex/Kevlar) • CNT facing down • One extra layer of Orthofabric **under** main coupon (Gore-tex touching Gore-tex) • Dust dropped over the back-side of second layer • Provides indication if Electric Field is effected/ diminished by the layer underneath the main coupon	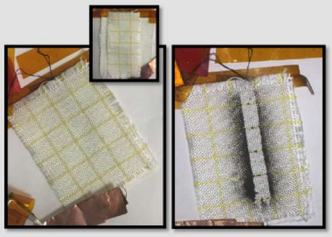	• Dust repulsion observed • Electric field is not affected
8	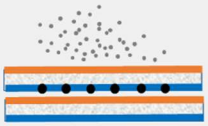	• CNT embedded coupon flipped with Back-side Up (Nomex/Kevlar) • CNT facing down • One extra layer of Orthofabric **under** main coupon (Gore-tex touching Nomex) • Dust dropped over the back-side of second layer • Provides indication if Electric Field is effected/ diminished by the layer underneath the main coupon	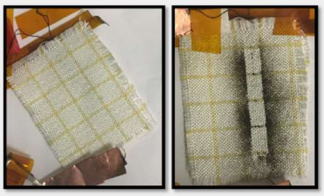	• Dust repulsion observed • Electric field is not affected

Table 8.9-2. Experiments with partial spacesuit material layup (Orthofabric, Aluminized Mylar, Polyurethane Coated Nylon)

	Configuration	Explanation	Results from Tests	Observations
1	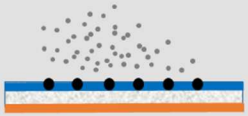	• CNT embedded coupon flipped with Back-side Up (Nomex/Kevlar) • CNT facing down • Dust dropped over the back-side • Provides indication if Electric Field propagates into the back side of the Orthofabric material	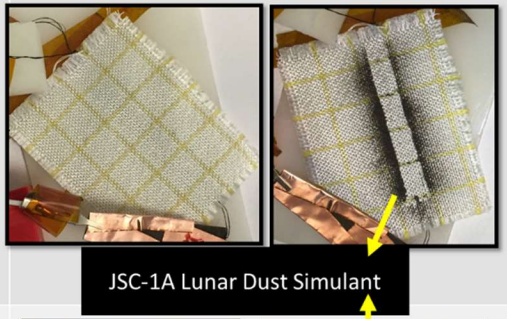	• Nominal operation of the dust cleaning system • Dust is repelled • Strong Electric Field observed
2	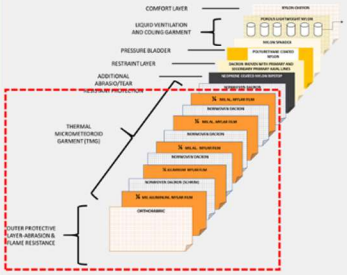	• 5 layers of Aluminum coated Mylar on the backside of Orthofabric (Nomex-Kevlar side) • Represents partial layout of the spacesuit • Dust dropped over the top most layer • Provides indication if Electric Field propagates through the Mylar layers		• No dust repulsion observed • Electric field intensity greatly diminished • Validated using ANSYS Maxwell simulation (graphic below from sim set-up)) 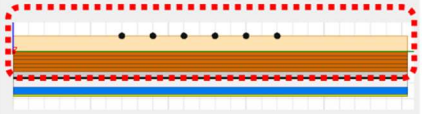
3	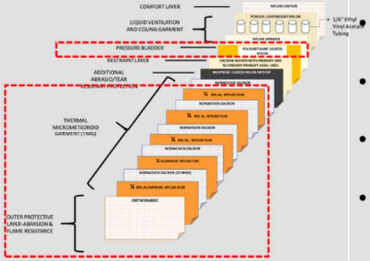	• Orthofabric+ 5 Mylar Layers+ Pressure Bladder Layer • Represents partial layout of spacesuit • Few intermediate layers not included (conservative case) • Dust dropped over the pressure bladder top most insulating layer • Provides indication if Electric Field propagates into the pressure bladder material	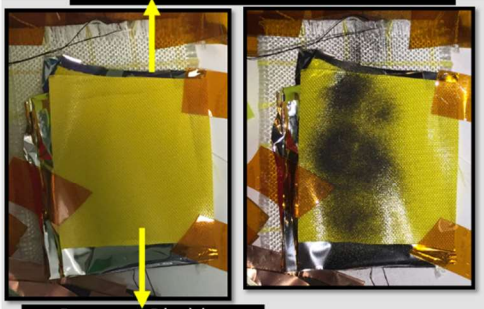	• No dust repulsion observed • Electric field intensity greatly diminished • Validated using ANSYS Maxwell simulation (graphic below from sim set-up) 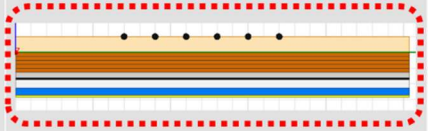

8.10. Recommendations for Safety

Astronaut safety is essential for human space exploration missions. Based on the analysis and experiments conducted here to identify the safety issues and hazards presented by the SPIcDER system, a few precautions would be required prior to implementing the SPIcDER into the spacesuit system. Although results from simulations and experiments show that the spacesuit layers provide the required protection from electric field leakage and touch potentials, recommendations in the design and operational aspects are provided for integrating SPIcDER into the spacesuit system to attain a stable protection level. Further analysis and details on these safety hazards is beyond the scope of this dissertation and recommended for future research plans if the system is implemented.

1. Recommendations for Spacesuit Material Lay-up

- **Shielding for electric field exposure**: Exposure to electric fields can be prevented by using Electromagnetic shielding techniques. The aluminum coating on the Aluminized Mylar layers is shown to be sufficient to provide shielding from electric field exposures. For effective shielding, the aluminum coating on the Mylar layers should be consistent without perforations and the metallized layers should be grounded to a common ground plane along with the power supply to help discharge any charge build up within the Mylar layers. Investigation of the effects of wear and tear were not included in the current analysis. Future analysis for flight suit implementation should evaluate the effects of wear and tear on the EF and voltage levels at the inner layers and identify if the assumptions made within this research hold. If the assumptions on consistency of the material properties are overcome by wear/tear and manufacturing defects of the materials, , an additional layer of flexible conductive material and/or Aluminized Mylar may be added to the suit lay-up and well-grounded for additional shielding to electric field radiation. As part of flight qualification of suits embedded SPIcDER system it is also recommended to include testing for the EMF and voltage levels at the inner layer.

- **Insulating the CNT electrodes:** Proof of concept experiments conducted during this research utilized uninsulated CNT electrodes. Insulating the CNT electrodes using flexible insulation material will help minimize direct exposure of CNT material to the astronauts (in addition to increasing the breakdown voltage of the electrode network and cleaning performance). Simulation showed that the addition of a 20 μm thick Teflon based insulation around each electrode results in approximately 10% decrease in the electric field magnitude only at the top

surface of the electrode at the same input voltage for that of an uninsulated electrode (1000 V, Figure 8.10-1). However, this reduction in the electric field magnitude can be overcome by increasing the operating voltage by just 50-100 V. This increase in operating voltage is still within the dielectric strengths of the suit materials and, the electric field magnitude and voltage values at the inner layer of the suit with the insulation are still an order of magnitude below the safety threshold levels established. Adding Teflon type insulating material will also help with the thermal properties by maintaining the α (solar absorptivity) at the same level as the Orthofabric material.

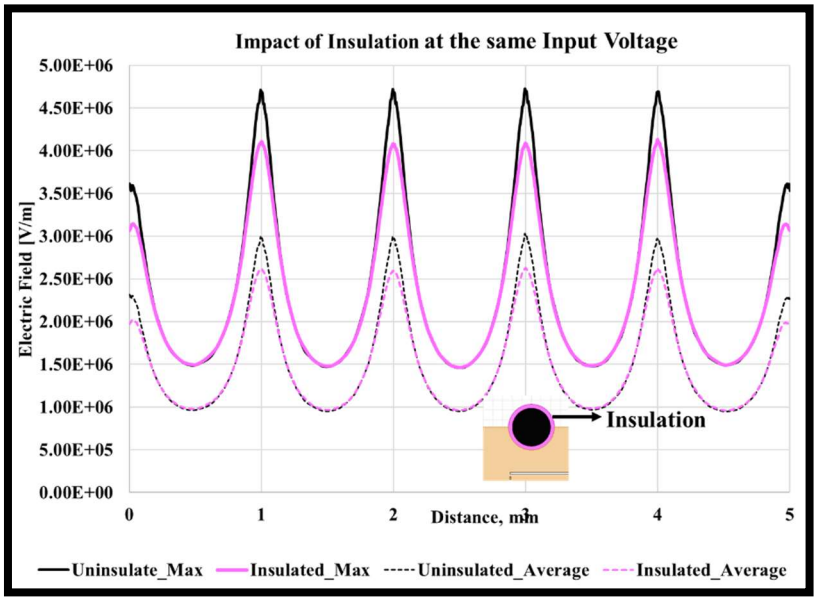

Figure 8.10-11. Impact of insulating electrodes on electric field magnitude at the same input voltage for uninsulated and insulated electrodes

2. Recommendations for EVA Operations

- **Operational Procedures**:

The SPIcDER system can be optimized to be operated in a continuous or pulse mode as explained in Chapter 7, section 7.3-2. To increase the safety margin during SPIcDER operations and to minimize any corona discharge or interference, a review and evaluation of the various operational modes to meet operational and safety requirements is necessary to fully implement the system. For example, in addition to continuously operating, the SPIcDER system can be operated in short bursts of time (short duration). This might be particularly helpful when the astronaut notices that the suit is already prone to dust and then powers ON the system to remove the accumulated dust. During experiments conducted in the laboratory using the SPIcDER system, this operational mode corresponds to the 'static dust' test series. Using this operational mode, the astronaut can pay attention to the operation while the system is powered ON and turn it off as needed. This could allow minimizing any potential for arcing while astronauts are on EVAs. Furthermore, various areas on the suit can be hooked up to multiple modes of operation, such that some of the areas can be operated in the pulse mode where astronauts can pay close attention to

the suit while the SPIcDER system is operational in case arcing occurs, while other areas that are less prone to overlapping electrodes may be operated continuously. For example, the electrode network on the backside of the suit, specially behind the knees can be operated after EVAs.

3. Recommendations for Electrode Fabrication to Minimize Arcing

- **Patterning/Fabrication of Electrodes**: To prevent arcing between different sections of the suit with embedded electrodes, fabrication of the electrodes into the outerlayer of the suit should be performed such that the electrodes do not contact or overlap. The posterior of the suit including the backside of the knee which tend to wrinkle/fold during regular walking motion fall into this category where normal fabrication and operation of the electrodes needs to be optimized. This can be achieved by fabricating segments of electrode networks that can be operated discretely (more details in Chapter 9, section 9.3-4). For example: The electrode network can be embedded in segmented fashion such that the front side of the suit SPIcDER system can be operated during EVAs, while the inner side of the knees/leg portions that could touch frequently while walking during EVA operations can be operated when the astronauts are stationary and upright and/or during post EVA operations. Additionally, a SPIcDER technique based tool/gloves/mittens may be utilized later to remove any dust particles adhered to this section of the suit. See Figure 8.10-2 for recommendations on areas that should could be embedded with segmented electrode patterns that can controlled and operated separately.

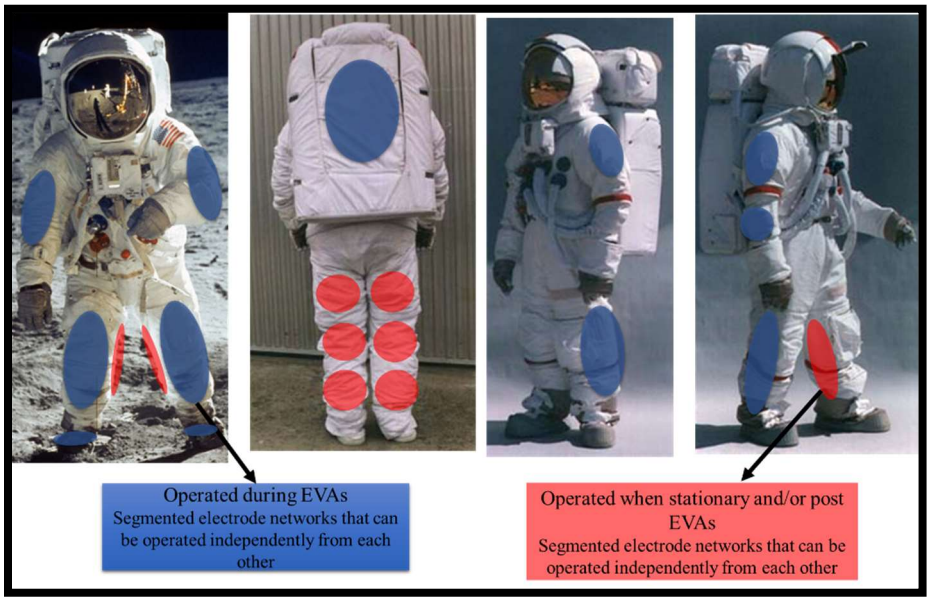

Figure 8.10-1 Recommendation for segmented patterns of the electrode network that can be operated independent from each section

- **Quality Inspection:** Inspections during manufacturing should include procedures on verifying tolerance on alignment of CNT electrodes, minimum spacing, and no overlapping of CNT electrodes. During routine maintenance of suits during real-time mission operations, procedures should include inspection checks for wear and tear of suits including unintended displacement of electrode wires within suit areas with embedded electrode network. Procedures for repair of wear and tear and suit maintenance should be provided.

4. **Recommendations for Electronics Design**
   - **Close access to power switch**: The power switch to turn on/off SPIcDER should be located on the suit such that the astronaut can easily reach to turn off the active system in case arcing between electrodes is observed. A recommendation would be to possibly locate the switch on the wrist or on the suit Display and Control (D&C) system that the astronaut can readily access. This will help to switch off the system if corona or arcing occurs between the suit and ground.
   - **Electronics Design**: The design of the voltage signal generator electronics circuit and power system should include a circuit breaker design such that the system trips when high current spikes/short circuit occurs. These events may be caused either due to electrical breakdown, arcing and/or when two electrodes come in contact. The circuit breaker will trip and shut off the electrical flow from the signal generator to the electrodes protecting any further arcing or damage to the SPIcDER system and potential hazards to the crew.
5. **Recommendations for Preventing Inadvertent Electromagnetic Exposure or Arcing to Other Equipment**
   - **Electromagnetic shielding**: Shielding will be required for other systems/electronic equipment within the spacesuit system susceptible to EF. All tools and equipment being used during EVAs that might interact with the suit embedded with active electrodes should be properly insulated and shielded to minimize any hazards. Use of bonding and grounding techniques are required to prevent buildup of potential differences on isolated conductive parts of a system.

8.11. Summary

Safety aspects related to implementing the SPIcDER system for flight suit implementation have been recognized and described in this chapter. The underlying assumption that the several

layers of the spacesuit would provide the required insulation and shielding to the crew from the active electrodes has been numerically analyzed. A 2D simulation model for evaluating the electric field and voltage intensities has been developed. The analysis was substantiated with experiments that demonstrated that the materials used in the Apollo and ISS EMU suits provide the required shielding to operate the SPIcDER system. Recommendations for improving safety margin to implement the SPIcDER system are also provided and are summarized in Table 8.11-1 below.

Table 8.11-1. Summary of suggested recommendations for preventing hazards due to SPIcDER Operations. 'X' represents hazards that can be prevented due to suggested changes.

Recommendations	Electric Field Exposure	Arcing	Potentials/ Contact	O2 Atmosphere	Toxicity of CNT
Spacesuit Layup					
Consistent Aluminized coating over Mylar layers	X		X	X	
High Dielectric Strength Materials	X	X	X	X	
CNT electrodes					
Insulation					X
Segmented Patterning		X			
Electronics Design					
EMF Shielding	X				
Circuit Breakber/Remote Power Conrol (RPC) trip		X			
Reachable location for power switch		X			
Operations					
Segmented Operations		X			
Pulse versues Continuous Modes		X			

PART IV
EXPERIMENTAL VALIDATION
SPIcDER Implementation on Spacesuit Prototype

CHAPTER 9: EXPERIMENTAL VALIDATION

"There is no such thing as a failed experiment, only experiments with unexpected outcomes"- *Buckminister Fuller*

Chapters 5-7 focused on small-scale demonstrations, detailed modeling, and key parameters that characterize the SPIcDER dust cleaning system and its performance for spacesuit application. Previous experiments using 2-3 inch samples of spacesuit orthofabric material embedded with CNT fiber electrodes have demonstrated that the SPIcDER system is capable of repelling > 80% of JSC-1A lunar dust simulant particles with grain sizes between 10-75 μm in ambient conditions, in both dynamic and static dust loading. This cleaning using the SPIcDER system resulted in less than 10% of the fabric area covered in residual lunar dust. In this chapter, the development and testing of a scaled functional prototype, representative of the joint knee section of a planetary spacesuit embedded with the SPIcDER system are discussed. Results are analyzed to assess the validity of the scalable functionality of the SPIcDER system. The prototype constructed for this research to demonstrate SPIcDER's scalability utilizes specifics of the NDX-2 lunar spacesuit developed by UND. It is expected that the scaled SPIcDER system provides comparable results observed during coupon testing documented in Chapter 5. The chapter correspondingly provides recommendations for manufacturing when scaling the system to cover larger areas of the spacesuit based on lessons learned from building and testing the prototype.

9.1. Test Objectives

Primary objectives of the experiment are two-fold

1. Assess the feasibility of manufacturing the SPIcDER system to a full-scale spacesuit leg, specifically the knee-joint section of a spacesuit
    - The knee portion has been chosen because of the substantial evidence from Apollo missions on the dust coverage and abrasion of the knee area of the suit and the complexity for manufacturing a joint section

2. Validate the dust cleaning performance of the SPIcDER system on a scaled model that was observed on small scale demonstrations.
    - The main performance metric in the scaled SPIcDER system is the residual (%) coverage of dust remaining after cleaning. Successful mitigation is defined as residual dust coverage less than 25% of the spacesuit fabric area shielded by electrodes.

Experiments were conducted in ambient conditions with the scaled model due to size constraints of the vacuum chamber available. Initial investigations on the feasibility of the SPIcDER system operation and performance in vacuum conditions were conducted utilizing 3-inch sized coupons in a vacuum chamber at the Electrostatics and Surface Physics Laboratory at KSC.

Secondary objectives of the experiment encompass the following

- Validating functionality of SPIcDER on a pressurized suit
- Identifying performance differences if any for straight and bent knee conditions
- Identify limitations of SPIcDER performance
- Identify manufacturing improvements to enhance dust cleaning performance

9.2. Methods and Materials

9.2.1. Prototype Development

The scaled prototype developed for this research is a knee-joint section of a spacesuit. Dimensions for the model are based on the NDX-2 lunar spacesuit prototype. NDX-2 is an advanced lunar EVA suit prototype developed by UND under a NASA grant to demonstrate usability for extended lunar missions with operating pressures of 4 psi (de Leon and Harris, 2011). NDX-2 features a malleable hard upper torso with a rear entry closure and soft lower torso elements. The restraint layer knee joints are an asymmetrical semi-toroid joint with elements from flat pattern joint. Figure 9.2-1 shows the NDX-2 lunar spacesuit prototype without the thermal insulation and outerlayer cover. The pressure bladder-restraint assembly is covered by orthofabric or similar candidate fabric to protect the internal components of the suit from dust, abrasion, flame resistance, MMOD and for thermal insulation.

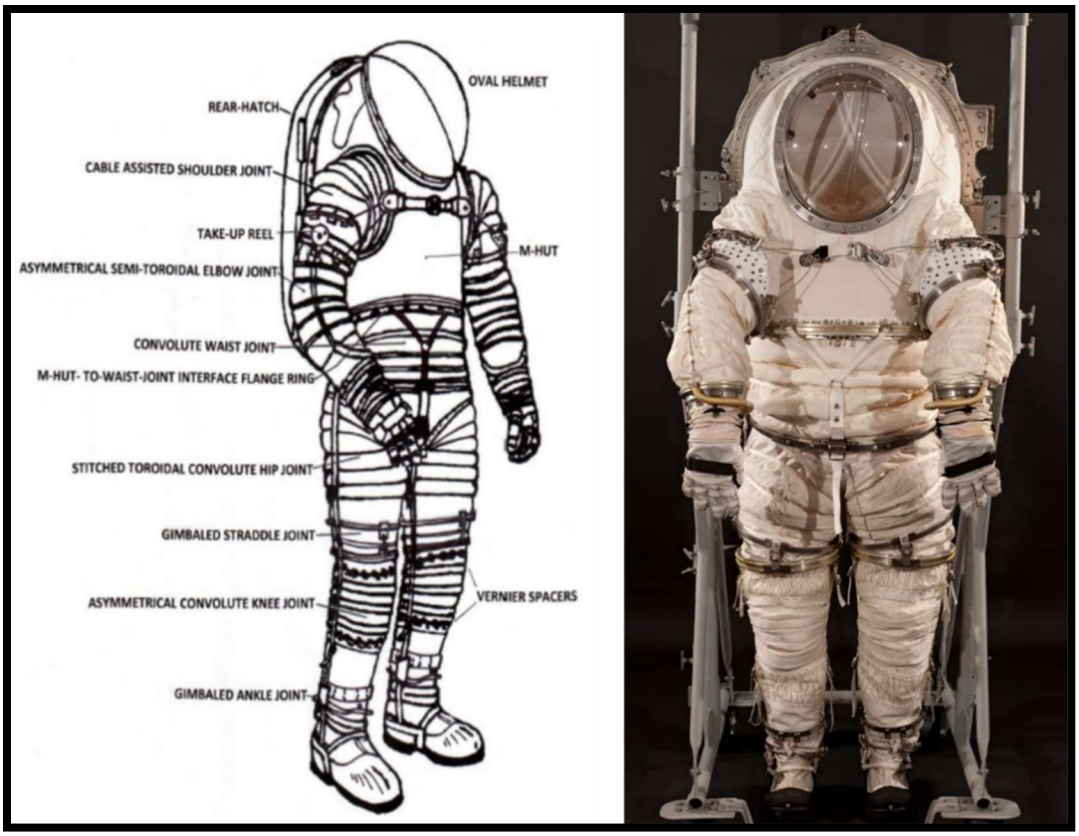

Figure 9.2-1. NDX-2 Lunar EVA spacesuit prototype built at UND (de Leon and Harris, 2011). *Model shown here is only the pressure garment with the white restraint layer. Orthofabric or other candidate fabric would cover the outerlayer*

9.2.2. Prototype Construction

There are two aspects of the prototype construction. First is the fabrication of the outerlayer made of orthofabric material and the placement of the CNT fiber electrodes. The second is the pressure bladder with the restraint layer that is constructed separately with aluminum sealed ends to facilitate build of a module that can be pressurized to conduct dust experiments on a pressurized module representative of the state of the spacesuit during an EVA on the lunar surface.

9.2.3. Outerlayer Construction and SPIcDER Fabrication

The outerlayer for the prototype was designed based on a flat pattern joint design utilized in the ISS EMU outerlayer and the NDX-2 lunar spacesuit outerlayer.

- **Flat-Pattern Joint Outerlayer**

The flat-pattern joint design is a commonly used pattern in spacesuit joint design, especially the outerlayer where joints are all fabric in most spacesuits. The flat pattern joint is an all fabric

joint fabricated using gore segments that are shaped as pleats with excess material built into the fabric on the outer sides of the joint. These gores are tucked into a series of transverse pleats/patterns in telescopic fashion. When pressurized and flexed, these pleats balloon out and form a series of semi-convolute shapes (Harris, 2011). The excess material built into the tensile side (font of the knee) of the joint provides sufficient material to stretch when the knee bends or flexes allowing the internal volume of the space suit to remain approximately constant. On the compressive side (back of the knee), the gores roll over one another when the joint bends. Longitudinal restraining straps are stitched along both sides of the joint (along the neutral axis). Shown in Figure 9.2.2 is an example of flat pattern joint from Harris (2011) and a close-up of the unpressurized ISS EMU outerlayer flat-pattern joint.

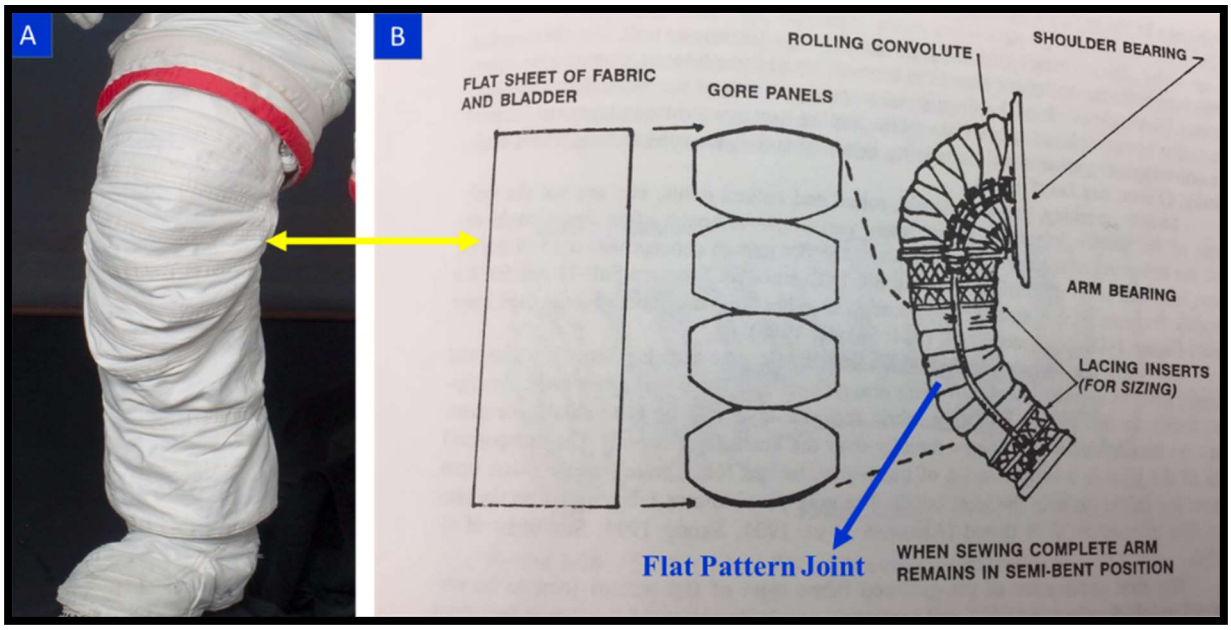

Figure 9.2-2. [A] Flat pattern knee joint of ISS EMU (unpressurized), [B] Flat Pattern knee joint concept (Harris, 2011)

The fabric flat pattern joint designed for the current experiments utilizes gores as shown in Figure 9.2-2. After the outer-layer was fabricated, it was embedded with the CNT electrode network in the orientation shown in Figure 9.2-3.

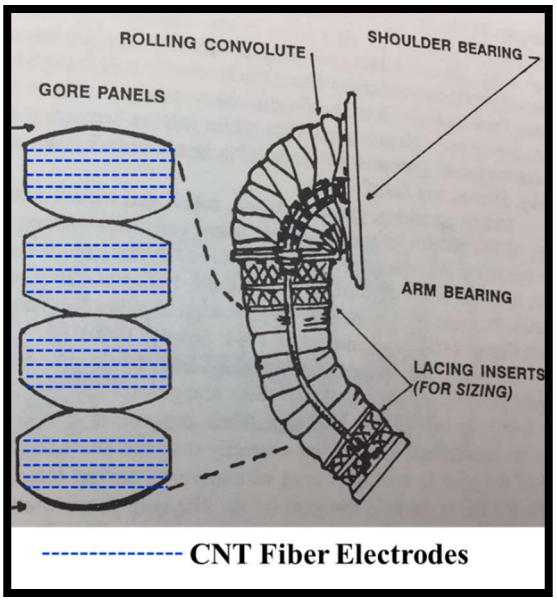

Figure 9.2-3. Orientation of CNT Fibers

- **CNT fiber Placement and Orientation**

The electrode characteristics for the scaled model were based on parameters that provided optimal results during the proof of concept demonstrations in Chapter 5, simulation studies from Chapter 6, and orientation of the weave of the orthofabric material, that provided optimal dust cleaning performance using the SPIcDER system.

CNT fibers on the model were embedded such that the parallel electrodes were circumferentially oriented throughout the length of the electrode covering the entire length of the front section of the knee. The major factor that impacted the decision for the orientation of the fibers was the ease of manufacturing and terminating the electrodes circumferentially rather than longitudinally. Another factor that played into this orientation is that if the electrodes were placed longitudinally, since the pleats expand longitudinally, embedding the electrodes might constraint opening of the pleats when the knee flexes. However, this was only an assumption and was not physically confirmed. The third factor that played a role in this orientation was the direction of electric field wave which in this case travels from top of the leg to the bottom of the leg moving the particles in the longitudinal direction. The assumption is that, the particles would be moved towards the bottom of the leg with gravity assisting the 'fall' of the particles.

Prior to embedding the CNT fibers on the main orthofabric material, a cotton fabric was fabricated to replicate the flat-pattern joint and test various methods for orientation, spacing, fabrication techniques and terminating the CNT fibers. Lessons learned from the practice session

were implemented on the final prototype. Figure 9.2-4 shows the cotton fabric with black threads representative of CNT fibers in the orientation that would be used for the final prototype.

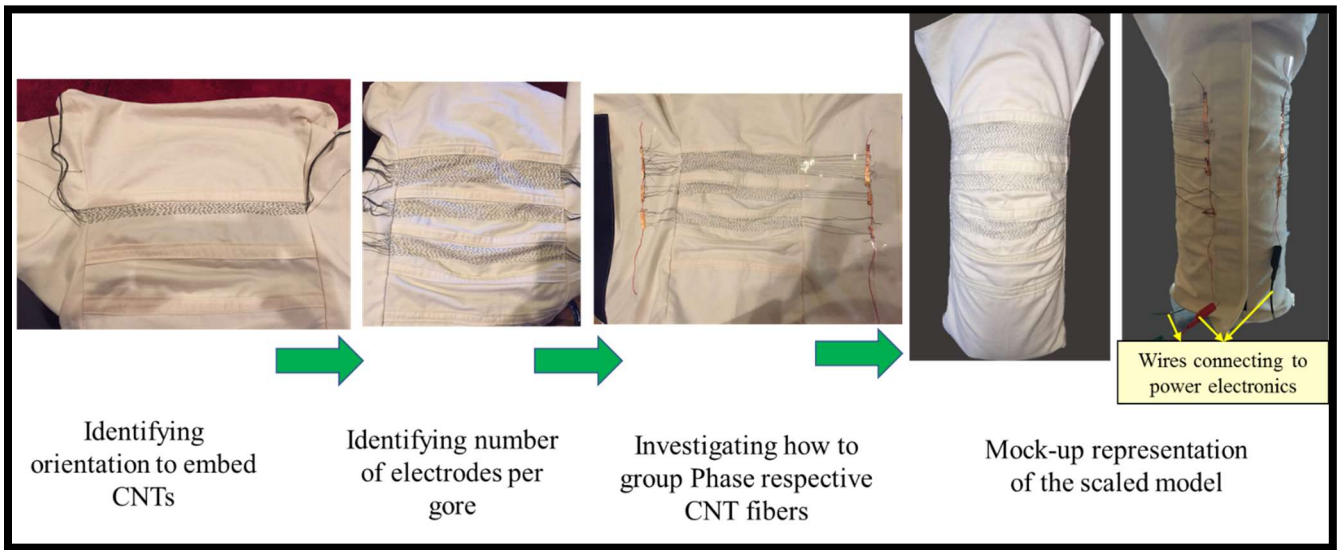

Figure 9.2-4. Investigating CNT fiber placement on scaled prototype using a cotton fabric prior to fabricating the final outerlayer with orthofabric

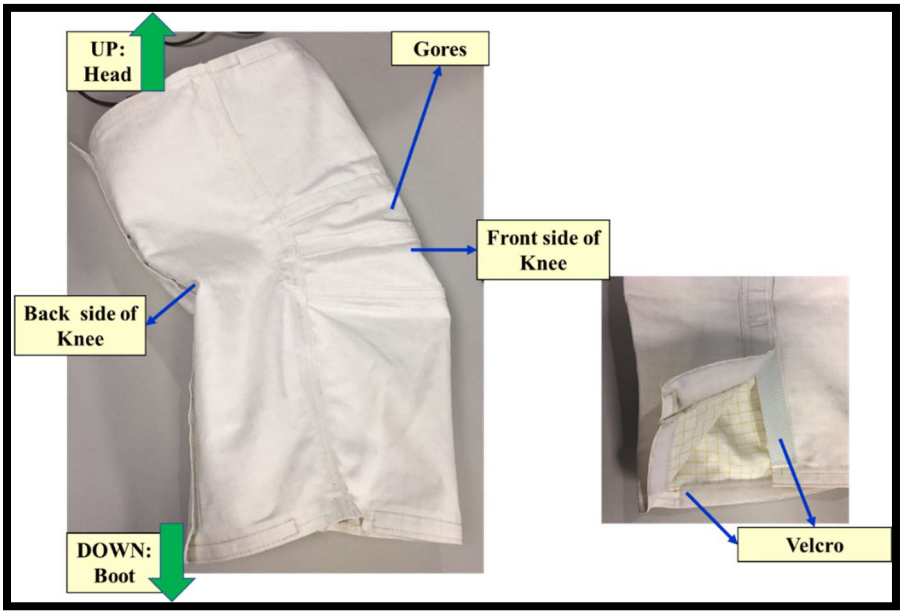

Figure 9.2-2. Orthofabric outerlayer built for the prototype prior to CNT placement

For the final configuration, the CNT fibers are embedded using the same techniques utilized for the coupons where each CNT fiber is carefully driven in the warp direction under every weft thread using a sewing needle. Automated methods for fabric making with the CNT fibers were not feasible at this time due to the unavailability of machinery and because of the novelty of the method, specifically in terminating the ends of the electrodes. Each of the individual CNT fibers

is terminated inches ~3 inches beyond the restraining strap to make necessary connections. CNT fibers of the respective phase are grouped together and attached to a conductive termination adapter (Copper Tape) placed longitudinally and stitched into the outerlayer. Kapton tape and adhesive glass fiber cloth were utilized as insulative termination adaptors to isolate electrode groups of distinct phases. Figure 9.2-6 illustrates the final outerlayer embedded with the CNT fiber electrode network at pre-specified spacing, diameter and number of phases.

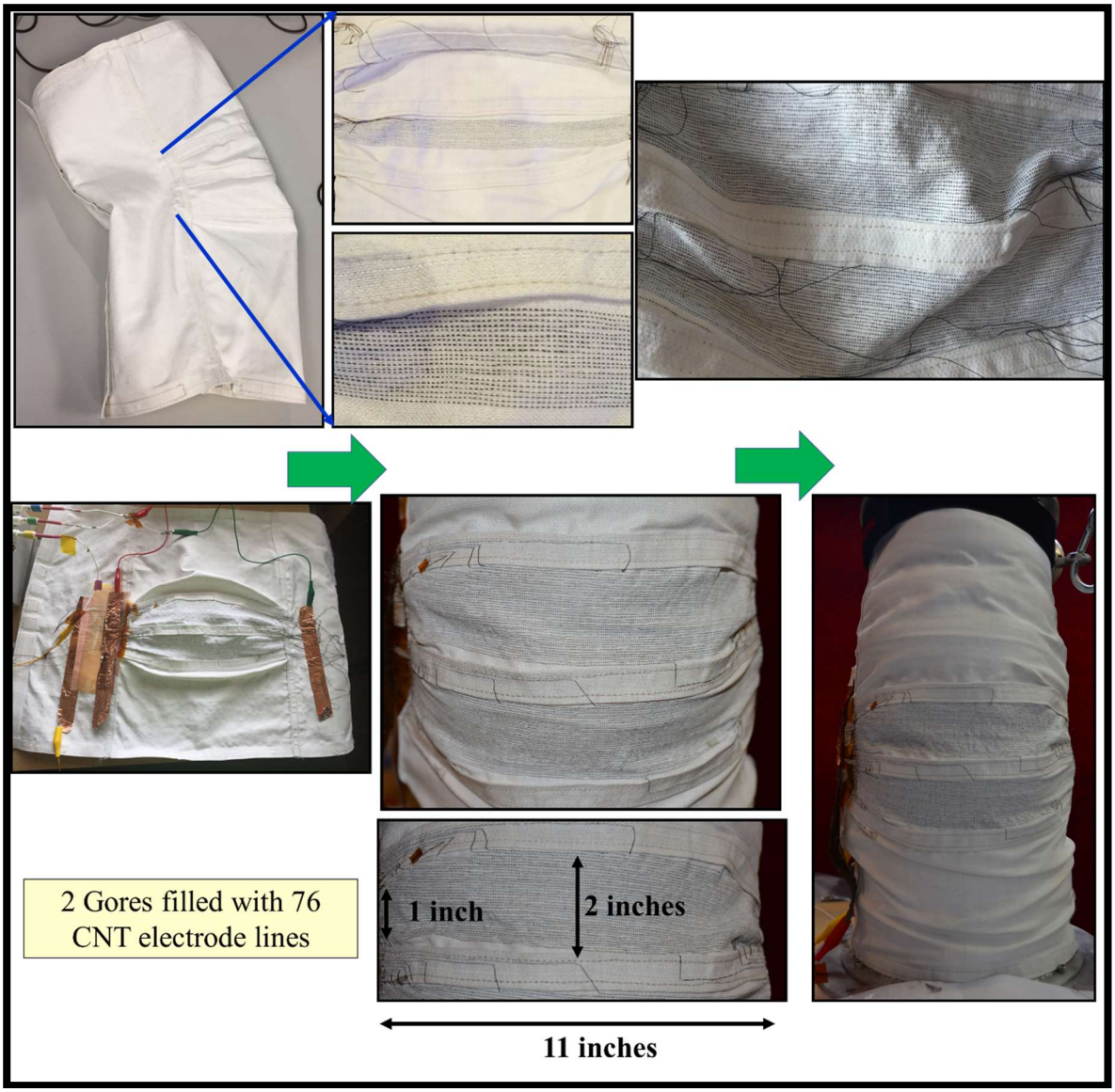

Figure 9.2-6. Joint-knee section embedded with CNT electrodes. Two gores filled with 76 number of electrodes with electrode characteristics show in Table 9.2-1

- **Pressure Bladder-Restraint Assembly Construction**

The pressure bladder along with the restraint layer for the knee section are constructed as one unit, separately from the outerlayer. Either ends of the leg-knee section is sealed with aluminum plates. The top and bottom of the module have provisions for pressurizing the module. The bottom valve interface was used to pressurize the module which is outfitted with a pressure gauge. The outerlayer with the embedded CNTs is attached to the pressure-restraint assembly using Velcro around the circumference of the top and bottom of the outerlayer. The pressure bladder utilized for the construction is the polyurethane coated nylon membrane, which is the same as the NDX-2 and the ISS EMU pressure bladder. The restraint layer is a nylon rip-stop which has similar characteristics as the ISS EMU restraint layer. Figures 9.2-7 through 9.2-9 show the pressure bladder-restraint assembly section of the prototype and the complete assembly with the outerlayer. The thermal insulation material (Aluminized Mylar) was not built into the outerlayer prototype due to constraints in fabrication and since as no data below the outerlayer was being collected. It is anticipated that because the insulation thermal layers are built into the outerlayer itself with a thickness less than 0.7 mm (per ISS EMU), there would not be an effect on the outside dust cleaning performance and the maneuverability of the prototype to different angles.

The operational pressure of the module was kept below 3 psi to prevent accidental burst of the module for the duration of the experiments. Since the module would undergo >50 pressurization cycles, it was decided to not go beyond this pressure although flight operating pressures for a spacesuit are between 3.5-4.3 psi. All the tests were conducted between 2.5-3 psi. It is anticipated that the geometry of the pressurized unit at 4.3 psi compared to 2.5-3 psi are not substantially different. The module is very rigid once pressurized to 2.5 psi. The results from the tests are applicable to a fully pressurized unit with no expected differences in the dust cleaning performance. Table 9.2.1 provides the details of the complete system configuration with materials, geometry and CNT properties utilized for the experiments.

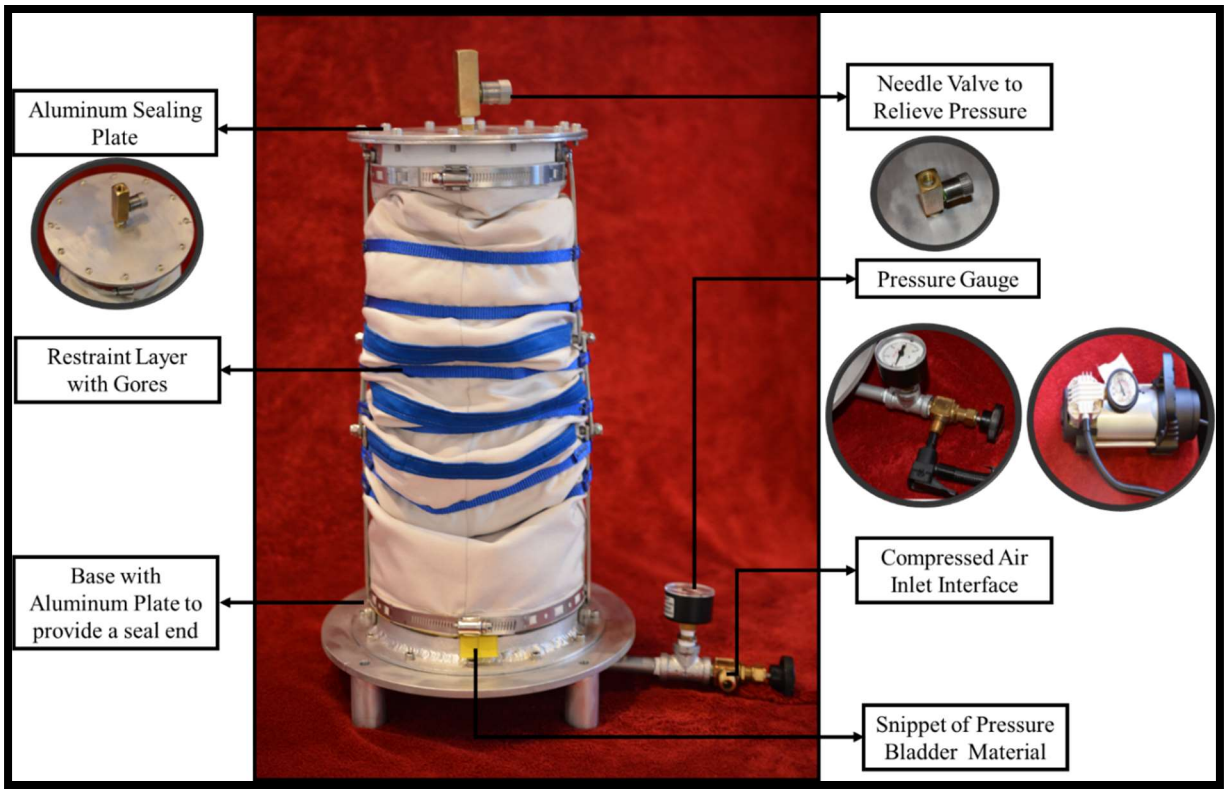

Figure 9.2-7. Pressure bladder-restraint assembly prototype

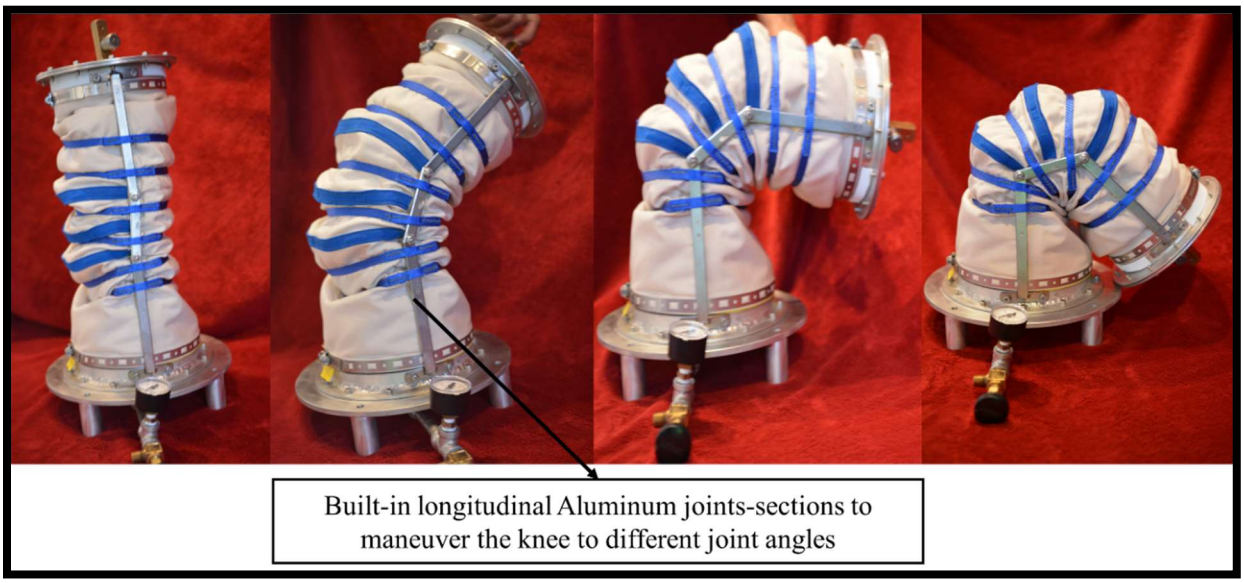

Figure 9.2-8. Maneuverability of the prototype when unpressurized

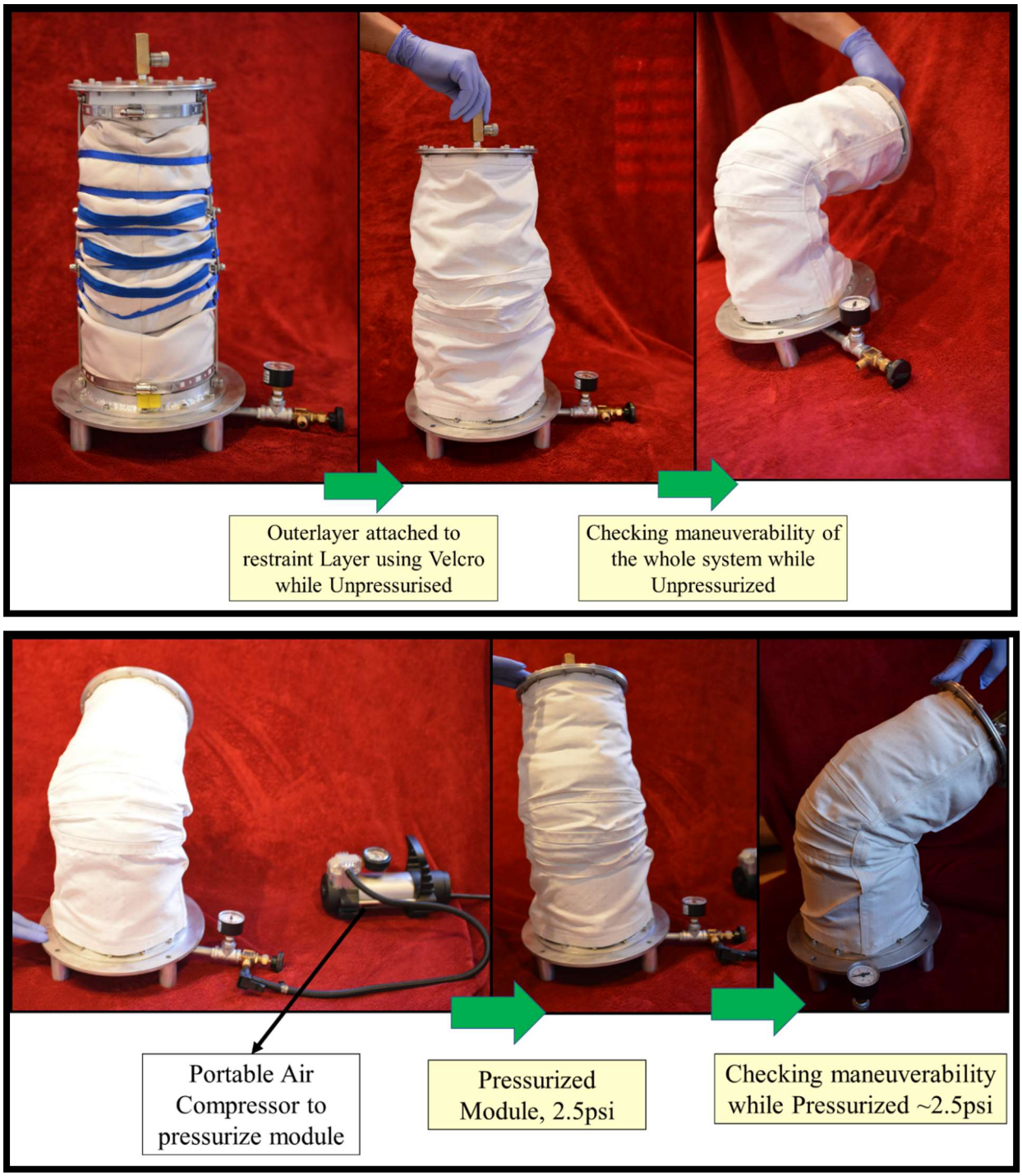

Figure 9.2-9. [Top] Attaching the outerlayer over the pressure-restraint system when module is unpressurized, [Bottom] Maneuvering the knee to various angles after pressuring. Note that the knee could not be flexed beyond 45º

\

Table 9.2-1. Configuration of the scaled prototype

Materials	
Suit Materials	
• Outerlayer	Orthofabric
• Pressure Bladder	Polyurethane coated Nylon (same as EMU)
• Restraint Layer	Nylon Rip-stop (same characteristics as EMU)
Electrode Material	CNT fibers uninsulated
Seals	Aluminum plates
Termination Adapters	
• Conductive	Copper Tape
• Insulative	Kapton, Glass Fiber Tape

CNT Electrode Properties	
Ply / Stranding	7/32 AWG
Diameter	212±7 µm
Length of electrode per line	10 in
Electrode Spacing	1-1.2 mm
Linear Density	25.7±0.4 tex
Density	0.72 g/cm^3
Resistance	18.4±0.2 Ω/m
Electrical Conductivity	1.5±0.1MS/m
Specific Conductivity	2100 Sm^2/kg
Tensile Strength	835± 40 MPa
Strength (Tenacity)	1.1 ±0.1N/tex

Geometry	
Length of entire unit	22 inches
Length of outerlayer	16 inches
Diameter (top)	20 inches
Diameter (bottom)	24 inches
Number of gores	2
Number of electrodes/gore	38
Neutral angle (pressurized)	15°

Environmental Parameters	
Temperature	22-25°C
Ambient Pressure	14.7 psi
Relative Humidity	39-41%
Lunar Dust Simulant	JSC-1A 50-75µm JSC- 1A 10-50 µm
Suit Pressure	2-2.5psi

Operational Parameters	
Input Voltages	880-970 V
Frequency	5 Hz
Waveform	Square
No. of Phases	3
Dust Loading	Amount of dust
• Dynamic	1g
• Static	1g

9.2.4. Experimental Set-Up

The entire module (knee-joint with the outerlayer layer, restraint-pressure bladder assembly) is placed on a bench top using a stand that holds the module in place at the specified angle. A plastic bottle with pierced lid is utilized to drop the dust over the knee section. The same 3 phase tunable power electronics from NASA utilized on the coupons is utilized for this experiment. Each of the conductive termination adapters for the 3 phases on the outerlayer was connected to the power supply using three insulated wires. The knee was pressurized using a portable Husky 120-Volt air compressor that interfaces with the valve on the bottom of the module. Figure 9.2-10 shows the complete module and test set-up.

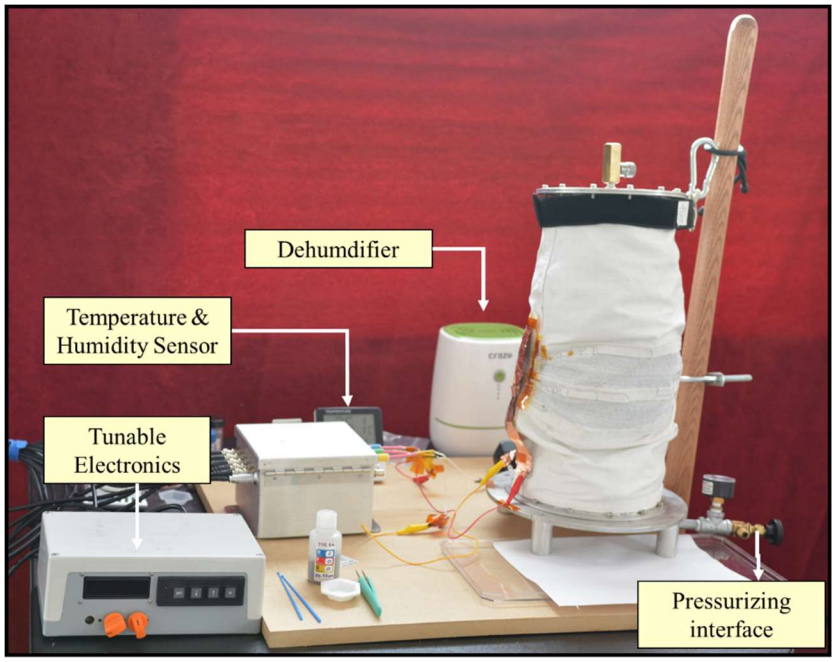

Figure 9.2-10. Experimental set-up of the scaled prototype

9.2.5. Test Conditions

The SPIcDER system on the scaled knee-joint section is evaluated at the three bend (flex) angles of the knee under two specific dust depositing conditions similar to the ones implemented on the coupon tests.

1. Dynamic Drop test
2. Static test

Three runs per angle were performed for each dust loading condition (dynamic and static) to identify repeatable performance, and data was collected and analyzed on two consecutive runs. JSC-1A lunar dust simulant with grain sizes 50-75 μm and 10-50 μm was utilized. All tests were conducted at room temperatures in the range 23-25 ºC and RH in the range 39-41%.

- **Dust Loading Conditions**

Like the proof of concept demonstrations, in the first case of 'Dynamic Drop test', the CNT fibers are first energized prior to depositing dust simulant over the knee. While the system was active, one gram of lunar dust simulant was continuously deposited/dropped over the entire knee area with electrodes using a bottle with punctured holes to easily drop the dust. This test case is presumed to represent lunar dust actively interacting with the suit when an astronaut is walking on the surface of the moon during an EVA and dust is being kicked up. In the second test case (static test), a measured amount of simulant is deposited over the knee covered with CNTs prior to

activating the system. This condition represents a scenario where the suit is pre-disposed to dust which has statically adhered and coated the spacesuits during an EVA.

The prototype was positioned perpendicular to the ground as shown in Figure 9.2.10, in an orientation representative of an astronaut standing/walking in a suit. Dust was dropped at an angle to the knee as shown in Figure 9.2-11 using a bottle with pierced holes. For the dynamic test, the dust was continuously dropped over the knee sweeping left to right to cover the area. For the static test, the dust was dropped to cover the knee area prior to activating the system. For the small grain size (10-50 μm), it was difficult to drop the dust evenly as the dust was cohesive, so the dust was manually spread out using gloved fingers to make the dust stick to the knee and had to be redone a few times if dust fell off the knee due to gravity. For the 15° angle, the prototype was also tested in the horizontal position so that sufficient dust stayed on the knee prior to activating SPIcDER for the static test. The 15° angle was almost vertical when placed perpendicular and was a challenge to keep the dust in position due to gravity. Using both orientations provided sufficient evidence that the SPIcDER system was clearing the dust. For the coupon tests, dust was dropped perpendicular to the coupon for both the dynamic and static tests. On the lunar surface, astronauts will be exposed to dust in various directions. Meaning, while walking the dust will get kicked up, during drilling operations dust would spread out and *'fall'* on the suit, while on the rover, the dust gets picked up by the wheels and sprayed onto the suits as seen

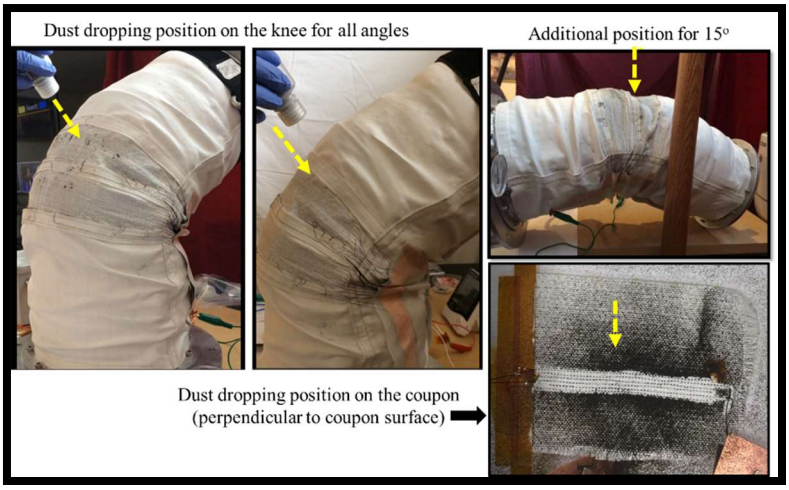

Figure 9.2-11. Dust loading method

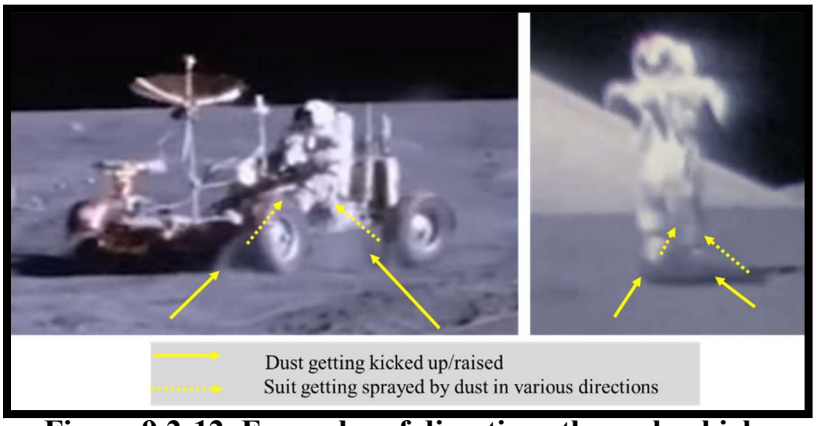

Figure 9.2-12. Examples of directions through which spacesuit is exposed to dust during surface operations (Background image credit: NASA)

in Apollo missions (See Figure 9.2-12). Therefore, the dust exposure during the experiments conducted here utilize only a subset of these different modes to provide an approximation of the dust exposure to validate the scalable functionality of the SPIcDER system. Future work would involve implementing test setups of the scaled SPIcDER system in realistic dust exposure settings simulating surface operations. For example: one test method would be to set-up an experiment in the lunar regolith bin at NASA KSC or the wind tunnel similar the ones performed on the NDX-1 spacesuit study by Gaier et al. (2010).

- **Bend Angles**

The bend angles of the knee correspond to the range of motion of the spacesuit, specifically the knee area when the astronaut is walking in the suit. Dust loading and cleaning for three specific angles of the knee are evaluated:

1. One that corresponds to the neutral position of the knee when the suit is pressurized (no flex). The neutral angle of the knee was determined after the module was pressurized prior to beginning the test procedures. This was observed to be approximately 15^{o} during the experiments.
2. An intermediate angle of 30^{o}.
3. A third angle of 45^{o}.

The original plan was to flex the knee to 90^{o} on the fourth configuration. However, the knee could not be flexed to 90^{o} when the module was pressurized due to the rigidity of the module. Even though there was provision built into the module to provide high maneuverability to flex the knee beyond 90^{o} angles as seen in the unpressurized module pictures (Figure 9.2-8), once pressurized, it was extremely difficult to bend the knee beyond 45-50 ^{o} and hold it place. When astronauts bend their knee inside a pressurized suit, they actively work against the extra resistance due to the gas pressure of the spacesuit. For the pressurized module, similar restrictions applied where the knee could not be bent beyond 45^{o} due to the rigidity and lack of active force being applied to move and maintain the knee beyond 45^{o} in a stable configuration. To prevent any damage to the test article, tests were limited to the 45^{o} angle. Figure 9.2-13 and Table 9.2-2 provide a representation of the three angles tested with the two dust loading conditions and test cases performed. It anticipated that for normal walking motions of the astronauts most of the movements are in the range of 10^{o} - 60^{o}, except when they sit on the rover or when they kneel. The results of the experiments conducted here can be extrapolated to 60^{o}-90^{o} without significant differences in cleaning performance.

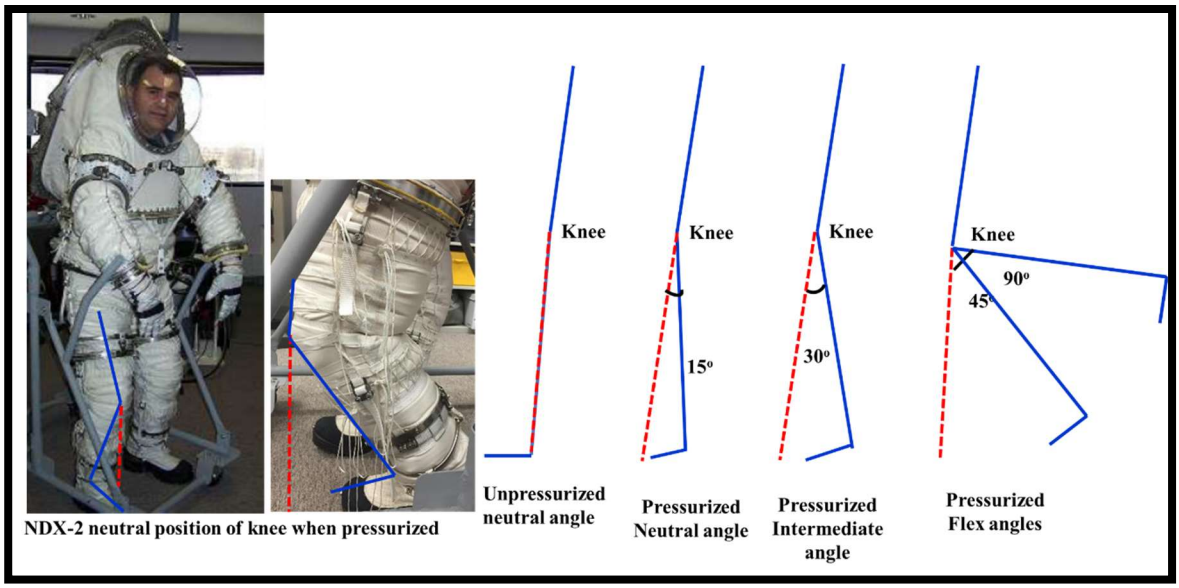

Figure 9.2-13. Angles of knee tested for dust cleaning performance of SPIcDER. *90° was planned but could not be tested when pressurized due to module constraints.*

Table 9.2-2. Test Conditions tested to investigate scalable functionality of the SPIcDER system

#	Dust Loading	Simulant (µm)	Knee Bend Angle (degrees)	Module Pressure (psi)	Temperature (°C)	Reletaive Humdity %	Voltage (V)	Frequency (Hz)
1	**Threshold Calibration**		Neutral- 15°	2.5	24	40	1010	5
2	**Threshold Calibration**		30°	2.5	24.1	40	1050	5
3	**Threshold Calibration**		45°	2.5	24	40	1090	5
4	**Dynamic**	50-75	Neutral- 15°	2.5	24	40	945	5
5	**Dynamic**	50-75	30°	2.5	23.2	40	945	5
6	**Dynamic**	50-75	45°	2.5	23.8	39	970	5
7	**Dynamic**	10-50	Neutral- 15°	2.5	23.5	40	900	5
8	**Dynamic**	10-50	30°	2.5	22.9	40	945	5
9	**Dynamic**	10-50	45°	2.5	24.1	39	970	5
10	**Static**	50-75	Neutral- 15°	2.5	23.9	40	900	5
11	**Static**	50-75	30°	2.5	24.9	40	945	5
12	**Static**	50-75	45°	2.5	24.1	40	970	5
13	**Static**	10-50	Neutral- 15°	2.5	24.5	40	900	5
14	**Static**	10-50	30°	2.5	24.4	40	945	5
15	**Static**	10-50	45°	2.5	23.7	39	970	5

9.2.6. Test Procedure

1. **Breakdown Voltage Calibration**
   - **a.** Prior to conducting the test cases mentioned in the Table 9.2-2, voltages where breakdown starts to initiate for each bend angle were calibrated. This was achieved by first energizing the electrodes without dust loading and slowly increasing the input voltage starting from 100 V in 50 V increments until arcing is evident. The voltage at which arcing occurs was noted for each bend angle.
   - **b.** When data was gathered in step 1a, the actual experiments with dust loading were conducted beginning with voltage values 200 V below the voltage where breakdown initiated in 1a. The operating voltages where best performance occurs for each bend angle that are no less than 100-50 V below the breakdown voltage were identified and utilized for the experiments.
2. **Test Runs**
   - **a.** Each of the test runs was conducted at 100 V below the threshold voltage for each bend angle that provided the best cleaning performance.
   - **b.** For dynamic tests runs, the knee was pressurized and positioned at the required angle. Images were taken prior to dust loading. Real-time video recording was set-up. The CNT fibers were energized with the required input voltage parameters as noted in the operating conditions in Table 9.2-2. A measured amount of dust simulant was continuously dropped over the knee. After all the dust was dropped (~1 min), the power system was turned off. Macroscopic and microscopic images of the condition of the knee were captured. After all required data/images were collected, the dust on the knee was cleared using puffs of air from a compressed air source. These steps were repeated for test cases 4-9.
   - **c.** For the static test runs, the knee was pressurized and positioned at the required angle. A measured amount of dust simulant was place over the knee area. Images were taken. CNT fibers were then energized until all visible dust seemed to clear the knee area (~60 seconds). The power was turned off. Images of the dust loading on the knee post cleaning operations were taken. After all required data/images were collected, the dust on the knee was cleared using puffs of air from a compressed air source. These steps were repeated for test cases 10-15.

9.2.7. Data Collection and Analysis Methods

Data was primarily collected using the following methods

1. Visual Observations
2. Microscopic and Macroscopic imaging
3. Videography

For the dynamic drop test condition, where SPIcDER was first activated, continuous video was recorded while dust was dropped over the coupon. The knee area was imaged in place after the system was powered off using a Celestron® handheld digital microscope and a Cannon® digital SLR camera. Similarly, for the static test, the knee area was imaged prior to dust deposition and after cleaning operations when the system was powered off. Microscopic images using the digital microscope were taken at 20X magnification to record the state of the coupons and dust distribution. Video during static cleaning operations was also recorded. Both the dynamic and static tests were repeated multiple times for each bend angle to observe repeatable and consistency of dust cleaning. Data was obtained for two consecutive runs.

Qualitative and quantitative analysis was used to assess the performance of the SPIcDER system and its scalable functionality. The capability of the dust cleaning system was evaluated using 1) Visual inspection via the videography data and images collected during the experiments to document observable dust cleaning capability for the qualitative aspect of the analysis 2) For the quantitative aspect, images were analyzed using ImageJ® software to estimate the overall percentage of dust covering the orthofabric before and after cleaning operations. Due to the large area of the knee and imaging capability using a digital microscope, for each run, analysis was performed on five smaller sections of the knee, each with an average area of 6 mm x 6 mm on five various locations on the knee. The locations were chosen based on worst and best-case dust coverage post cleaning operations. The microscopic images were loaded into the ImageJ image processing software. The contrasting shades of the white outerlayer fabric, and the dark dust particles and CNT fiber were leveraged using the color thresholding tool of the software to process the image.

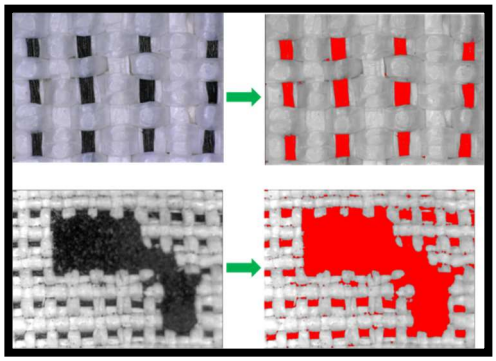

Figure 9.2-14. Image processing using ImageJ® software to estimate dust coverage area. *Shown here are examples of a clean farbic estimating CNT area and a sample covered in dust before cleaning operations.*

The total dark shaded area was estimated based on the color thresholding tool. This area was then subtracted with the area of the CNTs covering the fabric which provided the area of the fabric covered in just dust. Figure 9.2-14 shows how the color thresholding tool was used in ImageJ to process the images. Figure 9.2-15 shows a detailed flow chart of the steps involved in evaluating each of the 5 images per run and reaching the value for dust cleaning performance as explained in the following section.

- Voltage values

Two voltage values for each bend angle are reported. The threshold voltages where breakdown occurs and the operating voltages of the system used for dust cleaning operations where best performance was observed. Threshold voltages are collected for each bend angle. These values are compared to the threshold voltages observed during coupon tests where breakdown initiated. Results from the experiments and simulation for these breakdown voltages are compared and differences are analyzed.

- Dust Cleaning Performance

Based on lessons learned conducting coupon testing, for this scaled prototype, the percentage of dust coverage on the fabric area after cleaning operations has been utilized as the key parameter to evaluate dust cleaning performance. This is performed by obtaining images of the knee area on five separate locations per run. An average area of 6 mm x 6 mm was analyzed using ImageJ® as explained earlier. Unlike the coupon tests in Chapter 5, where it was feasible to take microscopic images of the entire electrode area divided into three sections and utilize ImageJ® for particle counting, the prototype tested here is a scaled unit with surface area more than an order of magnitude than the coupons. If similar method is used for the joint-knee section using ImageJ® for particle counting, it would be labor intensive requiring analyzing approximately 100 images per run per angle. Therefore, a decision was made to use five strategic locations over the knee area covered in electrodes to evaluate the microscopic images. These locations were analyzed to provide the percentage of area covered in dust before and after SPIcDER cleaning operations. Figure 9.2-15 illustrates the steps and equations utilized to analyze the performance of the system for the dynamic and static dust loading conditions.

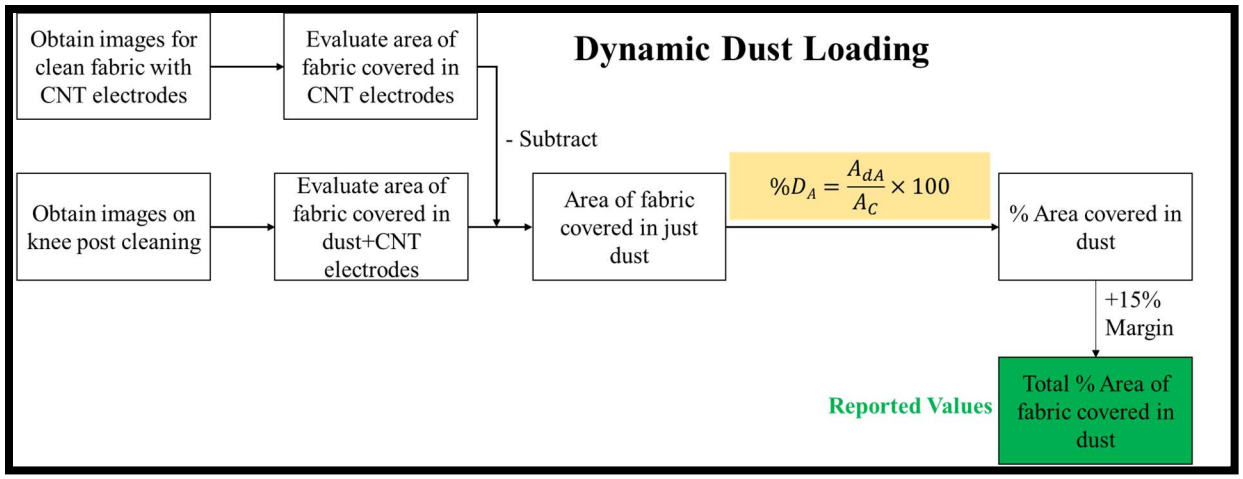

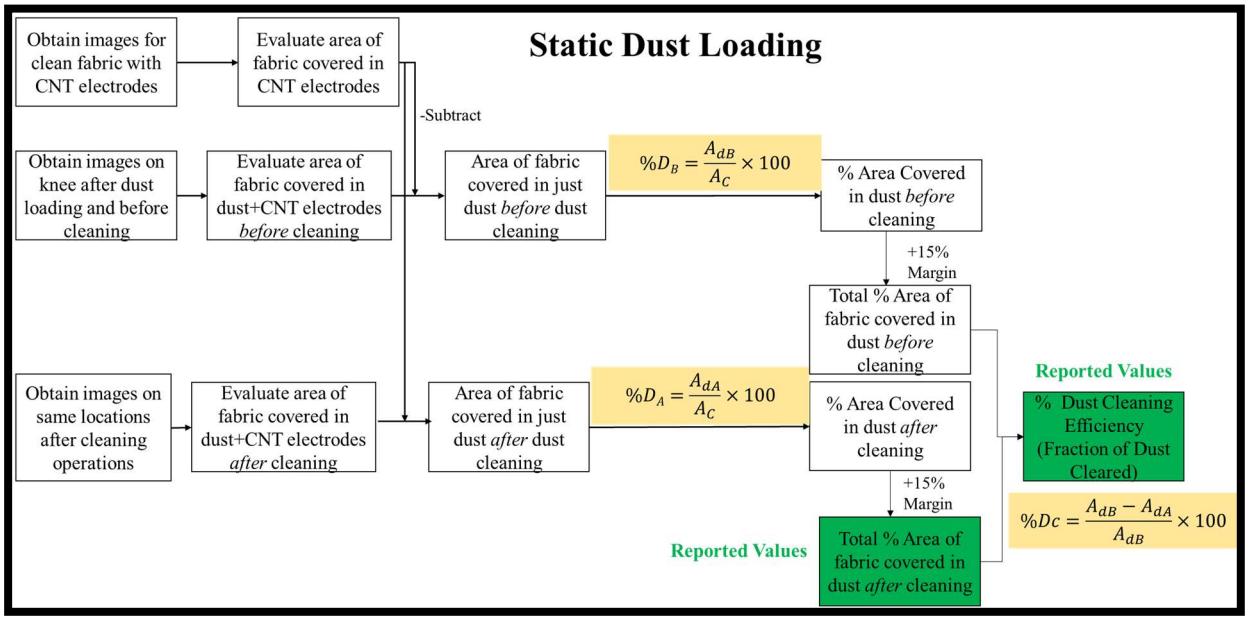

Figure 9.2-15. Flow chart illustrating the method to analyze percentage of fabric area covered in dust before and after dust cleaning and evaluation of SPIcDER's dust cleaning performance

The results from the three equations represented in the flow chart are reported in the subsequent results and discussion sections. The parameters of these equations are described below

- Dynamic Dust Loading

The percentage of dust covering the fabric is calculated using Equation 46, where $\%D_A$ is the percentage of dust covering the fabric post cleaning operations, A_C is the clean area of the fabric evaluated, A_{dA} is the area of the fabric covered in dust post cleaning. This value is obtained by subtracting visible CNT area to obtain area covered in just dust post cleaning operation.

$$\%D_A = \frac{A_{dA}}{A_C} \times 100 \tag{46}$$

- Static Dust Loading

The percentage of dust covering the fabric before dust cleaning is calculated using Equation 47, where $\%D_B$ is the percentage of dust covering the fabric prior to cleaning operations, A_C is the clean area of the fabric evaluated, A_{dB} is the area of the fabric covered in dust before cleaning.

$$\%D_B = \frac{A_{dB}}{A_C} \times 100 \tag{47}$$

The percentage of dust covering the fabric after dust cleaning for static test is also calculated using Equation 46.

The efficiency of the dust cleaning performance ($\%D_C$) of the SPIcDER system is then calculated using Equation 48 which provides the percentage of dust removed from the fabric due to cleaning compared to the original dust on the fabric before cleaning operations. This equation is applicable specifically for the static tests. For the dynamic tests, visual operations will be used to estimate the efficiency based on the equation 9.1. A 15% margin has been added to all the performance values for a conservative approach.

$$\%D_C = \frac{A_{dB} - A_{dA}}{A_{dB}} \times 100 \tag{48}$$

Results obtained are compared with the coupon tests, illustrated as 0° on the figures in subsequent sections.

9.3. Scaled Model Test Results and Discussion

9.3.1. Threshold/Breakdown and Operating Voltages

As explained in Chapter 6, section 6.8.5, the voltage where the surrounding medium breakdowns due to electric discharge causing visible sparks is dependent on the electrode configuration and the surrounding gas pressure. In the case of the joint-knee section, the knee angle impacts the fabric layout, i.e, the fabric might have wrinkles/folds/creases when unpressurized and when the knee is in a neutral position (no flex angle) when pressurized. These creases in the fabric may stretch/smooth out when the knee is in a flexed position. Therefore, the angles of the knee have an influence on how the embedded electrodes interact (spacing and overlap). There might be areas where the fabric creases so much that the electrodes might overlap impacting the value of

breakdown voltage. When pressurized, the pressure inside the module helps the outerlayer fabric to bubble outward allowing smoothing out of the creases normally observed while in unpressurized conditions. When flexed, these creases smooth out further. Figure 9.3-1 illustrates the fabric layout for unpressurized and pressurized module.

Figure 9.3-1. [A] Unpressurized and [B] Pressurized module. *Arrows point to creases in the knee area*

Calibration of the threshold voltages for the three knee angles was conducted with the module pressurized at 2.5 psi. Table 9.3.1 lists the observed voltages at the three angles tested and Figure 9.3.2 illustrates the difference in the threshold voltages observed during the knee experiments with results from simulation and coupon experiments for the electrode spacing of ~1.2 mm.

Table 9.3.1. Breakdown and operating voltages during experiments at knee angles tested

Knee Angle	V_B from Experiments	V_B from Simulations	Operating Voltages	Frequency
15° (neutral)	1010 V	1350	900-945 V	5 Hz
30°	1050 V	1390	945 V	5 Hz
45°	1090 V	1430	970 V	5 Hz

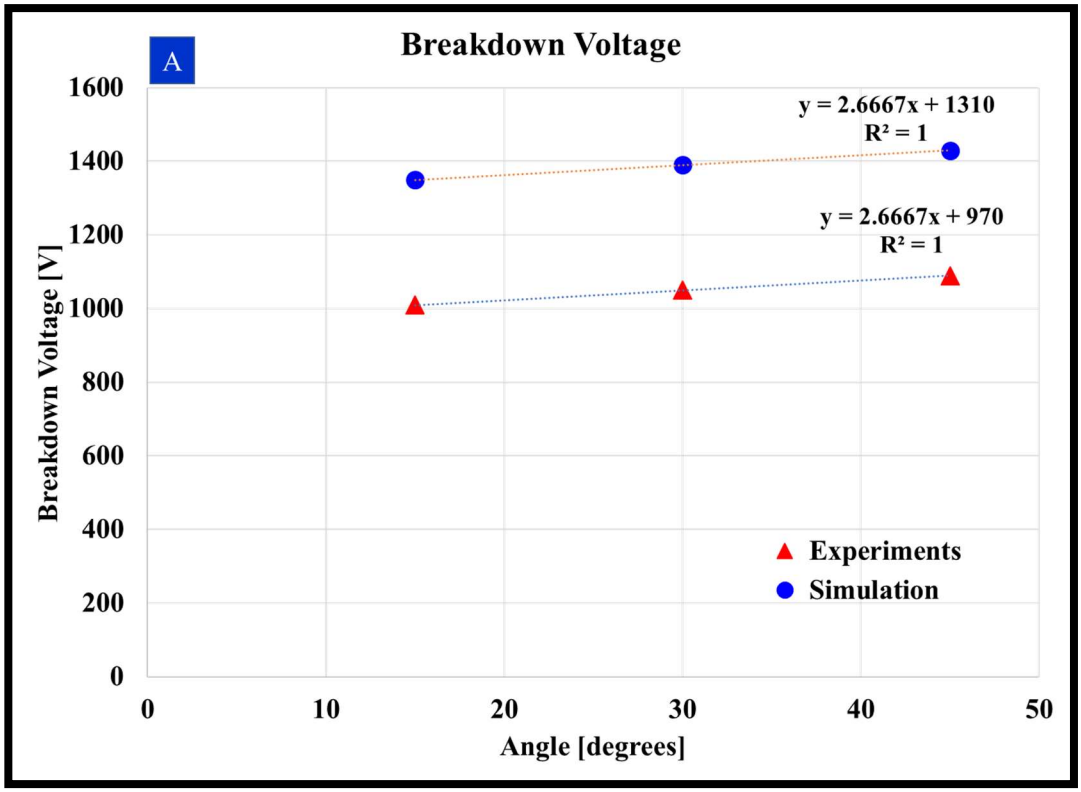

Figure 9.3.2. [A] Correlation of experimentally observed breakdown voltages with simulation produced breakdown voltages for the three angles tested.

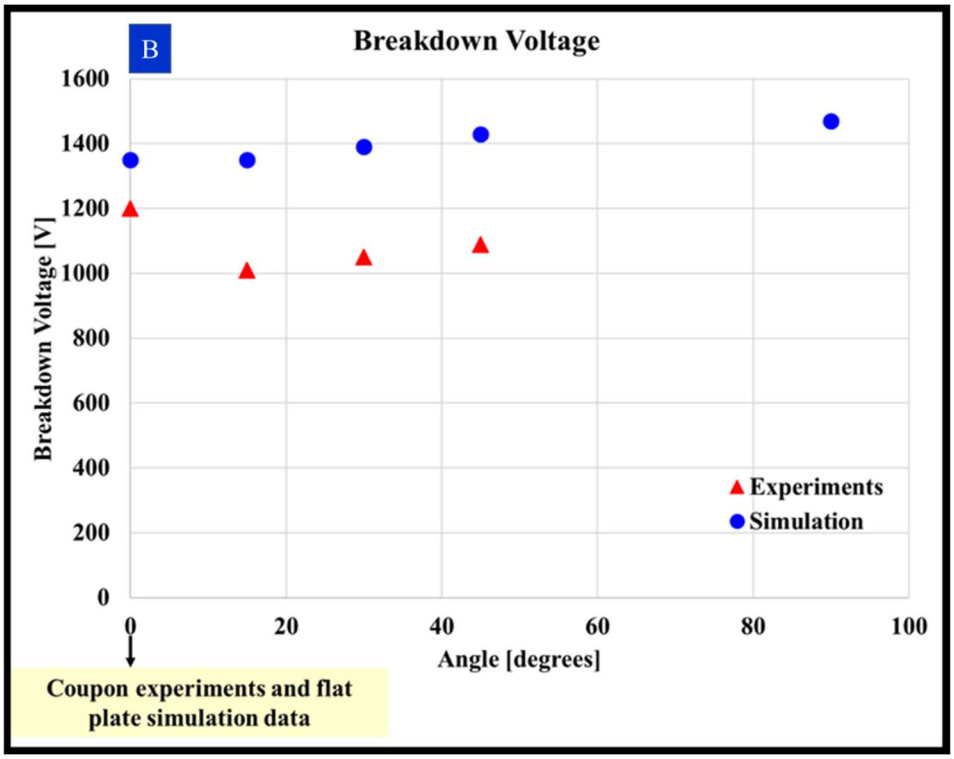

Figure 9.3.2. [B] Breakdown voltages for 90º and coupon experiment data. *Here 0º represents the coupon tests, horizontally placed.*

9.3.1.1. Discussion

9.3.1.1.1. <u>Difference in Threshold voltages between the knee angles:</u>

Both experimental and the simulation data show that there is a gradual increase in the voltage where breakdown initiates as the knee bend angle increases. The increasing trend of the threshold (breakdown) voltages for the 3 angles observed in the experiments correlate well with the trend observed in simulations (Figure 9.3-2A). There are two reasons predicted for the increase in the breakdown voltage as the knee angle increases.

- First, when the fabric is pressurized at lower angles, due to the nature of the fabric and patterning of the joint section, creases/folds develop in the fabric. As the knee flexes to a higher angle, these creases on the knee start to unfold, smoothing out the fabric. Figures 9.3-1 and 9.3-3 illustrate how the folds in the knee start to smooth out when the knee is flexed from 15º to 45º. Consequently, at the lower angle, the electrodes within the creases may start to overlap and compromise the electrode spacing (lower than 1.2 mm in this case) increasing the risk of breakdown occurring at lower voltages (left picture in Figure 9.3-3). As the knee angle increases

and creases smooth out, the electrode spacing is now at the intended spacing, and the voltage at which breakdown occurs is higher than at lower angles, as dictated by the Paschen law.

It is to be noted however that while the trend for breakdown voltage within both the experimental and simulation data show similar increase in the breakdown voltage with an increase in the knee flexion (~40 V increase with every 15° increase), the impact due to creases/folds are not replicated in the simulation. The difference between the experimental and simulation data however for each angle (~340 V reduction in breakdown voltage noticed between experiments compared to simulations for each angle) could be associated with these unanticipated folds of the fabric where breakdown initiated. Additionally, experiments demonstrated that the risk for breakdown is not at the corner of the knee as it is evident from Figure 9.3-3, that there is no significant difference in how the fabric bunches at the comers of the knee in both 15° and 45°.

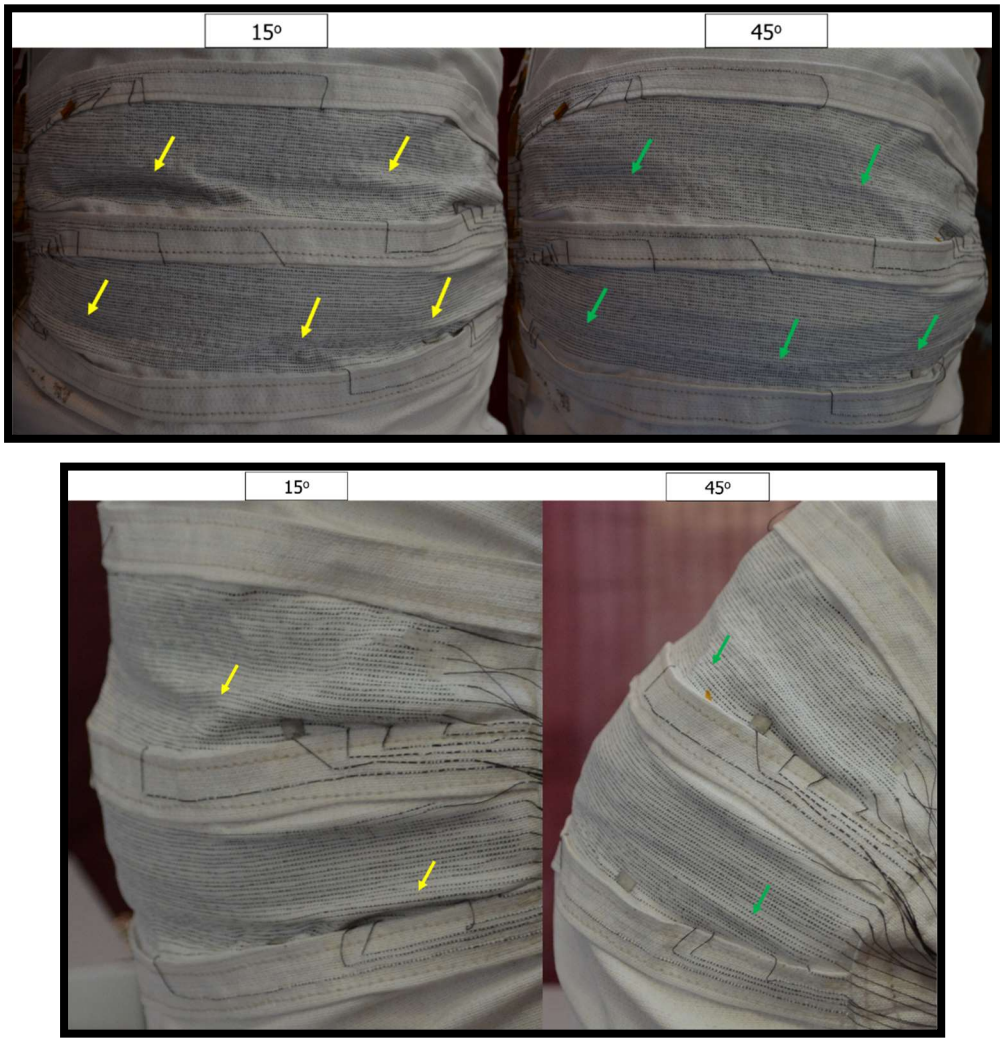

Figure 9.3-3. Fabric smoothing out as the angle of the knee increases

- Second, as the knee flexes and the fabric bends, there is a slight stretch in the fabric, the consequence of which is an increase in the electrode spacing. With an increase in electrode spacing, there is a corresponding increase in the breakdown voltage as dictated by the Paschen curve. Data from the simulations show that there is a minor increase in the electrode spacing ranging between 0.1 μm upto 140 μm depending on the location of the electrodes along the curvature due to the intrinsic property of the curved geometry surface (See Figure 9.3-4). Although the simulations do not replicate the fabric properties of the orthofabric material utilized in the experiments, electric field simulations for the four angles, show that voltages where breakdown initiates increase as one flexes the knee from 15^{o} to 90^{o} degrees at the rate of ~ 40 V increase for every 15^{o} increase in the knee flexion (See Figure 9.3-2). Due to this inherent increase in the electrode spacing due to geometry shown in the simulations combined with the experimental data, it could be concluded that the electrode spacing differences between the angles causes the observed increase in breakdown voltage.

To mitigate issues with breakdown during testing, the SPIcDER system was operated ~ 100 V below the threshold voltage at each angle which corresponds to operating voltage ranges between 900-970 V for the three knee angles. The performance of the system with these operating voltages was comparable to the results obtained on coupon tests as explained in subsequent sections. The impact of these different operating voltages and how this can be implemented operationally is captured in section 9.3.4.

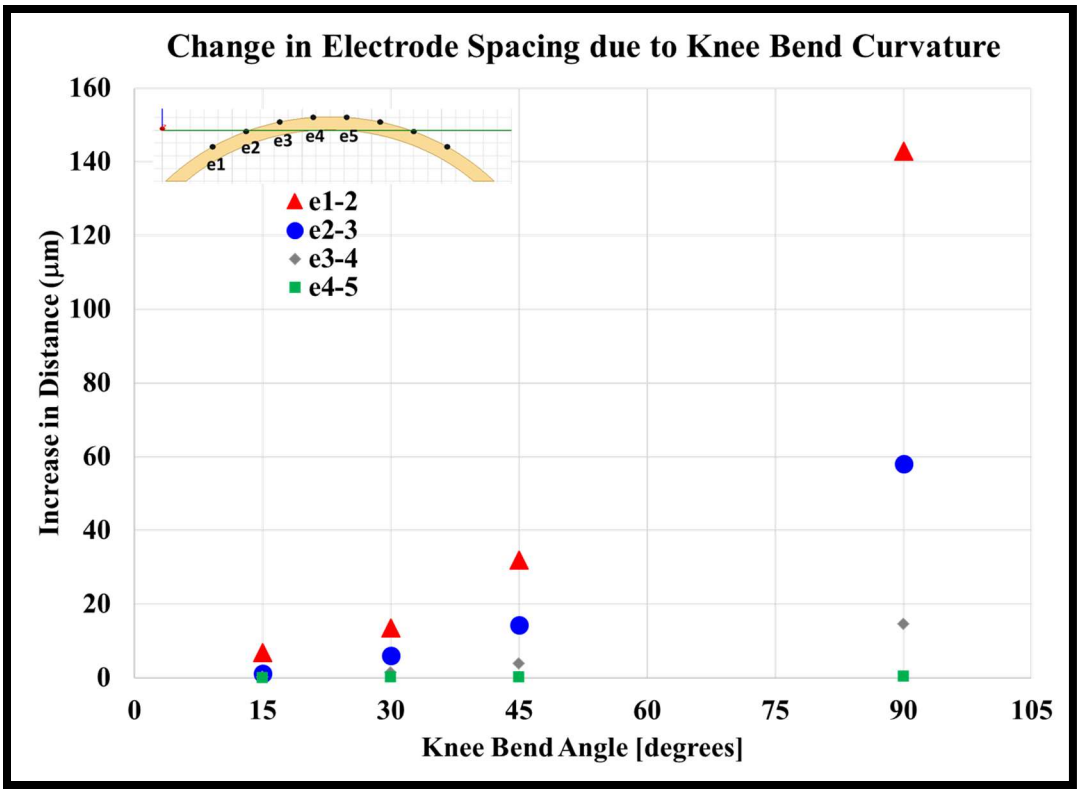

Figure 9.3-4. Increase in electrode spacing between each electrode group based on knee angle

9.3.1.1.2. Difference in threshold voltage between the coupon and scaled prototype experiments

The threshold and operating voltages during the knee prototype tests were ~100-150 V lower than the coupon experiments (1010-1090 V on knee versus 1150-1200 V on coupons). Figure 9.3-2B illustrates this difference in threshold voltages. While the threshold voltages for the prototype experiments was anticipated to be similar to that of the coupon tests due to the same average electrode spacing (~1.2 mm) between the two samples, three potential factors have been identified contributing to the decrease in the voltage, (1) Fold/creases (explained in previous section) (2) Inconsistent electrode spacing due to manufacturing process (3) fraying/hairs sticking out from the uninsulated CNT electrodes.

- As explained in the previous section, due to the nature of the fabric layout (pleats) within the knee section, we expect to see creases in the fabric, specially at lower angles. There were areas where the electrode spacing of the consecutive CNT electrodes was compromised due to folds/overlap causing breakdown at lower voltages than anticipated. In addition to the contribution from irregular spacing within the electrodes as part of the manufacturing process

(next paragraph), minor creases in the fabric even at the flexed position were discovered to be one of the reasons for lower threshold voltages on the scaled prototype when compared to the coupon experiments.

- Second, the coupons previously fabricated were much smaller samples relative to the scaled prototype. The ability to manually embed CNT electrodes and adjust the spacing and alignment of the electrodes was rather feasible on smaller coupons. However, with the larger prototype, embedding CNT electrodes manually was labor intensive and although care was taken to place the electrodes as properly oriented and aligned as possible within the warp threads, there were sections where it was difficult to pull the CNT electrodes under the weft threads. Once the entire electrode line was embedded, it was not feasible to adjust the spacing between two consecutive electrodes over large areas. Therefore, certain sections of the knee had electrode spacing less than other areas and vice versa (see Figure 9.3.5). While increase in the electrode spacing increases the voltage at which breakdown occurs, due to areas with <1.2 mm electrode spacing, breakdown initiated at lower than 1150 -1200 V as observed during the coupon tests. Hence, the threshold voltages of the knee was lower for all 3 knee angles when compared to the coupon tests (0^o). These inconsistencies occurred due to the fabrication process and can be prevented by using automated weaving methods. Recommendations to overcome such electrode spacing inconsistencies are described in section 9.3.4.

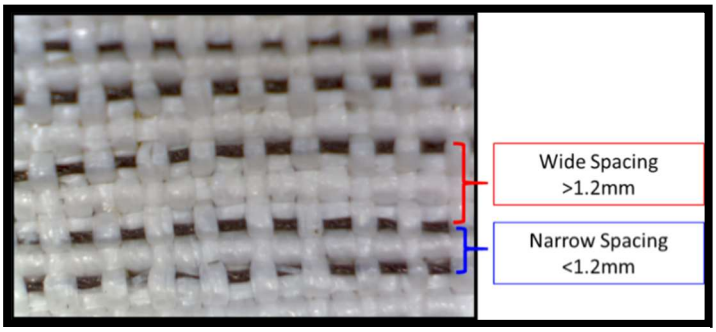

Figure 9.3-5. CNT electrode spacing irregularities using manual methods on scaled prototype

- Third, the electrodes embedded into the knee are uninsulated and bare. These CNT electrodes are made of several CNT fibers aligned together forming the larger diameter electrode 'thread' required for dust cleaning. As such the electrodes may have localized sections where micron sized CNT fibers might be sticking out as a result of handling the electrodes during the manual weaving process. On the coupons, care was taken post fabrication of the coupons to verify that all the CNT electrodes are aligned and any fibers sticking were rearranged accordingly. For the larger prototype, it was physically just not feasible to go through nearly 100 electrodes along the length of each electrode to check for the fibers and adjust. Therefore, it is anticipated that

the lower voltage might have also been caused if any fiber was frayed causing reduction in the electrode spacing in a localized area resulting in lower voltages. This issue can be certainly overcome by insulating the CNT electrodes in a flexible insulation material that would prevent any fraying of the electrode fibers.

9.3.2. Dynamic Runs

For the dynamic dust loading condition, the module was first pressurized to 2.5 psi and positioned in the required angle using the stand. Electrodes were activated by turning on the power supply at the set frequency and voltage as detailed in Table 9.3-1. One gram of lunar dust simulant was continuously dropped over the entire knee area. Visual observations were made while dropping the dust. Power system was turned off after all the dust was dropped. Microscopic images of the best and worst areas of dust loading were imaged and analyzed. Key observations and performance of the system in dynamic dust loading setting are described in the next section.

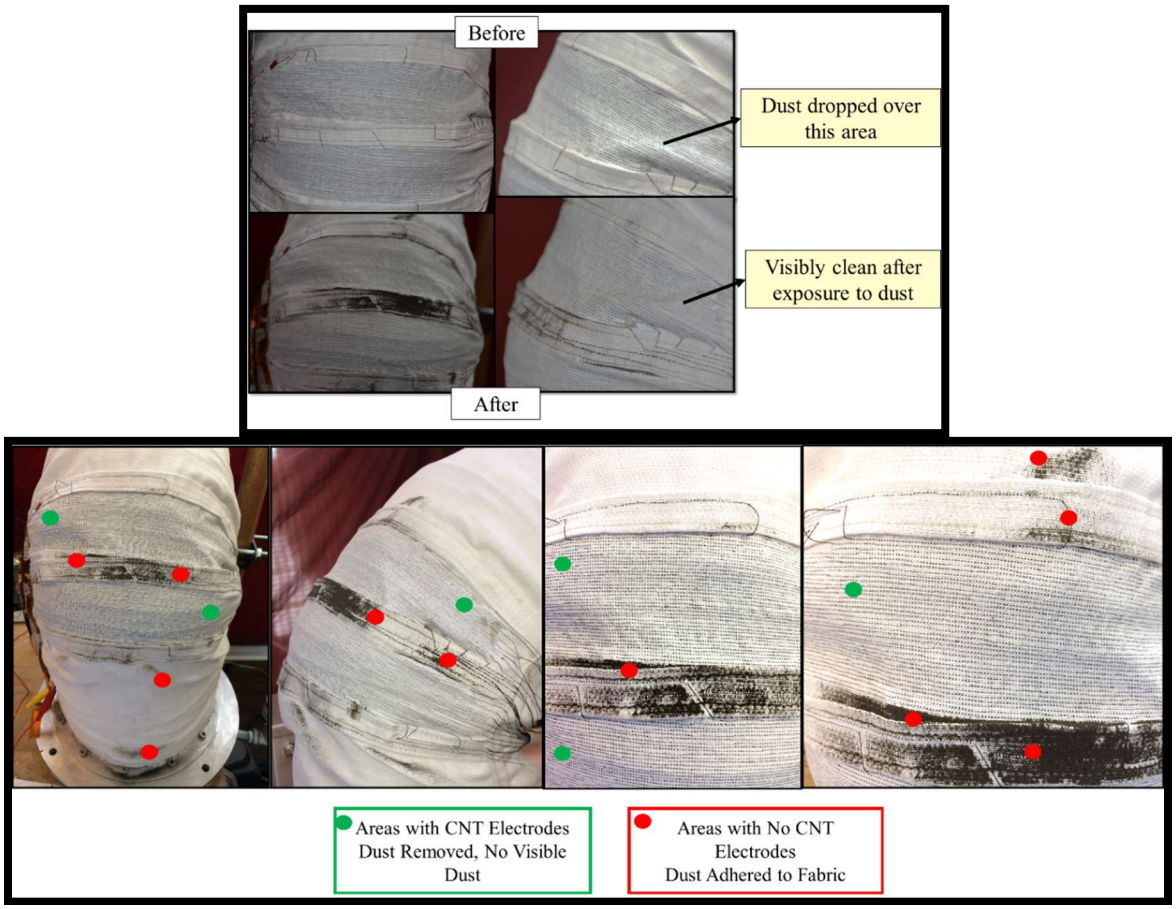

Figure 9.3-5 [Top] Images of the knee for dynamic dust cleaning operations, [Bottom] No visible dust within electrode area; dust collected in areas with no electrodes.

9.3.1.1. *Key Observations during Dynamic Dust Loading*

- The SPIcDER system clearly demonstrated its ability to repel dust when visually observed during dynamic dust loading. Dust was visibly cleared during the cleaning operations over the areas where CNTs were embedded, particularly the 50-75 μm in all knee angle positions. Figures 9.3-5 and 9.3-7 illustrate the cleaning ability of the SPIcDER system when embedded on the knee joint section.
- The operational voltage was chosen to be ~100 V below the threshold voltage where arcing would initiate
- Operating voltages had to be increased with increase in flex angle to obtain same performance. This correlates well with simulations conducted for curved surface due to increased electrode spacing
- At the threshold voltage, arcing was dominated by the area near the creases/folds
- Dust was also dropped on areas where there were creases and folds towards where CNTs were embedded and dust visibly cleared even from these areas
- Dust accumulated where no CNTs were embedded-towards the bottom of each gore and on the gore strips as seen in Figure 9.3-5
- While the 50-75 μm showed visibly excellent performance (quantitative numbers in next section), 10-50 μm dust was difficult to drop with uniform coverage over the entire knee. The small grain dust was very cohesive. Therefore, when the dust was dropped over the knee area, it dropped in clusters causing several layers buildup of dust. This impeded the performance and was not immediately comparable to that of 50-75 μm dust clearance.
- However, one of the critical observations during the 10-50 μm dust was that, even if clusters of dust adhered to the fabric, when additional dust, specifically the 50-75 μm was dynamically dropped over these areas with the cohesive dust, the new dust picked up the already adhered dust and visibly cleared the area (bottom picture in Figure 9.3-6). Details are captured in section 9.3.2.2.

Figure 9.3-6. Dynamic dust condition cleaning results

9.3.1.2. Dust Cleaning Performance

Quantitative analysis using ImageJ was conducted to estimate the performance of the system in dynamic dust conditions. The parameter used to determine the performance for the dynamic dust setting was the total amount of dust coverage over the knee covered in electrodes after dust cleaning operations. Microscopic observations on the amount of dust remaining over the fabric were analyzed. Figure 9.3-7 illustrates the results on the percentage of area covered by dust after cleaning operations obtained for each knee angle (15°, 30°, 45°) along with results from the coupon test (represented as 0° in the figure). The figure displays the average value of dust coverage calculated over the five sections on two repeated runs for each angle.

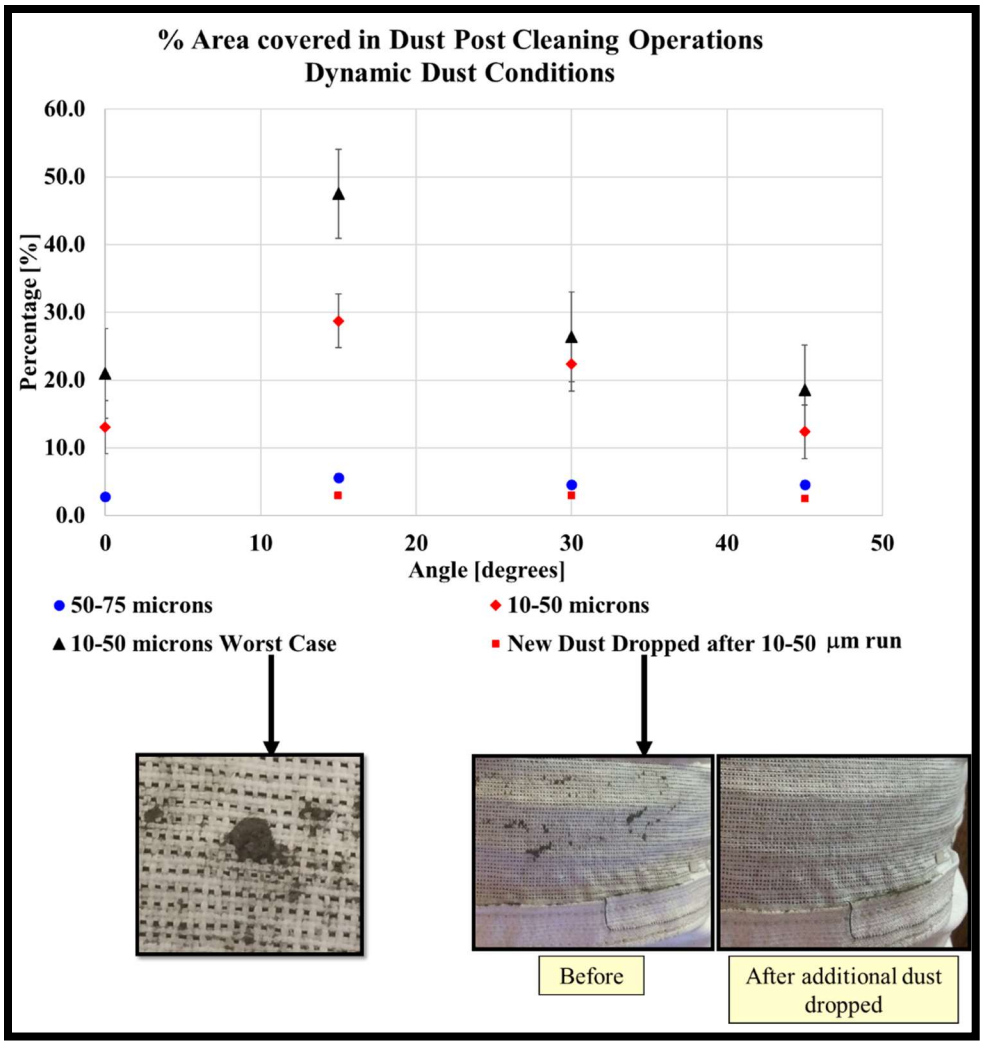

Figure 9.3-7. Percentage of fabric area covered in dust after dust cleaning operations

For the 50-75 µm dust loading, results show that the system can clear most of the dust dropped over the knee and the percentage of dust covering the knee post cleaning is within 5% of the fabric area at all angles. The difference in performance of the system was minor between all three angles tested, with the 15° position having the highest (5.4%) percentage of area covered by dust. Compared to the coupon tests, the knee experiments show an increase of approximately 2.5% in the dust remaining on the fabric. This minor difference is attributed to the 50-100 V decrease in the operating voltages while performing the knee experiments due reasons captured in section 9.3.1 (breakdown initiation at a lower voltage due to electrode distance change caused by creases/folds and manufacturing process). The decrease in the operating voltage impacts the electric field produced near the electrodes, thereby impacting the performance of dust cleaning ability. In this case the decrease of 100 V for example reduces the electric field produced by 11 %

that is translated into the 2.5% increase in the dust covering the fabric. The overall dust coverage however is less than 10% post cleaning operations for all knee angles.

For the 10-50 µm, the biggest challenge was to uniformly distribute the dust during the dynamic dust loading operations. Like the coupon tests, when this grain size simulant was dropped over the knee, there were areas where a dust dropped in clumps covering up the electrode region with several layers of dust (see left inset in Figure 9.3-7, and 9.3-8). Additionally, being able to drop the dust during the 15° knee position was also a challenge for the small grain size. Due to the angle of the knee, some of the dust did not get to the fabric. Therefore, the dust was dropped in multiple angles to be able to cover the fabric which resulted inconsistent dust loading. This impeded the performance of the system. Figure 9.3.-7 shows that the percentage of the fabric covered in dust after cleaning operations for some runs was >25%, However, the performance of the system for just the small grains is inconclusive (includes worst case areas where substantial amounts dropped in a single area (>5g).

Figure 9.3-8. 10-50 µm dust dropped over the knee. Clusters of dust covered a small section of the fabric

A critical observation made during the experiments was that when 50-75 µm dust was dropped over the residual 10-50 µm dust on the fabric while the system was still active, the new dust removed nearly 95% of the adhered 10-50 µm dust. These values are shown in the lower half of the Figure 9.3-9, that show how the % dust coverage from worst case areas represented by (▲) reduced to less than 5% dust coverage represented by (■). Based on the available data from Apollo missions, the lunar regolith includes ~ 45% of dust between 0-45 µm dust, and roughly 55% of the dust is above grain sizes of 45 µm (See Figure 9.3-9).

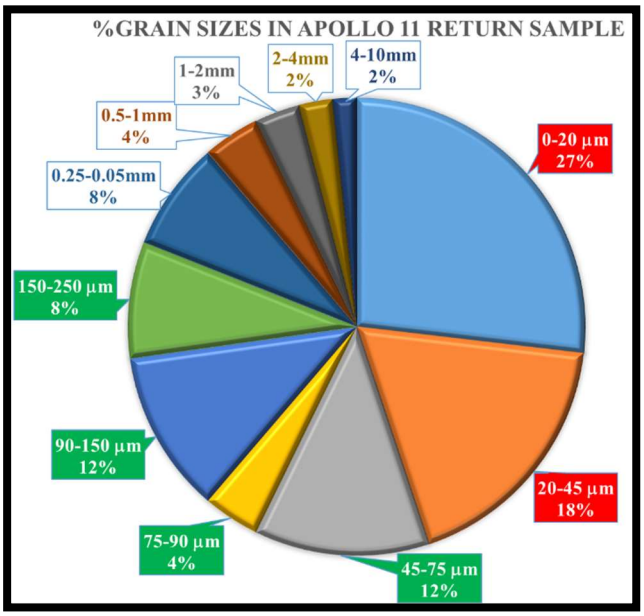

Figure 9.3-9. Lunar dust particle size distribution from Apollo 11 sample (McKay et al., 1989)

Therefore, the lunar dust is a mixture of assorted sizes and is not isolated to just the 10-50 μm dust as tested in the current experiments. It is anticipated from the available data and the observation during the experiments that the mixture of various dust grains would help solve most of the cohesion issues encountered during the 10-50 μm runs in the experiments and exposure to purely the <50 μm range during lunar operations may be rare. Tests in the future are recommended to be conducted with a mix of grain sizes ranging from 5-150 μm, to evaluate realistic dust loading conditions on the lunar surface rather than focusing on specific dust sizes due to the cohesive behavior of the dust when isolated to just small grain sizes.

9.3.3. Static Runs

For the static runs, after the module was pressurized, 1 gram of dust was measured and the knee area was covered with the dust simulant. Microscopic images were collected in this condition. The power system was then turned on to activate the CNT electrodes until all visible dust seemed to be repelled (approximately 60 seconds). The power system was then turned off and microscopic images of the dust coverage after cleaning operations were collected like the dynamic tests. Data was collected on two consecutive runs.

9.3.1.3. Key Observations during Static Dust Loading

- The SPIcDER system clearly demonstrated its ability to repel dust when visually observed during static dust loading. Statically adhered dust from the fabric was visibly cleared when the electrodes were energized, particularly the 50-75 μm in all knee angle positions. Figures 9.3-10 and 9.3-11 illustrate the cleaning ability of the SPIcDER system when embedded on the knee joint section.
- Results show that for the 50-75 μm, the system could clear between 90-94% of the statically adhered dust on the knee
- Results show that for the 10-50 μm, the system could clear between 75-88% of statically adhered dust. Similar to the dynamic runs, the 10-50 μm dust was difficult to load with uniform coverage over the entire knee due to its cohesiveness and specially on the 15^{o} angle position. The knee was almost vertical; therefore, it was a challenge to load the fabric with dust statically without some of it falling on the floor prior to activation. Therefore, for the 15^{o} angle, the knee was placed horizontally and dust was loaded. For rest of the

angles, dust was made to stick to the fabric by manually pressing with gloved fingers. For the 10-50 μm, due to challenges with dust loading limited data was usable for the analysis. This impeded the performance and was not immediately comparable to that of 50-75 μm dust clearance.

- One of the critical observation during the 10-50 μm dust loading was that, even if clusters of dust adhered to the fabric, when additional dust, specifically the 50-75 μm was dynamically dropped over these areas with dust, the new dust picked up the already adhered dust and visibly cleared the area. With this newly dropped dust, the system could once again clear nearly 96% of the previously adhered 10-50 μm dust over the knee
- At 15 °, uniform dust loading was a challenge in the vertical position of the knee. The presence of gravity resulted some of the dust dropping to the base during dust loading operations. It was much easier to load dust over the knee when in 30° and 45° knee angles
- Same operational voltages for each angle as utilized in the dynamic tests were utilized in the static runs
- Dust accumulated where no CNTs were embedded-towards the bottom of each gore and on the gore strips as seen in Figure 9.3-10

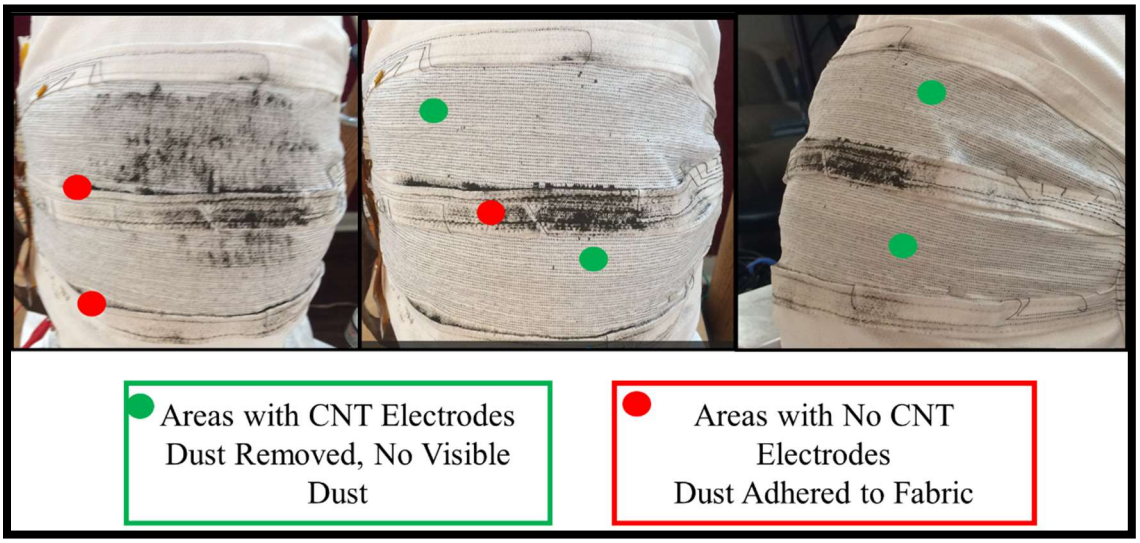

Figure 9.3-10. Before and after cleaning images of the static dust locating cleaning operations.

Angle	Before Dust Cleaning	After Dust Cleaning
15° Operating Voltage and Frequency : 900 V, 5Hz 50-75 µm		
30° Operating Voltage and Frequency : 945 V, 5Hz 50-75 µm		
45° Operating Voltage and Frequency : 970 V, 5Hz 50-75 µm		
45° Operating Voltage and Frequency : 945 V, 5Hz 10-50 µm followed by 50-75 µm		

Figure 9.3-11 Static dust condition cleaning results

9.3.1.4. Dust Cleaning Performance

Dust cleaning performance of the SPIcDER system was conducted using ImageJ analysis. Figure 9.3-12 illustrates the overall results on the percentage of fabric area covered by dust after cleaning operations for each knee angle (15°, 30°, 45°) along with results from the coupon test (0°). The figure displays the average value of dust coverage over the five sections on two repeated runs for each knee angle. For the 50-75 µm, all five data points for two consecutive runs were utilized. For the 10-50 µm, only limited data points (2-4) points over the two runs per angle were valid since the dust loading on the knee at the various angles was a challenge to uniformly distribute the dust over the knee. Results show that for the 50-75 µm, less than 7% of the fabric is covered by

dust after cleaning operations. Similar to the dynamic runs, the 10-50 µm dust was very cohesive and did not consistently drop over the fabric. The best-case scenarios showed that after cleaning operations less than 20% of the fabric was covered in dust. However, worst case scenarios where clusters of dust dropped and could not be cleared at initial system power on show nearly 30% of the area covered in dust (▲). However, when further dust (50-75 µm) was dropped over the adhered dust while the electrodes were active, the system could repel the adhered residual dust bringing the percentage area covered by due to less than 5% as shown in the figure (■).

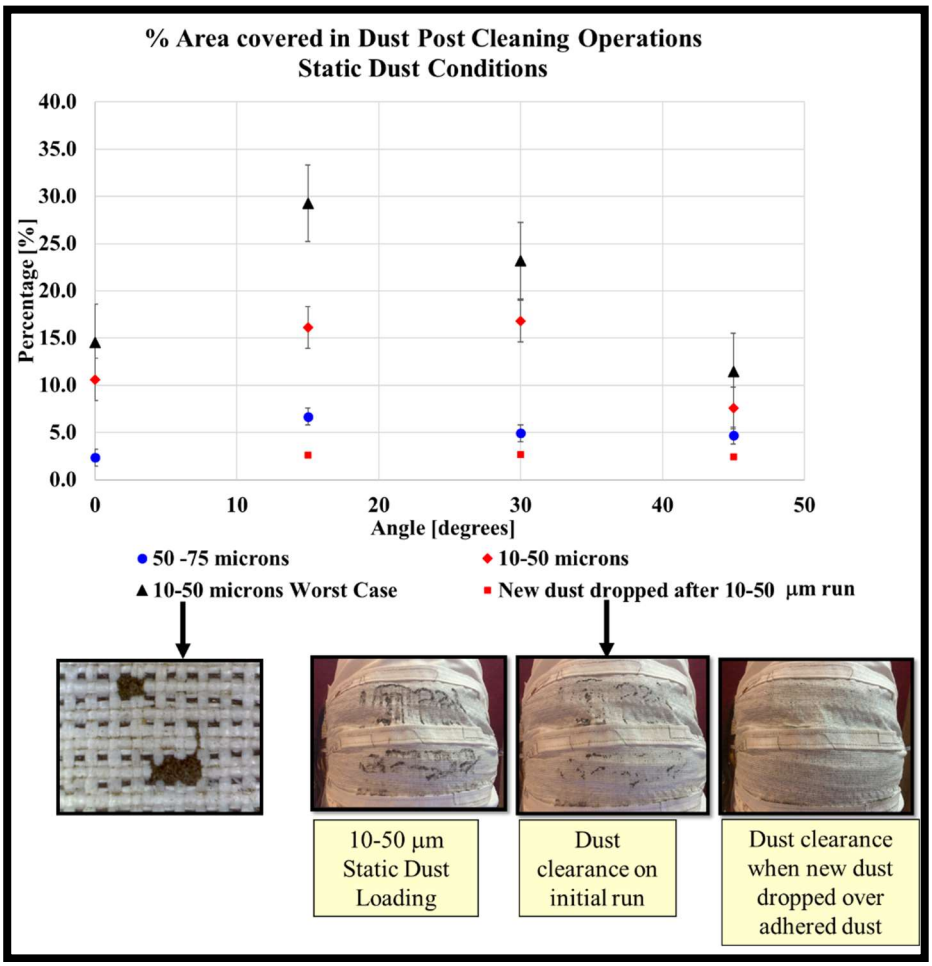

Figure 9.3-12. Overall data showing percentage of fabric covered in dust post dust cleaning operations for the 50-75 µm and 10-50 µm test runs at different angles. *The 0^{o} represents data from the coupon tests.*

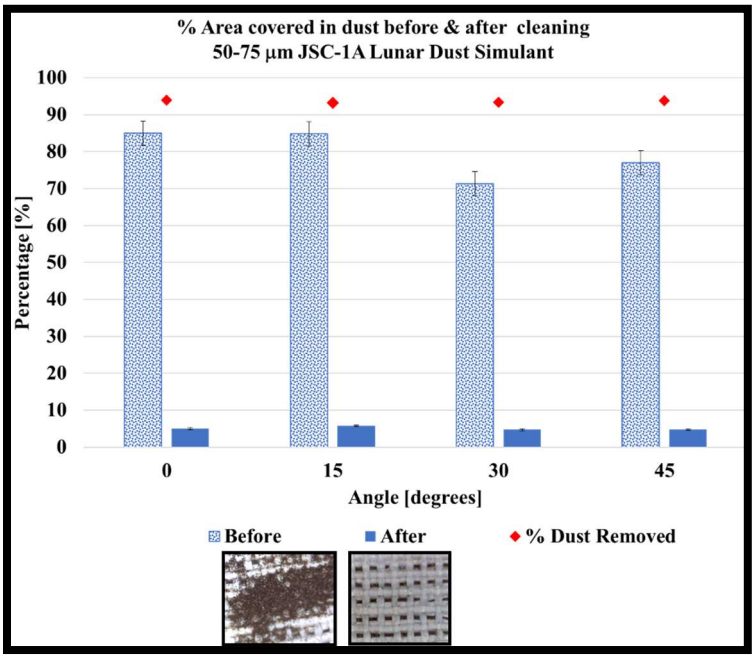

Figure 9.3-13. Percentage of area covered in dust before and after cleaning operations for 50-75 µm static dust

For the 50-75 µm dust, Figure 9.3-13 shows the percentage of the fabric covered in dust before and after dust cleaning operations along with the dust clearing performance (percentage of dust removed) which is between 92-95%. The system could clear most of the statically attached dust for all angles of the knee. Comparing the coupon test and the knee results, the percentage dust covering the coupons after dust cleaning was 2.3 % compared to the 4.9-7% dust coverage obtain in the current experiments. This difference can be attributed to two things, first the operating voltages for the coupons (0º), 15º and 45º knees angles, were 1000 V, 900-945 V and 970 V respectively. This ~50-100 V decrease in the operating voltage at the 15º angle has a direct impact on the electric field intensity produced (~11% decrease in electric field magnitude from simulation), with lower electric field compared to relatively higher electric field value on the coupon tests (0º) due to higher operating voltage.

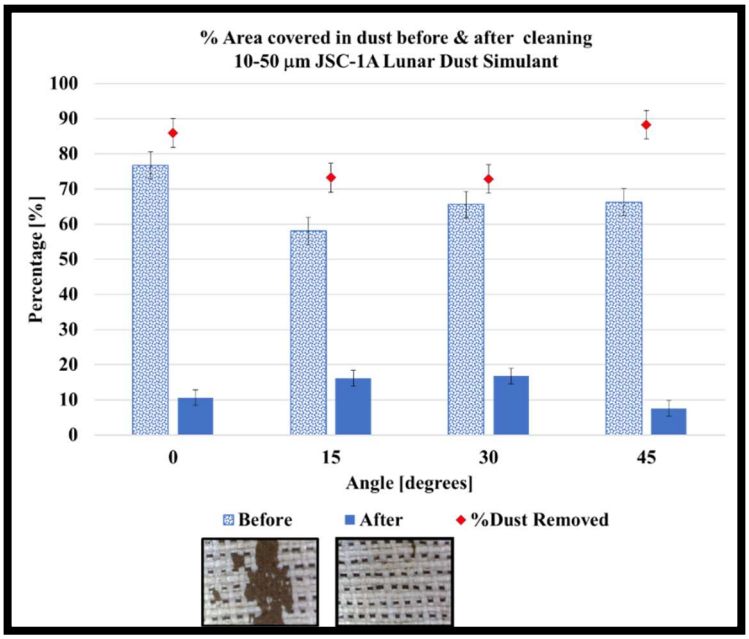

Figure 9.3-14. Percentage of area covered in dust before and after cleaning operations for 10-50 µm static dust

For the 10-50 µm dust loading, even though two consecutive runs were performed and data was collected, only part of the data was useful due to inconsistencies in being able to load the knee with uniform dust coverage. Figure 9.3-14 illustrates the before and after dust coverage and cleaning efficiency. It is noticeable that the efficiency of the

system to clear the dust at 15^{o} and 30^{o} is lower (~75%) when compared to the efficiency of the system at 45^{o} and the coupon test (0^{o}). Again, these are attributed to the lower operating voltages at the angles compared to the flat coupon. Additionally, the dust loading condition for the static case using the technique was not efficient as clusters of dust dropped in a small area and could not be distributed evenly. Nonetheless, the overall average amount of dust covering the fabric post cleaning operations is still under 17%.

9.3.4. Overall Observations of Scalable Functionality and Recommendations

9.3.4.1. Factors impacting performance

Key factors learned and identified during the experiments beyond the ones identified in Chapter 6 that need to be considered to implement the SPIcDER system on larger areas of the spacesuit, including joint sections that can be flexed are summarized in Table 9.3-2 and Figure 9.3-15 . Achievable recommendations to overcome these challenges are presented in the table and in the following section.

Table 9.3-2. Impacts of design, manufacturing and operational factors identified during prototype experiments. Recommendation provided to improve scalable functionality of the SPIcDER system.

Factor	Reason	Why it happens Observed /Validated	Result	Controls (Design, Manufacturing , Operational)	Recommendation	Improvement
Folds/Creases	Knee Angle	• At lower knee angles, fabric folds and creases due to fabric layout and gore patterning • As the knee angle increases, the folds/creases smooth out with increasing curvature • Observed in Experiments	• Compromises Electrode Spacing • Results in lower operating voltages lower knee angles	Operation and Design	• **Design** 1. Design Variable Operating voltage control into power electronics 2. Segmented electrode patterns in the corners of the knee, back of the knee (see next section for examples) 3. Improved electrode patterns to (See next section for examples) • **Operational** 1. Implement variable input voltages based on motion of knee 2. Implement dust cleaning for back of the knee after doffing suit	• Results in controllable operational voltage • Minimizes risks of arcing/breakdown during EVAs
Stretching of Fabric	Knee Angle	• With increase in knee angle curvature, fabric slightly stretched (~0.1-10%) • Observed in Experiments • Validation thoug simulations of inherent stretch due to curvature	• Increases Electrode Spacing • Higher operating voltages at higher angles needed for consistent dust cleaning	Operation	• **Design and Operational** 1. Variable Operating voltage control into power electronics 2. Example: when astronaut sitting on a rover, can operate at higher voltage, than when standing on the surface	• Results in consistent dust cleaning performance at all angles
Electrode Alignment/ Orientation	Manufacturing	• Manually embedding CNTs in large areas results in inconsistencies • Observed in Experimental prototype	Inconsistent Electrode Spacing	Manufacturing	• **Manufacturing** 1. Implement automated weaving method. Examples: ○ Include CNT electrodes into the fabric making process as the warp thread (See Chapter 4) ○ Utilized automatic machines to embed electrodes over finished fabric (See Chapter 4)	Results in higher EF forces
Fraying of electrodes	Manufacturing	• Micron sized fibers poking out of electrodes dur to handing of bare electrodes • Observed in Experimental prototype	Decrease in Electrode spacing results in arcing at lower voltages	Design and Manufacturing	• **Design** 1. Insulate CNT electrodes with flexible insulting material • **Manufacturing** 1.Implementation of insulation can be done at individual electrode level or overall electrode area	• Increased operating and threshold voltages • Increased cleaning performance • Decrease in risk of arcing • Decreased risk of fraying of electrodes

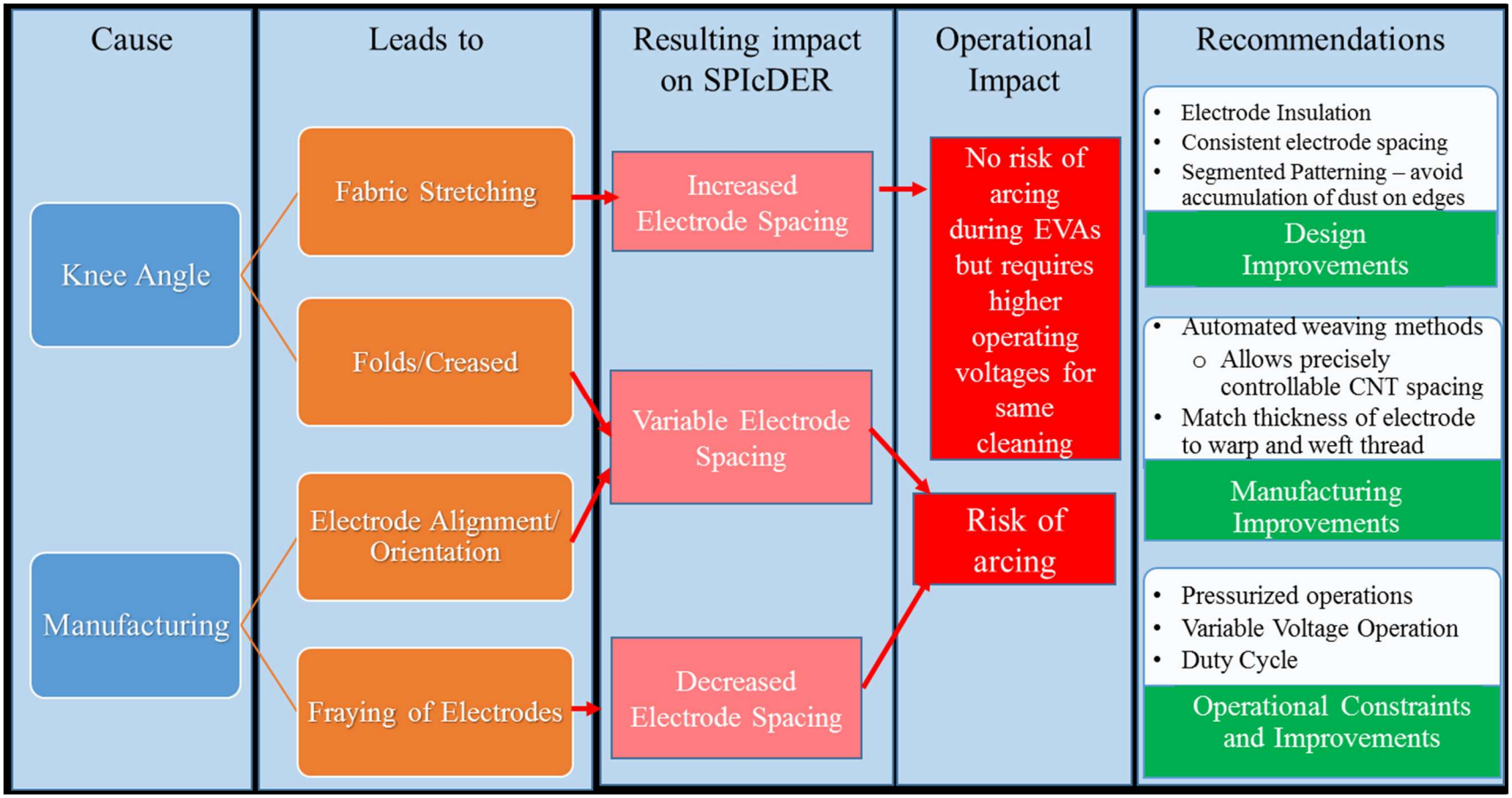

Figure 9.3-15. Summary of findings from prototype experiments on the knee joint section

9.3.4.2. Overall Dust Cleaning Performance

Based on visual observations and ImageJ analysis the overall performance of the SPIcDER system on a scaled unit shows promising results to further this technology for spacesuit dust cleaning operations. Based on data collection, the overall efficiency of the system for a pressurized module at different angles is estimated to be in the range 75-96% depending on particle size and knee angle. The worst-case scenarios are when the knee angle is 15°, specially when tested with the 10-50 µm grain size particles. This reduction is due to lower operating voltages at the angle which was driven by the creases in the fabric, and partly because within these creases there were areas were the fiber frayed and small micron sized hair form consecutive electrodes came in close contact, thereby reducing the threshold voltage. However, the performance significantly improved when fresh dust was dropped over the areas where dust already adhered (ex: changed from 25% dust coverage to 2% dust coverage). Some of the worst-case scenarios can be prevented using improved manufacturing techniques as stated in the Table 9.3-2 and the next section. Table 9.3-3 summarizes the performance results from the experiments for the scaled prototype.

Table 9.3-3. Summary of dust cleaning performance of the SPIcDER system on a scaled unit

	% Fabric area covered in dust post cleaning operations		Average % of Dust removed
Particle Size	Dynamic	Static	$\frac{A_{B\_dust} - A_{A\_dust}}{A_{B\_dust}} \times 100$
50-75 µm	4.4 % [average of all dynamic cases]	5.2% [average of all static cases]	94%
10-50 µm	15.4 % [average of all dynamic cases including worst case with heavy loading]	11 % [average of all dynamic cases including worst case with heavy loading]	87%
Overall Average for 10-75 µm particle size range	10.2 % [Average of all dynamic cases for both particle size range]	8% [Average of all static cases for both particle size range]	90% [average of all runs] [Worst case: 75%, Best case: 96%]
Standard Deviation	5 [All cases for both particle range]	5.1 [All cases for both particle range]	8.3

9.3.4.3. Recommendations for Improvements in SPIcDER Manufacturing and Design

The efficiency of the system can be improved by increasing the operating voltages and by minimizing overlap of the electrodes by maintaining consistent spacing between the electrodes as identified in Table 9.3-2. Based on lessons learned during building and testing the scaled prototype recommendations proposed in table 9.3-2 are detailed here. While some of these suggested recommendations are achievable, they could not be implemented during the duration of this research due to constraints with funding and equipment availability.

A. Manufacturing and Design Improvements

1. Electrode Insulation

One of the reasons for lower breakdown and operating voltages observed during the experiments was small micron sized fibers sticking out from the uninsulated CNT electrodes that were very close to the next electrode when the fabric was creased. These can be avoided by insulating the CNT fibers which would align the individual CNT filaments and avoid fraying of fibers, providing an increase in the operating voltages

2. ***Maintaining consistent electrode spacing***

Automated weaving techniques as explained in Chapter 4, to prepare the suit fabric (dust repelling fabric) would help with inclusion of the CNT fibers as part of the fabric making process. By doing so, the CNT fibers alignment and spacing can be precisely controlled. The CNT fibers can be part of the warp thread itself maintaining consistent spacing between the electrodes. The inconsistencies that were visible during the manual methods can be overcome as the spacing of the warp and weft threads in the automated process can be controlled while manufacturing the underlying fabric as well as by utilizing the required thickness of the warp and weft threads to space the parallel electrodes in a consistent manner. This helps to maintain a consistent breakdown voltage throughout the fabric allowing for consistent operating voltages.

Furthermore, if manual methods are utilized, the thickness of the electrodes could be increased to match the thickness of the warp and weft threads to maintain the alignment of the electrodes and consistent spacing between consecutive electrodes. This would also help with increase in the electric field force and the performance is anticipated to improve for smaller grain sizes.

3. Avoiding accumulation of dust on edges

The accumulation of the dust in the edges of the gores can be avoided by exploring new electrode arrangement patterns. Two new electrodes arrangements are suggested. 1.Spiral pattern of the electrodes within the gores and the which is possible if automated methods of embedding electrodes are utilized. 2. The orientation of the electrodes can also be changed to perpendicular direction than what is currently utilized (See Figure 9.3-16). Also exploring other unique ways of designing the gores to minimize pockets and fabric overlaps would help mitigate this problem. These suggested solutions proposed here are not implemented during the experimental work due to lack manufacturing equipment, however these solutions are thought to provide improved dust cleaning performance.

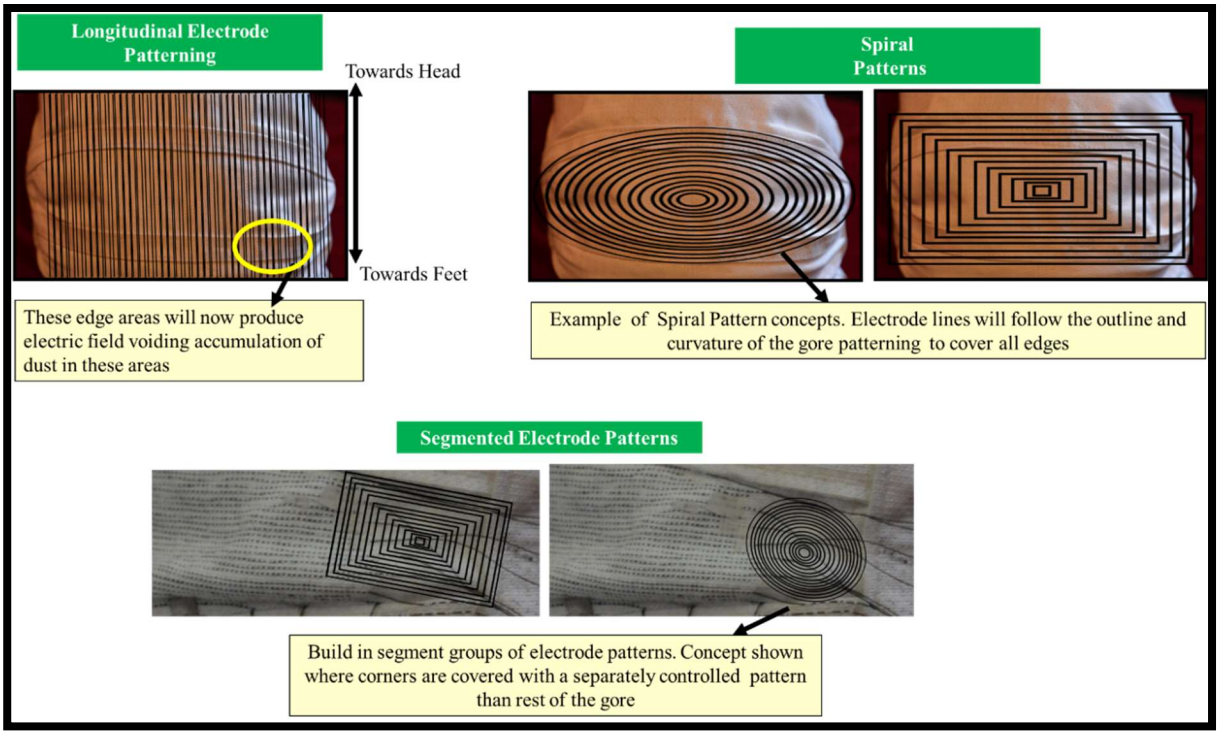

Figure 9.3-16. Suggested solutions to improvement dust cleaning, avoid areas of accumulation and overcome issues with bunching of fabric.

4. Terminal connections

To avoid overlap of the three phase terminals, one set of terminals may be connected on the inside of the fabric. The third set of electrodes can be passed through the backside of the fabric where they can be grouped and terminated to connect to the power system. The specific area on the back side where the electrodes penetrate can be covered with an extra layer of insulating fabric to avoid any contact to the inner layer

B. Operational Constraints and Improvements

1. *Pressurized versus unpressurized*

The joint-sections of the spacesuit are the most complex sections. The fabric folds and unfolds when the suit is unpressurized and pressurized respectively. The important requirement for stable functioning of the SPIcDER system is that the electrodes maintain the spacing between them and there is no overlap. During the EVAs, it is ideal to operate front side of the system when the suit is pressurized. Since the back side of the suit, specially the knee section will include folds/wrinkles the back side of the can be implemented with a separate segment of electrode pattern that is operated post EVAs. After EVAs, when the suit is unpressurized and doffed, the suit can be laid out and the areas with folds in the joint sections, especially the back side can be manually adjusted to smooth out the fabric and then operate the SPIcDER system to remove any adhered dust

2. Variable Voltage Operation

Experiments showed that even with folds at 15^{o} neutral angle, the fabric could repel and remove the dust from the areas. This was accomplished at lower operating voltages (900V versus 1000V) due to the lower threshold voltage. Since the motions of the astronaut during an EVA causes folds, implementing adjustable voltage inputs into the power electronics will aid in changing the input voltage as needed. The input voltage can be adjusted during different positions of the knee while conducting EVA operations, for example when the astronaut is seated on a rover, the knee is fully flexed, allowing an increase in the operating voltage.

3. Duty Cycle

It may be beneficial to operate the system in bursts of ~60-120 seconds every 30 minutes during EVA operations when the astronaut comes to a stop, at set intervals during the EVA. For situations where the astronauts are sitting on a rover with legs in flexed position, they can continuously operate the system. For drilling operations for example, where dust can continuously float and drop over the suit, the SPIcDER system can be activated to minimize dust sticking to the suit.

9.4. Vacuum Conditions

Two coupons were constructed to test the effectiveness of the SPIcDER system in vacuum conditions. Configuration of the two coupons are presented in Table 9.4.1. Based on lessons learned from vacuum tests listed in Chapter 5, two updates were made to the procedures:

1. Prior to embedding electrodes into the second orthofabric coupon, the CNT fiber was heated to 300ºC for 24 hours by the supplier to remove any acidic residuals from the fiber to prevent off-gassing in vacuum.
   a. The difference in properties for the CNT fiber before and after baking are listed in Table 9.4-2. There is nearly a 40% decrease in conductivity after baking the CNT fiber, however, the decrease in the conductivity would not impact the performance since the time constant τ (Resistance*Capacity) as explained in Chapter 6 is still on the order of 10^{-10}-10^{-11} seconds. This means the charge-discharge cycle on the electrodes is still the same order of magnitude between the unbaked and the baked samples.
2. Prior to depositing dust over the coupon in the chamber, calibration test to evaluate the threshold voltage at which breakdown occurs in vacuum is performed. Subsequent dust deposition was conducted at 50-100 V below the threshold voltage.

Table 9.4-1. Configuration of coupons tested in vacuum conditions

	Coupon 1	Coupon 2
Number of CNT electrodes	12	9
CNT fiber type	Unbaked	Baked at 300º C
Fiber Insulation	None	None
Coating	WFM coating	No Coating
Spacing	~1-1.2mm	~1-1.2mm
Phase	3 phase	3 phase
	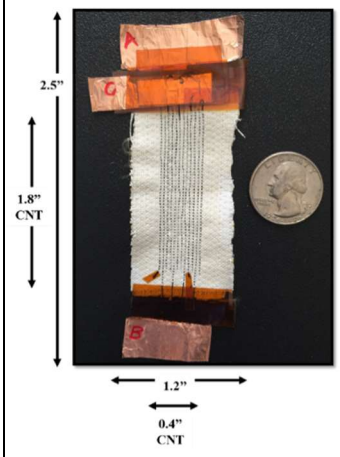	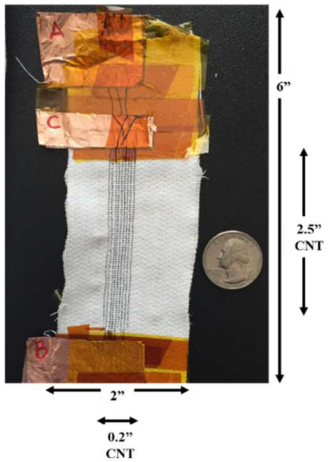

Table 9.4-2. CNT properties for the Vacuum chamber test coupon

CNT Electrode Properties		
	Unbaked	***Baked**
Diameter	212±7 μm	212±7 μm
Linear Density	30.5±0.5 tex	25.7±0.4 tex
Density	0.72 g/cm^3	0.72 g/cm^3
Resistance	10.5±0.2 Ω/m	18.4±0.2 Ω/m
Electrical Conductivity	2.7± 0.1MS/m	1.5± MS/m
Specific Conductivity	3100 Sm^2/kg	2100 Sm^2/kg
Tensile Strength	835± 40 MPa	835± 40 MPa
Strength (Tenacity)	1.1 ±0.1N/tex	1.1 ±0.1N/tex

9.4.1. Test Set-Up and Procedures

9.4.1.1. Vacuum Chamber

Vacuum tests were conducted at KSC in the ESPL lab. The vacuum chamber was custom built for the ESPL and can attain high vacuum down to 1.0e-6 torr. The chamber is made from stainless steel with internal dimensions of approximately 18" x 18" x 24". It has multiple 2.75" Conflat ports that can accommodate pumps, viewports, high voltage feed throughs, and other instrumentation.

9.4.1.2. Set-Up

Figure 9.4-1 illustrates the test set-up. The following paragraph provides a description of how the coupons were set-up inside the vacuum chamber.

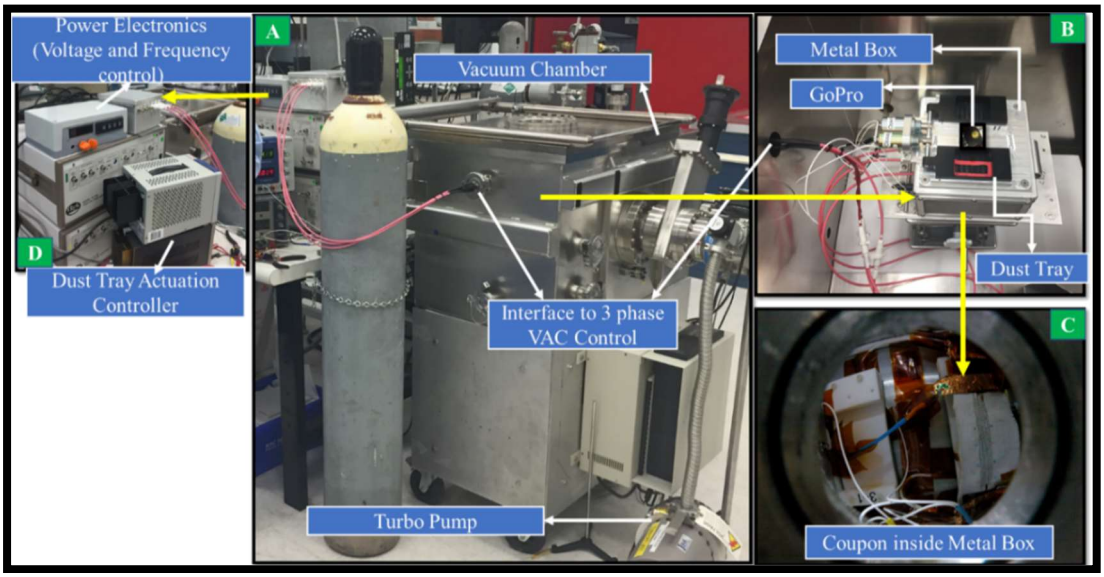

Figure 9.4-1. Vacuum chamber test set-up in the ESPL at KSC

- Each coupon was cleaned using puffs of compressed air and imaged under the microscope.
- The coupon was then placed inside the metal box on insulating plate holders. The metal box has interfaces to the power supply connections and is facilitated with a tray that holds the dust (Figure 9.4-1A). The tray can be actuated from outside the vacuum chamber to drop dust. Appropriate phase connections to the CNT electrodes were made inside the metal box first. The metal box was then placed inside the vacuum chamber. Interface connections to the power supply from the metal box exterior were mated. Additional interface connections to a LED light inside the metal box and the dust tray were mated.
- A GoPro® hero session camera was placed over the metal box to capture live video that could be controlled using an iPhone via Wi-Fi.
- The chamber was closed and pumped down to reach between 5-3e^{-4} torr. Due to a glitch in the chamber sealing, the chamber could not reach lower then 3e^{-5} torr.
- Once chamber pressure stabilized, the power system was turned on to verify threshold voltages.
- Based on the type of test, the actuation of the power supply and dust tray were as follows
  - Dynamic Test: The power was turned on first to energize the CNT electrodes followed by dust tray actuation to drop dust
  - Static Test: The dust tray was actuated first and the power was turned on after to energize the CNT electrodes

9.4.1.3. Test Sequence and Conditions

The following sequence was implemented to assess the SPIcDER system in vacuum conditions

A. Characterization of coupons using microscope
B. Calibration in Ambient Conditions
    a. Threshold voltage in ambient conditions
C. Vacuum Conditions
    a. Identify threshold voltage in vacuum conditions where breakdown initiates
    b. Dynamic Tests – collect data from two consecutive tests
        i. Lunar Simulant JSC-1A 50-75 μm

ii. Lunar Simulant JSC-1A 50-75 μm
iii. Martian Simulant JSC-1 Mars 50-100 μm

c. Static Test - collect data from two consecutive tests
i. Lunar Simulant JSC-1A 50-75 μm
ii. Lunar Simulant JSC-1A 50-75 μm
iii. Martian Simulant JSC-1 Mars 50-100 μm

9.4.1.4. Data Collection and Analysis

Similar to previous tests conducted in ambient conditions, qualitative and quantitative data was used to assess the feasibility of the SPIcDER system in vacuum conditions. GoPro® hero session camera was utilized to capture real time video inside the vacuum chamber. The camera was controlled using an iPhone from outside the chamber. Pre-and post-test microscopic images were taken using a handheld digital microscope. Both the dynamic and static tests were repeated multiple times. Data was obtained for two consecutive runs. After each run was completed, the vacuum chamber was positively pressurized and the chamber was opened. The coupon was imaged in place post-test using a handheld digital microscope to record the state of dust distribution. Microscopic images were taken at 20X magnification to record the state of the coupons and dust distribution. Table 9.4-3 provides a list of test cases performed in the vacuum chamber. The capability of the dust cleaning system was evaluated using

1) Visual inspection via the videography and images collected during the experiments to document observable dust cleaning capability for the qualitative aspect of the analysis

2) ImageJ® software was subsequently used to estimate dust particle coverage using microscopic images to approximate the amount of residual dust on the fabric for the quantitative portion of the analysis. Equations described in section 9.2.5 were used to calculate the dust cleaning performance of the system in vacuum conditions.

	Run Type	Particle Size (μm)	Dust amount (mg)	Operating Voltage (V)	Frequency (Hz)	Pressure (Torr)
Coupon 1	Threshold Voltage Calibration			450-500	5	5.2×10^{-4}
	Dynamic Dust Loading	50-75	130	350-400	5	3.8×10^{-4}
	Dynamic Dust Loading	10-50	165	350-400	5	5.2×10^{-4}
	Static Dust Loading	50-75	120	350-400	5	5.2×10^{-4}
	Static Dust Loading	10-50	132	350-400	5	5.5×10^{-4}
Coupon 2	Threshold Voltage Calibration			350-400	5	5.5×10^{-4}
	Dynamic Dust Loading	50-75	130	350-400	5	5.4×10^{-4}
	Dynamic Dust Loading	10-50	165	350-400	5	5.5×10^{-4}
	Static Dust Loading	50-75	130	350-400	5	5.7×10^{-4}
	Static Dust Loading	10-50	132	350-400	5	5.7×10^{-4}

Table 9.4-3 List of test cases performed in the vacuum chamber

9.4.2. Vacuum Chamber Test Results and Discussion

9.4.2.1. Threshold and Operating Voltages

The expectation in vacuum conditions is that the threshold voltage of the system where breakdown occurs would be at a voltage higher than what was observed during ambient conditions. At lower pressures, there are not sufficient ions in the surrounding medium which allows an increase in the voltage before the ions are energized by the electric field providing a conducting path causing breakdown. In ambient conditions, repeated experiments with multiple coupons with electrodes spaced at ~1.2 mm showed that breakdown occurs at 1200 V and 1600V for 2 mm spacing. Experiments in vacuum however showed that breakdown for both the coupons tested (~1-1.2 mm) was initiated around 450-500 V on repeated tests. When the voltage was increased to 700 V several bursts of sparks over the electrode area were noticed. These sparks were quick and short lived (milliseconds) unlike the continuous arcing that occurs during breakdown. This unexpected result from the vacuum tests are hypothesized due to the presence of micron sized fibers fraying from the uninsulated CNTs electrodes (see Figure 9.4-2). CNTs are also known to have a low threshold electric field for electron field emission (Chen and Zhou 2003). Field emission is a mechanism that extracts electrons under a sufficiently high external electric field and escapes to the vacuum level. Generally, for metals, the threshold fields are typically around 10^4 V/ μm which

is impractically high. Whereas this value is low for CNT fibers ~2-3 V/μm for a current density of 1 mA/cm^2 (Chen and Zhou, 2003).

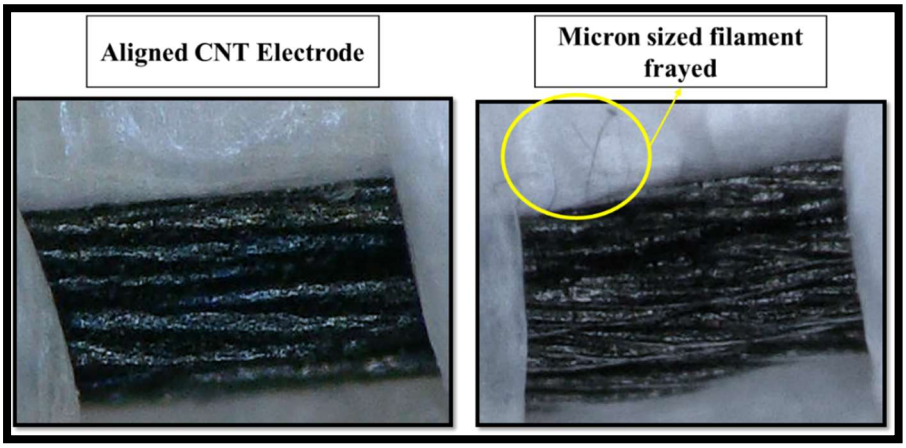

Figure 9.4-2 [Left] 200X magnification of a well aligned CNT electrode, [Right] A micron sized fiber sticking out of the CNT electrode alignment

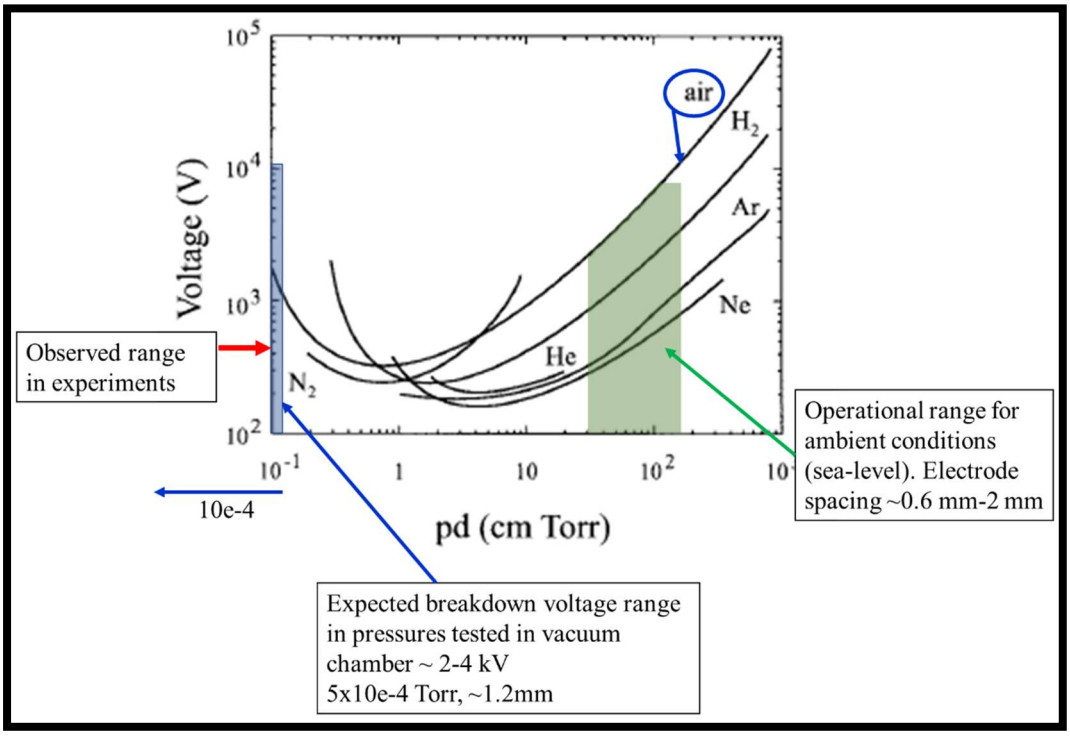

Figure 9.4-3. Expected versus observed breakdown voltage range during vacuum chamber experiments.

Figure 9.4-3 shows the theoretical expected breakdown voltage range for the pressures tested in the vacuum chamber. While the threshold voltages were shown to be lower in vacuum conditions using the CNT electrodes, the system could still repel and clean the dust on the fabric with the same efficiencies as seen in ambient conditions at much lower voltages (350 V in vacuum

compared to 1000 V). This is particularly advantageous for the present application due to the safety aspects reported in Chapter 8. Table 9.4-4 provides a comparison of the threshold voltages observed from ambient and vacuum conditions for the same configuration of the electrode arrangement on the orthofabric coupon.

Table 9.4-4. Threshold voltages experimentally observed in ambient and vacuum conditions

CNT electrode Spacing	Number of electrodes	Threshold Voltage in Ambient	Threshold Voltage in Vacuum
~1-1.2 mm spacing	9	1200V	450-500V
~1-1.2 mm spacing	12	1200V	450-500V
~1.6 mm spacing	6	1400V	750-800V

9.4.2.2. Dynamic Tests

Analogous to ambient conditions, real time observations of the drop test experiments in the vacuum chamber also demonstrated the ability of the SPIcDER system to repel and remove dust. As described in the previous section, cleaning was observed to occur at lower input voltages. When the SPIcDER system was activated and dust was dropped over the coupon by actuating the dust tray, it was evident that dust was repelled over the active area of the coupon. One of the critical observations during the tests was although threshold voltages initiated at 500 V, short-lived (millisecond rage) sparks were observed during the cleaning operations. This is once again attributed to the fibers fraying and electron field emission that releases electrons from the tips of the CNTs. These short sparks were favorable for cleaning performance as the frayed fibers with pointy tips would produce high localized electric field. These micro-sparks can be prevented by coating the CNT electrodes with a thin layer of insulative/dielectric material that would align the micron-sized fibers. Table 9.4-5 lists the input signal, dust loading conditions and before-after pictures to illustrate the dust removal capability of the system in vacuum conditions.

Table 9.4-5. Dynamic drop test observations in vacuum conditions

Description	Before Activation	After Activation
• 9 electrodes • ~1.2 mm spacing • 350V, 5z • 50-75µm JSC-1A Lunar Dust • ~130mg of dust dropped		
• 12 electrodes • ~1.2 mm spacing • 350V, 5z • 50-75µm JSC-1A Lunar Dust • ~130mg of dust dropped		
• 9 electrodes • ~1.2 mm spacing • 350V, 5z • 10-50µm JSC-1A Lunar Dust • ~165mg of dust dropped		
• 12 electrodes • ~1.2 mm spacing • 350V, 5z • 10-50µm JSC-1A Lunar Dust • ~165mg of dust dropped		
• 12 electrodes • ~1.2 mm spacing • 350V, 5z • 10-50µm JSC-1A Lunar Dust • >200mg of dust dropped • *Heavy dust loading		

Qualitative observations showed that the dust visibly cleared from the coupons. Quantitative analysis was performed to estimate the percentage of area of the coupon covered in dust post SPIcDER cleaning operations. This was achieved using ImageJ analysis to estimate dust coverage

over the coupon over an average area of 6 mm x 5 mm. The coupon was imaged over three sections analogous to ambient conditions and data was analyzed per run for an overall of 6 runs (3 runs per coupon). Figure 9.4-4 captures the percentage of the 30 mm^2 area covered in dust post cleaning. The data per run is averaged across the three sections.

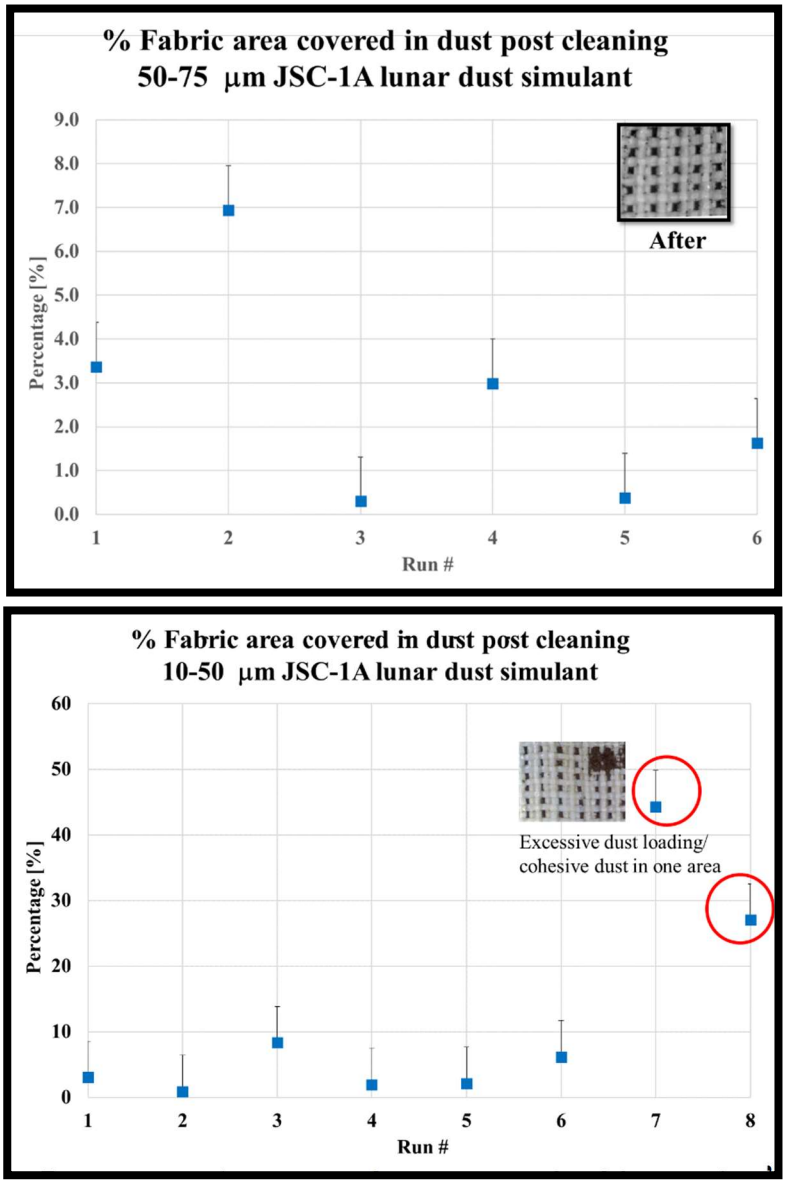

[Bottom] 10-50 µm. *Both showing % of the coupon area covered in dust post cleaning in vacuum conditions*

Results illustrate that for dynamic tests, less than 10% of the of the coupon is covered in dust after cleaning. The system could reproduce similar cleaning results on repeated drop tests. These results are comparable to the performance in ambient conditions. Similar level of cleaning performance in vacuum conditions was achieved at much lower voltages (350 V) when compared to higher voltages (1000 V) in ambient conditions. Two additional runs were conducted using the 10-50 µm with higher dust loading coverage (>200 mg). In this case, the small grain size simulant was observed to be cohesive, even though majority of the dust was cleared there were small sections on the coupon with clusters of dust that were more than a layer deep over the coupon (See Table 9.4-5). This is analogous to observations in ambient conditions.

9.4.3. Static Tests

Static tests in vacuum conditions also showed comparable cleaning performance results seen during ambient conditions. Higher amounts of dust loading (>100 mg in vacuum versus 10 mg in ambient) was used to test the system in vacuum settings. After desired vacuum level was achieved, the dust tray was first actuated to cover the coupon with the lunar simulant after which the CNT electrodes were energized at 350 V and 5Hz. Visual observations and microscopic images revealed that the system can repel between 80-95% of the dust statically attached to the coupons. Table 9.4-6 captures the before and after pictures of the static runs conducted in vacuum on both the coupons.

Table 9.4-3. Static Test observations in Vacuum conditions

Description	Before Activation	After Activation
• 9 electrodes • ~1.2 mm spacing • 350V, 5z • 50-75µm JSC-1A Lunar Dust • ~100mg dust loading		 Active area that cleared dust
• 12 electrodes • ~1.2 mm spacing • 350V, 5z • 50-75µm JSC-1A Lunar Dust • ~140mg dust loading		
• 9 electrodes • ~1.2 mm spacing • 350V, 5z • 10-50µm JSC-1A Lunar Dust • ~130mg dust loading		
• 12 electrodes • ~1.2 mm spacing • 350V, 5z • 10-50µm JSC-1A Lunar Dust • ~165mg dust loading *Heavy Dust Loading	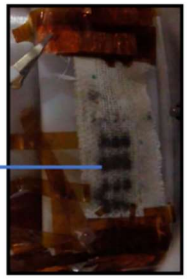	

Quantitative analysis was performed to evaluate the percentage of the coupon area covered in dust before and after dust cleaning operations. Figure 9.4-5 illustrates the percentage of the 30 mm^2 area of the coupon covered in dust before and after cleaning operations.

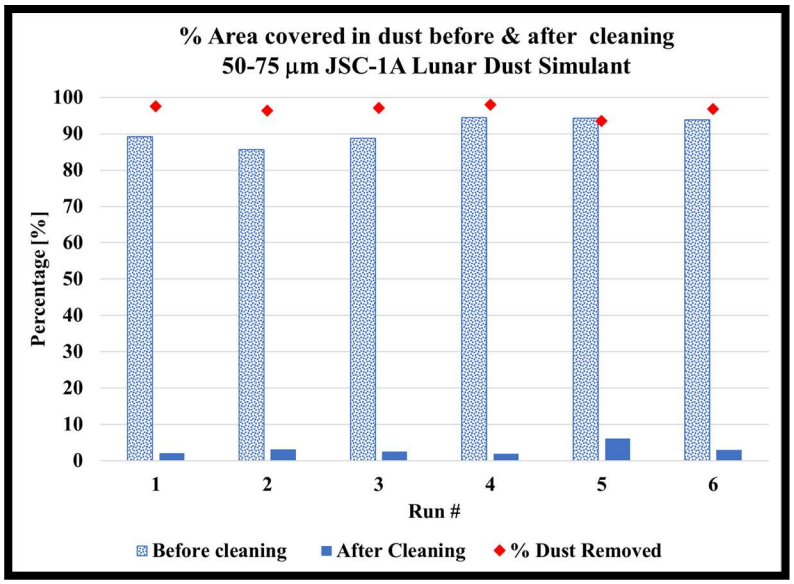

Results demonstrate that the system can clean majority of the static dust in the 50-75 µm range with less than 10% of the coupon covered in dust after cleaning operations. The system could reproduce similar cleaning results on repeated static tests on the same coupons. Similar to observations in ambient conditions and in dynamic drop tests with the smaller grain size particles (10-50 µm), some of the static runs showed heavy dust loading of the coupon in one area, where the dust on the coupon was observed to be cohesive. Although majority of the dust was cleared, there was a small section on the coupon with more than a layer deep over the coupon that was not entirely cleaned. However, it's been observed that these areas were cleaned later when the system was activated and additional dust was dropped over the coupon. The newly dropped dust could pick up the statically attached dust and clear the coupon.

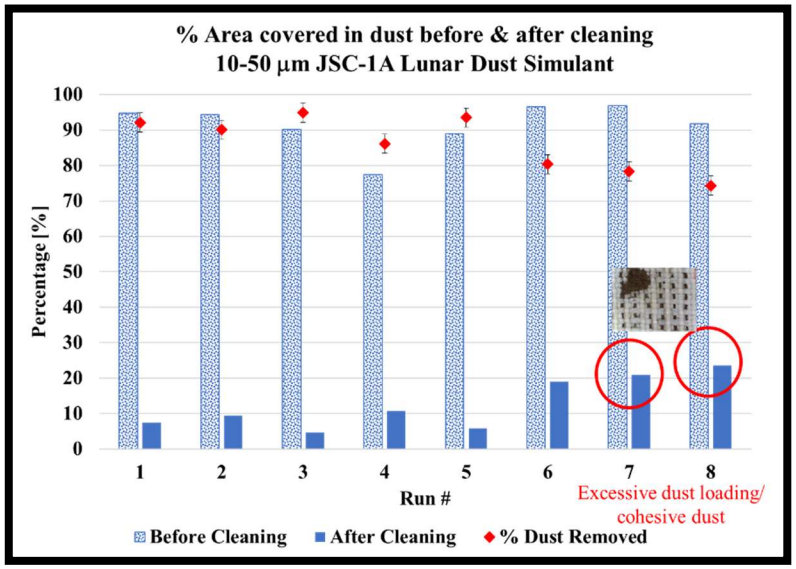

Figure 9.4-5. Static Test Results. [Top] 50-75µm, [Bottom] 10-50µm. *Plots show the percentage of the coupon area covered in dust*

9.4.4. Other Observations and Overall Performance in Vacuum Conditions

9.3.4.4. Critical Observations

1. The breakdown voltages in vacuum conditions were lower when compared to breakdown voltages in ambient conditions.

2. Based on previous observations in vacuum conditions, one of the coupons utilized CNT fiber that was oven baked to minimize off-gassing issues (9 electrodes coupon) while the other coupon (12 electrodes) was fabricated utilizing regular CNT electrodes. After operating both the coupons in vacuum conditions, the coupon that was not baked showed signs of discoloration around the electrode area (Shown in Figure 9.4-6). This discoloration is anticipated to be caused by both off-gassing as well as due to the micro sparks caused as result of microscopic frayed CNT fibers and possible field emission.

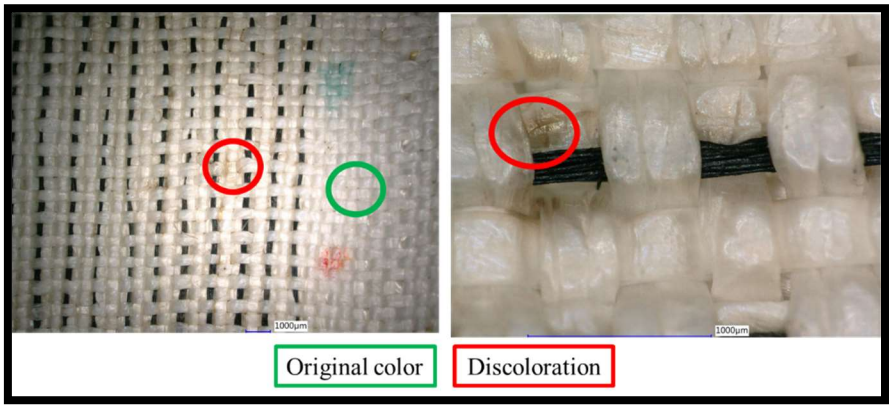

Figure 9.4-6. Change of color around the electrode area in vacuum conditions

9.4.4.1. Recommendations Based Vacuum Experiments

1. Insulate individual CNT electrodes in flexible dielectric material to align the CNT fibers within the electrode placement

2. Prior to insulating electrodes, expose electrodes to high temperatures (300°C) overnight to allow off gassing of dopant material. While this results in the reduction of conductivity, the overall performance of the system is not impacted due to the durations involved in charging the electrodes and creating an electric field to remove dust particles

9.4.4.2. Overall Dust Cleaning Performance

Based on visual observations and approximations using the ImageJ analysis to investigate the dust cleaning performance of SPIcDER, the average residual dust coverage over the coupon post cleaning is estimated to be as summarized in Table 9.4-6. The SPIcDER system is capable of repelling between 80-97% of lunar dust simulant in both dynamic and static conditions.

Table 9.4-6. Summary of dust cleaning efficiency from vacuum chamber experiments

	% Fabric area covered in dust post cleaning operations		Average % of Dust removed
Particle Size	Dynamic	Static	$\frac{A_{B\_dust} - A_{A\_dust}}{A_{B\_dust}} \times 100$
50-75 µm	3% [average of all dynamic cases]	3% [average of all static cases]	97%
10-50 µm	11.7% [average of all dynamic cases including worst case with heavy loading]	12% [average of all dynamic cases including worst case with heavy loading]	86%
Overall	7.8% [Average of all dynamic cases for both particle size range]	9% [Average of all dynamic cases for both particle size range]	91% [average of all runs] [Worst Case: 75% Best Case 97%]
Standard Deviation	3	5	7

9.5. Summary

Investigations of the SPIcDER system on a scaled joint section of a spacesuit provided insight that the dust cleaning concept proposed in this research is feasible to manufacture and operate over larger sections of a spacesuit (and other similar flexible surfaces). The experiments conducted on this prototype validate the dust cleaning performance observed during small scale demonstrations. From the data analyzed during the scaled tests, the percentage of area covered by dust after implementing the SPIcDER system is in the range 4-16%, below the set requirement of this research of 25%. Furthermore, the dust removing capability of the SPIcDER system is estimated to be between 75-96% on the scaled prototype depending on the dust exposure conditions (dynamic dust versus static dust) for lunar dust simulant particle sizes between 10-75 μm at three different knee angles. Limitations where lower performance (higher dust coverage of fabric after cleaning and lower dust removal efficiency) was observed is attributed to covering the fabric with several layers of dust, specially the 10-50 μm grain size that was cohesive. However, this was shown to overcome when dust contaminated fabric was exposed to fresh dust. It is anticipated that the lunar dust will include a mixture of 10-150 μm particle sizes and the issue with cohesive dust will be reduced. It is estimated that the results will improve if future tests utilize appropriate mixture of small and large particle size distributions replicating lunar dust particle size distribution. Recommendations for improving the manufacturability and the cleaning performance of the system have been provided based on lessons learned from the prototype fabrication and experiments.

Likewise, preliminary investigations of the SPIcDER system in vacuum conditions utilizing small scale (3-6 inches) experimental samples made of orthofabric material, integrated with the CNT fiber electrodes show proof that the concept also operates to remove lunar dust simulant in approximated lunar vacuum conditions. From the data analyzed during the repeated vacuum chamber tests, the percentage of area covered by dust after implementing the SPIcDER system is in the range 3-12%, below the set requirement of this research of 25% and with an overall dust removal efficiency between 75-97% depending on the dust exposure conditions (dynamic dust versus static dust) for lunar dust simulant particle sizes between 10-75 μm. It is estimated that the results will improve if future tests utilize appropriate mixture of small and large particle size distributions replicating lunar dust. It was also shown that cleaning performance is repeatable.

While results show the promising future of the proposed techniques, there are challenges to overcome to operate the system in vacuum conditions. Some of these are easily mitigated by utilizing flexible insulating material to wrap the electrodes. Table 9.5-1 summarizes the overall optimal dust cleaning parameters for the SPIcDER configuration from the studies conducted using the scaled prototype and vacuum experiments. Experiments have shown promising results to further improve this technology for use in spacesuits and similar flexible surfaces for dust mitigation to support future lunar exploration missions.

Table 9.5-1. Summary of optimal performance parameters of the SPIcDER system in vacuum conditions for uninsulated CNT electrodes

Parameter	Optimal Values in Ambient		Optimal Values in Vacuum	Comments
Electrode Spacing	~1.2 mm		~1.2 mm	
Operating Voltage	Flat Surface 90° knee	1000 V	350V	
	15°	900 V		
	30°	945 V		
	45°	970 V		
Frequency	5 Hz		5 Hz	Square wave form utilized. Limited investigation with waveforms due to constraints on availability of power electronics system
Dust Cleaning Performance 10-75 µm	75-96%		75-97%	Estimated using visual observations, ImageJ on repeated runs. Worst case includes several layers of dust. Average is on the order of 90%
Residual % of dust on fabric	4.4-15.4 %		3-12 %	

PART V
CONCLUSION
Research Contributions and Future Work

CHAPTER 10: RESEARCH SUMMARY, CONTRIBUTIONS, AND RECOMMENDATIONS FOR FUTURE

"It always feels impossible until it's done"- *Nelson Mandela*

10.1. Summary of Key Findings

This research developed a novel concept to address dust contamination of spacesuits for lunar surface operations with extendable application to other flexible surfaces. Leveraging technology built to clean rigid and smooth surfaces, the current research applied CNT fiber technology into the spacesuit outerlayer and designed fabrication techniques to create a smart fabric that can autonomously repel dust and protect planetary spacesuits (and similar flexible surfaces) from dust contamination for future planetary exploration missions. A comprehensive study was performed in a critical area to enable long duration planetary missions during this research by implementing a combination of experimental and simulation studies. This resulted in the development of core knowledge base and demonstration of the SPIcDER system. Key findings from this research are summarized as follows:

Table 10.1-1. Key findings of from this research

	KEY FINDINGS	DETAILS
Concept	• Conceptualized the SPIcDER system with active CNT electrode network enhanced by passive WFM coating to protect suits from lunar dust contamination by making it an integral part of the spacesuit outerlayer material • Leveraged existing spacesuit outerlayer structure to integrate the SPIcDER system for autonomous dust cleaning • The technology can be customized to various environments (Moon, Mars, asteroids, Earth) and flexible structures	Chapter 4
Feasibility	• Proof of feasibility of the SPIcDER concept for dust cleaning operations demonstrated using experiments on small coupons and scaled prototype for use on full scale spacesuits (and other flexible surfaces)	Chapters 5, 9
Dust Cleaning Performance	• Demonstration of the concept to remove upto 96% of adhered lunar dust simulant in the range 10- 75 μm dust in ambient and vacuum conditions	Chapters 5, 9

	KEY FINDINGS	DETAILS
	• Demonstration of cleaning performance where less than 3-16% of the fabric covered in dust post cleaning using SPIcDER system [established requirement <25%].	
Scaled Functionality	• Demonstration of the scaled functionality of the system to implement on larger areas of a spacesuit via construction of a knee joint-section of the spacesuit. Scaled prototype disclosed that the system can be optimized to remove upto 96% of adhered dust.	Chapter 9
Best Design Parameters	• 200-250 μm thick electrodes | 1-1.2 mm spacing | 1000 V | 5 Hz • Adjust thickness of yarns relative to thickness of warp and weft threads of outerlayer	Chapter 7
Operational Modes	• Effective in both continuous and pulse mode. Requires tradeoffs depending on type of EVA and payload/tool constraints	Chapter 7
Impacts of Environment	• Degradation in performance due to humidity (>50% RH), important for Earth based applications	
Astronaut Safety	• The system is operable with human in the loop during lunar surface operations. Suggested safety and operational controls described in the corresponding chapter	Chapter 8
Key Design Parameters	• Combination of parameters impacts dust cleaning performance. Optimize system based on application • Electrode properties and spacing | Substrate dielectric properties| Particle charge to mass ratio | Waveform characteristics | Substrate structure and weaving patterns	Chapter 6
Design and Manufacturing Improvements		
CNT electrodes	• Insulate CNT yarns to 1.Avoid fraying and field emissions from frayed micron sized fibers 2. Increase cleaning performance by increasing voltage 3. Reduce human exposures to bare CNTs and protection from possible arcing if fibers are frayed	Chapter 5, 8, 9
	• Expose yarns to high temperatures to remove off-gassing prior to embedding into spacesuit outerlayer	Chapter 5,9
Patterning	• Segmented patterning and control for moving components • Variable voltage operation	Chapter 9
Suit Material Layout	• Dielectric outerlayer| consistent Aluminized Mylar layer • There are minimum suit layer thicknesses required to prevent hazards	Chapter 8
Fabrication Methods	• Manual methods for small scale (inches), automated methods for larger scale (garment/spacesuit)	Chapter 4
Enhancing dust cleaning performance	Detailed recommendations listed in section 10.3	Section 10.3

	KEY FINDINGS	DETAILS
Applications of Technology	Dust mitigation of several flexible surfaces in various environments (Earth, Mars, Asteroids). Details on applications listed in section 10.2	Section 10.2

10.1.1. Hypotheses Assessment

Given the research conducted in this dissertation and results of the studies, the initial hypothesis is assessed as following:

Hypothesis 1: The SPIcDER cleaning system developed to address dust contamination for planetary spacesuits, with specific focus on lunar operations, should be capable of autonomously cleaning the spacesuit outerlayer. The efficiency of cleaning should meet the performance metric established where <25% of the fabric is covered in residual dust post cleaning operations.

Assessment: Validated

- This research designed, developed and tested the SPIcDER system concept that utilizes CNT flexible fibers embedded within the outerlayer of the spacesuit to generate an electric field that can actively levitate and repel the dust particles off the spacesuit outerlayer when energized using a multi-phase AC voltage signal.
- The concept has been demonstrated on coupons made of spacesuit orthofabric material in both ambient and vacuum conditions, and validated on a scaled prototype of a full size knee joint-section of a spacesuit using lunar dust simulant.
- The overall percentage of fabric covered in dust after cleaning operations in ambient and vacuum conditions was shown to be between 3-16%. The performance of the system across multiple coupon and knee prototype tests showed repeatable and consistent performance for similar dust loading conditions. The variation in test results (3 to 16%) showed that exposing the SPIcDER system to purely 10-50 μm dust caused localized areas of several thick layers of dust coverage due to cohesiveness within the dust particles. Further study of the grain size distribution of the lunar dust suggest that improvements in cleaning performance can be demonstrated by testing the system using lunar dust simulant PSD mixtures that replicate grain size mixture proportions of lunar dust.

Hypothesis 2: Demonstrate the feasibility of coating the spacesuit fabric embedded with CNT electrodes with WFM coating. Assess using a combination of the passive WFM coating with active system would not impact the cleaning performance of the active system.
Assessment: Validated in ambient conditions

- The feasibility of coating the CNT electrodes embedded within the spacesuit outerlayer fabric with WFM was demonstrated on coupons made of orthofabric material. Demonstrations of the cleaning ability with the integrated system were conducted in ambient conditions.
- Results showed that coating did not affect the fiber electrodes or the performance of the dust cleaning ability of the active electrode system and its breakdown characteristics in comparison with the uncoated samples.
- Despite the scope of the experiments being limited to ambient conditions, it was noticed that the coated samples had a statistically significant effect over uncoated samples in repelling specific particle sizes during the dynamic tests (0-10 μm and 70 μm, 90-100 μm).
- It was demonstrated in this research that the two technologies can be combined without diminishing the effects of each of their dust cleaning performance and capabilities.
- The effects of WFM are known to be significant and effective in vacuum and dry conditions, and when the dust is charged, as shown in previous studies (Gaier et al. 2011). Therefore, the effectiveness of WFM coating on minimizing adhesion of dust particles and enhancing the overall performance of the dust cleaning system alongside the CNT fiber embedded SPIcDER system should be further evaluated in vacuum and dry environments.

10.2. Other Applications and Implementation of SPIcDER beyond Spacesuits

Future long duration missions to the lunar surface (and other planetary surfaces) will include several pieces of hardware that would be exposed to the extreme environments of the lunar atmosphere. These exposed components would also need to be protected from dust contamination if they need to operate for long durations. A few examples of such hardware, specifically flexible surfaces for lunar missions where the SPIcDER concept can easily be extended to, are outlined below. The list explores potential future research implementing the SPIcDER system and not part

of this dissertation. Note that SPIcDER when extended to applications beyond spacesuits can be named ***SP***ecially ***I***ntegrated ***c***arbon nanotube ***D***ust/***R***ejection System

1. **Space Habitats/Inflatable Modules**:

Habitat structures will be a key component for human exploration missions. Such structures made of soft goods with flexible materials (to minimize launch mass) similar to Orthofabric/Vectran would be exposed to dust on a lunar or Martian base. The outer surface of these modules may be embedded with the SPIcDER system. Since the habitat structures are generally stationary, operational and design constraints due to moving components on breakdown voltages, and the packing of power electronics will be greatly minimized.

2. **Deployable Structures:**

Deployable structures such as flexible antennas, flexible solar cells, including thermal shrouds that are required to cover the outer surfaces of equipment can be embedded with the SPIcDER system.

3. **Earth Based Applications:**

Optimization of SPIcDER for hardware deployed in conditions where dust prevails (ex: desert regions) for applications not limited to canopy surfaces which are required to protect equipment, electrical fences, self-cleaning large flexible antenna dishes, dust protection for wearable communication, air filters, etc.

4. **Applicability to Other Planetary Surfaces:**

In addition to lunar surface exploration missions, dust mitigation is also a crucial environmental factor to overcome for potential missions to Mars and asteroids. Significant amounts of dust clouds are present in the Martian atmosphere. Tribocharging of Mars dust particles has known to contribute to strong adhesion of particles to solar panels and to optical windows as seen from previous missions and from studies conducted on ground using mars simulants (Gaier et al., 2010). Although the dust characteristics vary between lunar and other planetary surfaces, the SPIcDER system characteristics may be optimized to be effective in non-lunar surface environments to mitigate dust.

5. **Dual Use of the SPIcDER System**:

SPIcDER can also be configured to provide multiple functionalities in addition to dust mitigation. The system can be configured by adjusting the CNT electrode patterning and waveform characteristics to provide thermal protection leveraging the thermal conductivity of the CNT fibers. The CNT fibers themselves can also be embedded with devices such as piezoelectric-mechanical devices that utilized motion based energy for use in various applications such as providing heated garments for mountaineering and military applications.

6. **Particle Sorting:**

SPIcDER may also be applied to EVA tools used for collecting regolith for science. The electrodes may be embedded on the side of the EVA tool which contacts the lunar surface. The electrode spacing and waveform characteristics can be optimized to collect particles and transfer them into science bags. The fabrication methods detailed in Chapter 4 can implement multi-use functionality (dust removal, embedded sensing, or radiation protection for low and medium energy charged particles). This becomes possible because the fabrication methods allow implementation of predefined complex conductive fiber electrode patterning and corresponding waveforms.

10.3. Recommendations for Future Research Direction

This section identifies areas where further testing is required, enhancements for improving the technology and performance, and knowledge gaps to be filled that are beyond the scope of the current research to further mature the proposed SPIcDER technology for flight suit implementation.

1. **Enhancing Dust Cleaning Performance**

- WFM Coating:

It's been proposed in this research that the dust cleaning performance of the SPIcDER system can be enhanced by coating the outerlayer with WFM coating made of a material with similar composition as lunar dust as explained in Chapter 4. The current research with WFM coating was limited to identifying the viability of combining the active and passive techniques in ambient conditions. Future testing is recommended to validate the performance of this combined active and passive technology in vacuum conditions.

- Vibratory Actuators:

SPIcDER dust cleaning performance to may be enhanced by implementing battery operated micro vibratory actuators embedded within the fabric-material or within the CNT-fibers to remove any residual dust accumulated in between the fabric weaves that could not be eliminated using the electric fields. This method combines mechanical action with the electric field to enhance dust repelling action. The implementation of vibratory actuators may be performed in between the weaves of the fabric where electrodes are not embedded. Figure 10.3-1 provides a schematic of this combination of electro-mechanical SPIcDER system.

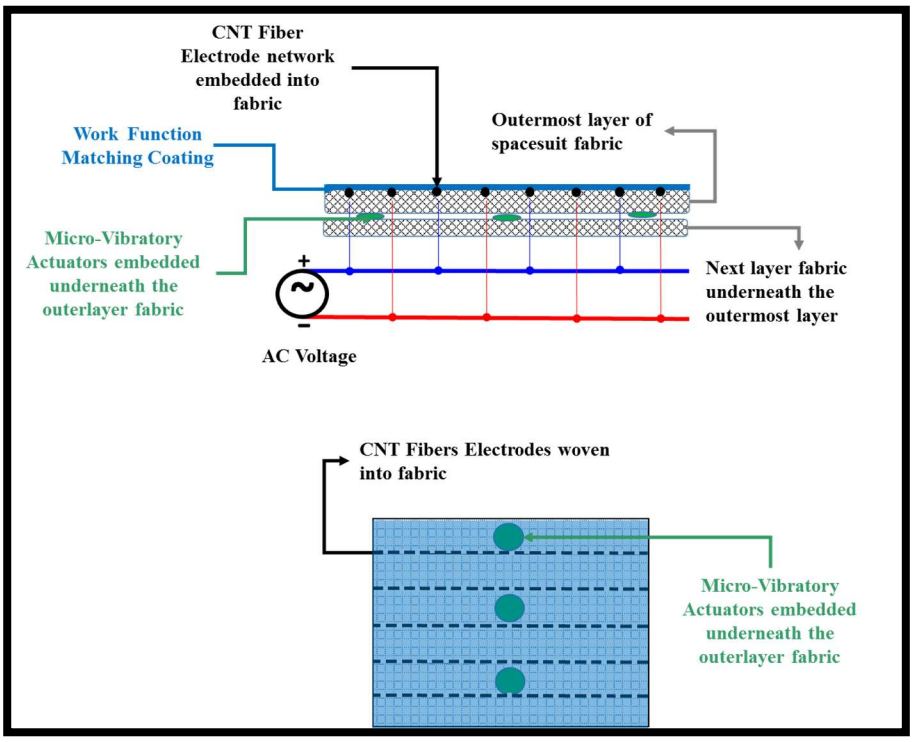

Figure 10.3-1. Enhancing SPIcDER with micro vibratory transducers, a future concept

Actuators that can provide frequency oscillations enough to create vibrations that can help overcome the adhesive forces between dust and the suit may be applied under the suit outerlayer fabric. The actuators may also be placed in between the outerlayer and the next layer below the outerlayer. These vibratory transducers can be built to be autonomously controlled or manually operated as needed. This activation could also be done in an incremental fashion to minimize power requirements. Parallels can be drawn from the field of wearable haptic feedback/ vibration alerting clothing being researched for other applications such as safety and rehabilitation.

- Active Mitts/Gloves with embedded CNT fibers:

One of the advantages of the CNT flexible electrode fibers is that, they can be embedded into various flexible materials and be configured into multiple patterns using various fabrication methods described in Chapter 4. Another implementation of the SPIcDER system for dust mitigation is embedding CNT electrodes into the palms of EVA gloves or a similar device that can be worn as a glove or a mitt. In addition to the spacesuit repelling dust in areas where CNT fibers are embedded, any residual dust on the suit may be removed during or post EVA by donning such SPIcDER mitts and moving the hand along areas on the spacesuit where dust is adhered. The dust accumulated may be levitated by the 'active' mitt and transported away from the suit. The same application can be implemented for several earth based applications to clean devices contaminated with dust.

- Monitoring amount of dust accumulation

Another area for further research could be developing sensors to identify maximum dust accumulation over an area to provide controlled SPIcDER activation for optimized cleaning. This would help tailor the energy required to operate the system over long durations. The sensors can be embedded within the outerlayer programmed to identify dust coverage and trigger the electronics to activate SPIcDER. The operational time and waveform characteristics can be adjusted based on data monitoring using these sensors.

2. CNT flexible fibers:

Three specific recommendations for future research to implement the CNT fiber for SPIcDER are provided based on lessons learned during the various experiments conducted in this research-

- CNT fiber insulation: Method to fabricate uniform flexible insulation for CNT fibers should be designed and implemented to prevent fraying of electrodes, minimize outgassing and prevent field emission. The dust cleaning performance of the SPIcDER system with insulated CNT electrodes in various environmental conditions should be tested as a logical next step.
- Characterization of CNT fiber properties to survive in space environmental conditions is needed. Post processing or fabrication methods to minimize off gassing are required.
- Abrasion characteristics of the insulated CNT fibers for long duration lunar dust exposure should be tested and quantified.

3. **Lunar Dust Simulants:**

- Test the SPIcDER system cleaning performance using complete PSD mixture ratios pf simulants replicating lunar dust PSD percentage (small and large dust particles combined).
- Developing lunar dust simulants that replicate the electrical properties of the actual lunar dust is crucial for characterizing and improving the SPIcDER system to be effective. Most of the dust related research studies conducted so far were conducted using lunar dust simulants. Differences between lunar dust and simulants as identified in Chapter 2 may result in redesign and/or other unrecognized impacts on the performance of the dust cleaning systems when the systems encounter real lunar dust. Therefore, it is imperative that simulants be developed that can closely replicate the lunar dust properties to appropriately characterize the dust cleaning performance of various technologies in simulated realistic conditions.
- The properties of the lunar return samples from the few lunar landing sites are not representative of the properties of dust on the entire lunar surface. The samples that were brought back by the Apollo astronauts and robotic missions are characterized by properties particular to their landing regions. Dust characteristics from other regions have not yet been sampled and analyzed (for example: lunar dust properties from the far side). If dust properties vary from site to site, dust mitigation technology research must consider these variations and systems development and testing must be implemented utilizing the most appropriate simulant that represent the various characteristics of lunar dust where the technologies would operate.

4. **Spacesuit Layers**

- Test SPIcDER with all layers within spacesuits. Aluminum coating within the Aluminized Mylar needs to be consistent. The Mylar insulation layers within the suit should be grounded.
- Hard versus Soft Suits

The effects of dust contamination may vary between hard and soft suits. Studies performed thus far have only included testing soft suit outerlayer fabrics. Smooth surfaces of hard suits may have different adhesion characteristics, but this has not been tested. Because of the ongoing research on hard and hybrid suit designs for future planetary missions, dust research studies should also evaluate best-suited dust mitigation strategies for both suit types. Applicability of SPIcDER to hard components could be evaluated.

- Chemical reactivity of dust to spacesuit elements, suit fabrics and its components need to be addressed for a comprehensive study of dust effects in addition to abrasion and penetration. The degradation effects of dust on metallic surfaces of suits is equally important. Long term chemical degradation of bearings, connectors, etc. should be included in future dust contamination effects on spacesuits

- The mechanical properties (tensile strength) of spacesuit elements after long-term dust exposures should be tested. So far, only Apollo 12 Alan Bean's suit fibers from the Apollo missions were tested for tensile test during abrasion studies. Characterization of the mechanical properties of future candidate fabric materials including the CNT embedded SPIcDER fabric exposed to dust should be performed.

5. Reduced Gravity Validation

The next logical step is to validate the performance of the SPIcDER system in vacuum conditions under reduced gravity settings with the CNT electrodes and WFM coating. The influence of particle charge to mass ratio in simulated lunar gravity on the cleaning performance can be characterized and the system can be further optimized using this data.

6. Supplemental Cleaning Options

While experiments showed that the SPIcDER system is capable of removing as high as 96% of the dust adhering to the outerlayer, the worst-case scenarios provide insight into the < 10 μm dust and dust that got settled in between the two electrodes that still need additional cleaning. While performing experiments, it was observed during post cleaning operations that when a puff of compressed air was utilized after SPIcDER was deactivated, the remaining small percentage of residual dust (3-16%) covering the knee was entirely removed. Therefore, while the SPIcDER system works to remove dust during EVA operations and provides a layer of defense against excessive dust accumulating over the suit surface, a secondary method post EVA could be implemented to remove any residual dust. Such immediate and quick measures post EVA could prevent extended hours of maintenance over long duration missions.

10.4. Summary of Research Contributions

The contributions from this research to the field of dust mitigation of planetary spacesuits and flexible surfaces are as follows

- A comprehensive assessment of past and current dust mitigation technologies that are applicable to spacesuits
- Development of a novel approach and technology using flexible CNT fibers and, design and development of a smart outerlayer spacesuit fabric that can repel dust
- SPIcDER system design and manufacturing methods for implementation on advanced spacesuit designs to prevent dust contamination of soft areas of suit
- Comprehensive experimental characterization of the SPIcDER dust cleaning system examining its behavior in small coupons and scaled prototype.
- First demonstration of an integrated, controllable active and passive technology for use on spacesuit outerlayer proving the practicality of the concepts proposed
- Development of a full-scale knee joint-section of the spacesuit. Uncovering operational issues and necessary improvements through the scaled prototype that go beyond the tests previously conducted. Important parameters such as the effects of variable electrode spacing and potential control of variable voltage inputs relative to astronaut movement discovered
- Development of analytical models for electric field generation by CNT electrodes and particle trajectory of a single dust particle to study the impacts of key design factors
- A detailed list of proposed improvements, alternative architectures, and future work to further mature the SPIcDER dust mitigation system

10.5. List of Associated Publications

Patents

1. Patent Submitted to USPTO, on Systems and Methods for Forming a Dust Mitigating Fabric, 2017
2. Patent Submitted to USPTO, on Dust Mitigation System Utilizing Conductive Fibers for Spacesuits, 2016

Journal Publications

3. Manyapu, K. K., De Leon, P., Peltz, L., Gaier, J. R., & Waters, D. (2017). Proof of concept demonstration of novel technologies for lunar spacesuit dust mitigation. Acta Astronautica.

Conference Proceedings

4. Manyapu, K. K., Peltz, L., de Leon, P. (2017, September) . Self-cleaning Spacesuits for Future Planetary Missions Using Carbon Nanotube Technology. 68th International Astronautical Conference (Paper Accepted, Manuscript in development).
5. Manyapu, K. K., De Leon, P., Peltz, L., Gaier, J. R., & Waters, D. (2017). Proof of concept demonstration of novel technologies for lunar spacesuit dust mitigation. 67th International Astronautical Conference
6. Manyapu, K. K., Peltz, L., de Leon, P., Gaier, J. R., Tsentalovich, D., Calle, C., & Mackey, P. (2016, July). Investigating the Feasibility of Utilizing Carbon Nanotube Fibers for Spacesuit Dust Mitigation. 46th International Conference on Environmental Systems.
7. Manyapu, K. K., de Leon, P (2015, October) Feasibility of Multi-Technology Integration Strategy for Dust Mitigation of Planetary Spacesuits. 66th International Astronautical Conference
    - *Best Interactive Presentation Award for Research Originality and Quality*
8. Manyapu, K. K., Gaier, J. R., de León, P. D., & Shiro, B. (2015, July). Effects of Dust Contamination on NDX-1 Planetary Spacesuit Material during Simulated EVAs. 45th International Conference on Environmental Systems.

Published Technical Press Articles Featuring Research

1. "*New Spacesuit System Could Repel Destructive Moon Dust"*- in Discovery News, June 2017. https://www.seeker.com/space/exploration/new-spacesuit-system-could-repel-destructive-moon-dust

2. *"How to solve the lunar dust problem"*- in The Economist Magazine, Nov 2016. http://www.economist.com/news/science-and-technology/21709943-sharp-jagged-dust-grains-get-everywhere-and-break-things-how-solve-lunar

Submitted Abstracts

11. Manyapu, K. K., Peltz, L (2017, July). Spacesuit Integrated Carbon Nanotube Dust Removal System: A Scaled Prototype. 47th International Conference on Environmental Systems (Abstract accepted)

12. Manyapu, K. K., Peltz, L**.** (2017, Feb). Spacesuit Integrated Carbon Nanotube Dust Ejection/Removal (SPIcDER) System: Space and Terrain Applications. Boeing Technical Excellence Conference

10.6. Final Comments

The studies conducted as part of this research, taken in aggregate, support the premise that spacesuit dust contamination issue can be greatly improved by embedding active CNT yarns into the outerlayer of the spacesuits and enhance with passive WFM coating to protect the soft areas of the suit from the charged and abrasive lunar dust particles. The design approach proposed in this research has the potential to improve the performance of both planetary spacesuits as well as other flexible surfaces not only for lunar operations but also for other planetary surfaces. This technology can also find its way in terrain applications such flexible solar cells.

For the first time, the application of CNT material and autonomous dust cleaning has been combined into the spacesuit outerlayer, addressing the issue of spacesuit dust contamination at a scalable level. The system has been analytically modeled, and the research provided an assessment of both the design and manufacturing space that dictate dust cleaning performance and provides proof of the practicality of the approach. Additionally, a prototyping methodology using CNT fibers is provided in this document which can be easily implemented by anyone with access to simple laboratory equipment and CNT fiber.

The underlying technology developed in this research unlocks new research opportunities for dynamic, wearable systems. The interest in integrating light weight and conductive materials for smart fabrics is growing and several avenues of applications in these areas are being continually discovered. Integrating a dust removal system into spacesuits for automatic cleaning and prevention of dust accumulation would also allow innovative research for smart self-cleaning fabrics beyond spacesuit application (a wearable garment and similar flexible structures). This study represents a significant step forward in the maturation of dust mitigation technologies to make future lunar surface exploration closer to reality.

APPENDICES

APPENDIX A

Lunar Dust Effects on Other Space Components

A survey of reported dust effects on other equipment and components during the Apollo missions was also conducted to provide a comprehensive overview of the dust effects on space hardware for future long duration lunar exploration missions.

A1.1 Thermal Control Surfaces

This section summarizes impacts to thermal control systems from the Apollo mission and ongoing research by NASA on thermal control degradation due to dust contamination. As explained in section 2.2-5, when spacesuit fabrics are dust coated, it essentially creates higher thermal load on due to the high solar absorptance of lunar dust (blackbody effect). In additional to the spacesuit fabric's thermal radiative capability, the EVA life support and heat rejection systems are also impacted by lunar dust contamination due to increased thermal load. Studying the degradation on thermal control surfaces are therefore essential to improve spacesuit design for protection from dust contamination.

For example, it was reported during the Apollo missions that the Lunar Roving Vehicle (LRV) radiator performance was substantially degraded after just single exposure to lunar dust, and none of the Apollo era contemporary cleaning techniques were effective in restoring the radiator performance (Gaier, 2007; Gaier et al., 2011).Table A.1-1 summarizes reported dust effects on thermal control surfaces from the Apollo missions based on data surveyed from various publications (McKay, 1971; Fuhs and Harris, 1992; Wagner 2006; Gaier, 2007; Christoffersen et al., 2008).

Table A.1-1. Dust Effects on Thermal systems during Apollo missions (*Author compiled data from various published sources)*

Mission	Dust Effect on Thermal Control Surfaces
Apollo 12	▪ Science mission objectives of Apollo Lunar Surface Experiment Package (ALSEP) were put at risk owing to overheating as a result of lunar dust exposure ▪ ALSEP experienced higher than predicted temperatures while on the lunar surface ▪ Dust laden exhaust plumes on Surveyor 3 spacecraft during Apollo 12 landing
Apollo 15	▪ Good battery cool-down of LRV between EVA-1 and EVA-2 ▪ But after EVA2, dust found its way onto the radiators. No cool down between EVA-2 and EVA-3 ▪ Both batteries warmed to about 47°C, about 4°C below their maximum rated operating temperature
Apollo 16	▪ LRV batteries only cooled down to 28°C instead of the 11°C ▪ Reached their operating limit at the end of the second EVA ▪ Batteries had only cooled about 2°C on beginning on EVA-3 ▪ At the end of the third EVA the LRV temperature had exceeded the maximum rated survival temperature
Apollo 17	▪ LRV battery temperature profile on Apollo 17 was similar to Apollo 16 ▪ Batteries exceeded their maximum operating temperature after a little more than 4 hours into EVA-3 ▪ By 6 hours, batteries had reached their maximum survival temperature

A.1.2. Thermal Control Surface Tests with Lunar dust during Apollo

NASA GRC evaluated the effects of lunar dust on thermal control surfaces from the Thermal Degradation Sample (TDS) experiment conducted during Apollo 14 mission (Gaier, 2012b). While the TDS experiments were performed in 1971, the samples that were returned after the mission were lost. Gaier's study investigated important results from this experiment using high resolution photographs on the 12 candidate thermal coatings exposed to lunar dust during Apollo 14.

The TDS experiment carried two duplicate arrays each containing 12 thermal coatings that were taken to the lunar surface during Apollo 14 to evaluate the effect of lunar dust on the optical properties (absorptivity and emissivity) of the thermal coatings (Table A.1-2). During the mission, astronauts covered the samples with dust and then removed the dust. Dust removal strategy varied

between the two samples. One tray was tapped to remove dust, while the other tray was cleaned with a nylon bristle brush. Gaier (2012b) notes in the report that it was unclear the exact method (shaking/tapping) used by astronauts to remove dust during the mission and if it was the same between the two sample trays. The brush used was 5 inches wide and 1.5 inches deep with 3-inch-long white nylon bristles. The study reported that while the qualitative results achieved were valid, if the samples were exposed to the lunar environment for a longer period the results might have been different. Exposure to the solar wind for longer duration would have likely cleaned terrestrial contamination from the sample surface, and dust would have adhered more strongly.

Table A.1-2. Candidate thermal control samples tested in the TDS experiment (Gaier, 2012b)

Sample #	Thermal control material
1	S-13G (white paint)
2	Z-93 (ZnO/potassium silicate white paint)
3	Goddard MS-74 (white paint)
4	Ag-FEP (Inconel back film, FEP side exposed)
5	Ag-Quartz (quartz side exposed)
6	Dow Corning 92-007 (TiO_2/silicone white paint)
7	Cat-a-lac White (TiO_2/epoxy)
8	3 M white velvet (400 series TiO_2/epoxy polyester)
9	Dacron on Al-Mylar fabric laminate
10	Oxidized SiO–Al-Kapton with SiO side exposed
11	Al–Kapton with Kapton side exposed
12	Anodized 6061 Al MIL-A-8625, type II, class I

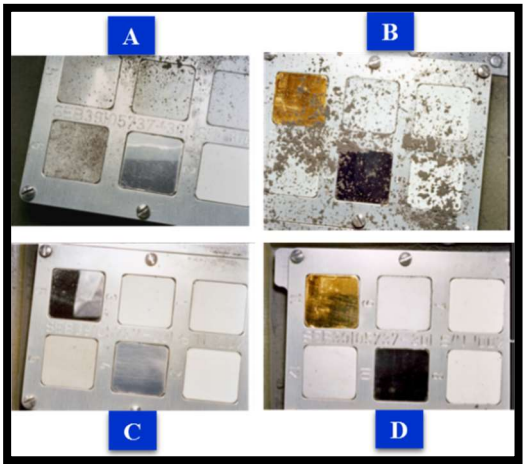

Figure A.1-1 [A, B] Condition of the TDS plates after scooping dust onto it and shaking it off. [C, D] Condition of the TDS plates after scooping dust onto it, shaking it off, and brushing it with a nylon brush. *Photos taken by astronauts during the mission* (Gaier, 2012b)

Important observations and results from evaluation of the TDS photographs were

- **General observations**
  - Lunar dust did not easily fall-off on its own and needed additional methods to remove the dust.

- **Effects of brushing**
  - Brushing affected the thermal surfaces in both positive and negative ways. Even though the nylon brush removed most of the dust, it scratched the soft polymer surfaces. This may probably be due to the dust particles being dragged across the surfaces by the bristles and/or the brush itself might have been dirty.
  - AgFEP and Al-Kapton were both noticeably scratched by brushing. Al-quartz appeared to sustain some scratching as well, though not to the same extent.
- **Adhesion of lunar dust to surfaces**
  - Images taken by the astronauts showed low adhesion than anticipated.
  - Study concludes this might be due to residual organic contamination not removed by the short exposure to the solar wind. Only Dow Corning 92-007 (TiO2/ silicone white paint) showed enhanced dust adhesion.
- **Cohesion between lunar dust particles**
  - Lunar soil exhibited more than anticipated cohesion.
  - There was dust remaining after shaking the plates.
  - Dust did not spread out in an even layer and formed clumps.
  - Further studies need to be conducted to understand greater cohesion effect compared to adhesion to thermal control surfaces.
- **Effects on thermal properties**
  - Thermal absorption results were not reported during the mission
  - Results from the study were based on photographic evidence. Ground test based studies conclude that the α of AgFEP may have increased by 3-10%, Z-93 by 10-65%. Under lab conditions, while using brush removed 90% of adhered dust, it only restored half of the α value (Wohl et al., 2011).

Relevant to this research, it can be concluded that lunar dust contamination causes increased thermal load, brushing may not be the best way to prevent dust contamination and may further abrade materials in addition to using valuable astronaut time.

A 1.3. Dust Effects on Solar Cell

Another study conducted by Gaier (1991) evaluated the effect of particle size on degradation of photovoltaic performance for Martian conditions. The study tested glass coverglass, and SiO_2

covered and uncovered silicon photovoltaic cells. The test was performed in the MARSWIT at NASA Ames. Martian soil simulant using artificial mineral of approximate elemental compositions was used. Results from the tests are summarized here

- **Particle Size effects**: Particles larger than 75 μm did not have sufficient forces to adhere to samples at angles of attack (AOA) ~ 27°. Smaller particles seemed to cause more occlusion while larger particles cause more abrasion.
- **Wind Velocity Effects**: It was observed that at higher wind velocities (>85 m/s), abrasion dominates as the degradation mode, while at lower wind velocities (>50 m/s), occlusion dominates as the degradation mode
- **Angle of Attack Effects**: It was observed that at higher (90°) AOA abrasion dominates as the degradation mode while at lower AOA (0°) occlusion dominates as the degradation mode

While there is no wind on the lunar surface, results from this study provide insight into elements to be considered for optimizing dust mitigation technologies for use on Martian surface.

APPENDIX B

Effects of Dust Contamination on NDX-1 Planetary Spacesuit Material during Simulated EVAs

Pre-cursor experiments utilizing Commercial Off-The Shelf (COTS) technology for passive coating were investigated prior to SPIcDER research. The effect of dust contamination on the outer layer materials on a Martian spacesuit prototype, the NDX-1 (North Dakota Experimental-1) spacesuit demonstrator, built by the Department of Space Studies at the UND was investigated. Two field tests were conducted at the Mars Desert Research Station (MDRS) to investigate dust interactions with the NDX-1 spacesuits and, investigate and improve the capability of the spacesuit materials to withstand dust abrasion and penetration for Mars analog studies. Kneepads constructed using NDX-1 restraint and pressure bladder suit materials were worn during several simulated EVAs at MDRS. The first test was conducted to examine material capability and degradation, the second test included improvements based on lessons from the first test. Hydrobead®, a passive hydrophobic and dust resistant outer surface coating was utilized to test the viability of the coating to reduce dust contamination effects on NDX-1 suit materials. Samples were analyzed using visual inspections, pre and post-test optical microscopy, and FESEM Microscopy at NASA GRC to determine the degree of wear on the outer layer materials and the corresponding dust permeation encountered in the subsequent layers. A very brief overview of the NDX-1 suit materials and samples prepared are provided here as a basis for future dust contamination and mitigation experiments. Results from the tests are captured in the ICES conference paper presented by the author and interested readers are referred to the paper (Manyapu et al., 2015).

B1.1. NDX-1 Suit Materials

The NDX-1 spacesuit design explores the feasibility of new suit materials using extremely rugged textiles for mobility joint fabrication and considered innovative and adaptable component designs for planetary exploration. It employs a hybrid design with a hard-upper torso garment and

a soft lower torso assembly. The suit features six layers of protective fabric to provide three major functions: 1) Pressure bladder, 2) Restraint layer, and 3) Outer Layer. The nylon-cotton outer layer is used to protect the suit from dust. The outer garment is integrated into the suit design covering the restraint layer, mechanical assemblies, and life support system to mitigate dust collection on the suit. However, the development of this outer layer is built for simple protection and is not a primary consideration for the suit construction. The restraint layer is a very strong material that is flame and cut resistant. It consists of a blend of 60% para-aramid and 40% polybenzoxazole fibers. The pressure bladder for the lower and upper torso consists of nylon-coated latex sewn with the same patterns as the restraint layer. The field tests noted above were performed to particularly evaluate the robustness of the restraint layer material for use in future planetary EVA suits. Table B1 provides the list of NDX-1 suit materials.

Table B.1-1. NDX-1 spacesuit materials

Layer	Material	Use
Pressure Bladder	Nylon-coated Latex	Provide a sealed pressurized environment
Restraint Layer	Millenia™ XT	Outside the pressure bladder to provide specific suit shape
Outer Layer	3 layer blend of Nylon (80%) Cotton (20%)	Prevent dust contamination of inner layers during analog studies

B1.2. Samples Constructed for Field Testing

A set of two kneepad pairs were constructed using the pressure bladder and restraint layer of the NDC-1 suit. Figure B.1-1 illustrates the fabricated samples, field test snapshots and analysis techniques utilized.

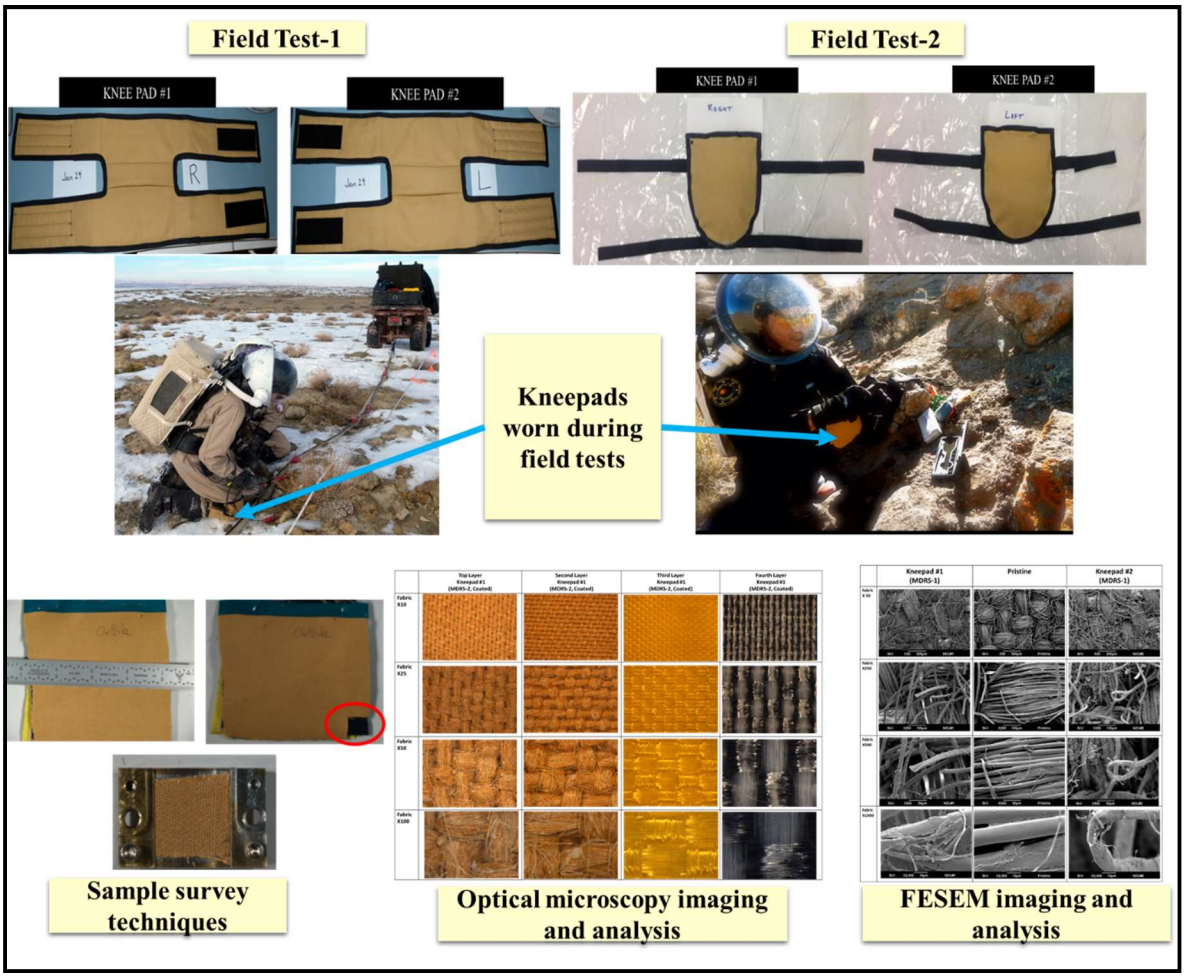

Figure B.1-1. Illustration of the investigations conducted on dust contamination of NDX-1 suit materials

BIBLIOGRAPHY

[1] Afshar-Mohajer, N., Wu, C. Y., Curtis, J. S., & Gaier, J. R. (2015). Review of dust transport and mitigation technologies in lunar and Martian atmospheres. *Advances in Space Research*, *56*(6), 1222-1241.

[2] Aga, K., Tarao, H., & Urushihara, S. (2016). Calculation of human body resistance at power frequency using anatomic numerical human model. *Energy Procedia,* (89), 401-407.

[3] Alfantazi, A. M., & Moskalyk, R. R. (2003). Processing of indium: a review. *Minerals Engineering*, *16*(8), 687-694.

[4] Alshibli, K. A., & Hasan, A. (2009). Strength properties of JSC-1A lunar regolith simulant. *Journal of Geotechnical and Geoenvironmental Engineering*, *135*(5), 673-679.

[5] AZoM, W. B. (2013, June 11). Gold - Physical, Mechanical, Thermal and Electrical Properties of Gold - World Gold Council. Retrieved January 2017, from http://www.azom.com/article.aspx?ArticleID=5147

[6] Banks, B. A., de Groh, K. K., Miller, S. K., & Haytas, C. A. (1999, October). Consequences of atomic oxygen interaction with silicone and silicone contamination on surfaces in low earth orbit. In *SPIE's International Symposium on Optical Science, Engineering, and Instrumentation* (pp. 62-71). International Society for Optics and Photonics.

[7] Batsura, I., Kruglikov, G. G., & Arutiunov, V. D. (1981). Morphology of experimental pneumoconiosis developing after exposure to lunar soil. *Bulletin of Experimental Biology and Medicine*, 92 (9), 376-379

[8] Berger, L.I. (2009). Dielectric Strength Of Insulating Materials In D.R. Lide (Ed.), *CRC Handbook of Chemistry and Physices* (90th ed., 42-26). Boca Raton, FL:Taylor & Francis, Boca Raton

[9] Berkebile. S, & Gaier J.R. (2012). Adhesion in a Vacuum Environment and its Implications for Dust Mitigation Techniques on Airless Bodies, *42nd International Conference on Environmental Systems*, San Diego, CA, 2012, 15-19 July.

[10] Berkebile. S, J.R. Gaier, Adhesion in a Vacuum Environment and its Implications for Dust Mitigation Techniques on Airless Bodies - NASA/TM-2012-217723. 42nd International Conference on Environmental Systems, 15-19 Jul. 2012, San Diego, CA, United States.

[11] Bernhardt, J. H., Brix, J., & Vogel, E. (1996). Established biological effects of extremely low frequency (ELF) fields, current protection concepts and research needs. In *IRPA9: 1996 International Congress on Radiation Protection. Proceedings. Volume 1*.

[12] Biener, M. M., Biener, J., Wichmann, A., Wittstock, A., Baumann, T. F., Bäumer, M., & Hamza, A. V. (2011). ALD functionalized nanoporous gold: thermal stability, mechanical properties, and catalytic activity. *Nano letters*, *11*(8), 3085-3090.

[13] Bikson, M. (2004). A review of hazards associated with exposure to low voltages. *New York: University of New York*.

[14] Bowell, E.L.G. (1971). Surface of the Moon. In J.Guest (Ed), *The Earth and Its Satellite,* (pp. 100-111). New York.

[15] Bulatov, V. P., Krasny, V. A., & Schneider, Y. G. (1997). Basics of machining methods to yield wear-and fretting-resistive surfaces, having regular roughness patterns. *Wear*, *208*(1), 132-137.

[16] Cadogan, D., & Ferl, J. (2007). *Dust Mitigation Solutions for Lunar and Mars Surface Systems* (No. 2007-01-3213). SAE Technical Paper.

[17] Cain, J. R. (2010). Lunar dust: The hazard and astronaut exposure risks. *Earth, Moon, and Planets*, *107*(1), 107-125.

[18] Calla, O. P. N., & Rathore, I. S. (2012). Study of complex dielectric properties of lunar simulants and comparison with Apollo samples at microwave frequencies. *Advances in Space Research*, *50*(12), 1607-1614.

[19] Calle, C. I., McFall, J. L., Buhler, C. R., Snyder, S. J., Arens, E. E., Chen, A., & Trigwell, S. (2008). Dust particle removal by electrostatic and dielectrophoretic forces

with applications to NASA exploration missions. In *Proceedings of the electrostatics society of America Annual meeting, Minneapolis* (pp. 17-19).

[20] Calle, C. I. (2011). The electrostatic environments of Mars and the Moon. In *Journal of Physics: Conference Series* (Vol. 301, No. 1, p. 012006).

[21] Calle, C. I., Buhler, C. R., Johansen, M. R., Hogue, M. D., & Snyder, S. J. (2011). Active dust control and mitigation technology for lunar and Martian exploration. *Acta Astronautica*, *69*(11), 1082-1088.

[22] Calle, C. I., Johansen, M. R., Mackey, P. J., Hogue, M. D., Cox, R. E., & Phillips III, J. R., (2015). History and Flight Development of the Electrodynamic Dust Shield. In *AIAA SPACE 2015 Conference and Exposition* (p. 4446).

[23] Campbell, C. (2012). Advanced EMU Portable Life Support System (PLSS) and Shuttle/ISS EMU Schematics, a Comparison. NASA/JSC, JSC-CN-26332.

[24] Campo, E. (2008). *Selection of polymeric materials : How to select design properties from different standards* (PDL handbook series. Y). Norwich, NY: William Andrew.

[25] Carrier, W.D., Olhoeft,G.R., Mendell,W. (1991). Physical Properties of the Lunar Surface, in The Lunar Sourcebook, edited by G. Heiken, D. T. Vaniman, and B. M. French, pp. 475-594, Cambridge Univ. Press, New York

[26] Chesnutt, J. K., & Marshall, J. S. (2013). Simulation of particle separation on an inclined electric curtain. *IEEE Transactions on Industry Applications*, *49*(3), 1104-1112.

[27] Christoffersen, R., Lindsay, J. F., Noble, S. K., and Lawrence, J. A. (2008). Lunar Dust Effects on Spacesuit Systems: Insights from the Apollo Spacesuits. LPI Contributions, 1446, 34.

[28] Cohen, M. M. (1989). *U.S. Patent No. 4,842,224*. Washington, DC: U.S. Patent and Trademark Office

[29] Colaprete, A., Schultz, P., Heldmann, J., Wooden, D., Shirley, M., Ennico, K., ... & Goldstein, D. (2010). Detection of water in the LCROSS ejecta plume. *Science*, *330*(6003), 463-468.

[30] Colwell, J. E., Batiste, S., Horányi, M., Robertson, S., & Sture, S. (2007). Lunar surface: Dust dynamics and regolith mechanics. *Reviews of Geophysics*, *45*(2).

[31] Corti, C. W., & Holliday, R. J. (2004). Commercial aspects of gold applications: From materials science to chemical science. *Gold bulletin*, *37*(1), 20-26.

[32] Dahm, M. M., Evans, D. E., Schubauer-Berigan, M. K., Birch, M. E., & Fernback, J. E. (2012). Occupational exposure assessment in carbon nanotube and nanofiber primary and secondary manufacturers. *Annals of Occupational Hygiene*, *56*(5), 542-556.

[33] David, L. (2016). Europe Aiming for International 'Moon Village' Retrieved December, 2016, from http://www.space.com/32695-moon-colony-european-space-agency.html

[34] Dhariwal, R. S., Torres, J. M., & Desmulliez, M. P. Y. (2000). Electric field breakdown at micrometre separations in air and nitrogen at atmospheric pressure. *IEE Proceedings-Science, Measurement and Technology*, *147*(5), 261-265.

[35] Dominik, C., & Tielens, A. G. G. M. (1997). The physics of dust coagulation and the structure of dust aggregates in space. *The Astrophysical Journal*, *480*(2), 647.

[36] DuPont. (2003). DuPont Nomex Technical Data Sheet. Retrieved August, 2016, from http://www2.dupont.com/Energy_Solutions/en_US/assets/downloads/418_419.pdf

[37] Eckart, P. (Ed.). (2006). *The lunar base handbook: an introduction to lunar base design, development, and operations*. McGraw-Hill.

[38] Ericson, L. M., Fan, H., Peng, H., Davis, V. A., Zhou, W., Sulpizio, J., ... & Parra-Vasquez, A. N. G. (2004). Macroscopic, neat, single-walled carbon nanotube fibers. *Science*, *305*(5689), 1447-1450.

[39] ESA. (2016). Moon Village: humans and robots together on the Moon. Retrieved January 2017, from http://www.esa.int/About_Us/DG_s_news_and_views/Moon_Village_humans_and_robots_together_on_the_Moon

[40] EVA Suit Layers. (n.d.). Retrieved October 2016, from http://www.nasa.gov/centers/johnson/pdf/513053main_V1-eva_suit_layers.pdf

[41] Frank, L. A., Sigwarth, J. B., & Craven, J. D. (1986). On the influx of small comets into the Earth's upper atmosphere II. Interpretation. *Geophysical research letters*, *13*(4), 307-310.

[42] Fuhs, S. & Harris, J. (1992). Dust protection for environmental control and life support systems in the lunar environment. *Arizona Univ., Proceedings of the Lunar Materials Technology Symposium*, 12 p.

[43] Gaier, J.R., & Perez-Davis, M. (1991). Effect of particle size of Martian dust on the degradation of photovoltaic cell performance - NASA-TM-105232. *International Solar Energy Conference,* International Solar Energy Conference, 4-8 April, Maui, HI, United States.

[44] Gaier, J. R. (2005). The Effects of Lunar Dust on EVA Systems During the Apollo Missions. NASA/TM-2005-213610

[45] Gaier, J. R. (2007). The effects of lunar dust on EVA systems during the Apollo missions.

[46] Gaier, J. R., & Jaworske, D. A. (2007). Lunar Dust on Heat Rejection System Surfaces: Problems and Prospects. In *Space Technology and Applications International Forum-STAIF 2007* (Vol. 880, pp. 27-34).

[47] Gaier, J. R., Meador, M. A., Rogers, K. J., & Sheehy, B. H. (2009). Abrasion of Candidate Spacesuit Fabrics by Simulated Lunar Dust - NASA/TM-2009-215800. *39th International Conference on Environmental Systems,* 12-16 Jul. 2009, Savannah, GA, United States.

[48] Gaier, J. R., de León, P. G., Lee, P., McCue, T., Hodgson, E., & Thrasher, J. (2010). Preliminary Testing of a Pressurized Space Suit and Candidate Fabrics Under Simulated Mars Dust Storm and Dust Devil Conditions - NASA/TM-2010-216787. *40th International Conference on Environmental Systems,* 11-15 Jul. 2010, Barcelona, Spain.

[49] Gaier, J.R, Waters, D., Banks, B., Misconin, R., & Crowder, M. (2011). Evaluation of Surface Modification as a Lunar Dust Mitigation Strategy for Thermal Control Surfaces - NASA/TM-2011-217230. *41st International Conference on Environmental Systems,* 17-21 July. 2011, Portland, OR, United States.

[50] Gaier, J.R, and Berkebile, S. (2012a). Implications of Adhesion Studies for Dust Mitigation on Thermal Control Surfaces - NASA/TM-2012-217213. *50th Aerospace Science Conference,* 50th Aerospace Science Conference, 9-12 Jan. 2012, Nashville, TN, United States.

[51] Gaier, J. R. (2012b). Interpretation of the Apollo 14 thermal degradation sample experiment. *Icarus*, *221*(1), 167-173.

[52] Gaier, J.R. (2012c). Degradation of Spacesuit Fabrics in Low Earth Orbit - NASA/TM-2012-217682. *42nd International Conference on Environmental Systems*, 15-19 July. 2012, San Diego, CA, United States.

[53] Geiss, J., Bühler, F., Cerutti, H., Eberhardt, P., & Filleux, C. (1972). Apollo 16 preliminary science report. *NASA SP-315*, *14*, 1-14.

[54] GoodFellow, W. B. (2013, June 11). Gold - Properties and Uses - Supplier Data by Goodfellow. Retrieved January 2017, from

[55] Graf, J. (1993). Lunar soils grain size catalog - NASA-RP-1265, Houston, Texas, USA 1265, 466 pp

[56] Grafix Plastics. (2007). Mylar® Film and Sheet Properties. Retrieved August 2016, from http://www.grafixplastics.com/mylar_prop.asp

[57] Green, N. G., Ramos, A., & Morgan, H. (2002). Numerical solution of the dielectrophoretic and travelling wave forces for interdigitated electrode arrays using the finite element method. *Journal of Electrostatics*, *56*(2), 235-254.

[58] Gustafson, G. (2009). JSC-1A lunar regolith simulant: availability and characterization. In *2009 Lunar Regolith Simulant Workshop*.

[59] Halekas, J. S., Delory, G. T., Brain, D. A., Lin, R. P., Fillingim, M. O., Lee, C. O., ... & Hudson, M. K. (2007). Extreme lunar surface charging during solar energetic particle events. *Geophysical research letters*, *34*(2).

[60] Hays, D.A. (1988) in: Particles on Surfaces 1: Detection, Adhesion and Removal, K.L. Mittal (Ed.) pp. 351–360, Plenum Press, NY.

[61] Heiken, G., Vaniman, D., & French, B. M. (Eds.). (1991). *Lunar sourcebook: A user's guide to the Moon*. CUP Archive.

[62] Hill, E., Mellin, M. J., Deane, B., Liu, Y., & Taylor, L. A. (2007). Apollo sample 70051 and high-and low-Ti lunar soil simulants MLS-1A and JSC-1A: Implications for future lunar exploration. *Journal of Geophysical Research: Planets*, *112*(E2).

[63] Holland, J. M., & Simmonds, R. C. (1973). The mammalian response to lunar particulates. *Space Life Sciences*, *4*(1), 97-109.

[64] Horenstein, M. N., Mazumder, M. K., Sumner, R. C., Stark, J., Abuhamed, T., & Boxman, R. (2013). Modeling of trajectories in an electrodynamic screen for obtaining maximum particle removal efficiency. *IEEE Transactions on Industry Applications*, *49*(2), 707-713.

[65] Hurlbert, K., Bagdigian, B., Carroll, C., Jeevarajan, A., Kliss, M., & Singh, B. (2012). Human Health, Life Support and Habitation Systems. *National Aeronautics and Space Administration (NASA): Washington, DC.*

[66] Indium Corporation. (n.d.). Physical constants of pure indium by Indium Corporation. Retrieved January 2017, from http://www.indium.com/metals/indium/physical-constants/

[67] J.T. James, Lunar dust inhalation standard, in: Exploration Science Mission Directorate Meeting, New Orleans, Louisiana, NASA Johnson Space Center, MS-SF2, Houston, TX, 2007.

[68] James, J. T., Lam, C. W., Santana, P. A., & Scully, R. R. (2013). Estimate of safe human exposure levels for lunar dust based on comparative benchmark dose modeling. *Inhalation toxicology*, *25*(5), 243-256.

[69] Järup, L., & Åkesson, A. (2009). Current status of cadmium as an environmental health problem. *Toxicology and Applied Pharmacology*, *238*(3), 201-208.

[70] JSC-1AF Characterization, Orbital Technologies Corporation (2007). Retrieved November 2014 from https://isru.msfc.nasa.gov/lib/Documents/JSC-1A_Bulk_Data_Characterization_draft.pdf.

[71] Katzan, C. M., & Edwards, J. L. (1991). Lunar dust transport and potential interactions with power system components - NASA-CR-4404.

[72] Kaufman and Zachary, D. (1997). Possible Health Effects of Exposure to Residential Electric and Magnetic Fields. *Energy Law Journal, 18*(2), 435-439.

[73] Kawamoto, H., & Hara, N. (2010). Electrostatic cleaning system for removing lunar dust adhering to space suits. *Journal of Aerospace Engineering*, *24*(4), 442-444.

[74] Kawamoto, H., & Hayashi, S. (2006). Fundamental investigation on electrostatic travelling-wave transport of a liquid drop. *Journal of Physics D: Applied Physics*, *39*(2), 418.

[75] Khan-Mayberry, N. (2008). The lunar environment: Determining the health effects of exposure to moon dusts. *Acta Astronautica*, *63*(7), 1006-1014.

[76] Kobrick, R. L., Klaus, D. M., & Street, K. W. (2011). Defining an abrasion index for lunar surface systems as a function of dust interaction modes and variable concentration zones. *Planetary and Space Science*, *59*(14), 1749-1757.

[77] Kopeliovic, D. (2015, March). Mechanisms of Wear. Retrieved March 2015, from http://www.substech.com/dokuwiki/doku.php?id=mechanisms_of_wear

[78] Koziol, K. K., Lekawa-Raus, A. E., Kurzepa, L., & Peng, X. (2016). *U.S. Patent No. 9,520,213*. Washington, DC: U.S. Patent and Trademark Office.

[79] Kramer, H. J. (2002). *Observation of the Earth and its Environment: Survey of Missions and Sensors*. Springer Science & Business Media.

[80] Kukowski, T. (2012). Lightweight CNT Cables Lightweight CNT Cables for Aerospace. NASA NDI Workshop-NESC NDE Technology Assessment Rep.). NASA.

[81] Kutsov, Y.D., Kruglikov, G. G., & Arutiunov, V. D. (1981). Morphology of experimental pneumoconiosis developing after exposure to lunar soil. *Bulletin of Experimental Biology and Medicine*, 92(9), 376-379.

[82] Lam, C. W., James, J. T., McCluskey, R., Arepalli, S., & Hunter, R. L. (2006). A review of carbon nanotube toxicity and assessment of potential occupational and environmental health risks. *Critical Reviews in Toxicology*, *36*(3), 189-217.

[83] Lam, C. W., Scully, R. R., Zhang, Y., Renne, R. A., Hunter, R. L., McCluskey, R. A., ... & McClellan, R. O. (2013). Toxicity of lunar dust assessed in inhalation-exposed rats. *Inhalation Toxicology*, *25*(12), 661-678.

[84] Launius, R. D. (2010). Can we colonize the solar system? Human biology and survival in the extreme space environment. *Endeavour*, *34*(3), 122-129.

[85] Lekawa-Raus, A., Patmore, J., Kurzepa, L., Bulmer, J., & Koziol, K. (2014). Electrical properties of carbon nanotube based fibers and their future use in electrical wiring. *Advanced Functional Materials*, *24*(24), 3661-3682.

[86] Li, M., & Zinkle, S. J. (2012). 4.20 Physical and Mechanical Properties of Copper and Copper Alloys. *Comprehensive Nuclear Materials*, 667-690.

[87] Linnarsson, D., Carpenter, J., Fubini, B., Gerde, P., Karlsson, L. L., Loftus, D. J and van Westrenen, W. (2012). Toxicity of lunar dust. *Planetary and Space Science*, *74*(1), 57-71.

[88] Liu, G. Q., & Marshall, J. S. (2010). Effect of particle adhesion and interactions on motion by traveling waves on an electric curtain. *Journal of Electrostatics*, *68*(2), 179-189.

[89] Liu, Y., Schnare, D. W., Eimer, B. C., & Taylor, L. A. (2008). Dry separation of respirable lunar dust: Providing samples for the lunar airborne dust toxicity advisory group. *Planetary and Space Science*, *56*(11), 1517-1523.

[90] Lucey, P. G., Blewett, D. T., & Hawke, B. (1998). Mapping the FeO and TiO2 content of the lunar surface with multispectral imagery. *Journal of Geophysical Research: Planets*, *103*(E2), 3679-3699.

[91] Mair, L. H., Stolarski, T. A., Vowles, R. W., & Lloyd, C. H. (1996). Wear: mechanisms, manifestations and measurement. Report of a workshop. *Journal of Dentistry*, *24*(1-2), 141-148.

[92] Malnar, B., Balachandran, W., & Cecelja, F. (2003, May). 3D simulation of travelling wave dielectrophoretic force on particles. In *ESA-IEEE Conference on Electrostatics* (Vol. 1).

[93] Manyapu, K. K., De Leon, P., Peltz, L., Gaier, J. R., & Waters, D. (2017). Proof of concept demonstration of novel technologies for lunar spacesuit dust mitigation. *Acta Astronautica*, *137*, 472-481.

[94] Manyapu, K. K., Peltz, L., de Leon, P., Gaier, J. R., Tsentalovich, D., Calle, C., & Mackey, P. (2016, July). Investigating the Feasibility of Utilizing Carbon Nanotube Fibers for Spacesuit Dust Mitigation. *International Conference on Environmental Systems,* 10-14 July, Vienna, Austria.

[95] Manyapu, K.K, Peltz, L., (*2016*).US Patent No. 62/312,931 . Washington, DC: U.S. Patent and Trademark Office, pending

[96] Manyapu, K.K., Peltz, L., (*2017*).US Patent (n.n) . Washington, DC: U.S. Patent and Trademark Office, pending

[97] Margiotta, D. V., Peters, W. C., Straka, S. A., Rodriguez, M., McKittrick, K. R., & Jones, C. B. (2010, August). The Lotus coating for space exploration: a dust mitigation tool. In *Optical System Contamination: Effects, Measurements, and Control 2010* (Vol. 7794).

[98] Margiotta, D. V., Peters, W. C., Straka, S. A., Rodriguez, M., McKittrick, K. R., & Jones, C. B. (2010, August). The Lotus coating for space exploration: a dust mitigation tool. In *SPIE Optical Engineering+ Applications* (pp. 77940I-77940I). International Society for Optics and Photonics.

[99] Marshall, J., Bratton, C., Kosmo, J., & Trevino, R. (1999). Interaction of Space Suits with Windblown Soil: Preliminary Mars Wind Tunnel Results. In *Studies of Mineralogical and Textural Properties of Martian Soil: An Exobiological Perspective* (Vol. 1, p. 79).

[100] McKay, D. S., & Ming, D. W. (1989). Mineralogical and chemical properties of the lunar regolith. *Lunar Base Agriculture: Soils for Plant Growth*, 45-68.

[101] McKay, D. S., Carter, J. L., Boles, W. W., Allen, C. C., & Allton, J. H. (1993). JSC-1: A new lunar regolith simulant. In *Lunar and Planetary Science Conference* (Vol. 24).

[102] McKay, D. S., G. Heiken, A. Basu, G. Blanford, S. Simon, R. Reedy, B. M. French, and J. Papike (1991), The lunar regolith. In G. Heiken, D. T. Vaniman, and B. M. French (Eds),*The Lunar Sourcebook* (pp. 285–356). Cambridge Univ. Press, New York.

[103] McKay, D. S., Heiken, G. H., Taylor, R. M., Clanton, U. S., Morrison, D. A., & Ladle, G. H. (1972). Apollo 14 soils: Size distribution and particle types. In *Lunar and Planetary Science Conference Proceedings* (Vol. 3, p. 983).

[104] Meyers, V. E., and Scully, R. R. (2015). Risk of adverse health and performance effects of celestial dust exposure. Human Research Program. NASA report (n.p).

[105] Miller, W. L. (1985). Mass loss of shuttle space suit orthofabric under simulated ionospheric atomic oxygen bombardment. NASA TM-87149.

[106] Mitchell, J. K., Houston, W. N., Scott, R. F., Costes, N. C., Carrier III, W. D., & Bromwell, L. G. (1972). Mechanical properties of lunar soil: Density, porosity, cohesion and angle of internal friction. In *Lunar and Planetary Science Conference Proceedings* (Vol. 3, p. 3235).

[107] Mitchell, K. C. (2010). Abrasion Testing of Candidate Outer Layer Fabrics for Lunar EVA Space Suits. 40t^{h} *International Conference on Environmental Systems*, 11-15 July. 2010, Barcelona, Spain.

[108] Mittal, K. L. (Ed.). (1988). *Particles on surfaces*. Plenum..

[109] Möller, P., Loewens, R., Abramov, I. P., & Albats, E. A. (1995). EVA suit 2000: A joint European/Russian space suit design. *Acta Astronautica*, *36*(1), 53-63.

[110] Mylar Technical Data [Specification Sheet]. (2010, May). San Leandro: Tap Plastics.

[111] Naidu, M., & Kamaraju, V. (1996). *High voltage engineering* (2nd ed.). New York: McGraw-Hill.

[112] NASA Technology Roadmaps (2015). TA 6: Human Health, Life Support, and Habitation Systems. Retrieved February 2016, from https://www.nasa.gov/sites/default/files/atoms/files/2015_nasa_technology_roadmaps_ta_6_human_health_life_support_habitation_final.pdf

[113] NASA, Asteroid Redirect Mission (2015). ARM Future Assessment Support Team Report. Retrieved January 2016 from https://www.nasa.gov/sites/default/files/atoms/files/fast-final-report-draft-for-public-comment.pdf

[114] Neerinck, & Vink. (1996). Depth profiling of thin ITO films by grazing incidence X-ray diffraction. *Thin Solid Films, 278*(1-2), 12-17.

[115] Neumann, I. B. (2016). *Russia and the idea of Europe: a study in identity and international relations*. Taylor & Francis.

[116] O'Brien, B. J., & Hollick, M. (2015). Sunrise-driven movements of dust on the Moon: Apollo 12 Ground-truth measurements. *Planetary and Space Science*, *119*, 194-199.

[117] Oberbeck, V. R. (1975). The role of ballistic erosion and sedimentation in lunar stratigraphy. *Reviews of Geophysics*, *13*(2), 337-362.

[118] Oberdörster, G., Castranova, V., Asgharian, B., & Sayre, P. (2015). Inhalation exposure to carbon nanotubes (CNT) and carbon nanofibers (CNF): Methodology and dosimetry. *Journal of Toxicology and Environmental Health, Part B*, *18*(3-4), 121-212.

[119] Olhoeft, G. R., & Strangway, D. W. (1975). Dielectric properties of the first 100 meters of the Moon. *Earth and Planetary Science Letters*, *24*(3), 394-404.

[120] Pabari, J. P., & Banerjee, D. (2016). Levitation of charged dust grains and its implications in lunar environment. *Current Science*, *110*(10), 1984-1989.

[121] Papike.J., Taylor.L., and Simon.S. (1991), Lunar Minerals. In G. Heiken, D. T. Vaniman, and B. M. French (Eds), *The Lunar Sourcebook* (pp. 121–181). Cambridge Univ. Press, New York.

[122] Park, J., Liu, Y., Kihm, K. D., & Taylor, L. A. (2006, March). Toxicity of lunar dust for humans at a lunar base. In *GSA Annual Meeting* (Vol. 38, No. 3, p. 69).

[123] Paschen, F. (1889). Ueber die zum Funkenübergang in Luft, Wasserstoff und Kohlensäure bei verschiedenen Drucken erforderliche Potentialdifferenz (On the potential difference required for the spark transfer in air, hydrogen and carbonic acid at various pressures). *Annals of Physics* , 273 (5), 69-96.

[124] Pieters, C. M., Goswami, J. N., Clark, R. N., Annadurai, M., Boardman, J., Buratti, B., ... & Hibbitts, C. (2009). Character and spatial distribution of OH/H2O on the surface of the Moon seen by M3 on Chandrayaan-1. *Science,* 326(5952), 568-572.

[125] Polyurethane (PUR) Typical Properties Generic PUR [Specification Sheet]. (October 2016). Kansas: UL Prospector®.

[126] Radmilovic-Radjenovic, M., Radjenovic, B., Klas, M., & Matejcik, S. (2012). Breakdown voltage curves in direct current discharges in molecular gases at microgaps. *IET Micro & Nano Letters*, *3*(7), 232-234.

[127] Ranade, M. B. (1987). Adhesion and removal of fine particles on surfaces. *Aerosol Science and Technology*, *7*(2), 161-176.

[128] Rawal, S., Brantley, J., & Karabudak, N. (2013). Development of carbon nanotube-based composite for spacecraft components. In *2013 6th International Conference on Recent Advances in Space Technologies (RAST)*. (pp. 13-19).

[129] Reasoner, D. L., & Burke, W. J. (1972). Characteristics of the lunar photoelectron layer in the geomagnetic tail. *Journal of Geophysical Research*, *77*(34), 6671-6687.

[130] Ruths, M., & Israelachvili, J. N. (2011). Surface forces and nanorheology of molecularly thin films. In *Nanotribology and Nanomechanics II* (pp. 107-202). Springer Berlin Heidelberg.

[131] Schrader, C., Rickman, D., Mclemore, C., Fikes, J., Wilson, S., Stoeser, D., ... & Botha, P. (2008). Extant and extinct lunar regolith simulants: Modal analyses of NU-LHT-1M and-2m, OB-1, JSC-1, JSC-1A and-1AF, FJS-1, and MLS-1. *Planetary and Terrestrial Mining Symposium*, 9-11 June. 2008, Montreal, Quebec, Canada.

[132] Schrenk, W. J., & Alfrey, T. (1969). Some physical properties of multilayered films. *Polymer Engineering & Science*, *9*(6), 393-399.

[133] Seybold, C. C. (1995, August). Characteristics of the Lunar Environment. Retrieved February 2017, from http://www.tsgc.utexas.edu/tadp/1995/spects/environment.html

[134] Slyuta, E. N. (2014). Physical and mechanical properties of the lunar soil (a review). *Solar System Research*, *48*(5), 330-353.)

[135] Strangway, D. W., Pearce, G. W., & Olhoeft, G. R. (1977). Magnetic and dielectric properties of lunar samples. *NASA Special Publication*, *370*.

[136] Stubbs, T. J., Halekas, J. S., Farrell, W. M., & Vondrak, R. R. (2007). Lunar surface charging: A global perspective using Lunar Prospector data. In *in Dust in Planetary Systems, ESA SP-643*.

[137] Taylor, G. F. (1924). A method of drawing metallic filaments and a discussion of their properties and uses. *Physical Review*, *23*(5), 655.

[138] Taylor, G. J. (1989). The environment at the lunar surface. *Lunar Base Agriculture: Soils for Plant Growth*, *1*, 37-44.

[139] Taylor, L. A., & James, J. T. (2007). Potential Toxicology of Lunar Dust. In *Space Resources Roundtable VIII: Program and Abstracts (LPI Contribution No. 1332)* (Vol. 1332, pp. 59-60).

[140] Taylor, L. A., Pieters, C. M., Keller, L. P., Morris, R. V., & McKay, D. S. (2001). Lunar mare soils: Space weathering and the major effects of surface-correlated nanophase Fe. *Journal of Geophysical Research: Planets*, *106*(E11), 27985-27999.

[141] Taylor, L. A., Pieters, C., Keller, L. P., Morris, R. V., Mckay, D. S., Patchen, A., & Wentworth, S. (2001). The effects of space weathering on Apollo 17 mare soils: Petrographie and chemical characterization. *Meteoritics & Planetary Science*, *36*(2), 285-299.

[142] Taylor, L. A., Schmitt, H. H., Carrier, W. D., & Nakagawa, M. (2005). The lunar dust problem: from liability to asset. *AIAA, 1st Space Exploration Mission*.

[143] Taylor, L.A., Liu, Y., Zhang, A. (2009). Taylor, L. A., Liu, Y., & Zhang, A. (2009, March). Shape and size relationship of several lunar dusts: preliminary results. In *Lunar and Planetary Science Conference* (Vol. 40).

[144] Taylor, S. R. (1982). *Planetary science: a lunar perspective* (Vol. 3303). Houston, TX: Lunar and Planetary Institute.

[145] The Gund Company Inc. (n.d.). Material Data Sheet Dacron/Mylar/Dacron 70 . Retrieved August 2016, from http://thegundcompany.com/wp-content/uploads/2016/11/DMD-from-The-Gund-Co.pdf

[146] Tranfield, E. M., van Eeden, S. F., Yatera, K., Hogg, J. C., & Walker, D. C. (2010). Ultrastructural changes in atherosclerotic plaques following the instillation of airborne particulate matter into the lungs of rabbits. *Canadian Journal of Cardiology*, *26*(7), e258-e269.

[147] Wagner, S. (2008). An assessment of dust effects on planetary surface systems to support exploration requirements. *NASA Technical Publication* TM –2008–213722. *Washington, DC: National Aeronautics and Space Administration*.

[148] Wagner, S. (2014). Asteroid, Lunar and Planetary Regolith Management A Layered Engineering Defense. *NASA Technical* Publication TP -2014-217399. *Washington, DC: National Aeronautics and Space Administration*.

[149] Wagner, S. A. (2006). The Apollo experience lessons learned for constellation lunar dust management. *NASA Technical Publication TP-2006-213726. Washington, DC: National Aeronautics and Space Administration*.

[150] Walton, O. (2007). Adhesion of Lunar Dust - NASA/CR-2007-214685.

[151] Walton, O. R. (2008). Review of adhesion fundamentals for micron-scale particles. *KONA Powder and Particle Journal*, *26*, 129-141.

[152] Wiesehahn, G. P., & Corash, L. (1993). *U.S. Patent No. 5,176,921*. Washington, DC: U.S. Patent and Trademark Office.

[153] Wohl, C. J., Connell, J. W., Lin, Y., Belcher, M. A., & Palmieri, F. L. (2011). Generation and Evaluation of Lunar Dust Adhesion Mitigating Materials. *3rd AIAA Atmospheric Space Environments Conference,* 27-30 Jun. 2011, Honolulu, HI, United States.

[154] World Health Organization. (2007). Environmental Health Criteria 238: Extremely Low Frequency (ELF) Fields. WHO, Geneva, Switzerland. ISBN 978-92-4-157238-5.

[155] Xu, F., Mo, X., Wan, S., Jiang, C., Hao, H., & Li, L. (2014). High-performance flexural fatigue of carbon nanotube yarns. *Chinese science bulletin*, *59*(29-30), 3831-3834.

[156] Zeng, X., He, C., Oravec, H., Wilkinson, A., Agui, J., & Asnani, V. (2009). Geotechnical properties of JSC-1A lunar soil simulant. *Journal of Aerospace Engineering*, *23*(2), 111-116.

[157] Zeimer, J. (2008). *Basics of Wear* (Rep.). Society of Tribologists and Lubrication Engineers. Retrieved 2015, from www.stle.org.